## Cover Photos

The images on the front cover intentionally suggest the appearance of television screens since the photographs were derived from videotape and depict the construction of the OMEGA laser system within the target bay.

During the construction, two video cameras, from fixed locations in the laser and target bays, remotely relayed signals to videocassette recorders, which documented day-to-day events for over two years. The recording times varied from continuous to segmented recordings, capturing 1 min every half hour, and resulted in over 250 hours of coverage.

To generate the cover images, 162 hours of videotape were edited; individual frames, including the 12 on the cover, were digitally captured and combined. The final 2-min, time-lapse movie shows a rapid motion view of the construction in the experimental area ending with the firing of the first 60 beams on target on 18 April 1995.

The video feeds are still active, and additional views have been added to augment security and to show visitors real-time activities in the target and laser bays, including beam profiles, pulse generation, and laser firings.



The work described in this volume includes current research at the Laboratory for Laser Energetics, which is supported by New York State Research and Development Authority, the University of Rochester, the U.S. Department of Energy Office of Inertial Confinement Fusion under Cooperative Agreement No. DE-FC03-92SF19460, and other agencies.

For questions or comments, contact Laboratory for Laser Energetics, 250 East River Road, Rochester, NY 14623-1299, (716) 275-5286.

Prepared for
U.S. Department of Energy
San Francisco Operations Office
DOE/SF/19460-106

Distribution Category UC712
October 1994–September 1995

Printed in the United States of America
Available from
National Technical Information Services
U.S. Department of Commerce
5285 Port Royal Road
Springfield, VA 22161

Price codes: Printed Copy A10
Microfiche A01

University of Rochester
Laboratory for Laser Energetics

DOE/SF/19460-106
January 1996

# LLE 1995 Annual Report

UR LLE

## October 1994 – September 1995

## Inertial Fusion Program and National Laser Users Facility Program

# Contents

# Executive Summary

The fiscal year ending September 1995 (FY95) concluded the third year of the cooperative agreement (DE-FC03-92SF19460) with the U. S. Department of Energy (DOE). This report summarizes research at the Laboratory for Laser Energetics (LLE) and reports on the successful completion of the OMEGA Upgrade.

**OMEGA Upgrade**

Previous annual reports describe the OMEGA Upgrade design. The preliminary design for the system was complete in October 1989 and the detailed design started in October 1990. The original 24-beam OMEGA system was decommissioned in December 1992 as construction for the OMEGA Upgrade began. We discuss the initial performance results (p. 99) of the upgraded OMEGA laser system. All acceptance tests were completed, and we demonstrated that all 60 beams can irradiate a target with more energy and better beam balance than was required by DOE's acceptance criteria. We are most proud that all program milestones were met or exceeded, and that the system was completed on time and on budget.

The purpose of the OMEGA laser is to execute an experimental program to validate the direct-drive approach to fusion. Because of the high efficiency, direct drive may give the Nation a laboratory microfusion capability on the National Ignition Facility (NIF). The NIF will be constructed to conduct both direct- and indirect-drive experiments. Highly uniform irradiation for direct-drive experiments can be produced by NIF if the design (see p. 62) is modified to allow one-half of the beams to be redirected to new ports closer to the equator of the target chamber and if beam-smoothing methods are implemented. The tolerances for energy imbalance among the beams, beam mispointing, and errors in target positioning will depend on how much long-wavelength nonuniformity the target can accept without a serious degradation in performance.

OMEGA is a 60-beam, frequency-tripled, Nd:glass laser in a master-oscillator, power-amplifier configuration. The power amplifiers consist of four stages of rod amplifiers and two stages of disk amplifiers. The 280-mm full-aperture beams are converted from the infrared (1.054 $\mu$m) to the ultraviolet (0.351 $\mu$m) using two KDP crystals arranged for Type II-Type II frequency conversion. The 60 beams are directed to a 3.3-m-diameter target chamber where they are symmetrically disposed about a sphere and focused with *f*/6 aspheric lenses.

At the completion of the Key Decision 4 (KD4) milestones set by DOE, OMEGA produced over 60 TW of UV light with up to 45 kJ of energy with better than an 8% rms energy balance. (The KD4 requirement was for 10% rms energy balance and greater than 30 kJ of UV light.) The system demonstrated the 1-h shot repetition rate required in a test that consisted of firing the laser 15 times at full energy in 14 h and 52 min. Conversion efficiencies on these tests were measured to be in excess of 75%.

Ultimately, high irradiation uniformity (>98.5%) will be obtained using smoothing by spectral dispersion and diffractive optics on each beam. Continuous distributed phase plates (DPP's) will provide efficient phase conversion for the system. A combination of continuous random phase and Fourier gratings will improve the far-field irradiance and energy efficiency. The continuous DPP's are inherently harmless to the laser system optics and provide for a flexible, effective, and affordable laser beam-smoothing system (pp. 126 and 170). Two-dimensional smoothing by spectral dispersion (SSD) and polarization rotators are being developed to achieve the final irradiation goals.

Flexible pulse shaping (p. 56) will be provided using various techniques. The optical-pulse-shaping system employs integrated-optic amplitude modulators operated in series and fabricated on a single, fiber-coupled $LiNbO_3$ waveguide. The system is capable of meeting future pulse-shaping requirements for OMEGA. In recent operational testing, this system has demonstrated the ability to produce shaped optical pulses with 50- to 100-ps structure over a pulse envelope of several nanoseconds.

Initial experiments (p. 145) were conducted on the system to activate and test the first diagnostics systems. The experiments demonstrated the successful overall functioning of the system and have produced high neutron yields and core temperatures in thermonuclear fuel. In fact, this first series of target implosions achieved a **new world record neutron yield ($1 \times 10^{14}$ neutrons).**

The OMEGA laser facility will be an important contributor to DOE's Science-Based Stewardship Program (SBSS) by providing continuity to the National ICF program and broadening its science base, by providing strong coupling to the NIF program, and by strengthening the links between the National laboratories and the educational and research strengths of the University of Rochester. Several specific missions of importance to the DOE Defense Programs (DP) will be addressed on OMEGA. The direct-drive experimental program will conduct a number of well-characterized physics campaigns. The results of this program can be used to enhance current predictive capabilities in the absence of nuclear testing, since many aspects of direct-drive implosions access physics regimes of interest in the SBSS program. Secondly, the increased energy of the OMEGA laser facility, the compatibility of the LLE target chamber and diagnostic systems with many existing Los Alamos National Laboratory (LANL) and Lawrence Livermore National Laboratory (LLNL) diagnostics, and the recent relaxation of the classification policy regarding ICF allow for experiments of interest in indirect-drive ICF to be conducted on OMEGA. Moreover, the OMEGA facility will most likely serve as a bridge facility for the Nation during NIF construction for advanced target- and laser-diagnostic development required for the NIF.

### Laser Facility Report

After completion of the OMEGA laser, the fourth quarter of FY95 was the first full quarter of operations on the upgraded laser. Both the first implosion campaign and the first planar-target campaign were successfully carried out (p. 188). The experimental campaign resulted in a total of 150 target shots and is consistent with plans to deliver 1000 target shots (one-shift operation) each year.

The shot summary for OMEGA was as follows:

| | |
|---|---|
| Driver | 187 |
| Beamline | 234 |
| Target | 150 |
| ***Total*** | **571** |

### Diagnostics Development

Present efforts on the OMEGA system are concentrating on activating an extensive set of diagnostics for target experiments. We discuss a krypton spectroscopy diagnostic for high-temperature implosions (p. 1). The addition of ~0.01 atm of krypton gas to the fuel allows the implosion temperature to be conveniently diagnosed through the spectrum of helium-like ($Kr^{+34}$) and hydrogen-like ($Kr^{+35}$) lines. The ratio of intensities for the two Kr lines as a function of temperature is sufficient to allow temperature measurements of up to ~10 keV with a maximum error less than ±10%. In related work (p. 155), improved calculations of krypton Stark profiles have been used to refine the diagnostic technique of doping the fuel with small amounts of krypton. Using different doping levels, krypton lines can be used to measure the electron and ion temperatures and the density-radius product of the compressed core.

A novel beam-energy diagnostic system, based on optical fibers, was implemented for OMEGA (p. 110). The system can measure the UV energy and the residual green and IR energies of all 60 beams with a relative beam-to-beam accuracy of a fraction of a percent.

Simulations of diagnostic x-ray emissions due to fuel-pusher mixing in laser-driven implosions have been carried out using the one-dimensional hydrocode *LILAC* (p. 170). The model describes the evolution of the mixed region near the unstable fuel-pusher interface and is fully incorporated into the hydrodynamics simulations. Calculations using the model support the feasibility of diagnosing mix using thin x-ray-emitting additive layers placed in the pusher near the unstable interface.

Diagnosing and characterizing direct-drive targets are important to all aspects of the experimental program on OMEGA. The uniformity requirements are stringent, both with respect to sphericity and wall thickness. We have developed a new technique to characterize transparent targets (p. 175). When irradiated with narrow-bandwidth, spatially incoherent light and viewed in a microscope, the shells display self-interference patterns that provide for a rapid assessment of wall thickness and uniformity.

### Laser and Optical Technology

An experimental technique to determine the group velocity walkaway of short pulses in nonlinear optical crystals has been developed based on frequency domain interferometry to di-

rectly measure polarization mode dispersion in birefringent media (p. 13). Measurement of walkaway dependence versus propagation angle in KDP-II crystals using this technique fits the theoretical prediction based on the material dispersion to within an accuracy of ±10%.

The isoelectric point of the polishing agent is a key process parameter to control for the rapid production of high-quality optical surfaces from silica-based glass types (p. 25). Combinations of slurry fluids and polishing agents in which the fluid pH value is larger than the polishing agent's isoelectric point consistently produced surfaces with the lowest surface roughness through inhibition of suspended particle agglomeration and enhanced dissolution of in-process glass constituents.

We have demonstrated an ability to readily induce uniform bulk molecular alignment in liquid crystalline polysiloxane elastomeric films by application of mechanical forces during the final crosslinking stage (p. 40).

The dominant damage feature in UV high-reflector coatings has been identified as submicron, lateral-sized craters that develop independently of the presence of micron-scale growth nodules and whose number density follows the intensity profile of the full laser beam (p. 49). Coupled with the observation that the smallest measured craters allow for starting absorber sizes of <10 nm, these results point toward randomly distributed nano-cluster absorbers as the sources involved in the energy transfer from the optical field to the porous film medium.

The terminal-level lifetimes for four different Nd:YLF samples as determined by small-signal-gain and transient excited state absorption measurements were found to be considerably longer than the pulse lengths encountered in mode-locked laser operation and amplification of up to nanosecond pulses (p. 71). Because the terminal-level-laser lifetime in these media approaches the length of a common $Q$-switched laser pulse, simple analytical models are inadequate to account for terminal-level relaxation during amplification of such pulses, and numerical solutions are required in order to calculate energy-extraction performance, operation, and amplification of up to nanosecond pulses.

Magnetorheological finishing is a new method being developed for the finish polishing of optics in which the polishing is performed using a fluid suspension stiffened by a magnetic field. This method is being studied using a pre-prototype machine at the Center for Optics Manufacturing (p. 135). Initial trials on the machine indicate excellent capability for smoothing ground glass surfaces, correcting figure errors, and eliminating sub-surface damage. Both spheres and aspheres can be finished with the same machine setup for a variety of optical glasses.

**Progress in Laser Fusion**

The electron plasma wave excited by the ion-acoustic decay instability was observed directly using a novel Thomson scattering diagnostic (p. 8). The electron temperature in the interaction region, as determined from the frequency of the detected wave obtained using this diagnostic, is in reasonably good agreement with the value predicted by computer simulations.

We have developed a new analytic model for calculating the cutoff wave number of the ablative Rayleigh-Taylor instability (p. 117). The model is self-consistent and valid for an arbitrary power-law dependence of the thermal conductivity ($K \sim T^{\nu}$). The formula for the cutoff wave number is valid for $\nu > 1$ and Froude numbers greater than unity. The results can be used for those equilibria (such as those for indirect-drive ICF) that cannot be described by electronic heat conduction.

**Advanced Technology**

A theoretical model of the flux dynamics in an optically irradiated YCBO thin-film superconducting switch has been developed and experimentally verified (p. 20). Both the magnitude of the peak switched voltage in the secondary coil and its response time show a marked dependence on the intensity of the laser pulse used to initiate switching. In related work on high-temperature superconductors, we report on electro-optic sampling being used for the first time to study the photoresponse signals from $YBa_2Cu_3O_{7-\delta}$ thin films (p. 131). Electrical transients as short as 1.5 ps have been observed and are the fastest photoresponse signals reported to date from YBCO thin films. Additionally, femtosecond pump-probe experiments were used to study the electronic structure of semiconducting YBCO (p. 183). The bandwidth of the O-2$p$ band has been measured to be approximately 1.9 eV.

Room-temperature photoluminescence with an efficiency between 0.1% and 10% has been observed in porous silicon (p. 77), and its luminescence spectrum, intensity, and lifetime have been shown to be highly sensitive to growth and processing parameters. The ability to vary the peak of the photoluminescence spectrum from the blue/violet to wave-

lengths past 1.5 $\mu$m makes these materials of interest in the fabrication of light-emitting devices operating over the same wavelength range.

The first experimental evidence of time-dependent reflection in dental hard tissues irradiated with a 9.6-$\mu$m $CO_2$ laser has been observed (p. 93) and is related to the temperature dependence of the absorption coefficient using known relationships between surface reflection and high-absorption coefficients. The results indicate that morphological surface modifications in dental hard tissue can be fine-tuned by making an appropriate choice of wavelength and pulse duration, which will allow optimization of the laser-irradiation conditions for the reduction of dental decay.

**National Laser Users Facility**

The National Laser Users Facility (NLUF) was active during the construction of the OMEGA Upgrade. Approved experiments are expected to have OMEGA system time scheduled during calendar year 1996. A description of NLUF activity can be found beginning on p. 189. A list of the approved NLUF proposals for FY95 can be found in Table 64.VI (p. 190). Proposals submitted for FY96 are listed in Table 64.VII (p. 191).

**Education at LLE**

As the only university participant in the National ICF Program, education continues to be a most important mission for the Laboratory. Graduate students continue to play an important role in LLE's research activities, and have had the opportunity to participate in designing, testing, and constructing the world's most powerful ultraviolet laser for fusion research in the OMEGA Upgrade project. Fourteen faculty from five departments collaborate with LLE's scientists and engineers. Presently, 56 graduate students are pursuing Ph.D. degrees at the Laboratory. The research interests vary widely and include theoretical and experimental plasma physics, laser-matter interaction physics, high-energy-density physics, x-ray and atomic physics, nuclear fusion, ultrafast optoelectronics, high-power laser development and applications, nonlinear optics, and optical materials and optical fabrication technology. The technology developed during some of the Ph.D. research is in routine use on the OMEGA laser system: liquid crystal optics, optical pulse shaping, high-density plasma diagnostics, high-resolution x-ray and alphas-particle imaging, and x-ray streak cameras. Technological developments from ongoing Ph.D. research will continue to play an important role on OMEGA.

Ninety-six University of Rochester students and 14 students associated with the NLUF program have earned Ph.D. degrees at LLE since its founding. The most recent University of Rochester Ph.D. graduates and their theses titles are listed below:

| | |
|---|---|
| X. Cao | *Propagation of Ultrashort Optical Pulses in Nonlinear Media and Their Applications* |
| H. Chen | *X-Ray Emission from Picosecond Laser Plasmas* |
| S. P. Palese | *Measurements and Effects of the Raman Active Nuclear Distribution in the Condensed Phase* |
| J. N. Sweetser | *Wave Packet-Modulated Coherent Emission and Amplification of Femtosecond Optical Pulses* |

In addition to the graduate research work, approximately 50 undergraduate students of the University of Rochester participated in work or research projects at LLE this past year. Student projects include maintenance of the OMEGA laser system, work in the materials and optical-thin-film coating laboratories, programming, and image processing. Advanced undergraduate students are able to participate in specific research projects at LLE. Senior Honors projects in Optics have included phase conversion with diffractive optics, liquid crystal optics, and the science of polishing. This is a unique opportunity for these students, many of whom will go on to pursue a higher degree in the area in which they have participated at the Laboratory.

LLE continues to run a summer high school student research program where eight to ten high school juniors spend eight weeks performing individual research projects. Each student is individually supervised by a staff scientist or an engineer. During the program the students attend two seminars per week on safety, science topics relevant to LLE, or ethics. At the conclusion of the program, the students make final oral and written presentations on their work. The written reports are published as an LLE report. In a recent survey of the 52 students who have participated in this program since 1989, 28 of the 34 responding students are pursuing degrees in science and technology. Both of the students who responded from 1989 are pursuing doctorates in science and technology.

**Robert L. McCrory**
*Director*

# Krypton Spectroscopy Diagnosis of High-Temperature Implosions

High-temperature implosions are planned for the OMEGA Upgrade experimental program. By using relatively thin shell targets, temperatures much higher than 1 keV at modest compressed densities (~1 to 5 g/cm$^3$) are predicted. The goal of this work is to demonstrate that by adding a small admixture of krypton gas (~0.01 atm) to the fuel, the temperature can be conveniently diagnosed through the spectrum of helium-like ($Kr^{+34}$) and hydrogen-like ($Kr^{+35}$) lines. By increasing the fill pressure, resonant Kr lines can become opaque, through self-absorption, and their relative intensities can be used to diagnose shell-fuel mixing.

As an example of predicted high-temperature implosion on the OMEGA Upgrade system, in Fig. 61.1 we show temperature and density profiles, at peak compression, calculated by the *LILAC* code for a CH shell of 1-mm diameter and 10-$\mu$m thickness, filled with a 10-atm pressure of DT. Typical Upgrade laser parameters (laser energy of 30 kJ in a Gaussian pulse of 650-ps width) were assumed. As Fig. 61.1 shows, the core temperature and density are fairly uniform at ~5 keV and ~4.5 g/cm$^3$, respectively. In the analysis that follows, the core profiles will be assumed to be uniform as well. The relatively high temperature of the shell is expected to play an important role in transmitting core radiation.

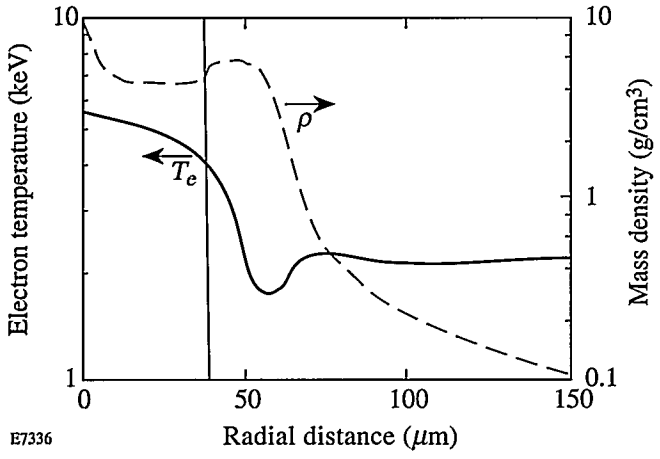


Figure 61.1
Electron temperature and mass density at peak compression, predicted by *LILAC*, for a DT-filled, high-temperature implosion on the OMEGA Upgrade system. The vertical line marks the fuel-shell interface.

### Observation of K-Shell Krypton Lines

The wavelengths and transition probabilities of Kr lines are not fully known from the literature. We have used atomic data calculated by M. Klapisch,[1] using a detailed relativistic atomic structure code that includes intermediate coupling, higher-multipole interactions, and many-body and QED effects. The K-shell lines are of much shorter wavelength than past spectral line emission from laser targets; for example, the $Kr^{+34}$ resonance line has a wavelength[1] of 0.94538 Å, or photon energy of 13.11347 keV. For this reason, we addressed the question of observability of these lines. A simple way to estimate the expected intensity of krypton lines is to make a comparison with past experiments on argon-filled targets. In recent experiments on OMEGA, strong helium-like and hydrogen-like argon lines were observed when the argon fill pressure was 0.1 atm (in 20-atm deuterium).[2] In other experiments the argon fill pressure was as low as 0.01 atm but still yielded significant spectral intensity. We chose to calculate the intensity of K-shell krypton lines using the corona approximation. This approximation was used to show only the intensity scaling; for the temperature-determination curves, the more general collisional-radiative model was used. The corona approximation is valid in the limit of low density, high temperature, and high nuclear charge $Z$, while the converse is true for the LTE approximation. The condition for the applicability of the corona model to excited states can be written as [Eq. (6-55) in Ref. 3]

$$N_e\left(\mathrm{cm}^{-3}\right) \ll 10^{18}\left(Z^7/n^{17/2}\right)\left(kT/E_i\right)^{1/2}, \qquad (1)$$

where $E_i$ is the ionization energy and $n$ is the highest principal quantum number for which the model applies. For helium-like krypton (of energy of ionization[4] $E_i = 17.296$ keV) and the predicted densities of up to $N_e \sim 10^{24}$ cm$^{-3}$ ($\rho \sim 4$ g/cm$^3$), the model applies to quantum numbers $n$ of up to at least $n = 3$, over the entire 1- to 10-keV temperature range. In the corona

approximation, the line intensity is given by the rate of excitation by electron collisions:[5]

$$I_\nu = h\nu\langle\sigma_{\text{exc}}v\rangle N_i N_e$$
$$= 1.6\times10^{-5} f\langle g\rangle N_e\left[\Delta E(kT)^{1/2}\right]^{-1}\exp\left[-(\Delta E/kT)\right], \quad (2)$$

where $\Delta E$ is the excitation energy, $N_i$ and $N_e$ are the densities of emitting ions and electrons, respectively, $f$ is the absorption oscillator strength, and $\langle g\rangle$ is the Maxwellian-averaged Gaunt factor[5] ($kT$ and $\Delta E$ are in eV). Thus, if the ratio $\Delta E/kT$ is maintained when krypton is used instead of argon, the intensity of the same transition should drop by a factor of ~8 since $\Delta E$ increases by a factor of 4. The actual drop in intensity would be much smaller for the following reasons: (a) For argon, Eq. (2) would yield an overestimate of the intensity since in the corona approximation every excitation leads to a photon emission, while for argon some of the excitations result in super-elastic collisions with free electrons; (b) whereas the predicted compressed density is comparable to what was achieved with argon, the krypton targets will be bigger and thus contain more mass (by a factor of ~64) for the same fill pressure. This leads to the conclusion that the strong K-shell krypton lines will be readily observable for temperatures ≥ 3 keV.

Supportive evidence can be found in the fact that the resonance line of $Kr^{+34}$ (at 0.94538 Å) was easily observable on previous short-pulse (100-ps) experiments[6] on OMEGA, using a Von-Hamos focusing spectrometer. The peak laser power in those experiments was ~6 TW, which is much lower than that of the OMEGA Upgrade (~30 TW).

### Determination of Temperature by Line-Intensity Ratio

We now calculate the temperature dependence of a particular Kr line-intensity ratio under steady-state conditions, using the collisional-radiative atomic code POPION.[7] Although the corona model is largely applicable for the cases under discussion, as was mentioned previously, the collisional-radiative model is more precise. For example, we examined the calculated relative specie and level populations for $Kr^{+34}$ and $Kr^{+35}$ ions. In Fig. 61.2 we show examples of level populations in $Kr^{+34}$ (helium-like krypton); the sum of populations in all levels of krypton ions adds up to 1. The ground-level population (especially at the higher temperatures) is essentially independent of the electron density $N_e$, which is a characteristic of the corona model [see Eq. (6-95) in Ref. 3]. At lower temperatures, the relative ground-level population approaches an inverse dependence on $N_e$, which in turn is a characteristic of the LTE model [as can be seen from the Saha equation, Eq. (6-29) in Ref. 3]. Also, the $n = 2$ population increases like $N_e$—also a characteristic of the corona model. The latter can be seen from Eq. (2), by equating $I_\nu$ with $h\nu\, N_i\, Q_n$, where $Q_n$ is the relative level population in the level $n$. On the other hand, at the lower temperatures the $n = 2$ level population approaches independence of $N_e$, a characteristic of the LTE model (where relative level populations depend only on the temperature, through the Boltzmann factors). Thus, to cover the whole relevant parameter space, a full collisional-radiative model is necessary.

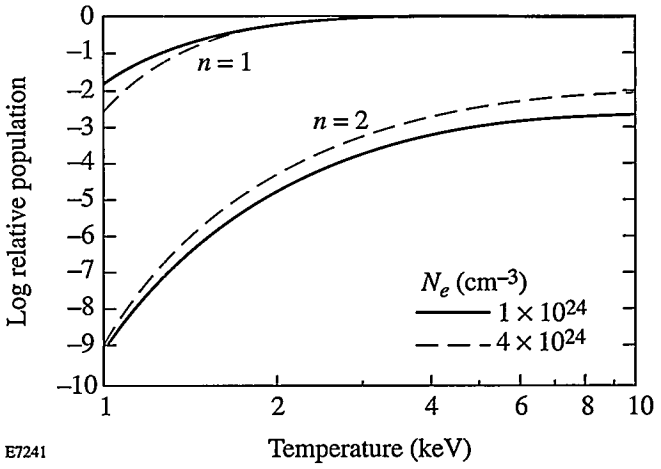


Figure 61.2
Relative populations in levels of $Kr^{+34}$ (helium-like krypton), as calculated by the POPION[7] atomic code. The sum of populations in all levels of krypton ions adds up to 1.

For a temperature-sensitive line-intensity ratio we choose the ratio of a hydrogen-like line to a helium-like line. To minimize opacity effects we use the following two lines: (a) the Lyman-$\alpha$ line of $Kr^{+35}$ of wavelength 0.9196 Å,[8] and (b) the helium-$\beta$ line of $Kr^{+34}$ of wavelength 0.8033 Å and absorption oscillator strength 0.1293.[1] We must show that the opacity of these lines will be negligible for the method to be applicable. We concentrate on the helium-$\beta$ line since the opacity of the Lyman-$\alpha$ line is much smaller. The line opacity at an energy separation $\delta E$ from the unperturbed position can be expressed as [see Eq. (8-14) in Ref. 3]

$$\tau(\delta E = 0) = \left(\pi e^2 h/Mmc\right)P(\delta E = 0) f\, \rho R\, \varepsilon Q_n, \quad (3)$$

where $M$ is the krypton ionic mass, $P(\delta E)$ is the line profile at $\delta E$ in inverse energy units, $f$ is the absorption oscillator

strength of the line, $\rho R$ is the total areal density (mostly that of the fuel), $\varepsilon$ is the fraction of krypton in the fuel (by mass), and $Q_n$ is the fraction of krypton ions in the absorbing level (i.e., the lower level of the transition). For unshifted lines one usually calculates $\tau_0 = \tau(\delta E = 0)$, but for the helium-$\beta$ line, which is shifted by the Stark effect, we designate $\tau_0$ as the maximum opacity at the shifted peak position. In either case, $P(0) \sim 1/\Delta E$, where $\Delta E$ is the line width. We assume the addition of 0.01 atm krypton to the DT-filled target implosion that was simulated in Fig. 61.1. In that implosion the DT fill pressure was 10 atm, and the total $\rho R$ at peak compression was ~16 mg/cm$^2$. According to the POPION code results (Fig. 61.2), $Q_1$ for helium-like Kr over a wide temperature range is very close to 1.

Next we need to estimate the line width, which is related to $P(0)$ in Eq. (3) as explained previously. The code results of Fig. 61.1 show that the ion temperature at peak compression is about twice the electron temperature, or $T_i \sim 10$ keV, for which the Doppler width of the helium-$\beta$ line is about 12.9 eV. A rough estimate of the Stark width of the $Kr^{+34}$ helium-$\beta$ line can be obtained by noting that for a given density and temperature the Stark width is proportional to $1/Z$. More specifically, the scaling for the Stark width of hydrogenic lines is[11] given by $\Delta E \sim \left(Z_p/Z\right)\left(n_i^2 - n_f^2\right)N_p^{2/3}$, where $Z_p$ and $N_p$ are respectively the nuclear charge and ion density of the perturber, $Z$ is the nuclear charge of the emitter, and $n_i$, $n_f$ are the principal quantum numbers of the initial and final levels of the transition. Although the ion under discussion is helium-like, the Stark width of the upper level, $1s3p\,^1P$, turns out to exceed the separation to the nearby $1s3d\,^1D$ level, which makes the transition close to hydrogenic (i.e., the level splitting increases linearly with the perturbing field as in single-electron ions). The above formula for the Stark width is only approximate and does not include such effects as perturbers correlation. However, we use its $Z$ scaling only for extrapolating the detailed calculations[10] for the same transition in argon at the same density and ignore the weak temperature dependence of the Stark broadening. The Stark width of the $Kr^{+34}$ helium-$\beta$ line at $\rho = 4.5$ g/cm$^3$ is thus estimated to be ~17 eV. Convolving this Stark width with the Doppler width yields a total width of ~26 eV, from which the normalized composite profile yields the value of $P(\delta E)$. Substituting these values into Eq. (3) yields an optical depth for the helium-$\beta$ line of $\tau_0 \sim 0.56$. This opacity value was estimated for an electron temperature of 5 keV ($T_i \sim 2\,T_e$) and density of 4.5 g/cm$^3$. For other temperatures (but the same doping fraction) the opacity will not change appreciably because (1) $Q_1$ is weakly dependent on $T$ in the range $T_e$ ~3 to 10 keV (see Fig. 61.2), and (2) the linewidth depends mainly on the density. For other densities the opacity will vary as $\sim\rho^{-2/3}$ due to the change in linewidth. The opacity of the Lyman-$\alpha$ line of $Kr^{+35}$ is much smaller than that of the helium-$\beta$ line because the ratio of $Kr^{+35}$ to $Kr^{+34}$ ground-state populations at $N_e = 10^{24}$ cm$^{-3}$ varies over the 1- to 10-keV temperature range from ~$10^{-10}$ to ~$10^{-1}$.

The curves in Fig. 61.2 and the temperature curves calculated below assume a steady-state situation. To justify this assumption we show in Fig. 61.3 the calculated ionization time $t_i$ of the $Kr^{+34}$ ion as a function of temperature for $N_e = 10^{24}$ cm$^{-3}$; $t_i$ depends inversely on $N_e$ and is given by $t_i = \left(\langle\sigma_{\text{ion}}v\rangle N_e\right)^{-1}$. The ionization rate was taken as[11]

$$\langle\sigma_{\text{ion}}\rangle = 2.5\times10^{-6}\,\eta\,E_i^{-3/2}\left(kt/E_i\right) \times\left[1+\left(kT/E_i\right)\right]^{-1}\exp\left[-\left(E_i/kT\right)\right], \quad (4)$$

where $E_i$ is the ionization energy (in eV) and $\eta$ is the number of outer-shell electrons ($\eta = 2$ for helium-like ions). The time constant for approaching a steady state of level populations for a given set of hydrodynamic conditions is given by $t_i$ since $t_i$ is the slowest of the relevant processes. An example can be found in the excitation rate from the ground level to the $2^1P$ level of $Kr^{+34}$, which is faster than the ionization rate by a factor that varies from ~700 at the low end of the temperature range to ~3 at the higher end. We see from Fig. 61.3 that for a value of $T$ of 5 keV, the ionization time $t_i$ is ~50 ps, which is about the time period $t_{\text{peak}}$ predicted for the volume-averaged temperature to be within ~90% of its peak value. Thus, the

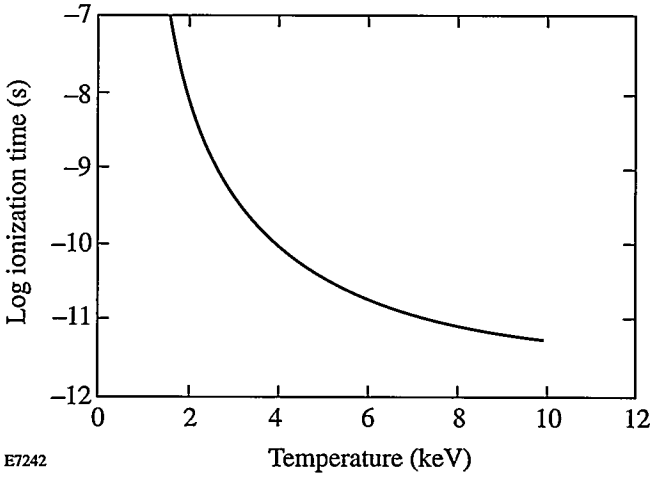


Figure 61.3
Calculated ionization time $t_i$ of $Kr^{+34}$ as a function of temperature, for $N_e = 10^{24}$ cm$^{-3}$. The ionization time serves as a time constant for approaching a steady state of level populations for a given set of hydrodynamic conditions.

density of hydrogen-like ions will reach only the fraction $\left[1-\exp\left(-t_{peak}/t_i\right)\right] \sim 0.63$ of its steady-state value. Neglecting this effect will result in an underestimate of the temperature (in the above example, 4.6 keV instead of 5 keV). An underestimate will also result if the spectral measurement is not time resolved, since the emission time of helium-like lines will be longer than that of hydrogen-like lines.

We show in Fig. 61.4 the calculated intensity ratio of the Lyman-$\alpha$ line of $Kr^{+35}$ to the helium-$\beta$ line of $Kr^{+35}$ as a function of temperature for two electron-density values. Clearly, the intensity-ratio change is sensitive to temperature, but the Lyman-$\alpha$ line may be too weak to be observed for temperatures smaller than ~4 keV. In going from $T = 10$ keV to $T = 4$ keV, both the ratio in Fig. 61.4 and the intensity of the helium-$\beta$ line drop by an order of magnitude, which causes the intensity of the Lyman-$\alpha$ line to drop by two orders of magnitude. Over a wide density range (changing by a factor of 20), the temperature-dependence curve changes very little. This behavior is due to the close resemblance to the corona model, where the line ratio is completely independent of density. If we know the density to be within this range, the maximum error in determining the temperature would be less than ±10%. The required precision in the intensity measurements is modest: to achieve a ±10% precision in the temperature, the intensity ratio must be measured with a precision of only a factor of ~3 (at $T = 4$ keV) or a factor of ~2 (at $T = 6$ keV). The attenuation of these two lines through the compressed CH polymer shell is of no concern, as a cold $\rho\Delta R$ of more than 1 g/cm$^2$ is needed to significantly attenuate them.

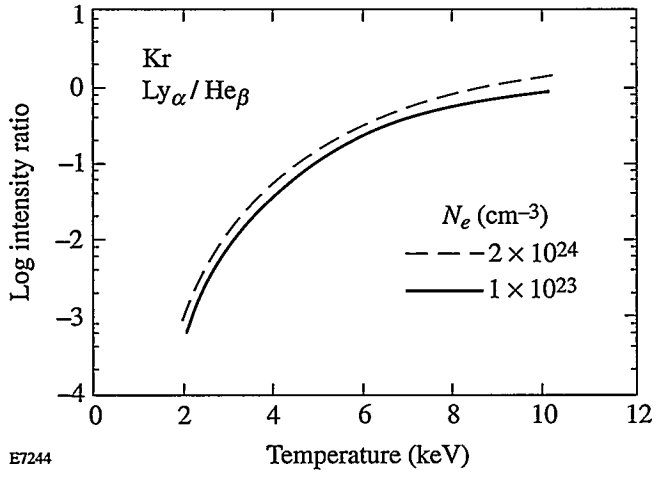


Figure 61.4
Intensity ratio of the Lyman-$\alpha$ line of $Kr^{+35}$ to the helium-$\beta$ line of $Kr^{+35}$ as a function of temperature at two electron-density values. The opacity of both lines, which was shown to be small, was neglected.

**Mixing Diagnosis Based on High-Opacity Kr Lines**

In the previous section the opacity of the helium-$\beta$ line of $Kr^{+34}$ for a fill pressure of 0.01 atm was shown to be smaller than 1 ($\tau_0 \sim 0.56$), and thus negligible. We now examine the case of much higher fill pressures, where the helium-$\beta$ line is optically thick at peak compression. Although the intensity ratio in Fig. 61.4 is then not applicable, a different type of information can be obtained on the target behavior. Anticipating the last section, we choose the helium-$\beta$ line rather than the higher-opacity helium-$\alpha$ line.

The intensity of an optically thick line emerging from the plasma volume is related to the escape factor parameter, which has been the subject of numerous publications.[12–15] The escape factor $G$ is defined by

$$G(\tau_0) = \int_{-\infty}^{\infty} P(\delta E)\exp\left[-\tau_0 P(\delta E)/P(\delta E = 0)\right] d(\delta E), \quad (5)$$

where $G(\tau_0)$ in spherical geometry corresponds to a point source at the center of the sphere and $\tau_0$ is the opacity over the radius. For a source uniformly distributed over the sphere, Mancini *et al.*[15] have shown that $G(\tau_0)$ is twice as big as the point-source case and depends primarily on the type of line profile. For example, for a Gaussian (i.e., Doppler) profile, $G(\tau_0)$ does not depend explicitly on the linewidth; for $\tau_0 >> 1$, $G(\tau_0) \sim 1/(\pi \ln \tau_0)^{1/2}\tau_0$. For Stark profiles the corresponding asymptotic relation was found to be $G(\tau_0) \sim 1/\tau_0^{3/5}$. For example, a Holtzmarkian profile (the simplest approximation to a Stark profile) yields the universal asymptotic expression[12]

$$G(\tau_0) = 0.451/\tau_0^{3/5} \qquad (\tau_0 >> 1). \quad (6)$$

Mancini *et al.*[15] have calculated $G(\tau_0)$ for the Lyman-$\alpha$ line of argon using complete Stark profiles. They showed that for an accurate value of $G$, a detailed calculation with an actual Stark profile should be performed. However, their curves (for a point source) can still be approximated by Eq. (6) if $G$ is expressed as a function of $\tau_0$, rather than as a function of $\tau_0/P(\delta E = 0)$, because an approximate Stark profile that changes only the line width without changing the profile shape will not affect Eq. (6).

A measurement of the escape factor of a high-opacity line can yield the value of $\tau_0$, using Eq. (6) or the equivalent result of a more detailed calculation.[15] As Eq. (3) shows, $\tau_0$ depends on $\rho R$ and, through $P(\delta E)$, on $\rho$. For a high-opacity line, most of the emergent intensity is located in the far wings of the

spectral profile. Because the Doppler profile drops much faster than the Stark profile, the wings are dominated by the latter, although the two separate linewidths are comparable. For this reason we consider the escape factor for a purely Stark profile. For the helium-$\beta$ line, $P_0 = P(\delta E = 0) \sim \rho^{-2/3}$, when the density is high enough to merge the $1s3p$ and $1s3d$ levels, which we have argued to be the case here. For the crude estimate of 17-eV Stark width, this relationship reads

$$P_0\left(\mathrm{eV}^{-1}\right) = 0.15\,\rho^{-2/3}, \tag{7}$$

where, as explained, $P_0$ refers to the peak of the profile rather than to the line center. On the other hand, in an imploding spherical target

$$\rho R = \left(3M_F/4\pi\right)^{1/3}\rho^{2/3} \tag{8}$$

in terms of the total fill mass (fuel and krypton) $M_F$. Thus $\tau_0$ is independent of the target compression because the opacity increases with increasing $\rho R$ but decreases due to the increasing width (or decreasing $P_0$). The two quantities change as $\rho^{2/3}$ and cancel each other's effect on $\tau_0$.

The foregoing discussion shows that measuring the escape factor cannot yield information on the density or $\rho R$. Mixing of shell material into the fuel, however, does affect the escape factor measurement because the $\rho R$ deduced from the absorption of Kr lines yields the $\rho R$ of only the fuel $(\rho R)_F$, whereas the Stark profile depends on the total density $\rho_T$, including shell material mixed into the fuel. Combining Eqs. (3), (7), and (8), we can relate the volume-averaged fraction of density due to mixing $\xi = \rho_{\mathrm{mix}}/\rho_F$ to $\tau_0$:

$$1 + \xi = \left[0.15\,\pi e^2 h\, f\left(eM_F/4\pi\right)/\left(mMc\,\tau_0\right)\right]^{3/2}. \tag{9}$$

We can understand the effect of mixing on the opacity as follows: Without mixing, the opacity $\tau_0$ is approximately constant during the compression because of the two opposing effects: (1) increase in the $\rho R$ of absorbing ions and (2) increase in the linewidth. The mixed shell material is involved only in the second effect, which causes a net reduction in the opacity.

The experimental determination of the mixing fraction consists of measuring the escape factor $G(\tau_0)$, deducing $\tau_0$ from Eq. (6) (or from a more detailed equivalent thereof), and, finally, finding $\xi$ from Eq. (9). In addition to using a crude Stark profile, Eq. (9) is correct only for a point source (central hot spot). As mentioned earlier, Mancini *et al.*[15] have shown that for a spherically uniform source, $G(\tau_0)$ is twice as big as for the point-source case. To determine which geometry conforms better to the experiment we can examine two experimental signatures: (a) for a uniform source, the core image size at high photon energy will be about the same as that at low photon energy, whereas for a hot-spot source the former will be much smaller than the latter; and (b) for a uniform source the observed line profile will be flat topped, whereas for a hot-spot source a self-reversal (or minimum) will be observed at the position of the profile peaks.

### A Method for Measuring the Escape Factor

The escape factor of a line can be measured by comparing its measured intensity to that of another line, both of which have the same upper level. The first should have an opacity $\tau_0 >> 1$, the second $\tau_0 << 1$. The two helium-like Kr lines we selected are (a) the Lyman-$\beta$ line, $1s3p\,^1P - 1s^2\,^1S$ (at 0.8033 Å) and (b) the Balmer-$\alpha$ line, $1s3p\,^1P - 1s2s\,^1S$ (at 5.0508 Å). Note that what we refer to here as Balmer-$\alpha$ is the helium-like, 3-2 transition that shares an upper level with the helium-$\beta$ line (and not, for example, to the stronger $1s3d\,^1D - 1s2p\,^1P$ transition at 5.3463 Å). Previously, we mentioned the helium-$\alpha$ line corresponding to the $1s2p\,^1P - 1s^2\,^1S$ transition. For krypton ions, both the transitions to the ground level and the 3-2 transitions are easily accessible to x-ray measurement. Thus, for argon, the 3-2 transitions are too soft ($\lambda > 20$ Å) for common x-ray crystal instruments, and they also suffer very high opacity in traversing the target.

By making an appropriate choice of the krypton fill pressure, the opacity (for resonant absorption) of the Lyman-$\beta$ line at peak compression will be >>1, while that of the Balmer-$\alpha$ will be <<1. It was estimated earlier that for a Kr fill pressure of 0.01 atm, the opacity $\tau_0$ of the helium-$\beta$ line will be ~0.5. Thus, for a fill pressure in the range of 0.1 to 1.0 atm, $\tau_0$ will be in the range of 5 to 50. The opacity of the Balmer-$\alpha$ line will still be negligible since it is absorbed by ions in the $n = 2$ shell (whereas the helium-$\beta$ line is absorbed by ground-level ions). Figure 61.2 shows that the population of $n = 2$ absorbing ions is smaller than that of $n = 1$ absorbing ions by several orders of magnitude. Due to the expected merging of the $1s3p\,^1P$ and $1s3d\,^1D$ levels, both ions in the $1s2p\,^1P$ and $1s2p\,^1S$ levels can absorb the broadened Balmer-$\alpha$ line; these constitute 1/3 of all $n = 2$ ions. With no merging, only 1/16 of the $n = 2$ ions can absorb the $1s3p\,^1P - 1s2s\,^1S$ transition. The high opacity of the resonance line $1s^2 - 1s2p\,^1P$

will also increase the $n = 2$ population (this effect is not included in Fig. 61.2).

In the absence of any absorption, the intensity ratio of these two lines $I_{Ly}/I_{Ba}$ would simply be given by the ratio of the Einstein $A$ coefficients (spontaneous emission probabilities) $A_{Ly}/A_{Ba}$ and be independent of any atomic modeling. Since $A$ (Lyman-$\beta$) = $4.453 \times 10^{14}$ s$^{-1}$ and $A$ (Balmer-$\alpha$) = $6.163 \times 10^{12}$ s$^{-1}$, $A_{Ly}/A_{Ba} = 72.25$. In the case discussed here, the observed intensity ratio $I_{Ly}/I_{Ba}$ will be lower than the ratio of the Einstein $A$ coefficients $A_{Ly}/A_{Ba}$, by the escape factor $G$ for the helium-$\beta$ line. Thus, $G$ can be found from

$$G = \left(I_{Ly}/I_{Ba}\right)/\left(A_{Ly}/A_{Ba}\right) = \left(I_{Ly}/I_{Ba}\right)/72.25. \quad (10)$$

It should be noted that the emergent intensity of a high-opacity line may not depend uniquely on the escape factor because of the possibility of re-emission of absorbed photons.[16] This is equivalent to allowing for the increased excited-level population (and thus emission) due to the absorption itself. In our case this effect is already included in the ratio of line intensity because the measured intensity of the optically thin Balmer-$\alpha$ line does reflect the actual excited-level population.

The nonresonant absorption by the target material (mostly the shell) should be negligibly small to insure the validity of this method. The attenuation of the Lyman-$\beta$ line through the shell is negligible: it takes a $\rho\Delta R$ of ~1.8 g/cm$^2$ of cold CH to attenuate that line by $1/e$. On the other hand, the Balmer-$\alpha$ line will be attenuated by the same amount in going through only a $\rho\Delta R$ of ~5.5 mg/cm$^2$ of cold CH. Figure 61.1 shows that the shell at peak compression is hot enough to minimize this attenuation. The opacity of the CH shell at a wavelength $\lambda$, due to inverse bremsstrahlung absorption, is given by[17] $\tau = 2.23 \times 10^{-3} \lambda^3 (\rho\Delta R)\rho/T^{1/2}$, where $\lambda$ is in Å and $T$ in keV. For the target profiles of Fig. 61.1, the inverse bremsstrahlung opacity is $\tau \sim 0.014$. The opacity of CH due to photoionization is given by[17] $\tau = 0.54\ \lambda^3(\rho\Delta R)\Psi$, where $\Psi$ is the fraction of carbon ions that are not stripped. Results from POPION calculations show that, at the given shell temperature and density values, $\Psi < 10^{-3}$ so that the photoionization opacity is $\tau < 10^{-3}$.

Finally we estimate the expected sensitivity of the method for measuring the degree of shell-fuel mixing. To find $G$ from Eq. (10) with a precision of approximately ±20%, the relative intensity of each of the lines must be measured with a precision of ±10%, which requires the relative calibration of two instruments for the two very different wavelengths used here. A suitable procedure is as follows: the intensity ratio $I_{Ly}/I_{Ba}$ for the case of a very low Kr fill pressure (~0.01 atm) is simply given by the known ratio $A_{Ly}/A_{Ba}$. Since, for Stark profiles, $G$ depends[15] asymptotically on $\tau_0$ like $1/\tau_0^{3/5}$, an error of ±20% in $G$ will result in an error of ±33% in $\tau_0$. Finally, finding the relative mixing from Eq. (9), this error translates into an error of ±50% in $1+\xi$. Thus, the method is useful only for extensive mixing, where $\xi$ is not much smaller than 1.

## ACKNOWLEDGMENT

This work was supported by the U.S. Department of Energy Office of Inertial Confinement Fusion under Cooperative Agreement No. DE-FC03-92SF19460, the University of Rochester, and the New York State Energy Research and Development Authority. The support of DOE does not constitute an endorsement by DOE of the views expressed in this article.

## REFERENCES

1. M. Klapisch (private communication).
2. B. Yaakobi, R. Epstein, F. J. Marshall, D. K. Bradley, P. A. Jaanimagi, and Q. Su, Optics Commun. **111**, 556 (1994).
3. H. R. Griem, *Plasma Spectroscopy* (McGraw-Hill, New York, 1964).
4. U. I. Safranova, Physica Scripta **23**, 241 (1981).
5. H. Van Regemorter, Astrophys. J. **136**, 906 (1962).
6. B. Yaakobi and A. J. Burek, IEEE J. Quantum Electron. **QE-19**, 1841 (1983).
7. R. Epstein, S. Skupsky, and J. Delettrez, J. Quant. Spectrosc. Radiat. Transfer **35**, 131 (1986).
8. G. W. Ericson, J. Phys. Chem. Ref. Data **6**, 831 (1977).
9. H. R. Griem, *Spectral Line Broadening by Plasmas* (Academic Press, New York, 1974).
10. C. F. Hooper (private communication).
11. H.-J. Kunze, A. H. Gabriel, and H. R. Griem, Phys. Rev. **165**, 267 (1968).
12. F. E. Irons, J. Quant. Spectrosc. Radiat. Transfer **22**, 1 (1979).

13. J. P. Apruzese, *ibid.* **34**, 447 (1985).

14. C. Chenais-Popovics, P. Alaterre, P. Audebert, J. P. Geindre, and J. C. Gauthier, *ibid.* **36**, 355 (1986).

15. R. C. Mancini, R. F. Joyce, and C. F. Hooper, Jr., J. Phys. B: At. Mol. Phys. **20**, 2975 (1987).

16. A. G. Hearn, Proc. Phys. Soc. (GB) **81**, 648 (1963).

17. B. Yaakobi, R. Epstein, and F. J. Marshall, Phys. Rev. A **44**, 8429 (1991).

# Direct Measurements of the Ion-Acoustic Decay Instability in a Laser-Produced, Large-Scale, Hot Plasma

The final experiment carried out on the 24-beam OMEGA laser (in collaboration with scientists from Lawrence Livermore and the University of California, Davis) involved the investigation of the ion-acoustic decay instability (IADI) in large-scale-length (~1-mm), hot (~1-keV) plasmas.

In the IADI, an electromagnetic wave (i.e., an incident laser beam) decays into an electron plasma wave (epw) and an ion-acoustic wave (iaw), near the critical density $n_c$ (where the electromagnetic wave frequency equals the plasma frequency). A unique feature of this experiment was the first direct observation of the epw using collective Thomson scattering (CTS). Further, it was possible from the spectral width of the CTS signal to estimate the electron temperature $T_e$ in the plasma, the result ($T_e = 1.5$ keV) being in reasonably good agreement with the value (1.1 keV) predicted by the two-dimensional code *SAGE*.

The IADI[1] is a fundamentally important subject in plasma physics that has been studied by numerous authors in the context of laser-plasma interactions,[2,3] microwave experiments,[4] and ionospheric studies.[5] It is potentially significant in the large-scale plasmas relevant to laser fusion because anomalous electron heating can occur even when the instability is relatively weak, if the unstable volume is sufficiently large. In addition, the instability can lead to anomalous dc resistivity and a reduction in electron thermal transport, and it has an application as a critical surface diagnostic. Despite the significance of the IADI to large-scale plasmas, all previous experiments have been carried out in relatively small-scale plasmas.

In this article we present two original results: (1) the first direct observation of the epw excited by the IADI, and (2) the first study of the IADI in a plasma that approaches laser-fusion conditions, in the sense of having a density scale length of the order of 1 mm and an electron temperature $T_e$ in excess of 1 keV. Previous observations of the epw's have been based on the second-harmonic emission, from which little can be inferred because the emission is produced by unknown pairs of epw's, integrated in a complicated way over wave-number space and real space. In contrast, we have directly observed the epw by using the 90°, collective Thomson scattering of a UV laser (at the third harmonic of the pump) from the epw's. Because the ratio of probe frequency to electron plasma frequency is only about 3, the scattering is collective (i.e., $k_{epw}\lambda_{De}$ is small, where $k_{epw}$ is the epw wave number and $\lambda_{De}$ is the Debye length), even though the scattering angle is large. The electron temperature can then be deduced from the ion sound velocity, obtained from the measurement of the frequency at which growth is maximum at the scattering wave number.

The experiments were carried out using a large-scale (~1-mm), hot (~1-keV) plasma[6] produced by the OMEGA laser in the geometry shown in Fig. 61.5. Two opposed sets of four UV beams, peaking at time $t = 1.0$ ns, were used to explode a polystyrene (CH) foil of 6-$\mu$m thickness and 600-$\mu$m diameter overcoated with 500 Å of Al. Four beams from each side were used as secondary heating beams and were incident later at $t = 1.6$ ns. The on-target laser energy was typically 50 to 60 J per beam with a pulse duration of 0.60 to 0.65 ns at a wavelength of 351 nm. One of the OMEGA beams was used as a 1.054-$\mu$m pump beam (at $\omega_0$) to drive the IADI and timed to peak at $t = 2.2$ ns. This beam was incident through a phase plate with 3-mm cells and an $f/3.6$ lens to produce a focal spot of 210-$\mu$m diam (at half-maximum), with 36 J in the central Airy lobe, giving a maximum intensity in space and time of ~$1.25 \times 10^{14}$ W/cm$^2$. Another beam was attenuated and used as the $3\omega_0$ probe. A wave plate was used to rotate the (elliptical) polarization of the pump beam to the optimum angle for exciting the epw's being diagnosed. The typical plasma had a center density of 1 to $2 \times 10^{21}$ cm$^{-3}$, which was maintained within a factor of 2 at $T_e \sim 1$ keV for approximately 1 ns. The scale length was of the order of 1 mm at $t = 2.2$ ns.

The scattering geometry is shown in Fig. 61.6. The CTS signal was collected by a focusing mirror at 90° to the Thomson scattering beam and focused onto the detector system (at the opposite port), which included a 1-m spectrometer, a UV streak camera, and a CCD camera. The measured wave vector

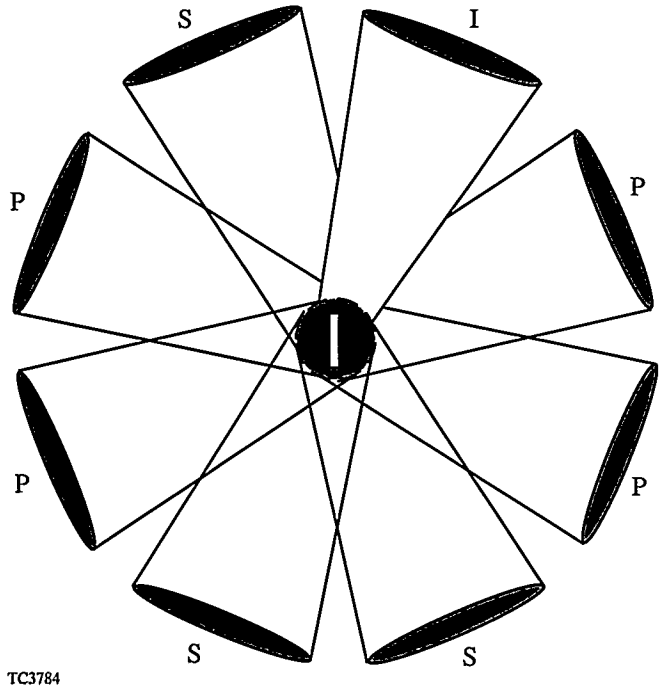


Figure 61.5
Configuration for long-scale-length plasma experiments. A plastic (CH) disk target is first irradiated by four near-normal-incidence, primary beams (P) from each side, forming an approximately spherical plasma. This plasma is then heated by four obliquely incident, secondary beams (S) from each side and one 1054-nm interaction beam (I). The interaction beam (shown shaded) is focused more tightly than the other beams.

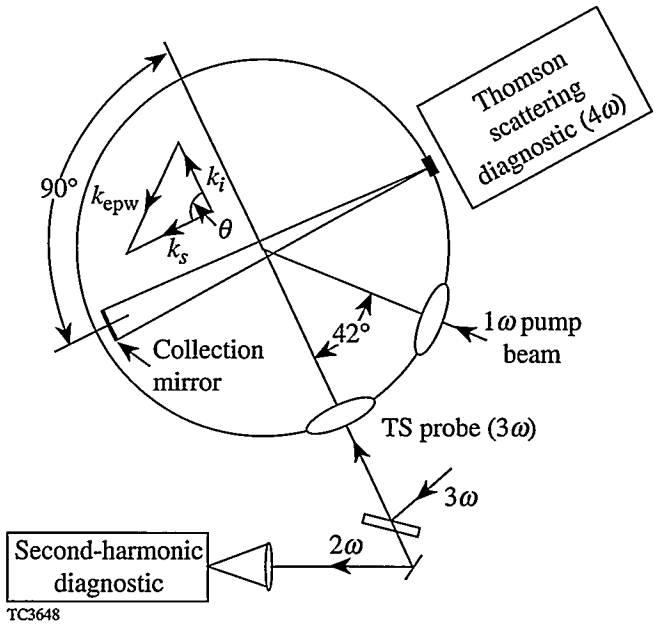


Figure 61.6
Schematic diagram of the experiment in the scattering plane. The IR pump beam is incident 6° below this plane. The initial target normal (the $z$ axis of the simulations) is in the plane perpendicular to the scattering vector $k_s$ and 69° below the scattering plane. It is also 69° from the pump beam. The $k$-matching diagram of the CTS is shown in the inset. Note that $k_{epw}$ is nearly perpendicular to the pump laser.

$k_{epw}$ was nearly parallel to the pump electric field. Simultaneously, the time-resolved, second-harmonic spectrum (through the Thomson-scattering port) was measured using a 1/3-m spectrometer, a streak camera, and another CCD camera.

Collective Thomson scattering[7] is a three-wave process satisfying the $k$-matching condition $k_s = k_i \pm k_{epw}$ and the energy conservation law $\omega_s = \omega_i \pm \omega_{epw}$. (The $k$'s and $\omega$'s are the wave vectors and frequencies of the three waves; the subscripts $i$, $s$, and epw refer to the incident and scattered probe beam and the electron plasma wave.) We have measured the up-shifted signal at $4\omega_0\left(=\omega_i+\omega_{epw}\right)$ to reduce the problems of incoherent harmonic emission and refraction. The scattering angle $\theta$ is given from the $k$-matching condition by $k_{epw}^2 = k_i^2 + k_s^2 - 2k_i k_s \cos\theta$. For the up-shifted scattering, we have $\omega_s \sim 4/3\ \omega_i$ and $k_s \sim 4/3\ k_i$. The geometry of the experiment selected a 90° scattering angle (Fig. 61.6) and $k_{epw} = 2.9 \times 10^5\ \text{cm}^{-1}$. At this angle the CTS signal intensity is maximum for out-of-plane polarization of the probe beam.[7] For $T_e \sim 1$ keV, the observed angle is close to the optimum scattering angle of 89° for measurement of the most unstable IADI mode, which has $k_{epw}\lambda_{De} \sim 0.23$. The density at which the observed $k_{epw}$ is resonant for the IADI depends upon $T_e$, becoming higher as $T_e$ decreases.

Our experiments were guided by two-dimensional calculations using the computer code *SAGE*.[8] Figure 61.7 shows spatial profiles of $n_e$, $T_e$, and ion temperature $T_i$ along the center $z$ axis at a time of 2.2 ns, corresponding to the peak of the pump beam. This timing was chosen so that the center plasma density would be slightly higher than the critical density $n_c \sim 10^{21}\ \text{cm}^{-3}$ of the pump laser. When the pump laser is applied to the preformed plasma, no significant density change is predicted, but the electrons in its path are heated by classical electron-ion collisions as is shown by the hump on the right-hand side of the $T_e$ curve. The peak value of $T_e$ is just above 1 keV. The *SAGE* calculations indicate that 15%–70% of the pump laser energy reaches the instability region, depending on the laser intensity.

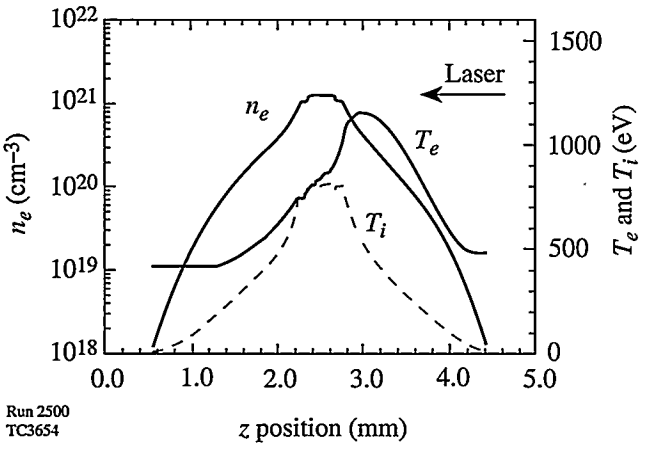


Figure 61.7
Calculated spatial profiles of the electron density $n_e$ and the electron and ion temperatures ($T_e$, $T_i$) at 2.2 ns. The pump laser enters from the right.

Owing to the three-dimensional nature of the experiment, some approximations were necessary. The pump beam was modeled as incident along the target normal ($z$), for consistency with the cylindrical symmetry about this direction assumed by *SAGE*, although the actual angle of incidence was 69°. At 2.2 ns the 0.86 $n_c$ contour, at which the measured epw ($k_{epw} = 2.9 \times 10^5$ cm$^{-1}$) is resonantly excited, is close to a prolate ellipsoid with diameters 560 $\mu$m along and 162 $\mu$m transverse to the $z$ axis. Typical rays are incident at 21° to the ellipsoid normal and see flow velocities $v_f$ of 1 to 2 × $10^7$ cm/s generally directed away from the plasma center. The experimental geometry is such that $v_f \cdot k_{epw} \approx 0$.

We verified that the measured signals were caused by CTS from the IADI-excited epw as follows: (1) the $4\omega_0$ intensity decreased rapidly as the pump laser intensity decreased, and the signal disappeared when the pump was below the IADI threshold (as determined by conventional second-harmonic emission measurements); (2) when the probe beam was turned off, no $4\omega_0$ signal was observed; and (3) the $4\omega_0$ intensity varied drastically (decreased about ten times) when the probe beam polarization was changed from out-of-plane to in-plane. Moreover, the measurements discussed in the remainder of this article are all consistent with standard instability theory for a uniform plasma.[1]

The experimental threshold value of the spatially averaged intensity in the instability region was estimated to be ~(1.4–2.8) × $10^{12}$ W/cm$^2$, based on the measured threshold laser energy for a CTS signal (5 J) and taking into account the collisional attenuation and refraction as estimated by *SAGE*. This result is in satisfactory agreement with the theoretical value[9] of ~(0.8–2.3) × $10^{12}$ W/cm$^2$ calculated using $T_e$ = 0.8 keV (appropriate for a low pump intensity), taking into account the swelling at the instability region and the multiple-species ion sound theory of Ref. 10.

Figure 61.8(a) shows a CTS measurement of the time evolution of the epw spectral density function with $k_{epw} = 2.9 \times 10^5$ cm$^{-1}$. A clear red shift relative to the $4\omega_0$ wavelength is evident. This Stokes peak is due to the primary IADI decay process: in these experiments, where the pump laser energy is less than 50 J, no cascade decay process[11] is observed. The solid curve in Fig. 61.8(b) shows the spectral density function at the time of the peak signal of Fig. 61.8(a) plotted against the normalized frequency shift $(\omega_0 - \omega_{epw})/\Omega_{iaw}$, where $\Omega_{iaw}$ is chosen to center the spectrum on a normalized shift of 1. The CTS timing is not known precisely, but Fig. 61.8(b) is presumed to correspond to 2.2 ns, the peak of the pump beam. The dashed curve gives the IADI growth rate calculated using the experimental parameters; its peak is calculated to occur at $\omega_0 - \omega_{epw} = \Omega_{iaw}$. The IADI resonance condition is thus satisfied, and the normal mode of the iaw is excited. The measured CTS spectrum is consistent with the growth-rate curve. If the pump laser intensity were instead much larger than ten times the threshold, the growth rate peak would shift to a higher frequency and the iaw frequency would increase with the laser intensity (driven mode).

We can now estimate the phase velocity of the iaw. Since the dipole approximation is valid in these experiments, the pump laser wave number is given by $k_0 \sim k_{epw} + k_{iaw} \sim 0$, so that the wave numbers $k_{iaw}$ and $k_{epw}$ are approximately equal in magnitude. The ion-acoustic wave frequency used for the normalization of Fig. 61.8(b) is given by

$$\Omega_{iaw} = 2\pi c \Delta\lambda / \lambda_{4\omega}^2 \approx 9 \times 10^{12} \text{ Hz},$$

where $\Delta\lambda$ is the wavelength shift of the peak of the CTS signal (3.3±0.2 Å). The phase velocity $\Omega_{iaw}/k_{iaw}$ of the iaw is then determined to be about $3 \times 10^7$ cm/s and may now be used to estimate the electron temperature.

The electron temperature depends on the ion-acoustic dispersion relation. To calculate this with greater accuracy, the multiple-ion nature of the plasma was included. Williams *et al.*[10] have obtained fast- and slow-wave solutions for CH plasmas and have shown that the slow wave is the important one, as it is eight times less damped than the fast wave. The phase velocity of the slow wave is effectively independent of

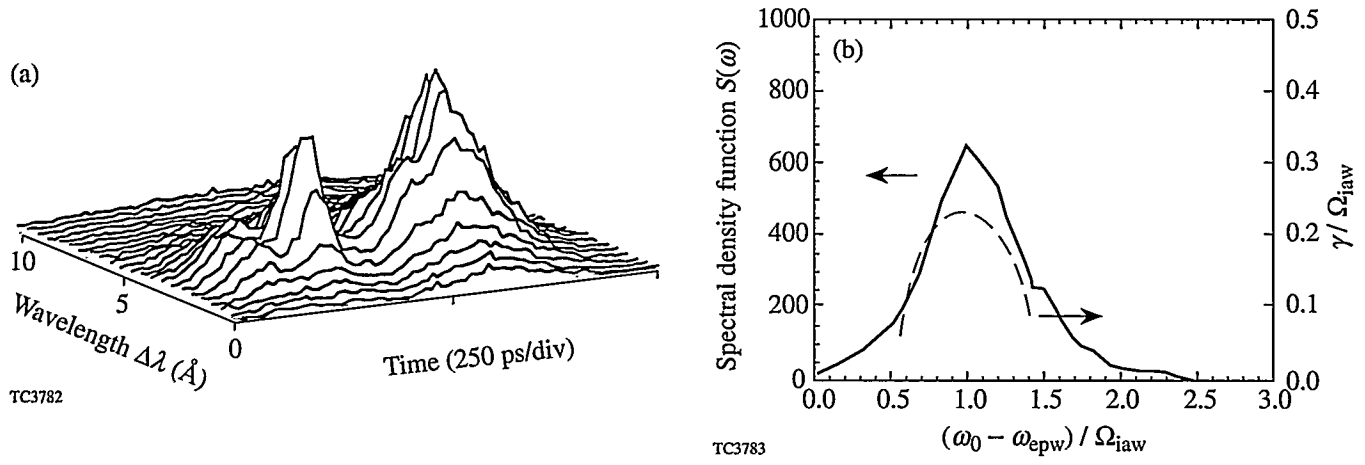


Figure 61.8
(a) Time evolution of the spectral density function of the epw (with $k_{epw} = 2.9 \times 10^5$ cm$^{-1}$) measured by CTS. (b) Solid line: the spectral density function of the same epw at $t \approx 2.2$ ns. Dashed line: the IADI growth rate calculated for a laser intensity five times threshold.

$T_i$ in the range $0.3 < T_i/T_e < 1$, being about 0.8 $(k_B T_e/M)^{1/2}$ or $1.87 \times 10^{-2}\, v_e$, where $M$ is the proton mass, $k_B$ is Boltzmann's constant, and $v_e$ is the electron thermal velocity. The slow iaw frequency at a given wave number is thus an excellent diagnostic for $T_e$: from the measured peak-signal frequency shift and the scattering wave vector (known from the geometry), one immediately obtains the slow iaw velocity and hence $T_e$. In this experiment, the iaw phase velocity is $3 \times 10^7$ cm/s, giving $T_e = 1.5$ keV and $v_e = 1.6 \times 10^9$ cm/s. The theoretical values ($v_e = 1.4 \times 10^9$ cm/s and $T_e = 1.1$ keV) given by the *SAGE* calculation (Fig. 61.7) are somewhat lower than the experimental values (about 13% for $v_e$ and 27% for $T_e$). However, if the complicated nature of the large-scale plasma produced, the possibility of hot spots within the focal spot, and the three-dimensional nature of the experiment are all taken into account, the theoretical and experimental values are in reasonably good agreement.

Several conditions were met that enabled the diagnostic to work well:

- The scattering angle was chosen to be large to measure the most unstable epw.
- Between the thresholds for the slow-ion-wave IADI ($I_{th}$) and the fast-ion-wave IADI (8 $I_{th}$), only the former was significantly excited.
- The refraction of the probe beam itself was small (less than 7% for this experiment) and that of the up-shifted signal even smaller.
- The complications of plasma flow effects on the diagnostic were minimized because the detection vector ($k_{epw} = k_s - k_i$) was perpendicular to the direction of plasma expansion.
- Because this is a collective scattering, the scattering rate is much larger than that from thermal electrons, and it is relatively easy to exceed the background bremsstrahlung emissions.
- The experimental design assured that only a narrow range of densities could contribute to the observed signals.[12]

We also measured the conventional second-harmonic signal (from the coupling between two epw's) and found its threshold laser energy to be comparable to that of the CTS threshold energy, consistent with the presence of the IADI. The Stokes signal is spread over a large wavelength range and decreases gradually without a distinct peak. This finding indicates that the epw intensity is spread over a wide range of wave numbers in the large-scale plasma.

In summary, we have studied the ion-acoustic decay instability in a large-scale-length (~1-mm), hot (~1-keV) plasma, which is relevant to a laser fusion reactor target, and have shown that the IADI threshold is low. We have also developed a novel collective Thomson scattering diagnostic for the interaction of a 1-$\mu$m pump laser near its critical density, using the third harmonic of the interaction laser at a 90° scattering angle, and we have used this diagnostic to measure the electron plasma wave excited by the ion-acoustic decay insta-

bility near the critical density ($n_e \sim 0.86\, n_c$). The frequency of the detected wave obtained from this diagnostic has been used to determine the electron temperature in the interaction region, yielding a result reasonably close to that predicted by the *SAGE* computer code.

## ACKNOWLEDGMENT

This work was carried out in collaboration with K. Mizuno, B. S. Bauer, J. S. DeGroot, R. P. Drake, and B. Sleaford of the Plasma Physics Research Institute at the Lawrence Livermore National Laboratory and the University of California at Davis. We thank T. W. Johnston and E. A. Williams for many useful discussions, and W. L. Kruer and E. M. Campbell for their help and encouragement. This work was supported by the U.S. Department of Energy National Laser Users Facility at the University of Rochester, the U.S. Department of Energy Office of Inertial Confinement Fusion under Cooperative Agreement No. DE-FC03-92SF19460, and the U.S. Department of Energy under contract W-7405-ENG-48 with the Lawrence Livermore National Laboratory.

## REFERENCES

1. W. L. Kruer, *The Physics of Laser Plasma Interactions*, Frontiers in Physics, Vol. 73 (Addison-Wesley, Redwood City, CA, 1988); K. Nishikawa, J. Phys. Soc. Jpn. **24**, 916 (1968); **24**, 1152 (1968).

2. C. Yamanaka *et al.*, Phys. Rev. Lett. **32**, 1038 (1974); K. Tanaka, W. Seka, L. M. Goldman, M. C. Richardson, R. W. Short, J. M. Soures, and E. A. Williams, Phys. Fluids **27**, 2187 (1984).

3. K. Mizuno, P. E. Young, W. Seka, R. Bahr, J. S. De Groot, R. P. Drake, and K. G. Estabrook, Phys. Rev. Lett. **65**, 428 (1990); K. Mizuno, R. P. Drake, P. E. Young, R. Bahr, W. Seka, and K. G. Estabrook, Phys. Fluids B **3**, 1983 (1991).

4. K. Mizuno *et al.*, Phys. Rev. Lett. **52**, 271 (1984); K. Mizuno, F. Kehl, and J. S. DeGroot, Phys. Rev. Lett. **56**, 2184 (1986).

5. D. F. DuBois, H. A. Rose, and D. Russell, Phys. Rev. Lett. **66**, 1970 (1991).

6. W. Seka, R. S. Craxton, R. E. Bahr, D. L. Brown, D. K. Bradley, P. A. Jaanimagi, B. Yaakobi, and R. Epstein, Phys. Fluids B **4**, 432 (1992).

7. J. Sheffield, *Plasma Scattering of Electromagnetic Radiation* (Academic Press, New York, 1975).

8. R. S. Craxton and R. L. McCrory, J. Appl. Phys. **56**, 108 (1984).

9. There is some uncertainty in this estimate, principally because the local electric field, which determines the IADI threshold, depends on the angle between the pump laser and the plasma density gradient at the instability region, due to the angular dependence of the swelling.

10. E. A. Williams *et al.*, submitted to Physics of Plasmas.

11. The cascade process for a fixed $k_{epw}$ is that $\omega_{epw}^{(n)} = \omega_{epw}^{(n+1)} + \omega_{iaw}^{(n+1)}$, and $k_{epw}^{(n)} = k_{epw}^{(n+1)} + k_{iaw}^{(n+1)}$ (which indicates that

$$\left|k_{epw}^{(n)}\right| = \left|k_{epw}^{(n+1)}\right| = 1/2\left|k_{iaw}^{(n+1)}\right| ,$$

where $n = 1, 2 \ldots$ , and $n = 1$ is the epw excited by the primary IADI process).

12. The epw's excited at densities above $0.86\, n_c$ have smaller wave numbers and cannot produce the observed wave vector by propagation. The epw's driven at densities much below $0.86\, n_c$ are very strongly Landau damped.

# Frequency-Domain Interferometer for Measurement of the Group-Velocity Walkaway of Ultrashort Pulses in Birefringent Media

A new technique based on frequency-domain interferometry (FDI)[1,2] has been used to measure the group-velocity walkaway (GVW) of ultrashort pulses in birefringent media. As the name implies, this technique is based on the spectral interference of two short pulses in the frequency domain and makes use of the intrinsic phase delay between the fast and slow modes of a birefringent medium. Due to the different group delays, two pulses launched along the fast and slow axes will come out of the medium at different times. In the frequency domain, two temporally separated pulses interfere in the same way that two waves with different frequencies do in the time domain. In the frequency-domain interferometer described here, measurement of the modulation period of the interference fringes in the frequency domain gives the GVW directly without the need for further assumptions about the properties of the light source. By analogy with an ordinary interferometer, the two optical axes of the birefringent medium can be regarded as two interfering arms. A polarizer placed at the output end of the medium combines the two field components to generate interference fringes in the frequency domain. Temporally separated pulses can interfere owing to the linear dispersion of the grating in a spectrometer.[1,2] Different frequency components propagate along different directions, resulting in a frequency-dependent time delay. Therefore, two temporally separated pulses can physically overlap on the detector surface of the spectrometer. In comparison with other methods, the experimental setup of our interferometer is quite simple, and the alignment is very easy. Of greater significance is the fact that the experimental data is directly related to the GVW and no further curve fitting is needed.

To understand the physics of the frequency-domain interferometer, we must understand the properties of a spectrometer. A simplified version of a spectrometer is shown in Fig. 61.9. The incident beam is collimated and has a diameter $D$. The incident angle to the grating is $i$, while the diffracted angle is $\alpha$. Assuming two pulses with pulse width $\tau_p$ that are separated by $T$, we find that the amplitude fronts of these two pulses are no longer parallel to the phase fronts after the grating. At the focus of the image lens, each pulse is temporally stretched to a duration of $DN\lambda/\cos(i)c$, where $N$ is the groove number of the grating, $\lambda$ is the wavelength of the pulses, and $c$ is the speed of light. The two separate pulses can physically overlap for a time $t_0$ in at the focal (frequency) plane, provided that the original separation $T$ is less than the grating-induced stretching $DN\lambda/\cos(i)c$ shown in Fig. 61.9.

### FDI for the Measurement of Polarization Mode Dispersion of Single-Mode Optical Fibers

Single-mode optical fibers have seen increasing use in coherent optical transmission systems and as polarization-dependent fiber-optic sensors. A knowledge of the polarization properties of single-mode fibers is of fundamental importance in these applications since these properties govern the degree and state of the polarization of the radiation. It is well-known that birefringence in optical fibers can be induced by

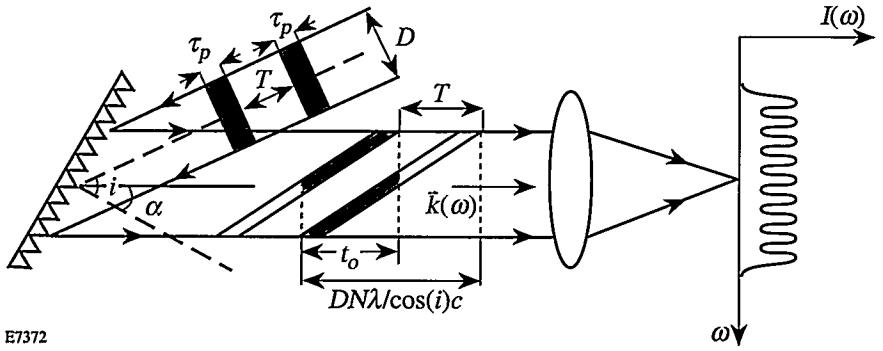


Figure 61.9
A simplified diagram illustrating temporal stretching of short pulses in a spectrometer. The incident angle to the grating is $i$; the diffracted angle is $\alpha$.

built-in stress or by geometric deformation of the fiber core. The most important parameters characterizing birefringent fibers are the polarization mode dispersion (PMD) and modal birefringence (MB). Polarization mode dispersion is the group delay time difference between two orthogonally polarized $HE_{11}$ modes, while modal birefringence is the refractive index difference between these two modes. In optical fiber communication systems, the presence of PMD results in bandwidth limitations.[3] Polarization mode dispersion has two contributions: one is the phase delay, which is proportional to modal birefringence; the other arises from dispersion difference between two modes. Since the first experimental verifications of PMD in birefringent optical fibers made by Rashleigh and Ulrich,[4] many methods for measuring PMD in single-mode fibers have been reported.[4–18] These methods fall into four categories: optical short-pulse methods,[7] frequency domain techniques,[8,9] interferometric methods,[4,8–16] and optical heterodyne techniques.[17–18] The white-light interferometric method has proved to be very accurate and applicable to meter-length samples.[4,16]

The configuration of the frequency-domain interferometer as used in our experiment is shown schematically in Fig. 61.10. The birefringent axes are labeled as $x$ and $y$; the laser light propagates along the $z$ direction. Two identical pulses temporally displaced by $T$ are launched into the birefringent fiber with their polarization directions aligned to the $x$ and $y$ axes, respectively. At the input plane ($z = 0$), the electric fields of these two pulses can be expressed by

$$\begin{aligned} E_x(t, z=0) &= E(t)\exp(i\,\omega_0\,t) \\ E_y(t, z=0) &= E(t-T)\,\exp[i\,\omega_0(t-T)], \end{aligned} \tag{1}$$

where $E(t)$ is the slowly varying envelope of the two pulses and $\omega_0$ is the carrier frequency of the laser pulses. At the exit end of the fiber, the Fourier transformations of the electric fields are

$$\begin{aligned} E_x(\omega, z=L) &= E(\omega-\omega_0)\exp[-i\,\beta_x(\omega)\,L] \\ E_y(\omega, z=L) &= E(\omega-\omega_0)\exp[-i\,\beta_y(\omega)\,L] \\ &\quad \times \exp(-i\,\omega\,T), \end{aligned} \tag{2}$$

where $E(\omega-\omega_0)$ is the Fourier transform of $E(t)$ and $\beta_x(\omega)$ and $\beta_y(\omega)$ are propagation constants of the $x$ and $y$ modes.

A polarizer with its transmission axis set to 45° with respect to the $x$ and $y$ axes combines the two electric fields:

$$E_{\text{out}}(\omega, z=L) = \frac{1}{2}\left[E_x(\omega, z=L) + E_y(\omega, z=L)\right]. \tag{3}$$

The power spectrum detected by a spectrometer can be expressed as

$$I(\omega) = \frac{1}{4}\left|E(\omega-\omega_0)\right|^2\left\{1+\cos\left[\Delta\beta(\omega)L+\omega T\right]\right\}, \tag{4}$$

where $\Delta\beta(\omega) = \beta_x(\omega) - \beta_y(\omega)$ is the modal birefringence and can be expanded as follows:

$$\begin{aligned} \Delta\beta(\omega) &= \Delta\beta(\omega_0) + \frac{d\Delta\beta(\omega_0)}{d\omega}\Delta\omega \\ &\quad + \frac{1}{2}\frac{d^2\Delta\beta(\omega_0)}{d\omega^2}\Delta\omega^2 + \ldots, \end{aligned} \tag{5}$$

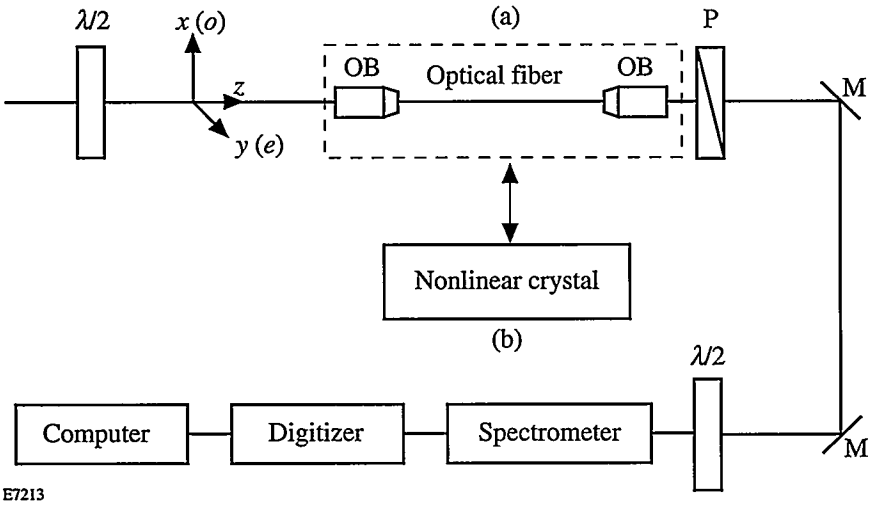


Figure 61.10
Experimental setup for measurement of GVW in birefringent media, where λ/2 = half-wave plate, OB = microscope objectives, P = polarizer, and M = mirror. Linearly polarized light is coupled into the birefringent sample with the polarization direction aligned 45° with respect to the optic axes. The microscope objectives and birefringent fiber (a) were replaced with CDA, KDP, or KD*P (b) for measurements of GVW in nonlinear crystalline media.

where $d\Delta\beta/d\omega$ is the polarization mode dispersion. The third term in Eq. (5) is the difference of group-velocity dispersion (GVD), which describes the difference in pulse spreading for the two principal axes. For subpicosecond pulses, the dispersion distance (the distance at which pulse width becomes twice the initial value) could be shorter than 1 m.[19] This term can be ignored, as pointed out in Ref. 4, since the difference in temporal spreading due to GVD is still negligible. Substituting Eq. (5) into Eq. (4) gives

$$I(\omega) = \frac{1}{4}\left|E(\omega-\omega_0)\right|^2 \times \left\{1+\cos\left[\Delta\beta(\omega_0)L+\frac{d\Delta\beta}{d\omega}\Delta\omega L+\omega T\right]\right\}. \quad (6)$$

From Eq. (6), the periodicity of the interference fringes is given by

$$\Omega = 2\pi\Big/\left(\frac{d\Delta\beta}{d\omega}L+T\right). \quad (7)$$

The polarization mode dispersion can be determined in terms of the measured quantity $\Omega$, the fringe spacing in the frequency domain. From Eq. (7), we have

$$\frac{d\Delta\beta}{d\omega} = \left(\frac{2\pi}{\Omega}-T\right)\Big/L. \quad (8)$$

A careful examination of Eq. (8) reveals that there are two possible methods of measuring PMD. In the first method, no optical delay is needed ($T=0$), and a measurement of the fiber length $L$ and interference spacing $\Omega$ gives the required result of PMD. This method has the advantage in that it is very simple to implement. The second method relies on adjustment of the temporal delay such that $\Omega=\infty$, which makes PMD $= -T/L$. Physically, this means that the predelay $T$ is set so that two pulses come out of the fiber at the same time, resulting in no interference in the frequency domain.

The experimental setup is shown in Fig. 61.10. The laser beam originates from an actively mode-locked Nd:YLF oscillator that produces a 50-ps pulse train at a 1054-nm wavelength with a 100-MHz repetition rate. The pulse train goes through an 800-m, single-mode optical fiber that increases the bandwidth from 0.3 Å to 31.6 Å through the combined effects of self-phase-modulation (SPM) and GVD.[20] The pulses are then temporally compressed to 1 ps by a double-pass grating pair. Two microscope objectives are used to couple the laser beam into and out of a highly birefringent fiber (3M product, FS-HB-5651). A $\lambda/2$-wave plate placed in front of the fiber was used to control the polarization direction of the incident laser beam. A polarizer placed at the exit end of fiber was used to combine the electric field components of the fast and slow modes. Finally the collimated output beam was sent to a spectrometer equipped with an optical multichannel analyzer (OMA). Another $\lambda/2$-wave plate placed in front of the spectrometer was used to match the polarization direction of the laser beam to that of the grating inside the spectrometer. The waveguide parameters of the fiber used in the experiment are listed in Table 61.I.

Table 61.I: Waveguide parameters of the fiber used in the experiment.

| | |
|---|---|
| Fiber length | 2.750 m |
| Mode field diameter | 6.8 $\mu$m |
| Fiber diameter | 100 $\mu$m |
| Operating wavelength | 1.060 $\mu$m |
| Cutoff wavelength | 1.000 $\mu$m |
| Birefringence | $4\times10^{-4}$ |
| Loss | <2 dB/km |

The input spectrum $\left[\left|E(\omega-\omega_0)\right|^2\right]$ is shown in Fig. 61.11. The power spectrum has nearly a square-top shape with a width of about 31.6 Å. In the experiment, the input polarization

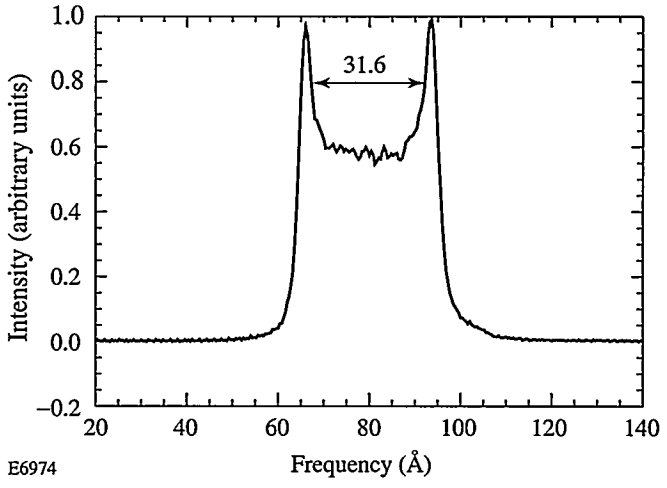


Figure 61.11
The spectrum of the incident pulses applied to the fiber. The spectrum shape is typical of the combined effects of SPM and GVD. The peak-peak width is 31.6 Å.

direction was adjusted to 45° with respect to the fast and slow axes of the birefringent fiber. The polarizer was also aligned to the same angle as described in Eq. (3). The frequency-domain interference fringes are shown in Fig. 61.12. The least-squares method was used to fit Fig. 61.12 using Eq. (6). The value of $\Omega$ was found to be 22.7±0.1 pixels, giving a modulational period of the interference fringes of 9.13±0.04 Å. The length of the fiber was measured to an accuracy of 1 mm. From Eq. (8), the PMD is found to be 1.42 ps/m with an accuracy of 1%. The term $d\Delta\beta/d\omega$ of Eq. (8) can also be expressed as

$$\frac{d\Delta\beta}{d\omega} = \frac{\Delta n}{c} + \frac{\omega}{c}\frac{d\Delta n}{d\omega}, \tag{9}$$

where $\Delta n$ is the modal birefringence and $c$ is the speed of light. Substituting the value for $\Delta\Omega$ from Table 61.I into Eq. (9) makes the first term on the right-hand side of Eq. (9) equal to 1.3±0.1 ps/m, which is very close to the measured PMD. The uncertainty comes from the fact that there is not enough information about the sample fiber. The contribution of the second term in Eq. (9) is much smaller than the first term, which is true in most stress-induced birefringent fibers.[20,21]

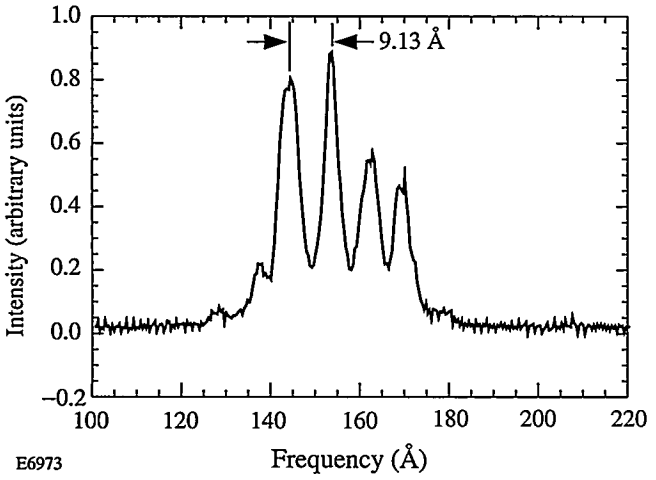


Figure 61.12
Frequency-domain interference fringes for the birefringent fiber. The fringe spacing is measured to be 9.13 Å.

### FDI for the Measurement of GVW in Nonlinear Crystals

Frequency conversion in nonlinear crystals is an important method for obtaining coherent radiation sources for wavelengths not covered by lasers and is especially valuable in applications involving ultrashort laser pulses. Frequency conversion includes second (and higher) harmonic generation,[22–24] optical parametric oscillators (OPO), and optical parametric amplifiers (OPA).[25,26] A major limitation in ultrashort frequency conversion is the GVW between the ordinary (o-wave) and extraordinary (e-wave) waves due to the different group velocities for the two polarizations.[27] Since birefringence and dispersion exist in all nonlinear crystals, the GVW effect becomes a fundamental factor in determining the frequency-conversion efficiency. The walkaway has been used to increase the conversion efficiency in type-II doubling of 1-$\mu$m, 1-ps laser pulses by using a second crystal to predelay the extraordinary wave relative to the ordinary wave.[22,23] It was also found that the pulse duration could be reduced from 1 ps to 200 fs.[28] Chien *et al.*[24] have studied the conversion efficiency of high-power ultrashort pulses and have found that the GVW between two polarizations causes reconversion of the second harmonic back to the fundamental frequency.

The GVW between the e- and o-wave is of fundamental importance in the frequency conversion of ultrashort pulses. Typically, the walkaway is inferred by measuring the refractive indices and the dispersion of the e- and o-waves. Most values of the refractive index have been obtained by the minimum-deviation method (MDM) and are accurate to the fifth decimal place.[29] Extensive measurements of refractive indices of nonlinear crystals isomorphic to $KH_2PO_4$ have been made by Kirby and DeShazer.[30] Although MDM provides an accurate measurement of the refractive indices of e- and o-waves, it is not convenient for many applications involving nonlinear frequency conversion. Since the MDM measurement requires a high-quality prism made from the sample crystal, this method can be expensive and impractical for ordinary frequency-conversion applications. The dispersion properties are usually obtained by fitting to the Sellmeier or Zernike formula,[31,32] which requires multiple measurements with different light frequencies. Since narrow spectral lines of different lamps are used in MDM, it is possible that no experimental data exists for some specific wavelength that is used in frequency-conversion experiments. Another disadvantage of this method is that the refractive indices of o- and e-waves are a function of propagation direction. All calculations require that the locations of optical axes and the propagation angle, as well as the relative angle between the propagation direction and the optical axis, be known accurately.

In this section we report on an alternative method that allows direct measurement of the GVW between the e- and o-waves in a birefringent crystal. There are several other advantages of this technique as far as nonlinear frequency conversion is concerned. In practical applications of frequency

conversion involving short pulses, it is desirable to know the walkaway parameter for the laser frequency involved. Since the walkaway can be measured using the same laser pulses that will be used in frequency conversion, the measured data about the walkaway is immediately relevant. For the applications involving cascade processes of frequency conversion of short pulses, it is crucial to know either the polarization direction or the crystal orientation that corresponds to the minimum walkaway, so that the orientations of nonlinear crystal for the next stage of frequency conversion can be optimized.[28] To our knowledge, this method provides the first direct measurement of angular dependence of the GVW.

From Eq. (4), the power spectrum detected in the spectrometer takes the following form:

$$I(\omega)=\frac{1}{4}\left|E(\omega-\omega_0)\right|^2\left[1+\cos(\phi_0+\Delta\tau\Delta\omega)\right], \qquad (10)$$

where $E(\omega-\omega_0)$ is the spectrum of the incident pulse, $\phi_0$ is a constant, $\Delta\tau$ is the temporal delay between the two pulses traveling along the fast and slow axes of the crystal, and $\Delta\omega=\omega-\omega_0$. The GVW is therefore equivalent to the periodicity of the interference pattern in the frequency domain.

The experimental setup is as shown in Fig. 61.10, except that the birefringent fiber and microscope objectives used for in-and-out coupling the incident light are replaced by a nonlinear crystal. The frequency-domain interference fringes for a 2.5-cm-thick CDA crystal are shown in Fig. 61.13. A least-squares method is used to fit Fig. 61.13 using Eq. (10), as shown by the dashed curve. There are three sources of error in the measurements: (1) measuring the length of the crystal, (2) calibrating the spectrometer, and (3) determining the spacing of the interference fringes. The error bar for thickness measurement is 1%. The calibration was performed using five spectral lines of a rubidium lamp ranging from 1053 nm to 1073 nm. The spectral lines were fitted with a Lorentzian line shape, and the overall error bar in the calibration was found to be 0.2%. The least-squares fit for the interference fringes gave an error of 0.3%. The largest source of error is in the measurement of the crystals' thickness. After taking into account these three error sources, we found that the error in determining the temporal walkaway is about 1%. The experimentally determined GVW values for several commonly used nonlinear crystals are listed in Table 61.II, along with the cut angles and lengths of the tested crystals. The last column of Table 61.II shows the calculated values of the GVW based on the dispersion data of Ref. 30; the measured results are very close to the calculated ones. As mentioned previously, this method can also be used to measure the length of a birefringent crystal if its GVW parameter is known. The last row of Table 61.II shows the length of a KDP-I crystal determined by this method using the calculated result of the walkaway; the resolution is about 50 $\mu$m.

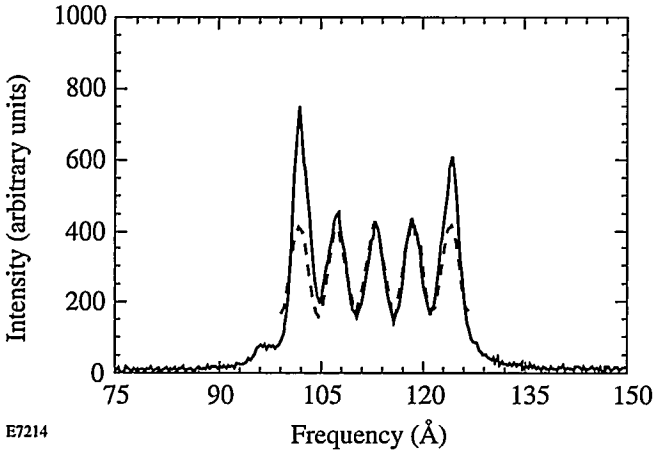


Figure 61.13
Frequency-domain interference fringes of the CDA-I sample. The fringe spacing is measured to be 6.7 Å. The solid line is the experimental data, while the dashed line is the theoretical fitting.

Table 61.II: Parameters of nonlinear crystals and measured walkaway.

| Crystal | Cut angle | Length ×2 (cm) | Walkaway[(a)] (ps/cm) | Walkaway[(b)] (ps/cm) |
|---|---|---|---|---|
| CDA I | 85.0° | 2.50 | 1.00±0.01 | 1.01 |
| KDP* II | 53.7° | 1.50 | 0.94±0.02 | 0.97 |
| KDP II | 59.2° | 1.90 | 1.35±0.02 | 1.33 |
| KDP I | 41.2° | 1.029±0.005 | – | 0.79 |

(a) Measured results
(b) Calculated results

Since the refractive index of the extraordinary wave is a function of propagation direction, the GVW will also be affected by the direction of propagation, as shown by the plot of walkaway dependence versus propagation angle in Fig. 61.14. The angle is measured with respect to the phase-matching angle of the crystal (KDP-II) in the YZ plane. The scattered triangles are experimental data, while the solid curve is the theoretical prediction based on the material dispersion.[24] The experimental data fits the theory very well, with an accuracy of 1%. The angle shown in Fig. 61.14 is the angle inside the crystal as obtained by Snell's law. The propagation

distance is also a function of angle due to the cube-shaped crystal, which has been taken into account in Fig. 61.14. In our experiment, the pulses were not transform limited (i.e., the pulses are slightly chirped). It is believed that the chirp may be responsible for the finite visibility of the interference patterns, which could affect the accuracy of the measurements when visibility is poor.

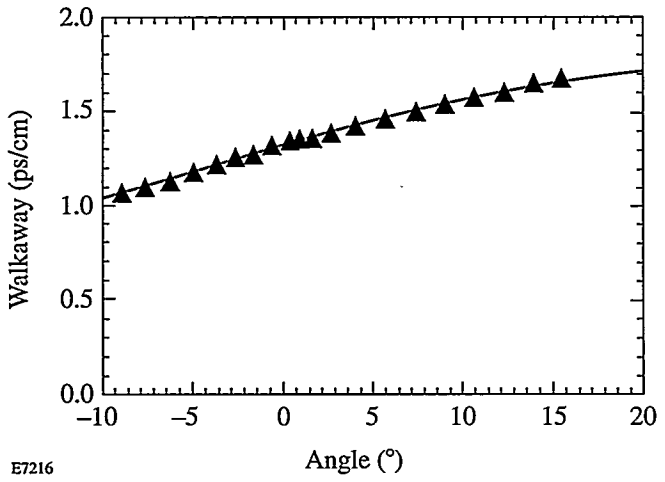


Figure 61.14
Dependence of the group-velocity walkaway on the propagation direction. The angle is measured with respect to the phase-matching angle of the sample (KDP-II).

## Conclusions

A new technique based on frequency-domain interferometry has been used to measure the polarization mode dispersion of birefringent media. In contrast to the usual interferometric methods that measure the interference visibility as a function of optical delay between two interfering arms, we measure the periodicity of the interference fringes in the frequency domain by using short, broadband optical pulses. No curve fitting is needed to find the values of PMD since the measured modulation period of the fringes is directly related to PMD. Two schemes of measurement, differing only in the requirements for an optical delay line, have been presented, and one method (without the delay line) was demonstrated experimentally. Advantages of this new method include (1) direct, real-time measurement of the group-velocity walkaway, which is useful for applications in which the GVW can be controlled by tuning the crystals; (2) values of GVW at the appropriate wavelength for most frequency-conversion applications since the source is the same as that used in the nonlinear frequency conversion; and (3) determination of the angular dependence of GVW, which is useful for experiments involving serial frequency conversion in that the walkaway can be compensated for in the second crystal.[28] Compared to other methods, the frequency-domain interferometric technique provides reasonably good accuracy, experimental simplicity, and linearity in the sense that it is not dependent on the laser power.

## ACKNOWLEDGMENTS

This work was supported by the U.S. Department of Energy, Office of Inertial Confinement Fusion under Cooperative Agreement No. DE-FC03-92SF19460, the University of Rochester, and the New York State Energy Research and Development Authority. The support of DOE does not constitute an endorsement by DOE of the views expressed in this article.

## REFERENCES

1. N. F. Scherer *et al.*, J. Chem. Phys. **95**, 1487 (1991).
2. E. Tokunaga, A. Terasaki, and T. Kobayashi, Opt. Lett. **17**, 1131 (1992).
3. I. P. Kaminow, IEEE J. Quantum Electron. **QE-17**, 15 (1981).
4. S. C. Rashleigh and R. Ulrich, Opt. Lett. **3**, 60 (1978).
5. Y. Sasaki, N. Shibata, and J. Noda, Electron. Lett. **18**, 997 (1982).
6. M. Monerie, P. Lamouler, and L. Jeunhomme, Electron. Lett. **16**, 907 (1980).
7. Y. Yamabayashi and M. Saruwatari, Electron. Lett. **19**, 239 (1983).
8. K. Mochizuki, Y. Namihira, and H. Wakabayashi, Electron. Lett. **17**, 153 (1981).
9. N. Shibata, M. Tateda, and S. Seikai, IEEE J. Quantum Electron. **QE-18**, 53 (1982).
10. N. Imoto and M. Ikeda, IEEE J. Quantum Electron. **QE-17**, 542 (1981).
11. S. C. Rashleigh, Opt. Lett. **7**, 294 (1982).
12. S. C. Rashleigh, *ibid.* **8**, 336 (1983).
13. A. B. Grudinin, G. L. Dyankov, and V. B. Neustruev, Sov. J. Quantum Electron. **16**, 1522 (1986).
14. L. Thévenaz, V. de Coulon, and J.-P. Von der Weid, Opt. Lett. **12**, 619 (1987).
15. J.-P. Von der Weid, L. Thévenaz, and J.-P. Pellaux, Electron. Lett. **23**, 151 (1987).
16. W. J. Bock and W. Urbanczyk, Appl. Opt. **32**, 5841 (1993).
17. N. Shibata, M. Tsubokawa, and S. Seikai, Electron. Lett. **20**, 1055(1984).
18. N. Shibata, M. Tsubokawa, and S. Seikai, Opt. Lett. **10**, 92 (1985).
19. G. P. Agrawal, *Nonlinear Fiber Optics* (Academic, Boston, 1989), Chaps. 3–5.
20. N. K. Sinha, Phys. Chem. Glasses **18**, 66 (1978).

21. N. Shibata *et al.*, J. Opt. Soc. Am. **73**, 1972 (1983).

22. Y. Wang and R. Dragila, Phys. Rev. A **41**, 5645 (1990).

23. Y. Wang, B. Luther-Davis, Y.-H. Chuang, R. S. Craxton, and D. D. Meyerhofer, Opt. Lett. **16**, 1862 (1991).

24. C. Y. Chien, G. Korn, J. S. Coe, J. Squier, G. Mourou, and R. S. Craxton, submitted to Optics Letters.

25. R. L. Byer, J. Opt. Soc. Am. B **10**, 1656 (1993).

26. R. L. Byer, *ibid.* **10**, 2148 (1993).

27. R. W. Boyd, *Nonlinear Optics* (Academic Press, San Diego, 1992).

28. Y. Wang and B. Luther-Davies, Opt. Lett. **17**, 1459 (1992).

29. W. L. Wolfe, "Properties of Optical Materials," in *Handbook of Optics*, edited by W. G. Driscoll (McGraw-Hill, 1978), Sec. 7, pp. 7-1–7-157.

30. K. W. Kirby and L. G. DeShazer, J. Opt. Soc. Am. B **4**, 1072 (1987).

31. M. Born and E. Wolf, *Principles of Optics*, 6th ed. (Pergamon, Oxford, 1986).

32. F. Nernike, Jr., J. Opt. Soc. Am. **54**, 1215 (1964).

# Transient Flux Dynamics in Optically Irradiated YBCO Thin-Film Switches

Fast switching using thin films of high-temperature superconductor (HTS) has been a subject of interest in recent years. Several high-power applications, including fault current limiters, generation of fast current pulses, and energy extraction from superconducting magnetic energy storage (SMES), require an opening switch with high current-carrying capacity and fast rise times. The property requirements of the opening switch are diverse and depend on the application.[1] In this article, we discuss a contactless, inductively coupled opening switch that employs $YBa_2Cu_3O_{7-x}$ (YBCO) thin films.

In its simplest form, the switch consists of a film of HTS placed between the primary and secondary coils of a transformer, shown conceptually in Fig. 61.15.[2] A current source drives current in the primary coil. If the film is superconducting, it screens the magnetic flux, and there is no flux coupling between the two coils. If a load is connected across the secondary coil, the voltage across the load is zero. Upon illumination by a laser pulse, the film makes a transition to the normal state, allowing magnetic flux produced by the primary current to couple into the secondary coil. The temporal change of flux through the secondary coil results in an induced voltage $\left(V = -\partial\Phi/\partial t\right)$ across the load. A similar contactless arrangement has been used to measure critical temperature and critical current density of films.[3] Optically thick films (500–800 nm) were used in our experiment to enhance the current-carrying capacity. A ring of 5-mm width, 1-mm thickness, and 20-MA/cm$^2$ current density will correspond to a current of 1 kA that can produce a field $\left(B = \mu_0 I/2a\right)$ of about 0.12 T at the center of the ring. This order-of-magnitude estimate suggests that a large field can be excluded using thin films with very high critical current density ($J_c$).

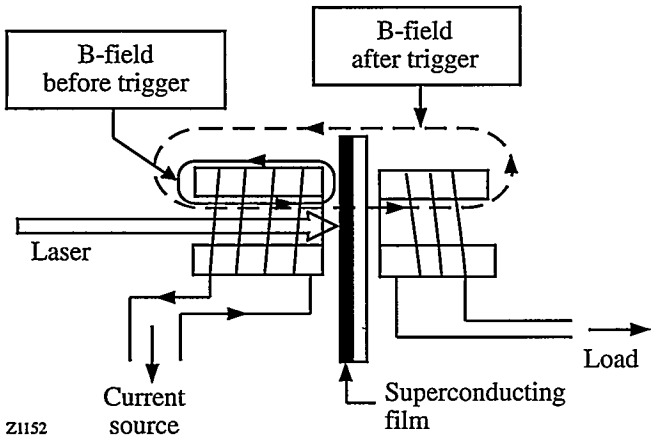


Figure 61.15
A conceptual diagram of the high-temperature superconducting thin-film switch. The superconducting film acts as a magnetic shield until triggered.

Figure 61.16 shows the configuration of our switching system, which has three components: the source (the primary coil in our discussion), the switch (the superconducting film), and the load circuit (the secondary coil and load). The superconducting magnet serves as the primary coil (source), while two superconducting films (switch) are placed on either side of the secondary coil.

## Theory

For the described switch configuration, if the applied field, which is perpendicular to the film surface, is below the lower critical field ($H_{c1}$) of the superconductor, the superconductor is in a reversible Meissner state and will initially screen the flux produced by the magnet from coupling to the secondary coil. When it is driven to its normal state by heating with a laser pulse, the magnetic flux moves radially inward and produces a voltage pulse across the secondary coil. As the film cools down and returns to its superconducting state, it will expel the flux. Repetitive switching can then be performed with a train of laser pulses.[2] If the applied field exceeds $H_{c1}$, the flux will still be excluded from the superconductor up to a certain field strength depending upon the critical current density of the film (critical state model). Beyond this point, only a partial flux exclusion will take place as the screening currents in the superconductor redistribute to exclude the flux from the center of the film. Single-shot switching can still be performed under these conditions, allowing the excluded flux to couple to the secondary coil. As the film cools into the superconducting

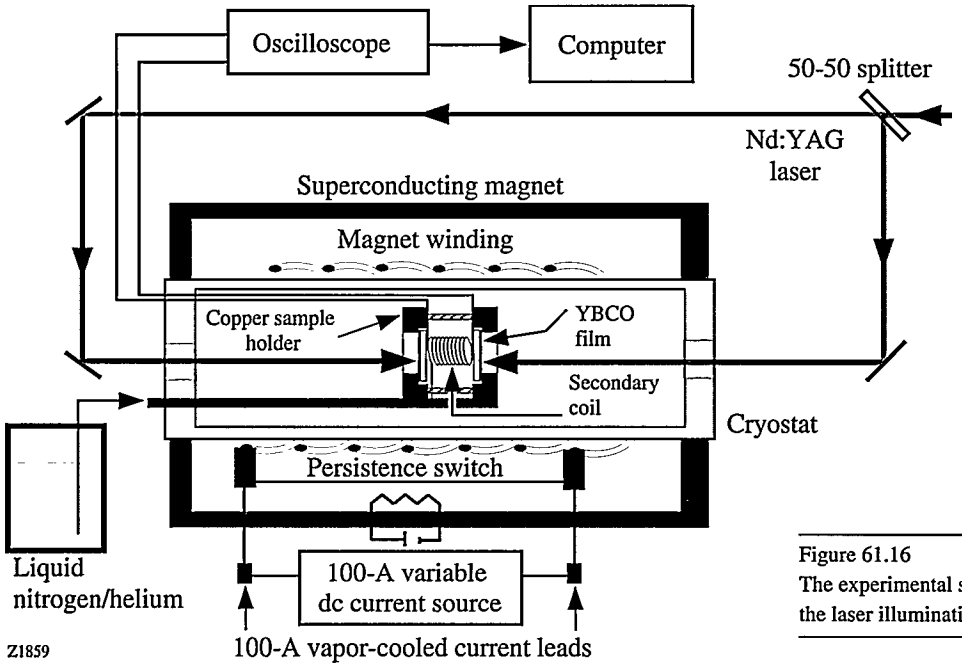


Figure 61.16
The experimental setup for the high-field experiments showing the laser illumination scheme and the data acquisition system.

state, however, it will no longer expel the penetrated flux. Because the thin-film geometry produces a large demagnetization factor that causes enhancement of the magnetic field at the edges of the film, some field penetration occurs at the edges, even when the applied field is less than $H_{c1}$.

To understand the motion of flux inside the superconductor following its transition into the normal state, we must analyze the distribution of screening currents and magnetic fields. Temporal variation of the flux in the secondary coil, which is inductively coupled to the superconducting films, must also be investigated.[4] We first calculate the current and field distribution in a film of thickness $t$, shaped like a circular disk of radius $R$, for a given externally applied field ($B_{ext}$) and critical current density ($J_c$) by dividing the disk into a set of $n$ concentric circular strips of equal width ($w = R/n$, where $n = 25$ for our calculation). Starting from the current-density distribution $J(r)$ required for complete flux exclusion inside the film, the $J_c$-limited distribution is calculated iteratively. At each step of the iteration the field is allowed to penetrate from the edge by the width of one ring more than the previous step. If the field penetrates to a radius $a$, $J(r < a)$ is recalculated to make the region $0 < r < a$ flux free, and $J(r > a)$ is set equal to $J_c$. For a single film and field-independent critical current, our result, shown in Fig. 61.17, exactly matches the analytical expression given by Mikheenko and Kuzovlev.[5]

We then proceed to calculate the temporal evolution of current distributions in the two films and the secondary coil. This is done by treating each ring in the two films and the secondary coil as $(2n+1)$ circuits. We then solve a set of linear equations of the form $[L]d[I]/dt + [R][I] = 0$, where $[L]$ and $[R]$ are matrices of dimension $(2n+1) \times (2n+1)$ and $[I]$ is a column vector. The diagonal elements of $[L]$ are the inductances of each circuit, and off-diagonal elements are the appropriate mutual inductances. $[R]$ is a diagonal matrix with elements equal to the normal-state resistances of the circuits. The elements of $[I]$ represent the current in each circuit. Using

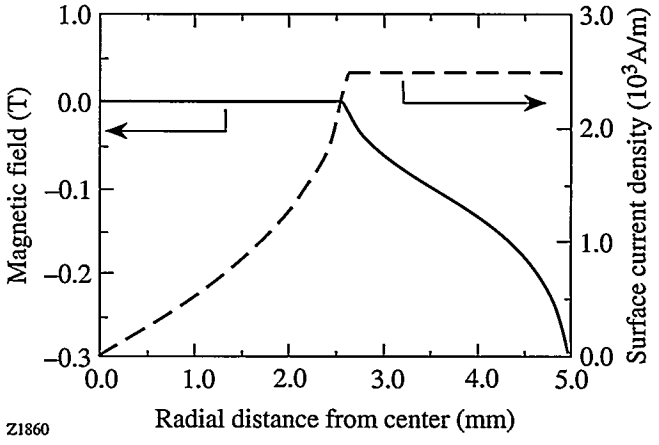


Figure 61.17
Static $J_c$-limited surface current and z-component of the magnetic field for a 1-cm-diam, thin superconducting disk of 500-nm thickness. A constant critical current density of $5.10^7$ A/cm$^2$ and an externally applied field of −0.2 T are assumed.

this analysis we calculate the current in the secondary coil as a function of time; Fig. 61.18 shows the result of this calculation. The matrix formulation of the problem enables us to take advantage of the computationally efficient, matrix manipulation tools in commercial software packages such as MATLAB™. The numerical method discussed above can easily incorporate additional details,[4] e.g., field-dependent critical current densities $J_c(B)$ and field-dependent superconducting flux-flow resistances.

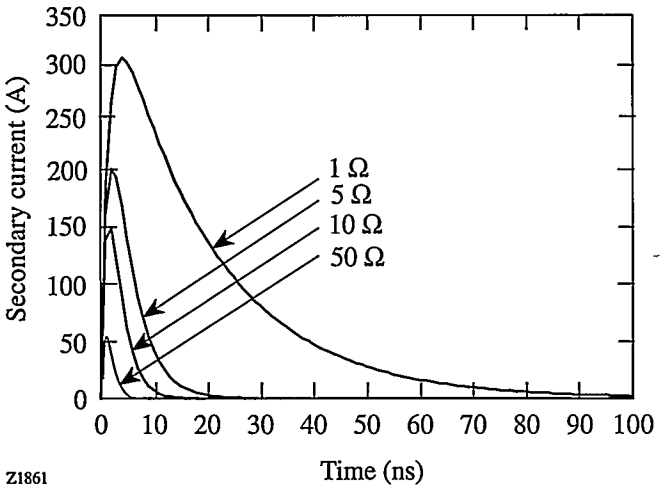


Figure 61.18
The simulated current pulse produced at a single-turn secondary coil for different values of load resistance. Two identical, 1-cm-diam, 500-nm-thick, disk-shaped superconducting films with $J_c = 5.10^7$ A/cm$^2$ are placed on either side of the secondary coil at a distance of 1 mm. The externally applied field ($B_{ext}$) is –0.2 T.

## Experimental Results and Discussion

The magnet used in our experiment is a Nb-Ti solenoid cooled by liquid helium, rated at 100 A and a maximum field of 4 T. A schematic drawing of the entire experimental setup, including the cryostat and magnet, is shown in Fig. 61.16.

The secondary coil is a single-turn inductor patterned on a printed circuit board. The sample holder consists of two 2-in.-diam circular copper disks with 1-cm × 1-cm-sq windows. The films, 500-nm-thick YBCO on 1-cm × 1-cm $LaAlO_3$ substrates with $T_c > 88$ K, are placed on either side of the secondary coil and supported by the copper disks.

A Nd:YAG laser beam ($\lambda$ = 1064 nm; pulse width = 150 ps) was used to illuminate the films from either side through a splitter arrangement (Fig. 61.16). A stainless steel, semirigid coaxial cable carries the secondary voltage signal out of the cryostat to a computer-interfaced oscilloscope for viewing (Fig. 61.16).

After cooling the sample to the desired temperature using liquid nitrogen or helium in zero magnetic field, the magnet was then charged at a ramp rate of 0.1 A/s up to the desired level and was maintained in persistent current mode. The magnetic field strength was measured using a Hall probe and a gaussmeter.

With the magnet charged, the switch was illuminated by the laser. The YBCO films screening the secondary coils were driven normal by this laser irradiation, which allowed the flux to penetrate. A secondary voltage (of negative sign) appeared across the load. The magnet was then discharged by heating the persistent switch, leaving some of the flux trapped in the superconductor. Driving the films normal again expelled the trapped flux, and the corresponding secondary voltage signal (of positive sign) was observed.

Figure 61.19 shows a comparison of the experimentally observed secondary voltage signal at an applied field of –0.2 T with the one obtained with the theoretical analysis described in the previous section. The simulation was done by varying $J_c$ to match the flux associated with the output voltage pulse. The peak voltage of the simulated pulse is higher than the experimentally observed pulse because instantaneous transition to the normal slate was assumed. The critical current density required to match the flux was $1.33 \times 10^6$ A/cm$^2$, which

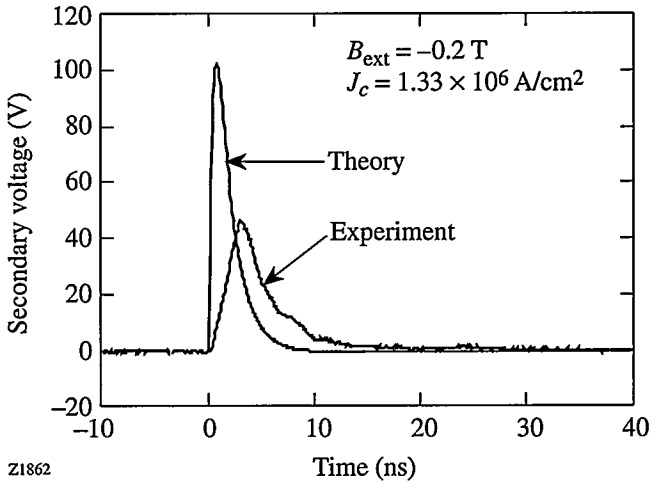


Figure 61.19
A comparison of experimentally obtained secondary voltage with the simulated voltage pulse representing the same flux. The experiment was carried out at 12.4 K, in –0.2-T field, and 8 mJ of laser energy per film.

is of the right order of magnitude but slightly lower than the value of $J_c$ at zero field, as quoted by the film manufacturer. Possible sources of reduced effective $J_c$ might include suppression in the magnetic field or sample inhomogeneity.

The variation of the secondary voltage signal for different laser energies is shown in Fig. 61.20. At lower laser energies, the entire bulk of the film is not heated instantaneously above the transition temperature. The 500-nm film thickness is greater than the optical penetration depth (≈120 nm); consequently the upper section of the film absorbs most of the energy when the laser pulse is incident on the film. The heat is eventually redistributed by diffusion, elevating the temperature of the entire film above the critical temperature. The heat is then redistributed throughout the remaining bulk of the film by thermal diffusion.[6] If we divide the film into a series of layers normal to the propagation direction of the incident laser radiation, the bottom layers will remain superconducting and carry the screening currents even after the top layers become nonsuperconducting. These screening currents continue to exclude flux and retard its motion. Since the secondary voltage is the temporal derivative of the flux, the peak voltage goes down, and rise and fall times increase, with the decrease in laser fluence. However, as shown in Fig. 61.20, the time integral of the secondary voltage pulse, representing the total flux that has traversed the film, is the same for pulses triggered by laser irradiation of varying intensity. Based on these results,

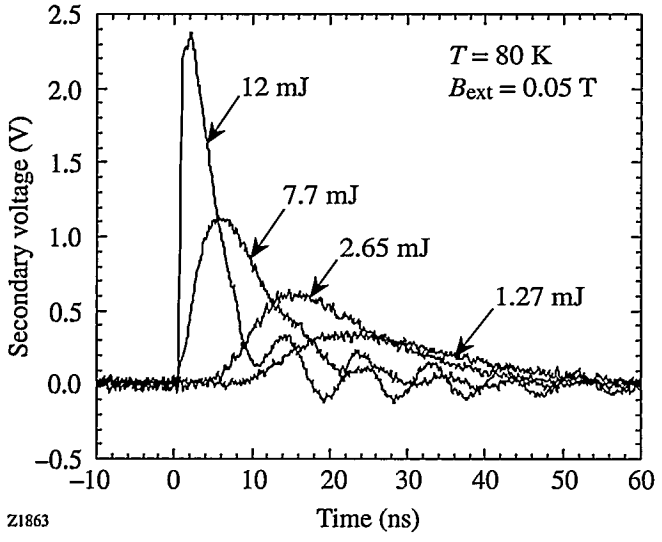


Figure 61.20
The speed of flux motion depends on the incident laser energy. For lower laser energy the bottom part of the film remains superconducting for a while, impeding the motion of flux. The film was a 1-cm-diam disk with a thickness of 500 nm.

we can conclude that higher laser fluence will give rise to faster signals with higher peak voltage. The energy ($E$) delivered to the load is given by $E = 1/R \int V^2(t)dt$, where $R$ is the load resistance and $V(t)$ is the voltage across the secondary. For the same flux, $\Phi = \int V(t)dt$, a faster signal will deliver higher energy in the load. Both the peak voltage and the flux are larger at lower temperatures because $J_c$ is higher.

An inductively coupled switch of the type we have described lends itself to a variety of applications. For example, in a current multiplication circuit using programmed inductive elements (PIE),[7] storage inductors are charged in series and discharged sequentially in stages that are connected in parallel with the load through a set of isolating closing switches. This circuit can be used to deliver a large load current using switches that are rated at a fraction of that current. The most important constraint in such a circuit is the synchronization of the opening switches with the closing switches. If the opening switches in this circuit are not triggered within a short temporal window, transient high current or voltages will catastrophically destroy the circuit elements. Optical triggering provides accurate timing. The optically triggered inductive opening switch will be suitable in circuits with such constraints.

The contactless arrangement of our switch is especially suited for applications such as energy extraction from SMES,[8–9] though there are some unresolved problems. The main application of SMES is as a backup source of energy to be delivered to the load in a crisis situation. If an opening switch is placed in series with the magnet winding, the finite closed-state resistance of the switch results in a continuous loss of energy while the system is idle. A contactless switch will solve this problem; the film properties, however, will need to be significantly improved for this design to be practical for high-power applications.

## Conclusion

We have described the flux dynamics in a contactless opening switch. The switching is performed by the optical heating of YBCO thin films, which in their superconducting state screen the flux coupling between two inductively coupled circuits. A single-turn secondary coil with a small $L/R$ time produces a fast voltage pulse. The rise time of the output signal is about 1 ns. At lower temperatures the critical currents are higher and can screen higher fields. Fast voltage pulses of 100 V and higher are possible and may have switching applications. We have developed a theoretical model, supported by experimental evidence, that can be used as a diagnostic tool to study flux motion.

## ACKNOWLEDGMENT

This work was supported by BMDO through ONR Contract #N00014-92-J-1993, Rochester Gas and Electric, NSF Grant #DMR-9122727, the New York State Energy Research and Development Authority, and the Frank J. Horton Graduate Fellowship Program.

## REFERENCES

1. E. M. Honig, in *Opening Switches,* edited by A. Guenther, M. Kristiansen, and T. Martin, Advances in Pulsed Power Technology, Vol. 1 (Plenum Press, New York, 1987), pp. 1–48.

2. D. Gupta, W. R. Donaldson, K. Kortkamp, and A. M. Kadin, IEEE Trans. Appl. Supercond. **3**, 2895 (1993).

3. J. H. Claassen, M. E. Reeves, and R. J. Soulen, Jr., Rev. Sci. Instrum. **62**, 996 (1991).

4. D. Gupta, W. R. Donaldson, and A. M. Kadin, submitted to the Journal of Applied Physics.

5. P. N. Mikheenko and Yu. E. Kuzovlev, Physica C **204**, 229 (1993).

6. D. Gupta, W. R. Donaldson, K. Kortkamp, and A. M. Kadin, in *Optically Activated Switching II,* edited by G. M. Loubriel (SPIE, Bellingham, WA, 1992), Vol. 1632, pp. 190–195.

7. T. Burke *et al.* (private communication); also presented at the IEEE's High Voltage Workshop, Monterey, CA, March 1988.

8. W. R. Donaldson, D. Gupta, and A. M. Kadin, U. S. Patent No. 5,339,062 (16 August 1994).

9. D. Gupta, W. R. Donaldson, and A. M. Kadin, in *Advances in Cryogenic Engineering,* edited by P. Kittel (Plenum Press, New York, 1994), Vol. 39, Part B, pp. 2015–2020.

# Slurry Particle Size Evolution During the Polishing of Optical Glass

Significant advances have been made in the fabrication of glass optical components since Newton's time, especially in the mechanically dominated grinding operations; however, optical polishing remains a very challenging finishing operation, primarily because of uncontrolled chemical factors and associated chemo-mechanical interactions. Most modern fabrication shops still rely on the specialized skills of experienced opticians to manage the complex system of polishing agent, fluid, glass work, and polishing tool. As an added source of difficulty, the proprietary nature of compositional data for some of the system elements (especially the glass work and polishing agent) means that knowledge of the initial process conditions is usually incomplete. Coupled with inherently low glass removal rates, the optician's labor makes polishing the most expensive operation in precision optical fabrication.

In this article, evolution of the slurry particle size distribution during aqueous glass polishing is investigated. Our primary focus is on the role of slurry fluid chemistry, which can also be influenced by the in-process dissolution of glass constituents.[1] This issue is especially significant in commercial polishing processes, where recirculation of the slurry is an economic necessity. The discussion here is limited to three glass types (Corning 7940 fused silica, Schott BK7 borosilicate crown, and Schott SF6 dense flint) and three polishing agents ($CeO_2$, monoclinic $ZrO_2$, and nanocrystalline $\alpha$-$Al_2O_3$). A more extensive treatment of the subject, including materials of purely academic interest, may be found in Ref. 2.

## Introduction

In the fabrication of typical precision optical elements, the purpose of polishing is threefold: (1) to shape the glass work to within 0.1 $\mu$m ($\lambda/5$, $\lambda = 0.5$ $\mu$m) or less of the desired surface form, (2) remove subsurface damage (SSD) created by the preceding grinding operations, and (3) reduce the peak-to-valley (PV) surface roughness to less than 5 nm ($\lambda/100$). The mechanism of glass removal, while not entirely understood, is generally accepted as plastic scratching of the hydrated or corroded glass surface by a polishing agent suspended in an aqueous fluid.[3] This mechanism is considered to be the essence of the chemo-mechanical theory of glass polishing. The most common polishing agents are $CeO_2$ and $ZrO_2$ with mean particle sizes ranging from 0.01 to 3 $\mu$m. The polishing agent is supported by a viscoelastic tool made of pitch (wood or petroleum based) or polyurethane foam. Since the polishing agent sinks into the tool until the smallest grains are load-bearing, the glass removal rate is not strongly dependent on the particle size distribution within some poorly specified upper limit.[4] The total glass thickness removed is about 25 $\mu$m, with removal rates ranging from 0.1 to 1 $\mu$m/min. The creation of SSD is not an issue in the polishing of glass because, unlike grinding, there is no fracturing of the surface.

The mechanical aspects of polishing have been modeled as an area-averaged wear process using Preston's equation[5,6]

$$\frac{dz}{dt} = C_p \frac{L}{A}\frac{ds}{dt}, \tag{1}$$

where $z$ is the height at a point on the surface of the glass work, $C_p$ is Preston's coefficient (units of area/force), $L$ is the total load, $A$ is the area over which wear occurs, and $s$ is the path traveled by the work relative to the tool. This equation predicts that the glass removal rate at any point on the surface is proportional to the local pressure ($L/A$) and velocity ($ds/dt$). The term $C_p$ is generally used as either a fitting parameter or an empirical measure of polishing efficiency.[7,8] The latter use is made clear by solving Eq. (1) for $C_p$ in terms of polishing process parameters:

$$C_p = \frac{1}{\rho L}\frac{\Delta m}{\Delta s}, \tag{2}$$

where $\rho$ is the density of the glass work, $\Delta m$ is the mass lost by the glass work during a given interval of polishing time, and $\Delta s$ is the total path length traveled by the tool across the work during the same time interval. Typically reported values of $C_p$ are of the order of $10^{-14}$ cm$^2$/dyne ($10^{-13}$ Pa$^{-1}$ or $9.806 \times 10^{-7}$ mm$^2$/kgf).[4,8,9]

Preston's deceivingly simple model lacks an explicit accounting of the role of process chemistry. This point is clarified by the work of Brown *et al.* on purely abrasive (i.e., chemically inactive) polishing of metals.[10] For this specific case, they proposed an expression for $C_p$ that is proportional to the inverse of Young's modulus of the bulk metal. If glass polishing was also a purely abrasive process, then there would be no hydrated surface layer. The corresponding value of $C_p$, calculated using the value of Young's modulus for the bulk glass, would be of the order of $10^{-12}$ cm$^2$/dyne, which is two orders of magnitude larger than typically reported empirical values. A major portion of this discrepancy is most likely due to three chemistry-related processes: (1) the complex hydration/corrosion of multicomponent silicate glass, (2) redeposition of silica species during polishing, and (3) surface charging of the glass work and the polishing agent. Cook's review of these processes and his proposed rate model suggested a number of interesting experiments, particularly relating to the influence of surface charge on mass transport during polishing.[4] This was a precursor to the trend of increasing interest in surface charge effects in the microgrinding[11] as well as polishing[9,12,13] of optical glass.

Hunter has summarized the mechanisms for the spontaneous separation of electric charges in systems consisting of oxides and fluids.[14] The mechanisms relevant to such systems consisting of two material phases are

(a) differences in the affinity of the two phases for ions of opposite charge, and

(b) ionization of surface groups.

Mechanism (a) involves the differential adsorption of anions or cations from the fluid onto the oxide surface as well as the differential dissolution of one type of ion over another from the oxide into the fluid. Equilibrium is established when the electrochemical potential is the same in both the oxide and fluid phases for any ion that can move freely between them.

For mechanism (b), the degree of charge development (and its sign) at the fluid-oxide interface due to ionization of surface groups on the oxide depends on the pH of the fluid. Metal-oxide surfaces typically possess a high density of amphoteric hydroxyl groups that can react with either $H^+$ or $OH^-$ depending on the pH:

$$MOH_2^+ \xleftarrow{H^+} M-OH \xrightarrow{OH^-} MO^- + H_2O. \quad (3)$$

This behavior may be regarded as a specific example of mechanism (a), with $H^+$ and $OH^-$ acting as the freely moving ions. These types of reactions can occur at the surface of a metal-oxide polishing agent particle as well as at an optical glass surface.

Well-developed techniques based on electrokinetic effects exist for measuring surface charge in systems containing either microscopic particles suspended in a fluid[15] or macroscopic solid bodies immersed in a fluid.[16] For suspended microscopic particles, measurement of the velocity of the particles under the influence of a known externally applied electric field permits the determination of the mobility of the particle. The mobility is related to the net electric charge, or surface potential, of the particle with respect to the bulk fluid. This technique is known as particle electrophoresis.

For the case of a macroscopic solid body, the surface charge can be determined by constraining the fluid to flow along a surface under the influence of a pressure gradient. Ionic charges at the surface tend to be swept along with the moving fluid, which results in an accumulation of charge downstream. The resultant potential difference induces an upstream electric current by ionic conduction through the fluid. A steady state is quickly established, and the measured potential difference along the portion of the surface over which the fluid is flowing is called the streaming potential. This streaming potential is related to both the pressure gradient driving the fluid motion and the surface potential of the solid with respect to the bulk fluid.

The above descriptions of electrokinetic measurement techniques refer to the term "surface potential." What is typically calculated from electrokinetic measurement data is known as the zeta ($\zeta$) potential, defined as the average electric potential at the "surface of shear" near the solid (microscopic particle or macroscopic body) with respect to the bulk fluid potential. This surface of shear is an imaginary hydrodynamic boundary in the region of the fluid-solid interface. Between the solid surface and the surface of shear, the fluid is considered to be stationary in the reference frame of the solid.

Recent literature on polishing has referred to both the $\zeta$ potential[9,12] and the isoelectric point (IEP)[4] of the polishing agent and the glass work. The relationship between the IEP and the $\zeta$ potential can be readily understood in terms of the preceding discussion. The IEP of a hydrated surface is defined as the pH at which there is no net charge within the surface of shear, which clearly corresponds to $\zeta = 0$.

In spite of the complexity of the task, there has been recent progress toward the development of a deterministic glass-polishing model. Based on empirical data from two different sources, a polishing rate model has been proposed by Cook[4] that accounts for the single oxygen bond strength of the metal-oxide polishing agent (R-O, in kcal/mole), the pH of the fluid, and the IEP of the polishing agent:

$$R_c = \frac{1}{\log_{10}\left[(\mathrm{R-O}) \times |\mathrm{pH} - \mathrm{IEP}|\right]}. \quad (4)$$

The rate factor ($R_c$) is a predictor of the relative polishing activity of metal-oxide polishing agents.

Our earlier research with an atomic force microscope (AFM) showed that electrostatic forces between planar glass disks and individual metal-oxide polishing agent particles can be easily controlled by manipulating the pH of the surrounding fluid.[13] In this work, we investigate the manifestations of such chemically modulated forces in a planar continuous-polishing process and assess the effectiveness of manipulating the slurry chemistry to produce higher-quality surfaces in less time.

## Experiment

Commercially available products were used in our experiments whenever feasible. Optical glass disks and polishing slurries were characterized in terms of the $\zeta$ potential. Slurries were further characterized in terms of the particle size distribution, and planar glass polishing experiments were conducted with a commercially compatible continuous polishing machine. Particle electrophoresis and streaming potential measurements were used to determine the IEP's of metal-oxide polishing agents and silicate glass types prior to actual polishing experiments.

### 1. Materials

Three glass types commonly used for precision optical components were examined in this study: Corning 7940 (fused silica),[17] Schott BK7 (borosilicate crown), and Schott SF6 (dense lead silicate flint).[18] Their chemical compositions[19,20] along with some of their fundamental properties[2,19,21] are listed in Tables 61.III and 61.IV, respectively. The action of three high-purity metal-oxide polishing agents on these three glass types was evaluated at three levels of slurry fluid pH (4, 7, and 10), spanning the range of values normally encountered in polishing. Two of the three polishing agents, Transelco $CeO_2$[22] and Norton monoclinic $ZrO_2$,[23] are supplied as aqueous slurries with a median particle size of 1 $\mu$m. The third polishing agent, Norton nanocrystalline $\alpha$-$Al_2O_3$,[24] is also supplied as an aqueous slurry but with a median particle size of 0.6 $\mu$m. It is engineered for greater friability (i.e., a lower resistance to crumbling) than conventional $\alpha$-$Al_2O_3$ grinding abrasives, thereby improving the prospects for successful glass polishing.[25]

Table 61.III: Composition of the three glass types (weight %).

| Glass Type | $SiO_2$ | $B_2O_3$ | $Na_2O$ | $K_2O$ | BaO | PbO | $As_2O_3$ |
|---|---|---|---|---|---|---|---|
| 7940 | 99.9 | – | – | – | – | – | – |
| BK7 | 68.9 | 10.1 | 8.8 | 8.4 | 2.8 | – | 1.0 |
| SF6 | 26.9 | – | 0.5 | 1.0 | – | 71.3 | 0.3 |

The scope of our core experimental program was thus defined as the evaluation of 27 different combinations ($3^3$) of glass, polishing agent, and fluid.

### 2. Equipment and Methods

a. Preparation of glass surfaces. To ensure consistent initial conditions for each polishing experiment, a uniform planar

Table 61.IV: Some thermal and mechanical properties of the three glass types.

| Glass Type | Transition Temp. ($T_g$) (°C) | $\alpha$ ($10^{-6}$C) (a) | Density (g/cm$^3$) | Young's Modulus (GPa) | $H_v$ (kgf/mm$^2$)(b) | $K_c$ (MPa m$^{1/2}$)(c) |
|---|---|---|---|---|---|---|
| 7940 | 1075 | 0.5 | 2.20 | 73.1 | 953 | – |
| BK7 | 559 | 7.1 | 2.51 | 81.0 | 772 | 0.86 |
| SF6 | 423 | 8.1 | 5.18 | 56.0 | 465 | 0.44 |

(a) Linear thermal expansion coefficient ($\alpha$) of 7940 determined over a temperature range of 5°C to 35°C.[9] $\alpha$ of BK7 and SF6 determined over a range of –30°C to 70°C.[21]
(b) Vickers hardness ($H_v$) measured using 0.05 kgf with samples immersed in water.[2]
(c) Fracture toughness ($K_c$) also measured using 0.05 kgf with samples immersed in water.[2] $K_c$ is undefined here for fused silica because it does not fracture radially under such a low load.

disk geometry was adopted for all glass samples. Fine annealed plates were rough ground to a thickness of 15 mm and then core drilled to produce at least two dozen 40-mm-diam disks of each glass type. The individual disks were beveled and then processed using a controlled grinding strategy to minimize the depth of subsurface damage (SSD).[26] A cast iron tool and Microgrit #9 $Al_2O_3$ abrasive,[27] which has a median particle size of 5.75 $\mu$m, were used in the last fine-grinding operation. The resultant PV surface roughness was measured over a 4-mm scan length using a Pocket Surf III roughness gage,[28] and the depth of SSD was measured using a modification of the Itek ball method.[29] All surface sampling measurements, including PV roughness and SSD, were taken at five sites per disk: the center site plus the four sites within 5 mm of the edge at the 3, 6, 9, and 12 o'clock positions.

b. $\zeta$ potential and particle-size analysis. The $\zeta$ potential values of the three optical glass types were determined using a Brookhaven EKA electrokinetic analyzer.[30] Six disks of each glass type were cut and rough ground to the rectangular dimensions (33 × 20 × 5 mm) required to line the fluid cell of the Brookhaven EKA. One large face of each rectangular sample was fine ground as specified above and then polished using a pitch tool with an aqueous slurry of monoclinic $ZrO_2$. The polished surfaces were planar to within $\lambda/2$ with a scratch/dig quality of 60/40.[31] Samples of a given glass type were cleaned and mounted end-to-end in the upper and lower recesses of the EKA streaming potential cell with the polished surfaces exposed to the fluid. The streaming potential that developed along the surface of the glass-lined channel was measured while an electrolyte solution ($1 \times 10^{-3}$ M aqueous KCl) was forced, by external pressure, to flow along the surface. The pH values were varied between 3 and 10 by adding either HCl or NaOH to the transport electrolyte. The $\zeta$ potential values, calculated from the streaming potential measurements using the Briggs method,[15,16] were plotted as a function of fluid pH. The corresponding IEP values of each glass type (pH at which $\zeta = 0$) were obtained by interpolation.

The $\zeta$ potential values of the three polishing agents were determined using a Brookhaven ZetaPlus zeta potential analyzer,[32] which measures the electrokinetic mobility of particles suspended in a fluid using electrophoretic light scattering (ELS). The $\zeta$ potential, calculated from the electrokinetic mobility using the Smoluchowski equation,[15] was measured with the polishing agents suspended in water as well as in aqueous solutions of NaCl and catechol ($1,2\text{-}(HO)_2C_6H_4$). Catechol was chosen as a fluid additive because of its reported role as a potential silica sequestering agent during polishing with pitch tools.[4,9,33] Since a salt-rich, aqueous environment is known to effectively screen out electrostatic interactions near macroscopic oxide surfaces[34] and between particles in colloidal systems,[35,36] NaCl was also chosen as a fluid additive. Samples of each of the three slurries as received from the manufacturers were diluted (10:1) with three different carrier fluids: deionized water, aqueous catechol (500 ppm, $4.5 \times 10^{-3}$ M), and aqueous NaCl [500 ppm, (0.01 M)]. The catechol concentration was chosen based on the maximum conceivable evolution of analogous compounds from a pitch polishing tool in recirculated slurry systems.[37] The maximum salt concentration was limited by the electrolytic current handling capability of the ZetaPlus instrument. Small working volumes of the nine polishing agent/fluid combinations were prepared at three pH values (4, 7, and 10) adjusted by the addition of HCl or NaOH. Measured $\zeta$ potential values of each polishing agent/fluid combination were then plotted as a function of pH, and the corresponding IEP values were obtained by interpolation.

The particle size distribution of polishing slurries was measured using a Horiba LA900.[38] This instrument optically determines the size of particles suspended in a fluid over a range of 0.04 to 1000 $\mu$m by combining Fraunhofer diffraction and Mie scattering information.[39] Typically, two or three droplets of a given slurry were dispersed directly into the carrier fluid ($V \approx 250$ ml) of the LA900. An aqueous solution of an anionic surfactant [$(NaPO_3)_6$, 0.2% by weight] was used as the carrier fluid to prevent any agglomeration of the suspended metal-oxide particles. The diluted slurry was recirculated through the LA900 until the forward-scattered red light ($\lambda = 633$ nm) signal stabilized, indicating uniform mixing. The particle size distribution was then measured and stored as a 74-bin histogram.

c. Glass polishing experiments. Glass polishing experiments were conducted on a custom-built, 535-mm-diam continuous polishing machine (CPM) with a 297-mm-diam conditioner and a pair of 178-mm-diam work rings (for individual work pieces). The theory and operational considerations of this planar polishing machine have been presented elsewhere by Preston[5] and Cooke *et al.*[40] and will not be discussed here. Unique features of our CPM include a vacuum-activated slurry agitation/recirculation system,[11] a mechanical agitator in the outer catchment trough to prevent liquid/solid separation by settling, and *in situ* measurement of the frictional force ($F_T$) between the polishing tool and an individual 40-mm-diam glass work piece using an Entran load cell.[41] The overall sensitivity of the frictional force measurement system is approximately ±0.1 N.

Given the ambitiously large number of material combinations to be evaluated and the need to eliminate any chemical carryover between experiments, polyurethane foam was used instead of pitch as the polishing tool. Although this choice simplifies tool replacement between experiments, the surface figure of the work, or edge roll-off, was compromised. On the basis of cost and the availability of die-cut sheets large enough to cover the 535-mm-diam turntable of our CPM, we selected a 0.5-mm-thick blown polyurethane pad, Rodel HSP.[42] The open cellular structure of this material provides a high density of sites for retaining polishing agent particles, which is a necessary condition for efficient glass removal during polishing with any polyurethane tool.[43]

The primary role of the CPM conditioner in our polishing experiments was to dominate the process chemistry by providing a significant surface area for tool/slurry/glass interactions. The conditioner also functioned as a truing device by shearing off any local asperities on the surface of the polyurethane tool.[44] To isolate glass-specific chemical effects, a separate conditioner was prepared for each of the three glass types that were polished. Each conditioner was fabricated by blocking 17 individual glass disks (40-mm diam, 15 mm thick) to a large Pyrex disk (297-mm diam, 25 mm thick). Since the functional surface of the conditioner was made of the same glass type as the individual work piece in the frictional force measurement system, only the particular glass type being studied in a given experiment participated in the process chemistry. This choice of common glass types essentially eliminated any competing effects that could be attributed to a different conditioner material.

A consistent CPM operational procedure was followed in each of the glass polishing experiments. Since chemistry-related issues were our primary concern, constant values of pressure (40 gf/cm$^2$) and synchronous rotation rate (9 RPM for the turntable and work rings) were maintained throughout the experiments.

At the conclusion of each experiment, the roughness of a blocked disk near the center of the conditioner was measured using a Zygo Maxim-3D laser interference microscope.[45] The surface figure of the glass work and the conditioner disk was evaluated using a Davidson Optronics Fizeau interferometer, which has a He-Ne laser source ($\lambda = 632.8$ nm) and a 127-mm-diam reference flat for testing planar surfaces.[46]

The glass removal rate ($\Delta z/\Delta t$) was calculated from the mass loss ($\Delta m$) of the glass work over a given time interval ($\Delta t$) using[11]

$$\frac{\Delta z}{\Delta t} = \frac{1}{\rho A}\frac{\Delta m}{\Delta t}, \tag{5}$$

where $\rho$ is the glass density and $A$ is the area of the work in contact with the polyurethane pad. The mass loss was determined by weighing the work before and after polishing using an analytical balance with a reproducibility (one standard deviation) of 20 $\mu$g. The maximum uncertainty in the reported glass removal rates was 3%.

A typical polishing experiment required approximately 7 h, including cleanup time. The polyurethane pad was replaced whenever an experiment called for a change in glass type or polishing agent. New pads were preconditioned by an 8-h polishing session with the slurry and glass type of interest, which ensured that the pad was fully charged with polishing agent particles.

## Results and Discussion

1. Glass Surface Conditions prior to Polishing

The surface conditions of each glass type following fine grinding with #9 $Al_2O_3$ abrasive are summarized in Table 61.V in terms of the PV roughness and depth of SSD. The results clearly demonstrate that the performance of a given loose abrasive grinding operation is highly dependent on the glass type. From Table 61.V, we see that only 7940 follows the constant SSD-to-PV roughness ratio of 4.0 (±0.4) for loose abrasive grinding advanced by Aleinikov.[47] The two multicomponent glass types, BK7 and SF6, have significantly lower SSD-to-PV roughness ratios.

Table 61.V: Roughness and subsurface damage of the three glass types after fine grinding with #9 $Al_2O_3$ abrasive.

| Glass Type | PV Roughness ($\mu$m) (average of five sites) | Standard Deviation ($\mu$m) | SSD Depth ($\mu$m) (average of five sites) | Standard Deviation ($\mu$m) |
|---|---|---|---|---|
| 7940 | 2.2 | 0.3 | 8.1 | 0.6 |
| BK7 | 2.4 | 0.5 | 5.3 | 0.4 |
| SF6 | 4.2 | 0.7 | 4.0 | 0.2 |

2. Isoelectric Point (IEP) Values of Optical Glasses and Polishing Agents

The pH dependence of the $\zeta$ potential values obtained for each glass type using the Brookhaven EKA instrument is

shown in Fig. 61.21. The corresponding IEP values of each glass type, obtained by interpolation, are listed in the legend.

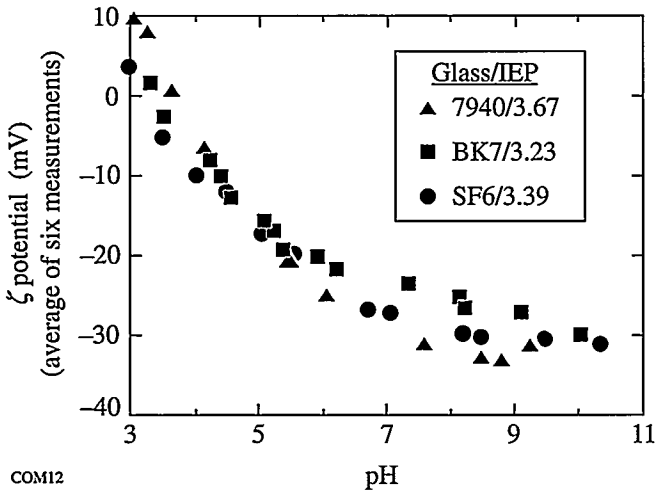


Figure 61.21
Zeta potential of 7940, BK7, and SF6 versus fluid pH. The pH was adjusted by the addition of HCl or NaOH to the transport fluid ($1 \times 10^{-3}$ M aqueous KCl). Error bars ≤ ±2 mV (±3 standard deviations) have been omitted for clarity.

Several important observations can be made concerning the results shown in Fig. 61.21:

- The measured value of the IEP of 7940 is in excellent agreement with that reported by Jednacak *et al.* for vitreous silica.[48]

- The ζ potential values of the three glass types are all negative (i.e., the surfaces are negatively charged due to the dissociation of OH groups) for the entire range of pH values usually encountered in optical polishing ($4 \leq pH \leq 10$).

- While the presence of significant amounts of intermediates and/or modifiers in BK7 and SF6 results in only a modest reduction of their IEP values relative to that of 7940, the ζ potential values are fairly distinctive for pH values between 6 and 9. This behavior is caused by differences in the density and charging characteristics of active surface oxide species, ostensibly due to the compositional differences between the three glass types.

The ζ potential values of each polishing agent were measured in all nine combinations of fluid additive and pH using the Brookhaven ZetaPlus instrument. The results for each polishing agent/fluid combination, when plotted as a function of pH, allowed us to determine the IEP values by interpolation, as shown for nanocrystalline $Al_2O_3$ suspended in aqueous catechol in Fig. 61.22. The IEP values for the eight remaining combinations of polishing agent and fluid additive were obtained by similar means and are summarized in Table 61.VI. The IEP values published by Cook[4] are also included in the table for reference.

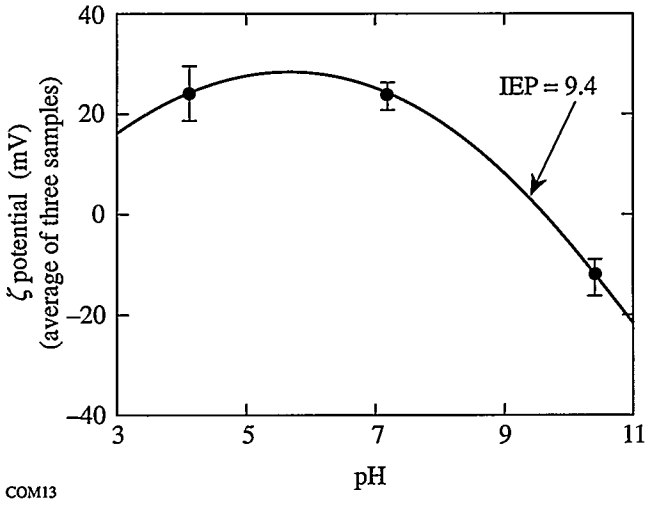


Figure 61.22
Zeta potential of the nanocrystalline $Al_2O_3$ polishing agent diluted in aqueous catechol (500 ppm, $4.5 \times 10^{-3}$ M) versus fluid pH. The pH was adjusted by the addition of HCl or NaOH to the fluid. The data shown represents an average of three samples with ±1 standard deviation error bars.

A remarkable feature of the data in Table 61.VI is the consistency between the measured and previously published IEP values for nanocrystalline $Al_2O_3$, which is an indication of the lack of specifically adsorbed ions on the surface of the polishing agent.[49] Conversely, the IEP values of $CeO_2$ and $ZrO_2$ are very sensitive to the fluid chemistry. The presence of either additive reduces the IEP values of both polishing agents, which suggests that catechol and NaCl provide ions that are specifically adsorbed at the surfaces of $CeO_2$ and $ZrO_2$. These results are considered valid only in the absence of mechanical action since individual polishing agent particles are not subjected to mechanical forces that might cause them to crumble during ζ potential measurements. The total active surface area of the polishing agent particles also remains essentially constant, unlike the case when glass is polished.

3. Original Particle Size Distribution and Friability of the Polishing Agents

The original particle size distribution of each slurry as re-

Table 61.VI Isoelectric point (IEP) values of the three polishing agents in deionized water, aqueous catechol, and aqueous sodium chloride.

| Polishing Agent | IEP previously published (Ref. 4) | IEP measured in deionized water | IEP measured in catechol (aq) ($4.5 \times 10^{-3}$ M) (500 ppm) | IEP measured in NaCl (aq) ($1.0 \times 10^{-2}$ M) (584 ppm) |
|---|---|---|---|---|
| $CeO_2$ | 6.8 | 8.8 | 7.0 | 7.3 |
| m-$ZrO_2$ | 6.2 | 6.3 | 3.0 | 5.0 |
| n-$Al_2O_3$ | 9.5 | 9.3 | 9.4 | 9.3 |

ceived from the manufacturers was measured using the Horiba LA900 instrument. All three polishing agents fall within the median particle size range of 0.01 to 3.0 $\mu$m that is typical of precision polishing operations, as shown in Table 61.VII.

Table 61.VII Original particle size statistics of the three polishing agents.

| Polishing Agent | Median Size ($\mu$m) | Maximum Size ($\mu$m) | Minimum Size ($\mu$m) |
|---|---|---|---|
| $CeO_2$ | 1.00 | 4.47 | 0.23 |
| m-$ZrO_2$ | 1.34 | 5.12 | 0.23 |
| n-$Al_2O_3$ | 0.59 | 5.12 | 0.26 |

The friability of each polishing agent was assessed by evaluating particle size distribution in recirculated slurry samples exposed to 20-kHz, 40-W ultrasound in the LA 900 instrument. These measurements were conducted between successive, 3-min exposures to ultrasound.

Figure 61.23 illustrates the effect of ultrasonic energy on the particle size distribution of $CeO_2$. The initial distribution ($t$ = 0 min) is bimodal, with the dominant mode representing the larger particles in the population. After 3 min of ultrasonic exposure, the distribution character is reversed, with the dominant mode representing the smaller particles in the population. Evidently, the ultrasonic energy induced a significant fraction of the $CeO_2$ particles to break apart. After 6 min (not shown) and 9 min of ultrasonic vibration, the size distribution shifts further toward smaller particle diameters, but not as dramatically as within the first 3 min.

The effect of ultrasonic energy on the median particle size of all three polishing agents is shown in Fig. 61.24. Based on the decaying exponential character of the size dependence shown in the figure, we can define an empirical ultrasonic friability index $F_{us}$ as

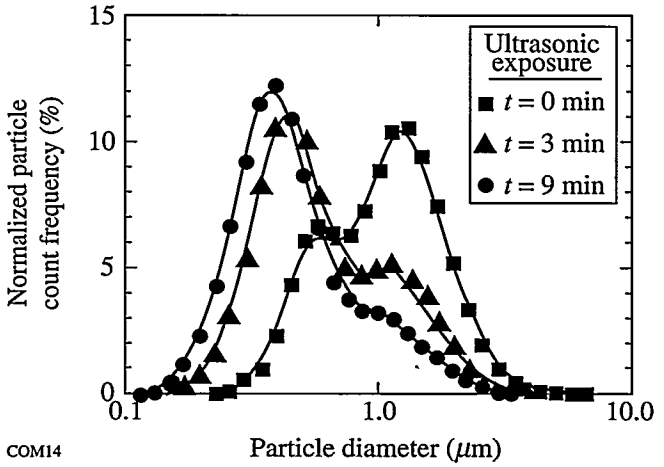


Figure 61.23
Effect of ultrasonic energy on the particle size distribution of the $CeO_2$ slurry. Particle size measurements were performed between successive 3-min exposures to ultrasound (40 W, 20 kHz). For clarity, the $t$ = 6 min. distribution has been omitted.

$$F_{us} = -\frac{1}{U}\ln\left(\frac{D}{D_0}\right), \tag{6}$$

where $D$ is the median particle size measured after exposure to ultrasonic energy $U$ and $D_0$ is the original median particle size. This friability index $F_{us}$ is a useful measure of the relative change in median particle size per unit of ultrasonic energy, i.e., the more friable the polishing agent, the larger the value of $F_{us}$.

The median particle size and corresponding value of $F_{us}$ for all three polishing agents after 3 and 6 min of ultrasonic exposure are listed in Table 61.VIII. The original median particle size ($t$=0) is also given in Table 61.VIII for convenient reference. In terms of $F_{us}$, nanocrystalline $Al_2O_3$ is the most friable polishing agent, followed in decreasing order by $CeO_2$ and monoclinic $ZrO_2$.

Table 61.VIII: Median particle size and ultrasonic friability index of the three polishing agents.

| Polishing Agent | Median Size ($\mu$m) ($t$ = 0 min) | Median Size ($\mu$m) ($t$ = 3 min) | $F_{us}$ ($t$ = 3 min) ($\times 10^{-5}$/J) | Median Size ($\mu$m) ($t$ = 6 min) | $F_{us}$ ($t$ = 6 min) ($\times 10^{-5}$/J) |
|---|---|---|---|---|---|
| $CeO_2$ | 1.00 | 0.50 | 9.6 | 0.43 | 5.9 |
| m-$ZrO_2$ | 1.34 | 0.89 | 5.7 | 0.87 | 3.0 |
| n-$Al_2O_3$ | 0.59 | 0.29 | 9.9 | 0.21 | 7.2 |

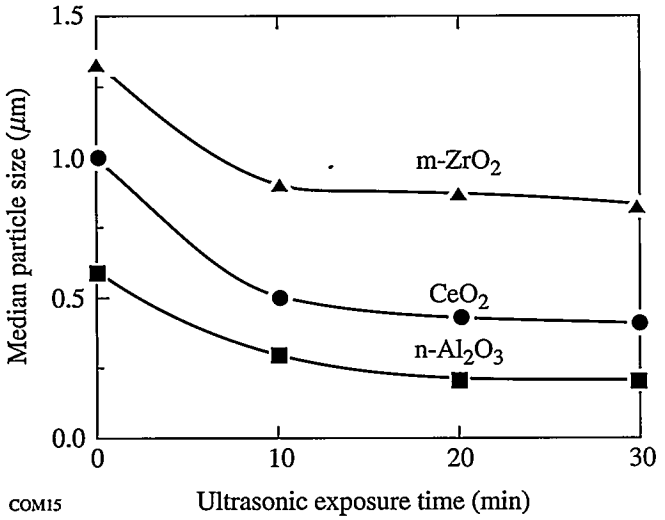


Figure 61.24
Effect of ultrasonic exposure time on the median particle size of the polishing agents.

4. Glass Polishing Experiments

Two preliminary experiments with the CPM were conducted using the most commercially important glass and polishing agents, BK7 and $CeO_2$, respectively. The goals of these experiments were

- to assess the in-process evolution of slurry particle size over a prolonged period of polishing, and
- to study the effect of catechol and NaCl as slurry additives.

The core experiments were then conducted using all 27 combinations of polishing agent, glass type, and slurry fluid pH. The results of each experiment are discussed below.

a. Assessment of in-process particle size evolution. The effective working lifetime of the polyurethane pad and slurry was initially determined by running the CPM with a new pad, a BK7 work and conditioner, and a fresh batch of $CeO_2$ slurry at pH 7 for 30 consecutive hours. The mass loss of the work and the slurry particle size distribution were measured hourly for the first 8 h, then at 15- and 30-h intervals.

The resulting glass removal rate and median particle size are plotted versus polishing time in Fig. 61.25. The glass removal rate is seen to stabilize after 6 h, which validates the need to condition new pads for at least this length of time. Between 8 and 30 h of polishing, the glass removal rate is essentially constant. This experiment established a reasonable minimum pad lifetime of 30 h, which was never exceeded during the remaining CPM experiments.

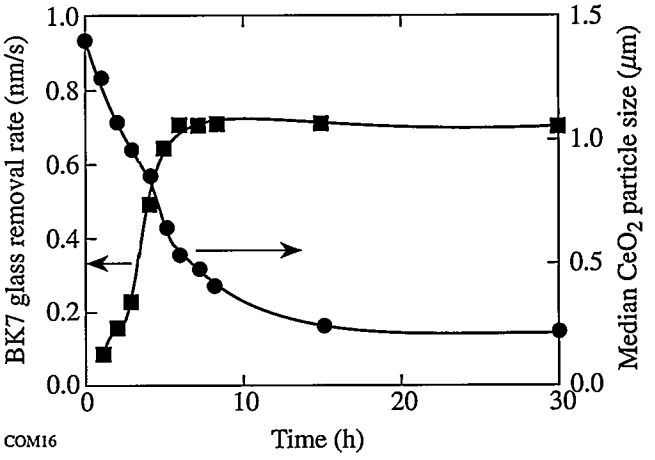


Figure 61.25
Removal rate of BK7 and the corresponding median size of the $CeO_2$ polishing agent versus polishing time.

After 6 h of polishing, the median $CeO_2$ particle size was reduced to 0.64 $\mu$m (approximately 50% of the initial value). Comparison of Figs. 61.24 and 61.25 suggests an equivalence relationship between 6 h of BK7 polishing under these conditions with 3 min of ultrasonic vibration in the Horiba LA900. These results also serve as a reminder that the glass polishing process also functions as a milling process for the polishing agent.

b. Effect of catechol and sodium chloride as slurry additives. Our earlier AFM screening experiments[13] revealed that catechol and NaCl function only to buffer mildly the forces between individual metal-oxide particles and polished glass surfaces. Their strong influence on the measured IEP values of $CeO_2$ and $ZrO_2$, as indicated in Table 61.IV, suggests the possibility of more-complex interactions between slurry particles. To resolve this issue, we studied the effect of catechol and NaCl as slurry additives using the CPM.

The average BK7 glass removal rate obtained during 4 h of polishing with aqueous $CeO_2$ slurries containing no slurry fluid additive, aqueous catechol (500 ppm, $4.5 \times 10^{-3}$ M), and NaCl (5% by weight, 0.86 M) is plotted as a function of slurry pH in Fig. 61.26. At each of the three pH levels, the relative effect of the additives on the glass removal rate was quite consistent. The additive-free slurry fluid yielded the maximum removal rate, followed by aqueous catechol and aqueous NaCl. The maximum removal rate was obtained with no additive at pH 7. In contrast with the glass removal rate, the final rms surface roughness values (average of five measurements) of the conditioner for all nine combinations of slurry fluid additive and pH were nearly indistinguishable, averaging from only 10 to 16 Å.

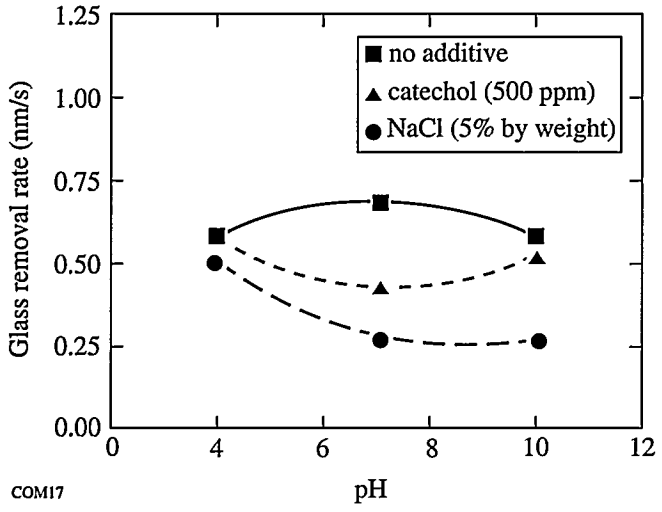


Figure 61.26
Glass removal rate as a function of slurry pH and slurry additive for polishing of BK7 with $CeO_2$.

These results demonstrate that, in terms of final BK7 surface roughness, the performance of $CeO_2$ is insensitive to significant variations in fluid chemistry. This insensitivity to fluid chemistry variations implies that an insignificant level of specifically adsorbed ions evolve from BK7 glass during the polishing process. There also is a penalty for using either catechol or NaCl as a slurry additive between pH 4 and pH 10, as evidenced by the lower glass removal rate. Since these additives made no significant impact on the polishing process, they were excluded from the remaining experiments.

c. Core glass polishing experiments. The results of the 27 core polishing experiments with $CeO_2$, monoclinic $ZrO_2$, and nanocrystalline $Al_2O_3$ are summarized in Table 61.IX. The range of data presented includes the average glass removal rate (RR) during each 4-h polishing session, the corresponding value of Preston's coefficient ($C_p$), the coefficient of friction ($\mu$) between the work and the polyurethane pad, the final rms surface roughness of the conditioner, and the ratio of the final and original median particle size ($D_f/D_0$) of the slurry.

A careful review of Table 61.IX shows that polishing slurries containing monoclinic $ZrO_2$ are clearly the least sensitive to glass type or slurry pH, while those containing nanocrystalline $Al_2O_3$ are the most sensitive to these chemistry-related process factors. The $CeO_2$ results are intermediate to the other two polishing agents. This ordering of chemical sensitivity is identical to the ultrasonic friability index ordering (Table 61.VIII) but is contrary to the IEP stability (Table 61.VI). This apparent inconsistency can be reconciled if the available surface area of the polishing agent is taken into account. From Eq. (3), the total number of hydroxyl groups able to participate in ionization reactions scales with the combined surface area of the polishing agent particles in the recirculated slurry. Highly friable polishing agent particles will crumble progressively with use, exposing new active surface groups and accentuating the chemical aspect of their performance.

The coefficient of friction ($\mu$) has been shown previously to be a good quantitative indicator of the efficiency of glass removal[9,12] and, as such, is a useful element with which to begin quantitative interpretation of the data in Table 61.IX. In Fig. 61.27, $C_p$ is plotted as a function of $\mu$ for all 27 core polishing experiments. Although there are a number of outlying points, the reasonably good linear correlation ($r^2 = 0.718$) confirms quantitatively that $\mu$ may be regarded as a measure of the useful mechanical work done during polishing. Those process conditions that induced a value of $\mu$ in excess of 0.4 always resulted in a value of $C_p$ characteristic of efficient mass transport away from the work ($\geq 10^{-13}$ cm$^2$/dyne).

If one studies the effect of slurry pH on the efficiency of glass removal, an interesting pattern emerges from the data.

Table 61.IX: Results of the core polishing experiments.

| Polishing Agent | Glass Type | Slurry pH | RR (nm/s) | $C_p$ ($\times 10^{-14}$ cm$^2$/dyne) | Friction Coefficient ($\mu$) | rms Roughness (Å) | $D_f/D_0$ |
|---|---|---|---|---|---|---|---|
| $CeO_2$ | 7940 | 4 | 0.141 | 2.2 | 0.27 | 13 | 1.22 |
| " | " | 7 | 0.215 | 3.3 | 0.31 | 12 | 1.11 |
| " | " | 10 | 0.200 | 3.1 | 0.30 | 10 | 0.61 |
| " | BK7 | 4 | 0.582 | 8.9 | 0.32 | 16 | 2.36 |
| " | " | 7 | 0.680 | 10.4 | 0.41 | 13 | 0.55 |
| " | " | 10 | 0.580 | 8.8 | 0.29 | 11 | 0.25 |
| " | SF6 | 4 | 0.270 | 4.1 | 0.32 | 478 | 1.78 |
| " | " | 7 | 0.104 | 1.6 | 0.28 | 308 | 0.37 |
| " | " | 10 | 0.788 | 12.0 | 0.48 | 13 | 0.51 |
| m-$ZrO_2$ | 7940 | 4 | 0.307 | 4.7 | 0.35 | 13 | 0.85 |
| " | " | 7 | 0.241 | 3.7 | 0.35 | 12 | 0.20 |
| " | " | 10 | 0.253 | 3.8 | 0.33 | 13 | 0.47 |
| " | BK7 | 4 | 0.673 | 10.3 | 0.38 | 19 | 2.15 |
| " | " | 7 | 0.530 | 8.1 | 0.40 | 16 | 0.80 |
| " | " | 10 | 0.524 | 8.0 | 0.37 | 14 | 0.62 |
| " | SF6 | 4 | 1.110 | 16.9 | 0.49 | 24 | 1.36 |
| " | " | 7 | 0.733 | 11.2 | 0.48 | 21 | 0.83 |
| " | " | 10 | 0.778 | 11.8 | 0.48 | 14 | 0.76 |
| n-$Al_2O_3$ | 7940 | 4 | 0.123 | 1.9 | 0.28 | 243 | 0.54 |
| " | " | 7 | 0.033 | 0.5 | 0.25 | 167 | 3.92 |
| " | " | 10 | 0.147 | 2.2 | 0.31 | 16 | 0.56 |
| " | BK7 | 4 | 0.353 | 5.4 | 0.32 | 24 | 0.64 |
| " | " | 7 | 0.029 | 0.4 | 0.24 | 66 | 3.75 |
| " | " | 10 | 0.364 | 5.5 | 0.29 | 10 | 0.29 |
| " | SF6 | 4 | 0.713 | 10.9 | 0.38 | 19 | 0.80 |
| " | " | 7 | 0.077 | 1.2 | 0.34 | 609 | 4.00 |
| " | " | 10 | 0.966 | 14.7 | 0.41 | 12 | 0.56 |

Except for the case of $CeO_2$ and SF6, a glass prone to selective corrosion of the PbO network modifier in acidic to neutral fluids,[50] each polishing agent exhibits a unique, glass-independent optimum pH for the maximum removal rate. For $CeO_2$, monoclinic $ZrO_2$, and nanocrystalline $Al_2O_3$, the glass removal rates were maximized at pH 7, 4, and 10, respectively. Returning to Table 61.VI, these optimum pH values roughly correspond to the respective IEP values measured in the presence of specifically adsorbed ions (i.e., in 0.01-M aqueous NaCl). An abundance of such ions was assumed to be present during our polishing experiments because of the dissolution of glass constituents and the use of HCl or NaOH to adjust the slurry pH. Given this assumption, our results are partially consistent with Cook's rate model, which predicts a maximum glass removal rate for a given polishing agent if the slurry pH is close to the IEP of the polishing agent [Eq. (4)]. However, as shown in Figs. 61.28–61.31, the reliability of the rate constant ($R_c$) as a predictor of glass removal rates is suspect. This reliability issue is especially apparent in Figs. 61.30 and 61.31, which show that $R_c$ is not positively correlated with removal rates obtained in fluids that are corrosive to the glass.

The optimum pH for maximum glass removal did not result necessarily in the smoothest possible surfaces, which is a primary objective of polishing. Minimum surface roughness values for all nine combinations of polishing agent and glass

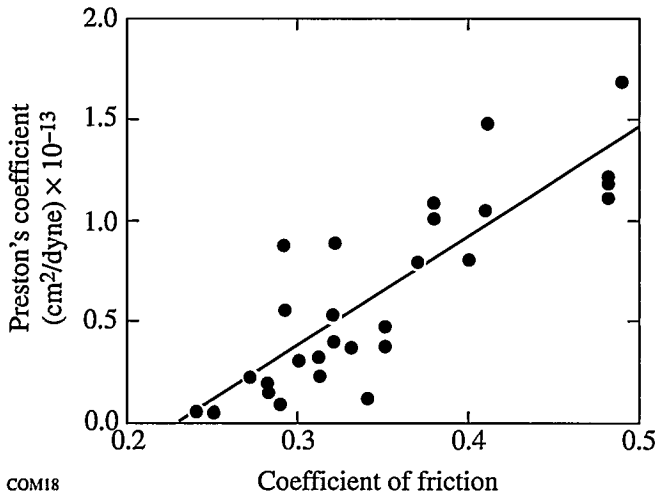


Figure 61.27
Preston's coefficient versus the coefficient of friction between the glass work and the polyurethane pad.

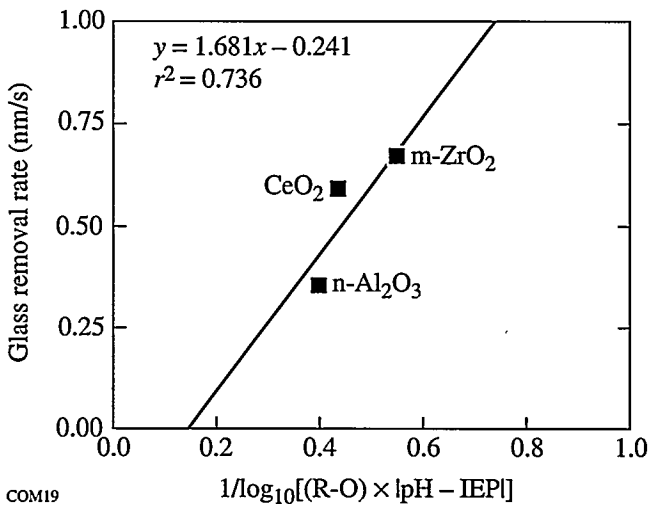


Figure 61.28
Glass removal rate versus the rate constant [4] for BK7 polishing at pH 4. (R-O) is the single oxygen bond strength (units of kcal/mole) of the polishing agent.

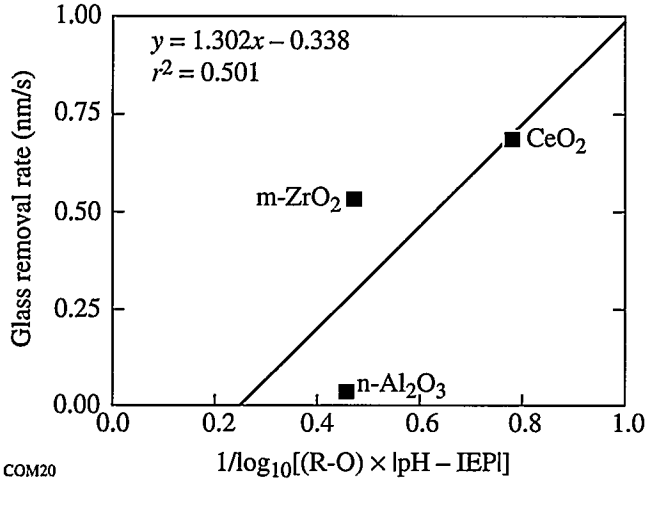


Figure 61.29
Glass removal rate versus the rate constant [4] for BK7 polishing at pH 7. (R-O) is the single oxygen bond strength (units of kcal/mole) of the polishing agent.

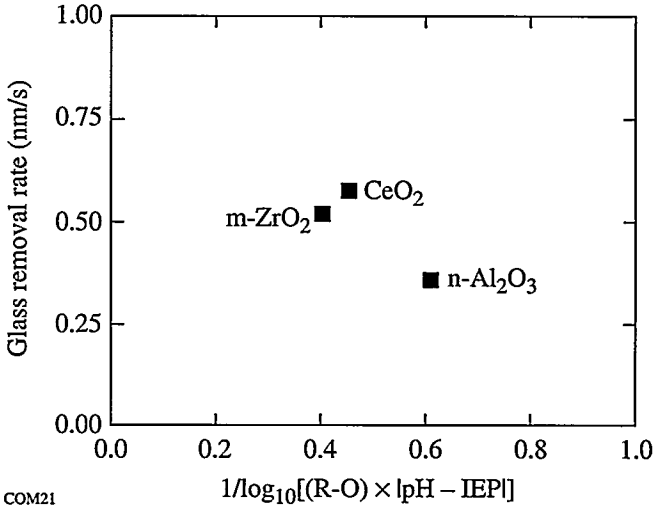


Figure 61.30
Glass removal rate versus the rate constant [4] for BK7 polishing at pH 10. (R-O) is the single oxygen bond strength (units of kcal/mole) of the polishing agent.

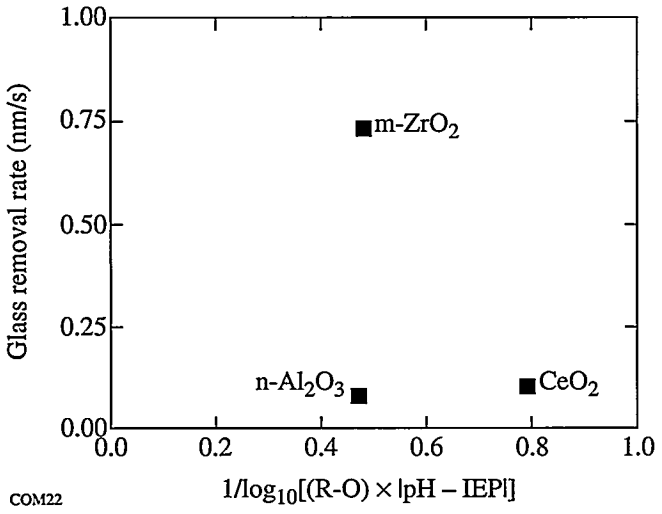


Figure 61.31
Glass removal rate versus the rate constant [4] for SF6 polishing at pH 7. (R-O) is the single oxygen bond strength (units of kcal/mole) of the polishing agent.

type were obtained when the slurry was maintained at pH 10. To understand this result, it should first be noted that all three polishing agents and all three glass types have a negative surface charge density at pH 10. As indicated by $D_f/D_0$, significant in-process reduction of the mean slurry particle size occurred for all nine combinations of polishing agent and glass type at this pH level. The repulsive electrostatic interparticle forces induced by the basic fluid environment inhibit the formation of agglomerates in the slurry, thereby preventing the formation of deep scratches or sleeks on the surface of the glass work. The aqueous solubility of silica, which forms the network of all three glass types, is also sharply accelerated above pH 8.[51] At pH 10, it is therefore quite plausible to expect preferential dissolution of any microscopic irregularities on the silicate surface because of their relatively high surface-area-to-volume ratios. Supportive evidence for the above can be found in the scatter diagram of Fig. 61.32, which is a plot of the average rms surface roughness values on a logarithmic scale obtained at the conclusion of each of the 27 core polishing experiments versus the difference between the fluid pH and the IEP values of the polishing agents. Each plotted symbol in Fig. 61.32 represents one polishing session for the indicated glass type and polishing agent at a given pH value. The abscissa, pH–IEP, is an opposite indicator of the sign of the surface charge on the polishing agent. Note that for pH values larger than the IEP of the polishing agent (i.e., for which the polishing agent and glass are negatively charged), the surface roughness values were, without exception, quite low. When the pH is less than the IEP, large values of roughness were observed for some combinations of polishing agent, glass type, and pH; we term this phenomenon the *slurry charge control effect.*

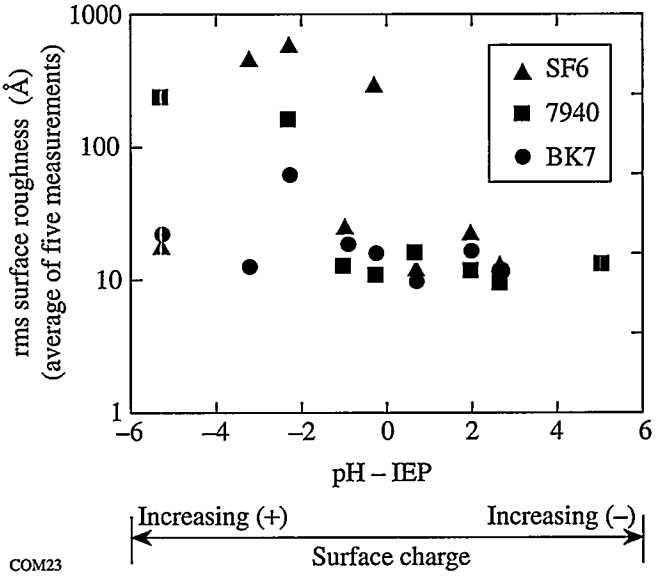


Figure 61.32
Dependence of the glass surface roughness on the difference between the fluid pH and the isoelectric point of the polishing agent (measured in 0.01-M aqueous NaCl). Each data point corresponds to a unique combination of polishing agent ($CeO_2$, monoclinic $ZrO_2$, or nanocrystalline $Al_2O_3$), glass type (7940, BK7, or SF6), and slurry pH (4, 7, or 10).

Interpretation of the slurry charge control effect is quite simple as summarized in Table 61.X. For glass types with a silica network, the combination of fluid and polishing agent should be selected so that the fluid pH is always larger than the IEP of the polishing agent. This precaution ensures that both the polishing agent particles and any silica species have surface charge of the same sign. As was mentioned previously, the corresponding repulsive electrostatic force inhibits agglomeration of any particles suspended in the slurry, resulting in the smoothest possible surface finishes.

Referring to Figs. 61.33 and 61.34, the polishing of 7940 with nanocrystalline $Al_2O_3$ provides an excellent example of the slurry charge control effect. In terms of both removal rate and surface roughness, the best results were obtained at pH 10, where both the polishing agent particles and the glass work had relatively large negative charge densities. At pH 7, where the polishing agent particles and the glass work were oppositely charged, significant agglomeration occurred, causing an increase in the surface roughness and a decrease in the removal

Table 61.X: Qualitative summary of the slurry charge control effect. *The smoothest surfaces are obtained using combinations of polishing agent and glass type with surface charge of the same sign.*

| Materials | IEP | Surface Charge State at pH 4 | Surface Charge State at pH 7 | Surface Charge State at pH 10 |
|---|---|---|---|---|
| Polishing Agents | | | | |
| $CeO_2$ | 7.3[a] | ++ | $0^+$ | – |
| m-$ZrO_2$ | 5.0[a] | + | – | –– |
| n-$Al_2O_3$ | 9.3[a] | ++ | + | – |
| Glass Types | | | | |
| 7940 | 3.7[b] | $0^-$ | – | –– |
| BK7 | 3.2[b] | – | – | –– |
| SF6 | 3.4[b] | – | – | –– |

(a) Measured in aqueous NaCl (0.01 M) using electrophoretic light scattering
(b) Measured in aqueous KCl (0.001M) using the streaming potential technique
++ Relatively large positive charge density
+ Relatively small positive charge density
$0^+$ Slight positive charge density (pH close to the IEP)
$0^-$ Slight negative charge density (pH close to the IEP)
– Relatively small negative charge density
–– Relatively large negative charge density

rate. At pH 4, no agglomeration occurred since the polishing agent particles had a relatively high positive charge density, while the glass work had only a slight negative charge density. The removal rate in this system was nearly as high as with the pH 10 slurry. The corresponding large value of surface roughness at pH 4 is probably due to the reduced solubility of silica in the acidic environment, which inhibited corrosion of the network.

Landingham *et al.* have previously encountered agglomeration problems in the pitch polishing of fused silica with $Al_2O_3$.[52] In hindsight, this is not surprising since their investigation was limited to slurry pH values between 7.4 and 9.0, where silica and $Al_2O_3$ are oppositely charged. Although the more recent success of Tesar *et al.*[12] in the pitch polishing of fused silica with $CeO_2$ and monoclinic $ZrO_2$ at pH 4 appears to be at odds with the slurry charge control effect, their slurries were dispensed at a very low rate (1.2 ml/min.) and were not recirculated. These two process features reduced the tendency of the polishing agent to agglomerate because the accumulation of silica species in the slurry was negligible. Since no results were reported by Tesar *et al.* at pH 10, we were unable to make a more direct comparison of their results with our own.

## Conclusions

The concepts and analytical tools of colloid science for characterization of surface charge effects were used in this work to demonstrate the strengths and limitations of a newly proposed polishing process rate model. The pivotal role of slurry fluid chemistry, particularly pH, in maintaining

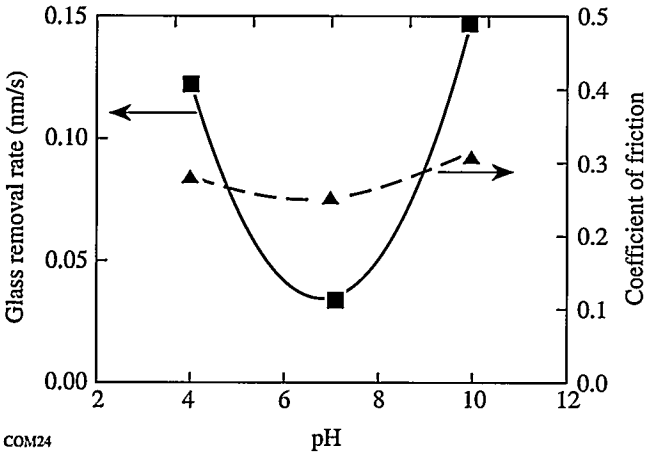


Figure 61.33
Glass removal rate and coefficient of friction between the work and the polyurethane pad as a function of slurry pH for polishing of 7940 with nanocrystalline $Al_2O_3$.

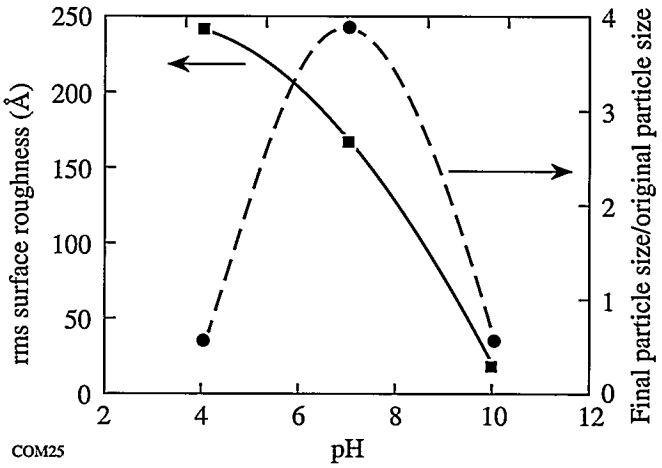


Figure 61.34
Surface roughness and the final median particle size of the slurry divided by the original median particle size as a function of slurry pH for polishing of 7940 with nanocrystalline $Al_2O_3$.

electrokinetically favorable conditions for a well-dispersed polishing agent was also identified and explored. For the silicate glass types studied here, these electrokinetically favorable conditions were sufficient for obtaining the smoothest possible surfaces. A relationship between fluid pH and the isoelectric point of the polishing agent, termed the slurry charge control effect, was also established, and its importance in controlling surface roughness was demonstrated. Our results have shown that there are chemically modulated forces present in the polishing system that can be equal to and, in some cases, exceed the mechanical forces and that these chemically modulated forces exert their effect at the interparticle level, not between individual particles and the glass work. The latter was most clearly demonstrated by the performance of nano-crystalline $Al_2O_3$, which was limited by the slurry fluid pH and not by the mechanical friability of individual polishing agent particles. The pH of the fluid and the IEP of the polishing agent were also shown to be the process parameters that, if carefully controlled, can lead to the production of higher-quality surfaces in less time.

## ACKNOWLEDGMENTS

The authors extend their thanks to the following individuals and organizations for providing many helpful suggestions: T. S. Izumitani (Hoya Corporation) and L. M. Cook (Rodel Products Corp.). Glass samples were prepared under the skillful guidance of the University of Rochester's master opticians, K. H. Kubath and A. Maltsev. Generous financial support was provided by Bausch & Lomb, the Center for Optics Manufacturing (COM) through the U.S. Army Mantech Program, the New York State Center for Advanced Optical Technology (NYSCAOT), and the U.S. Department of Energy Office of Inertial Confinement Fusion under Cooperative Agreement No. DE-FC03-92SF19460.

## REFERENCES

1. R. H. Doremus, *Glass Science* (Wiley, NY, 1973), Chap. 13, pp. 229–252.
2. M. J. Cumbo, "Chemo-Mechanical Interactions in Optical Polishing," Ph.D. thesis, University of Rochester, 1993.
3. T. S. Izumitani, *Optical Glass* (AIP Translation Series, NY, 1986), Chap. 4, pp. 91–146.
4. L. M. Cook, J. Non-Cryst. Solids **120**, 152 (1990).
5. F. W. Preston, J. Soc. Glass Technol. **11**, 214 (1927).
6. G. M. Sanger and S. D. Fantone, in *CRC Handbook of Laser Science and Technology*, Vol. V, Part 3, edited by M. J. Weber (CRC Press, Boca Raton, FL, 1987), pp. 461–500.
7. N. J. Brown, Lawrence Livermore National Laboratory Report MISC 4476, p. 6 (1990).
8. A. A. Tesar and B. A. Fuchs, in *Optical Fabrication and Testing Workshop*, OSA Technical Digest, Vol. 24, WB9-1 (Optical Society of America, Washington, DC, 1992), pp. 137–140.
9. A. A. Tesar and B. A. Fuchs, in *Advanced Optical Manufacturing and Testing II*, edited by V. J. Doherty (SPIE, Bellingham, WA, 1991), Vol. 1531, pp. 80–90.
10. N. J. Brown, in *Contemporary Methods in Optical Fabrication*, edited by C. L. Stonecypher (SPIE, Bellingham, WA, 1981), Vol. 306, pp. 42–57.
11. D. Golini and S. D. Jacobs, Appl. Opt. **30**, 2761 (1991).
12. A. A. Tesar, B. A. Fuchs and P. P. Hed, Appl. Opt. **31**, 7164 (1992).
13. M. J. Cumbo and S. D. Jacobs, Nanotechnology **5**, 70 (1994).
14. R. J. Hunter, *Zeta Potential in Colloid Science: Principles and Applications* (Academic Press, New York, 1981), pp. 17–18.
15. *Ibid.*, pp. 59–178.
16. D. Fairhurst and V. Ribisch, "Zeta Potential Measurements of Irregular Shape Solid Materials," in *Particle Size Distribution II*, American Chemical Society Symposium Series, No. 472, 337–353 (1991).
17. Corning 7940 fused silica, courtesy of L. Sutton, Corning Inc., Canton, NY 13617.
18. Schott BK7 (borosilicate crown) and Schott SF6 (dense flint), courtesy of A. Marker, Schott Glass Technologies Inc., Duryea, PA 18642.
19. "Corning Premium-Quality Fused Silica Low Expansion Material Code 7940," Corning Inc., Corning, NY 14830.
20. T. S. Izumitani, *Optical Glass* (AIP Translation Series, NY, 1986), p. 21.
21. Optical Glass Catalog, Schott Glass Technologies, Duryea, PA.
22. CE-RITE HP, High Purity Cerium Oxide, Code 480-G, lot # 910876, courtesy of D. Coller, Transelco Div., Ferro Corp., Penn Yan, NY 14527.
23. Zirconia Q, batch #15030492, courtesy of D. Rostoker, Saint Gobain/Norton Industrial Ceramics Corp., Worcester, MA 01615.
24. NANO-SIZE ALPHA, batch #0001-92, courtesy of D. Rostoker, Saint Gobain/Norton Industrial Ceramics Corp., Worcester, MA 01615. This is a blocky a-$Al_2O_3$ abrasive with individual crystallite sizes of the order of 50 nm (patent pending).
25. T. Izumitani, in *Treatise on Material Science and Technology*, edited by M. Tomozawa and R. H. Doremus (Academic, New York, 1979), Vol. 17, pp. 138–140.
26. S. D. Jacobs, "Optical Glasses and Optical Fabrication," Optics 443 course notes, University of Rochester (1994), Chap. 6, p. 11.
27. "Microgrit WCA Specifications," Micro Abrasives Corporation, Westfield, MA 01086.

28. Pocket Surf III, Federal Products Corp., Providence, RI 02905.

29. A. Lindquist, S. D. Jacobs, and A. Feltz, in *Science of Optical Finishing*, OSA Technical Digest, Vol. 9., SMC3-1 (Optical Society of America, Washington, DC, 1990), pp. 57-60. SSD measurements courtesy of T. M. Rich, Center for Optics Manufacturing, University of Rochester.

30. Brookhaven EKA, Brookhaven Instruments Corp., Holtsville, NY 11742.

31. MIL-0-13830A, Revision L, (1980).

32. Brookhaven ZetaPlus, Brookhaven Instruments Corp., Holtsville, NY 11742.

33. F. M. Ernsberger, J. Am. Ceram. Soc. **42**, 373 (1959).

34. J. Jednacak, V. Pravdic and W. Haller, J. Colloid Interface Sci. **49**, 16 (1974).

35. R. J. Hunter, *Zeta Potential in Colloid Science: Principles and Applications* (Academic Press, London, 1981), p. 249.

36. R. H. Ottewill, "Electrokinetic Properties," Fifth Annual Short Course on Colloid Science Principles & Practice, University of Massachusetts (1992), p. 7.10.

37. L. M. Cook, Rodel Products Corp., Newark, DE 19713 (personal communication, 1992).

38. Horiba LA900, Horiba Instruments Inc., Irvine, CA 92714.

39. J. S. Reed, *Introduction to the Principles of Ceramic Processing* (John Wiley & Sons, NY, 1988), pp. 90–92.

40. F. Cooke, N. Brown and E. Prochnow, Opt. Eng. **15**, 407 (1976).

41. EL Load Cell, Model #ELF-1000-100, Entran Devices, Inc., Fairfield, NJ 07004.

42. HSP, Rodel Products Corp., Scottsdale, AZ 85258.

43. J. J. Bohache, "A Study of the Optical Polishing Process," Ph.D. thesis, University of Rochester, 1978, p. 143.

44. As suggested by H. Koch, Planar Optics, Inc., Webster, NY 14580 (personal communication, 1992).

45. Zygo Maxim-3D Model 5700, Zygo Corp., Middlefield, CT 06455. Using a 20X Mirau objective, this noncontact optical profiler has a 0.1-nm vertical resolution, a field of view of $0.453 \times 0.411$ mm, and a 1.75-$\mu$m lateral resolution.

46. Davidson D305LV, Davidson Optronics Inc., West Covina, CA 91790.

47. F. K. Aleinikov, Sov. Phys.-Tech. Phy. **27**, 2529 (1957).

48. J. Jednacak, V. Pravdic, and W. Haller, J. Colloid Interface Sci. **49**, 16 (1974). The authors confined most of their study to chemically durable silica-rich glass types.

49. R. J. Hunter, *Zeta Potential in Colloid Science: Principles and Applications* (Academic Press, London, 1981), p. 233. Any ion whose adsorption at a surface is influenced by factors other than the electrical potential there (e.g., covalent bonding with surface atoms) is regarded as being specifically adsorbed.

50. J. H. Escard and D. J. Brion, J. Am. Ceram. Soc. **58**, 296 (1975).

51. R. H. Doremus, *Glass Science* (Wiley, NY, 1973), p. 243.

52. R. L. Landingham, A. W. Casey, and Roy O. Lindahl, in *The Science of Ceramic Machining and Surface Finishing II*, edited by B. J. Hockey and R. W. Rice, NBS Special Publication 562 (U.S. Government Printing Office, Washington, DC, 1979), pp. 231–245.

# Effect of Thermal and Mechanical Processing on Molecular Ordering in Liquid Crystal Elastomers

Liquid crystalline polymers have been the focus of intensive research in recent years because of their potential for use in a wide range of optical as well as photonic applications.[1–3] Although the macroscopic alignment required for practical applications can be achieved by surface treatment and the application of an external electric or magnetic field, the effectiveness of these processing techniques is limited to films with a thickness less than 100 $\mu$m.[4] To overcome this problem, liquid crystalline (LC) *elastomers* have been explored in view of the relative ease with which mesogenic moieties can be aligned by stretching.[5–11] An additional feature of these materials is the ability to "lock-in" this stress-induced alignment via crosslinking of reactive side-chains to produce a three-dimensional polymer network.

Finkelmann *et al.*[12] have previously described a novel two-stage reaction scheme for the preparation of LC elastomers; this process is shown in Fig. 61.35. In the first stage, a hydrosilylation reaction was conducted on the terminal methylene groups of the polymer to obtain a partially crosslinked elastomer carrying two pendant groups: a nematogen and a methacrylate. In the second stage, a constant stress was applied to produce uniform nematic alignment followed by a second crosslinking step by means of the less-reactive methacryloyl groups. Poly(methylhydrosiloxane), with a degree of polymerization $n$ of 120, was employed exclusively in these experiments.

In this article we describe the preparation of mesogenic elastomer systems based on two commercially available polysiloxanes, poly(methylhydrosiloxane) ($n = 40$) and poly(ethylhydrosiloxane) ($n = 80$), and their characterization by Fourier transform infrared (FTIR) spectroscopy, differential scanning calorimetry (DSC), hot-stage polarized optical microscopy, stress-strain analysis, and x-ray diffraction to elucidate the dynamic features of preparation and processing of LC elastomers.

## Experimental Section

1. Materials

Poly(methylhydrosiloxane) (PMHS), $-[(CH_3)SiH-O-]_{40}-$, (0.30 Stoke, Spectrum Chemicals); poly(ethylhydrosiloxane) (PEHS), $-[(C_2H_5)SiH-O-]_{80}-$, (1.00 Stoke, Gelest); toluene (anhydrous, 99+% Aldrich Chemical Company); and a Pt-catalyst (PC072, United Chemical Technologies) were all used as received without further purification. The nematic monomer and cross-linking agents were synthesized by standard literature methods, as shown in Figs. 61.36 and 61.37.

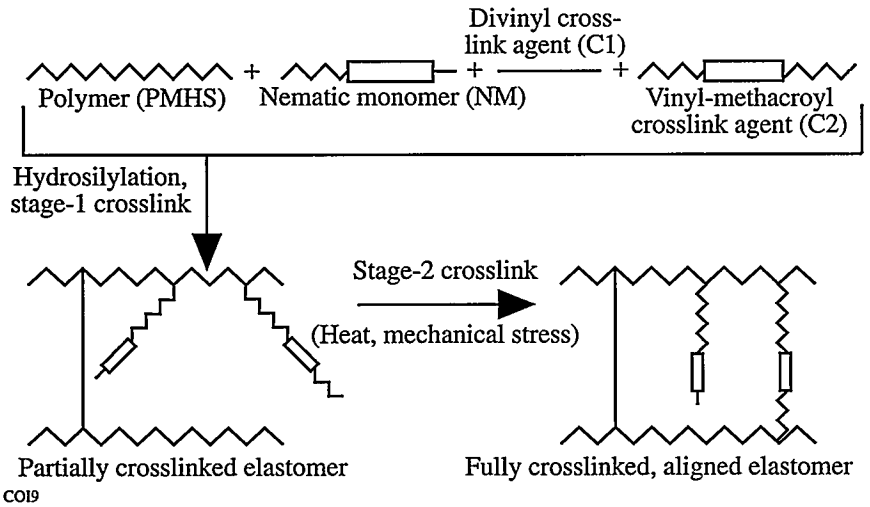


Figure 61.35
The two-step process for the preparation of aligned LC elastomers. The components are combined and reacted to form a partially crosslinked elastomer; the combination of heat and mechanical stress completes the crosslinking reaction and aligns the mesogenic pendant groups.

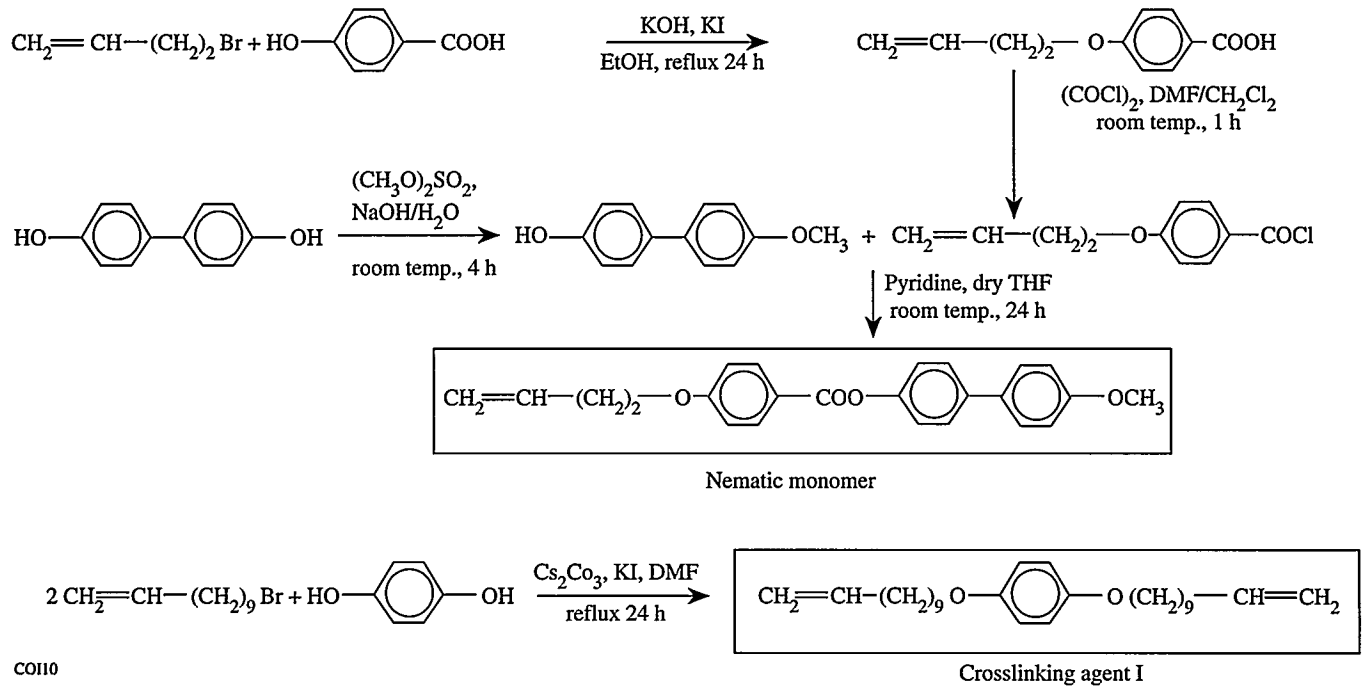


Figure 61.36
Synthesis scheme for the preparation of the nematic monomer and the diacrylate crosslinking agent used for elastomer preparation.

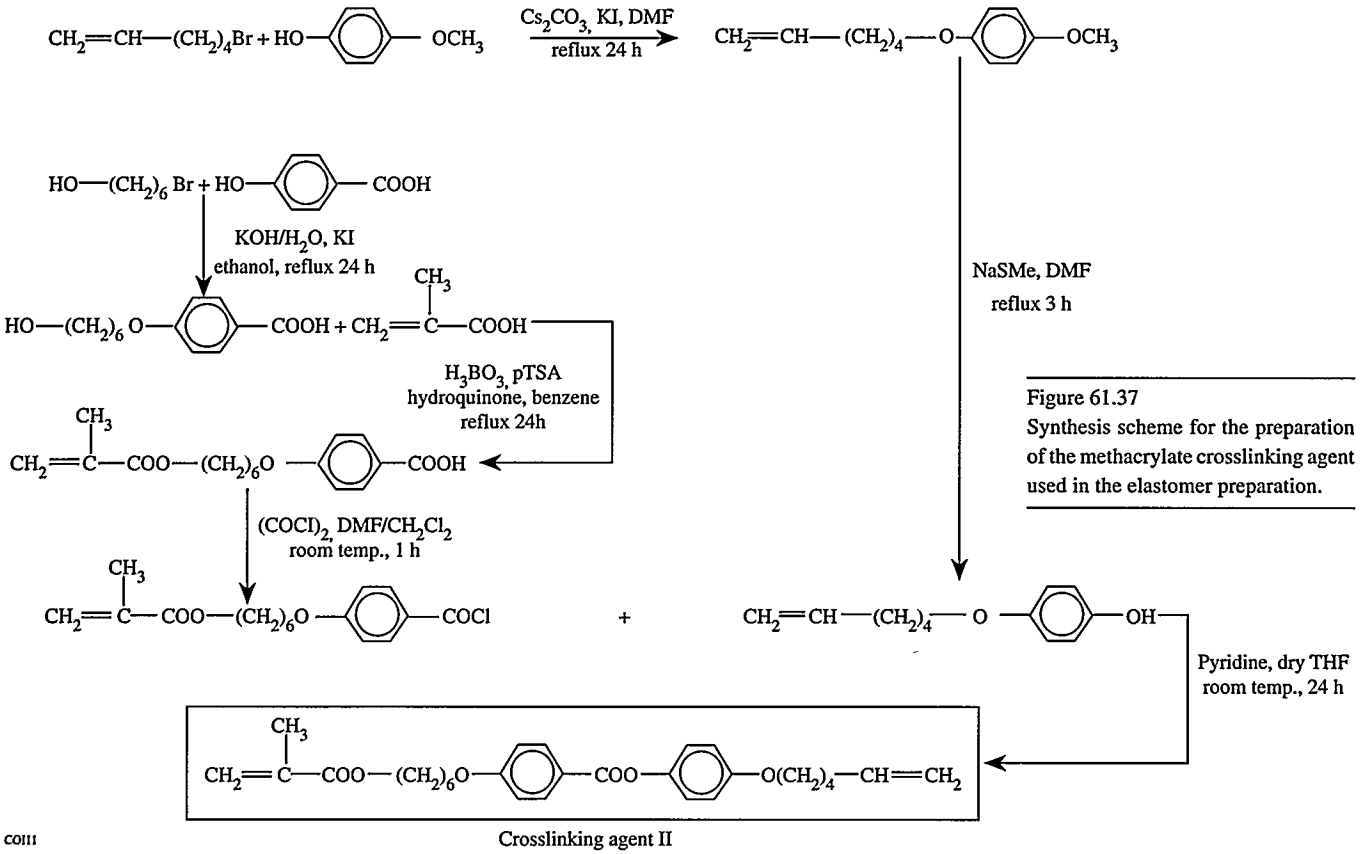


Figure 61.37
Synthesis scheme for the preparation of the methacrylate crosslinking agent used in the elastomer preparation.

2. Preparation of Elastomers

To prepare the elastomers, appropriate quantities of the nematic monomer (NM), the first crosslinking agent (C1), and the second crosslinking agent (C2), as shown in Fig. 61.38, were added to PEHS or PMHS in a round-bottomed reaction flask to ensure a polymer:NM:C1:C2 molar ratio of 1:0.3:0.1:0.1. Upon addition of toluene (13.6 ml/g-material), the flask was sealed, flushed with nitrogen, and heated to ensure dissolution of solids. The catalyst was added ([Pt/$CH_2$ = CH–] ≈ 0.002), and the flask was shaken vigorously for 30 s before quickly transferring the contents to a heated Teflon™ mold kept overnight at 60°C under a nitrogen purge (first-stage reaction). The elastomer was carefully removed from the mold, stretched by the desired amount, and left for three days on a hot plate at 60°C to complete the elastomer preparation (second-stage reaction). This method of elastomer preparation is similar to that reported by Finkelmann *et al.*,[12] with the exception that a constant *strain*, as opposed to a constant *stress*, was used in our experiments. The extent of reaction was monitored using FTIR spectroscopy. The elastomers prepared from PEHS and PMHS parent polymers were denoted as ES and MS, respectively.

3. Methods of Characterization

The degrees of polymerization of PEHS and PMHS were evaluated from a viscosity versus molecular weight relationship derived from product data (United Chemical Technologies). Infrared spectra of both the parent polymers and the elastomers were obtained using a Nicolet 20SXC FTIR spectrophotometer. Differential scanning calorimetry (DSC) data were collected using a Perkin Elmer DSC-4 at +20°C/min under a helium purge with liquid nitrogen cooling. A hot-stage polarized optical microscope (Leitz Orthoplan-Pol and a Mettler FP52 hot stage) was used for mesophase identification and verification of transition temperatures determined by DSC. Mechanical characterization of elastomers was conducted in a water bath at 55±1°C using an Instron Table Model 1102 instrument. The stress $\sigma$ is determined in terms of the original cross sectional area, and the strain is defined as $\varepsilon = (l - l_0)/l_0$, where $l$ and $l_0$ are the length at the time of data collection and original length, respectively.

Two-dimensional, flat-plate x-ray diffraction patterns were collected using a Statton box camera with a sample-to-film distance of 5.0 cm. An image-plate storage phosphor detector was utilized in place of x-ray film to reduce data-collection time.[13] Samples were irradiated with nickel-filtered copper radiation. A qualitative assessment of orientation and liquid crystallinity was accomplished using the flat-plate diffraction data. The x-ray diffraction patterns were obtained with a Rigaku RU-300 pole figure goniometer used in the Bragg-Brentano geometry. This diffractometer was equipped with a copper rotating anode operated at 50 kV and 280 mA, a diffracted-beam nickel filter, and a scintillation detector. Reflection-mode $\theta/2\theta$ scans provided information on planar orientation, while symmetrical transmission-mode $\theta/2\theta$ scans provided a preliminary assessment of in-plane orientation. A quantitative orientation analysis was performed by an azimuthal diffraction technique.[14] Data were collected using the Rigaku RU-300 pole goniometer as mentioned above. Azimuthal analysis involved positioning a sample at a fixed angle $\theta$ in the symmetric transmission mode with the detector

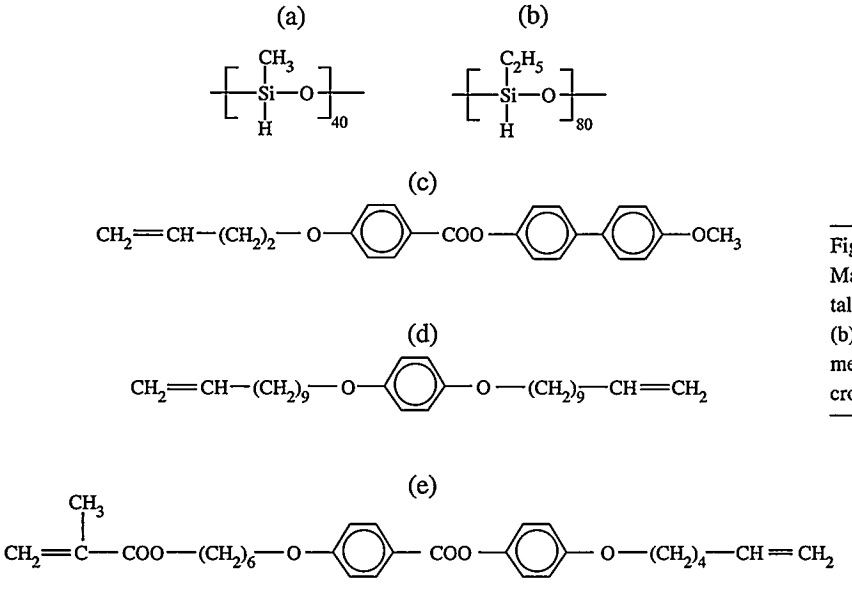


Figure 61.38
Materials used in the preparation of the liquid crystalline elastomers: (a) poly(methylhydrosiloxane); (b) poly(ethylhydro-siloxane); (c) nematic monomer; (d) first crosslinking agent; and (e) second crosslinking agent.

at a fixed $2\theta$ to detect a desired Bragg diffraction peak. The sample was then rotated 360° around the normal to the sample plane, defined as the $\chi$ rotation. In this study the transverse direction was mounted at zero azimuthal angle, i.e., parallel to the plane of the x-ray beam. Azimuthal data allowed the determination of in-plane orientation. Orientation distribution was quantified by the use of the Herman's orientation distribution function ($HOF_A$) defined for in-plane alignment as[14]

$$HOF_A = \frac{3\langle \cos^2 \chi \rangle - 1}{2} \tag{1}$$

with $\langle \cos^2 \chi \rangle$ defined as

$$\langle \cos^2 \chi \rangle = \frac{\Sigma I(\chi) \sin \chi \cos^2 \chi}{\Sigma I(\chi) \sin \chi}, \tag{2}$$

where $I(\chi)$ denotes intensity as a function of azimuthal angle $\chi$. The value of $HOF_A$ ranges from –0.5 to 1 for in-plane orientation distribution, with a value of –0.5 indicating a perfect alignment of polymer chains along the strain direction, a value of 0 indicating a random or balanced alignment, and a value of 1 indicating perfect alignment of polymer chains along the transverse direction.[14]

**Results and Discussion**

Fourier transform infrared spectrometry was used to monitor the extent of hydrosilylation reaction, as illustrated in Fig. 61.39 for elastomer MS, where a comparison of scans recorded after the first- [Fig. 61.39(a)] and second-stage [Fig. 61.39(b)] reactions shows the expected reduction in the intensity of the Si-H stretching band at 2160 $cm^{-1}$. The effect of reaction on the mechanical properties of both the ES and MS elastomers is illustrated in the stress versus strain curves of Fig. 61.40. In light of the reported effect of crosslink density on glass transition ($T_g$) and liquid-crystal-to-isotropic transition temperatures,[4–11] it is important to ensure that a valid comparison of ES to MS elastomers is made. The crosslink density in terms of the molecular weight between crosslinks, $M_c$, is related to the elastic modulus $E$ ($N/mm^2$) at low strains and at temperatures above $T_g$ by Eq. (3):[6]

$$E = \frac{3\rho RT}{M_c}, \tag{3}$$

where $\rho$ is the density estimated at 1.0 $g/cm^3$,[8,11] $R$ the ideal gas constant, and $T$ the temperature (°K). Since the data were collected at a temperature (55°C) that is above the $T_g$ for all samples considered, Eq. (3) is appropriate for evaluating $E$ from Fig. 61.40. Using Eq. (3), an $M_c$ of 660 g/mole ($E$ = 12.4 $N/mm^2$) and 560 g/mole ($E$ = 14.6 $N/mm^2$) were found for the ES and MS elastomers, respectively. Figure 61.37 also shows the expected increase in $E$ (*i.e.*, a decrease in $M_c$) with an increased extent of reaction. Since samples must be stretched during the second-stage reaction to achieve bulk alignment of the nematic pendant groups, the maximum strain sustained, $\varepsilon_b$, is an important parameter. For our elastomer composition as defined earlier, ES and MS possessed an $\varepsilon_b$ value of 0.31 and 0.16, respectively. The difference in $\varepsilon_b$ is attributed to the higher molecular weight of the ES system since the degrees of polymerization of the PEHS and PMHS polymers are 80 and 40, respectively.

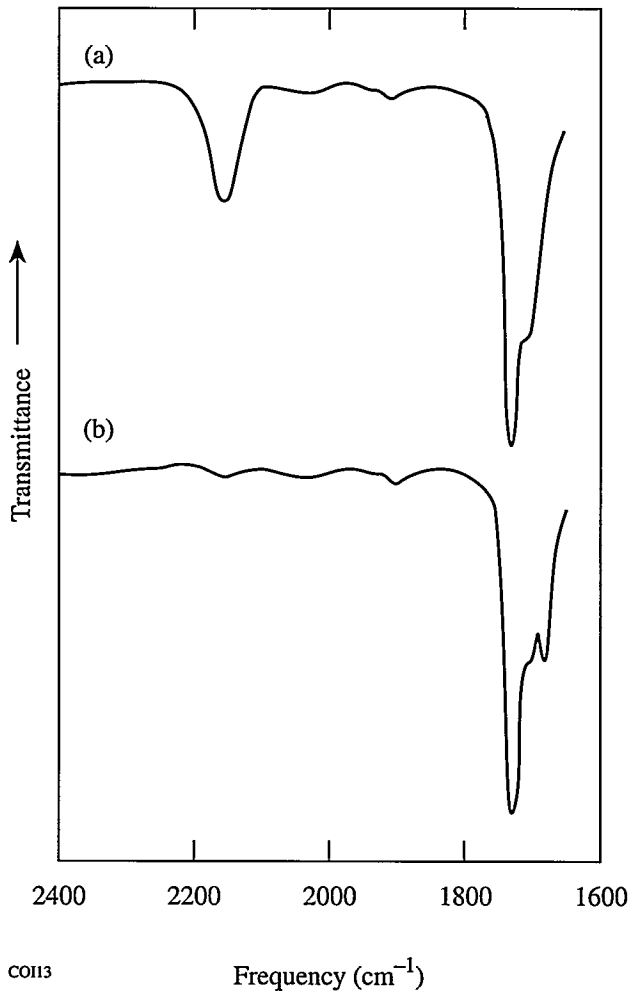


Figure 61.39
FTIR spectra of the MS elastomer after (a) first-stage and (b) second-stage reaction.

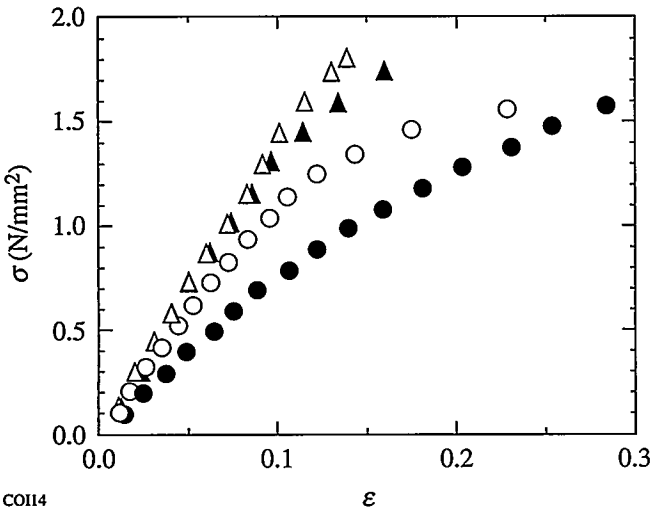


Figure 61.40
Stress ($\sigma$) versus strain ($\varepsilon$) recorded at 55°C for MS elastomer after first-stage (▲) and second-stage reaction (△), and ES elastomer after first-stage (●) and second-stage reaction (○).

The DSC thermograms of ES and MS are presented in Fig. 61.41, where the subscripts *s* and *n* refer to samples that were stretched and not stretched, respectively, during the second-stage reaction. Samples described as "stretched" are those that were strained to the fullest possible extent without tearing during the second-stage reaction. Since the glass transitions of pure PEHS and PMHS are −149°C and −140°C, respectively, the substitution and crosslinking reactions would appear to be responsible for the elevated glass transitions of both polymer hosts. This factor is consistent with the increase in $E$ observed in Fig. 61.40. In the first heating scan of the ES elastomer prepared without stretching, an endotherm occurs at 82°C [Fig. 61.41(a)] due to a nematic-to-isotropic transition. A lower value for the transition enthalpy ($\Delta H$) was obtained for an equivalent sample that had been stretched. After the ES sample is heated through this transition temperature and slowly cooled to room temperature, the nematic-isotropic endotherm now appears at 63°C [Fig. 61.38(b)] with a greatly reduced $\Delta H$. If this same ES elastomer sample is instead rapidly cooled to low temperatures (i.e., quenched) from 90°C and then annealed at 60°C, subsequent heating gives an endotherm at 70°C with a $\Delta H$ of 1.9 J/g, identical to the value shown in Fig. 61.38(b). These results infer that the $\Delta H$ for the nematic-isotropic transition is independent of thermal history applied after the initial heating cycle, while, in contrast, the nematic-isotropic transition temperature ($T_{n\text{-}i}$) displays total thermal history dependence. For the MS elastomer [Fig. 61.41(c)], the endotherm at 80°C is accompanied by a reduced $\Delta H$ as compared to the ES elastomer, even though the nematic texture was clearly visible between $T_g$ and 80°C by hot-stage polarizing microscopy. The absence of an endotherm for elastomer MS when the same sample is rescanned [Fig. 61.41(d)] suggests a lack of nematic ordering. Finkelmann *et al.*,[12] however, have reported values for $T_g$, $T_{n\text{-}i}$, and $\Delta H_{n\text{-}i}$ of 0°C, 83°C, and 1.7 J/g°K, respectively, for the elastomer prepared from PMHS with a degree of polymerization of 120. Other than the differences in the chain length of the starting PMHS and in the

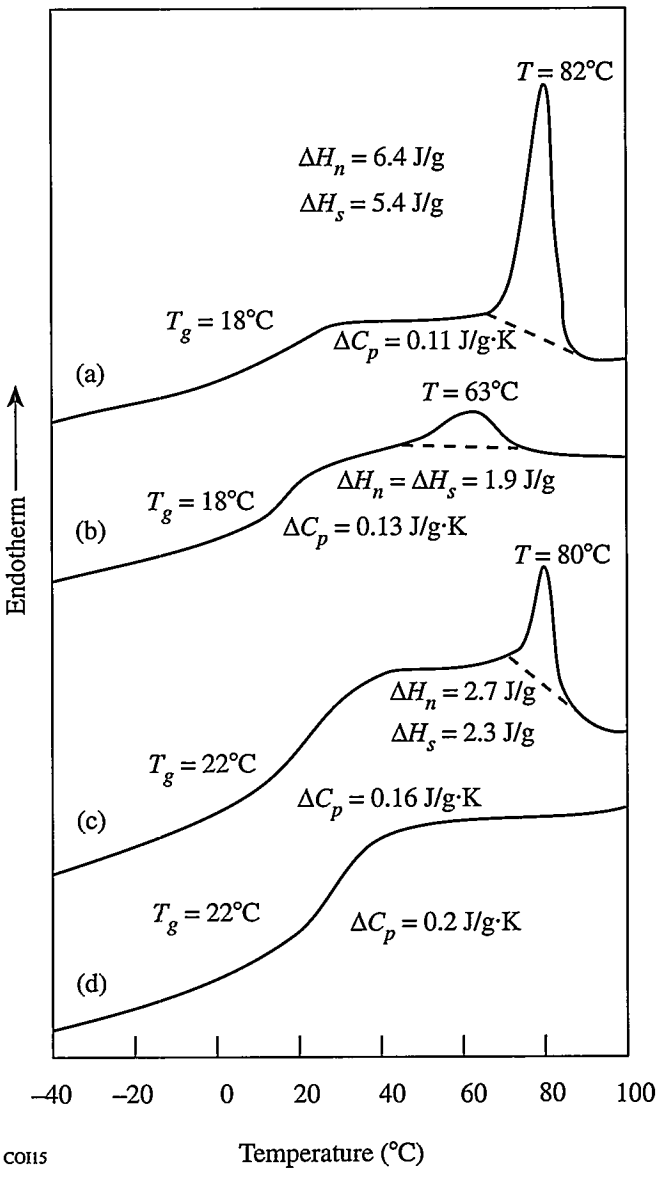


Figure 61.41
DSC thermograms recorded at 20°C/min. of (a) ES elastomer; (b) second heating scan of ES elastomer after the sample was first heated to 90°C and cooled at 5°C/min to room temperature; (c) MS elastomer; and (d) second heating scan of MS elastomer after the sample was heated to 90°C and cooled at 5°C/min to room temperature.

crosslink density, no explanation can be offered for the discrepancy with our experimental results. It appears that the observed values of $\Delta H_n$ and $\Delta H_s$ of the ES and MS elastomers without any previous thermal history are both greater than those that can be properly accounted for by a typical nematic-to-isotropic transition.

To gain further insights into the relationship between molecular ordering and the endotherms acquired during the first heating scans of the ES and MS elastomers, we turned to x-ray diffraction techniques. The flat-plate diffraction pattern for the unstretched ES sample [Fig. 61.42(a)] shows two broad diffraction rings characteristic of a polydomain nematic, as was also observed for the unstretched MS elastomer. Interplanar spacing calculations reveal that the inner and outer rings have *d*-spacings of 8.8 Å and 4.38 Å, respectively. Upon stretching the elastomers, in-plane orientation occurs, as evidenced by the formation of arcs in the flat-plate diffraction pattern for the ES elastomer with $\varepsilon = 0.3$ [Fig. 61.42(b)], which is characteristic of a monodomain nematic.[15] Due to the lower sustainable strains in the MS elastomer (see Fig. 61.40), the effect of strain on orientation in this system is not pronounced, as evidenced by the lack of arc formation in the flat-plate camera photographs. In the ES samples, the majority of the diffraction scatter lies in the equatorial position (zeroth order) in the flat-plate pattern, which indicates that the 8.8-Å and 4.38-Å diffraction peaks are of the type (*hk*0). In the following discussion, the term "thermal treatment" indicates that the samples were heated at 90°C for 10 min and then cooled to room temperature. Upon thermal treatment of the stretched ES elastomer, the nematic order is retained, as evidenced by the absence of any discernible effect on arc formation in comparing Figs. 61.42(b) and 61.42(c). In fact, the $\Delta H_{n\text{-}i}$ at 63°C, 1.9 J/g as noted in Fig. 61.41(b), is typical of a nematic-to-isotropic transition. Thus, the $\Delta H_{n\text{-}i}$ observed in Fig. 61.41(a) appears to be caused by a combination of nematic-to-isotropic transition and molecular relaxation.

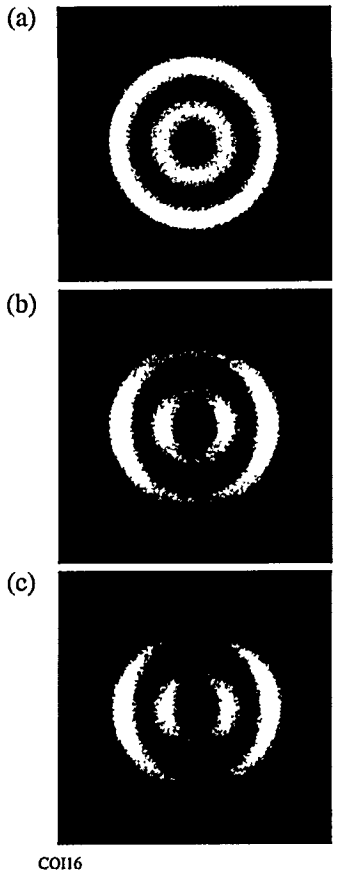


Figure 61.42
Flat-plate x-ray diffraction patterns of ES elastomer: (a) unstretched; (b) stretched to $\varepsilon = 0.3$; and (c) as in (b) but first heated to 90°C and then cooled to room temperature.

Transmission-mode x-ray diffraction data were collected for elastomer ES over a selected range of $2\theta$, as shown in Fig. 61.43. An inspection of Fig. 61.43 reveals that, for both unstretched [I(a)] and stretched [II(a)] ES samples, the 4.38-Å peak (corresponding to the outer ring shown in Fig. 61.42) observed in the flat-plate diffraction data actually comprises *two* peaks with *d*-spacings of 4.47 Å and 4.13 Å. The two peaks can be resolved because of the 20-cm sample-to-detector distance, as compared to the 5-cm distance utilized in the flat-plate diffraction work. The intensity of the 4.13-Å peak relative to that of the 4.47-Å peak is clearly diminished by stretching. The 4.13-Å peak disappears with an increase in intensity of the 4.47-Å peak with thermal treatment, as revealed in comparing I(b) to I(a) and II(b) to II(a) (Fig. 61.43). These observations indicate that stretching and thermal treatment may induce some degree of molecular relaxation, consistent with the facts that $\Delta H_n > \Delta H_s$ and that $\Delta H_n$ and $\Delta H_s$ both decrease to 1.9 J/g upon thermal treatment (see Fig. 61.41).

Azimuthal diffraction data collected on the 4.47-Å peak, as shown in Fig. 61.44, permit a quantitative assessment of molecular relaxation resulting in an enhanced order reflected by the $HOF_A$ parameter defined by Eq. (1). These data suggest that the unstretched ES sample has no in-plane alignment, which implies a near-random distribution of lattice planes based on a $HOF_A$ value of 0.02. For the stretched ES sample, the peaks at 0° and 180° azimuthal positions in Fig. 61.44 (along the sample transverse direction) and a $HOF_A$ value of 0.35 reveal the effect of stretching on the preferred orientation of (*hk*0) lattice planes. Thermal treatment of the stretched sample shows an enhancement of the azimuthal intensity along the transverse direction, resulting in an increased $HOF_A$ value of 0.43 apparently due to the alignment of nematic domains. To be consistent with the observed order in which the $HOF_A$ value

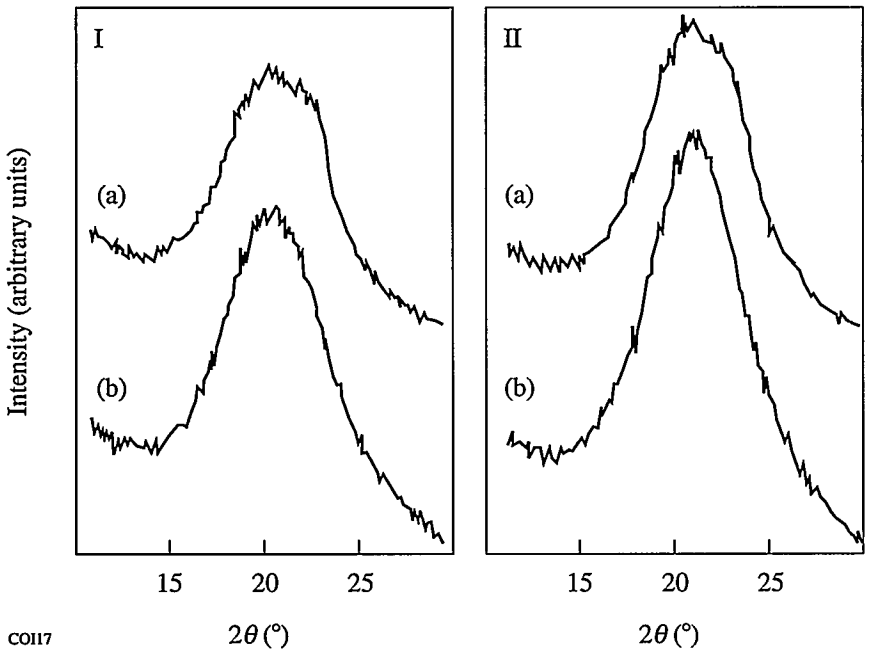


Figure 61.43
X-ray diffraction patterns of ES elastomer: I(a) unstretched, no thermal processing; I(b) sample I(a) heated at 90°C for 10 min and by cooled to room temperature; II(a) stretched to $\varepsilon = 0.3$, no thermal processing; II(b) stretched as in II(a) followed by heating at 90°C for 10 min and cooled to room temperature.

increases upon stretching and thermal treatment, the DSC thermograms in Figs. 61.41(a) and 61.41(b) should be interpreted in terms of stored enthalpy at the molecular scale that is released to some extent by stretching during the second-stage reaction and completely released by thermal treatment. This mode of enthalpy storage does not seem to contribute to the experimentally quantified $HOF_A$ parameter on a relatively macroscopic scale in the case of nematic ordering.

From the x-ray diffraction and thermal analysis data reviewed above, we can make several observations regarding the effect of processing on mesomorphic behavior:

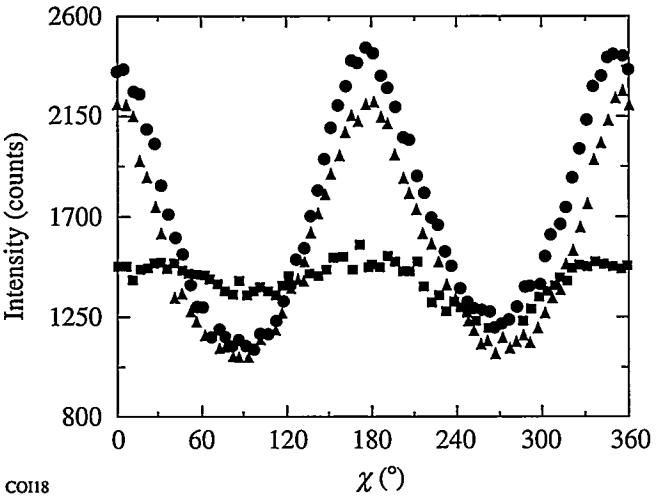


- Based on the flat-plate x-ray diffraction pattern, an imposed strain gives rise to a monodomain nematic character, whereas a polydomain character is observed in the absence of applied strain. Furthermore, the monodomain character achieved with the application of strain is retained when the sample is heated above the nematic-isotropic transition temperature and cooled back to room temperature.

- The DSC thermograms, coupled with the transmission-mode x-ray diffraction data, suggest that (a) enthalpy is stored in the freshly prepared elastomer; (b) the imposed strain helps to release the stored enthalpy to some extent; and (c) the stored enthalpy is almost completely released upon thermal cycling between the nematic-isotropic transition and room temperature.

- The transmission mode and azimuthal x-ray diffraction data demonstrate that, although the stored enthalpy does not lead to an increased order parameter ($HOF_A$), the enthalpy is released through molecular relaxation upon stretching or thermal treatment. This enthalpy release appears to enhance nematic ordering and increase $HOF_A$ values.

Figure 61.44
X-ray diffraction azimuth plots for ES elastomer at $2\theta = 19.8°$, i.e., the 4.47-Å peak in Fig. 61.40: unstretched (■), stretched to $\varepsilon = 0.3$ (▲), and stretched to $\varepsilon = 0.3$ (●) while heating at 90°C for 10 min followed by cooling to room temperature.

**Summary**

Liquid crystalline elastomers derived from siloxane polymers, PMHS and PEHS, were prepared following a two-stage reaction scheme to investigate the effects of processing conditions and thermal treatment on mesomorphic characteristics. A thorough analysis of these elastomers by a combination of FTIR, DSC, mechanical analysis, polarized hot-stage optical microscopy, and x-ray diffraction techniques has shown that the chain length of the precursor siloxane polymer plays an important role in achieving bulk alignment via stretching during the second-stage reaction. The imposed strain was also demonstrated to be critical in achieving a monodomain nematic character, which is completely recoverable after repeated thermal cycling from $T_{n\text{-}i}$ to room temperature. The latter feature is especially important in the preparation of freestanding, optical-quality birefringent films for laser and other optical device applications.

ACKNOWLEDGMENT

This work was supported in part by the Army Research Office under Contract #DAAL03-92-G-0147, the Contact Lens Division of Bausch & Lomb, Inc., the U.S. Department of Energy Office of Inertial Confinement Fusion under Cooperative Agreement No. DE-FC03-92SF19460, and the University of Rochester. The support of DOE does not constitute an endorsement by DOE of the views expressed in this article. The authors would like to thank Craig Barnes of Eastman Kodak Company for assistance in gathering the x-ray data, Eric J. Leibenguth and Linda Slapelis of Bausch & Lomb for assistance in the stress-strain analysis, Dr. Jay F. Kunzler of Bausch & Lomb for helpful discussions, Darin Phelps of the Department of Chemical Engineering for assistance in monomer synthesis, and Professor Burns of the Department of Mechanical Engineering, University of Rochester for helpful discussions.

REFERENCES

1. (a) H. Finkelmann, Angew. Chem. Int. Ed. Engl. **26**, 816 (1987); (b) H. Finkelmann, in *Liquid Crystallinity in Polymers: Principles and Fundamental Properties*, edited by A. Ciferri (VCH Publishers, New York, 1991), p. 315.
2. G. W. Gray, in *Side Chain Liquid Crystal Polymers*, edited by B. McArdle (Chapman and Hall, New York, 1989), p. 106.
3. V. Percec and Q. Zheng, J. Mater. Chem. **2**, 475 (1992).
4. J. Schätzle and H. Finkelmann, Mol. Cryst. Liq. Cryst. **142**, 85 (1987).
5. W. Gleim and H. Finkelmann, in *Side Chain Liquid Crystal Polymers*, edited by C. B. McArdle (Chapman and Hall, New York, 1989), p. 287.
6. F. J. Davis, J. Mater. Chem. **3**, 551 (1993).
7. M. Brehmer and R. Zentel, Mol. Cryst. Liq. Cryst. **243**, 353 (1994).
8. T. Tsutsui and R. Tanaka, Polymer **22**, 117 (1981).
9. (a) R. Zentel and M. Benalia, Makromol. Chem. **188**, 665 (1987); (b) R. Zentel and G. Reckert, Makromol. Chem. **187**, 1915 (1986).
10. H. Loth and A. Euschen, Makromol. Chem., Rapid Commun. **9**, 35 (1988).
11. (a) J. Küpfer and H. Finkelmann, Macromol. Chem. Phys. **195**, 1353 (1994); (b) J. Schätzle, W. Kaufhold, and H. Finkelmann, Makromol. Chem. **190**, 3269 (1989); (c) H. Finkelmann, H.-J. Kock, and G. Rehage, Makromol. Chem., Rapid Commun. **2**, 317 (1981).
12. J. Küpfer and H. Finkelmann, Makromol. Chem., Rapid Commun. **12**, 717 (1991).
13. T. N. Blanton, in *Advances in X-Ray Analysis* (Plenum Press, New York, in press), Vol. 37.
14. L. E. Alexander, *X-Ray Diffraction Methods in Polymer Science* (Wiley-Interscience, New York, 1969).
15. J. Falgueirettes and P. DeLord, in *Liquid Crystals & Plastic Crystals, Vol 2: Physicochemical Properties and Methods of Investigation*, edited by G. W. Gray and P. A. Winsor (Halsted Press, New York, 1974), p. 63.

# An Intrinsic Laser-Damage Mechanism in Next-Generation OMEGA UV Multilayer Coatings

Laser-induced damage has always been and remains as vexing as it is expensive. Despite a quarter century of work, the problem has not been eliminated or even fully defined—only the technical limits have been increased. Although dielectric thin films have improved over the last 25 years, they remain especially difficult subjects to deal with owing to the multiparameter nature of the nonequilibrium deposition methods used in their preparation. As new analytical methods and tools become available, however, better insight into the laser-damage enigma is gained.

The importance of nodular film-growth defects in originating laser damage was one such key insight that was recently offered through a series of pioneering papers by the Optical Coatings Group at Lawrence Livermore National Laboratory.[1–4] These results were achieved through a combination of (1) analytical modeling of laser-field effects in and around growth nodules; (2) mapping of these growth nodules under atomic-force microscopy; and (3) physical analysis of the nodules by focused-ion-beam cross sectioning and Auger spectroscopy. In conjunction with conventional laser-damage-threshold measurements, this approach yielded the broad conclusion that nodular growth defects are the dominant laser-damage drivers in thin films. From a systems design viewpoint, nodules became the coating affliction to be eradicated for laser-damage thresholds to improve.

As results for the fundamental and second-harmonic-wavelength laser-damage characteristics of multilayer coatings were being disseminated, prototype development and actual production of OMEGA Upgrade transport coatings were proceeding at LLE. In this article we report our observations on laser damage in these $3\omega$ (351-nm) high reflectors (HR's), obtained by combining conventional $3\omega$ laser-damage investigations with mapping of damaged and undamaged sites on production witness pieces by atomic force microscopy. These findings differ from the earlier ones for 1054-nm and 527-nm conditions in that the nodules are capable of surviving fluences that cause crater formation by other mechanisms. These mechanisms confine crater origination to the top two layers of the multilayer, high-reflector stack.

### Samples and Experimental Conditions

Two types of oblique-incidence, $3\omega$ high reflectors were analyzed: (1) a 46° angle-of-incidence, 37 alternating quarter-wave stack HR made from $HfO_2$ and $SiO_2$, with the first and third $HfO_2$ layers replaced by $Sc_2O_3$ to make the coating strippable; and (2) a 50° angle-of-incidence, 53 alternating quarter-wave stack of $Sc_2O_3$ and $SiO_2$, with 47 layers of exact quarter-wave optical thicknesses and the top six layers adjusted in thickness for reduced electric-field intensity at the layer interfaces. Both coatings were deposited by conventional e-beam methods. One of the primary goals in the deposition process was to minimize the formation of growth nodules.

Witness pieces from these production coatings were irradiated at the respective angles using frequency-tripled, 0.7-ns pulses from a Nd:glass slab laser. At optimized conversion efficiency and under weak focusing by a 10-m focal-length silica lens, fluences up to 14 J/cm$^2$ within a 600-$\mu$m spot diameter were delivered to the test piece. Damage was identified by dark-field microscopy (110-times magnification) as an agglomeration of very fine, low-light-level scattering sites (nebula). The damage thresholds in 1-on-1 irradiation mode ($p$-polarization, scaled to 0° incidence for systems design engineering convenience) were 5.6±0.2 J/cm$^2$ in the case of the $HfO_2/SiO_2$ system, and 5.4±0.1 J/cm$^2$ for $Sc_2O_3/SiO_2$. Sites later mapped by atomic force microscopy experienced damage at ~5% above threshold (defined as "weak" damage sites) and at 15%–20% above threshold fluences (defined as "moderate" damage sites).

Analysis of both irradiated and unirradiated (control) sites was carried out using a Nanoscope III (Digital Instruments, Inc.) atomic force microscope (AFM) operated in contact mode. "Oxide-sharp" $Si_3N_4$ probes proved adequate for resolving both nanometer-scale film morphology and any laser-modified structures, although rapid wear required fre-

quent probe replacement. Typical "stickiness" between the sample and probe of dielectric oxide films during scans was counteracted by making adjustments in scanning speeds and feedback loop parameters. The contact force was routinely minimized to ensure an unmodified scan area during repeated scans. Adjacent, 5-$\mu$m × 5-$\mu$m sections were mapped with the goal of accumulating statistically significant numbers of various damage features, such as cracks, craters, or domes. For a given sample and irradiation condition, this number is of the order of 100 for each irradiated site. Each feature observed was subsequently analyzed in high-resolution closeups.

## Results and Discussion

1. Morphology of Unirradiated Films

In both the $HfO_2/SiO_2$ and $Sc_2O_3/SiO_2$ stacks, the terminating (top) layer is the respective high-refractive-index medium (i.e., $HfO_2$ or $Sc_2O_3$). Figures 62.1 and 62.2 show the typical oxide-film columnar structures for these materials, with 25- to 40-nm grain size and 3.3- to 3.6-nm vertical rms roughness. Taking into account an AFM probe tip radius $R_{tip}$ ~10 nm (according to manufacturer specifications) and the recently reported image-distortion criterion,[5] i.e., $R_{grain}/R_{tip} < 2$, we find our imaged grain size to be overestimated. The magnitude of this error, however, is not large, as we were able to resolve the 10-nm-scale granular structure of $Ta_2O_5$ monolayer films using the same probes.[6] These features are less than half the scale length of the $HfO_2$ and/or $Sc_2O_3$ characteristic grains.

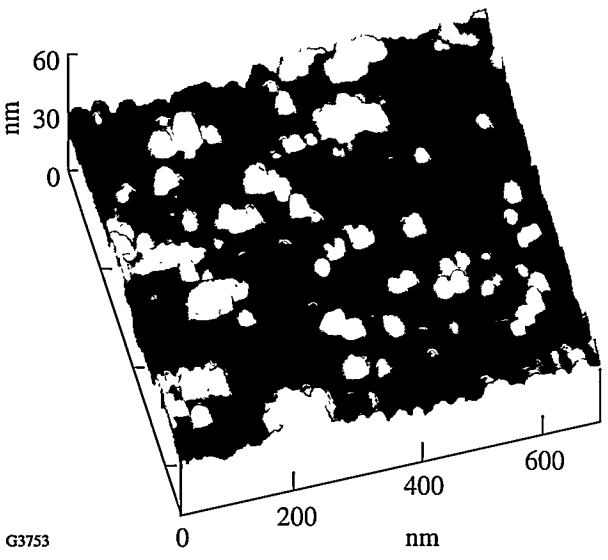


Figure 62.1
Columnar structure of the $HfO_2$ top surface (700 × 700-$\mu$m scan) of a $HfO_2/SiO_2$ multilayer HR stack.

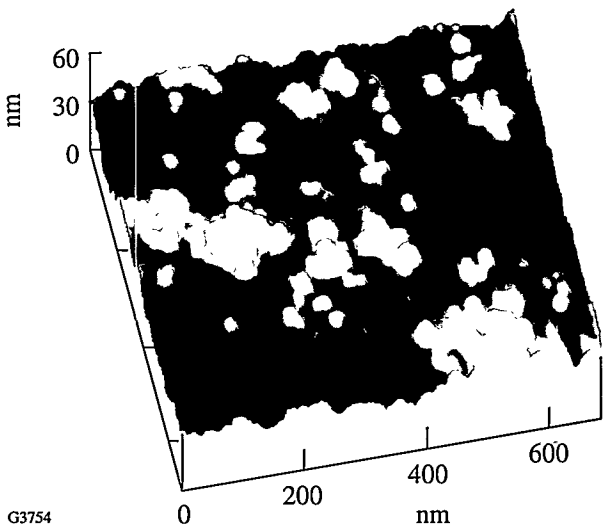


Figure 62.2
Columnar structure of the $Sc_2O_3$ top surface (700 × 700-$\mu$m scan) of a $Sc_2O_3/SiO_2$ multilayer HR stack with reduced *E*-field design.

2. Laser-Induced Morphology

In both $HfO_2/SiO_2$ and $Sc_2O_3/SiO_2$ coatings, craters on the scale of 200 nm to 700 nm across and up to 130 nm deep are the main laser-damage features (Figs. 62.3 and 62.4). Their spatial correlation with the incident beam-fluence profile recorded in a sample equivalent plane by a CID camera is weak or nearly nonexistent. Under weakly damaging conditions,

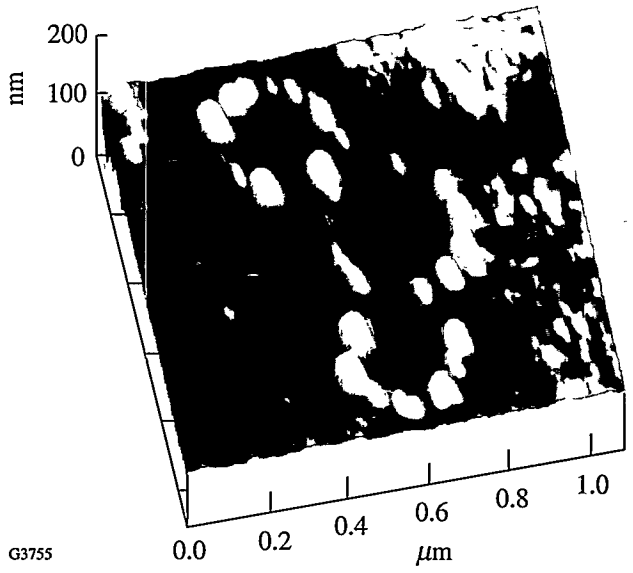


Figure 62.3
Conventional laser-damage craters formed by 351-nm radiation in the $HfO_2/SiO_2$ film. The area shown corresponds to the periphery of a moderate-damage site.

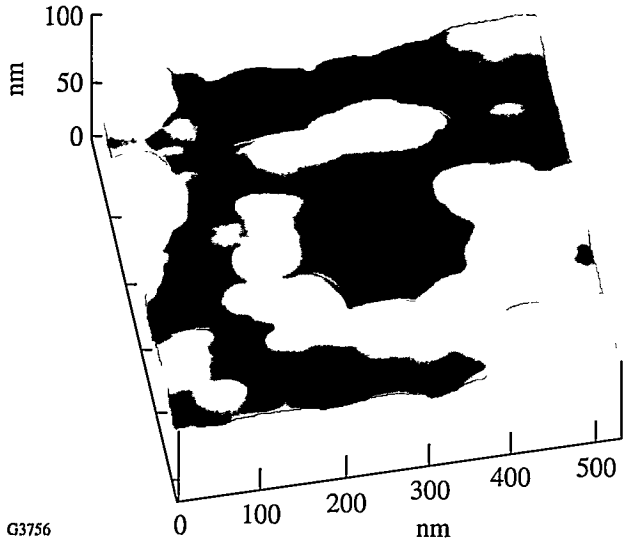


Figure 62.4
Conventional laser-damage crater formed by 351-nm radiation in the $Sc_2O_3/SiO_2$ film. The crater is 38 nm deep and, on average, 300 nm in diameter.

crater-to-crater average distances are 2.4 $\mu$m for $HfO_2/SiO_2$ and 2.7 $\mu$m for $Sc_2O_3/SiO_2$. In agreement with our earlier findings on 1054-nm laser-irradiated monolayer films,[6] such craters develop independently of whether or not micron-scale growth nodules are present. Figure 62.5 demonstrates that growth nodules and inclusions can remain unaffected, even under 351-nm irradiation, while other defect-driving mechanisms dominate crater formation in the nodules' immediate vicinity. Up to now, we have been unable to offer similar evidence for 1054-nm HR stacks. Within that constraint, the current evidence suggests that growth nodules *are not always* the dominating cause of damage. We have, in fact, no AFM evidence or visible-light microscopy record for any observable feature that could be used as a landmark for predicting the occurrence of these craters.

Closer analysis of these craters offers some interesting conclusions regarding their potential source. In agreement with LLNL findings from 1981,[7] under near-threshold conditions the majority of craters are very shallow, originating in either or both of the top two layers; i.e., 29% of $HfO_2/SiO_2$ craters and 17% of $Sc_2O_3/SiO_2$ craters are less than 20 nm deep. If a compact absorber is postulated as the damage originator, one can deduce immediately from this crater depth that such an absorber would have to be limited in extent to ~10 nm.

Modern AFM tools now permit greater insight into crater cross-sectional features than were observed 14 years ago. We have found many instances in which a conventional, cone-edged crater is superimposed on a second, deeper crater (see Fig. 62.6). These complex craters occur mainly in $Sc_2O_3/SiO_2$ with an abundance level of 37%. Conventional craters show conical walls that are normally smooth and without any grain

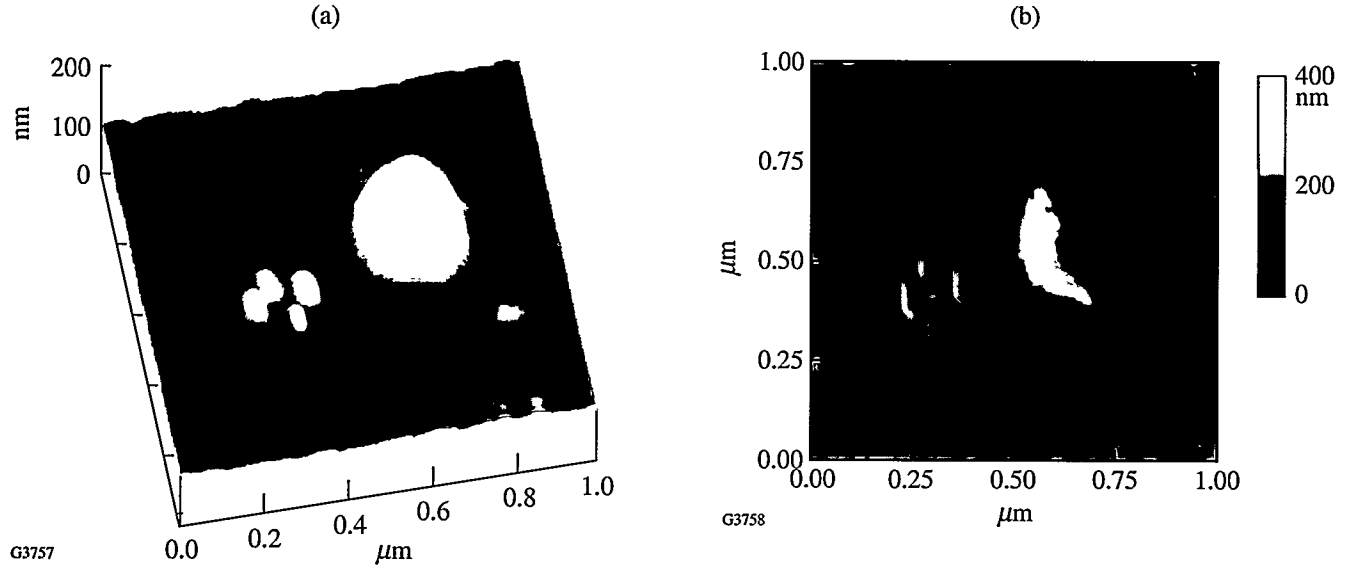


Figure 62.5
(a) Crater formed in the vicinity of an unaffected nodular growth defect in the $HfO_2/SiO_2$ film. The columnar structure of the nodule surface is masked by the saturating dome height (~200 nm) relative to the only 15-nm peak-to-valley excursions characteristic for the columnar structure. (b) High-pass filtered version of the image in Fig. 62.5(a), highlighting the columnar structure and nodular nature of the defect.

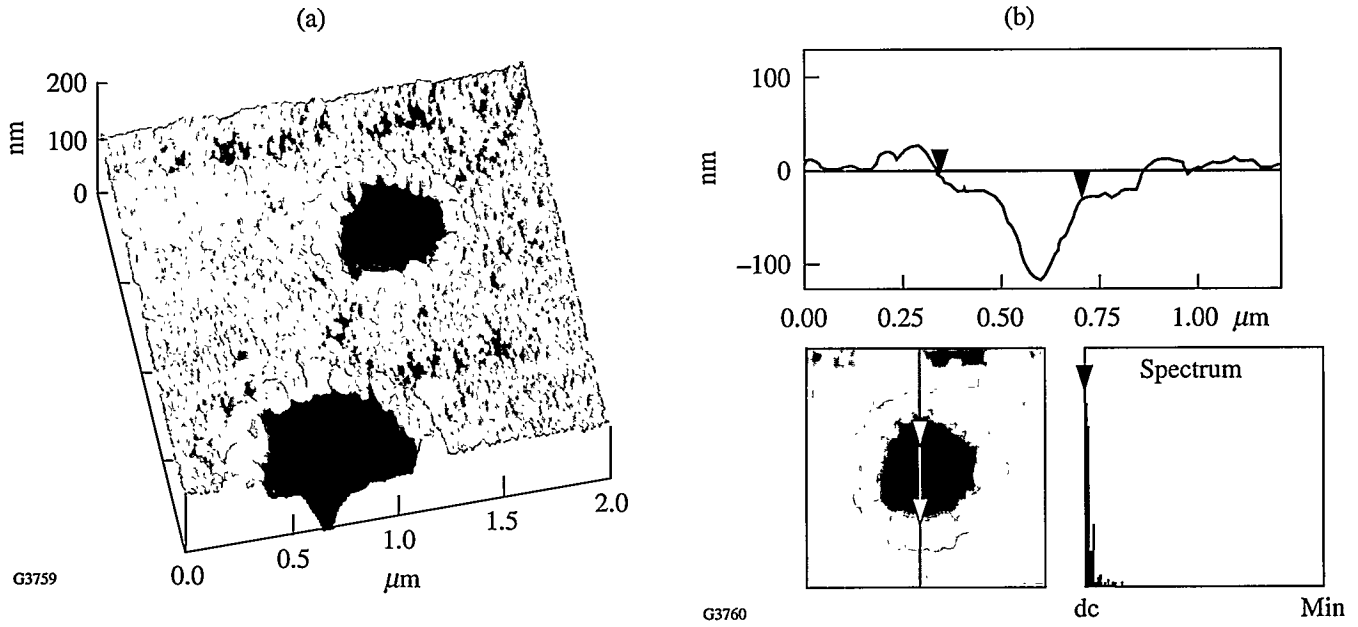


Figure 62.6
(a) Complex crater(s) in the $Sc_2O_3/SiO_2$ film show the preserved columnar structure within the outer, larger-diameter cone. This indicates that melting remains localized within the inner cone volume, i.e., the $SiO_2$ layer. (b) Cross section through the complex crater in the $Sc_2O_3/SiO_2$ film. The double-cone structure is clearly pronounced here, as well as the 32.8-nm step formed by the outer cone.

structure with ridges elevated above the film surface average (Fig. 62.7). In complex craters, the inner, deeper cone also shows smooth, glassy walls, while the outer cone and the horizontal interface clearly preserve columnar structure. Although the horizontal step between the outer and inner cones occurs reproducibly at 32.8±0.3 nm from the nominal top surface average (36 craters were sampled for this value by AFM determination) and intuitively corresponds to the $Sc_2O_3/SiO_2$ interface, the top-layer ($Sc_2O_3$) physical thickness determined during evaporation by quartz-microbalance and optical-monitoring methods is supposed to be 25.4±3 nm. We ascribe this discrepancy to the uncertainty in material-density and refractive-index values for evaporated thin films when extracting physical thickness data from mass deposition and interference numbers.

Without detailed simulation, it remains unclear whether the observed double-cone damage is driven by starting events in the first or the second layer. In each scenario, the large difference in melting temperature between $SiO_2$ ($T_m = 1753°C$) and $Sc_2O_3$ ($T_m$ ~2400°C) is essential in explaining the observed morphology. As the $SiO_2$ crater walls yield no columnar-structure indicators, we can assume that melting has occurred in the $SiO_2$ layer. Conversely, the columnar spatial frequencies typical of the unirradiated film are maintained around the $Sc_2O_3$ crater walls and ridges, which rules out large-scale melting in that layer [Fig. 62.6(a)]. Temperatures insufficient for melting in $Sc_2O_3$ are adequate to produce thermal expansion and possible buckling of the 25- to 32-nm top layer that, with or without further pressure from the underlying, melted $SiO_2$ layer, severed along grain boundaries and "popped out." In the event that the initiating absorber was lodged in the second ($SiO_2$) layer, the melting of that layer preceded the thermal distortion of the top layer. If the absorber was instead in the top layer, heat from that layer must first propagate across the layer boundary at a flow rate that supports melting of $SiO_2$ columns before the top layer pops out. On the basis of post-mortem evidence alone, the dominant or most likely mechanism cannot be determined with any certainty.

Superimposed, double-crater damage is absent in the $HfO_2/SiO_2$ system. Conventional craters become more numerous and, if sufficiently adjacent to one another, merge as the level of damage increases in this system (Fig. 62.8). In spite of earlier reports to the contrary[8] that rank quarter-wave layers of $SiO_2$ at nearly a factor of 2 higher in 351-nm thresholds than equivalent $HfO_2$ layers of the same thickness, all merging craters in our samples originate in the $SiO_2$ layer after exposure to fluences *above threshold*. This issue will be discussed in detail in the next section.

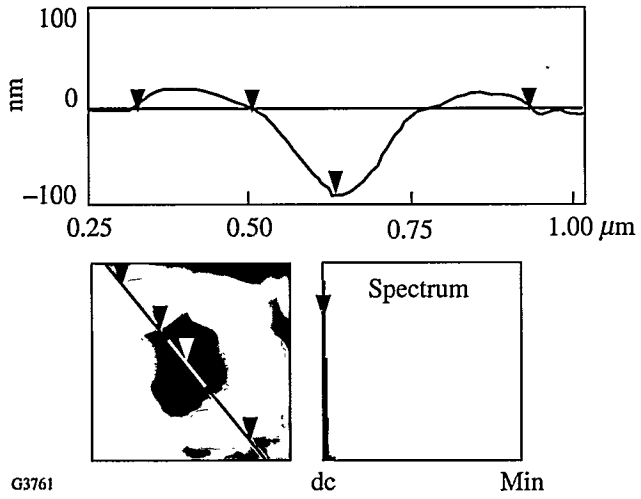


Figure 62.7
Cross section through the 46-nm-deep conventional crater in the $Sc_2O_3$/$SiO_2$ film. Smooth, glassy walls offer evidence of melting as part of the damage process.

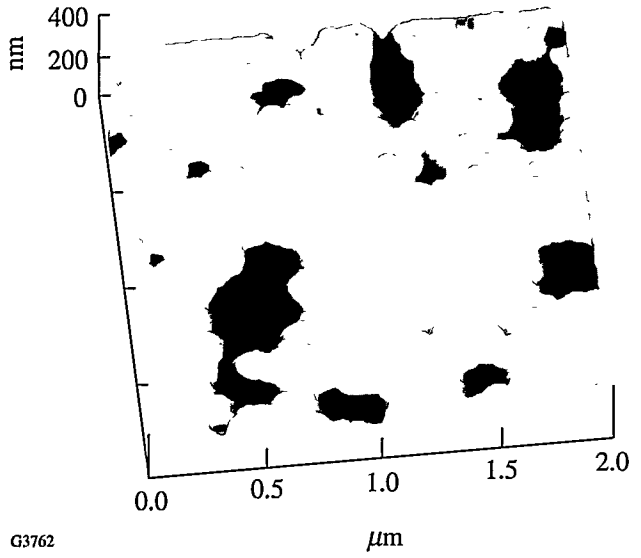


Figure 62.8
Merging craters in the central portion of a moderate-damage event in the $HfO_2/SiO_2$ film.

3. Crater-Depth Distribution

For both material systems, crater-depth distributions were recorded for three irradiation conditions: (1) weak damage, attained at fluences ~5% above the threshold average; (2) moderate damage at 15%–20% above threshold; and (3) the periphery condition of moderate damage, estimated to correspond to a fluence condition intermediate between (1) and (2). Damage-crater histograms were assembled using 10-nm-wide bins as a matter of convenience, with the understanding that for other bin sizes the crater-count distribution would vary. The arguments in the following sections are therefore not focused on exact depths, but rather on trends.

a. $HfO_2/SiO_2$. The weak-damage results summarized in Fig. 62.9 show that craters originate in the first or second layer only, with the majority originating in the 46-nm-thick $HfO_2$ layer. The distribution peaks at a depth near 20 nm and shifts to greater depths with increasing fluence. At the periphery of moderate damage (Fig. 62.10), two peaks appear in the distribution at 30 nm and 80 nm, respectively; in the center of moderate damage, craters appear only infrequently in the $HfO_2$ layer, while the distribution peak centers around 75 nm (Fig. 62.11). In the latter case, a few damage events originate near the interface between the second and third layers, but none were observed protruding into the next $HfO_2$ layer. Concurrent with this shift of craters to greater depths is an increase in both their density (more than an order of magnitude higher for moderate damage than for near-threshold damage) and their tendency to merge.

Energy-balance considerations suggest that the amount of energy near threshold needed for removal of a cone volume (anticrater) is met predominantly by absorbers closer to the surface. We assume here that (1) the crater bottom is either at or very near the location of the absorbing defect, and (2) the defect characteristics and depth do not vary significantly from one AFM mapping area to the next. At energy values further above threshold, deeply located defects absorb sufficient energy to remove material and form a crater, while those closer to the surface not only cause material removal but also dissi-

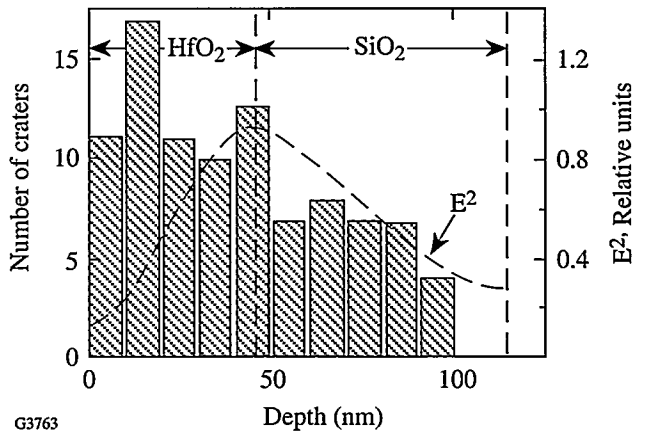


Figure 62.9
Crater-depth distribution (histogram) for weak-damage conditions (~5% above threshold fluence) in the $HfO_2/SiO_2$ system. The majority of craters originate within the top $HfO_2$ layer.

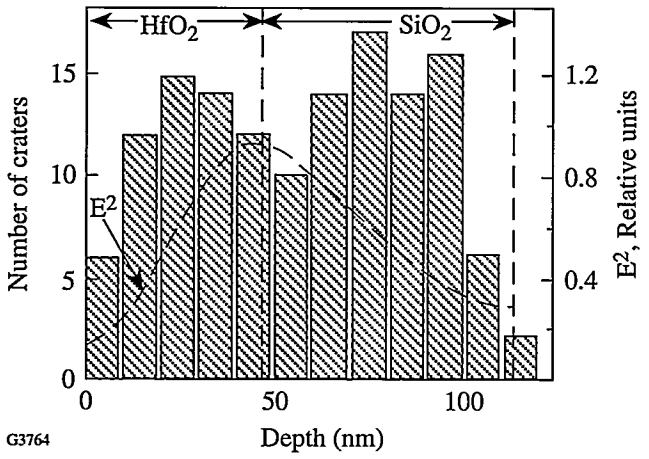


Figure 62.10
Crater-depth distribution (histogram) for moderate-damage (periphery) conditions in the $HfO_2/SiO_2$ system. The second peak at 80-nm depth may be attributed to the combined effects of excess energy (relative to weak-damage conditions) and heat propagation from the higher-melting-point $HfO_2$ layer to the lower-melting-point $SiO_2$ layer.

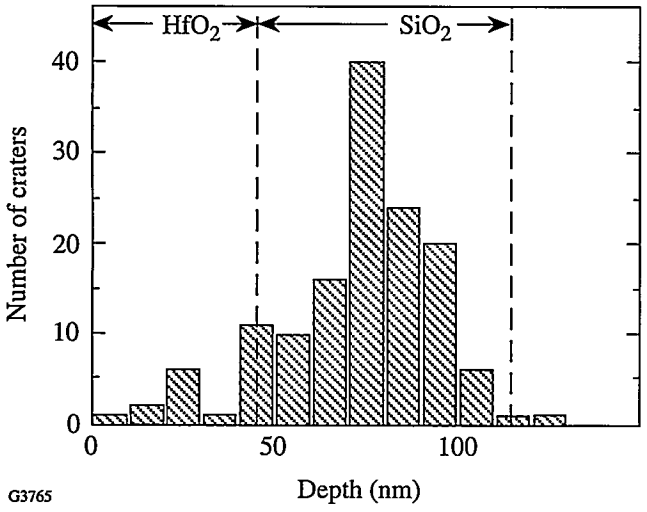


Figure 62.11
Crater-depth distribution at the central portion of a moderate-damage area (~20% above threshold fluence) in the $HfO_2/SiO_2$ system. The distribution is now fully shifted into the $SiO_2$ layer, indicative of the dominance of heat-propagation effects under the 20%-above-threshold fluence conditions.

pate heat into the lower layer, extending the effective material modification to greater depths. This process is eased by the lower melting point of the second layer.

Figures 62.9 and 62.10 show also the $E^2$-optical-intensity dependence inside the first two stack layers, which peak exactly at the interface. Other local maxima are located at the interface between the third and fourth layers, etc., with each deeper maximum dropping in value relative to the previous one. In good coatings, it is therefore not surprising to find that, at values near threshold, only the absorbers near the largest intensity maximum contribute to crater formation.

It has long been suspected that, either for manufacturing reasons or owing to intrinsic physics, the discontinuities associated with interfacial areas are absorber locations themselves and, as such, are drivers for laser damage. The lack of any clear evidence for crater depths peaking at interfaces (the apparent interface peak in Fig. 62.9 is not nearly strong enough not to disappear after a small bin-size adjustment) suggest that, for state-of-the-art coatings, interface issues have ceased to be damage-critical issues.

b. $Sc_2O_3/SiO_2$. In the $Sc_2O_3/SiO_2$ system the top $Sc_2O_3$ layer is only 25.4 nm thick, and the peak of the $E^2$-intensity distribution has been designed to not coincide with the layer interface. For this system, the intensity peaks at a depth of 65 nm. Both factors bias the crater-depth distribution toward the $SiO_2$ layer, as seen in Figs. 62.12 and 62.13 for the cases of weak damage and peripheral moderate damage. As was true for $HfO_2/SiO_2$, no craters originate from beneath the second layer. However, the shift of the distribution peak in going from weak to moderate damage (~40 nm in $HfO_2/SiO_2$) is more modest in this system. The 10-nm difference between distribution peaks in Figs. 62.12 and 62.13 is too small to be considered significant in light of the 10-nm bin width.

The trailing edges of the distributions shown in Figs. 62.12 and 62.13 drop faster with depth than the incident intensity,

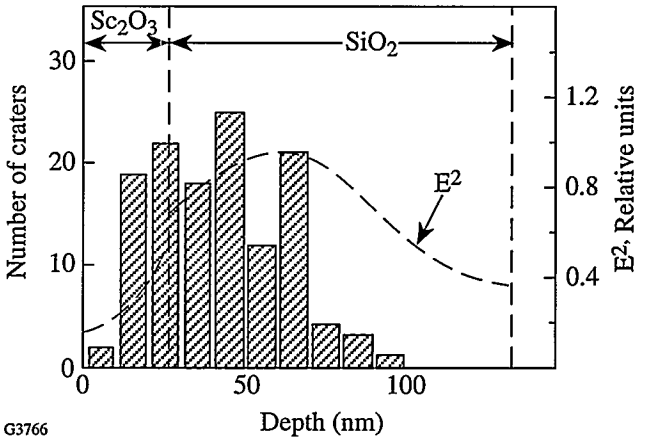


Figure 62.12
Crater-depth distribution (histogram) for weak damage in the $Sc_2O_3/SiO_2$ system. Owing to the relatively thin (25.4-nm) $Sc_2O_3$ layer, the *E*-field, i.e., intensity, peaks inside the $SiO_2$ layer.

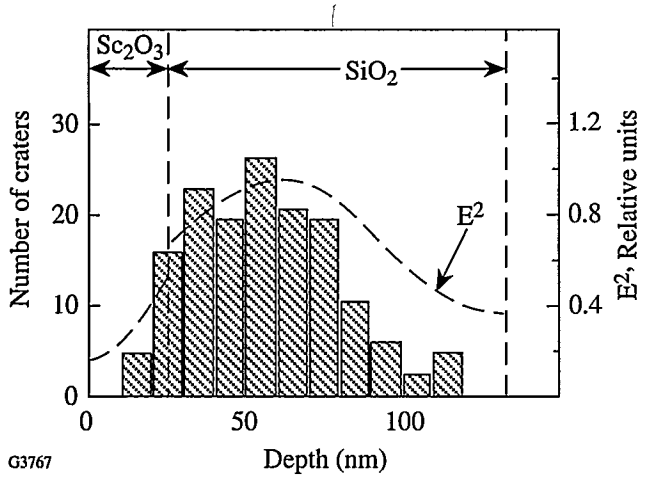


Figure 62.13
Crater-depth distribution (histogram) for moderate-damage (periphery) conditions in the $Sc_2O_3/SiO_2$ system. The distribution is almost fully bracketed within the $SiO_2$ layer.

which is not unexpected based on energy-balance grounds. If one simply assumes that for a conical crater to be formed the entire conical volume will be uniformly affected by heat, then the energy required for such heating will scale with the cone depth $h$ as, at most, $h^3$. In reality, this dependence is probably less severe. The distribution's trailing edge already scales nearly as $1/h^3$, indicating that the exponent must be significantly smaller in light of the monotonously declining intensity dependence over the same depth interval.

## Conclusions

Mapping of pulsed-laser-induced damage morphologies in UV high-reflector coatings by AFM has shown the dominant damage feature to be submicron-lateral-sized craters that appear to be independent of micron-scale film growth defects (nodules). The local number density of these defect craters follows the intensity profile over the full laser-beam profile (hundreds of microns) but appears random over scale lengths of a few microns. The 700°K to 1000°K difference in the melting point between the high- and low-index medium in these stacks results in peculiar crater formation in the $Sc_2O_3/SiO_2$ system, where crater-wall structural evidence shows melting and glass forming in the $SiO_2$ layer, while the crater walls along the $Sc_2O_3$ layer maintain columnar structure. A preponderance of craters originating in the second ($SiO_2$) layer points toward heat transfer across the interface and lower-layer melting by absorbers located in the top layer as the primary cause. Together with the observation that the smallest measured craters allow for starting absorber sizes of <10 nm, this distribution points toward randomly distributed nano-cluster absorbers as the sources involved in the energy transfer from the optical field to the porous film medium. Whether these nano-clusters owe their absorptivity to unbound charges of metallic character or to charges localized in broken-stoichiometry states (point-defect states) remains to be resolved. The oxide deposition process certainly does not rule out bursts of impurity or non-stoichiometric events during which such nano-clusters could be dispersed into the coating stack. Similarly, at this time details of the damage kinetics are still speculative. The very low number density of nodules encountered leaves no doubt that few, if any, of these nano-clusters act as seeds for growth nodules, and that the nodules themselves may survive irradiation even though craters are formed within their immediate vicinity.

## ACKNOWLEDGMENT

This work was supported by the U.S. Department of Energy Office of Inertial Confinement Fusion under Cooperative Agreement No. DE-FC03-92SF19460, the University of Rochester, and the New York State Energy Research and Development Authority. The support of DOE does not constitute an endorsement by DOE of the views expressed in this article. This work was carried out on equipment of the Center for Optics Manufacturing (COM)—a DOD Center of Excellence by the U.S. Army Materiel Command.

## REFERENCES

1. M. R. Kozlowski *et al.*, in *Scanning Microscopy Instrumentation*, edited by G. S. Kino (SPIE, Bellingham, WA, 1991), Vol. 1556, pp. 68–78.
2. M. C. Staggs *et al.*, in *Laser-Induced Damage in Optical Materials: 1991*, edited by H. E. Bennett *et al.* (SPIE, Bellingham, WA, 1992), Vol. 1624, pp. 375–385.
3. M. C. Staggs *et al.*, in *Laser-Induced Damage in Optical Materials: 1992*, edited by H. E. Bennett *et al.* (SPIE, Bellingham, WA, 1993), Vol. 1848, pp. 234–242.
4. R. J. Tench, R. Chow, and M. R. Kozlowski, in *Laser-Induced Damage in Optical Materials: 1993*, edited by H. E. Bennett *et al.* (SPIE, Bellingham, WA, 1994), Vol. 2114, pp. 415–425.
5. K. L. Westra and D. J. Thomson, J. Vac. Sci. Technol. B **12**, 3176 (1994).
6. S. Papernov and A. Schmid, "A Comparison of Laser-Induced Damage Morphology in Three Model Thin-Film Systems: $HfO_2$, $Y_2O_3$, and $Ta_2O_5$," to be published in SPIE's *Laser-Induced Damage in Optical Materials: 1994*.
7. W. H. Lowdermilk and D. Milam, IEEE J. Quantum Electron. **QE-17**, 1888 (1981).
8. T. W. Walker, A. H. Guenther, and P. E. Nielsen, IEEE J. Quantum Electron. **QE-17**, 2041 (1981).

# The OMEGA Laser Pulse-Shaping System

Laser-fusion experiments require that high-energy, temporally shaped optical pulses be generated and applied to fusion targets. On the OMEGA laser, low-energy optical pulses will be shaped with amplitude modulators and injected into the laser system for amplification and delivery to the laser-fusion targets. A layout of the pulse-shaping system is shown in Fig. 62.14. The output of a single-mode Nd:YLF laser is sliced to produce a 10- to 15-ns square optical pulse. This pulse is sent through two integrated-optic amplitude modulators operated in series and fabricated on a single, fiber-coupled $LiNbO_3$ waveguide. Shaped electrical pulses, synchronized with the input optical square pulse, are applied to the modulators. This shaped optical pulse from the modulators is then preamplified in a regenerative amplifier (regen) and sent to the OMEGA amplifier chains. The shaped electrical pulses are produced using optically activated Si photoconductive (PC) switches and variable impedance microstrip lines. Activation of the Si PC switches is achieved using an optical pulse that has been steepened by the stimulated Brillouin scattering process.

Given the desired optical pulse shape and energy on target, the required output optical pulse shape from the modulator is determined by modeling the temporal pulse distortions introduced by the OMEGA laser system from all sources and then using this model as a transfer function to relate the input to output pulse shapes from the system. This model, available in the form of a computer code (*RAINBOW*), takes into account such factors as the effects of the frequency-tripling process and gain saturation in the amplifiers. Since the optical transfer function of a modulator is well known in terms of the voltage waveform applied to the modulator, a knowledge of the optical pulse shape required on target uniquely determines the required voltage waveform that must be applied to the modulator.

### Optical Modulators

A schematic of a typical dual-amplitude, fiber-coupled, waveguide integrated-optic modulator is shown in Fig. 62.15. The input and output fibers are single-mode polarization-preserving fiber with industry-standard FC/APC connectors. Light launched into the input fiber is coupled into a waveguide in the $LiNbO_3$ electro-optic crystal. A Y-branch is used to split the signal and form two arms of a Mach-Zehnder interferometer. Electrodes are placed around the interferometer arms so that a voltage applied to the RF port produces a phase shift in each arm of the interferometer. The polarity of these electrodes is arranged such that the device operates in a push-pull fashion,

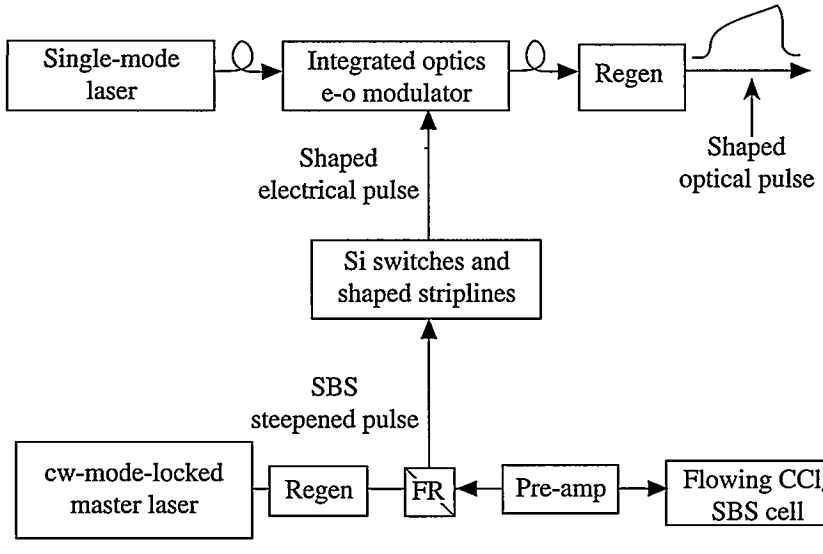


E7021

Figure 62.14
A block diagram of the OMEGA optical-pulse-shaping system. The electrical-pulse-generation portion of the system uses Si photoconductive switches that are activated with an SBS-steepened optical pulse.

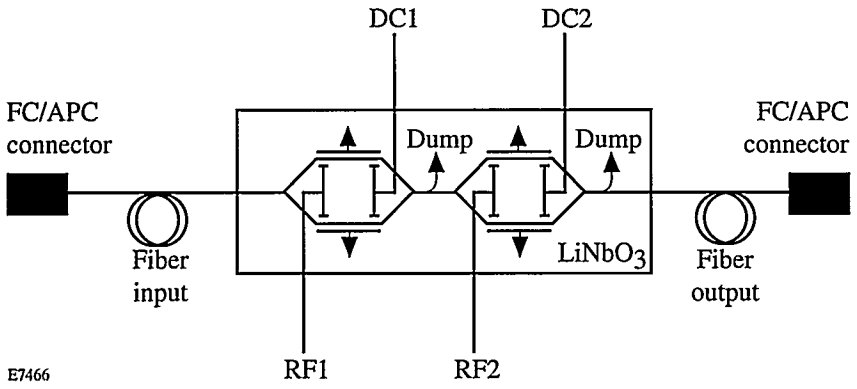


Figure 62.15
The dual-amplitude, Mach-Zehnder, waveguide integrated-optic modulator used for pulse shaping. Shaped voltage waveforms are applied to the RF input ports, and each modulator has a DC input port for setting the dc offset.

i.e., the phase shift in the two arms is cumulative. A second Y-branch is used to coherently combine the two beams and send the shaped pulse to the next stage, while the unwanted radiation is sent to an appropriate beam dump. The device incorporates two identical modulators in series. The output optical pulse intensity from a modulator is given by

$$I(t) = I_0(t)\cos^2\left[\frac{\pi}{2}\,\frac{V(t)}{V_\pi} + \phi\right], \qquad (1)$$

where $I_0(t)$ is the input optical pulse intensity to the modulator, $V(t)$ is the applied voltage, $V_\pi$ is the half-wave voltage [the voltage required to drive the modulator from its maximum to its minimum transmission (<10 V)], and $\phi$ is an overall phase that can be controlled by an applied 0- to 10-V dc bias (provided by a computer with an A/D board). In our case, the input optical pulse to the modulator is a square optical pulse (~10-ns FWHM) obtained by "slicing out" the center of a single-longitudinal-mode Nd:YLF laser pulse (pulsewidth ~100-ns FWHM) using conventional Pockels cells. The modulators are designed for 1054-nm-wavelength operation and have traveling wave electrodes to provide an 8-GHz bandwidth.

### Electrical Waveform Generation

To produce shaped optical pulses from the modulators, temporally shaped voltage waveforms [$V(t)$ in Eq. (1)] must be applied to the modulators. (The modulator is dc biased so that $\phi = \pi/2$.) The electrical-pulse-generation system that shapes the voltage waveforms applied to the modulators is modeled after a design developed at Lawrence Livermore National Laboratory (LLNL).[1] The system consists of two Si PC switches, a microstrip charge line, and a variable impedance microstrip line as shown in Fig. 62.16. The microstrip charge line is placed between two PC switches and is charged to approximately 80 V. The opposite side of one PC switch is connected to the modulator, while the opposite side of the other PC switch is connected to the terminated variable-impedance microstrip line. When the PC switch near the variable-impedance microstrip line is activated (closed), a square pulse is sent to the

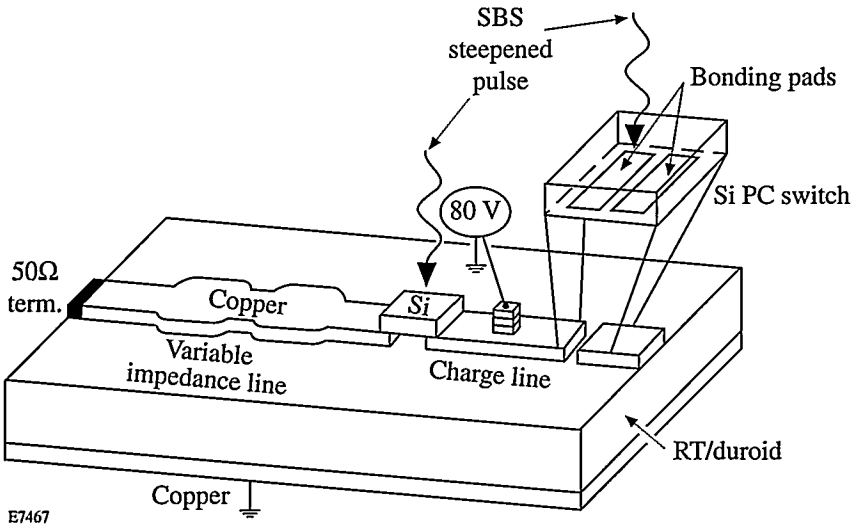


Figure 62.16
A detailed view of the electrical-pulse-generation system consisting of two optically activated Si PC switches, a microstrip charge line, and a terminated variable-impedance microstrip line.

variable-impedance microstrip line. A voltage waveform is then reflected from the variable-impedance line with a specific shape depending on the impedance mismatches along the length of the line. This shaped voltage waveform propagates back through the PC switch and charge line toward the modulator. Just before the waveform reaches the modulator PC switch, this switch is activated, allowing the voltage waveform to be applied to the RF input port of the modulator. The exact shape of the voltage waveform can be controlled by the judicious placement of impedance variations along the length of the variable-impedance microstrip line.

The system of microstrip lines and switches is designed to be impedance matched to the 50-Ω input impedance of the modulators and test equipment used. Microstrip lines were chosen instead of strip lines to minimize the impedance mismatch at the Si switches. The charge line and variable-impedance microstrip lines are fabricated in 0.79-mm-thick RT/duroid 5880 microwave laminate having 36-μm-thick Cu on both sides. An impedance variation along the line is obtained by adjusting the width of the top Cu electrode. The exact geometry is easily calculated knowing the required voltage waveform that must be produced. The reflection coefficient along the line can be calculated using a layer-peeling technique.[2] The impedance as a function of position along the line is then obtained from the reflection coefficient along the line. Finally the width of the electrode along the line is calculated using simple relationships between the material parameters and the impedance variations.[3] To fabricate the microstrip line, the Cu material on one side is machined with a precision programmable milling machine to produce the desired width as a function of length. The charge line is a constant 50-Ω microstrip line (Cu width = 2.38 mm) with a 2-mm gap at both ends to facilitate Si switch mounting. The Si switches, 2 mm long by 2.38 mm wide (to match the width of the 50-Ω charge line) by 0.5 mm thick, have bonding pads with 1-mm separation. The switches are low temperature soldered across each gap in the charge line with the bonding pads facing the Cu of the microstrip line, as shown in Fig. 62.16. The switches are illuminated from the back (opposite side from the contact pads) using 1054-nm laser radiation with ~0.5 mJ of energy per pulse. The laser radiation is absorbed throughout the entire volume of the 0.5-mm-thick Si switch, which results in switch activation. When illuminated with a laser pulse, the switch resistance changes from its dark value of approximately 600 kΩ to its activated resistance of less than 1 Ω as the absorbed photons generate electron hole pairs in the Si and reduce the resistivity of the material.

The square pulse sent to the variable-impedance microstrip line must contain frequency components high enough to reflect the pulse shapes of interest. Photoconductive switches can be activated (closed) in a time comparable to the rise time of the activating optical pulse (<100 ps), which in this case is a pulse that has its leading edge steepened by the stimulated Brillouin scattering (SBS) process. A typical square pulse produced by activating one switch only is shown in Fig. 62.17. The rising edge of the electrical pulse is approximately 80 ps, as measured with a Tektronix 7250 oscilloscope (~10-GHz bandwidth).

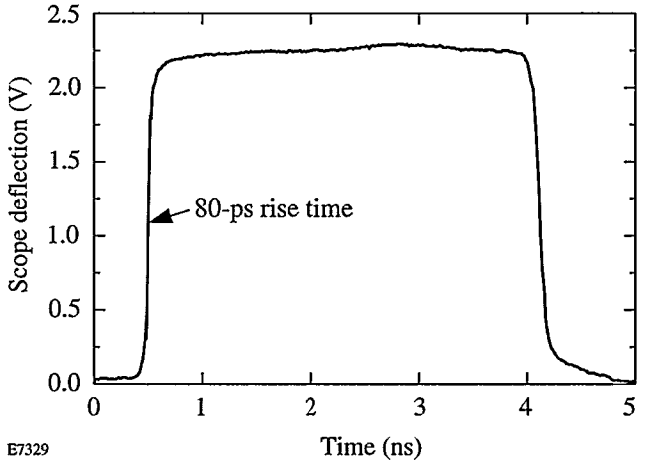


Figure 62.17
A square electrical pulse generated by the charge line and a Si PC switch. The pulse has a rise time of approximately 80 ps.

High bandwidth must be maintained throughout the entire system. High-bandwidth SMA end launchers and cables are used to transfer the electrical pulses from the microstrip line to the modulator or test equipment being used. Care is taken to minimize the impedance mismatch in the charge line at the point where the charging voltage is applied; this is done by charging through three board-mounted chip resistors (~10 kΩ each) stacked in series, as shown in Fig. 62.16. Less than 0.6% reflection at 10 GHz is produced by this process, as determined from time-domain reflectometer (TDR) measurements. A TDR of the complete microstrip line can be taken by soldering copper strips across the gaps in place of the Si switches. Figure 62.18 shows (1) the TDR measurement of a variable impedance microstrip line (taken with a 20-GHz-bandwidth HP 5420B TDR oscilloscope) with Si switches removed, compared to the design shape, and (2) the shaped electrical pulse transferred into the Tektronix 7250 oscilloscope after passing through the two Si switches that have been activated as described above. From Fig. 62.18 we see that, although the

present Si switches clearly degrade the inherent frequency response of the system, high-bandwidth shaped electrical pulses can ultimately be achieved with this pulse-generating system. Research is continuing in this area to improve the overall system performance.

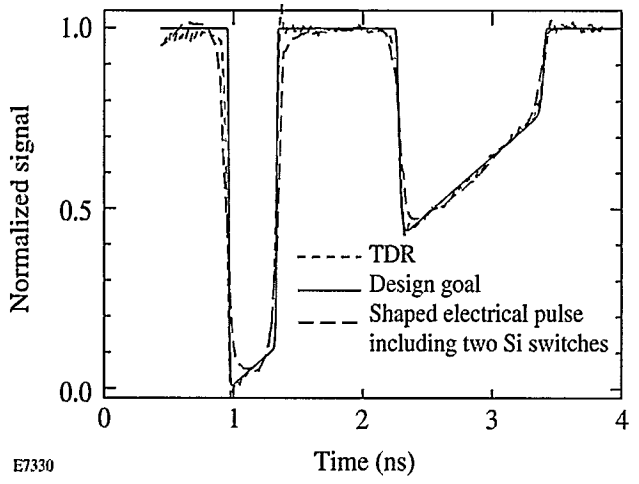


Figure 62.18
Time-domain reflectometer (TDR) measurement of a variable impedance microstrip line (dotted line) compared to the design goal (solid line). The dashed line is the measured shaped electrical pulse after propagation through two Si PC switches.

### PC Switch Activation

To produce fast closing times the PC switches must be activated by illuminating them with optical energy in as short a time as possible. Once the switches are closed, they must stay closed for a long time in comparison to the desired electrical pulse shapes of interest (~10 ns). Silicon PC switches were chosen for this application because of their long recombination times (100 to 200 $\mu$s). The switches are activated with fast-rise-time, high-contrast optical pulses generated by the SBS process.[4–5] The experimental setup is shown in Fig. 62.14.

A 1054-nm, 1- to 3-ns FWHM pulse (controlled by intracavity etalons[6]) from a Nd:YLF regen is amplified to 3 to 5 mJ and focused into a liquid cell containing carbon tetrachloride ($CCl_4$). A Brillouin-Stokes pulse is generated in the backward direction from this cell due to the SBS process. The SBS process is an intensity-dependent, nonlinear process where the incident laser Bragg-scatters in the backward direction from a driven acoustic wave in the medium. The process can be modeled as a pure gain process whereby a backward-traveling Brillouin noise signal experiences exponential-type gain throughout the focal region of the laser and grows into the Brillouin-Stokes signal. The gain coefficient depends on the laser intensity and the response time of the Brillouin medium (less than 1 ns for $CCl_4$).[7] The low intensity at the beginning of the laser pulse is transmitted through the cell, with little energy converted to the Brillouin signal. As the laser intensity in the cell increases during the laser pulse, the cell begins to generate Brillouin Stokes energy very rapidly due to the nonlinear buildup of the acoustic wave. The process quickly saturates, after which the laser scatters into the Stokes wave with high efficiency. The backscattered Brillouin pulse from the SBS cell has a fast-rising edge (<100-ps measurement limited) due to this Brillouin pulse steepening, while the back of the pulse approximates that of the laser. The reflected Brillouin pulse is sent back through the preamplifier and switched out using polarization optics and a Faraday rotator (FR). The SBS pulse is then split and used to activate both PC switches by introducing an appropriate timing delay between the two pulses.

Typical SBS reflected pulses for different incident laser energies are shown in Fig. 62.19. As the incident laser energy is varied, the location in time of the fast-rising edge of the SBS pulse changes. As seen in Fig. 62.19, as we increase (decrease) the laser energy, the SBS process turns on earlier (later). Hence, amplitude fluctuations in the laser may result in timing jitter of the electrical-pulse-generation system. To obtain electrical waveforms from the pulse-generation system that are

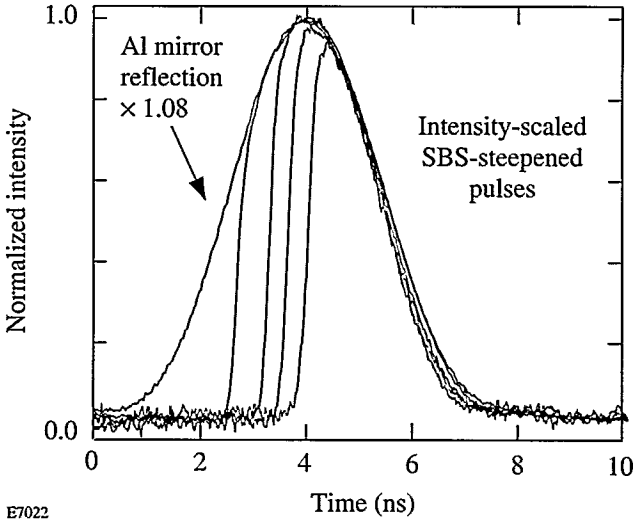


Figure 62.19
Fast-rise-time optical pulses produced by SBS pulse steepening with varying laser input energy. As the incident laser energy is increased (decreased), the SBS pulse turns on earlier (later). The reflected SBS pulse has a rise time of less than 100 ps.

accurately synchronized to a master timing reference, the laser that activates the PC switches must be amplitude stable. The laser amplitude in our setup is actively stabilized to within 3% using an optical feedback system that controls the cavity losses during the pulse build-up phase. A shaped optical pulse from the pulse-shaping system (including the Si PC switches, variable-impedance microstrip line, optical modulator, and regen preamplifier) was produced, and the shot-to-shot timing jitter between the shaped optical pulse and the master cw-mode-locked laser pulse injected into the regen that activates the PC switches was measured. An absolute timing jitter of less than 30 ps was measured using the Tektronix 7250 oscilloscope (~10-GHz bandwidth) and fast detectors (~3.5-GHz bandwidth).

The SBS process has an additional advantage when using Si PC switches. The SBS process is nonlinear, and for low incident laser energy into the SBS cell, essentially no Brillouin energy is reflected; hence, all laser prepulse noise is eliminated, resulting in a very-high on/off contrast ratio. This is important for Si switch applications because the recombination times are long (100 to 200 $\mu$s) and the switch will integrate the incident energy during this recombination time. Elimination of all prepulse optical noise ensures proper switch performance.

### System Performance

Optical pulses have been produced with the pulse-shaping system described above. Figure 62.20 shows an optical pulse shape produced by the system (solid line). To produce this shape, a square optical pulse (~10-ns FWHM) is used as input to the modulator. This pulse is obtained by slicing out the center of a single-longitudinal-mode Nd:YLF laser pulse (pulse width ~100-ns FWHM) using conventional Pockels cells, as was mentioned previously. The square pulse is then transferred to the modulator through optical fibers. Synchronized with this optical pulse is the electrical pulse (Fig. 62.18) that was produced by the electrical pulse generator described above. Figure 62.20 also shows the optical pulse shape expected from the modulator (dashed line) if the design goal of Fig. 62.18 is substituted into the modulator transfer function [Eq. (1)], and the optical pulse shape expected from the modulator (dotted line) if the measured shaped electrical pulse of Fig. 62.18 is substituted into the modulator transfer function [Eq. (1)].

The optical pulse in Fig. 62.20 was measured at the output of the modulator with a 25-GHz bandwidth detector (New Focus 1414). The energy at this point in the pulse-shaping system is approximately 10 nJ per pulse and is too low to make temporal measurements of a single pulse. The measurement

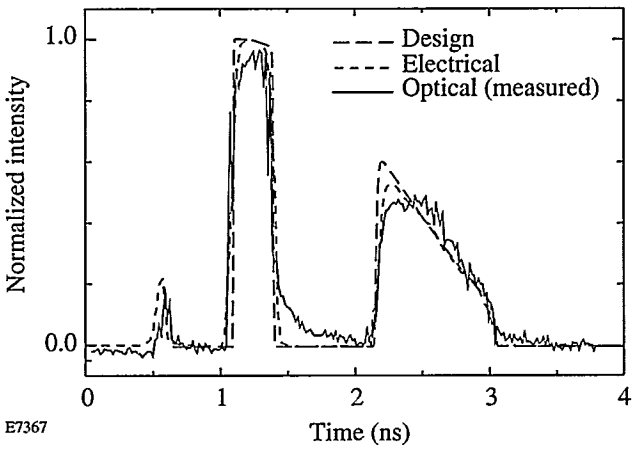


Figure 62.20
A comparison of expected and observed optical pulse shapes from the OMEGA laser's pulse-shaping system. Actual measured optical pulse shape from the modulator (solid line); optical pulse shape expected from the modulator if the design goal of Fig. 62.18 is substituted into the modulator transfer function [Eq. (1)] (dashed line); optical pulse shape expected from the modulator if the measured shaped electrical pulse of Fig. 62.18 is substituted into the modulator transfer function [Eq. (1)] (dotted line).

was taken with a high-bandwidth sampling oscilloscope (HP 5420B) and includes averaging over many pulses. The optical pulse shape in Fig. 62.20 appears to deviate from the expected pulse shape. We believe that the deviations are largely due to the detector response. In fact, our measurements show that large discrepancies occur between high-bandwidth detectors when measuring the same optical pulse. These detectors are designed to measure short pulses with fast rise times but have varying responses when trying to measure long pulses with fast rising structure. Work is continuing in this area to make accurate measurements of these shaped pulses. A streak camera will be used to measure these pulses and is expected to provide more accurate results.

In summary, an optical-pulse-shaping system has been designed that is capable of meeting the future pulse-shaping requirements for the OMEGA laser. The system has been tested and is capable of producing shaped optical pulses with 50- to 100-ps structure over a several-nanosecond pulse envelope.

ACKNOWLEDGMENT

This work was supported by the U.S. Department of Energy Office of Inertial Confinement Fusion under Cooperative Agreement No. DE-FC03-92SF19460, the University of Rochester, and the support of the Frank Horton Graduate Fellowship Program. The support of DOE does not constitute an endorsement by DOE of the views expressed in this article.

## REFERENCES


1. R. B. Wilcox *et al.*, in *Laser Coherence Control: Technology and Applications*, edited by H. T. Powell and T. J. Kessler (SPIE, Bellingham, WA, 1993), Vol. 1870, pp. 53–63.

2. S. C. Burkhart and R. B. Wilcox, IEEE Trans. Microw. Theory Tech. **38**, 1514 (1990).

3. B. C. Wadell, *Transmission Line Design Handbook* (Artech House, Boston, 1991).

4. T. de Saxce and P. Picart, in *Optically Activated Switching III*, edited by R. A. Falk (SPIE, Bellingham, WA, 1993), Vol. 1873, pp. 262–271.

5. A. Okishev, M. D. Skeldon, and W. Seka, in *CLEO '94, 1994 Technical Digest Series, Volume 8*, Anaheim, CA, 8–13 May 1994, paper CTuQ5.

6. M. D. Skeldon and S. T. Bui, J. Opt. Soc. Am. B **10**, 677 (1993).

7. W. Kaiser and M. Maier, in *Laser Handbook*, edited by F. T. Arecchi and E. O. Schulz-Dubois (North-Holland, Amsterdam, 1972), Vol. 2, p. 1077.

# Direct-Drive Irradiation Uniformity for the NIF

The National Ignition Facility (NIF) can have the flexibility to perform direct-drive experiments, in addition to indirect drive, if two key elements are included in its design: (1) The facility must be able to redirect 24 of the beam clusters to new beam ports near the "equator" of the target chamber, and (2) two-dimensional smoothing by spectral dispersion[1] (2-D SSD) must be implemented.

In this article, we first address how the indirect-drive irradiation geometry must be modified to accommodate direct drive. Emphasis is placed on finding an acceptable direct-drive geometry that minimizes the amount of reconfiguration. Tolerances for energy imbalance, beam mispointing, and target-positioning errors are discussed for the proposed irradiation geometry. The beam uniformity that can be achieved using 2-D SSD is also examined. One related laser design issue that affects the level of uniformity is pinhole size. The pinholes determine the maximum amount of angular spectral dispersion that can be used with SSD. The dependence of uniformity on pinhole size is discussed. Finally, the SSD-smoothed beam profile is combined with the direct-drive beam geometry to calculate the irradiation uniformity on a spherical target with multiple overlapping beams.

**Beam Placement**

Because the NIF will have only a single target chamber (designed primarily for indirect drive), a direct-drive component must be integrated into the system without major modifications. The current design for beam placement at the NIF target chamber, given in Table 62.I, has 48 beams in eight latitudinal rings clustered near the poles. Each beam consists of a cluster of four beamlets, separated in wavelength by about 5 Å. Such an irradiation scheme, taken as a whole, does not lend itself to direct drive. However, a portion of the beam positions would be suitable if additional beam ports were added near the equator. Such configurations have been considered by Mark,[2] who pointed out that direct-drive beams need not be uniformly disposed but could be placed in rings at polar angles given by the zeros of a Legendre polynomial. However, in general, the beams from different rings must have different energies, corresponding to the weights of Gaussian quadrature. One such configuration, which closely meshes with the current NIF design, is based on rings of beams at the zeros of the $P_6$ Legendre polynomial, with polar angles given by $\theta = 21.17°$, 48.60°, 76.19°, 103.81°, 131.40°, and 158.83°. Examination of the beam-port positions in Table 62.I shows that four of the rings in that design correspond very well to four of these angles, namely the ports at 23.49°, 48.27°, 131.73°, and 156.73°. For half of the beam ports, no modification would be required (except possibly for a small pointing correction so that the beam axes pass through the target surface, closer to the required latitudes). The remaining 24 beam clusters would have to be redirected into new beam ports positioned at 76.19° and 103.80° (Table 62.II).

The number of beam clusters in each ring for this direct-drive configuration is 4, 8, and 12 for the upper hemisphere, and similarly for the lower. The laser energies coming from each of these rings must be in the proportion of 1 to 2.105 to 2.731. Distributing this energy among the beams in each ring, we find that the relative energies for beams from different rings are 0.95, 1.00, and 0.86, which implies that beams from the polar and equatorial rings must be reduced in energy relative to beams from the ring at $\theta = 48°$. The net result is that ~8% of the available laser energy cannot be used for target irradiation, which represents a relatively small energy penalty for the flexibility of adding a direct-drive option to the current NIF design.

The irradiation uniformity for this 48-cluster configuration is shown in Fig. 62.21. The rms nonuniformity is plotted as a function of how much the beam overfills the target, for a smooth eighth-order supergaussian beam profile. (The edge of the beam was defined as the 5% intensity contour.) The nonuniformity is entirely long-wavelength structure, characterized by how well the 48 overlapping clusters of beams can cover a sphere. (The effect of short-wavelength nonuniformity from structure on the individual beams is examined in the next section.) For conditions at the onset of irradiation, the beam-to-target ratio should be chosen to be about 1.1. As the target implodes, this ratio becomes larger, and the long-wavelength

Table 62.I: NIF beamport assignments — indirect drive

| Port # | $\theta$ | $\phi$ | Port # | $\theta$ | $\phi$ |
|---|---|---|---|---|---|
| n01 | 23.4895 | 78.750 | n25 | 123.3311 | 5.625 |
| n02 | 23.4895 | 168.750 | n26 | 123.3311 | 50.625 |
| n03 | 23.4895 | 258.750 | n27 | 123.3311 | 95.625 |
| n04 | 23.4895 | 348.750 | n28 | 123.3311 | 140.625 |
| n05 | 31.9844 | 33.750 | n29 | 123.3311 | 185.625 |
| n06 | 31.9844 | 123.750 | n30 | 123.3311 | 230.625 |
| n07 | 31.9844 | 213.750 | n31 | 123.3311 | 275.625 |
| n08 | 31.9844 | 303.750 | n32 | 123.3311 | 320.625 |
| n09 | 48.2682 | 16.875 | n33 | 131.7317 | 28.125 |
| n10 | 48.2682 | 61.875 | n34 | 131.7317 | 73.125 |
| n11 | 48.2682 | 106.875 | n35 | 131.7317 | 118.125 |
| n12 | 48.2682 | 151.875 | n36 | 131.7317 | 163.125 |
| n13 | 48.2682 | 196.875 | n37 | 131.7317 | 208.125 |
| n14 | 48.2682 | 241.875 | n38 | 131.7317 | 253.125 |
| n15 | 48.2682 | 286.875 | n39 | 131.7317 | 298.125 |
| n16 | 48.2682 | 331.875 | n40 | 131.7317 | 343.125 |
| n17 | 56.6688 | 39.375 | n41 | 148.1055 | 56.250 |
| n18 | 56.6688 | 84.375 | n42 | 148.1055 | 146.250 |
| n19 | 56.6688 | 129.375 | n43 | 148.1055 | 236.250 |
| n20 | 56.6688 | 174.375 | n44 | 148.1055 | 326.250 |
| n21 | 56.6688 | 219.375 | n45 | 156.7317 | 11.250 |
| n22 | 56.6688 | 264.375 | n46 | 156.7317 | 101.250 |
| n23 | 56.6688 | 309.375 | n47 | 156.7317 | 191.250 |
| n24 | 56.6688 | 354.375 | n48 | 156.7317 | 281.250 |

nonuniformity degrades slightly. The solid line in Fig. 62.21 is the result of pointing the polar ring of beams to the correct latitude on the target surface; the dashed line is without this correction. The effect of the beam-pointing correction is to reduce this contribution to nonuniformity by 30% to 50%.

The effect on uniformity produced by energy imbalance among the beams is shown in Fig. 62.22. (The energy fluctuations among beams within a cluster were assumed uncorrelated.) Conditions with the same rms variation in energy can produce a relatively large spread in nonuniformity, as indicated by the bars in the figure, but it is all very-long-wavelength structure, corresponding to spherical harmonic modes 1 through 4. Similar results were obtained for cluster pointing errors (Fig. 62.23). Target positioning errors, shown in Fig. 62.24, predominantly affect only the mode $\ell = 1$. Generally, the combined contributions from these factors will add harmonically. These factors will make less than a 1% contribution to nonuniformity if the energy imbalance is less than ~5%, cluster pointing is better than 5% of the target radius, and target positioning errors are less than about 2% of the target radius.

The 8% reduction in laser energy can be avoided if the beamports for indirect drive can be shifted by a few degrees

Table 62.II: NIF beamport assignments — direct drive

| Port # | $\theta$ | $\phi$ | Port # | $\theta$ | $\phi$ |
|---|---|---|---|---|---|
| n01 | 23.4895 | 78.750 | n25 | 103.8000 | 15.000 |
| n02 | 23.4895 | 168.750 | n26 | 103.8000 | 45.000 |
| n03 | 23.4895 | 258.750 | n27 | 103.8000 | 75.000 |
| n04 | 23.4895 | 348.750 | n28 | 103.8000 | 105.000 |
| n05 | 48.2682 | 16.875 | n29 | 103.8000 | 135.000 |
| n06 | 48.2682 | 61.875 | n30 | 103.8000 | 165.000 |
| n07 | 48.2682 | 106.875 | n31 | 103.8000 | 195.000 |
| n08 | 48.2682 | 151.875 | n32 | 103.8000 | 225.000 |
| n09 | 48.2682 | 196.875 | n33 | 103.8000 | 255.000 |
| n10 | 48.2682 | 241.875 | n34 | 103.8000 | 285.000 |
| n11 | 48.2682 | 286.875 | n35 | 103.8000 | 315.000 |
| n12 | 48.2682 | 331.875 | n36 | 103.8000 | 345.000 |
| n13 | 76.1900 | 0.000 | n37 | 131.7317 | 28.125 |
| n14 | 76.1900 | 30.000 | n38 | 131.7317 | 73.125 |
| n15 | 76.1900 | 60.000 | n39 | 131.7317 | 118.125 |
| n16 | 76.1900 | 90.000 | n40 | 131.7317 | 163.125 |
| n17 | 76.1900 | 120.000 | n41 | 131.7317 | 208.125 |
| n18 | 76.1900 | 150.000 | n42 | 131.7317 | 253.125 |
| n19 | 76.1900 | 180.000 | n43 | 131.7317 | 298.125 |
| n20 | 76.1900 | 210.000 | n44 | 131.7317 | 343.125 |
| n21 | 76.1900 | 240.000 | n45 | 156.7317 | 11.250 |
| n22 | 76.1900 | 270.000 | n46 | 156.7317 | 101.250 |
| n23 | 76.1900 | 300.000 | n47 | 156.7317 | 191.250 |
| n24 | 76.1900 | 330.000 | n48 | 156.7317 | 281.250 |

without affecting indirect-drive target performance. One possibility[3] is to move the rings at 23.49° and 48.27° to new positions at 21.00° and 46.50°. The additional ring of 12 beams, in the upper hemisphere, would be placed at 75.75° rather than 76.19°. The rings in the lower hemisphere would be at 104.25°, 133.50°, and 159.00°. The direct-drive uniformity for this configuration is similar to the solid curve in Fig. 62.21, but with all beam axes now passing through the center of the target. The uniformity requirement for direct drive can be met by either configuration. Clearly, options requiring no energy reduction are preferred.

**Beam Smoothing by Spectral Dispersion (SSD)**

This section examines issues related to beam smoothing by spectral dispersion (SSD). The starting point for the calculations presented here is the SSD configuration proposed for the NIF by D. Eimerl[4] during the ICFAC meeting at the University of Rochester on 18 May 1994. A key design issue for the NIF that affects optimization of SSD is the angular acceptance of the pinholes, which determines the amount of spectral dispersion that can be used by SSD. It will be shown below that if twice the dispersion specified by Eimerl is imposed (in just one dimension), then a substantial improvement in uniformity can be achieved.

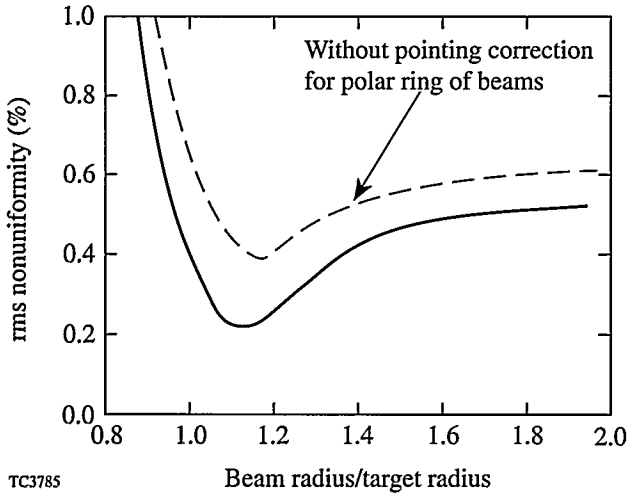


Figure 62.21
The rms nonuniformity for the 48-beam configuration as a function of the ratio of beam size to target size. An eighth-order supergaussian beam profile was used. (The effect of structure on the beams is shown in Fig. 62.29.) The solid line is the result of pointing the polar ring of beams to the optimal position on the target surface. The dashed line is without this correction.

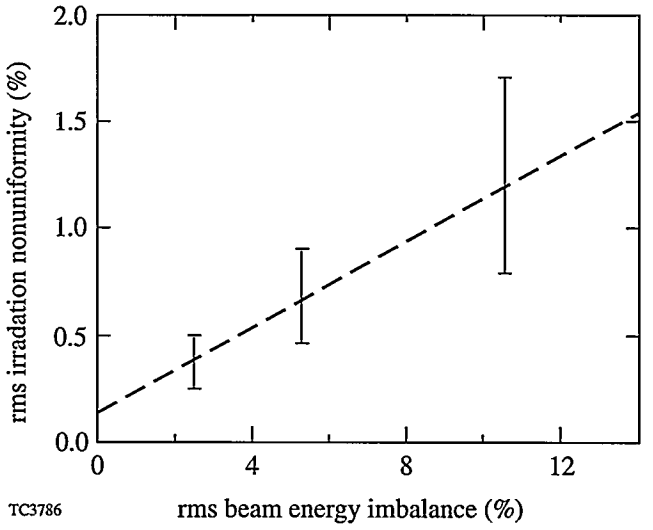


Figure 62.22
The rms irradiation nonuniformity as a function of the rms energy imbalance among the beams. The bars show the spread in irradiation nonuniformity that can occur for a given energy imbalance. Energy fluctuations among beams in a cluster were assumed to be uncorrelated.

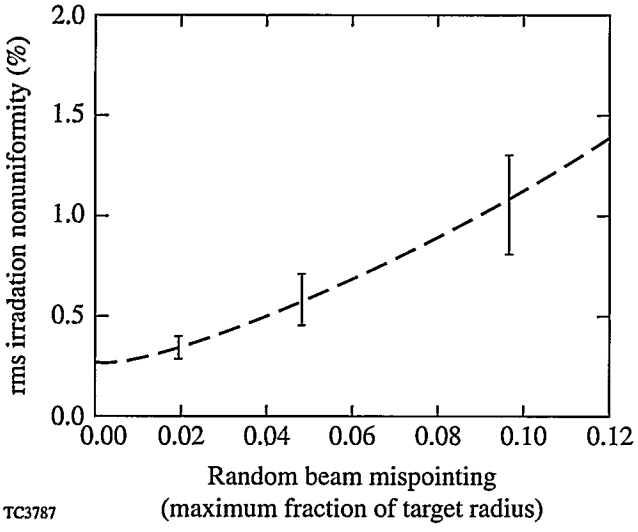


Figure 62.23
The rms irradiation nonuniformity as a function of cluster pointing error. All beams within a cluster were assumed to be pointed in the same direction.

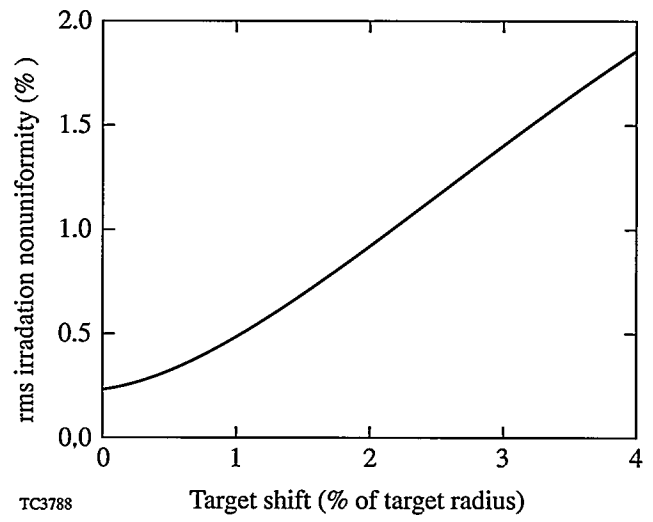


Figure 62.24
The rms irradiation nonuniformity as a function of target positioning error.

The three sets of parameters that determine the single-beam uniformity achievable by SSD are those related to the phase plate, the polarization rotator (or shifter), and the spectrally dispersed bandwidth. The first two parameter sets will be mentioned only briefly as any adjustable parameters associated with them will affect mainly long-wavelength nonuniformities. The third parameter set will be discussed in more detail since this provides the primary smoothing mechanism for short-wavelength structure in the beam and a large number of options are available.

1. Phase Plate

The calculations presented here use a binary phase plate with an array of 250 × 250 square elements, which produces a $\text{sinc}^2$ intensity envelope in the target plane. Superimposed upon this envelope is highly modulated speckle from the interference between rays from different phase-plate elements. Most of this structure is smoothed out by SSD. The distance $D$ between the first zeros of the envelope is equal to 250 times the beam's diffraction limit (for the phase plate considered), i.e.,

$$D = 250 \times \left(2\lambda F^{\#}\right).$$

For an $f$-number ($F^{\#}$) of 17.5 and $\lambda = 0.35$ mm, we have $D =$ 3 mm, which should correspond to the diameter of the target. Current direct-drive designs for the NIF use targets about 30% larger, which would require a larger number of phase-plate elements (i.e., ~350 × 350 for the above example). More phase-plate elements (of smaller size) would produce a small shift in nonuniformity to shorter wavelengths relative to the target size, but the shift would not be large enough to significantly affect the results presented in the next section.

Current phase-plate strategies involve the use of continuously varying phases[5] and kinoforms[6] to avoid the energy loss around the target associated with the sharp variations in binary phase plates. These will also provide greater control over the shape of the intensity envelope in the target plane. It remains to be determined what effect these new phase plates will have on short-wavelength nonuniformities. They can significantly affect long-wavelength structures (spherical harmonic modes $\ell < 20$) through the envelope shape. (It should be emphasized that any phase-plate envelope shape will be slightly modified by SSD and polarization dispersion.) As target designs and phase-plate strategies develop, their characteristic features can be incorporated into the uniformity calculations to determine their effects.

2. Polarization Dispersion

A birefringent wedge placed at the end of each beamline will cause the speckle pattern from one polarization to shift relative to the other.[7] If the shift is more than about 1/2 of a speckle width (which is roughly the coherence length), then the effect is similar to adding two different random-intensity patterns.[8] The rms nonuniformity will be reduced instantaneously by a factor of $\sqrt{2}$. This effect was demonstrated at LLE using a liquid crystal (LC) wedge,[7] but any other birefringent material, such as KDP, could be used. Figure 62.25 shows the experimental results of how the speckle modulation from a phase plate has been reduced using the LC wedge. An analysis of the intensity fluctuations around a smooth envelope

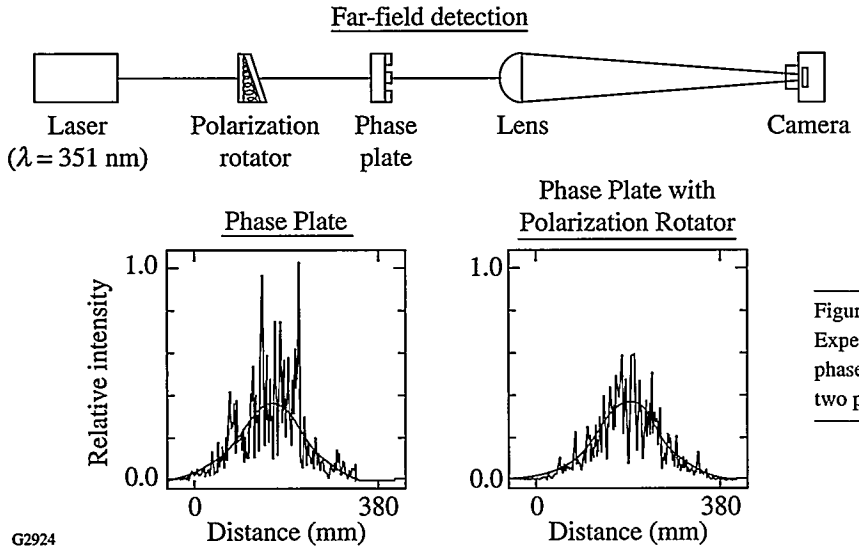


Figure 62.25
Experimentally observed reduction in nonuniformity from a phase plate using a birefringent wedge to spatially separate the two polarization components.

showed that the rms variation was reduced by roughly a $\sqrt{2}$, as predicted. This superposition of shifted speckle patterns is similar to the smoothing mechanism produced by SSD, which shifts the speckle patterns for different spectral modes of the bandwidth. Optimized smoothing is achieved when the polarization and spectral shifts are complementary, as discussed below.

3. SSD Considerations

As the baseline configuration for 2-D SSD, we adopt the parameters described by Eimerl (Fig. 62.26). The one departure from that design, examined here, is the option for increased angular dispersion in one of the directions. It remains to be determined what effect such increased dispersion would have on laser performance and whether the amount of improved laser uniformity is large enough to justify a possible degradation in energy output.

One strategy for combining two-dimensional spectral dispersion of the bandwidth with polarization dispersion from a birefringent wedge is illustrated in Fig. 62.27, which shows the modal positions in the target plane. The minimum separation between modes should not be closer than ~1/2 the diffraction limit of the beam (i.e., 1/2 a speckle size) for good smoothing. The symbols "x" and "o" represent orthogonal components of polarization. This configuration allows for the smallest amount of angular dispersion through the laser but requires the maximum polarization dispersion. To keep the beam nearly circular, either twice as many modes must be used in the direction perpendicular to polarization dispersion (i.e., twice the angular spread) or the beam envelope must be adjusted using the phase plate to compensate for unequal angular dispersion.[1]

To examine the effect of increasing the angular dispersion in one direction, we considered the example where the parameters associated with the 3-GHz modulator (Fig. 62.26) were kept constant and parameters of the other modulator were varied. The 1-Å IR bandwidth from the 3-GHz modulator produces about 31 spectral lines upon frequency tripling. These lines were spectrally dispersed to a separation of 1/2 a speckle distance in the target plane, i.e., a total angular spread of 15 times the beam's diffraction limit (to be denoted by 15 × DL). This was chosen to be the direction of polarization dispersion, which was also 15 × DL, corresponding to the horizontal direction in Fig. 62.27. The total angular deflection in this direction is now 30 × DL.

For spectral lines from the first modulator in Fig. 62.26, the modes were also dispersed to a separation of 1/2 DL in the target plane, but the number of modes (i.e., the total angular spread) was allowed to vary while keeping the bandwidth constant. The bandwidth was maintained at a value near 4 Å (IR) by varying the modulation frequency $\nu_1$ inversely with the number of spectral lines. (This bandwidth is about 10% lower than the value used by Eimerl.) A secondary constraint—that the frequencies from the two modulators should be incommensurate—could have been imposed. However, to simplify the calculation, it was only required that $\nu_1$ should be an odd multiple of 0.5 GHz. This approach assured that when its modes were combined with those from the 3-GHz modulator, the resultant modes would have equally spaced frequencies separated by $\delta\nu$=0.5 GHz. (The resultant modes have frequencies composed of a harmonic from one modulator plus a harmonic from the second.) Beam smoothing will then occur for averaging times up to 2 ns $(1/\delta\nu)$, which is the time required to smooth nearest-neighbor modes. If longer smoothing times are applicable, then $\nu_1$ can be chosen so that the resultant modes are more closely spaced in frequency.

Figure 62.28 shows the effect of increasing the angular dispersion in one direction. The rms nonuniformity for a single beam versus averaging time is plotted. Here, the rms nonuniformity is defined as the intensity fluctuation around the

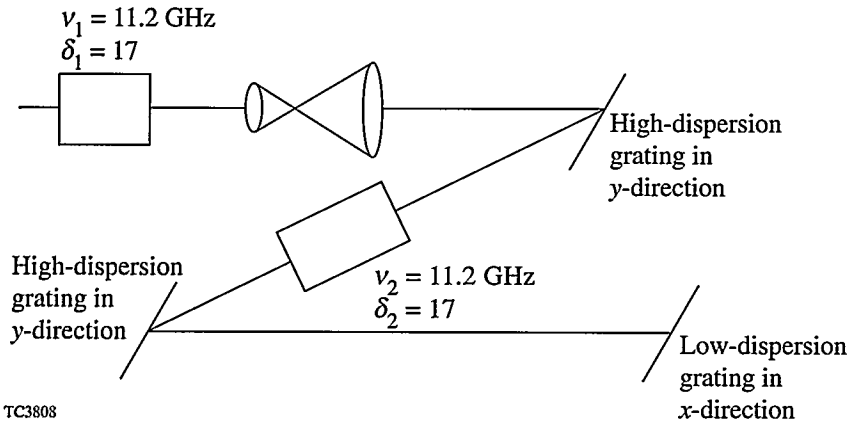


Figure 62.26
Configuration for 2-D SSD proposed for the NIF laser (Ref. 4). Here $\nu_1$ and $\nu_2$ are the modulation frequencies for the two modulators, and $\delta_1$ and $\delta_2$ are the modulation indices, corresponding to 1/2 the number of spectral modes.

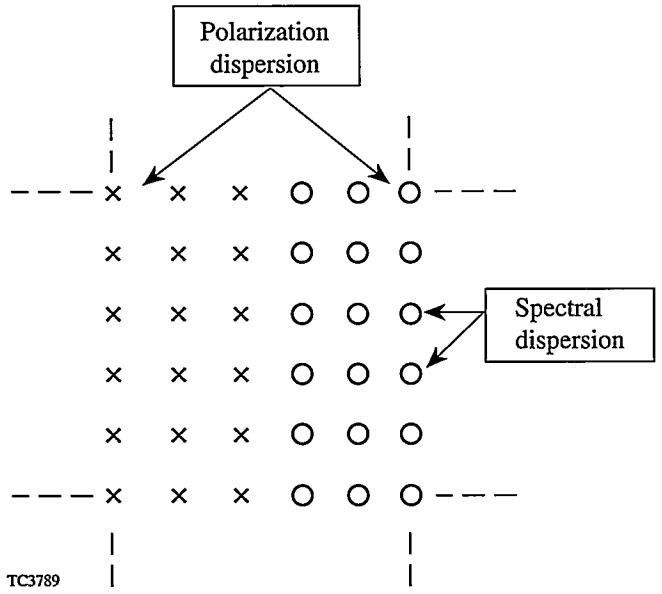


Figure 62.27
Strategy for combining 2-D SSD with polarization dispersion. The "x" and "o" positions represent the locations of the dispersed spectral modes for the two polarization components. The components should be separated by at least 1/2 of a speckle distance.

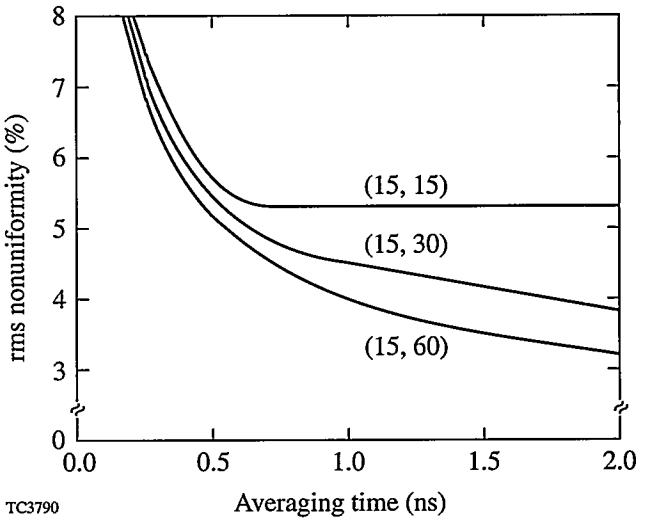


Figure 62.28
Improved irradiation nonuniformity with increased pinhole size. The numbers in parentheses indicate the angular dispersion for the two perpendicular directions, in terms of the beam's UV diffraction limit.

diffraction-limited envelope that would be produced if interference between all phase-plate elements were absent. The rms value was evaluated at the center of the beam, over a square region given by ±0.1 times the target radius in each direction. This gives a good sampling of the short-wavelength structure. (Long-wavelength nonuniformity is more appropriately discussed in conjunction with the effects of multiple-beam overlap.) The three curves in Fig. 62.28 are labeled by the angular deflection (in terms of the beam's UV diffraction limit) in each direction.

The single-beam results in Fig. 62.28 show that if we are interested only in averaging times less than ~500 ps, then there is little advantage to increasing the angular dispersion. However, if averaging times of ~1 ns or larger are relevant, then substantial improvements in uniformity can be achieved from increased dispersion. The majority of the effect is achieved at 30 × DL: For a 2-ns averaging time, the rms nonuniformity is reduced by 40%, compared with the 15 × DL result. (For 60 × DL, the reduction is increased to 65%.) The improved uniformity is probably the result of smoothing some of the longer-wavelength nonuniformities that become accessible with increased angular dispersion. (All three cases in Fig. 62.28 use the same bandwidth.) Table 62.III summarizes some of the SSD parameters and results.

The uniformity results for spherical illumination, using multiple beam overlap, are shown in Fig. 62.29, which uses the configuration of 48 clusters of 4 beams from Table 62.II with the pointing correction for the polar ring of beams. The axes of the beams in each cluster were also shifted by 20% of the target radius (using wedges) to produce an intensity envelope for the cluster that was less center-peaked than for the individual beams. (This could also be accomplished by using the phase plate to shape the envelope.) The beams were mapped directly onto the target surface, and the nonuniformity was expressed in terms of spherical harmonics for modes up to 512. No refractive smoothing or thermal smoothing in a plasma atmosphere was used, except indirectly by neglecting the very-short-wavelength structure with spherical harmonic modes greater than 512. Interference between the beams was not included in the calculation. This is justified for the interference between beams within a cluster and between beams from different clusters with different frequencies, as this structure will smooth within ~5 ps. Interference between beams (of the same frequency) from different clusters was not considered because this nonuniformity has spatial wavelengths that are much shorter than the minimum considered here. Such very-short-wavelength nonuniformity would be smoothed by thermal conduction within the target, over distances of only a few microns.

Table 62.III: Parameters related to the large-bandwidth modulator and the resultant single-beam rms nonuniformity.

| | Total Angular Dispersonx(DL) | | |
|---|---|---|---|
| | 15 | 30 | 60 |
| Modulation frequency (GHz) | 13.50 | 6.5 | 3.5 |
| Bandwidth (Å, IR) | 4.05 | 3.9 | 4.2 |
| Single-beam nonuniformity | | | |
| $\Delta t$ = 500 ps | 5.9% | 5.7% | 5.4% |
| $\Delta t$ = 2 ns | 5.3% | 3.9% | 3.3% |

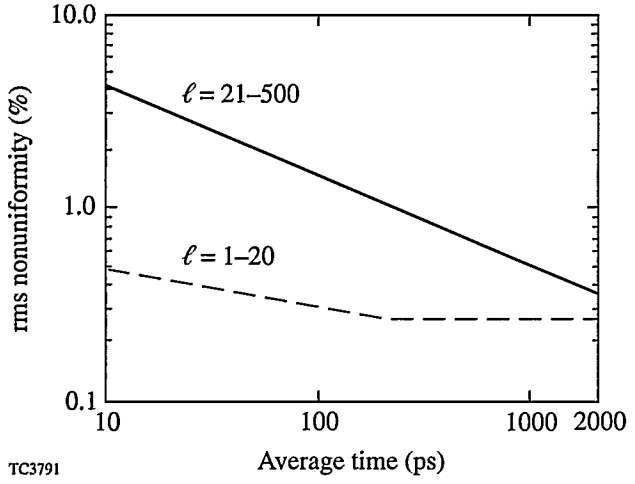


Figure 62.29
Irradiation nonuniformity for spherical irradiation as a function of averaging time. The $\ell$ values indicate the spherical harmonic modes for the two curves shown.

The nonuniformity for spherical irradiation (Fig. 62.29) has been separated into a long-wavelength component, with spherical harmonic modes $\ell \leq 20$, and a shorter-wavelength component with $21 \leq \ell \leq 512$. The long-wavelength modes are relatively static and are dominated by the shape of the cluster intensity envelope and the number of clusters. It is possible that this component of nonuniformity could be further reduced by modifying the envelope shape as part of the phase-plate design. The shorter-wavelength modes (21–512) decrease with averaging time $t$ roughly as $t^{-1/2}$. This is the same scaling as ISI[9] and is obtained from the superposition of different random speckle patterns.

Finally, it should be pointed out that there is still additional nonuniformity present, with $\ell > 512$, from structure in the individual beams. As an example, Fig. 62.30 shows the modal decomposition for an averaging time of 2 ns. The nonuniformity clearly extends even above 512. The largest mode number that should be present can be estimated as follows: The largest mode $\ell_{max}$ is related to the wavelength of the smallest structure $\delta\lambda$ and to the target diameter by

$$\ell_{max} = \pi D/\delta\lambda.$$

The smallest wavelength should correspond roughly to the beam's diffraction limit (i.e., one speckle). Since $D$ is 250 times larger for this calculation, we have $\ell_{max} \sim 800$. It remains to be determined what effect the very-short-wavelength structure has on target performance.

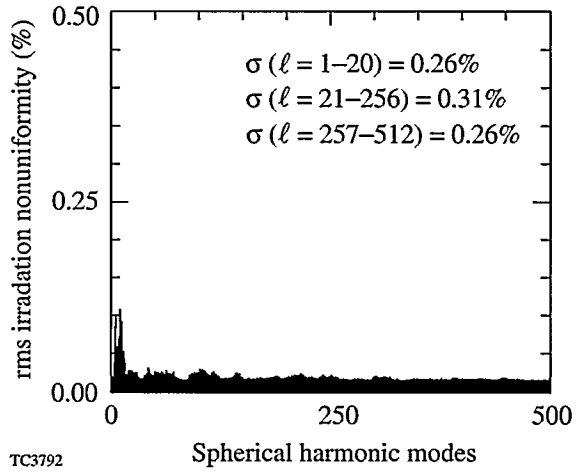


Figure 62.30
Spherical harmonic decomposition of the nonuniformity from Fig. 62.29 for 2-ns averaging time.

## Summary

The NIF can produce highly uniform irradiation for direct-drive experiments if one-half of the beams are redirected to new ports closer to the "equator" of the target chamber and if 2-D SSD is implemented with polarization dispersion. The tolerances for energy imbalance among the beams, beam mispointing, and errors in target positioning depend on how much long-wavelength nonuniformity (spherical harmonic modes 1–4) the target can accept without serious degradation in performance. Using 1% for the maximum nonuniformity in these modes, we have the following constraints: (1) energy imbalance among the beams should be less than ~5%; (2) cluster mispointing should not exceed ~5% of the target radius; and (3) the target positioning error should be less than ~2% of the target radius.

The optimal pinhole size for SSD is another issue that depends on the target design. If intensity-averaging times greater than ~1 ns are of interest, then there is a definite advantage for the pinhole to be able to accommodate a divergence of 30 × DL in one direction and 15 × DL in the other for UV irradiation. It would be useful to determine what effect this would have on laser performance. If these divergences are available, it might be possible to optimize target designs to take advantage of the resultant higher uniformity for longer smoothing times.

## ACKNOWLEDGMENT

This work was supported by the U.S. Department of Energy Office of Inertial Confinement Fusion under Cooperative Agreement No. DE-FC03-92SF19460, the University of Rochester, and the New York State Energy Research and Development Authority. The support of DOE does not constitute an endorsement by DOE of the views expressed in this article.

## REFERENCES

1. S. Skupsky, R. W. Short, T. Kessler, R. S. Craxton, S. Letzring, and J. M. Soures, J. Appl. Phys. **66**, 3456 (1989).
2. J. W.-K. Mark, Phys. Lett. **114A**, 458 (1986).
3. D. Eimerl (private communication).
4. D. Eimerl, presented at the 5th Meeting of the Inertial Confinement Fusion Advisory Committee/Defense Programs (ICFAC/DP), University of Rochester, Rochester, NY, 18–20 May 1994.
5. T. J. Kessler, Y. Lin, J. J. Armstrong, and B. Velazquez, in *Laser Coherence Control: Technology and Applications,* edited by H. T. Powell and T. J. Kessler (SPIE, Bellingham, WA, 1993), Vol. 1870, pp. 95–104.
6. S. N. Dixit *et al.*, Opt. Lett. **19**, 417 (1994).
7. Laboratory for Laser Energetics LLE Review **45**, NTIS document No. DOE/DP40200-149, 1990 (unpublished), p. 1.
8. S. N. Dixit (private communication); also J. W. Goodman in *Laser Speckle and Related Phenomena*, Topics in Applied Physics, Vol. 9, edited by J. C. Dainty (Springer-Verlag, Berlin, 1984), Chap. 2, pp. 9–75.
9. R. H. Lehmberg, A. J. Schmitt, and S. E. Bodner, J. Appl. Phys. **62**, 2680 (1987).

# Direct Measurements of Terminal-Level Lifetime in Nd:YLF

The terminal-level lifetime of a four-level laser fundamentally affects its gain saturation performance since slow relaxation rates from this level can form a "bottleneck" when the saturating pulses are significantly shorter than the terminal-level lifetime. As a result, the terminal-level lifetime is an important design parameter in achieving maximum energy extraction from high-peak-power laser amplifiers and $Q$-switched oscillator systems.

Terminal-level lifetimes reported in the literature for even the most common laser media such as Nd:YAG differ by as much as several orders of magnitude;[1–4] references for Nd:YLF[2,3] are less common and subject to the same uncertainty.

For most solid-state laser materials, the terminal-level lifetime is dominated by nonradiative relaxation processes involving the emission or absorption of host material phonons. Closely spaced energy levels within a Stark manifold thermalize extremely rapidly (<10 ps)[5,6] through nonradiative processes involving single phonons, while relaxation between different Stark manifolds proceeds at significantly slower rates since multiple phonons are required to bridge the typically larger intermanifold energy gaps. When the total multiphonon, nonradiative relaxation out of the terminal laser level manifold is much slower than the intramanifold thermalization, the distribution of population within the manifold can be treated as a system in quasi-thermal equilibrium and described by a Boltzmann distribution. For laser systems in which the terminal laser level contains a significant proportion of its thermalized manifold population, gain saturation properties are determined by both the relaxation rate of the entire manifold and the quasi-thermal occupation factor in the terminal laser level. The manifold relaxation rate, often characterized by its lifetime, determines whether any "bottlenecking" occurs, and the thermal occupation factor determines the degree to which accumulation of population in the terminal-level manifold reduces population inversion during lasing.

Measured lifetimes for other energy levels can yield relevant information since multiphonon nonradiative relaxation rates generally follow a phenomenological model[7,8] that depends only on temperature, energy gap to the next lower energy level, and a single phonon frequency. Measured relaxation rates for high-order phonon processes ($n > 3$) substantially support this model;[9,10] however, it is generally invalid for low-order processes ($n \leq 3$). Anomalies have also been observed in some materials[8] due to selection rules or when a high degree of resonance exists between an intermanifold energy gap and a sum of phonon energies corresponding to peaks in the host material's phonon spectrum. In addition, significantly different lifetimes for nonradiative transitions covering nearly identical energy gaps have been reported for Nd:YAG[3,11] that suggest either a breakdown in the model or a dependence on the measurement technique.

Direct measurement of the $^4I_{11/2}$ terminal-level relaxation is performed ideally under prototypical energy extraction conditions to ensure meaningful results. Sensitive and accurate measurement of the relaxation rate demands operating in a regime that clearly isolates the multiphonon nonradiative decay process from radiative processes. Saturating pulses substantially shorter than the terminal-level lifetime can yield a true impulse response that is easily analyzed without the need for deconvolving input beam pulse shapes or applying complicated models of the population dynamics. Any practical method should by design also minimize the amount of sample required and avoid nonlinear optical processes, such as self-focusing or self-phase modulation, that might damage the sample or otherwise introduce unquantifiable effects into the measurement.[12]

## Theory

Figure 62.31 represents the energy levels in Nd:YLF important to laser action. The 1475-cm$^{-1}$ energy gap[13] between the $^4I_{11/2}$ terminal-level manifold and the $^4I_{9/2}$ ground-state manifold is less than three times the phonon cutoff energy of 566 cm$^{-1}$ in YLF,[14] which places this nonradiative decay process near the limit of validity for the single-frequency model.

In this work, the $^4F_{3/2}$ initial-laser-level manifold is pumped directly from the $^4I_{9/2}$ ground-state manifold. Laser action at

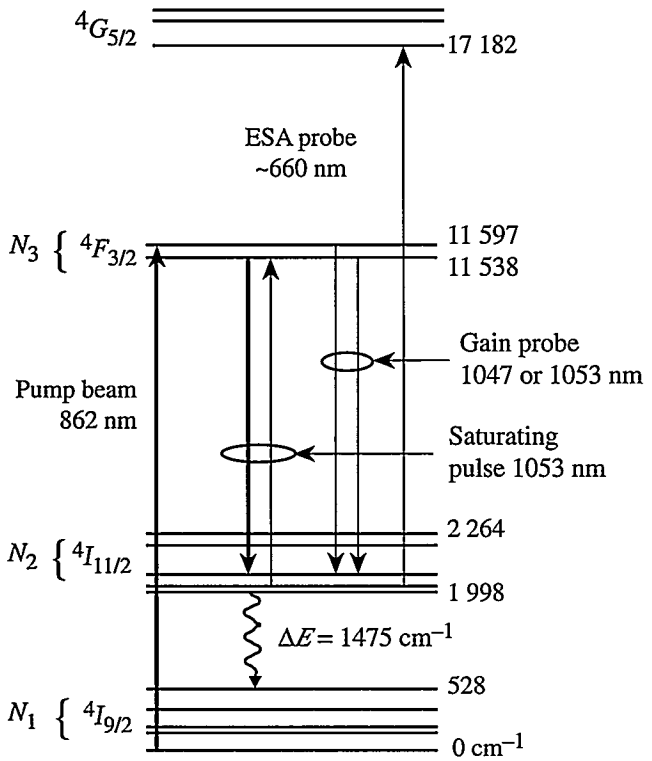


Figure 62.31
Energy-level diagram for lasing in Nd:YLF. The $^4I_{9/2}$ ground state and $^4I_{11/2}$ terminal laser state are separated by a 1475-cm$^{-1}$ energy gap that is less than three times the maximum phonon energy in YLF[14] (~566 cm$^{-1}$). The thick upward (downward) arrow represents the pump (saturating pulse) laser transitions. The thin downward (upward) arrow represents the small-signal-gain (excited-state absorption) probe transitions.

the 1053-nm laser transition occurs between the lowest sublevel in the $^4F_{3/2}$ manifold and the second lowest level in the $^4I_{11/2}$ manifold. Since both the initial and terminal laser levels are strongly coupled to their respective Stark manifolds and each contains a substantial portion of its manifold's population, the relevant population dynamics are best described by rate equations for the total populations $N_3$ and $N_2$ of the initial ($^4F_{3/2}$) and terminal ($^4I_{11/2}$) laser-level manifolds, respectively,

$$\frac{dN_3(\bar{r},t)}{dt} = W_{\text{pump}}(t)\cdot N_1(\bar{r},t) - W_{\text{sat pulse}}(t) \times \left[f_3 N_3(\bar{r},t) - f_2 N_2(\bar{r},t)\right] - N_3(\bar{r},t)/\tau_3, \quad (1a)$$

$$\frac{dN_2(\bar{r},t)}{dt} = W_{\text{sat pulse}}(t) \times \left[f_3 N_3(\bar{r},t) - f_2 N_2(\bar{r},t)\right] - N_2(\bar{r},t)/\tau_2, \quad (1b)$$

where $W_{\text{pump}}$ and $W_{\text{sat pulse}}$ are the radiative transition rates associated with the pump and saturating pulses, respectively, given by $W(t) = I(t)\cdot\sigma/h\nu$, where $I(t)$ is the intensity, $\sigma$ is the corresponding pump absorption or laser-stimulated emission cross section, and $h\nu$ is the photon energy; $\tau_3$ and $\tau_2$ are the lifetimes of the initial and terminal-laser-level manifolds, respectively; and the thermal occupation factors of the actual Stark sublevels of the laser transition, $f_3$ and $f_2$, are given by $f_i = e^{-E_i/kT}/Z_i$, where $E_i$ is the energy of the sublevel within the manifold and $Z_i$ is the partition function for the manifold. Given that no other energy levels accumulate significant populations, all relevant population dynamics are described by Eq. (1) plus the closure condition $N_0 = N_1 + N_2 + N_3$, where $N_0$ is the doping concentration of the crystal and $N_1$ is the total population of the $^4I_{9/2}$ ground-state manifold.

The rapid thermalization of the initial and terminal laser levels within their respective Stark manifolds can also be addressed in analytic solutions for laser-energy extraction performance[15] when saturating pulse lengths are short compared to the lifetime of the entire terminal-level manifold but long compared to the intramanifold thermalization processes. In a manner analogous to applying level degeneracy factors,[16] the expression for saturation fluence can be modified to include the thermal occupation factors $F_{\text{sat}} = h\nu/(f_3 + f_2)\sigma_{\text{se}}$, where $\sigma_{\text{se}}$ is the spectroscopic stimulated emission cross-section. This expression reduces to the well-known value of $F_{\text{sat}} = h\nu/\sigma_{\text{se}}$ for an ideal four-level system $(f_3 = 1,\ f_2 = 0)$, and $F_{\text{sat}} = h\nu/2\sigma_{\text{se}}$ for a three-level system $(f_3 = 1,\ f_2 = 1)$. Simple analytical models are inadequate for the intermediate case where laser pulse lengths are comparable to the terminal-laser-level manifold lifetime.

Figure 62.31 also shows small-signal-gain and excited-state absorption probes used in measuring the terminal-level lifetime. The small-signal-gain probe measures the population inversion $\Delta N = f_3 N_3 - f_2 N_2$, while the excited-state absorption probe monitors directly the population of the terminal manifold.[12,17] Assuming a plane-wave interaction, the time dependence of small-signal probe beams propagating in the $x$ direction are determined by the population dynamics of the initial and terminal laser levels according to simple exponential growth and absorption laws

$$G_{ss}(t) = \exp\left\{\int_{x=0}^{L} \Delta N(x,t)\sigma_{se}\, dx\right\}, \quad (2a)$$

$$T_{ESA}(t) = \exp\left\{-\int_{x=0}^{L} f_2 N_2(x,t)\sigma_{ESA} dx\right\}, \quad (2b)$$

where $\sigma_{se}$ and $\sigma_{ESA}$ are the stimulated emission and excited-state absorption cross sections, respectively, and $L$ is the sample thickness. The exponential arguments are integrated along the path traveled in the sample by the probe beams since the populations may vary spatially. Zero population in the ${}^4G_{5/2}$ upper level of the excited-state absorption transition is assumed in Eq. (2b) for small probe signals.

After the initial-laser-level pumping has stopped and after an impulse-like saturating pulse has extracted stored energy at time $t_0$, Eqs. (1a) and (1b) become uncoupled differential equations with simple exponential solutions

$$N_3(x,t) = N_3(x,t_0)\cdot\exp\left[-(t-t_0)/\tau_3\right]$$

and

$$N_2(x,t) = N_2(x,t_0)\cdot\exp\left[-(t-t_0)/\tau_2\right],$$

where $N_3(x,t_0)$ and $N_2(x,t_0)$ are the population densities of the initial and terminal laser manifolds, respectively, left by the saturating pulse at $t_0$.

Substituting into Eq. (2) gives

$$G_{ss}(t>t_0) = G_{final}\cdot\exp\left\{-\alpha_{se}(t_0)L\cdot e^{-(t-t_0)/\tau_2}\right\}, \quad (3a)$$

$$T_{ESA}(t>t_0) = \exp\left\{-\alpha_{ESA}(t_0)L\cdot e^{-(t-t_0)/\tau_2}\right\}, \quad (3b)$$

where

$$\alpha_{se}(t_0) = \frac{1}{L}\int_{x=0}^{L} f_2 N_2(x,t_0)\sigma_{se} dx$$

and

$$\alpha_{ESA}(t_0) = \frac{1}{L}\int_{x=0}^{L} f_2 N_2(x,t_0)\sigma_{ESA} dx$$

represent the effective excited-state absorption coefficients for the small-signal probes at time $t_0$. Since the ${}^4F_{3/2}$ initial laser-level lifetime is extremely long compared to the lower-level lifetime,[6,18] the upper-laser-level population can be taken as constant with a value $N_3(t) \sim N_3(t_0)$. The final small-signal gain after relaxation of the terminal laser level is given by

$$G_{final} = \exp\left\{\int_{x=0}^{L} f_3 N_3(x,t_0)\sigma_{se} dx\right\}.$$

**Experimental Setup**

Figure 62.32 illustrates the experimental setup. Thin Nd:YLF samples approximately 1 and 2 mm thick with nominal 1-at.-% doping concentrations are intracavity pumped directly into the ${}^4F_{3/2}$ initial-laser-level manifold by a free-running, tunable Cr:LiSAF pulsed laser. The pump laser is tuned to the weak Nd:YLF absorption band at ~860 nm using a birefringent tuning filter made from four crystalline quartz plates positioned at Brewster's angle. Horizontal polarization is further enforced by orienting the stronger $\pi$-polarization emission of the Cr:LiSAF rod to match the low-loss horizontal polarization of the Brewster tuning plates. The crystalline axis of the Nd:YLF sample is also horizontal to match the horizontal pump polarization with the stronger $\pi$-polarization absorption for Nd:YLF[18] $\left(\alpha_{max} \approx 0.3\ \text{cm}^{-1}\right)$. Operation in the $TEM_{00}$ mode is accomplished with an intracavity aperture in the nearly hemispherical resonator. Pump pulses with overall durations of approximately 70 $\mu$s and numerous relaxation oscillations were obtained typically, as shown in Fig. 62.33. Uniform pumping is expected since the sample is optically thin at this wavelength. Furthermore, multiple-longitudinal-mode operation of the pump laser should smooth out any spatial hole burning that might occur early during the pump pulse. The diameter of the Nd:YLF sample's pumped region is approximately 1 mm in the vertical direction and elongated in the horizontal direction since it is also positioned at Brewster's angle inside the pump laser cavity to minimize reflection losses from the uncoated sample.

A saturating pulse is generated from an ~70-ps (FWHM) pulse picked from the output of a cw mode-locked Nd:YLF laser operating at 1053 nm and amplified to the millijoule regime in an unstable, regenerative ring amplifier.[19] The

Table 62.IV: Measured values for the terminal-level lifetime of four different Nd:YLF samples using small-signal-gain ($G_{SS}$) recovery and transient excited-state absorption (ESA) methods are consistent within experimental accuracy.

| Sample | Thickness (mm) | Lifetime (ns) | Standard Deviation (ns) | Method |
|---|---|---|---|---|
| 1 | 1.015 | 21.9 | ±0.2 | 1047-nm $G_{SS}$ recovery |
| 2 | 1.100 | 21.9 | ±0.2 | 1047-nm $G_{SS}$ recovery |
| | | 21.4 | ±0.4 | 1053-nm $G_{SS}$ recovery |
| | | 21.8 | ±0.2 | transient ESA |
| 3 | 1.435 | 21.4 | ±0.2 | transient ESA |
| 4 | 2.230 | 21.3 | ±0.3 | 1047-nm $G_{SS}$ recovery |
| | | 21.7 | ±0.7 | transient ESA |

## Conclusions

The terminal-level lifetime for Nd:YLF measured in this work is long compared to the pulse lengths encountered for mode-locked laser operation and amplification of up to nanosecond pulses. In these cases, Nd:YLF must be treated as a three-level system amenable to standard Frantz-Nodvik gain saturation analysis with a modified expression for the saturation fluence that accounts for rapid thermalization of the initial and terminal laser levels within their respective Stark manifolds. Since common $Q$-switched laser pulse lengths are comparable to the terminal-laser-level lifetime measured in this work, simple analytical models are inadequate to account for terminal-level relaxation during amplification of such pulses, and numerical solutions are required to calculate energy-extraction performance.

## ACKNOWLEDGMENTS

The authors wish to acknowledge Lightning Optical Corporation for providing the Nd:YLF samples. The authors also wish to thank S. A. Letzring for technical support related to high-speed instrumentation and electro-optic elements used throughout the experiments. This work was supported by the U.S. Department of Energy Office of Inertial Confinement Fusion under Cooperative Agreement No. DE-FC03-92SF19460 and the University of Rochester. The support of DOE does not constitute an endorsement by DOE of the views expressed in this article.

## REFERENCES

1. F. E. Hovis *et al.*, IEEE J. Quantum Electron. **28**, 39 (1992).
2. K. Palombo *et al.*, in *OSA Proceedings on Advanced Solid-State Lasers, 1993*, edited by A. A. Pinto and T. Y. Fan (Optical Society of America, Washington, DC, 1993), Vol. 15, pp. 78–80.
3. C. Bibeau, S. A. Payne, and H. T. Powell, in *OSA Proceedings on Advanced Solid-State Lasers, 1994*, edited by T. Y. Fan and B. H. T. Chai (Optical Society of America, Washington, DC, 1994), Vol. 20, pp. 74–76.
4. W. Koechner, *Solid-State Laser Engineering*, 2nd rev. and updated ed., Springer Series in Optical Sciences, Vol. 1 (Springer-Verlag, New York, 1988), p. 49.
5. T. Kushida, Phys. Rev. **185**, 500 (1969).
6. A. L. Harmer, A. Linz, and D. R. Gabbe, J. Phys. Chem. Solids **30**, 1483 (1969).
7. H. W. Moos, J. Lumin. **1,2**, 106 (1970).
8. L. A. Riseberg and M. J. Weber, in *Progress in Optics*, edited by E. Wolf (North-Holland, New York, 1976), Vol. XIV, pp. 91–159.
9. M. J. Weber, Phys. Rev. B **8**, 54 (1973).
10. H. P. Jenssen, Ph.D. thesis, Massachusetts Institute of Technology, 1971.
11. T. T. Basiev *et al.*, J. Lumin. **53**, 19 (1992).
12. N. E. Bykovskii *et al.*, Sov. J. Quantum Electron. **18**, 783 (1988).
13. A. A. S. da Gama *et al.*, J. Chem. Phys. **75**, 2583 (1981).
14. E. Schultheiss, A. Scharmann, and D. Schwabe, Phys. Stat. Sol. (b) **138**, 465 (1986).
15. L. M. Frantz and J. S. Nodvik, J. Appl. Phys. **34**, 2346 (1963).
16. A. E. Siegman, *Lasers* (University Science Books, Mill Valley, CA, 1986), pp. 153–157.
17. V. A. Sychugov and G. P. Shipulo, Sov. Phys. JETP **31**, 438 (1970).
18. J. R. Ryan and R. Beach, J. Opt. Soc. Am. B **9**, 1883 (1992).
19. D. Y. Park, W. Seka, Y. Lin, and D. L. Brown, in the *Proceedings of the International Conference on Lasers '89*, edited by D. G. Harris and T. M. Shay (STS Press, McLean, VA, 1990), pp. 449–456.

# Light-Emitting Porous Silicon: Materials Science, Properties, and Device Applications

Silicon-based, light-emitting devices (LED's) should find numerous uses in optoelectronics. For example, the integration of silicon LED's with silicon microelectronics could lead to reliable and inexpensive optical displays and optical interconnects. Until recently, however, it had not been possible to obtain efficient room-temperature luminescence from silicon. The demonstration in 1990 that a form of silicon called "porous" can emit bright photoluminescence in the red region of the spectrum triggered worldwide research efforts aimed at establishing the mechanisms for the unexpected luminescence and at fabricating efficient and durable LED's. In less than five years, significant progress has been achieved on both fronts. LED's emitting throughout the visible spectrum have been demonstrated, and the best measured external electroluminescence efficiency has risen from $10^{-5}$% to better than 0.01% at room temperature. The photoluminescence efficiency of the best samples is near 10% at room temperature, and light-emitting porous silicon (LEPSi) that luminesces from the blue part of the spectrum to the infrared beyond 1.5 $\mu$m has been produced. In this article, we first review why silicon is a poor light emitter and then define porous silicon and its main properties. We then focus on the properties of the three luminescence bands ("red," "blue," and "infrared") and present the results of femtosecond time-resolved optical measurements. Next, we report progress toward the fabrication of LED's and discuss some specific device structures. Finally, we outline what is necessary for commercial LEPSi LED's to become a reality and report on experimental results that suggest the possible integration of LEPSi with standard microelectronic devices.

## Porous Silicon

### 1. Silicon Light Emission

Radiative recombination of an electron with a hole across the bandgap of semiconductors produces luminescence. The emitted photons have an energy equal to the bandgap energy (e.g., 1.4 to 1.5 eV in GaAs) and negligible momentum. Thus, the electron and the hole must be located at the same point in the Brillouin zone, which is the case in direct-gap semiconductors such as GaAs. Under these conditions, the radiative recombination rate is large, which means that the radiative lifetime is short (typically of the order of a few nanoseconds). To obtain a large luminescence efficiency, the nonradiative recombination rate must be lower than the radiative recombination rate. The efficiency is defined as

$$\eta = \tau_{\text{nonrad}} / (\tau_{\text{nonrad}} + \tau_{\text{rad}}), \qquad (1)$$

where $\eta$ is the quantum efficiency, $\tau_{\text{rad}}$ is the radiative lifetime, and $\tau_{\text{nonrad}}$ is the nonradiative lifetime. Nonradiative recombination occurs both at the surface and in the bulk. To minimize it, the surface should be well passivated leading to a low surface recombination velocity $S$, and the bulk must be free of defects that act as radiation killers. The efficiency of good-quality, direct-gap III–V semiconductors exceeds 1% at room temperature and 10% at cryogenic temperature.

Because silicon is an indirect-gap semiconductor, electrons and holes are found at different locations in the Brillouin zone and recombination by emission of a photon alone is not possible. Photon emission is possible only if another particle capable of carrying a large momentum, such as a phonon, is involved. In this case, both energy and momentum can be conserved in the radiative transition. The participation of a third particle in addition to the electron and the hole makes the rate of the process substantially lower and the radiative lifetime typically in the millisecond regime. Thus, the efficiency drops by several orders of magnitude, even in the case of high-purity materials and good surface passivation. At room temperature, the typical efficiency of crystalline silicon is of the order of $10^{-5}$%, which makes it unsuitable for LED's.[1] Several attempts have been made to improve the luminescence efficiency of silicon and silicon-based alloys, including the use of silicon-germanium alloys and superlattices,[2] isoelectronic impurities[3] in a manner similar to nitrogen in GaP, and erbium doping.[4] The strategy in these attempts can be divided into two classes: increasing the radiative rate or decreasing the nonradiative rate. The former can be achieved by "bandgap engineering" or "defect engineering," which essentially consists of "convincing" the electron and the hole that they do not

require a phonon to recombine radiatively. This process can be accomplished through zone folding in thin superlattices or with isoelectronic impurities whose energy level extends throughout the Brillouin zone. The latter consists of confining the electron and the hole to a small volume where the probability of finding a nonradiative center is equal to zero. This can be accomplished in the Ge-rich regions of SiGe and is realized to some extent with isoelectronic impurities. Such approaches have led to very good photoluminescence efficiencies (up to 10% in some cases) and good electroluminescence efficiency in some structures (approaching 1%), but only at cryogenic temperatures. At room temperature, these numbers drop to the range of $10^{-4}$% to $10^{-5}$%, and it is not clear how they can be increased to the 0.1% to 1% level.

## 2. Porous Silicon

Porous silicon is a material that has been known for nearly 40 years.[5] It has found limited use in microelectronics,[6] especially in the silicon-on-insulator (SOI) technology, as porous silicon becomes a good insulator after oxidation. In the 1980's, several studies of the optical properties of porous silicon were published, and photoluminescence in the deep red/near infrared was detected at cryogenic temperatures.[7] In 1990, Canham[8] reported that when porous silicon is further etched in concentrated aqueous HF for 6 h after preparation, it emits bright red light when illuminated with blue or UV light. Longer etching in HF was demonstrated to lead to brighter photoluminescence at shorter wavelengths, which was ascribed to quantum confinement. Longer etching increases the porosity, which produces, on the average, smaller nanocrystalline columnar structures. When the dimension of the columns decreases below 5 nm, the bandgap widens by quantum confinement in the conduction and valence bands and thus smaller columns produce larger bandgaps. In Canham's original model, the luminescence was attributed to band-to-band recombination across the bandgap. He also suggested that porous silicon might have a direct bandgap, which would explain the increase in efficiency by several orders of magnitude. Interestingly, at the same time as Canham was publishing his seminal paper, Lehmann and Gosele[9] independently showed that the bandgap of porous silicon is larger than that of crystalline silicon and attributed this increase to quantum confinement as well.

Lehmann and Gosele's proposal allowed them to provide a new and elegant explanation for the mechanism of pore formation. Injection of holes from the substrate to the surface is required for etching in HF. In their model, the thinning of the silicon columns formed when the pores are created continues until quantum confinement produces a barrier against hole transport into the columns. Although there are attractive competing models,[10] which for example rely on electrostatic effects near the pore's tip, this model has received partial experimental confirmation.[11] It must be noted that neither Canham's model for the luminescence nor Lehmann and Gosele's model for pore formation is universally accepted, and other models have been proposed.[12–16] Note also that the nanostructure of porous silicon is quite complicated. Even though columnar crystalline structures are present in some samples, the shape, thickness, and orientation of these columns or wires are not uniform. In other samples, no wires are detected, and the crystalline objects appear to be more or less spherical ("dots"). In all cases, however, light emission appears to be well correlated with the presence of crystalline structures smaller than 5 nm.[17]

Figure 62.36 shows the schematic arrangement for a typical electrochemical cell used to produce porous silicon. The arrangement is very simple and inexpensive. The wafer (anode) and the metal cathode are immersed in an aqueous solution containing HF. Typically, the HF concentration is kept around 25% by weight, and ethanol or methanol is added to improve the penetration of the solution into the pores and to minimize hydrogen bubble formation. Maintaining a constant current density of 1 to 100 mA/cm$^2$ for several minutes results in the formation of a porous silicon film with a thickness ranging from ~1 $\mu$m to tens of microns. Both the thickness and the photoluminescence spectrum of the porous layer depend

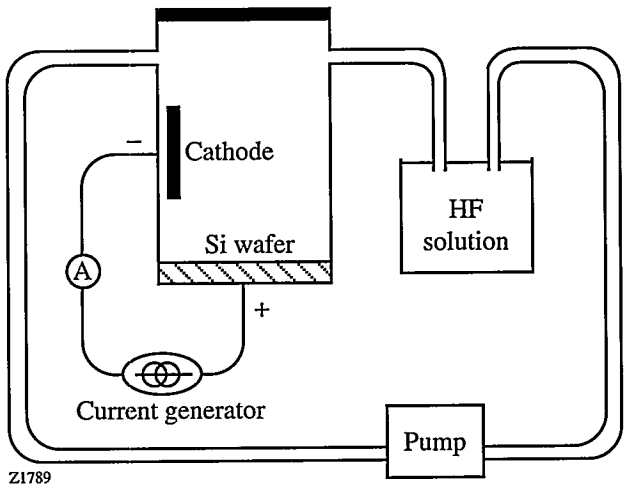


Figure 62.36
Schematic of the electrochemical cell used for the production of porous silicon. The HF solution circulates in Teflon™ tubing and through a Teflon™ pump.

strongly on many parameters, such as doping level and sign, current density, solution concentration and pH, and duration of the anodization. However, it should be stressed that light-emitting porous silicon can be produced over a wide range of most of these parameters. For example, holes, which play a critical role in the formation of porous silicon, cannot be injected from the bulk to the surface of an *n*-type wafer. This shortcoming can be eliminated by illuminating the wafer during anodization, as holes are photogenerated near the surface. Even if the porous layer is not of the luminescent type, further etching in HF in the open circuit configuration or by anodic oxidation in water can produce bright luminescence.

Figure 62.37 shows a LEPSi luminescence spectrum and its time evolution after pulsed excitation at 3.5 eV. The peak photoluminescence wavelength is typical, but it can easily be tuned between 850 nm and 550 nm, as discussed later. The full-width at half-maximum (FWHM) of the spectrum is between 150 meV and 500 meV. The most widely accepted explanation for this very large width is that the spectrum is "inhomogeneous," i.e., corresponds to bandgap or near-bandgap emission coming from nanocrystallites with a distribution of sizes. The decay of the photoluminescence following excitation takes place on a microsecond time scale at room temperature and increases to the millisecond regime at cryogenic temperatures.[18] Furthermore, the short-wavelength components usually decay faster than the long-wavelength components, a fact that also supports the hypothesis that a distribution of crystallite sizes produces the wide spectrum. This spectral diffusion with time varies from sample to sample. The decay of the full band or that of any individual wavelength component does not follow a simple law and can be fitted very well using a stretched exponential function.[19] Stretched exponentials may result from the random walk of carriers on a finite distribution of discrete sites in real space, as is known to occur in amorphous silicon. Regardless of the details of the physical mechanisms, there are well-known procedures to define the average or most probable lifetime; this lifetime value is usually quoted in the literature. After removing a possible fast decay component in the nanosecond time domain (to be discussed later), the lifetime of the red luminescence is in the microsecond time domain.

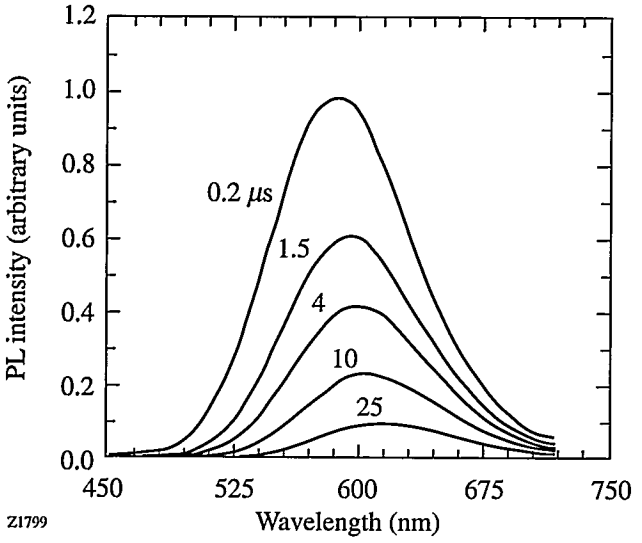


Figure 62.37
Time-resolved photoluminescence spectra measured at different times following excitation with a picosecond laser pulse at 3.5 eV. The overall decay at room temperature is in the microsecond time domain, but the decay is not exponential and is faster at shorter wavelengths.

### The Three Luminescence Bands

1. The Red Band

As mentioned earlier, the "red" luminescence band actually extends from the near infrared to the orange/green regions. Tuning can be achieved by changing any one of many parameters.[20] Here, we focus on results obtained by changing the anodization time under light assistance and by annealing in air. The LEPSi samples were prepared from *p*-type Si substrates in the dark (DA) or from *p*- and *n*-type Si substrates with light assistance (LA). The substrates were (100) oriented with a resistivity in the 1- to 10-Ω-cm range. Anodization with LA was performed using a 300-W, white-light halogen lamp.

The photoluminescence (PL) spectra from DA and LA samples are rather different.[21] The DA LEPSi has a broad peak centered near 740 nm, which is typical of samples prepared in the dark. In contrast, the PL spectra of the LA samples can be easily tuned from the infrared to the yellow/orange by increasing the anodization time. For a given solution and a constant current density, a longer anodization time produces a thicker LEPSi layer and shifts the PL peak toward shorter wavelengths. Figure 62.38 shows the relation between PL intensity, PL peak wavelength, and anodization time for *n*-type Si wafers prepared in an aqueous solution (no alcohol) with LA using a current density $j$ of 10 mA/cm$^2$.[22] Under these conditions, the maximum PL intensity corresponds to a peak wavelength near 700 nm. A proper choice of solutions and current density allows us to obtain homogeneous LEPSi samples that have good PL efficiency. Using blue excitation, the highest quantum efficiency we have measured on a red LEPSi sample at room temperature is approximately 5%. After optimization of the growth conditions, the PL of LEPSi samples is comparable to that emitted at room temperature by direct-gap III–V semiconductor compounds.

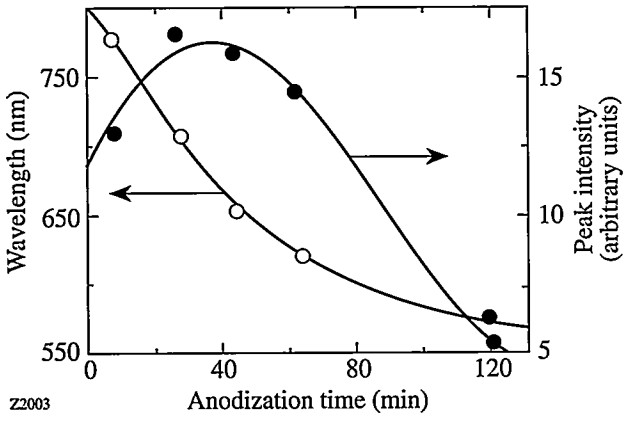


Figure 62.38
Photoluminescence intensity and peak wavelength as a function of the anodization time. The current density is 10 mA/cm$^2$, the substrate is a 10-Ω-cm *n*-type Si wafer, and light assistance is employed.

The PL peak wavelength has also been tuned by thermal annealing in a tube furnace in ambient air for 5 min at various temperatures.[23] In this case, the LEPSi layers were formed by anodization in the dark of 10-Ω-cm *p*-type Si wafers in a 1:1:2 solution of HF, $H_2O$, and methanol. Figure 62.39 summarizes results obtained with a variety of samples, either freshly prepared, annealed in air, or oxidized in $HNO_3$. The PL peak wavelength shifts to shorter values as the ratio of Si-O bonds to Si-H bonds increases. The ratio of the concentration of Si-H and Si-O bonds present on the surface of the nanocrystallites as shown in Fig. 62.39 is not the absolute ratio, since the cross section for infrared absorption of Si-O bonds is stronger than that for the Si-H bonds. Thus, the horizontal scale in Fig. 62.39 is a relative scale only. These results demonstrate a clear correlation between surface chemistry and PL peak wavelength. Freshly anodized samples that contain a very small but detectable amount of Si-O bonds and chemically oxidized samples that have almost no remaining Si-H bonds fit nicely at the two extremes of the data. Furthermore, annealing of freshly prepared samples at moderate temperature leads to data points that coincide with the data points obtained with aged samples.

The results of Fig. 62.39 are more easily understood if we assume that the PL is related to recombination involving surface states[24] rather than if it is strictly due to confinement[8] since the low-temperature treatments reported here have no effect on the particle size. For a particular surface coverage of the nanocrystallites present in LEPSi, we expect to find a specific set of surface states. When the coverage is changed, the nature and the energetic position of the surface states within the bandgap should change; thus, the PL spectrum is expected to change as well. It may be reasonable to model the wide PL spectrum as due to several bands associated with recombination involving different surface species.

It is worth noting that the origin of the "red" luminescence remains highly controversial. Many models have been proposed, ranging from those involving specific defects and molecular compounds to those involving quantum confinement.[12–16,25] Of all these models, two have received strong experimental support. The "pure" quantum confinement originally proposed by Canham,[8] which is consistent with many observations, has recently received support from resonant photoluminescence experiments.[26,27] In these experiments the low-temperature luminescence was not excited by a short-wavelength laser but by a laser tuned inside the broad PL spectrum to provide size-selective excitation. Under these conditions, the PL spectrum shows discrete steps that coincide with the zone-edge phonons of crystalline silicon that are known to be involved in the bandgap absorption and emission in crystalline silicon. These results not only indicate that silicon is the absorbing and luminescing species in LEPSi but also strongly suggest that luminescence occurs at the silicon crystallite bandgap. Other experiments, however, suggest that the luminescence occurs well below the bandgap and is affected by more than quantum confinement. Some examples include the results shown in Fig. 62.39 and the difference between the measured PL peaks and the measured or calculated bandgap,[28,29] which can be as large as ~1 eV.

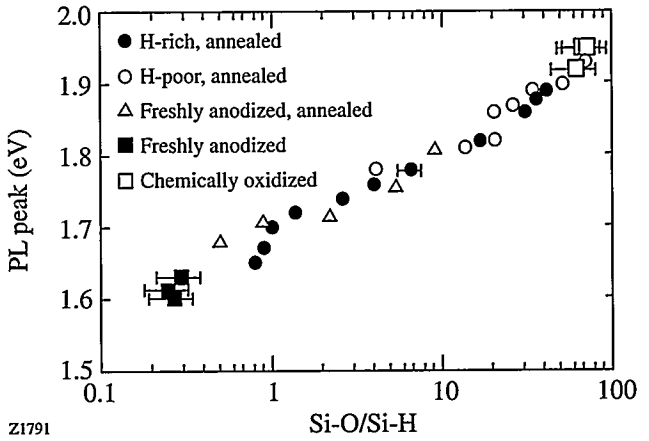


Figure 62.39
Relationship between the peak of the photoluminescence spectrum and the surface coverage, as measured by the ratio of Si-O bonds over Si-H bonds obtained by infrared absorption measurements. This ratio does not take into account the difference in the infrared absorption cross sections between Si-H and Si-O bonds.

Since the PL intensity and spectrum depend strongly on the surface coverage, one can expect some problems with long-term stability of the PL. For hydrogen-covered surfaces, the surface can become depassivated by hydrogen loss through heating[30] or exposure to short-wavelength light.[31] A solution to this problem is passivation with silicon dioxide instead of hydrogen. Such samples are much more resilient[21] but they also tend to luminesce in the blue.

2. The Blue Band

Recent literature contains several reports of strong blue PL in LEPSi after rapid thermal oxidation (RTO) at high temperature ($T_{ox} \geq 1000°C$),[32,33] as well as several reports of weaker blue PL in various samples. We conducted a systematic investigation of the properties of blue samples and have evaluated methods for obtaining them. The LEPSi layers were formed by anodization of 5-Ω-cm $p$-type silicon wafers in a 1:1:2 solution of HF, $H_2O$, and methanol. To change the sample's properties we varied the current density from 1 mA/cm$^2$ to 30 mA/cm$^2$. Anodization was performed either in the dark or with light assistance. Oxidation of the LEPSi layers was achieved in a tube furnace with a dry oxygen atmosphere. Samples of LEPSi first anodized in the dark at a current density $j = 10$ mA/cm$^2$ and then oxidized for 2 min at 1100°C in dry oxygen[34] display the reported blue PL band (Fig. 62.40). Infrared absorption measurements show a strong line at 1080 cm$^{-1}$ related to the asymmetric stretching vibrational mode of the Si-O-Si oxygen bridge (Fig. 62.40, inset). Other LEPSi samples anodized at a smaller current density (1 mA/cm$^2$) with light assistance and subjected to no further treatments have only one strong peak at 1070 cm$^{-1}$ in the infrared spectrum, which corresponds to Si-O-Si bridges in a configuration close to stoichiometry. Thus, the infrared spectra show no significant difference in the chemical composition between these two types of samples. Although we refer to these samples as "fully oxidized" in the following discussion since no Si-H bonds remain, this does not imply that there are no silicon nanocrystallites left in these samples.

The time-resolved PL spectra of both samples show a broad PL band (FWHM > 0.5 eV) with a peak near 2.6 eV that decays on a nanosecond time scale. The PL spectra have not been corrected for the spectral sensitivity of our detection system and are likely to extend to shorter wavelengths. The decay is nonexponential as for the red band, but in contrast to the red band, no significant wavelength dependence of the blue PL decay has been observed when the detection wavelength was changed from 440 nm to 650 nm, unlike what is seen in the red PL. The decay dynamics did not change appreciably when the measurements were performed at cryogenic temperatures. The observed nonexponential decay may indicate a distribution of carrier lifetimes, with the most probable lifetime being close to 1 ns. The estimated quantum efficiency of the blue PL is greater than 0.1%, roughly one order of magnitude below the efficiency of a good red sample.

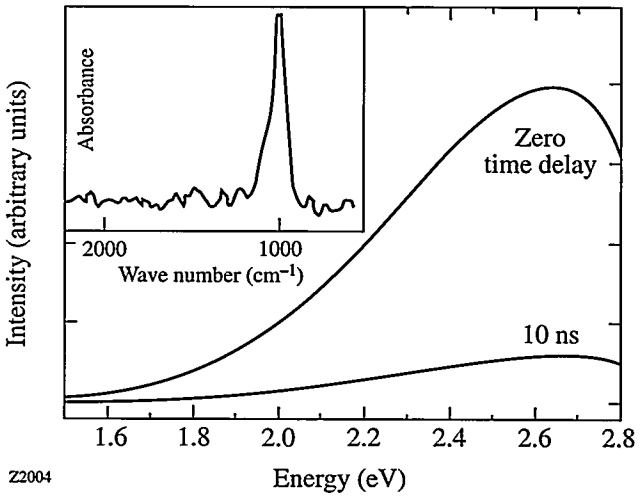


Figure 62.40
Time-resolved photoluminescence spectra of oxidized LEPSi after excitation with a picosecond laser pulse at 3.5 eV. The infrared absorption spectrum of the same sample shown in the inset indicates that the sample contains no Si-H bonds and only Si-O bonds.

The blue PL is also observed in samples that are oxidized chemically by immersion in 10% $HNO_3$ for 2 min or in freshly anodized samples after handling in air.[34] Measurements of the blue PL dynamics in the chemically oxidized sample also show a nonexponential decay with a characteristic time close to those of the fully oxidized samples. The time-resolved PL spectra of the freshly anodized samples measured right after excitation again show a weak but clearly observable blue PL band whose spectrum is similar to that of the "fully oxidized" samples. The presence of a very small amount of Si-O bonds is apparent in the infrared spectra of freshly anodized samples. Due to the low intensity of this blue band we were not able to analyze the decay in detail, but the characteristic decay time is much less than 15 ns.

Our results suggest two possibilities for the origin of the blue PL. Silicon dioxide is known to luminesce efficiently in the visible under appropriate conditions,[35] and it has been shown that blue PL with a nanosecond decay time can be excited by 4-eV photons in high-purity, wet synthetic silica.[36] Thus, the blue PL in oxidized LEPSi could originate not from

the silicon crystallites themselves, but from the oxide surrounding them. The second possibility is that special Si-O configurations produce the luminescence. These special configurations could be present at the Si nanocrystal/silicon dioxide interface, or in Si-rich regions produced in the oxide after nearly complete oxidation of the crystallites. It appears that we can exclude the hypothesis that the blue PL would originate from the interior of sub-3-nm Si crystallites. If this were the case, subjecting the oxidized crystallites to chemical agents should not affect the luminescence. We have exposed blue-emitting oxidized porous silicon to liquid methanol and observed a quenching of the blue PL.[37] This quenching is consistent with luminescent centers near the oxide surface. Specific chemical configurations such as silanol[38] have been proposed, but there remains considerable uncertainty as to the exact origin of the blue PL.[39] Note finally that the stability of the blue samples in air is much improved compared to that of the red samples.[21] This improvement can be traced to the presence of silicon dioxide, which is much less fragile than the Si-H bonds that passivate the surface of freshly prepared LEPSi.

3. The Infrared Band

Very few reports of infrared PL have appeared in the literature.[8,24,40–42] Some of these measurements were interpreted as bandgap or near-bandgap PL from crystalline silicon. Another explanation has been proposed for this IR PL, in which emission is associated with mid-gap dangling bonds on the surface of the nanocrystallites.[24] We have performed a careful measurement of the IR PL in several LEPSi samples.[41] In our experiments, the samples were placed in an ultrahigh vacuum (UHV) chamber where they were annealed *in situ*. The 422-nm line of a HeCd laser excites the PL, which in turn is detected by a Ge detector with a cutoff of ~0.7 eV. In the results reported below, the PL spectrum was recorded at room temperature, following vacuum annealing at temperatures as high as ~500°C for 5 min.

Figure 62.41 shows the room-temperature PL spectra for one sample before annealing and after annealing at two temperatures. The broad IR PL peak of the as-prepared sample is small but measurable at room temperature. As the annealing temperature is increased, its relative intensity increases until it dominates the spectrum. The IR PL appears to be most intense after annealing at a temperature where the red PL disappears, i.e., when most of the hydrogen that passivates the LEPSi surface has been desorbed, since heat treatment at such a temperature produces many dangling bonds. It is thus tempting to interpret the IR PL as due to recombination involving carriers in mid-gap dangling bonds. We also prepared samples in which the IR PL peak energy was ~0.7 eV. After annealing around 350°C, the integrated PL intensity measured at room temperature was comparable to the integrated intensity of the initial red PL peak. Preliminary results obtained with a luminescence detection system that is sensitive to wavelengths up to 5 $\mu$m indicate that these samples luminesce well past 2 $\mu$m. The conditions required for obtaining such samples are as of yet not well understood.

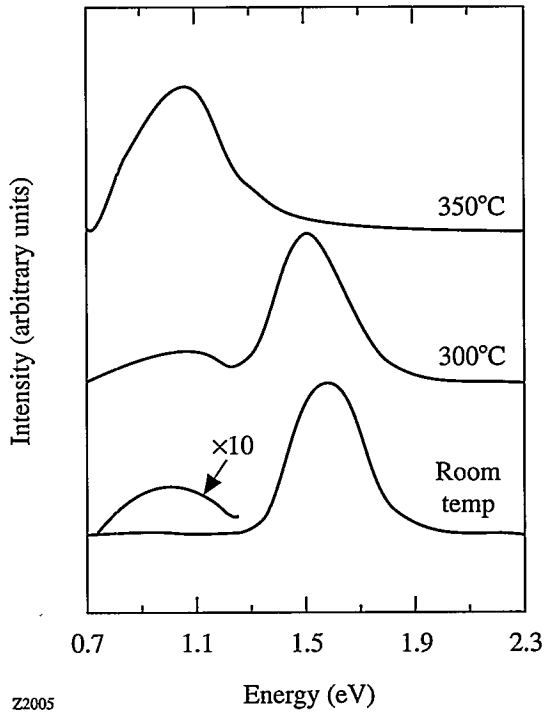


Figure 62.41
Normalized room-temperature PL spectra for LEPSi held in ultrahigh vacuum, before and after annealing for 5 min at two temperatures.

Time-resolved PL measurements[42,43] indicate a decay in the range from tens of nanoseconds to ~10 $\mu$s at 77 K, which is faster than the red PL decay in the same range of temperature. This decay may be consistent with calculations of the radiative recombination in the infrared due to dangling bonds present at nanocrystallite surfaces.[44] Finally, the long-term stability of the infrared band has not been established. If it is related to the presence of dangling bonds, it is reasonable to expect poor stability since the concentration and nature of dangling bonds on the surface can be modified by many factors. Our preliminary results so far support this hypothesis.

**Femtosecond Photoinduced Absorption**

1. Experimental Techniques and Sample Preparation

The femtosecond time-resolved experiments have been

performed with the standard pump/probe arrangement. The pump beam excites electrons and holes across the bandgap, while the probe beam monitors the changes in transmission (and reflection) induced in the sample by photoinjection of carriers by the pump beam. The pump and probe beams are synchronized since they are produced by the same laser pulse. Thus, the time evolution of the changes in transmission (and reflection) is monitored by increasing the beam path of the probe, which produces a time delay between the pump and probe beams. These experiments, which we routinely perform in semiconductors,[45–47] have a time resolution limited by the pulse duration (in the present case, 100 fs). Once the results have been recorded, the changes in optical properties are related to the dynamics of the photoinjected carriers, which may include thermalization, cooling, trapping, and recombination. In cases where nonradiative recombination occurs rapidly across the bandgap,[47,48] it is also possible to record the dynamics of the temperature increase of the sample due to the production of a large number of phonons.

Femtosecond photoinduced measurements were performed using two different laser systems. In the first type of experiments,[49] the laser source was a colliding-pulse, mode-locked dye laser, amplified at 8.5 kHz using a copper vapor laser. The pulses are <100 fs long at 620 nm (2 eV). A portion of these pulses is used to generate a white light continuum from which 100-fs-long pulses tunable from the green to ~900 nm were selected. In the second type of experiments,[50] the laser source was a titanium sapphire laser producing 90-fs-long pulses tunable between 800 and 900 nm (1.55 to 1.38 eV) with a repetition rate of 85 MHz. Pulses at half the wavelength (twice the photon energy) were obtained by frequency doubling in a BBO nonlinear crystal.

To perform the transmission measurements, the samples must first be removed from their silicon substrates, as the substrates would absorb all the light at wavelengths shorter than 1 $\mu$m. In the present work, we used both oxidized mesoporous films[49] and very-high-quality films deposited on sapphire.[50,51] These latter films were produced using a current density of 14 mA/cm$^2$ passing through a circular area of 1.76 cm$^2$ from 25 s to 30 min depending on the desired thickness. The anodization occurred in the dark and the (100) polished c-Si wafers were either moderately or highly doped. To remove the porous silicon film from the substrate, electropolishing was employed in which the silicon atoms were removed layer by layer and the porous silicon film was separated from the wafer (lifted off). The process was converted from porous silicon formation to electropolishing by diluting the HF while increasing the current density to approximately 100 mA/cm$^2$. The freestanding LEPSi films were kept wet in ethanol to protect them from breaking during drying, and layers thinner than ~5 $\mu$m were deposited wet on sapphire windows and allowed to dry in air. Afterward, the LEPSi films remained attached to the windows by van der Waals or electrostatic forces, similar to a technique used to mount ultrathin III–V semiconductor films.[45] We chose sapphire windows because of their optical flatness, high heat conductivity, and high transparency from the IR to the UV. Figure 62.42 summarizes some of the properties of a typical high-quality ultrathin LEPSi film.

2. Experimental Results

Figure 62.43 shows results obtained with the pump at 2 eV (which is well above the PL peak of 1.65 eV) and various probes at photon energies ranging from above to below the PL peak energy.[49] Qualitatively similar results have been obtained on all films, irrespective of whether they were pumped at 2 or 3 eV, in the entire probe wavelength range. These traces have several interesting features:

- At all probe wavelengths, the absorption increases instantly, then recovers in part very promptly to a photoinduced absorption "plateau."
- When the induced absorption is measured on a much longer time scale, this "plateau" corresponds in fact to a slow recovery of the photoinduced absorption.
- The recovery is nonexponential and depends on the photoinjected carrier density: at low injected carrier density, the prompt recovery is extremely fast and the slower recovery takes tens of picoseconds, whereas at high injected carrier density, the prompt recovery slows down and the slower recovery speeds up.

The challenge is to interpret these results.

Our results indicate that porous silicon is not a direct-gap semiconductor. In direct-gap semiconductors, bleaching is observed after femtosecond excitation.[45,46,52] This bleaching results from the partial occupation of the final and initial states by the photoinjected electrons and holes respectively, which decreases the absorption at all probe wavelengths and especially near the pump wavelength immediately after excitation. In the present experiments, we instead observe photoinduced absorption, which occurs either in indirect-gap semiconductors[53,54] or in amorphous semiconductors,[48,55] and is indicative

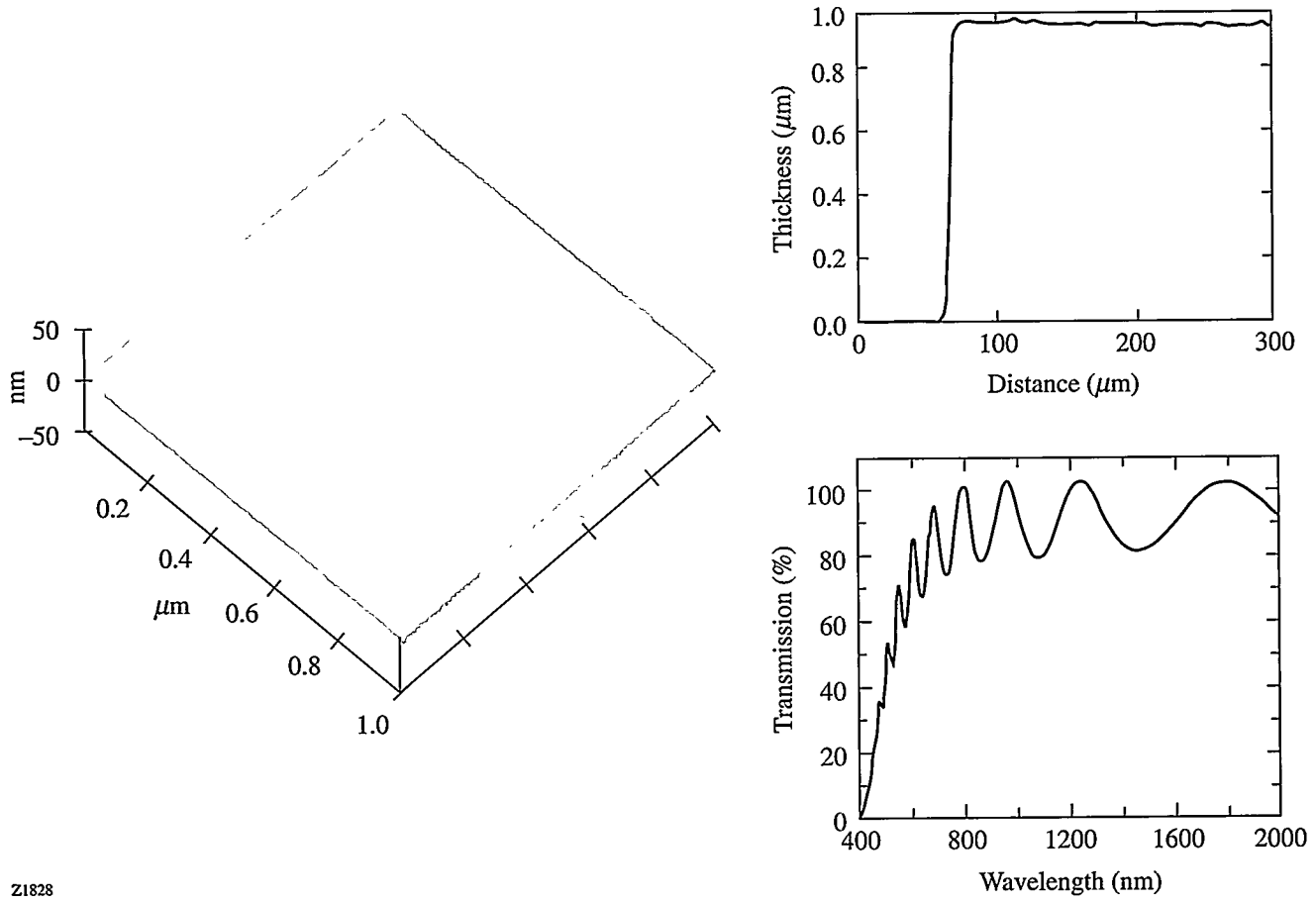


Figure 62.42
Atomic-force-micrograph, thickness measurement, and optical transmission spectrum of a thin, porous film that has been lifted off the c-Si substrate and deposited on a sapphire substrate.

of Drude absorption by free carriers. This observation confirms recent theoretical[56] and experimental[26,27] work, which also suggested that red-emitting porous silicon remains an indirect bandgap semiconductor. Figure 62.44 compares femtosecond time-resolved data obtained under similar conditions with GaAs (a direct-gap semiconductor), a-Si:H (an amorphous semiconductor), c-Si (an indirect-gap semiconductor), and porous silicon. Clearly, porous silicon and c-Si have a very similar response, which in turn is quite distinct from that of GaAs and a-Si:H.

The dynamics of the photoinduced absorption recovery are consistent with the following model. The prompt recovery is due to carrier trapping, presumably at the nanocrystallite surfaces. The fact that trapping occurs on a ~100-fs time scale should not be surprising since a classical electron moving at the thermal velocity will "hit" the surface every 30 fs. However, not all nanocrystals have a "fast" trap, and the ratio of the amplitude of the slower recovery to that of the prompt recovery is a measure of the ratio of the number of nanocrystals without a fast trap to that of nanocrystals with a fast trap. In those nanocrystals that have no fast trap, the photoinjected carriers can only recombine or be trapped in "slow" traps. Assuming that the slower recovery is due to recombination, we can explain the intensity dependence. When the number of electron-hole pairs injected per nanocrystallite is less than 1, recombination is probably radiative and relatively slow; when the number of pairs injected exceeds 1 per nanocrystal, Auger recombination becomes possible. In this process, one electron recombines with one hole, and the excess energy is given to another electron (or hole). This process is relatively efficient at large carrier densities in bulk crystalline silicon and is expected to be very efficient in nanometer-size crystallites, where the overlap between the wave functions of the carriers is strong and the momentum conservation rules that limit the Auger rate in bulk silicon are somewhat relaxed. Furthermore, the

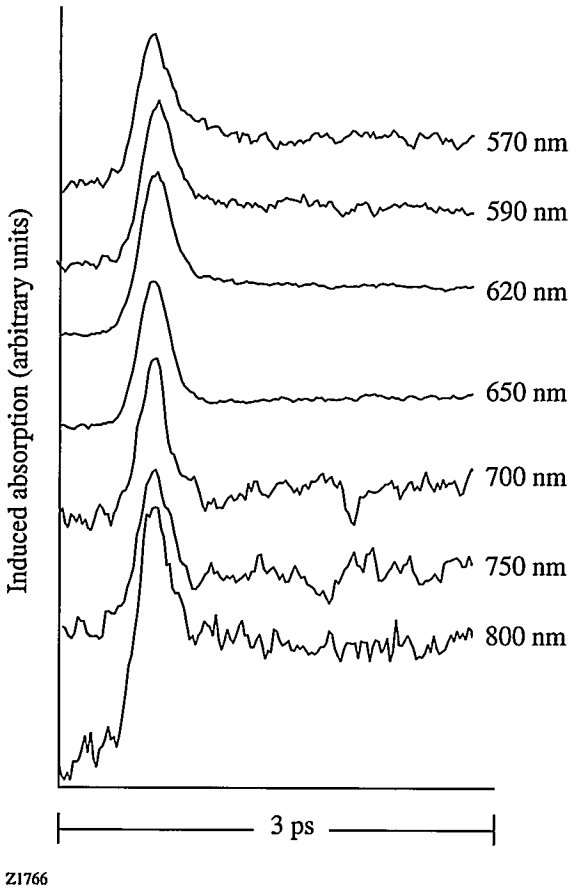


Figure 62.43
Induced absorption measured with a probe pulse at different wavelengths following carrier injection with a 100-fs-long, 2-eV pump pulse in a sample that luminesces near 1.65 eV. The traces are similar at all wavelengths.

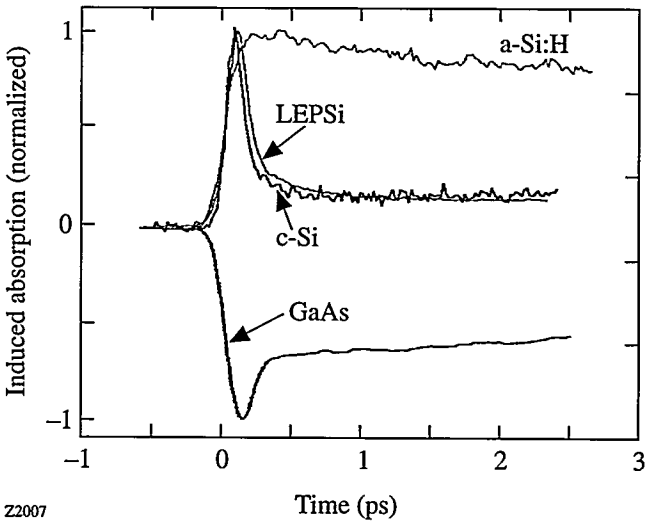


Figure 62.44
Room-temperature photoinduced absorption measurements performed in the pump-probe geometry at 2 eV in GaAs, crystalline silicon (c-Si), porous silicon (LEPSi), and amorphous hydrogenated silicon (a-Si:H).

relative amplitude of the prompt recovery is expected to decrease since in nanocrystallites with one trap the second photoinjected pair can no longer undergo fast trapping.

We thus attribute the initial recovery to trapping of the photoexcited carriers from extended states into surface states. The intensity dependence of the fast recovery is consistent with trap saturation. These traps are most likely not responsible for the luminescence because trapping tends to become more efficient when the luminescence efficiency decreases after exposure to high-intensity UV light. However, the changes in the ultrafast optical response remain small even after the luminescence efficiency drops by at least one order of magnitude.

### Electroluminescent Devices

Electroluminescence (EL) was observed in LEPSi shortly after the discovery of its strong photoluminescence.[57–61] It was first detected during anodic oxidation in the electrochemical cell.[61] This EL and electrolyte electroluminescence were shown to have a spectrum similar to the PL spectrum, with an efficiency larger than 0.1%. Bsiesy *et al.*[62] reported on tuning the electrolyte EL throughout the broad PL spectrum by simply changing the applied voltage from 0.8 V to 1.5 V.[62] Cathodoluminescence has also been reported.[63,64] In this section, we focus on *solid-state* electroluminescent devices. In these light-emitting devices (LED's), electrons and/or holes are injected into the porous layer where radiative recombination occurs.

The first LED made of porous silicon was demonstrated in 1991.[57] It consisted of a metal/porous silicon/crystalline silicon structure similar to a Schottky barrier or more accurately to a metal/insulator/semiconductor (MIS) structure. Although the device did electroluminesce, its efficiency measured at room temperature was of the order of $10^{-4}$% to $10^{-5}$%. The threshold voltage for observable EL was at first very high (>> 10 V) but has since been reduced to less than 5 V. In our recent work, we have been able to detect EL for applied voltages below 1 eV in more complicated structures.[65] Such LEPSi MIS devices are very easy to fabricate since after fabrication of the porous layer, the only additional step is the evaporation of a thin metal film. Variations on this device structure have since been published by many groups. The PL and EL spectra are usually similar to each other, although in some cases not identical[66,67] for reasons that are not clear. The efficiency of these devices has remained low, although efficiencies in the range of $10^{-2}$% and even higher have been

quoted.[68,69] Some of the most obvious reasons for the poor efficiency are (1) the mechanism of carrier injection is not clear and possibly inefficient; (2) the semitransparent metal contacts absorb part of the luminescence; and (3) it is extremely difficult to make a good contact over the large microscopic surface area of porous silicon using line-of-sight deposition techniques. In other LED's indium tin oxide (ITO) is used as the top electrode[58] instead of a metal. This approach has several advantages, including potentially better contacts and less light absorption by the ITO. We have found in our devices that the efficiency of LED's using ITO is consistently higher than that of LED's using metals such as Au or Ag. Contacts made of conducting polymers have also been demonstrated[70] but the efficiency remained low.

The best published efficiency for porous silicon LED's was achieved using a somewhat more complicated device structure.[69] Figure 62.45 shows the proposed band structure and the current-voltage (I-V) relationship for a similar device.[66,71] The porous silicon $p$-$n$ junction LED's were fabricated in $p$-type substrates with a resistivity of 5 to 10 Ω cm. A high-dose phosphorus implant was followed by a period of thermal annealing to yield junction depths ≤1 μm. Because holes are required in the anodization process, light assistance is essential to create $n$-type LEPSi. The LEPSi layers were thus formed by electrochemical etching in a 1:1:2 solution of HF, $H_2O$, and ethanol, using a constant current density of 15 mA/cm$^2$ for 5 to 30 min. This anodization process produces LEPSi at a rate of approximately 1 μm/min. To improve the homogeneity of the LEPSi layer, the backside of the wafers was heavily doped with boron, and a sintered Al film was used to create an intimate backside ohmic contact. Following LEPSi layer formation, a semitransparent, 100-Å gold film was deposited to form patterned 0.2-cm$^2$ contacts. Using similar structures, electroluminescence has been achieved from the near infrared to the blue with nearly constant efficiencies (e.g., 0.005% in the blue using indium contacts[72]).

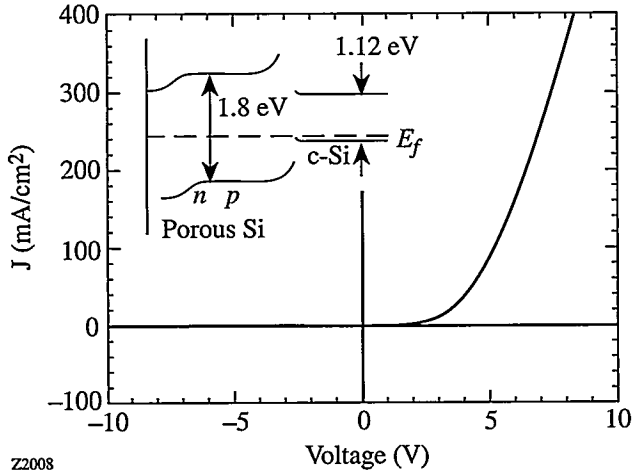


Figure 62.45
Current-voltage relationship of a light-emitting porous silicon $p$-$n$ junction LED. The inset shows the proposed band diagram.

The band diagram proposed in Fig. 62.45 is based on an analysis of the I-V curve, its temperature dependence, and the C-V data.[71] The Fermi level for $n$- and $p$-type LEPSi is taken to be ~0.2 eV above and below the midgap respectively. Thus, a small amount of band-bending is created within the LEPSi layer. The presence of a $p$-$n$ junction in the LEPSi layer affects carrier transport, resulting in a rectifying I-V relationship that is nearly exponential in forward bias [i.e., $I = I_0\left(e^{eV/nkT} - 1\right)$]. The extracted ideality factor $n$ was found to be 2.1 at applied forward bias voltages of less than 0.5 V and at room temperature. At higher voltages there is a large deviation from this behavior.[71]

Frequency modulation measurements were performed on LEPSi LED's.[66] In this experiment, a peak-to-peak ac signal of 10 V was applied to the device under a forward dc bias of 30 V. The modulated EL signal, detected and amplified with a lock-in amplifier, is shown in Fig. 62.46. The output power of an LED is related to the modulation frequency $\omega$ by

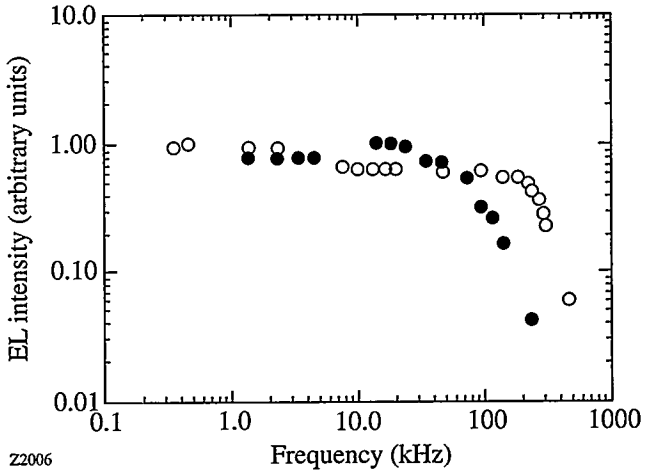


Figure 62.46
Frequency modulation response of the electroluminescence of porous silicon $p$-$n$ junction LED's with (○) 0.2-μm junction depth and 5-μm LEPSi layer; (●) 1-μm junction depth and 10-μm LEPSi layer. The 3-dB bandwidth can exceed 100 kHz.

$$\frac{P(\omega)}{P(0)} = \left[\frac{1}{1+(\omega/\omega_0)^2}\right]^{1/2}, \qquad (2)$$

where $P(0)$ is the dc power, $P(\omega)$ is the power at frequency $\omega$, and $\omega_0$ is the cutoff frequency. Table 62.V shows the relationship between the cutoff frequency of different device structures and the corresponding PL lifetime $\tau_{PL}$. The fact that $2\pi/\omega_0$ is comparable to $\tau_{PL}$ suggests that the EL response is controlled by the carrier lifetime; thus, it appears that the maximum speed of the red *p-n* junction LEPSi LED's is ~1 MHz.

Table 62.V: Comparison of the EL time constant and the PL lifetime

| Sample Description | $2\pi/\omega_0$ ($\mu$s) | $\tau_{PL}$ ($\mu$s) |
|---|---|---|
| Au/LEPSi, 30-min etching | 30 | 13 |
| *p-n*, 1 $\mu$m, 10-min etching | 15 | 17 |
| *p-n*, 0.2 $\mu$m, 5-min etching | 0.86 | 0.7 |

When we prepare LEPSi MIS structures, not only is the efficiency lower but the I-V curve indicates that the transport mechanism is different and the maximum modulation speed is lower. Figure 62.47 shows that the current-voltage curve in forward bias follows a power law $I \sim V^n$, with $n > 2$ in devices where EL is detected.[67,73] Such a behavior is typical of a space-charge-limited current.[74] If the LEPSi layer can be modeled as a perfect insulator, then

$$J = \varepsilon\, \varepsilon_0\, \mu V^2/d^3,$$

where $\varepsilon$ is the dielectric function of LEPSi, $\varepsilon_0 = 8.854\ 10^{-12}$ F/m, $\mu$ is the drift mobility in LEPSi, and $d$ is the thickness of the LEPSi layer. If deep traps or interface traps are present, the current may increase faster than $V^2$, and if the mobility is electric field dependent, the current is no longer proportional to $V^2$. When frequency-dependent EL measurements are performed, we find as expected that the drift time across the LEPSi layer limits the device speed to at most 10 KHz.[71] Using these results, we have deduced a drift mobility of ~$10^{-5}$ cm$^2$/V-s in LEPSi layers prepared from 5- to 10-Ω-cm *p*-type substrates under light assistance.[71] Finally, we note that when the LEPSi layers were prepared so that the surface passivation involved Si-O bonds and no Si-H bonds, the LED's did not degrade even after 100 h of continuous operation.[67,73]

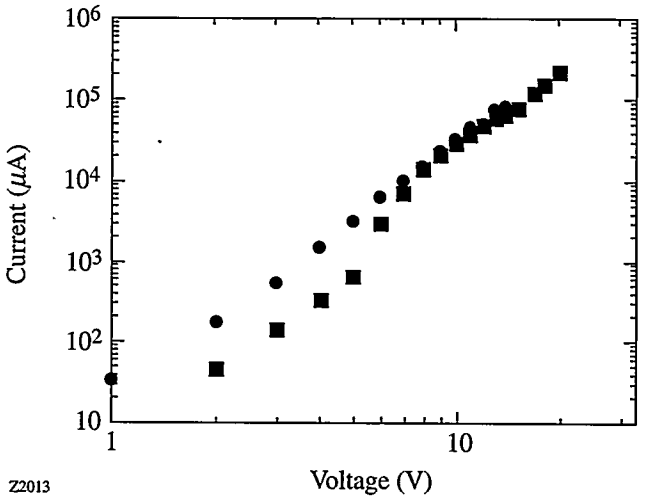


Figure 62.47
Current-voltage relationship of two metal/porous-silicon/crystalline-silicon light-emitting devices.

## Prospects for Commercial Devices

Light-emitting porous silicon has given a new impetus to silicon-based optoelectronics. Since the first report of efficient photoluminescence in the red/orange part of spectrum, much progress has been achieved. Efficient luminescence has been observed from the blue/near UV to past 1.5 $\mu$m, as shown in Fig. 62.48. The quantum efficiency of LEPSi LED's has improved by at least four orders of magnitude since the first solid-state EL device was demonstrated. Nevertheless, much remains to be done before commercial applications of these materials becomes a reality.[75] Research should focus on improving either the efficiency or the speed of LED's. Better efficiencies are required for optical display applications. In addition, to be cost competitive, displays must be made using silicon thin films, and not bulk wafers. Optical interconnect applications, in contrast, do not require extremely high efficiencies but do require data-transfer rates in excess of 1 Mbit/s. Thus, for interconnects, the best hope seems to be the blue luminescence. In this section, we briefly discuss four points of relevance for technological applications. These are (1) ion implantation and oxidation of LEPSi; (2) uniformity of LEPSi; (3) mechanical stability of LEPSi; and (4) manufacture of micron-size LEPSi structures.

The major advantage of LEPSi LED's is that they could be made on the same chip as Si electronic devices or integrated circuits, which raises the important issue of their compatibility with various microelectronic processing steps. We have performed several studies[76–80] that have yielded encouraging results. Ion implantation, a technique that is widely used in

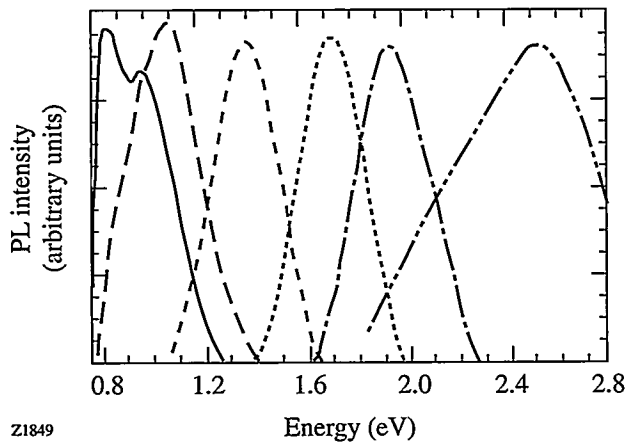


Figure 62.48
Normalized room-temperature photoluminescence spectra of various porous silicon samples, as prepared ("red" region), after oxidation ("blue" region), and after vacuum annealing ("infrared" region). The cutoff near 1.5 $\mu$m is due to the Ge photodetector.

semiconductor technology, consists of bombarding the wafer with donor or acceptor ions to produce the desired doping profile. We have demonstrated[76,77] that LEPSi can retain its strong photoluminescence after ion implantation with phosphorus and boron, provided that the dose does not exceed ~$10^{14}$ $cm^{-2}$. Another important processing step is oxidation. As was discussed previously, oxidation at elevated temperatures ($T_{ox} \geq 1000°C$) produces LEPSi that emits in the blue. If the oxidation is performed at very low temperatures ($T_{ox} \leq 600°C$), the red luminescence disappears.[22,81] At these temperatures, all the hydrogen that passivated the surface of the as-grown LEPSi has been desorbed, and the oxide that is formed is of extremely poor quality. The surface is thus covered by dangling bonds,[82] which act preferentially as nonradiative recombination centers. However, as $T_{ox}$ is raised from 600°C to ~1000°C, the quality of the thermal oxide improves, the density of dangling bonds decreases, and the PL intensity recovers. Near 1000°C, the PL intensity of high-efficiency LEPSi samples recovers to within a factor of 3 of the initial intensity. The peak PL wavelength is also blue shifted after oxidation above 600°C, in agreement with the expected decrease of the silicon crystallite size after oxidation of several silicon monolayers.[22]

For device applications, it is highly desirable that the porous layers have good cross-sectional and lateral uniformity. Previously published[83,84] studies of depth uniformity lead us to conclude that most samples are not uniform as a function of depth, with the possible exception of thin LEPSi layers prepared in the dark using $p$-type substrates. Spatially resolved photoluminescence and Raman measurements have shown that the first few microns usually possess a different nanostructure from that of the deeper layers. As a result, both the PL spectrum and its intensity change as a function of depth. However, we have shown[50,51] that manufacturing of LEPSi layers thicker than 10 $\mu$m with homogeneous cross-sectional PL properties is possible under specific conditions. More work must be done in this area to identify the conditions that lead to uniform LEPSi layers with good luminescence efficiency. Another issue is lateral uniformity, where we distinguish three length scales. Uniformity over large areas (>>1 $cm^2$) can be maintained if the electrochemical cell is designed carefully. On a scale of 1 to 100 $\mu$m, however, uniformity is more difficult to maintain. High-porosity layers tend to crack when they are removed from the solution and dried, which leads to a surface with a morphology reminiscent of a dry lake bed.[83] Spatially resolved photoluminescence (SRPL) maps of such surfaces taken with 1-$\mu$m spatial resolution show large differences in the local PL intensity, with regions that appear dark (no PL) and bright (visible PL). Even layers that show no evidence of cracking are often not homogeneous on a micron scale. Using SRPL maps, we have shown[83] that the surface of apparently uniform samples is in fact made of a very large number of small (~1-$\mu$m) regions that emit very bright PL and are separated by ≥1 $\mu$m. With the knowledge that longer anodization times generally produce less homogeneous surfaces, we have been able to produce LEPSi layers that appear homogeneous on a 1-$\mu$m scale by properly choosing the anodization parameters.[83] Perfect uniformity on a scale of 10 to 100 nm is almost impossible to achieve since the crystallite sizes are in the nanometer range, although the results of Fig. 62.42 show that, at least under specific conditions, the surface can be of optical quality.

As mentioned previously, high-porosity samples have a tendency to crack when dried. In addition, all LEPSi samples, with the exception of those that have been oxidized at elevated temperatures, have poor mechanical properties. A method that improves the mechanical properties and allows the production of high-porosity (≥95%) films without cracking and degradation of the crystallinity has been demonstrated.[85] In this technique, the as-prepared layers are supercritically dried in $CO_2$ for a period of several hours. This "gentle" drying, which maintains the structural integrity of highly porous materials, has been previously used in sol-gel technology. Supercritical drying of porous silicon appears promising. Further work will help determine whether it is a necessary step for the development of LEPSi LED's.

Finally, if LEPSi LED's are to be integrated with silicon microelectronic circuits for optical interconnects or other applications, at least two developments are necessary:

- the size of the LED's must decrease from ~1 $mm^2$ to a few $\mu m^2$; and
- the regions of the wafer where porous silicon is not produced should be protected during anodization.

Very few studies have addressed these important issues.[78,80,86] We have developed several processes that allow us to make LEPSi lines narrower than 0.5 $\mu$m and to protect the adjacent silicon material (see Fig. 62.49). Although we have yet to demonstrate a practical device employing this feature, the ability to produce such ultranarrow lines suggests that integration of miniature porous silicon LED's with conventional VLSI is indeed possible.

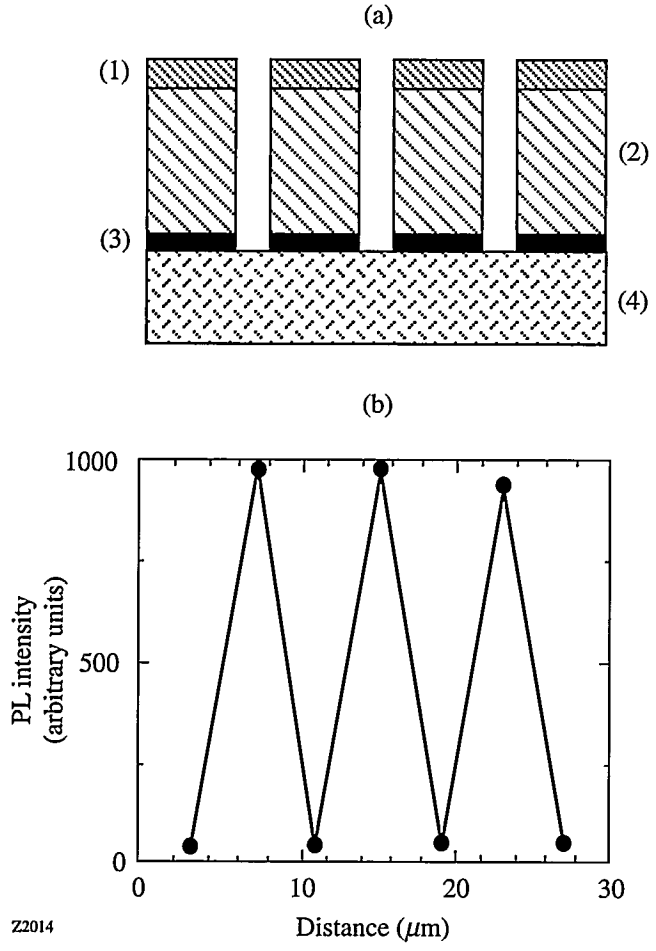


Figure 62.49
(a) Pre-anodization schematic of the mask structure. Layer (4) c-Si substrate, (3) 100-nm-thick $Si_3N_4$, (2) 5-$\mu$m-thick crosslinked photoresist, and (1) 1-$\mu$m-thick capping resist. (b) PL map after anodization.

## Conclusions

Porous silicon, a promising new material for silicon optoelectronics, has been demonstrated to photoluminesce at room temperature with an efficiency between 0.1% and 10%. Its luminescence spectrum, intensity, and lifetime are highly sensitive to the growth and processing parameters. Light-emitting devices (LED's) made of porous silicon have already been demonstrated throughout the visible range. Since the peak of the photoluminescence spectrum of porous silicon can be changed from the blue/violet to wavelengths past 1.5 $\mu$m, it is conceivable that LED's will be made over the same range of wavelengths. Despite some impressive progress, much work still remains to be done before commercial LED's can be envisioned, even in the visible range. Nevertheless, because of its compatibility with silicon microelectronics, porous silicon is a material worthy of further scientific and technological investigations.

## ACKNOWLEDGMENTS

This work was supported by grants from Rochester Gas & Electric and the New York State Energy Research & Development Authority, with additional support from the National Science Foundation Center for Photo-Induced Charge Transfer, Xerox, and Link fellowships.

## REFERENCES

1. S. S. Iyer and Y.-H. Xie, Science **260**, 40 (1993).
2. J. C. Sturm *et al.*, in *Silicon-Based Optoelectronic Materials*, edited by M. A. Tischler *et al.*, Materials Research Society Symposium Proceedings, Vol. 298 (Materials Research Society, Pittsburgh, PA, 1993), pp. 69–78.
3. P. L. Bradfield, T. G. Brown, and D. G. Hall, Appl. Phys. Lett. **55**, 100 (1989).
4. F. Y. G. Ren *et al.*, in *Silicon-Based Optoelectronic Materials*, edited by M. A. Tischler *et al.*, Materials Research Society Symposium Proceedings, Vol. 298 (Materials Research Society, Pittsburgh, PA, 1993), pp. 415–423.
5. A. Uhlir, Jr., Bell Syst. Tech. J. **35**, 333 (1956).
6. G. Bomchil, A. Halimasui, and R. Herino, Microelectron. Eng. **8**, 293 (1988).
7. C. Pickering *et al.*, J. Phys. C: Solid State Phys. **17**, 6535 (1984).
8. L. T. Canham, Appl. Phys. Lett. **57**, 1046 (1990).
9. V. Lehmann and U. Gosele, Appl. Phys. Lett. **58**, 856 (1991).
10. R. L. Smith and S. D. Collins, J. Appl. Phys. **71**, R1 (1992).
11. H. Koyama and N. Koshida, J. Appl. Phys. **74**, 6365 (1993).

12. *Light Emission from Silicon*, edited by S. S. Iyer, R. T. Collins, and L. T. Canham, Materials Research Society Symposium Proceedings, Vol. 256 (Materials Research Society, Pittsburgh, PA, 1992).

13. *Microcrystalline Semiconductors: Materials Science & Devices*, edited by P. M. Fauchet *et al.*, Materials Research Society Symposium Proceedings, Vol. 283 (Materials Research Society, Pittsburgh, PA, 1993).

14. *Silicon-Based Optoelectronic Materials*, edited by M. A. Tischler *et al.*, Materials Research Society Symposium Proceedings, Vol. 298 (Materials Research Society, Pittsburgh, PA, 1993).

15. *Optical Properties of Low Dimensional Silicon Structures*, edited by D. C. Bensahel, L. T. Canham, and S. Ossicini, NATO ASI Series E, Applied Sciences, Vol. 244 (Kluwer Academic Publishers, Dordrecht, 1993).

16. *Light Emission from Silicon*, edited by J.-C. Vial, L. T. Canham, and W. Lang, (North-Holland, Amsterdam, 1994).

17. A. G. Cullis and L. T. Canham, Nature **353**, 335 (1991).

18. J. C. Vial *et al.*, in *Microcrystalline Semiconductors: Materials Science & Devices*, edited by P. M. Fauchet *et al.*, Materials Research Society Symposium Proceedings, Vol. 283 (Materials Research Society, Pittsburgh, PA, 1993), pp. 241–246.

19. Y. Kanemitsu, Phys. Rev. B **48**, 12357 (1993).

20. P. M. Fauchet, C. Peng, L. Tsybeskov, J. Vandyshev, A. Dubois, A Raisanen, T. E. Orlowski, L. J. Brillson, J. E. Fouquet, S. L. Dexheimer, J. M. Rehm, G. L. McLendon, E. Ettedgui, Y. Gao, F. Seiferth, and S. K. Kurinec, in *Semiconductor Silicon/94: Proceedings of the 7th International Symposium on Silicon Materials Science and Technology*, edited by H. R. Huff, W. Bergholz, and K. Sumino (The Electrochemical Society, Pennington, 1994), pp. 499–510.

21. L. Tsybeskov, C. Peng, S. P. Duttagupta, E. Ettedgui, Y. Gao, P. M. Fauchet, and G. E. Carver, in *Silicon-Based Optoelectronic Materials*, edited by M. A. Tischler *et al.*, Materials Research Society Symposium Proceedings, Vol. 298 (Materials Research Society, Pittsburgh, PA, 1993), pp. 307–311.

22. C. Peng, L. Tsybeskov, and P. M. Fauchet, in *Microcrystalline Semiconductors: Materials Science & Devices*, edited by P. M. Fauchet *et al.*, Materials Research Society Symposium Proceedings, Vol. 283 (Materials Research Society, Pittsburgh, PA, 1993), pp. 121–126.

23. L. Tsybeskov and P. M. Fauchet, Appl. Phys. Lett. **64**, 1983 (1994).

24. F. Koch *et al.*, in *Microcrystalline Semiconductors: Materials Science & Devices*, edited by P. M. Fauchet *et al.*, Materials Research Society Symposium Proceedings, Vol. 283 (Materials Research Society, Pittsburgh, PA, 1993), pp. 197–202; F. Koch, in *Silicon-Based Optoelectronic Materials*, edited by M. A. Tischler *et al.*, Materials Research Society Symposium Proceedings, Vol. 298 (Materials Research Society, Pittsburgh, PA, 1993), pp. 319–329.

25. *Microcrystalline and Nanocrystalline Semiconductors*, edited by R. W. Collins *et al.*, Materials Research Society Symposium Proceedings, Vol. 358 (Materials Research Society, Pittsburgh, PA, 1995).

26. P. D. J. Calcott *et al.*, J. Lumin. **57**, 257 (1993).

27. P. D. J. Calcott *et al.*, in *Microcrystalline and Nanocrystalline Semiconductors*, edited by R. W. Collins *et al.*, Materials Research Society Symposium Proceedings, Vol. 358 (Materials Research Society, Pittsburgh, PA, 1995), pp. 465–476.

28. T. van Buuren *et al.*, in *Microcrystalline and Nanocrystalline Semiconductors*, edited by R. W. Collins *et al.*, Materials Research Society Symposium Proceedings, Vol. 358 (Materials Research Society, Pittsburgh, PA, 1995), pp. 441–446.

29. S. Schuppler *et al.*, Phys. Rev. Lett. **72**, 2648 (1994).

30. M. B. Robinson *et al.*, Appl. Phys. Lett. **61**, 1414 (1992).

31. R. T. Collins, M. A. Tischler, and J. H. Stathis, Appl. Phys. Lett. **61**, 1649 (1992).

32. V. Petrova-Koch *et al.*, in *Microcrystalline Semiconductors: Materials Science & Devices*, edited by P. M. Fauchet *et al.*, Materials Research Society Symposium Proceedings, Vol. 283 (Materials Research Society, Pittsburgh, PA, 1993), pp. 179–184.

33. Y. Kanemitsu *et al.*, in *Silicon-Based Optoelectronic Materials*, edited by M. A. Tischler *et al.*, Materials Research Society Symposium Proceedings, Vol. 298 (Materials Research Society, Pittsburgh, PA, 1993), pp. 205–210.

34. L. Tsybeskov, J. V. Vandyshev, and P. M. Fauchet, Phys. Rev. B **49**, 7821 (1994).

35. J. H. Stathis and M. A. Kastner, Phys. Rev. B **35**, 2972 (1987).

36. A. Anedda *et al.*, J. Appl. Phys. **74**, 6993 (1993).

37. J. M. Rehm, G. L. McLendon, L. Tsybeskov, and P. M. Fauchet, to appear in Applied Physics Letters.

38. H. Tamura *et al.*, Appl. Phys. Lett. **65**, 1537 (1994).

39. R. E. Hummel, P. M. Fauchet, M. H. Ludwig, Ju. V. Vandyshev, S.-S. Chang, and L. Tsybeskov, to appear in Solid State Communications.

40. C. H. Perry *et al.*, in *Light Emission from Silicon*, edited by S. S. Iyer, R. T. Collins, and L. T. Canham, Materials Research Society Symposium Proceedings, Vol. 256 (Materials Research Society, Pittsburgh, PA, 1992), pp. 153–158.

41. P. M. Fauchet, E. Ettedgui, A. Raisanen, L. J. Brillson, F. Seiferth, S. K. Kurinec, Y. Gao, C. Peng, and L. Tsybeskov, in *Silicon-Based Optoelectronic Materials*, edited by M. A. Tischler *et al.*, Materials Research Society Symposium Proceedings, Vol. 298 (Materials Research Society, Pittsburgh, PA, 1993), pp. 271–276.

42. G. Mauckner *et al.*, in *Microcrystalline and Nanocrystalline Semiconductors*, edited by R. W. Collins *et al.*, Materials Research Society Symposium Proceedings, Vol. 358 (Materials Research Society, Pittsburgh, PA, 1995), pp. 489–494.

43. P. M. Fauchet, C. Peng, L. Tsybeskov, Ju. V. Vandyshev, A. Dubois, L. McLoud, S. P. Duttagupta, J. M. Rehm, G. L. McLendon, E. Ettedgui, Y. Gao, F. Seiferth, S. K. Kurinec, A. Raisanen, T. E. Orlowski, L. J. Brillson, and G. E. Carver, in *Advanced Photonics Materials for Information Technology*, edited by S. Etemad (SPIE, Bellingham, WA, 1994), Vol. 2144, pp. 34–50.

44. M. Lannoo, presented at the International School on Luminescence of Porous Silicon and Silicon Nanostructures, Les Houches, France, February 1994; M. Lannoo, C. Delerue, and G. Allan, J. Lumin. **57**, 243 (1993).

45. T. Gong, W. L. Nighan, Jr., and P. M. Fauchet, Appl. Phys. Lett. **57**, 2713 (1990).

46. J. F. Young, T. Gong, P. M. Fauchet, and P. J. Kelly, Phys. Rev. B **50**, 2208 (1994).

47. P. M. Fauchet, A. Antonetti, D. Hulin, J. Kolodzey, A. Migus, and S. Wagner, Phys. Rev. Lett. **57**, 2438 (1986).

48. P. M. Fauchet, D. Hulin, R. Vanderhaghen, A. Mourchid, and W. L. Nighan, Jr., J. Non-Cryst. Solids **141**, 76 (1992).

49. P. M. Fauchet, Y. Kostoulas, Ju. V. Vandyshev, and V. Petrova-Koch, in *Ultrafast Phenomena IX*, edited by P. F. Barbara *et al.* (Springer-Verlag, Berlin, 1994), p. 283.

50. J. von Behren, K. B. Ucer, L. Tsybeskov, Ju. V. Vandyshev, and P. M. Fauchet, to appear in the Journal of Vacuum Science and Technology (1995).

51. J. von Behren, L. Tsybeskov, and P. M. Fauchet, Appl. Phys. Lett. **66**, 1662 (1995).

52. J. L. Oudar *et al.*, Phys. Rev. Lett. **55**, 2074 (1985).

53. M. C. Downer and C. V. Shank, Phys. Rev. Lett. **56**, 761 (1986).

54. P. M. Fauchet and W. L. Nighan, Jr., Appl. Phys. Lett. **48**, 721 (1986).

55. A. Mourchid, D. Hulin, R. Vanderhaghen, W. L. Nighan, Jr., K. Gzara, and P. M. Fauchet, Solid State Commun. **74**, 1197 (1990).

56. M. S. Hybertsen, Phys. Rev. Lett. **72**, 1514 (1994).

57. A. Richter *et al.*, IEEE Electron Device Lett. **12**, 691 (1991).

58. N. M. Kalkhoran, F. Namavar, and H. P. Maruska, in *Light Emission from Silicon*, edited by S. S. Iyer, R. T. Collins, and L. T. Canham, Materials Research Society Symposium Proceedings, Vol. 256 (Materials Research Society, Pittsburgh, PA, 1992), pp. 89–94.

59. E. Bassous *et al.*, in *Light Emission from Silicon*, edited by S. S. Iyer, R. T. Collins, and L. T. Canham, Materials Research Society Symposium Proceedings, Vol. 256 (Materials Research Society, Pittsburgh, PA, 1992), pp. 23–26.

60. N. Koshida and H. Koyama, in *Light Emission from Silicon*, edited by S. S. Iyer, R. T. Collins, and L. T. Canham, Materials Research Society Symposium Proceedings, Vol. 256 (Materials Research Society, Pittsburgh, PA, 1992), pp. 219–222.

61. A. Halimaoui *et al.*, Appl. Phys. Lett. **59**, 304 (1991).

62. A. Bsiesy *et al.*, Phys. Rev. Lett. **71**, 637 (1993).

63. A. G. Cullis *et al.*, in *Microcrystalline Semiconductors: Materials Science & Devices*, edited by P. M. Fauchet *et al.*, Materials Research Society Symposium Proceedings, Vol. 283 (Materials Research Society, Pittsburgh, PA, 1993), pp. 257–262.

64. S. M. Pillai *et al.*, Jpn. J. Appl. 2, Lett. **31**, L1702 (1992).

65. L. Tsybeskov *et al.*, unpublished data.

66. C. Peng, P. M. Fauchet, K. D. Hirschman, and S. K. Kurinec, in *Microcrystalline and Nanocrystalline Semiconductors*, edited by R. W. Collins *et al.*, Materials Research Society Symposium Proceedings, Vol. 358 (Materials Research Society, Pittsburgh, PA, 1995), pp. 689–694.

67. L. Tsybeskov, S. P. Duttagupta, and P. M. Fauchet, to appear in Solid State Communications.

68. N. Koshida, presented at the International School on Luminescence of Porous Silicon and Silicon Nanostructures, Les Houches, France, February 1994.

69. P. Steiner *et al.*, in *Microcrystalline Semiconductors: Materials Science & Devices*, edited by P. M. Fauchet *et al.*, Materials Research Society Symposium Proceedings, Vol. 283 (Materials Research Society, Pittsburgh, PA, 1993), pp. 343–351; W. Lang, P. Steiner, and F. Kozlowski, J. Lumin. **57**, 341 (1993).

70. N. Koshida *et al.*, Appl. Phys. Lett. **63**, 2655 (1993).

71. C. Peng *et al.*, submitted for publication to Applied Physics Letters.

72. W. Lang, presented at the International School on Luminescence of Porous Silicon and Silicon Nanostructures, Les Houches, France, February 1994.

73. L. Tsybeskov, S. P. Duttagupta, and P. M. Fauchet, in *Microcrystalline and Nanocrystalline Semiconductors*, edited by R. W. Collins *et al.*, Materials Research Society Symposium Proceedings, Vol. 358 (Materials Research Society, Pittsburgh, PA, 1995), pp. 683–688.

74. M. A. Lampert and P. Mark, *Current Injection in Solids* (Academic Press, New York, 1970), p. 351.

75. P. M. Fauchet, in *Porous Silicon*, edited by Z. C. Feng and R. Tsu (World Scientific, Singapore, 1994), pp. 429–465.

76. C. Peng, P. M. Fauchet, J. M. Rehm, G. L. McLendon, F. Seiferth, and S. K. Kurinec, Appl. Phys. Lett. **64**, 1259 (1994).

77. C. Peng, L. Tsybeskov, P. M. Fauchet, F. Seiferth, S. K. Kurinec, J. M. Rehm, and G. L. McLendon, in *Silicon-Based Optoelectronic Materials*, edited by M. A. Tischler *et al.*, Materials Research Society Symposium Proceedings, Vol. 298 (Materials Research Society, Pittsburgh, PA, 1993), pp. 179–184.

78. S. P. Duttagupta, C. Peng, P. M. Fauchet, S. K. Kurinec, and T. N. Blanton, to appear in the Journal of Vacuum Science and Technology (1995).

79. S. P. Duttagupta, L. Tsybeskov, P. M. Fauchet, E. Ettedgui, and Y. Gao, in *Microcrystalline and Nanocrystalline Semiconductors*, edited by R. W. Collins *et al.*, Materials Research Society Symposium Proceedings, Vol. 358 (Materials Research Society, Pittsburgh, PA, 1995), pp. 381–386.

80. S. P. Duttagupta, P. M. Fauchet, C. Peng, S. K. Kurinec, K. Hirschman, and T. N. Blanton, in *Microcrystalline and Nanocrystalline Semiconductors*, edited by R. W. Collins *et al.*, Materials Research Society

Symposium Proceedings, Vol. 358 (Materials Research Society, Pittsburgh, PA, 1995), pp. 647–652.

81. V. Petrova-Koch *et al.*, Appl. Phys. Lett. **61**, 943 (1992).

82. H. Linke *et al.*, in *Microcrystalline Semiconductors: Materials Science & Devices*, edited by P. M. Fauchet *et al.*, Materials Research Society Symposium Proceedings, Vol. 283 (Materials Research Society, Pittsburgh, PA, 1993), pp. 251–256.

83. E. Ettedgui, C. Peng, L. Tsybeskov, Y. Gao, P. M. Fauchet, G. E. Carver, and H. A. Mizes, in *Microcrystalline Semiconductors: Materials Science & Devices*, edited by P. M. Fauchet *et al.*, Materials Research Society Symposium Proceedings, Vol. 283 (Materials Research Society, Pittsburgh, PA, 1993), pp. 173–178.

84. F. Kozlowski and W. Lang, J. Appl. Phys. **72**, 5401 (1992).

85. L. T. Canham *et al.*, Nature **368**, 133 (1994).

86. N. M. Kalkhoran, in *Microcrystalline Semiconductors: Materials Science & Devices*, edited by P. M. Fauchet *et al.*, Materials Research Society Symposium Proceedings, Vol. 283 (Materials Research Society, Pittsburgh, PA, 1993), pp. 365–370.

# Time-Dependent Reflection and Surface Temperatures during $CO_2$ Laser Irradiation of Dental Hard Tissues with 100-$\mu$s Pulses

Lasers, including $CO_2$ lasers operating around $\lambda \approx 10\ \mu m$, are being used frequently in dental soft tissue surgery and some dental hard tissue applications. In addition, pulsed $CO_2$ laser irradiation has been applied successfully for *in vitro* caries (dental decay) prevention or retardation.[1] For this application the laser is used for very localized surface heat treatment with or without inducing visible changes in the surface morphology.

For all laser applications to dental hard tissue the temperature increase in the pulpal region must be kept below ~4°C lest the pulp be damaged. If thermally induced modifications at or near the (enamel) surface are desirable while avoiding excessive subsurface thermal assault, it is advantageous to use a laser wavelength whose absorption length is very small, i.e., whose absorption coefficient is very large. For $CO_2$ laser radiation around 10 $\mu$m the absorption coefficients are very large[2] (see Fig. 62.50), ranging from ~5,000 $cm^{-1}$ at 10.6 $\mu$m to 31,000 $cm^{-1}$ at 9.6 $\mu$m, with corresponding absorption depths between 2 and 0.3 $\mu$m. These high absorption coefficients are due to intrinsic molecular vibrations of the phosphate ions (P–O stretching modes) of the mineral constituent (carbonated hydroxyapatite) of the dental hard tissue. Past research has found this region of the spectrum to be of particular interest for caries retardation.[1]

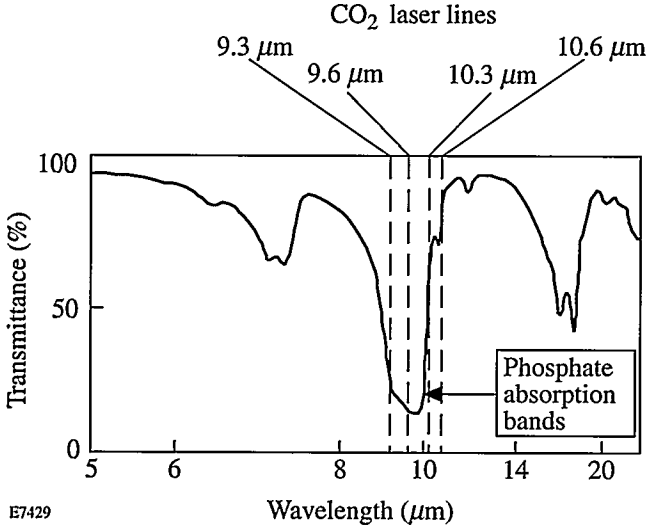


Figure 62.50
Absorption spectrum of dental enamel around the four major $CO_2$ laser lines. The absorption band in this region is due to vibrational bands in the phosphate bonds.

Pulses of appropriately short duration, in addition to short absorption lengths, are essential to avoid excessive subsurface heating. To avoid excessive heating at depths $\Delta x > 10\ \mu m$, one must choose pulse durations of the order of, or less than, the relaxation time ($\tau \approx \Delta x^2/4\kappa \approx 60\ \mu s$, $\kappa \approx 4 \times 10^{-3}\ cm^2/s$ = thermal diffusivity) associated with this distance. While only approximate, these numbers are useful guides. Longer pulses or smaller absorption coefficients will heat thicker layers.

Very high absorption coefficients typically occur near resonances. All resonance transitions are typically temperature sensitive. For electronic transitions the peak absorption decreases with temperature while its width increases, but the resonance frequency remains constant. For vibrational resonances, S. S. Mitra[3] shows the temperature dependence of vibrational resonances in nonmetallic solids (e.g., MgO). The peak absorption coefficient drops rapidly between room temperature and ~600°C, and the absorption band broadens and shifts toward longer wavelengths. The frequency shifts are at least partly due to the lengthening of the bond distances. The resonances are typically asymmetric, and their shapes and values depend on the particular material.

Basic optics theory relates the absorption coefficient and index of refraction through the Kramers-Kronig relations.[4] The textbook index of refraction typically has a maximum on the long-wavelength side of the resonance and a minimum on its short-wavelength side. For vibrational transitions the behavior is qualitatively similar, though generally more complex. Nevertheless, as the temperature increases and the absorption decreases and shifts toward longer wavelengths, the index of refraction exhibits similar behavior, i.e., its peak values drop

and the resonance broadens and shifts toward lower frequencies (longer wavelengths). We note that a similar temperature dependence of the strong absorption coefficient for water near $\lambda = 3\ \mu$m has been reported in the literature.[5–7]

Associated with the index of refraction, $n$, is the well-known Fresnel reflection given by $R = (1-n)^2/(1+n)^2$. When the absorption coefficient is very strong (as it is typically near a resonance transition), the index of refraction becomes complex and can be written as $n = n_r + ik$, where $n_r$ is the real part of the index of refraction, $i = \sqrt{-1}$, and $k$ is the extinction coefficient. The extinction coefficient is related to the absorption coefficient by $\alpha = 4\pi k/\lambda$. Under these conditions the above Fresnel-reflection formula is rewritten as

$$R = \left[(1-n_r)^2 + k^2\right] \Big/ \left[(1+n_r)^2 + k^2\right]. \qquad (1)$$

We note that for either $n_r$ or $k$ (or both) >> 1, the reflection coefficient approaches 100%! In fact, for enamel at $\lambda = 9.6\ \mu$m we find $R \approx 50\%$, while for $\lambda = 10.6\ \mu$m we find $R \approx 13\%$. These measurements were first reported by Duplain[2] for bovine enamel and have been verified in our laboratory for both bovine enamel and human enamel. Thus, if either $k$ and/or $n_r$ decreases due to their temperature dependence, the corresponding surface reflection decreases. While this observation certainly holds in the immediate vicinity of a resonance, farther away the reflection losses could actually increase with temperature due to the temperature dependence of the complex index of refraction.[2] The most dramatic changes in both $n_r$ and $k$ occur at rather modest temperatures below 600°C to 900°C with changes by factors of ≥2 being quite plausible.[3]

Since the surface temperatures during $CO_2$ laser irradiation can easily reach 1000°C or more, we can expect significant changes in the reflection coefficient during the laser pulse. Concomitant with a reduced reflection is increased energy coupling to the irradiated substrate; thus, the apparently paradoxical situation can arise where the absorption coefficient decreases while the absorbed energy increases, albeit over a greater volume.

In this article we report on time-dependent reflection and surface temperature measurements for laser-irradiated dental hard tissue at two of the four major $CO_2$ laser wavelengths (9.6 and 10.6 $\mu$m). These wavelengths were chosen for their potential usefulness in caries retardation if appropriate irradiation conditions are chosen.[1]

## Method

Time-resolved reflection and surface temperature measurements were carried out using the experimental setup illustrated in Fig. 62.51. The light collector for the surface temperature measurements is an elliptical, rhodium-coated mirror (left side in Fig. 62.51) with an entrance hole at the top for the $CO_2$ laser beam. All thermal radiation emitted into the upper hemisphere was collected and imaged onto the HgCdZnTe detector, which has a time response of ~1 $\mu$s. The broadband filter shields the detector against scattered laser radiation and passes the thermal radiation between 5 and 9 $\mu$m. The signal from the detector was acquired by a digital oscilloscope (TEK2440) and recorded by a personal computer.

The time-resolved reflection measurements were made using a gold-coated integrating sphere as a light collector (right side in Fig. 62.51) with a broadband filter in front of the detector. The filter passes the laser light and adjusts the light level at the detector for optimum detection.

The recorded pyrometric signals were converted to surface temperatures using a calibration procedure described by Fried *et al.*[8] Synthetic carbonated hydroxyapatite (CAP) heated in a furnace at a known temperature of up to ~1000°C was employed as a calibration standard. A known area of the sample was imaged onto the detector using the same broadband filters as in the actual experiment. The results indicate that the emissivity is close to unity, i.e., the thermal emission from our samples is close to blackbody emission. However, we have no independent measurement of the absorption depths in the region between 5 and 9 $\mu$m. For the moment we assume that this absorption depth is small compared to the depths over which a given temperature is measured. This assumption is tenuous and must always be kept in mind when interpreting temperature measurements.

The strong temperature dependence of the total blackbody emission ($A\sigma T^4$, $A$ = emitting area, $\sigma$ = Stefan-Boltzmann constant, and $T$ = absolute temperature) renders such a measurement insensitive to the exact value of $A$. Likewise, this strong temperature dependence strongly biases the measurement toward the peak temperature. Our actual measurements are carried out, however, in a fixed and limited wavelength interval (5 to 9 $\mu$m) causing the measured signal to follow a lower-power law (smaller exponent in $T$), which furthermore changes with temperature. While the calibration procedure takes this effect into account, the temperatures deduced from these measurements are more sensitive to the exact value of $A$

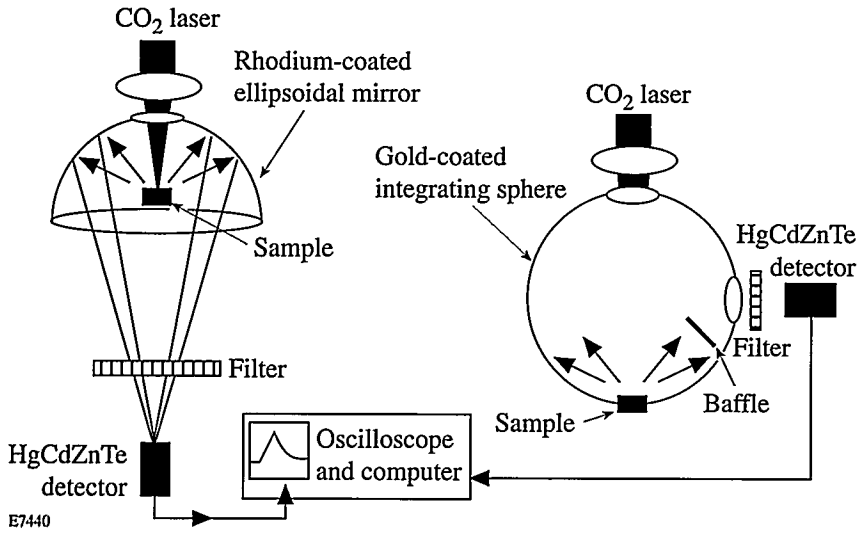


Figure 62.51
Experimental arrangement for measuring the time-dependent surface reflection (right side) and surface temperature (left side) of laser-irradiated dental hard tissue.

and less strongly biased to the maximum temperature in the area measured. As a consequence, assigning error bars to these measurements is rather difficult.

The tooth samples are unerupted, human third molars with a polished (1-$\mu$m grit size) enamel or dentin surface. The polished teeth are sonicated to remove the smear layer and polishing debris; the efficacy of this procedure is verified using scanning electron microscopy.

Our wavelength-tunable $CO_2$ laser (Pulsed Systems, Los Alamos, NM) is capable of delivering up to 200 mJ in pulses of 50 $\mu$s to 1 ms and is tunable from 9.3 to 9.6, 10.3, and 10.6 $\mu$m. At present we believe that the 100-$\mu$s pulse duration is the most suitable for caries retardation applications.

## Results and Discussion

1. Time-Resolved Reflection in Dental Enamel

Typical time-resolved reflection measurements of human dental enamel are shown in Fig. 62.52 for $\lambda = 10.6$ and 9.6 $\mu$m. These wavelengths have the largest difference in absorption coefficient (see above) and therefore are expected to exhibit the largest difference in thermal behavior. For both wavelengths the reference pulse shown represents the reflection from an enamel surface irradiated at low fluence (~1 J/cm$^2$) scaled to 6 J/cm$^2$ (i.e., six times the reflected signal at 1 J/cm$^2$).

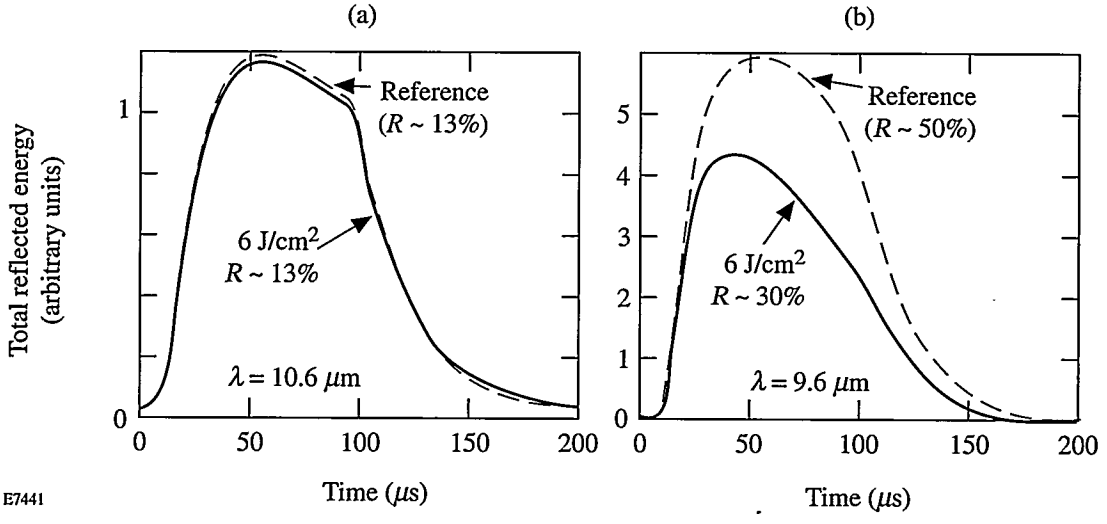


Figure 62.52
Time-resolved reflection from polished human dental enamel for two $CO_2$ laser wavelengths at low (~1-J/cm$^2$) and high (~6-J/cm$^2$) fluence, (a) $\lambda = 10.6$ $\mu$m, (b) $\lambda = 9.6$ $\mu$m. The reference (low-fluence reflection) is linearly scaled to that expected at high fluence and mirrors the incident pulse shape. The overall low-fluence reflections are ~13% and ~50% at 10.6 $\mu$m and 9.6 $\mu$m, respectively.

This reference is identical in shape to the incident laser pulse, implying no change in reflectivity during the pulse at that fluence. For the 10.6-$\mu$m reflection data [Fig. 62.52(a)] there is essentially no change in reflectivity as the fluence is raised from 1 J/cm$^2$ to 6 J/cm$^2$. In contrast, for $\lambda = 9.6$ $\mu$m [Fig. 62.52(b)] there is a very marked difference between the reflection signals registered for the two fluence levels. While the overall reflection loss at low fluence is ~50%, the reflection losses drop to ~30% at 6 J/cm$^2$; thus the amount of energy actually absorbed by the enamel increases at the higher fluence. These observations are consistent with the temperature-dependent absorption and reflection coefficients that are expected to decrease for the most highly absorbing $CO_2$ line at ≥6 J/cm$^2$, while remaining quite unaffected at 10.6 $\mu$m. At 10.6 $\mu$m the absorption is low and relatively far from the main vibrational resonances (see Fig. 62.50). On the basis of qualitative similarities with MgO we would expect no significant changes in either the absorption or reflection coefficient this far from the main resonance.[3]

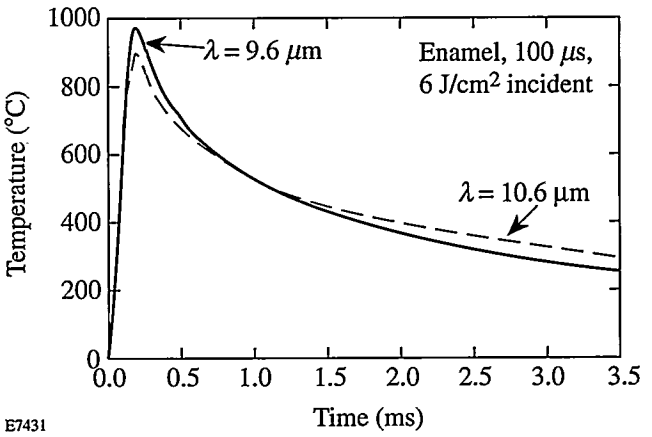


Figure 62.53
Time-resolved temperatures for enamel irradiated with 100-$\mu$s $CO_2$ laser pulses at 9.6 and 10.6 $\mu$m and a fluence of ~6 J/cm$^2$. The peak surface temperature for 9.6-$\mu$m irradiation is slightly larger than at 10.6 $\mu$m due to the higher absorption coefficient and in spite of the higher surface-reflection losses at this wavelength.

2. Time-Resolved Temperatures in Dental Enamel

Time-resolved temperature measurements show a great variety of behavior depending on whether enamel or dentin is irradiated and whether one looks at the first, second, tenth, or subsequent pulses.[9] At present we believe that these initial pulse-to-pulse changes in the temperature measurements relate to burnoff (blowoff) of the organic constituents of the dental hard tissue as well as some surface melting and recrystallization of the mineral substrate. After approximately ten pulses, the surface typically stabilizes, and temporal temperatures like those shown in Fig. 62.53 are obtained reproducibly. We note that for 9.6- and 10.6-$\mu$m irradiation with single, 6-J/cm$^2$, 100-$\mu$s pulses, the peak surface temperatures are quite similar for the two wavelengths with the peak surface temperature at 9.6 $\mu$m being slightly higher. The energy coupled into the sample is smaller by ~25% at 9.6 $\mu$m due to reflection losses (see preceding section). The deposited energy density near the surface is still larger, however, at 9.6 $\mu$m due to the higher absorption coefficient (shorter absorption depth)—even after allowing for the temperature dependence of the absorption coefficient and heat conduction into the interior of the target. The crossover of the two curves reflects the fact that at 9.6 $\mu$m less energy is deposited in the sample over a shorter distance than at 10.6 $\mu$m. This leads to higher surface temperatures at early times, while at later times, when thermal diffusion has heated a larger part of the sample, the detailed laser-energy deposition is unimportant and the measured surface temperatures reflect only the total energy deposited. We also note that at lower fluences (such as 4 J/cm$^2$) the temperature profiles for 9.6- and 10.6-$\mu$m irradiation of dental enamel are quite different, with 9.6 $\mu$m giving a markedly higher peak temperature.[9]

3. Time-Resolved Reflection in Dentin

The time-resolved, high-fluence (>6-J/cm$^2$) reflection from dentin surfaces exhibits a similar wavelength dependence to enamel. Here, too, we plot the time-resolved reflection after a number of pulses have stabilized the dentin surface. The reflection curves for prior shots are clearly affected by the blowoff of the organic constituents and water. After ~20 shots, scanning electron microscope (SEM) images at 60,000× magnification reveal a melted and recrystallized mineral surface devoid of organic material and quite like that obtained with enamel. All subsequent shots cause no further material blowoff from the surface as judged either optically or acoustically. Lower-magnification SEM images show differences between multiply irradiated dentin and enamel samples with, e.g., the dentinal tubules remaining open. The differences between the reference profile and the 6-J/cm$^2$ reflection profile at 9.6 $\mu$m [Fig. 62.54(b)] appear noticeably smaller than for enamel [Fig. 62.52(b)]. These differences largely disappear when one takes into account that the low-fluence reflectivity of irradiated dentin increases[9] from $R \approx 17\%$ to $R \approx 22\%$ after the dentin surface has been recrystallized by multiple irradiation at 6 J/cm$^2$. We therefore surmise that the basic absorption process is the same for irradiated enamel and dentin but the density of dentin near the surface is still somewhat lower than that of enamel. Under these conditions the overall absorption and reflection coefficients would be re-

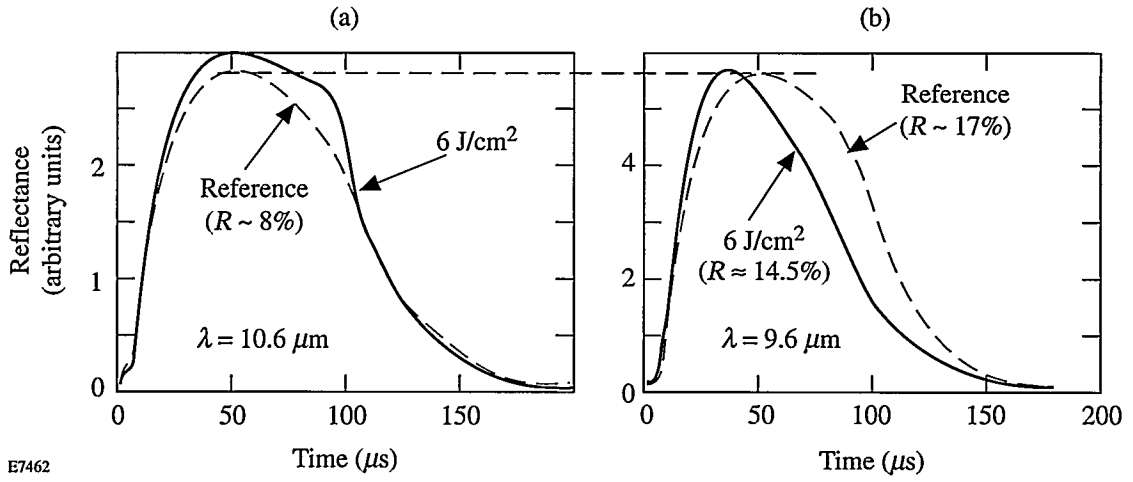


Figure 62.54
Time-resolved reflection from dentin irradiated at (a) 10.6 $\mu$m and (b) 9.6 $\mu$m. The reference pulse is the reflection at 1 J/cm$^2$ scaled to 6 J/cm$^2$ and is identical to the incident pulse shape. The strong wavelength dependence of the reflection at 9.6 $\mu$m is connected with the temperature-dependent absorption coefficient as in Fig. 62.52.

duced, but the relative change in reflection due to the temperature-dependent absorption coefficient would remain unchanged, consistent with our observations.

## Conclusions

We have observed the first experimental evidence of time-dependent reflection in $CO_2$-laser-irradiated dental hard tissue at 9.6 $\mu$m, while no differences in reflectivity were observed at 10.6 $\mu$m. Using the known relationships between surface reflection and high absorption coefficients, we have related the reduced reflection for the high-fluence, 9.6-$\mu$m data to the temperature dependence of the absorption coefficient. This temperature dependence is much more pronounced in the immediate vicinity of the strong vibrational bands of the phosphate ions (9.6 $\mu$m) than farther away (10.6 $\mu$m). We have also seen direct evidence of this temperature-dependent absorption in time-resolved temperature measurements using fast photodetectors.

These data show that an appropriate choice of wavelength and pulse duration allows fine tuning of morphological surface modifications of irradiated dental hard tissue. Such fine tuning is expected to permit optimization of the laser-irradiation conditions for the purpose of caries reduction in dental hard tissue.

## ACKNOWLEDGMENT

This work was supported by NIH/NIDR Grant DE 09958.

## REFERENCES

1. J. D. Featherstone and D. G. Nelson, Adv. Dent. Res. **1**, 21 (1987).
2. G. Duplain, P. A. Belanger, and R. Boulay, Appl. Opt. **26**, 4447 (1987).
3. S. S. Mitra, in *Handbook of Optical Constants of Solids*, edited by E. D. Palik (Academic Press, Orlando, 1985), Chap. 11, pp. 213–270.
4. M. Born and E. Wolf, *Principles of Optics: Electromagnetic Theory of Propagation, Interference, and Diffraction of Light*, 2nd rev. ed. (Macmillan, New York, 1964).
5. J. T. Walsh, Jr. and J. P. Cummings, Las. Surg. Med. **15**, 295 (1994).
6. K. L. Vodop'yanov, Sov. Phys. JETP **70**, 114 (1990).
7. K. L. Vodop'yanov, J. Chem Phys. **94**, 5389 (1991).
8. D. Fried, S. F. Borzillary, S. M. McCormack, R. E. Glena, J. D. B. Featherstone, and W. Seka, in *Laser Surgery: Advanced Characterization, Therapeutics, and Systems IV*, edited by R. R. Anderson and A. Katzir (SPIE, Bellingham, WA, 1994), Vol. 2128, pp. 319–328.
9. D. Fried, R. E. Glena, J. D. B. Featherstone, and W. Seka, in *Lasers in Dentistry*, edited by H. A. Wigdor, J. D. B. Featherstone, and J. M. White (SPIE, Bellingham, WA, 1995), Vol. 2394 , pp. 41–50.

# Initial Performance Results of the OMEGA Laser System

An important step in the U.S. inertial fusion effort toward demonstrating ignition and modest gain in the laboratory is the validation of high-performance direct-drive fusion capsules. The scientific program at UR/LLE[1] is aimed at studying near-ignition conditions in direct-drive capsules that achieve ion temperatures of 2 to 3 keV and fuel areal densities of 0.2 g/cm$^2$. Such capsules are expected to achieve convergence ratios greater than 20 and experience Rayleigh-Taylor (R-T) growth factors in excess of 500. The OMEGA laser system has been upgraded to demonstrate these near-ignition conditions. The system has now produced up to 37 kJ of UV energy on target in 60 beams. Ultimately, the system will provide versatile pulse shapes and produce high irradiation uniformity (1%–2%) on the capsule.

The preliminary design[2] for the upgraded OMEGA system was completed in October 1989. Detailed design commenced in October 1990. In December 1992, the 24-beam OMEGA laser fired its last shot before being decommissioned to allow for the construction of the upgraded system. Ten months later, the building modifications were completed and laser construction began. In January 1994, the pulse generation room (PGR) began operations, and, in April 1994, the entire driver was activated. The first full OMEGA beamline was completed in December 1994 and produced 800 J in the IR and 606 J in the UV. In February 1995, a single UV beam irradiated a target. In March, the first 60-beam laser shot was fired, and in April, all 60 beams irradiated a target. The final acceptance tests for the system were performed on 2 May 1995.

The acceptance criteria for the upgraded system were the demonstration of target irradiation with 30 kJ of UV energy in 60 beams with ~750-ps Gaussian pulses and the achievement of a beam-to-beam energy balance of 10% rms. This article provides a brief description of the laser system and then presents the initial system performance results that met and exceeded the acceptance criteria. Specifically, targets were irradiated with UV energies up to 37 kJ, and the beam-to-beam energy balance was better than 8%. Overall frequency-conversion efficiencies of 75% were routinely obtained. The full laser system was operated for 15 shots with a 1-h shot cycle, including nine consecutive target shots.

OMEGA is a Nd:glass laser in the master oscillator–power amplifier (MOPA) configuration (see Fig. 63.1). It uses rod amplifiers up to a beam diameter of 9 cm, followed by disk amplifiers up to an output aperture of 20 cm in the IR. Each amplifier is followed by a spatial filter. The 60 IR beams are expanded in the final spatial filters to a 28-cm aperture and converted to 351 nm using KDP crystals in the type II/type II polarization-mismatch frequency-tripling configuration developed at LLE.[3,4] The beams are uniformly distributed around a 3.3-m-diam target chamber and focused onto target with *f*/6 lenses. (The effective *f* number based on the beam diameter is approximately 6.7.) Details of the design and configuration of the laser system can be found in other LLE Review articles. In Ref. 5, an updated description of the system included design changes since the preliminary design.[2] More details were given in Ref. 6 (laser drivers and laser amplifiers), Ref. 7 (power conditioning, control systems, optomechanical systems, major structures, and the target area), Ref. 8 [the large-aperture ring amplifiers (LARA's)], and Ref. 9 (the final design review prepared for the Department of Energy). This article presents performance results for the driver, the power amplifiers, frequency conversion, the harmonic energy diagnostic system, the temporal laser pulse shape, and the target-bay alignment and pointing systems.

**Driver**

The OMEGA driver generates optical pulses that are amplified, frequency converted, and eventually irradiate the target. To provide precise control of the on-target irradiation for fusion experiments, the driver must provide a beam that is stable and appropriately shaped in space, time, and frequency. In the acceptance tests the amplitude stability of the OMEGA driver was demonstrated to be better than 2% rms.

Figure 63.2 depicts the configuration of the driver, which begins with a master oscillator that produces ~10-nJ, 80-ps Gaussian pulses at a rate of ~76 MHz. These pulses seed

feedback-stabilized regenerative amplifiers (regens), which produce ~0.5 mJ per pulse with a pulse width ranging from 0.5 ns to 5 ns. A pulse-shaping system, not yet implemented and not shown in Fig. 63.2, will temporally shape the master-oscillator pulses before injection into these regens. It will be possible to inject independent pulse shapes into each of the three regens (main pulse, foot pulse, and backlighter). For the acceptance tests described here, a Gaussian pulse of ~800-ps duration was produced using an etalon in the main-pulse regen. The pulse-shaping system and the foot-pulse and backlighter beams were not required.

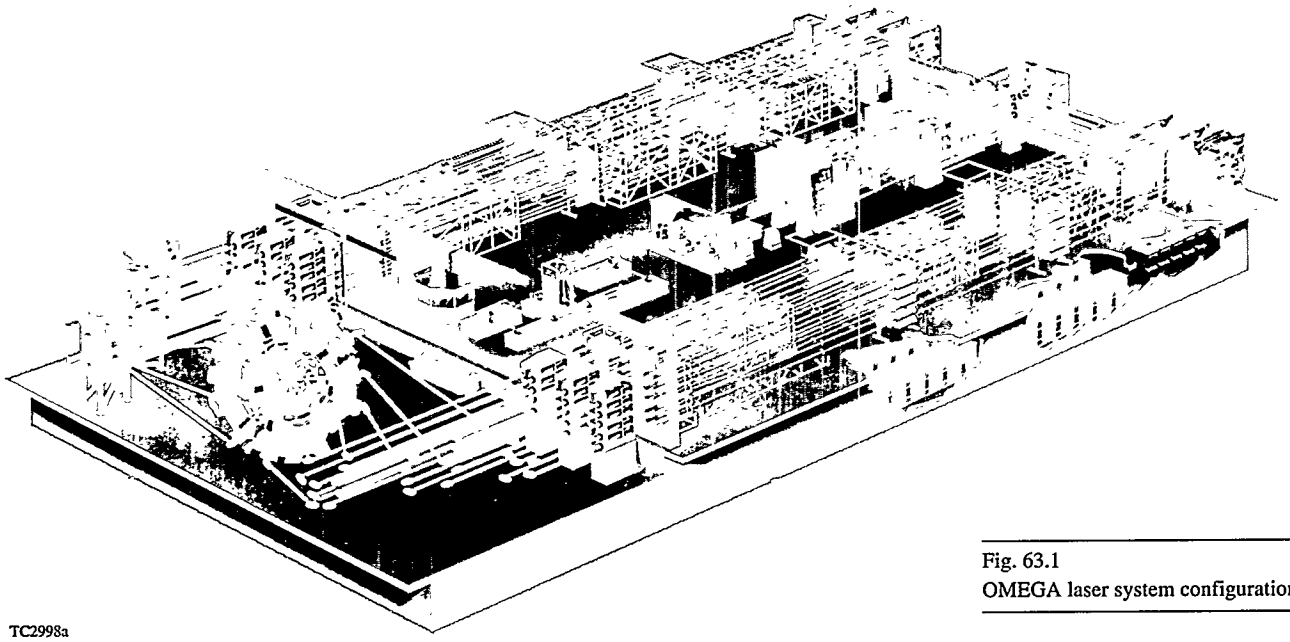

TC2998a

Fig. 63.1
OMEGA laser system configuration.

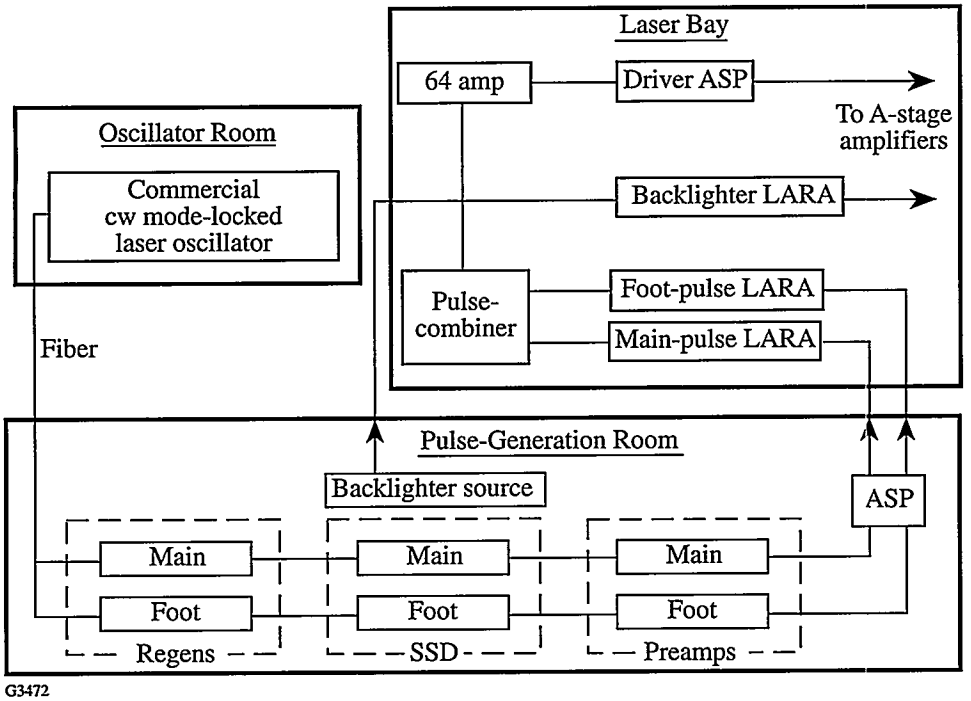


G3472

Fig. 63.2
Driver configuration for the OMEGA laser as used during the performance tests. Three optical pulses of independent temporal shapes (main, foot, and backlighter) can be generated in each of three separate drivers and subsequently amplified in three large-aperture ring amplifiers (LARA's).

The regens largely dictate the stability and reproducibility of the driver, which is why an amplitude feedback mechanism was implemented. This approach to stabilization has produced output pulses that have amplitudes and pulse widths with shot-to-shot variations of ≲1.5% rms. In addition, the time jitter between pulses from separate oscillators has been measured to be ≲30 ps rms. This low jitter permits the operation of synchronized oscillators for the main, foot, and backlighter pulses as well as ancillary oscillators/amplifiers to drive fiducials and probe beams needed for the diagnosis of fusion experiments. The wavelength of the pulses is monitored on every shot using Fabry-Perot interferometers that provide 0.05-Å wavelength resolution; care is taken to ensure that the wavelength remains constant to that accuracy so as not to compromise the frequency-conversion crystal (FCC) alignment.

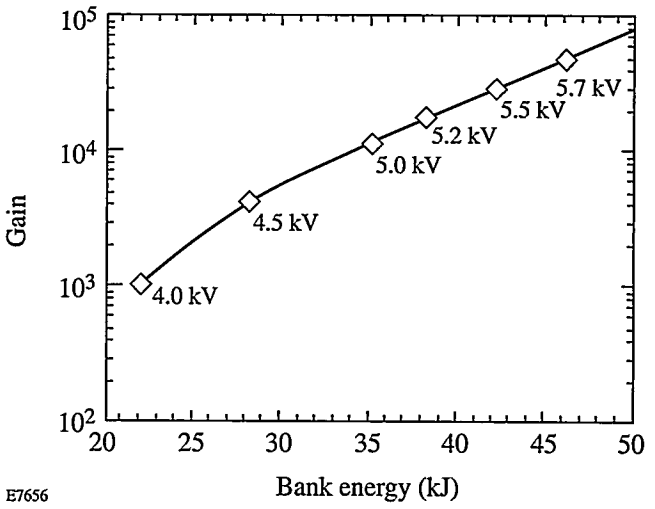


Fig. 63.3
Performance results for the main-pulse LARA. The gain is given as a function of bank energy for four-pass operation. The bank energy is determined from the charging voltage indicated.

To conserve space in the laser bay and enhance performance reliability, most of the driver gain is provided by a large-aperture ring amplifier (LARA). For the acceptance tests, LARA amplified the regen output from <1 mJ to ~1 J and a single-pass, 64-mm amplifier then amplified the pulse to ~5 J. LARA is a 40-mm, four-pass, imaging ring amplifier capable of producing energies ≳15 J in 1 ns. LARA is compact and fits easily on a 5-ft × 10-ft optical table. Figure 63.3 demonstrates the LARA gain performance in its four-pass configuration. Gains of up to ~$4 \times 10^4$ have been achieved. This performance largely exceeds current requirements and thus ensures that schemes to improve the irradiation uniformity, which require additional driver gain, can be accommodated without compromising the full output-energy performance of the system. The high quality of the output beam from LARA is clearly demonstrated by the near-field image and interferogram (Fig. 63.4) obtained during tests at full aperture (37 mm) for a pulse width of ~1 ns. The peak-to-valley phase distortion [Fig. 63.4(b)] was measured to be less than one wave at $\lambda = 1\ \mu$m, while random intensity fluctuations were ≲10% rms. Under normal operating conditions on OMEGA, only the ~20-mm central region of the LARA aperture is used, resulting in ≲$\lambda/4$ phase error (peak to valley). The slight edge enhancement of the near-field image is due to the input beam apodizer that was designed for a lower output energy.

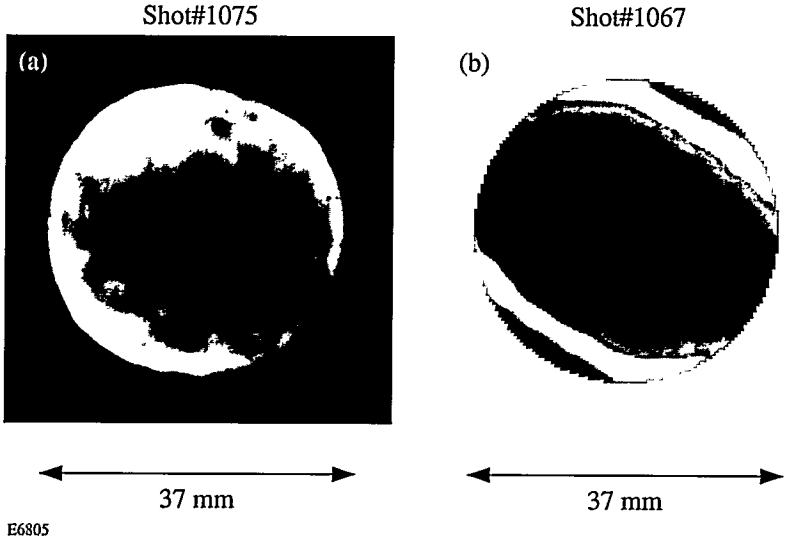


Fig. 63.4
(a) Near-field image and (b) interferogram of 37-mm-diam beams at the LARA output. The beam energy was 13.7 J in (a) and 17.8 J in (b).

The OMEGA driver is used to shape the output spatial profile of the laser (see Fig. 63.5). This is characterized by two features: the intensity profile and the location of the outer "edge" of the beam. (To maintain alignment and prevent modulations due to vignetting of the beam, an edge is needed to define the beam.) Each of these features is determined by the profile at an image plane in the driver that is relayed through the system by the spatial filters. To ensure high extraction efficiency in the disk amplifiers and high frequency-conversion efficiency, it is important that the output spatial profile of the laser be flat. The input beam profile must therefore compensate for the radial gain variation exhibited by the rod amplifiers of the system (stages A through D). This is done by placing a serrated apodizer[10] at the input to LARA and irradiating it with an appropriately sized beam from the PGR. Using a laser propagation code (*RAINBOW*) and the measured radial-gain profiles of each class of amplifier (40, 64, and 90 mm), the apodizer transmittance and input beam size have been designed to produce the desired beam intensity profile at the output of the system (the solid line of Fig. 63.5). For the tests reported here, the apodizer was used to shape the spatially Gaussian beam from the PGR. The beam edge is set entirely by the transmittance of the apodizer. The LARA spatial filter removes the high spatial frequencies created by the serrations while preserving the desired low-frequency beam shape. As a consequence, the pinhole in this filter is the tightest in the whole laser system—just five times the diffraction-limited size for its 2.0-cm beam.

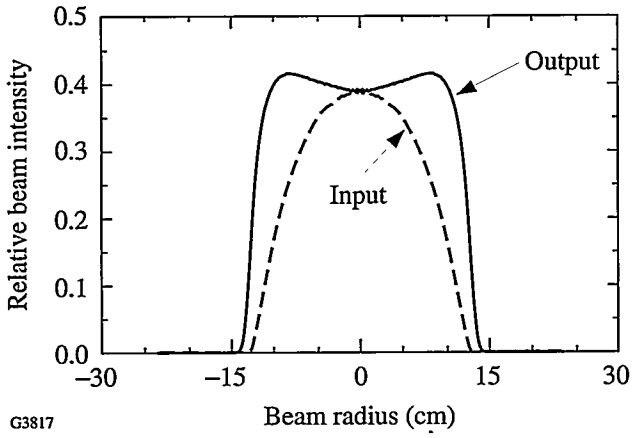


Fig.63.5
One-dimensional lineouts of the IR spatial intensity profile at the input to the amplifier chain (dashed line, scaled with the beamline paraxial magnification) and at the output of the final (stage-F) spatial filter (solid line). The input profile is strongly center-peaked to compensate for the radial gain profiles in the rod amplifiers.

**Power Amplifiers**

The OMEGA system has been designed to propagate the complex temporal pulse shapes required for direct-drive targets.[11] The system is staged for equivalent Gaussian pulse widths in the range of 0.5–3.0 ns. The 0.5-ns pulses are sufficiently short that it has been necessary to emphasize high gain in order to minimize B-integral effects.[12] For 3.0-ns pulses, on the other hand, the performance is limited by the damage fluences.

A staging diagram of the OMEGA laser is shown in Fig. 63.6. Values are given for the energy, fluence, and accumulated B-integral at various points for a 750-ps, temporal-Gaussian, spatially flat-topped pulse. Circular polarization is propagated through all of the 64- and 90-mm rod amplifiers to reduce non-azimuthally symmetric (i.e., "Maltese cross") beam modulation due to component birefringence (particularly in the rods), to reduce the B-integral in the rods,[13] and to reject retroreflections from optical components at the circular polarizers.[14] The laser performance used for the acceptance tests was approximately as shown in Fig. 63.6.

The beam splitting necessary to produce the requisite 60 beams is performed using a combination of wave plates and polarizing beam splitters. The first split is the stage-A split, in which the driver is split into three beams before the A amplifiers. The other splits are similar, except for the number of output beams, and will not be described in detail. The input to the stage-A splitter is first repolarized by a liquid-crystal circular polarizer[14] to eliminate changes in the split ratio in the event that the input polarization were to change. The input beam is then converted to linear polarization by an adjustable quarter-wave plate followed by a polarizing beam splitter that divides the beam into a high-contrast *p*-polarized beam and an *s*-polarized beam containing a small amount (<4% of the input intensity) of residual *p*-polarization. The *p*-polarized beam constitutes one of the three split outputs. The *s*-polarized beam passes through an adjustable half-wave plate and is split two ways by another polarizing beam splitter, forming the remaining two output beams. Each of the three output beams is reconverted to circular polarization by a rotatable quarter-wave plate and repolarized by another circular polarizer before leaving the split. The optical paths in the legs of the split are equalized to maintain relative beam timing. All mirror and beam-splitter reflections are kept in the same plane.

For the acceptance tests, the input energy to the A split was ~5 J. Each of the resulting three beams was amplified by a

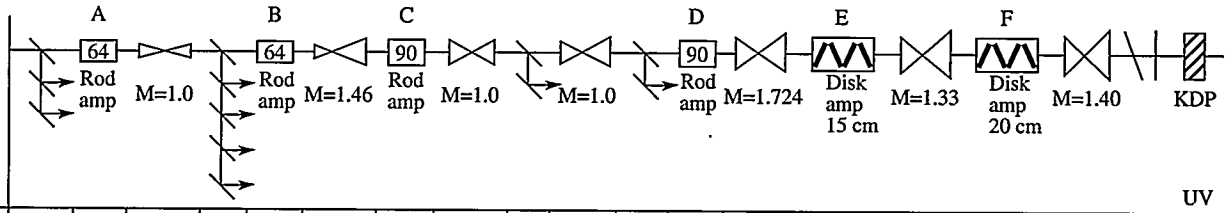


| | | | | | | | | | | | | | | | | | | |
|---|---|---|---|---|---|---|---|---|---|---|---|---|---|---|---|---|---|---|
| Energy (J) | 1.1 | 12.0 | 11.7 | 2.0 | 21.2 | 20.7 | 103 | 99.4 | 48.2 | 47 | 22.0 | 124 | 118 | 402 | 398 | 1040 | 978 | 750 |
| Avg. fluence ($J/cm^2$) | 0.1 | 0.87 | 0.85 | 0.15 | 1.3 | 0.56 | 2.3 | 2.2 | 1.1 | 1.0 | 0.48 | 2.3 | 0.71 | 2.5 | 1.35 | 3.5 | 1.7 | 1.4 |
| B-integral (radians) | 0.26 | 0.46 | 0.5 | 0.5 | 0.79 | 0.83 | 1.5 | 1.7 | 1.7 | 1.8 | 1.9 | 2.5 | 2.6 | 2.9 | 3.0 | 3.5 | 3.8 | ---- |

G3578

Fig. 63.6
Staging diagram of an OMEGA beamline through stages A–F (not to scale) for an input Gaussian pulse of 0.82-ns FWHM.

factor of 10 by a 64-mm-diam, stage-A rod amplifier (with a 61-mm clear aperture). After spatial filtering, each of these beams was split vertically into five beams in the stage-B split, for a total of 15 beams with ~3 J per beam. This provided adequate drive for the subsequent 64-mm and 90-mm rod-amplifier combination (stages B and C) located in each of the 15 beamlines to produce ~100 J at the final, four-way, stage-C split. (This is essentially identical to a beamline of the old OMEGA system where a 2-J drive in each of 24 beamlines produced just over 100 J at the output.) The final three amplifiers in each beamline in the upgraded system (the stage-D rods and the disk amplifiers of stages E and F) generate 97% of the system output energy for a 0.7-ns pulse. A drive of 22 J at the stage-D rod produces over 1 kJ of IR energy at the output of the stage-F amplifier.

### Frequency Conversion

The IR output of OMEGA is frequency tripled to 351 nm using two type-II KDP crystals per beam.[3,4] To guarantee high harmonic conversion it is necessary to maintain the proper phase-matching angles in the crystals. This requires precise control of the crystal orientation, the beam wavelength, and the crystal temperature. In addition, to ensure the optimum ratio of fundamental and second harmonic in the second (tripler) crystal, high-contrast linear polarization is required at the input to the first (doubler) crystal. For this reason a large-aperture polarizer is placed in each beam just before the crystals. The wavelength of the driver is constantly monitored by diagnostics with 0.05-Å resolution, and care is taken to maintain a constant wavelength. The crystals are maintained at the ambient temperature of the laser bay, which is nominally controlled to ±0.5°F. Variations in crystal temperature will be actively compensated for by using empirical temperature-tuning curves, although this has not yet proven necessary.

Prior to the installation of the crystals, the peaks of the angle-tuning curves for the doublers and triplers were found by using an off-line tuning procedure that used one of the remaining two OMEGA drivers not required for system activation. Configured to produce 100-ps, 2-mJ pulses at 5 Hz, this driver irradiated frequency-conversion cells (including the doubler and tripler) with a weakly converging beam of about 1 cm in diameter [see Fig. 63.7(a)]. This produced a spread of angles that included the optimum phase-matching angle for each of the crystals.[15] By properly referencing the experimental setup, the tuning peaks and thus the correct orientations for the doubler and tripler crystals could easily be determined in a single 20-shot (4-s) exposure of a CCD camera. Figure 63.7(b) shows one such exposure. The central lobes of the characteristic $\text{sinc}^2(x)$ intensity distributions for the green from the doubler (band AB) and the UV from the tripler (band CD) intersect at the optimum tuning position (marked with an "x"). The other broad band across the image (EF) is produced by rays that are phase matched for doubling in the tripler. The broadness of the second-harmonic (green) bands results from the relative insensitivity of doubling to changes in the ray angle along the *o* axis of each crystal. The CCD image is produced by a combination of all three wavelengths, with greatest sensitivity to the UV. Thus, there are many bands parallel to AB corresponding to green side lobes in the doubler, mostly imperceptible in the image; however, whenever these lobes intersect the line CD, i.e., are phase-matched for tripling, the UV generated is evident as a series of elliptical images. These images are narrower in the tripler tuning direction (parallel to AB) than in

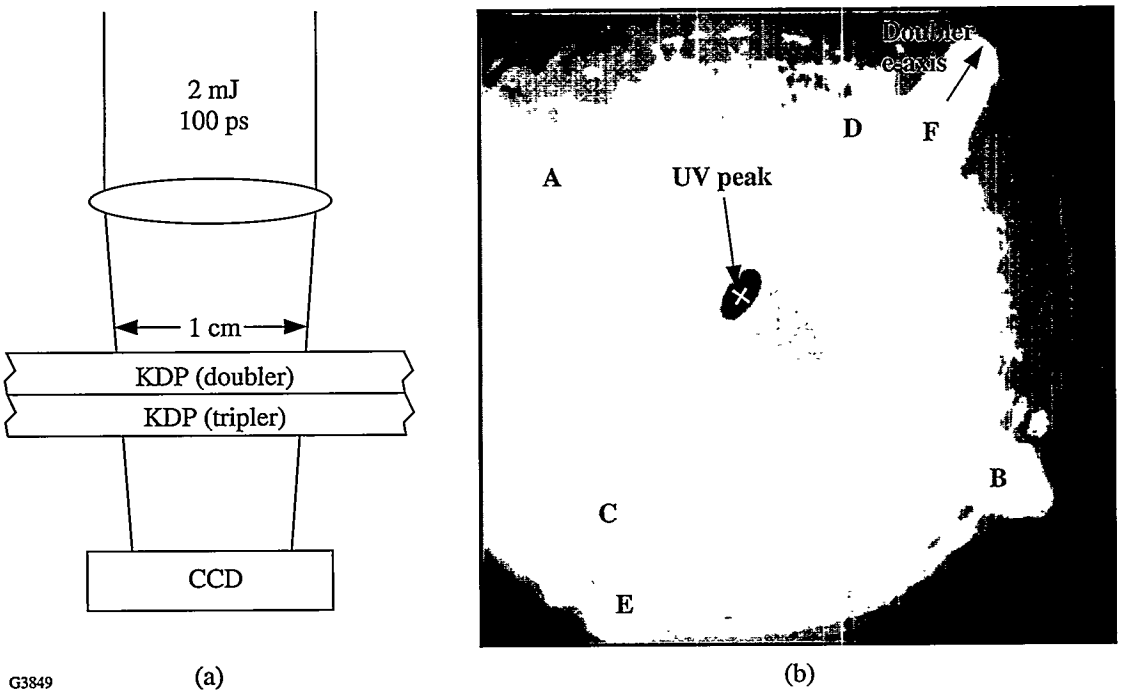


Fig. 63.7
(a) Off-line tuning technique for the frequency-conversion crystals (FCC's). A small-aperture (1-cm) beam is weakly focused through the FCC's onto a CCD camera; (b) resulting spatial pattern on the CCD. By identifying the ray in the converging beam that generates optimum UV, indicated by an "x," the necessary angle tilts of the FCC assembly in each of the two orthogonal directions may be determined. The arrow indicates the *e* axis of the doubler and the *o* axis of the tripler.

the doubler tuning direction (parallel to the arrow) because of the greater sensitivity of the tripler to the detuning angle.

The crystals were installed in the OMEGA system at the peak position as determined by the off-line tuning system. High-power angle-tuning scans were then performed about that position at 30% beam energy (300 J IR) with just three shots each for the doubler and tripler. In this procedure the doubling and tripling conversion efficiencies are fitted to the respective theoretical tuning curves, which are well represented as quadratic. The peak tuning positions were determined with a precision of ±50 μrad. The differences between the high-power peak tuning positions and those found from the off-line procedure were less than 125 μrad rms. This difference was presumed to be due mainly to a temperature differential between the off-line tuning setup and the location of the crystals in the OMEGA system. Even though no temperature compensation was applied to the crystal positions during high-power tuning, remarkably stable frequency-conversion efficiencies (70%–75%) were routinely achieved over a two-week period of activation shots. These results demonstrate the stability of the opto-mechanical alignment and the temperature control in the OMEGA facility.

Figure 63.8 is a plot of the $3\omega$ conversion efficiency versus the IR intensity incident on the crystals. The conversion efficiency is defined as the UV energy output from the crystals divided by the IR energy input to the crystals. The incident intensity is calculated using the input IR energy inferred from the energy measurement system, the IR beam profile shown in Fig. 63.5 (which has a nominal diameter of 27 cm), and the measured IR pulse width of 725 ps at the input to the crystals.

The achievement of frequency-conversion efficiencies greater than 70% is the result of a concerted effort to produce input IR beams that are highly suited for conversion. The beams have nearly flat intensity profiles with fill factors of ~90%. [The fill factor is the ratio of the integral of the actual beam shape to that of a flat (i.e., ideal) beam filling the clear aperture.] The intrinsic polarization purity of the disk amplifi-

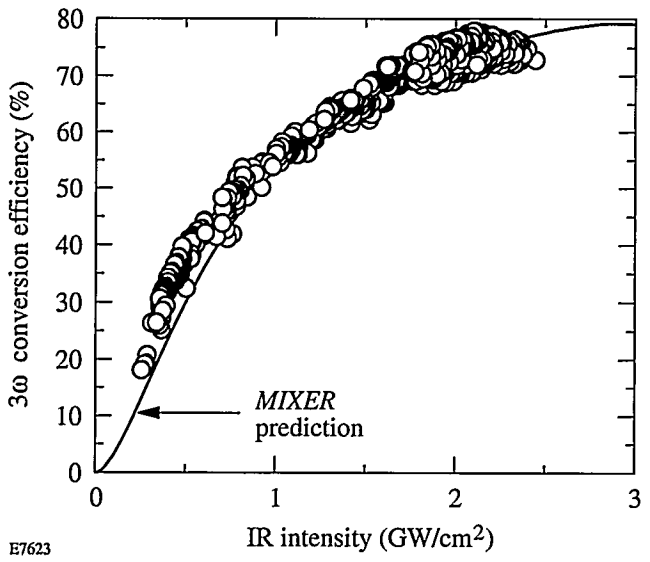


Fig. 63.8
Measured and predicted $3\omega$ energy conversion efficiency as a function of input IR intensity. The predictions take into account the experimental spatial profile of Fig. 63.5.

ers (depolarization <1% at any point in the clear aperture) and the low stress birefringence induced in the spatial-filter lenses produce beams that contain pure linear polarization with a contrast greater than 100:1 at all points in the clear aperture. The high-contrast linear polarizers (contrast of ~500:1) then produce beams that have a very high resultant contrast at the input to the crystals. Also, the laser was designed to produce high wavefront quality: in each beamline the accumulated B-integral is less than 4 radians (at 1 ns), and the optical tolerances are consistent with beams that are <14 times diffraction limited at 351 nm. (Measurements of the optical wavefront quality of OMEGA beamlines are planned for early FY96.)

The measured conversion efficiencies shown in Fig. 63.8 are generally in good agreement with predictions of the code *MIXER*.[4] However, some differences may be noted. In particular, the system seems to generate slightly more UV than predicted, especially at the lower intensities. One possible explanation is that the nonlinear coefficient $d_{36}/\varepsilon_0$ used in the code for Fig. 63.8 is a little too low. The value used for both crystals, $d_{36}/\varepsilon_0 = 0.39$ pm/V, is the same as that inferred from the experiments of Ref. 3 and subsequently accepted as standard.[16] (This value is quoted according to the now-agreed definition of Ref. 16, which is a factor of 2 lower than the definition used in Ref. 4, where $d_{36}/\varepsilon_0$ was quoted as 0.78 pm/V.) A higher value of $d_{36}$ in the tripler, which could be within the measurement error bounds of Ref. 3, would have the effect of shifting the theoretical curve to the left. The scatter in the experimental data probably reflects variations in the crystal temperatures, which were not compensated for during the acceptance tests, so it is the upper envelope of data points that should be compared with the theory. Also, variations in the laser spatial profile at differing input intensities and during the laser pulse have not been included. Additional experiments are needed to resolve the (minor) differences between prediction and experiment.

### System Output Energy

To ensure optimal performance, the energy at the crystal output is measured at all three harmonic wavelengths—IR, green, and UV. This is performed with the harmonic energy diagnostics (HED's). The output (stage-F) alignment sensor package (F-ASP) for each beamline contains an optical pickoff that directs a fraction of the beamline energy (at all three wavelengths) to an integrating sphere for that beam. A single fiber optic samples the energy in the sphere and transports that signal to one of two HED's, where imaging spectrometers separate the three signals by wavelength. Each HED diagnoses 30 beams. In each HED, the 30 fibers are arranged such that, after dispersion, they form three 10×3 arrays, i.e., an image of every fiber in the IR, green, and UV. Figure 63.9 is a composite of the images from the two HED's for a single shot. Each of the beamlines, arranged in six ten-beam clusters, produces three images. The spatially integrated signal for each individual beam image is used as a measure of the energy in the beam at each wavelength. The HED's are calibrated by a full-aperture calorimeter located directly behind the F-ASP optical pickoff and at present provide energy measurements with an absolute accuracy (one standard deviation) of 2% and a relative accuracy of 1.9%. The relative accuracy is expected to improve to <1% in the near future. This system is described in detail in the following article.

The HED's were used to diagnose the beamline energy and overall beam balance for the acceptance tests. The system output energy was measured on numerous 60-beam shots, some of which were target shots. The system consistently produced >30 kJ with typical beam balances of 6%–8%. Figure 63.10 is a plot of the UV output energy versus the beamline IR energy at the crystal, including data for all beamlines for more than 20 shots. The data included some lower-energy shots produced during calibration and energy ramp-up procedures. The highest-energy 60-beam shot produced over 40 kJ of UV, and tests on an individual beam demonstrated that a beamline energy of 1 kJ IR can produce 750 J of UV. This is equivalent to a full-system output of 45 kJ UV, which, at 660 ps, corresponds to 68 TW.

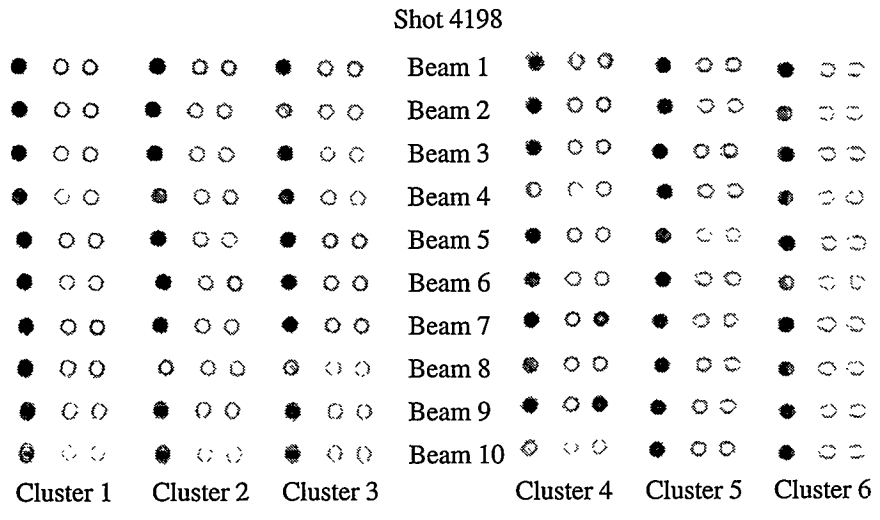


Fig. 63.9
Output of the harmonic energy diagnostic (HED) system. This produces images indicating the output energy at each of the UV, green, and IR wavelengths (from left to right) for each beam. A shot with the crystals detuned was used to illustrate the capability of the HED system—normally, very little signal is seen in the IR and green images.

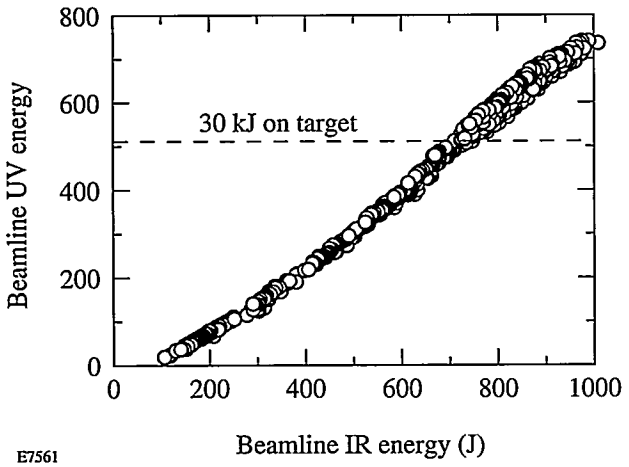


Fig. 63.10
Energy performance of the OMEGA laser. The UV energy at the FCC output is plotted against the IR energy at the FCC input for individual beams. The horizontal dashed line indicates the individual beam output energy required to produce a total energy on target of 30 kJ, taking into account transport losses from the FCC's to the target.

### Temporal Pulse Shape

Figure 63.11 shows the temporal histories of the IR pulse at the input to the driver line and the output UV pulse measured on beam 45 on a shot in which 750 J of IR was produced at the input to the crystals. The steepened rise and slower falloff of the output pulse (compared with the input pulse) are caused by saturation effects in the amplifiers. The intensity dependence of frequency conversion results in the FWHM of the UV output pulse being shortened by about 10% with respect to the IR pulse at the input to the crystals. (At high conversion efficiency, the change in FWHM due to frequency conversion is minimal.) For a near-Gaussian pulse shape at the driver input, a 0.82-ns (FWHM) pulse is shortened to about 0.73 ns in the IR at the output of the last amplifier and to 0.66 ns in the UV.

The dashed curve in Fig. 63.11 is the predicted pulse shape from the laser propagation code *RAINBOW* when the measured input pulse shape is used as input to the code. This agreement indicates that the system meets the design specifications and performs as expected. Proper characterization of the system and normalization of the analysis tools are important for control of the on-target pulse shapes. Eventually, the laser propagation code will be used to propagate the desired on-target pulse shape backward through the system to determine the requisite driver pulse shape that must be produced by the pulse-shaping system. The good agreement seen in Fig. 63.11 provides confidence that accurate control of the on-target UV pulse shape will be possible.

Further verification of the accuracy of the code was provided by measurement of the pulse shape of the residual IR on a shot where the crystals were tuned (see Fig. 63.12). One curve is the signal as measured with a fast photodiode and oscilloscope, while the other is the residual IR predicted by the energy

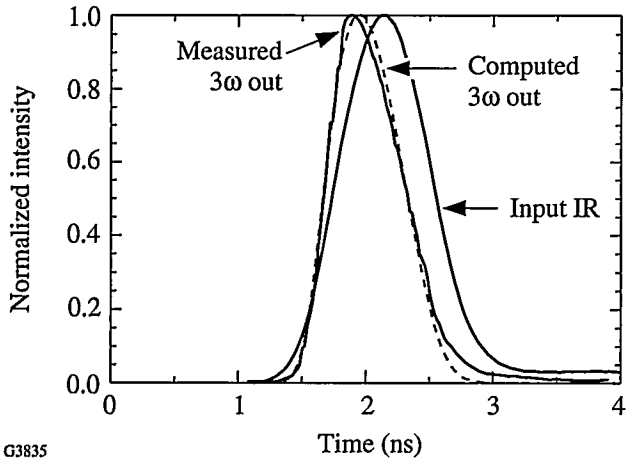


Fig. 63.11
Temporal pulse shapes measured at the input to the driver line and at the output of the FCC's. The measured output pulse shape is very close to that calculated by the propagation code *RAINBOW* (dashed curve).

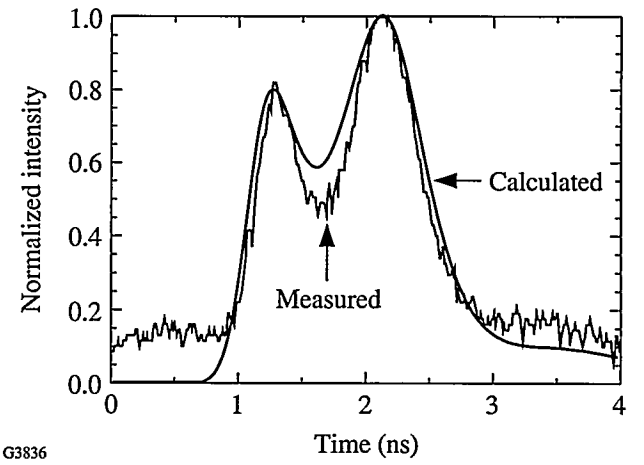


Fig. 63.12
Measured and predicted temporal pulse shape of the residual IR from a high-conversion shot, with 600 J of IR at the input to the FCC's. The *RAINBOW* prediction is shown as the smooth curve. The two peaks in time are associated with the intensity dependence of frequency conversion: maximum conversion, and thus a minimum in the residual IR, occurs at the peak of the pulse. The maximum residual IR intensity is ~13% of the maximum input IR intensity.

transport code *RAINBOW*. The two curves were normalized to match at the peak. The measured pulse shape has not been smoothed or had its pedestal removed. The predicted pulse shape was calculated by propagating the IR temporal pulse shape, measured at the input to the driver, through the driver, the system, and the frequency-conversion crystals. The calculated residual red output was then convolved with a falling-exponential (simple RC) approximation to the impulse response of the measurement's fast photodiode and oscilloscope to obtain the second plot. Even using this simple approximation, the major features of the data are replicated by the prediction. The central dip is due to the higher conversion efficiency at the center of the pulse, where conversion is maximum. The first peak is narrower than the second due to the steeper rise of the input IR pulse in comparison with its slower fall. The increased steepness of the leading edge is due to both a temporal asymmetry of the input to the driver and further steepening due to gain saturation. Since the conversion process responds essentially instantaneously for these time scales, the amplitudes of the two peaks are expected to be equal. Approximately 5% of the observed inequality is due to a change in the spatial pulse shape from early in the pulse to later times. The remainder is due to the convolution with the 180-ps impulse response of the diode and oscilloscope. The long, low intensity tail appearing in the calculation is due to an instrumental tail on the measured pulse shape used as the input to the code; its apparent agreement with the late-time background of the measured signal is fortuitous and of no significance.

### Target Irradiation Tests

Each of the 60 UV output beams from the laser is transported to the target chamber using two high-reflection UV mirrors, and then focused onto target with an *f*/6.4 aspheric lens. The beams are symmetrically distributed around the target chamber in the stretched soccer-ball geometry[2] with the beams located at the vertices of the hexagons and pentagons.

For the acceptance tests, large, gold-coated CH targets were irradiated with 60 beams. The targets were 1600-$\mu$m-diam solid plastic spheres, coated with 0.4 $\mu$m of gold, with an outer 4-$\mu$m layer of CH to reduce the x-ray flux. The resulting x rays were viewed with six pinhole cameras to provide verification of the positioning of all beams on target. Figure 63.13 shows two such images, viewing the target from opposing directions. The focus lenses were set to the surface-focus position, resulting in the relatively small spot sizes (<150-$\mu$m diameter).

The hexagonal/pentagonal configuration can be seen in Fig. 63.13. For this shot the pointing accuracy was 26 $\mu$m rms, dominated by a few beams with significant pointing errors. This result was achieved using only the cw alignment system; i.e., no adjustment of the beam alignment based on these x-ray pinhole images was performed during the acceptance tests.

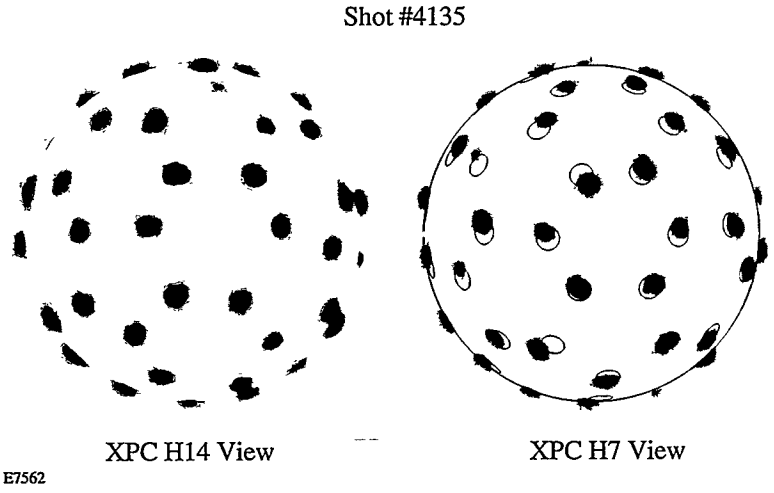


Fig. 63.13
Opposing x-ray pinhole images of a 1.6-mm-diam gold-coated target irradiated with 37 kJ in 60 tightly focused UV beams. The pentagonal and hexagonal patterns characteristic of the soccer-ball irradiation geometry are easily seen.

Significantly better pointing accuracy is expected when the alignment system is fully calibrated and between-shot feedback iterations are performed. Once calibrated, the maximum pointing error of any beam is expected to be less than 20 $\mu$m, which corresponds to 5% of the radius of a typical target. This accuracy will be more than sufficient for precision laser-fusion experiments, both direct drive and indirect drive.

### Future Work

The project to upgrade the OMEGA laser system was aimed at creating a system that can be enhanced in various stages to meet the progressively more stringent demands of the planned fusion experiments. The achievement of 40 kJ of UV at ~7% beam balance, while exceeding system acceptance criteria, is only part of what will enhance the probability of success of the LLE experimental plan.[1] This plan calls for distributed phase plates (DPP's), two-dimensional smoothing by spectral dispersion (SSD), and initial pulse shaping (at ~20:1 contrast) to be implemented during FY96. These enhancements are expected to produce on-target irradiation with (rms) nonuniformities below ~5%. Ultimately, high-contrast pulse shaping (400:1), power balance control, and additional uniformity enhancements are needed to reduce nonuniformities below 2%, to enable OMEGA to be used for the implosion of high-performance capsules under near-ignition conditions.

### Conclusions

The acceptance tests for OMEGA have demonstrated performance results that exceed requirements. The driver produces output pulses that are highly stable in amplitude, pulse width, and wavelength, resulting in stable and predictable performance of the entire laser system. Separate tests have also shown that the driver has the excess gain capability necessary for the future implementation of SSD and pulse shaping.

The OMEGA laser has produced over 40 kJ in the UV and has irradiated targets with up to 37 kJ with <8% rms imbalance in the energies of the 60 beams. The consistent achievement of high frequency-conversion efficiency (~75%) is indicative of good beam quality and control of the various beam and crystal parameters. The consistency of this performance over many days of operation is proof of the overall optomechanical stability of the system. Also, a 15-shot series including nine consecutive target shots has demonstrated the 1-h shot cycle that is necessary for a productive experimental program.

OMEGA is now a well-characterized system that performs above specifications. Once the planned enhancements for the control of pulse shape and uniformity are in place, the system will be uniquely capable of conducting precision direct- and indirect-drive fusion experiments.

### ACKNOWLEDGMENT

This work was supported by the U.S. Department of Energy Office of Inertial Confinement Fusion under Cooperative Agreement No. DE-FC03-92SF19460, the University of Rochester, and the New York State Energy Research and Development Authority. The support of DOE does not constitute an endorsement by DOE of the views expressed in this article.

### REFERENCES

1. OMEGA Upgrade Program Plan, University of Rochester, Laboratory for Laser Energetics (May 1994).
2. R. S. Craxton, ed., *OMEGA Upgrade Preliminary Design*, Laboratory for Laser Energetics Report DOE/DP 40200-101, University of Rochester (1989).
3. W. Seka, S. D. Jacobs, J. E. Rizzo, R. Boni, and R. S. Craxton, Opt. Commun. 34, 469 (1980).
4. R. S. Craxton, IEEE J. Quantum Electron. QE-17, 1771 (1981).

5. Laboratory for Laser Energetics LLE Review **55**, NTIS document No. DOE/DP/40200-257, 1993 (unpublished), p. 178.

6. Laboratory for Laser Energetics LLE Review **56**, NTIS document No. DOE/DP/40200-277, 1993 (unpublished), p. 225.

7. Laboratory for Laser Energetics LLE Review **57**, NTIS document No. DOE/SF/19460-02, 1993 (unpublished), p. 32.

8. Laboratory for Laser Energetics LLE Review **58**, NTIS document No. DOE/SF/19460-17, 1994 (unpublished), p. 90.

9. T. R. Boehly, Ed., *OMEGA Upgrade Project Final Design Review* (KD3′), September 1993.

10. D. R. Speck, Lawrence Livermore National Laboratory Laser Program Annual Report 1988/89, UCRL-50021-88/89 (1993), pp. 4-10–4-12.

11. Proposal for Renewal Award for Cooperative Agreement DE-FC03-85-DP402000 (US DOE/LLE, October 1991), pp. 2.70–2.84.

12. D. C. Brown, in *High-Peak-Power Nd:Glass Laser Systems* (Springer-Verlag, New York, 1981), Vol. 7.7, pp. 227–235.

13. D. C. Brown, op. cit., p. 43.

14. S. D. Jacobs, K. A. Cerqua, T. J. Kessler, W. Seka, and R. Bahr, in *Laser Induced Damage in Optical Materials: 1984*, Nat. Bur. Stand. (U.S.) Spec. Publ. 727 (U.S. Government Printing Office, Washington, DC, 1984), p. 15.

15. W. L. Smith and T. F. Deaton, Lawrence Livermore National Laboratory Laser Program Annual Report 1979, UCRL-50021-79 (1980), p. 2-209.

16. D. Eimerl, Ferroelectrics **72**, 95 (1987).

# A Novel Energy Measurement System for the OMEGA Laser

Target experiments conducted using the OMEGA laser system will require an on-target, beam-to-beam UV energy balance of 3%–4%. As a prerequisite, we have implemented an accurate beam-energy diagnostic system. This system is capable of measuring the UV laser energy and the residual green and IR energies of all 60 beams with a relative beam-to-beam accuracy of a fraction of a percent.

**Overview of the Harmonic Energy Diagnostic (HED)**

The stringent requirements imposed on the harmonic energy diagnostic (HED) system stimulated the adoption of a novel approach that is fundamentally different from the system implemented previously on the 24-beam OMEGA laser (see Fig. 63.14). The only common element is the use of integrating spheres that sample fractions of all three wavelengths emerging from the frequency-conversion crystals. The previous system [Fig. 63.14(a)] used discrete PIN diode detectors, with colored glass filter stacks, to isolate and sample the wavelengths of interest. The electrical signals generated by these detectors were carried by long triax cables to a central diagnostic location where they were digitized and processed by a computer. It was generally accepted that this measurement technique would be too expensive and not sufficiently precise for the 60-beam system. In the new approach [Fig. 63.14(b)] a fiber-optic delivery system coupled to a CCD detector array is used. Fibers carry the light at all three wavelengths from the integrating spheres, one per beamline, to a common location for measurement. By separating each wavelength at the output end of these fibers, only one fiber is required for each sphere, thus reducing the number of components. Furthermore, by separating the wavelengths for all the fiber-optic outputs simultaneously, the fiber outputs can be optically coupled to a

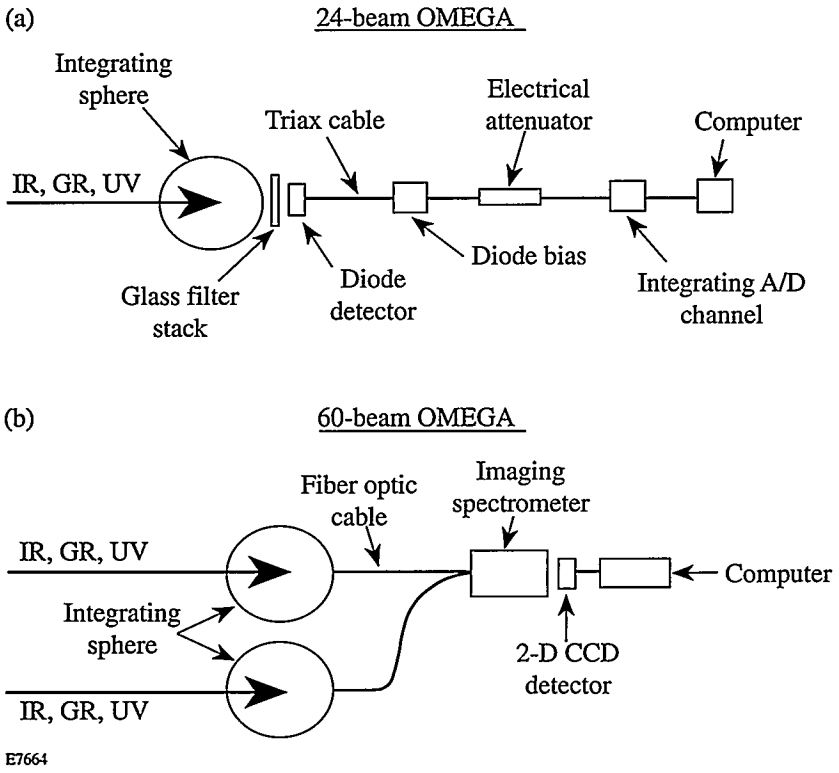


Fig. 63.14
Techniques used for laser-energy measurement on (a) the original, 24-beam OMEGA system and (b) the upgraded, 60-beam system. In the original system PIN photodiode detectors looked into an integrating sphere through three filter stacks, one for each wavelength (IR, green, and UV), and the signals were transmitted electrically to a computer. In the new system, a 300-$\mu$m-diam optical fiber samples the three wavelengths at each integrating sphere and is connected to one of two imaging spectrometers. The images are read out by a CCD detector.

single, large-format, two-dimensional CCD array detector. This architecture eliminates the need for individual detectors and acquisition channels.

Within each stage-F alignment sensor package (F-ASP) there is a three-wavelength energy pickoff, one for each beamline. The optical system is shown schematically in Fig. 63.15. The pickoff is a wedged, full-aperture piece of fused silica that is tilted at 5° to the incoming beam. The surfaces of the pickoff are curved, with radii chosen to produce a net optical power of zero in transmission. The first surface is uncoated and provides a Fresnel reflection of ~4% for each of the three wavelengths. The second surface is antireflection coated; approximately 0.5% of the beam energy is reflected from this surface but, because of the wedge, this reflection is prevented from entering the integrating sphere (see below). A second ~4% reflection occurs from a 5-in.-diam flat wedge, also made of fused silica and also tilted at 5°. The beam then passes through a window into a vacuum tube, through focus, and through a lens that recollimates it at a diameter of 36 mm before it enters the integrating sphere. A 2-in. disk of Spectralon™[1] (sintered Teflon, a highly diffusing material with a high damage threshold) is placed in the directly irradiated portion of the integrating sphere. The remainder of the sphere is painted on the inside with $BaSO_4$.

The second wedge is uncoated and serves two purposes. First, it attenuates the beam energy to 0.16% of its initial value to avoid damaging the inside of the integrating sphere. Second, it is tilted in the orthogonal plane to that of the first wedge so that the net attenuation of both wedges is the same for both "*s*" and "*p*" polarizations; this is important because the polarization of the residual IR is indeterminate. The vacuum tube is used to avoid air breakdown in the vicinity of focus, where a knife edge eliminates reflections off the second surface of each wedge. (Both wedges are in the same plane.) Laser energy transmitted through the second wedge is absorbed by a piece of 19-mm-thick filter glass. The optical design ensures that the integrating sphere is located at a system image relay plane. Thus, if co-propagation[2] is added to the system, the main and foot pulses will be spatially separated at the rear of the integrating sphere. A second sphere will then be added to diagnose the foot pulse.

The energy in each integrating sphere is sampled using a large-core, 300-$\mu$m-diam, silica optical fiber. These fibers are routed through dedicated fiber-optic conduits that protect the fibers and make them less susceptible to bending-radius changes caused by incidental touching or bumping during routine system maintenance. (Changing the bending radius changes the transmission through the optical fiber.[3]) The fibers are bundled in an ordered array of rows and columns and connected to the input of the HED measurement system. This is a spectrometer that images the output ends of all fibers onto a single CCD detector. The dispersion of the spectrometer provides for the formation of three discrete images of each fiber, one for each wavelength (see Fig. 63.16). The integrated intensity of each image is proportional to the energy in the associated beamline at the selected wavelength. The constant of proportionality is obtained from cross-calibration with conventional full-energy, full-aperture absorption calorimeters. These calorimeters are located at the output of the F-ASP structures and are rotated into the beamlines when recalibration is required. These calorimeters provide absolute energy calibration at each wavelength for each beamline.

### Integrating Sphere

Significant measurement errors due to speckle can result when sampling coherent light from an integrating sphere. These errors originate from natural shot-to-shot pointing and wavefront variations in the laser output and occur when the number of speckles incident on the detector, or fiber in this

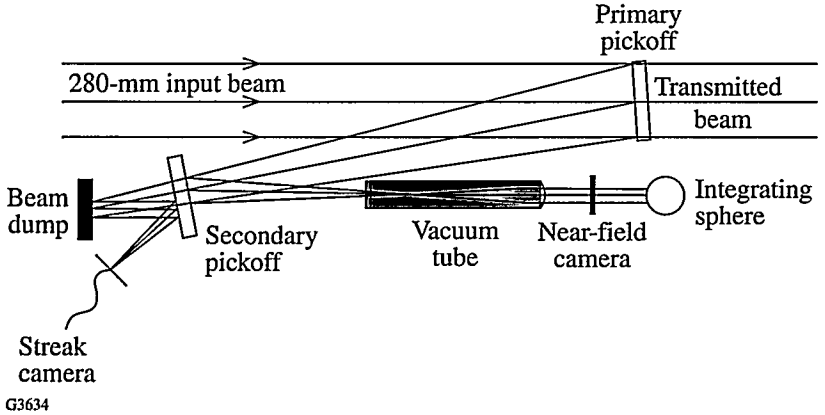


Fig. 63.15
Optical layout within the stage-F alignment sensor package (F-ASP). A small fraction of the energy in each beam is split off by the combination of a curved primary pickoff and a flat, wedged secondary pickoff and down-collimated to a 6-in.-diam integrating sphere.

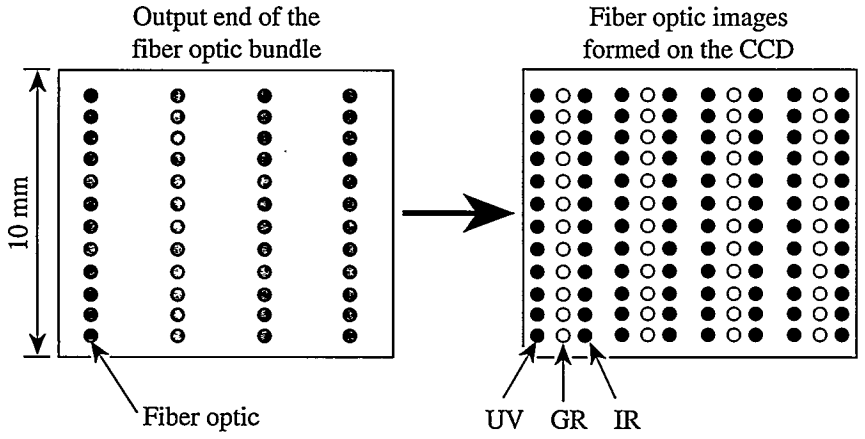


Fig. 63.16
Schematic of the output end of one of the two fiber-optic bundles (left). Each 300-$\mu$m fiber is shown as a dark circle. The spectrometer images this 10-mm-square bundle onto the CCD array as shown on the right, creating three images of each fiber, one for each wavelength. There are 96 inputs for each spectrometer. Of the 48 inputs shown, 30 are used for beam-energy measurements.

case, is small enough to produce poor sampling statistics. In the HED implementation, the 300-$\mu$m-diam fiber was tested to determine if it was compatible with the performance requirements of this instrument. A prototype integrating sphere and fiber-optic system were set up for this purpose. Two fibers were attached at different points to this sphere and imaged onto a single CCD detector (see Fig. 63.17). The sphere was illuminated with coherent light from a pulsed laser system, and the ratio of the signals from the fiber images on the CCD was recorded. The ratio of the two CCD signals remained constant, indicating that the detection system was insensitive to changes in the speckle pattern.

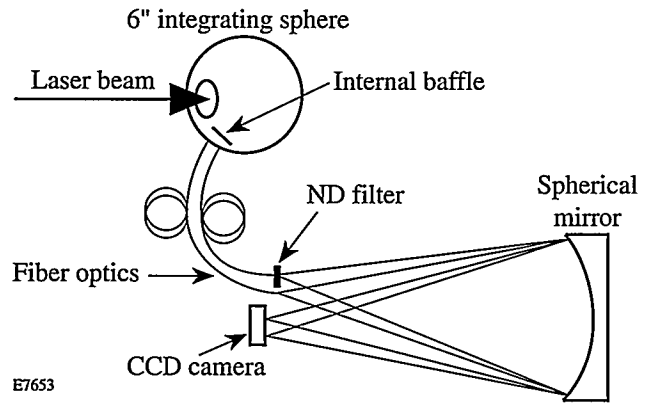


Fig. 63.17
Setup for determining the energy measurement sensitivity to speckle. Two fibers are linked to one integrating sphere and imaged onto the same CCD array. The ratio of the two CCD images remains constant from shot to shot, indicating insensitivity to changing speckle patterns.

## CCD Detector

Considerable testing of the detection system (integrating sphere, fiber, spectrometer, and CCD array) was carried out to establish its efficacy in terms of both performance and cost. The linearity of the CCD detector response was tested over four orders of magnitude for short-pulse (<1-ns) signals in the IR, the green, and the UV. The same setup as Fig. 63.17 was used for this purpose, with one of the two fiber outputs attenuated by a factor of 5 relative to the other fiber using neutral density filters at the output of the fiber. The intensity ratio of the two images remained constant within a small but measurable deviation (see Fig. 63.18). A better fit was obtained by assuming that the CCD signal $S$ was of the form $S = aE + bE^2$, where $E$ is the optical input signal. Best fits for the coefficients $a$ and $b$ were found for the operating range of interest (a relative input signal in the range of 0.1–1.0) as

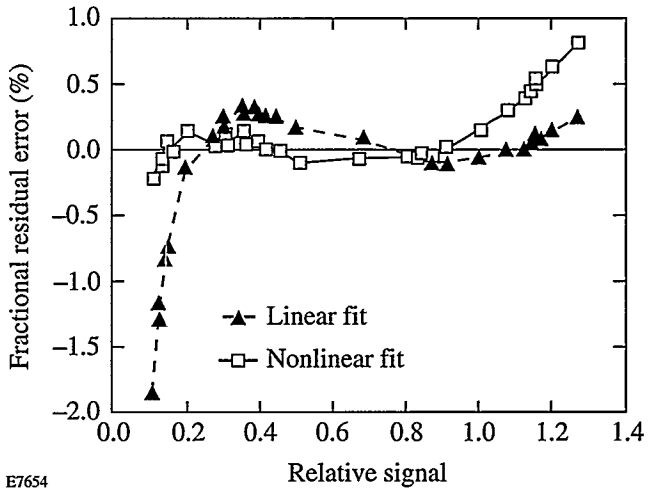


Fig. 63.18
Results from a linearity test on the CCD array. Two signals were imaged onto the CCD array, as in Fig. 63.17, but with one signal attenuated by a factor of 5. Deviations of the ratio of measured signals from this factor are plotted on the vertical axis assuming a linear fit (dashed curve) and a nonlinear fit that corrects for deviations from linearity using a small quadratic term (solid curve). The quadratic term is a fraction 0.027 of the linear term at a relative signal of 1.0. The nonlinear fit is optimized for relative signals in the range 0.1–1.0.

shown in Fig. 63.18, which illustrates the linear and nonlinear fits for the UV wavelength. The residual error corresponding to the nonlinear fit represented a very small (~0.2%) overall measurement error that can remain uncorrected. The nonlinear correction is in fact not strictly necessary for beam energy balance since all beams are equally affected by the small nonlinearity, which is only 2.7% at the maximum optical energy $E$ (i.e., $bE/a = 0.027$ at this point). Figure 63.18 also validates the speckle-insensitive nature of the HED detection system.

### Optical Design of the HED Spectrometer

The spectrometer for the HED energy measurement system is designed to match the characteristics of the fiber-optic input bundle, the CCD array, and the imaging system. The HED system is a low-dispersion instrument with fast (*f*/1.6) optics that match the numerical aperture of the fibers in the ultraviolet for maximum collection efficiency. The fiber-optic bundle does not need to be imaged near the diffraction limit of the *f*/1.6 system since it is sufficient for the light from each fiber in the bundle to be collected and concentrated into a confined spot. In fact, 50 times diffraction-limited performance (50 XDL) is sufficient to concentrate all the light into a circle of diameter less than 500 $\mu$m at the detector, allowing large amounts of astigmatism, coma, and field curvature to be tolerated. This permitted a cost-effective, all-reflective spectrometer design using parabolic mirrors. An on-axis Pfund[4] parabolic system using flat mirrors with central holes in combination with the parabolic mirrors was selected (Fig. 63.19). The parabolic mirrors were diamond turned to a figure tolerance of half a wave and then post-polished to remove the grooves. After post-polishing, the final figure of the parabolas deviated by as much as two waves, which was well within the specifications for the HED application. This loose surface figure specification made the post-polishing step easy and cost effective. Additionally, the post-polishing ensured a final surface roughness of less than 5 Å rms. All mirror surfaces have protected, enhanced UV aluminum coatings with insignificant reflective losses. Scattered light due to the central hole in the flat pickoff mirrors is minimal. Ray-trace evaluation determined that the fiber images, although heavily aberrated, especially at the edge of the field, concentrated the light into well-defined regions on the detector. An example of a digitized CCD image of a single fiber is shown in Fig. 63.20.

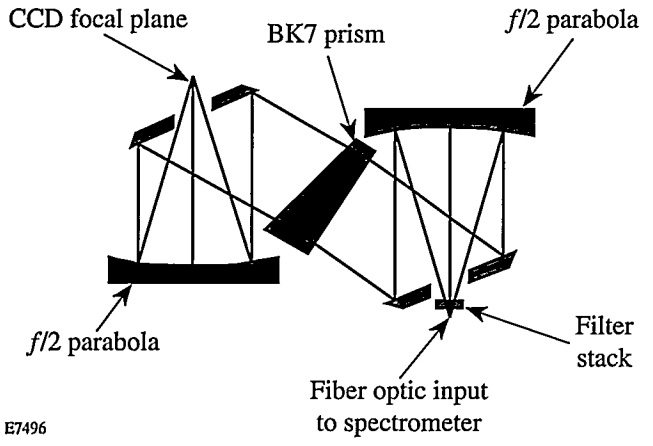


Fig. 63.19
Optical design of the HED spectrometer. This is based on Pfund's use of plane mirrors with central openings to avoid astigmatism when using parabolic collimating and focusing elements. A BK7 prism is used as the dispersive element. A single glass filter stack is used at the input to attenuate the IR, green, and UV light from each fiber.

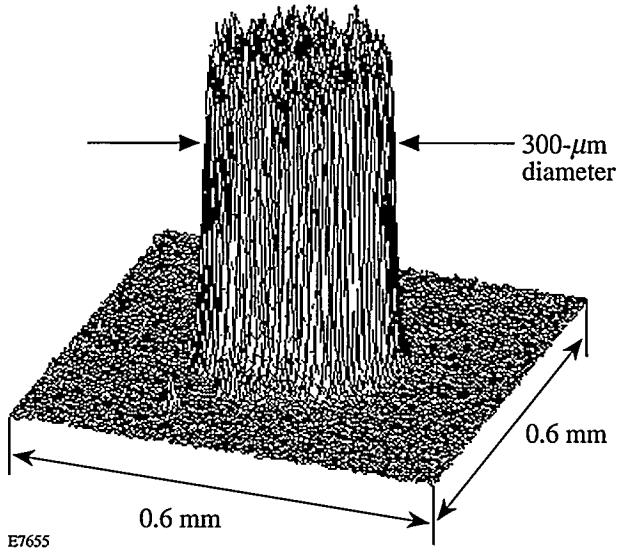


Fig. 63.20
Isometric view of a digitized CCD image of a single fiber from the multifiber bundle as imaged by the spectrometer. The fiber image is well confined within a square region of the array.

The dispersive element chosen for the HED is a single-pass, uncoated, 6° BK7 glass prism, which provides the required dispersion of ~400 nm/mm. Ray-trace analysis determined that multiple-order surface reflections from the prism faces and other reflective surfaces do not reach the detector plane.

To ensure adequate performance of the HED system it was essential to remove the vacuum window from the CCD camera. This was done primarily because this window created a serious reflected-light problem at the detector surface (see Fig. 63.21). The CCD array surface is reflective, allowing the converging light cone that focuses on this surface to be reflected back to the input vacuum window. This reflection, which is now diverg-

ing, is reflected back to the CCD detector surface by the window, showing up as a halo of light around the initial focal spot. The multiple reflections supported by this geometry result in the signal being spread for several millimeters across the detector surface. A three-wavelength antireflection coating for the window would have at best a reflectivity of a few tenths of 1% from each surface, and the image quality would still be spoiled. Tilting the window enough to walk the reflections off the array would introduce significant astigmatism. Operating the CCD camera without a vacuum window requires purging of the spectrometer with dry nitrogen (at 1 psi above ambient pressure) to protect the cooled CCD array from the condensation of atmospheric moisture. This requirement significantly affected the mechanical design of the spectrometer housing.

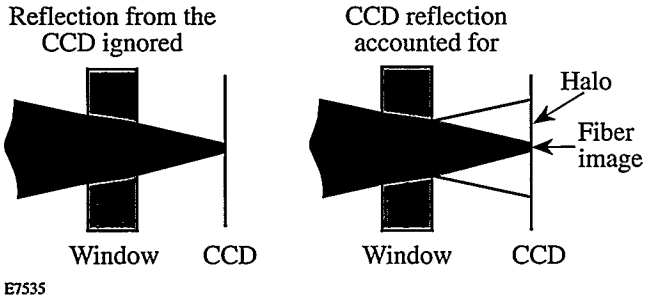


Fig. 63.21
Influence of the CCD camera window on image quality. The converging cone of light rays is focused on the CCD plane (left). With a window, some light is reflected from the CCD surface (right) and back from the window onto the CCD, leading to a halo around the image and errors in the energy measurement.

## Mechanical Design of the HED Spectrometer

The primary considerations for the HED spectrometer enclosure were mechanical stability, operational simplicity, and nitrogen purging. These considerations ruled out some designs found in several commercially available spectrometers. For example, some larger spectrometers used a thick, flat mounting plate for the optical elements and a light-tight, sheet-metal cover, but this design would have been hard to seal and maintain at a positive pressure. Ray-trace analysis showed that the 50 XDL imaging requirement results in tolerances in the range of milliradians and hundreds of microns. Thus it was sufficient to machine optical mounting stations directly into the spectrometer housing without any positioning adjustments, allowing the spectrometer housing to be fabricated from solid blocks of aluminum. The housing is rigid and stable and contains the HED optics folded into a compact 20-in. × 16-in. × 9-in. package. A photograph of the spectrometer is shown in Fig. 63.22. The only adjustable component in the system is the mount for the fiber-optic bundle. This mount allows for $x$, $y$, $z$, and $\theta$ motion for proper centering, focusing, and angular orientation of the images on the CCD. O-ring gaskets are used to seal the spectrometer, allowing for the 1-psi overpressure and a small flow of dry nitrogen.

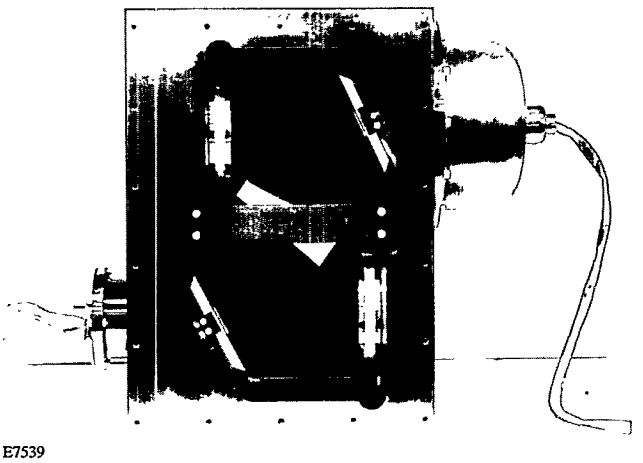


Fig. 63.22
View of the imaging spectrometer, showing the interior cavity that has been hollowed out from a solid block of aluminum. The optical elements (two parabolic mirrors, two flat mirrors, and a prism) are viewed edge-on. The fiber-optic bundle is inserted into the port on the upper right side. The CCD camera is mounted on the lower left side with the array behind the flat mirror. A gasketed plate is used to cover the front.

## Multichannel Fiber-Optic Input Bundle

Fabrication of the 96-fiber bundle (300-$\mu$m core diameter) presented some challenge. This number of fibers was needed to accommodate 30 (three-color) input channels for UV conversion measurements, 30 channels for passive IR beam-balance measurements (taken from flip-in pickoffs in the final, stage-F spatial filters), and several spare channels. At the other end of the bundle each fiber terminates with a fiber-optic patch panel. Each fiber in the bundle is 1 m long.

The fiber-bundle array facing the HED spectrometer is arranged in eight columns of 12 fibers (see Fig. 63.23). Each fiber must be held at a precise transverse location within the bundle. Only the rotation of the fiber-optic core relative to the optical axis of the fiber is uncontrolled—and unimportant. To ensure that the image of each fiber optic reaches the CCD detector within a few pixels of the desired location, the horizontal and vertical position tolerance of each fiber within the

bundle is 50 μm. The tip-tilt angle of the fiber relative to the output surface normal is held to better than 2 mrad to prevent signal loss and unnecessary scattering of light due to miscentering on the clear aperture of the spectrometer imaging optics. Finally, all fibers must be in the same plane to within 25 μm to ensure that the image from each fiber is focused at the detector surface.

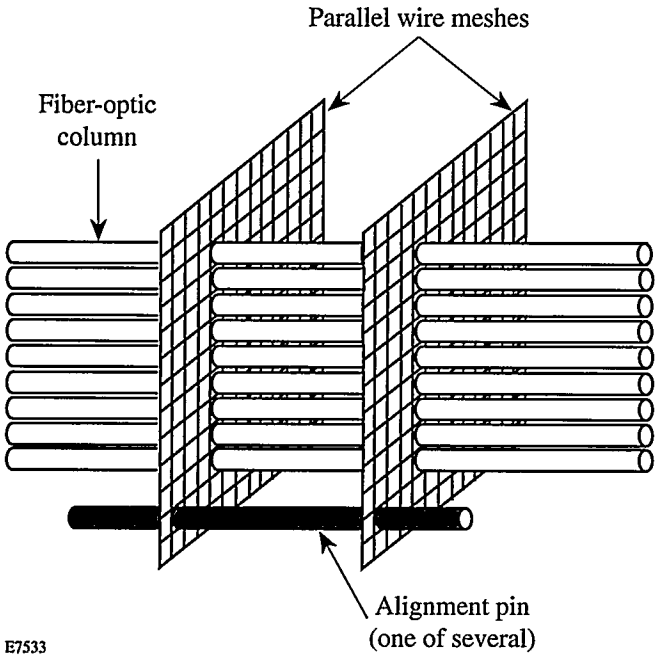


Fig. 63.23
Wire meshes used to hold the fiber bundle in position. Metal alignment pins around the perimeter (one shown) support the meshes. Nine fibers from a column are shown; the mesh holds 96 fibers in total (8 columns of 12).

This precision is achieved using two parallel wire meshes spaced 8 mm apart (Fig. 63.23). The wire meshes are coated with 5 to 10 μm of parylene prior to insertion of the fibers to prevent scratching of the fibers. The pitch and wire diameter of the mesh are selected such that the outer diameter of the fiber-optic plastic buffer fits tightly into the mesh opening. The wire meshes are cut into 25-mm squares and secured with several pins around the perimeter. Before inserting the fibers into the mesh assembly, a 10-mm length of the plastic buffer is removed (to prevent interference with the subsequent polishing operation), exposing the glass-clad core of the fiber.

During the assembly process, each fiber is inserted such that the plastic buffer extends a few millimeters beyond the second mesh. After insertion, each column of 12 fibers is held in position with a small amount of fast-curing epoxy. After all eight columns are in place, an enclosure around the fibers and the supporting mesh is filled with epoxy. The selected epoxy is one that cures with minimal shrinkage, is opaque from the IR to the UV, and can be coarse ground and polished. In addition, it has a low viscosity and is slow curing in order to fill in the spaces between the fibers and the supporting mesh and allow trapped air to escape. Once the epoxy is fully cured, the forms are removed and the exposed epoxy block is ground into a 1-in.-long, 5/8-in.-diam, cylindrical shape. The fiber output end is then coarse ground until all 96 fibers are exposed. A 3/4-in.-diam stainless steel tube with 1/32-in.-thick walls is slid over this epoxy rod such that the output end of the epoxy assembly extends about 1/8 in. beyond the end of the stainless steel tube. Additional epoxy is used to fill the gap between the epoxy rod and the stainless steel tube. Once cured, the output end of this assembly is fine ground and polished. A 3-in.-diam, 1/2-in.-thick aluminum disk with a 3/4-in.-diam hole for the bundle to slide into ensures that the output face of the bundle is ground flat. All work is done using a figure-eight rubbing motion under a steady stream of cold water. Approximately two hours of polishing with abrasive grit sizes ranging from 30 μm to 0.3 μm produces a polished bundle free of any scratched or cracked fiber-optic ends when viewed under an optical microscope.

### Installation of the HED System

Fully assembled, each HED spectrometer, together with its supporting electronics and utilities, weighs about 300 lbs. Half the weight is due to the spectrometer housing, with the remaining weight due to the steel enclosure, power supplies, and CCD cooling units. Each system is housed in an EMI-shielded rack and placed on top of an F-ASP structure (see Fig. 63.24). The optical fibers from the integrating spheres are connected to the patch panels on the enclosures. A 70-psi dry nitrogen line, a fiber-optic communications connection to the remote computer network, a 120-V ac power feed, and an RG58 coax cable from the timing system are all connected to the HED unit. A trigger signal is provided by the timing system 10 s before the laser system fires so the HED can initiate internal preshot preparations. These preparations include blanking the CCD array to ensure that any residual charge has been cleared from each pixel before new data is taken. The spectrometer shutter is opened from 25 ms prior to a laser shot to 25 ms after the shot to ensure capture of the images on the CCD array. The CCD frame is later transferred from the HED unit via a computer network to the data acquisition, analysis and archiving computers. These computers reduce the data to determine the energies and conversion efficiencies and the beam-to-beam energy balance.

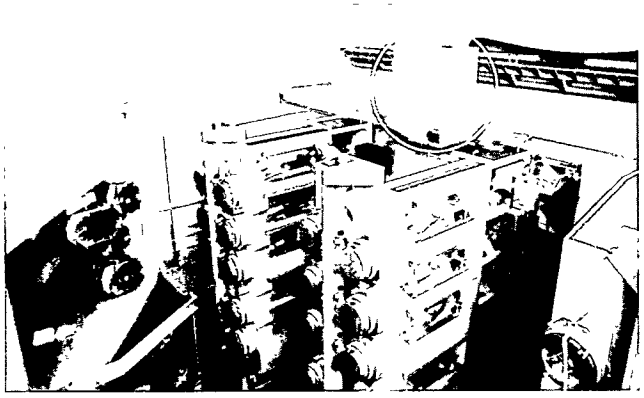

E7540

Fig. 63.24
HED enclosure shown inside the white circle on top of the F-ASP structure. The fiber optics are routed from each integrating sphere, through the square conduits, to the back of the HED rack.

## Conclusion

The harmonic energy diagnostic (HED) is now an integral part of the OMEGA laser system. Data collected by the HED has been used to perform on-line, high-power, fine tuning of the frequency-conversion crystals for the 60-beam system. In addition, the HED system has provided the energy measurements used to confirm that the laser system meets its output-energy and beam-to-beam energy-balance acceptance specifications. In the future the HED, together with other instrumentation, will provide crucial measurements needed to improve the on-target energy balance.

## ACKNOWLEDGMENT

This work was supported by the U.S. Department of Energy Office of Inertial Confinement Fusion under Cooperative Agreement No. DE-FC03-92SF19460, the University of Rochester, and the New York State Energy Research and Development Authority. The support of DOE does not constitute an endorsement by DOE of the views expressed in this article.

## REFERENCES

1. "Spectralon" is a proprietary product available from Labsphere, N. Sutton, NH 03260.
2. R. S. Craxton, ed., *OMEGA Upgrade Preliminary Design*, Laboratory for Laser Energetics Report DOE/DP 40200-101, University of Rochester (1989).
3. A. A. P. Boechat *et al.*, Appl. Opt. **30**, 321 (1991).
4. R. A. Sawyer, *Experimental Spectroscopy*, 3rd ed. (Dover Publications, NY, 1963).

# Self-Consistent Cutoff Wave Number of the Ablative Rayleigh-Taylor Instability

The Rayleigh-Taylor instability occurs at the interface between heavy and light fluids when the heavy fluid is accelerated by the light fluid. The classical treatment[1] of a sharp interface shows that a small perturbation at this boundary will grow as $e^{\gamma t}$, where $\gamma = \sqrt{A_T kg}$ is the linear growth rate, $k$ is the mode wave number, $g$ is the acceleration, and

$$A_T = (\rho_h - \rho_l)/(\rho_h + \rho_l)$$

is the Atwood number ($\rho_h$ and $\rho_l$ are the heavy- and light-fluid densities, respectively). The ablation front of an inertial-confinement-fusion (ICF) imploding target is subject to this instability because the compressed target is accelerated by the low-density ablating plasma. If small perturbations caused by either target imperfections or illumination nonuniformity grew classically, they would grow to sufficient amplitude to destroy the shell of the target and degrade the performance of the implosion. However, because the shell material is ablated by the laser, the growth is reduced with respect to the classical value and, for sufficiently short wavelengths, the instability is suppressed.[2–12] Thus, only those modes with wave number $k$ smaller than a critical value ($k < k_c$, where $k_c$ is the cutoff wave number) are unstable.

The calculation of the cutoff wave number of the unstable spectrum has been previously attempted by several authors.[7,8,10] The most common analytic models of the Rayleigh-Taylor instability of laser-illuminated pellets consider inviscid and incompressible fluids. The incompressible model[7,8] is not self-consistent as the equilibrium and the perturbations are described by different equations. In this model, the equilibrium flow is compressible ($\nabla \cdot \mathbf{U} \neq 0$), but the perturbation is assumed to be divergence-free ($\nabla \cdot \tilde{\mathbf{v}} = 0$). The incompressibility condition leads to a fourth-order differential equation for the perturbation that can be analytically solved. In other models,[5,6] the assumption of a divergence-free perturbation has been removed by retaining the effects of finite thermal conductivity. However, because of the difficulties in determining the analytic solutions, a sharp-boundary model has been used in representing the equilibrium.[5] Such an approximation to the equilibrium is not self-consistent since the plasma density in the blowoff region cannot be approximated by a flat profile. Subsequently, the growth rate has been calculated using a sharp-boundary model for the perturbations and a diffuse density profile for the equilibrium.[11] The density jump across the ablation front is calculated by retaining the thermal conductivity, and the derived growth rate is in good agreement with Takabe's numerical results.[1] Nevertheless, such a model is still not self-consistent since the equilibrium and perturbed quantities satisfy different equations. A more accurate treatment of the effect of finite thermal conductivity in a diffuse density profile can be found in Ref. 9, where the growth rate of the instability is calculated semi-analytically by matching the analytic solution in the overdense region with the numerical solution in the blowoff region. The first truly analytical estimate of the cutoff wave number for direct-drive ICF without radiation effects ($\nu = 2.5$), including the effects of finite thermal conductivity, is derived in Ref. 10. In that work, the Wentzel-Kramers-Brillouin (WKB) approximation is used to determine the solution in the downstream region assuming that the mode wavelength is smaller than the density-gradient scale length and the cutoff wave number is derived by connecting that solution with the one in the upstream region.

It is noteworthy that numerical simulations of indirect-drive ICF capsule implosions have shown a different growth rate of the instability in comparison with direct drive. We attribute this difference to the mechanism of energy transfer that, in indirect-drive ICF, is dominated by radiation transport over electronic thermal conduction. According to the simple model of Ref. 13, the heat flux transported by radiation heat conduction is

$$\mathbf{q} = -(lc/3)\nabla U_p = -(lc/3)\nabla\left(4\sigma T^4/c\right),$$

where $U_p = 4\sigma T^4/c$ is the equilibrium radiation energy density and $l$ is the Rosseland mean free path. The energy flux can be written in terms of the gradient of temperature and an effective radiation thermal conductivity $K = 16\sigma T^3 l/c$, where the radiation mean free path $l$ is assumed to be proportional to some power of the temperature and density. Since the pressure-

gradient scale length is much larger than the density and temperature gradient scale length in the ablation front ($p \simeq$ const), the radiation heat conduction has a strong dependence on the temperature. Thus, it became clear that a cutoff wave number formula valid for a general thermal conduction law was needed. In this article, the formula for the cutoff is derived for an arbitrary power-law dependence of the thermal conductivity ($K \sim T^{\nu}$) with $\nu > 1$, and it can be applied to a wide class of equilibria described by different values of $\nu$. The corresponding eigenfunction is found by performing a "boundary layer" analysis of the solution in different regions of the density profile. The asymptotic matching of the eigenfunction through the boundary layers leads to an eigenvalue equation for the cutoff wave number. The analytically derived formula for the cutoff wave number is in excellent agreement with the numerical results of Ref. 6 for $\nu > 1$.

## The Model

We consider an ablatively accelerated fluid in steady state. In the frame of reference of the ablation front, the evolution of the mass density $\rho$ and the velocity $\mathbf{v}$ are described by the isobaric model of Kull and Anisimov[5]

$$\frac{\partial \rho}{\partial t} + \nabla \cdot \rho \mathbf{v} = 0 \tag{1}$$

$$\rho\left(\frac{\partial \mathbf{v}}{\partial t} + \mathbf{v} \cdot \nabla \mathbf{v}\right) = -\nabla p + \rho g \tag{2}$$

$$\nabla \cdot \left(\mathbf{v} + L_0 V_a \frac{\nabla \xi}{\xi^{\nu+2}}\right) = 0, \tag{3}$$

where $\mathbf{g} = g\mathbf{e}_y (g < 0)$, $\xi = \rho/\rho_a$ is the density normalized to its peak value $\rho_a$, and $L_0$ is the typical length of the ablation front

$$L_0 \equiv \frac{\gamma_h - 1}{\gamma_h} \frac{AK_a}{\rho_a V_a}. \tag{4}$$

Here, $K_a$ is the thermal conductivity at the peak density, $A = m_i/(1 + Z)$ is the average particle mass, and $\gamma_h$ is the ratio of specific heats. The parameter $L_0$ can be related to the density-gradient scale length $L = \rho(d\rho/dy)^{-1}$. Following Ref. 6, the equilibrium density profile can be obtained by combining Eqs. (1) and (3) into a single first-order differential equation

$$\frac{d\xi}{dy} = \frac{1}{L_0} \xi^{\nu+1}(1 - \xi) \tag{5}$$

with the boundary condition $\xi(y \to \infty) = 1$. Equation (5) yields the density-gradient scale length $L = L_0/[\xi^{\nu}(1-\xi)]$, and its minimum value[6] is proportional to

$$L_0\left(L_{\min} = \left[(\nu + 1)^{\nu+1}/\nu^{\nu}\right] L_0\right).$$

Although Eq. (5) cannot be solved analytically, an approximate solution can be found in the proximity of the peak density ($\xi \approx 1$ or overdense region) and the blowoff region ($\xi << 1$):

$$\xi^{\text{heavy}} \approx 1 - e^{-y/L_0} \qquad \xi^{\text{blowoff}} \approx \left(\frac{-L_0}{\nu y}\right)^{1/\nu}. \tag{6}$$

Equation (6) shows that the density gradient is sharp near the peak density where $L \simeq L_0$ and becomes smooth in the blowoff region where $L \simeq -\nu y$ and $-y >> L_0$. It is important to observe that the density-gradient scale length is determined by the thermal conductivity coefficient, the mass ablation rate, and the exponent $\nu$. The density profile becomes smoother as $K_a$ or $\nu$ increases.

## Linear Stability Analysis

Since the equilibrium depends on the spatial coordinate $y$ only, the perturbation can be Fourier decomposed in the $x$ direction; i.e. $Q_1 = \tilde{Q}(y) \exp(ikx + \gamma t)$ where $\gamma \to 0^+$ for wave numbers approaching the cutoff $(k \to k_c^-)$. The linearized conservation equations can be written in the following dimensionless form:

$$\left(\Gamma_a \xi + \partial_{\hat{y}}\right) \tilde{n} + \frac{\tilde{u}_y}{\hat{L}} \frac{\xi}{\epsilon_c} + \xi \hat{\nabla} \cdot \tilde{\mathbf{u}} = 0 \tag{7a}$$

$$\tilde{\pi} - i\left(\Gamma_a \xi + \partial_{\hat{y}}\right) \tilde{u}_x = 0 \tag{7b}$$

$$\left(\Gamma_a \xi + \partial_{\hat{y}} - \frac{1}{\epsilon_c \hat{L}}\right) \tilde{u}_y + \partial_{\hat{y}} \tilde{\pi} + \tilde{n}\left(\frac{\xi}{\epsilon_c Fr} - \frac{1}{\epsilon_c \hat{L} \xi}\right) = 0 \tag{7c}$$

$$\hat{\nabla} \cdot \tilde{u} - \epsilon_c \tilde{\nabla}^2 \tilde{\Phi} = 0, \tag{7d}$$

where

$Fr = V_a^2/|g|L_0$ is the Froude number, $\hat{y} = ky$, $\Gamma_a = -\gamma/kV_a$, $\hat{\nabla} = k^{-1}\nabla$, $\epsilon_c = k_c L_0$ ($k_c$ is the cutoff wave number), $\hat{L} = L/L_0$, and

$$\tilde{n} = \frac{\tilde{\rho}}{\rho}; \quad \tilde{\mathbf{u}} = -\frac{\tilde{\mathbf{v}}}{V_a}; \quad \tilde{\pi} = \frac{\tilde{p}}{\rho_a V_a^2}; \quad \tilde{\Phi} = \frac{\tilde{\rho}}{\xi^{\nu+2}}. \tag{7e}$$

Equations (7a)–(7d) can be easily combined into a single fifth-order differential equation for the density perturbation:

$$\left[\partial_{\hat{y}}\left(\Gamma_a\xi + \partial_{\hat{y}}\right)\partial_{\hat{y}} - \left(\Gamma_a\xi + \partial_{\hat{y}}\right)\right]\epsilon_c\,\hat{L}$$

$$\left[\left(\Gamma_a\xi + \partial_{\hat{y}}\right)\tilde{\Phi}\xi^{\nu} + \epsilon_c\,\hat{\nabla}^2\tilde{\Phi}\right]$$

$$+\partial_{\hat{y}}\left(\Gamma_a\xi + \partial_{\hat{y}}\right)\left[\partial_{\hat{y}}\tilde{\Phi}\xi^{\nu} + \epsilon_c\,\hat{\nabla}^2\tilde{\Phi}\right]$$

$$+\epsilon_c\,\hat{\nabla}^2\tilde{\Phi} + \tilde{\Phi}\frac{\xi^{\nu+2}}{\epsilon_c\,Fr} = 0. \tag{8}$$

Here, $V_a > 0$ and $\Gamma_a \to 0^-$. Equation (8) is an eigenvalue equation for the cutoff wave number $k_c\left(\epsilon_c = k_c L_0\right)$. We focus on equilibria characterized by $Fr > 1$, $\nu > 1$, and we order $\epsilon_c \sim Fr^{\nu/1-\nu}$. The validity of this assumption will be verified later by the matching conditions for the eigenfunction. In ICF, the Froude number varies significantly according to the target acceleration and the thermal conduction law. For the set of equilibria parameters considered in Ref. 4, $5 < Fr < g$, and it can be significantly lower for the equilibria considered in Ref. 14. The eigenfunction must satisfy the boundary conditions of vanishing perturbation at infinity; i.e., $\tilde{\mathbf{v}}(\pm\infty) = 0$, $\tilde{p}(\pm\infty) = 0$, and $\tilde{\rho}(\pm\infty) = 0$. Because of the variable scale length of the eigenfunction, three regions have been identified (Fig. 63.25): the overdense region (heavy fluid), the ablation front, and the blowoff region.

1. The Overdense Region

In ICF capsule implosions, the overdense portion of the shell represents the heavy-fluid region where $\hat{y} \sim 1$, $\rho \simeq \rho_a$, $\xi = 1 - \exp(-\hat{y}/\epsilon_c) + O\left[\exp(-2\hat{y}/\epsilon_c)\right]$, and $L >> L_0$. In this region and to lowest order in $\exp(-\hat{y}/\epsilon_c)$, Eq. (8) reduces to a constant-coefficient fifth-order differential equation

$$\left(\partial_{\hat{y}}^2 - 1\right)\left(\Gamma_a + \partial_{\hat{y}}\right)$$
$$\left(\epsilon_c\,\partial_{\hat{y}}^2 - \partial_{\hat{y}} + \Gamma_a - \epsilon_c\right)\tilde{\Phi}^h \exp\left(\hat{y}/\epsilon_c\right) = 0, \tag{9}$$

where $\Gamma_a \to 0^-$ and the superscript $h$ denotes the heavy-fluid region. The solution of Eq. (9) can be written in the following form:

$$\tilde{\Phi}^h = \left(a^h e^{-\hat{y}} + b^h e^{\alpha^-\hat{y}} + c^h e^{\hat{y}} + d^h e^{-\Gamma_a\hat{y}} + q^h e^{\alpha^+\hat{y}}\right)e^{-\hat{y}/\epsilon_c}, \tag{10}$$

where $a^h$, $b^h$, $c^h$, $d^h$, $q^h$ are integration constants and

$$\alpha^{\pm} = \left[1 \pm \sqrt{1 + 4\epsilon\left(\epsilon - \Gamma_a\right)}\right]/2\epsilon.$$

To satisfy the boundary conditions of vanishing perturbation for $\hat{y} \to +\infty$, $c_h = d_h = q_h = 0$ and Eq. (10) reduces to the simple form

$$\tilde{\Phi}^h = \left[a^h e^{-\hat{y}} + b^h e^{\left(1 - \sqrt{1+4\epsilon_c^2}\right)\hat{y}}\right]e^{-\hat{y}/\epsilon_c}. \tag{11}$$

It is important to observe that the incompressible theory $\left(\nabla\cdot\tilde{\mathbf{v}} = 0\right)$ yields only the sonic solution

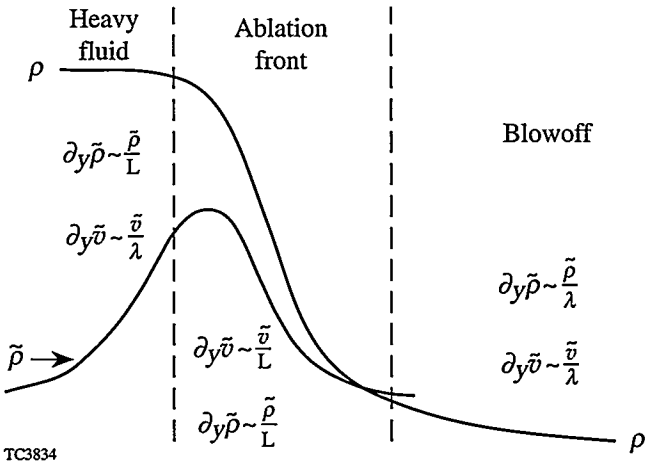


Fig. 63.25
Density profile with regions of different scale length of the perturbations. Here $\lambda$ is the mode wavelength.

$$\tilde{\rho}^{\text{sonic}} \sim \exp\left[-\hat{y}-\hat{y}/\epsilon\right].$$

Equation (11) shows that a new solution is introduced by the finite thermal conductivity. Because of the diffusive character of thermal conduction, we denote the second term in Eq. (11) as the diffusion or entropy solution. Since the mode amplitude is arbitrary, we set $a_h+b_h=1$, define the ablation front variable $z=\hat{y}/\epsilon_c$, and expand the solution for $z\sim 1$ and $\epsilon_c \ll 1$. A short calculation yields

$$\tilde{\Phi}^h = e^{-z}\left\{1-\left(1-b^h\right)\left[\epsilon_c\, z-\epsilon_c^2\,\frac{z^2}{2}\right.\right.$$

$$\left.\left.+\epsilon_c^3\,\frac{z^3}{6}+O\left(\epsilon_c^4\right)\right]-\epsilon_c^2\, b^h z\right\}. \qquad (12)$$

Each power of $z$ in Eq. (12) needs to be matched to the ablation front solution.

2. The Ablation Front Region

The ablation front is the region where the density, velocity, and temperature profiles undergo a sharp variation. In this region, $\hat{y}\sim\epsilon_c$, $L\sim L_0$, and $\xi\sim 1$. Since $\xi\sim 1$, Eq. (5) cannot be solved in this region, and an explicit expression for the spatial dependence of the density profile cannot be found. Thus, it is more convenient to use $\xi$ as the independent variable. By denoting with $\tilde{\Phi}^a$ the solution in the ablation region and after some straightforward manipulations, Eq. (8) can be rewritten in the following operator form:

$$\left(\mathcal{L}_0+\epsilon_c^2\,\mathcal{L}_2+\epsilon_c^3\,\mathcal{L}_3+\epsilon_c^4\,\mathcal{L}_4\right)\tilde{\Phi}^a = 0, \qquad (13)$$

where

$$\mathcal{L}_0 = \partial_z^3\left(\hat{L}\partial_z+1\right)\left(\xi^\nu+\partial_z\right) \qquad (13a)$$

$$\mathcal{L}_2 = -\partial_z^3\hat{L}-\partial_z\hat{L}\left(\partial_z\xi^\nu+\partial_z^2\right) \qquad (13b)$$

$$\mathcal{L}_3 = \frac{\xi^{\nu+2}}{\epsilon_c\, Fr} \qquad (13c)$$

$$\mathcal{L}_4 = \partial_z\hat{L}-1. \qquad (13d)$$

Here, $\partial_z=\xi^{\nu+1}(1-\xi)\partial_\xi$, $\hat{L}=\xi^{-\nu}/(1-\xi)$, and $z=\hat{y}/\epsilon_c$ is the ablation front coordinate ($z\sim 1$ in the ablation front region). We look for a solution of Eq. (13) in the form of an $\epsilon_c$–series $\left(\hat{\Phi}^a=\sum_{j=0}^{\infty}\hat{\Phi}_j^a\,\epsilon_c^j\right)$, and we calculate all the terms up to third order in $\epsilon_c$:

$$\mathcal{L}_0\hat{\Phi}_0^a = 0 \qquad (14a)$$

$$\mathcal{L}_0\hat{\Phi}_1^a = 0 \qquad (14b)$$

$$\mathcal{L}_0\hat{\Phi}_2^a = -\mathcal{L}_2\hat{\Phi}_0^a \qquad (14c)$$

$$\mathcal{L}_0\hat{\Phi}_3^a = -\mathcal{L}_2\hat{\Phi}_1^a-\mathcal{L}_3\hat{\Phi}_0^a. \qquad (14d)$$

Equation (14a) yields the following five homogeneous solutions:

$$\Psi_0=\frac{1-\xi}{\xi} \qquad \Psi_1=\frac{1-\xi}{\xi}z(\xi) \qquad (15a)$$

$$\Psi_2=\frac{1-\xi}{\xi}\left[\frac{z^2}{2}+\frac{1}{\nu}\int_1^\xi\frac{1+\nu\eta^\nu(\eta-1)-\eta^\nu}{\eta^{2\nu+1}(1-\eta)^2}\,d\eta\right] \qquad (15b)$$

$$\Psi_3=\frac{1-\xi}{\xi}\left[\frac{z^3}{6}-\int_1^\xi\frac{d\eta}{\eta^{\nu+1}(1-\eta)^2}\int_1^\eta z(\theta)\frac{1-\theta^{\nu+1}}{\theta^{\nu+1}}\,d\theta\right] \qquad (15c)$$

$$\Psi_4=\frac{1-\xi}{\xi}\int_{\xi_0}^\xi\frac{d\eta}{\eta^{\nu+1}(1-\eta)^2}, \qquad (15d)$$

where the function $z(\xi)$ is derived from Eq. (5):

$$z(\xi)=\int_{\xi_0}^\xi\frac{d\tau}{\tau^{\nu+1}(1-\tau)} \qquad (16)$$

($\xi_0$ is the density at $z=0$). Matching the zeroth and first-order solutions with the heavy-fluid solution yields $\tilde{\Phi}_0^a=\Psi_0$ and $\tilde{\Phi}_1^a=-\left(1-b^h\right)\Psi_1$. The second- and third-order equations [Eqs. (14c) and (14d)] are not homogeneous and require a combination of homogeneous and particular solutions to match the heavy-fluid solution. A long calculation leads to the following form of $\tilde{\Phi}_2^a$ and $\tilde{\Phi}_3^a$:

$$\tilde{\Phi}_2^a = \frac{1-\xi}{\xi}\frac{z^2}{2} - b^h\left(\Psi_1 + \Psi_2\right) \tag{17a}$$

$$\tilde{\Phi}_3^a = -\frac{1-\xi}{\xi}\left(1-b^h\right)\frac{z^3}{6} - \frac{1-\xi}{\xi}\int_1^{\xi}\frac{d\theta}{\theta^{\nu+1}(1-\theta)^2}\int_1^{\theta} ds$$

$$\times \int_1^s dx\,\frac{1-x^{\nu}}{x^{2\nu+1}(1-x)}\left[\frac{1}{\nu\,\epsilon_c\,Fr} + \frac{1-b^h}{\nu+1}\frac{1}{x}\right]. \tag{17b}$$

3. The Blowoff Region

The light-fluid or blowoff region is located downstream with respect to the ablation front. In this region, $-\hat{y} \sim 1$, $L >> L_0$, and $\xi \simeq \left(-L_0/\nu y\right)^{1/\nu} << 1$. The analysis can be simplified by introducing the new variable $\varsigma = \epsilon_c/\nu\xi^{\nu}$ and rewriting Eq. (8) in the following form:

$$M\tilde{\Phi}^l = 0, \tag{18a}$$

where

$$M = \partial_{\hat{y}}^4 + \partial_{\hat{y}}^3\frac{1}{\nu\varsigma} - 1 + \partial_{\hat{y}}\hat{\nabla}^2\frac{\nu\varsigma}{1-\xi}\left(\partial_{\hat{y}}\frac{1}{\nu\varsigma} + \hat{\nabla}^2\right) + \frac{1}{\nu\,\epsilon_c\,Fr}\left(\frac{\epsilon_c}{\nu}\right)^{2/\nu}\frac{1}{\varsigma^{1+2/\nu}}. \tag{18b}$$

Here, $\partial_{\hat{y}} = -\left(1-\xi\right)\partial_{\varsigma}$ and $\xi = \left(\epsilon_c/\nu\varsigma\right)^{1/\nu}$. Equation (18a) cannot be analytically solved for arbitrary $\nu$. However, since $\nu > 1$ for both direct- and indirect-drive ICF, one could attempt to solve Eq. (18a) by performing a $1/\nu$ expansion of the operator and eigenfunction. Such an approach is reasonable for radiation-dominated transport in a fully ionized plasma as described in Ref. 13 ($\nu \sim 5$–$8$) but less convincing for electronic transport with $\nu = 2.5$. Thus, to check the validity of the expansion, we compare the analytical solution with the numerical results for $\nu = 2.5$. Based on that comparison, we deduce whether or not the $1/\nu$ expansion is a valid approach to the solution of Eq. (18a) in the regimes of interest for direct-drive ICF.

The next step is to rewrite the operator $M$ and the eigenfunction $\tilde{\Phi}^l$ as power series in $1/\nu$:

$$M = \sum_{n=0}^{\infty} M_n\left(\frac{1}{\nu}\right)^{n-1} \tag{19}$$

$$\tilde{\Phi}^l = \sum_{n=0}^{\infty}\tilde{\Phi}_n^l(\hat{y})\left(\frac{1}{\nu}\right)^n. \tag{20}$$

Substituting Eqs. (19) and (20) into Eq. (18a) and collecting terms up to the first two orders in $1/\nu$ leads to the following equations:

$$\partial_{\hat{y}}\left(\partial_{\hat{y}}^2 - 1\right)\varsigma\left(\partial_{\hat{y}}^2 - 1\right)\tilde{\Phi}_0^l = 0 \tag{21a}$$

$$\partial_{\hat{y}}\left(\partial_{\hat{y}}^2 - 1\right)\varsigma\left(\partial_{\hat{y}}^2 - 1\right)\tilde{\Phi}_1^l + \left[\left(1-\delta\right)\left(\partial_{\hat{y}}^4 - 1\right) + \partial_{\hat{y}}\left(\partial_{\hat{y}}^2 - 1\right)\varsigma\partial_{\hat{y}}\frac{1}{\varsigma} - \frac{\delta}{1-\delta}\partial_{\hat{y}}\left(\partial_{\hat{y}}^2 - 1\right)\varsigma\ln\varsigma\left(\partial_{\hat{y}}^2 - 1\right)\right]\tilde{\Phi}_0^l = 0, \tag{21b}$$

where $\delta = \left(\epsilon_c/\nu\right)^{1/\nu}$. We first solve the lowest-order equation [Eq. (21a)]. The solution of Eq. (21a) that satisfies the boundary conditions of vanishing perturbations at infinity can be written as a linear combination $\left[\tilde{\Phi}_0^l = A^l\tilde{\Phi}_A^l + B^l\tilde{\Phi}_B^l + C^l\tilde{\Phi}_C^l\right]$ of the following homogeneous decaying solutions:

$$\tilde{\Phi}_A^l = e^{\hat{y}} \qquad \tilde{\Phi}_B^l = e^{-\hat{y}}\int_{-\infty}^{\hat{y}} dx e^{2x}\int^x \frac{d\eta}{\varsigma(\eta)} \tag{22a}$$

$$\tilde{\Phi}_C^l = e^{\hat{y}}\int_o^{\hat{y}} dx e^{-2x}\int_{-\infty}^x d\eta\frac{e^{2\eta} - e^{\eta}}{\varsigma(\eta)}. \tag{22b}$$

(Note that in the light-fluid region $-\infty < \hat{y} < 0$.) To determine the constants of integration ($A^l$, $B^l$, $C^l$), the solution in the ablation front must be asymptotically matched to the solution in the light-fluid region. To perform the matching of the eigenfunction, it is necessary to expand the ablation front solution in powers of $(1/\nu)$. A short calculation yields

$$\tilde{\Phi}^a = \frac{1-\delta}{\delta}+\frac{1}{\nu}\frac{\ln\varsigma}{\delta}+\frac{\varsigma}{\delta}\left(1-b^h\right)\left[1+\frac{1}{\nu}\left(\ln\varsigma+\frac{\delta}{1-\delta}\right)\right]$$

$$+\frac{\varsigma^2}{2(1-\delta)^2}\left\{\frac{1-\delta}{\delta}+\frac{1}{\nu}\left[2-b^h+\left(\frac{1}{\delta}-2\right)\ln\varsigma\right]\right\}$$

$$+\frac{\varsigma^3\left(1-b^h\right)}{6\delta(1-\delta)^2}\left\{1+\frac{1}{\nu}\left[\frac{1+5\delta+2\ln\varsigma(1-3\delta)}{2(1-\delta)}\right.\right.$$

$$\left.\left.+\frac{\delta\left(1-b^h\right)^{-1}}{2\,\epsilon_c\,Fr}\right]\right\}+O\left(\frac{1}{\nu^2}\right). \qquad (23)$$

Matching the lowest power of $1/\nu$ yields $A^l=(1-\delta)/\delta$, $B^l=0$, and $C^l=0$. The next step is to determine the first-order correction to $\tilde{\Phi}^l$ by substituting $\tilde{\Phi}_0^l$ into Eq. (21b) and solving for $\tilde{\Phi}_1^l$. Combining $\tilde{\Phi}_0^l$ and $\tilde{\Phi}_1^l$ gives the solution of the light-fluid equation up to first order in $1/\nu$:

$$\tilde{\Phi}^l \simeq \frac{1-\delta}{\delta}e^{\hat{y}}\left(1+\frac{1}{\nu}\frac{\ln\varsigma}{1-\delta}\right)+\frac{1-\delta}{\nu}\,C_1^l\,\tilde{\Phi}_C^l, \qquad (24)$$

where $C_1^l$ is determined by matching Eq. (24) with the ablation front solution [Eq. (23)]. To perform the matching, we rewrite $\tilde{\Phi}^l$ for $\varsigma\to 0$:

$$\tilde{\Phi}^l(\varsigma\to 0)\simeq\frac{1-\delta}{\delta}+\frac{1}{\nu}\frac{\ln\varsigma}{\delta}$$

$$-\frac{\varsigma}{\delta}\left\{1+\frac{1}{\nu}\left[\ln\varsigma+\frac{\delta}{1-\delta}\left(1-C_1^l\ln 2\right)\right]\right\}$$

$$+\frac{\varsigma^2}{2(1-\delta)^2}\left\{\frac{1-\delta}{\delta}\right.$$

$$\left.+\frac{1}{\nu}\left[1-C_1^l+\left(\frac{1}{\delta}-2\right)\ln\varsigma\right]\right\}$$

$$+\frac{\varsigma^3}{6(1-\delta)^3}\left\{-\frac{1-\delta}{\delta}+\frac{1}{\nu}\left[C_1^l\left(\ln 2+\frac{1}{2}\right)-3\right.\right.$$

$$\left.\left.+\left(3-\frac{1}{\delta}\right)\ln\varsigma\right]\right\}+O\left(\varsigma^4\right). \qquad (25)$$

Matching equal powers of $1/\nu$ in Eqs. (23) and (25) leads to the following relations:

$$C_1^l=b^h=2\left(1-\frac{\ln 2}{\nu}\frac{\delta}{1-\delta}\right) \qquad (26)$$

$$\frac{1}{\epsilon_c\,Fr}\simeq\left(\frac{\epsilon_c}{\nu}\right)^{-1/\nu}+2\left[1-\left(\frac{\epsilon_c}{\nu}\right)^{1/\nu}\right]^{-1}. \qquad (27)$$

In Eq. (27) all the terms up to first order in $1/\nu$ are retained. Higher-order terms in $1/\nu$ can be derived by solving Eq. (18a) to next order in $1/\nu$ and matching the solution with the $1/\nu$ expansion of the ablation front solution.[15] Using the results of Ref. 15, Eq. (27) can be rewritten in the following form:

$$\epsilon_c=\frac{\mu_0(\nu)}{Fr}\epsilon_c^{1/\nu}\,A_T(\epsilon_c) \qquad A_T(\epsilon_c)=\frac{1-\mu_0(\nu)\,\epsilon_c^{1/\nu}}{1+\mu_0(\nu)\,\epsilon_c^{1/\nu}}. \qquad (28)$$

Here, $\mu_0(\nu)=(2/\nu)^{1/\nu}/\Gamma(1+1/\nu)$, $\epsilon_c=k_cL_0$, and $A_T$ is an effective Atwood number depending on the mode wavelength.

**Discussion**

The physical interpretation of the Atwood number in Eq. (28) is straightforward and may help to resolve the controversy about the right value of $A_T$ to be used in the growth rate formulas. The classical definition of the Atwood number for a heavy fluid of constant density $\rho_h$ superimposed on a light fluid of constant density $\rho_l$ is $A_T=(\rho_h-\rho_l)/(\rho_h+\rho_l)$. However, for a monotonic diffuse density profile, the appropriate definition is $A_T=\left(\rho^+-\rho^-\right)/\left(\rho^++\rho^-\right)$, where $\rho^+$ and $\rho^-$ are the fluid densities calculated at some points where the eigenfunction is evanescent. For long-wavelength modes ($\epsilon_c=k_cL_0<<1$), the eigenfunction for $\tilde{v}$ decays exponentially $\tilde{v}\sim e^{-k|y|}$ and becomes evanescent at a distance $d$ of some wavelengths $\lambda$ from the peak $y=0$ ($d=\theta\lambda$, where $\theta$ is a constant of order unity). Thus, the Atwood number should be defined by setting $\rho^+=\rho(d)$ and $\rho^-=\rho(-d)$. Using the equilibrium density profile $\rho=\xi\rho_a$ yields

$$\rho(d)=\rho_a+O\left(e^{-1/\epsilon_c}\right)$$

and

$$\rho(-d)\simeq\rho_a(\epsilon_c/\nu)^{1/\nu}/(2\pi\theta)^{1/\nu},$$

and the Atwood number of Eq. (28) is recovered by choosing $\theta = 1/2\pi\nu\mu_0^\nu$. It is important to observe that Eq. (28) can also be obtained by balancing the classical growth rate $\gamma_{cl} = \sqrt{A_T(\epsilon)kg}$ with an effective ablation damping $\gamma_{ab} = -kV_{\text{eff}}$, where $V_{\text{eff}}$ is the geometric average of the ablation velocity evaluated at distances $d$ and $-d$ from the peak of the eigenfunction, $V_{\text{eff}} = \sqrt{V(d)V(-d)}$. Setting $\gamma \simeq \gamma_{cl} + \gamma_{ab} = 0$ yields Eq. (28) for the cutoff wave number.

To test the validity of the $1/\nu$ expansion, we compare the cutoff wave number obtained by solving Eq. (28) with the numerical results available in the literature. Figure 63.26 shows a plot of the normalized cutoff wave number $k_c V_a^2/g$ versus the inverse Froude number. The solid line represents the solution of Eq. (28), and the dashed-dotted line represents the numerical results of Ref. 6 for $\nu = 2.5$. The remarkable agreement shown in Fig. 63.26 implies that the $1/\nu$ expansion is quite accurate even for $\nu = 2.5$. The disagreement in the regime of $Fr << 1$ is due to higher-order $\epsilon_c$ corrections that become important for modes with wavelength shorter than the thickness of the ablation front. Figure 63.27 shows a plot of the normalized cutoff wave number versus $\nu$ for $Fr = 5$. The solid line represents the solution of Eq. (28) and the dots are the numerical results of Ref. 6. Observe the excellent agreement between the analytic and numerical results even in the region $\nu \sim 1$.

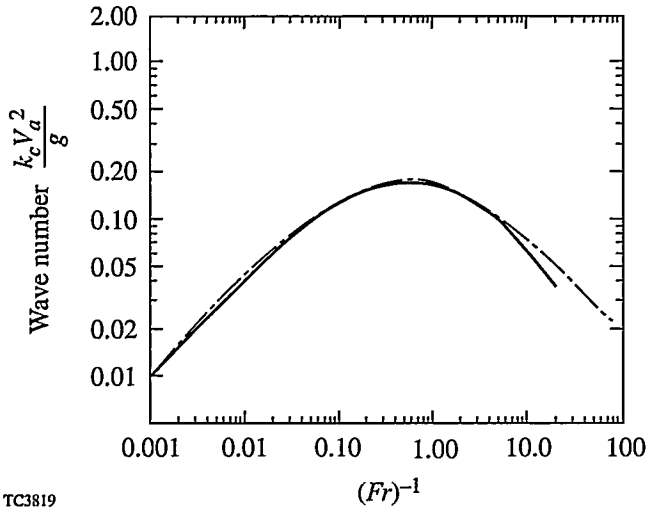


Fig. 63.26
Comparison of the normalized cutoff wave number $(k_c V_a^2/g)$ obtained from Eq. (28) (solid line) with the numerical results of Ref. 6 (dashed-dotted line).

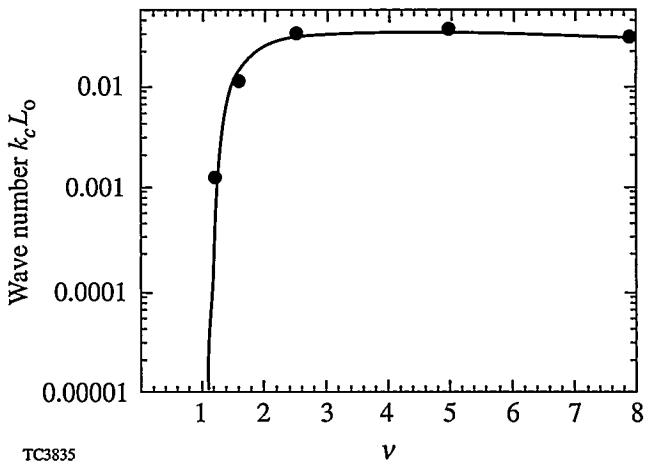


Fig. 63.27
Plot of normalized cutoff wave number $k_c L_0$ versus $\nu$ for $Fr = 5$. The solid line represents the solution of Eq. (28) and the dots are the numerical results of Ref. 6.

For electronic thermal conduction $\nu = 2.5$ and Eq. (28) can be compared with the analytic estimate of Ref. 10 that can be written in the following form:

$$\epsilon_c = \frac{\epsilon_c^{2/5}}{Fr}\,\frac{1-\epsilon_c^{2/5}}{1+\epsilon_c^{2/5}}. \tag{29}$$

Observe that Eq. (29) differs from Eq. (28) by terms $\mu_0(2.5)$. Since $\mu_0(2.5) = 1.03$, Eqs. (28)–(29) yield very similar results for electronic heat conduction. However, when diffusive radiation transport[13] dominates over electronic heat conduction, the thermal conductivity has a strong dependence on the temperature ($\nu \sim 5$–$8$) and Eq. (29) is not valid. In this case, the general formula (valid for arbitrary $\nu > 1$) derived in this article must be used to calculate the cutoff wave number. According to Ref. 13, $\nu = 6.5$ for a fully ionized gas; Fig. 63.28 shows the corresponding normalized cutoff wave number as a function of the inverse Froude number obtained by solving Eq. (28). We recognize that an accurate estimate of the cutoff wave number requires a more complete model of thermal conduction than the one described here. A multigroup treatment of the diffusive transport, as adopted in sophisticated codes such as *LASNEX*,[16] would probably lead to a more accurate result than the one of Eq. (28). Nevertheless, by judiciously choosing the values of $\nu$ and $L_0$, it is possible to fit

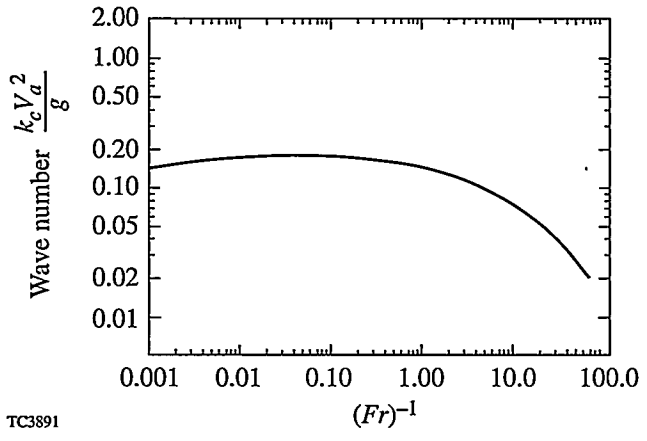


Fig. 63.28
Plot of the normalized cutoff wave number $(k_c V_a^2/g)$ obtained from Eq. (28) for $\nu = 6.5$ as a function of the inverse Froud number.

the equilibrium density profile obtained in the numerical simulations with the solution of Eq. (5). Obviously, different equilibria require different values of $\nu$ and $L_0$. Using such values in Eq. (28) should produce a reliable formula for the cutoff wave number with the appropriate values of the Atwood number and the ablative stabilization term.

To simplify the use of Eq. (28), the scale length $L_0$ is related to the distance $L_e$ between the peak density and the $1/e$ point. The latter is the characteristic scale length widely reported in the literature. The isobaric model used here does not produce a maximum in the density and, in the overdense region, the density profile approaches the maximum value at infinity. Nevertheless, one can define an equivalent length as the distance between the point where the density is $\xi = 1/e$ and the point where the density is $\xi = \xi_0$, where $\xi_0 = 0.95$. A different choice of $\xi_0$ such as $\xi_0 = 0.99$ or $\xi_0 = 0.999$ would only slightly change the results as the density becomes exponentially flat in the overdense region. To determine $L_e$, the density profile is implicitly calculated by using Eq. (16), where $z = y/L_0$ and $\xi_0 = 0.95$. The integration in Eq. (16) can be carried out for integer or half-integer values of $\nu$. A short calculation yields

$$\frac{L_e}{L_0} = z\left(\frac{1}{e}\right) = \sum_{i=0}^{m} \frac{e^{\nu-i}}{\nu-i}$$

$$+\ln\frac{\sqrt{\xi_0}\left(\sqrt{e}-1\right)}{\left(1-\sqrt{\xi_0}\right)} \qquad (\nu = n,\ m = n-1); \qquad (30)$$

$$\frac{L_e}{L_0} = z\left(\frac{1}{e}\right) = \sum_{i=0}^{m} \frac{e^{\nu-i}}{\nu-i}$$

$$+\ln\frac{2\sqrt{\xi_0}\left(\sqrt{e}-1\right)}{\left(\sqrt{e}+1\right)\left(1-\sqrt{\xi_0}\right)} \qquad (\nu = n+1/2, m = n). \qquad (31)$$

Equation (31) yields $L_e \simeq 14\, L_0$ and $L_e \simeq 190\, L_0$ for $\nu = 2.5$ and $\nu = 6.5$, respectively. Lastly, we compare the cutoff wave number derived here with the one produced by the incompressible theory of long-wavelength modes ($kL \ll 1$) or sharp boundary models.[2,17] These non-self-consistent derivations lead to growth rates of the form $\gamma = \sqrt{A_T kg} - \beta k V_a$, where $A_T = (\rho_h - \rho_l)/(\rho_h + \rho_l)$ is the Atwood number for flat profiles and $\beta = 1$ or 1.5. By setting $\gamma = 0$, the incompressible model yields a cutoff wave number $\epsilon_c = A_T/(\beta^2 Fr)$, quite different from the one satisfying Eq. (28).

## Conclusions

The cutoff wave number of the ablative Rayleigh-Taylor instability is calculated self-consistently for an arbitrary power-law dependence of the thermal conductivity ($K \sim T^{\nu}$). The cutoff formula is valid for $\nu > 1$ and $Fr = V_a^2/gL_0 > 1$. Here $V_a$, $g$, and $L_0$ are the ablation velocity, the target acceleration, and the typical thickness of the ablation front, respectively. The derivation is carried out by expanding the eigenvalue equation in powers of $1/\nu$ and $\epsilon = kL_0$ and by performing a boundary layer analysis and asymptotic matching of the eigenfunction. The validity of the formula has been tested with the numerical solution of Ref. 6 up to values of $\nu$ close to 1, and the formula can be used for those equilibria (such as in indirect-drive ICF) that cannot be described by electronic heat conduction ($\nu = 2.5$ and $Fr \sim 5$).

## ACKNOWLEDGMENT

This work was supported by the U.S. Department of Energy Office of Inertial Confinement Fusion under Cooperative Agreement No. DE-FC03-92SF19460, the University of Rochester, and the New York State Energy Research and Development Authority. The support of DOE does not constitute an endorsement by DOE of the views expressed in this article. Some of this work was carried out at the Institute for Theoretical Physics of the University of California at Santa Barbara, where the support of Prof. S. Cowley and the National Science Foundation (Grant No. PHY94-07194) is acknowledged.

## REFERENCES

1. Lord Rayleigh, *Scientific Papers* (Cambridge University Press, Cambridge, England, 1900), Vol. II, pp. 200–207.

2. S. Bodner, Phys. Rev. Lett. **33**, 761 (1974).

3. C. P. Verdon, R. L. McCrory, R. L. Morse, G. R. Baker, D. I. Meiron, and S. A. Orszag, Phys. Fluids **25**, 1663 (1982).

4. H. Takabe, K. Mima, L. Montierth, and R. L. Morse, Phys. Fluids **28**, 3676 (1985).

5. H. J. Kull and S. I. Anisimov, Phys. Fluids **29**, 2067 (1986).

6. H. J. Kull, Phys. Fluids B **1**, 170 (1989).

7. A. B. Bud'ko and M. A. Liberman, Phys. Fluids B **4**, 3499 (1992).

8. R. Betti, V. Goncharov, R. L. McCrory, E. Turano, and C. P. Verdon, Phys. Rev. E **50**, 3968 (1994).

9. J. Sanz, Phys. Rev. Lett. **73**, 2700 (1994).

10. V. V. Bychkov, S. M. Golberg, and M. A. Liberman, Phys. Plasmas **1**, 2976 (1994).

11. J. G. Wouchuk and A. R. Piriz, Phys. Plasmas **2**, 493 (1995).

12. K. O. Mikaelian, Phys. Rev. A **46**, 6621 (1992).

13. Ya. B. Zel'dovich and Yu. P. Raizer, *Physics of Shock Waves and High-Temperature Hydrodynamic Phenomena* (Academic Press, NY, 1966), p. 152.

14. S. V. Weber, B. A. Remington, S. A. Haan, B. G. Wilson, and J. K. Nash, Phys. Plasmas **1**, 3652 (1994).

15. R. Betti, V. N. Goncharov, C. P. Verdon, and R. L. McCrory (in press).

16. G. B. Zimmerman and W. L. Kruer, Comments Plasma Phys. Controlled Fusion **11**, 51 (1975).

17. R. Betti, R. L. McCrory, and C. P. Verdon, Phys. Rev. Lett. **71**, 3131 (1993).

# Distributed Phase Plates for Super-Gaussian Focal-Plane Irradiance Profiles

Various phase-plate designs have been investigated to provide different focal-plane irradiation profiles for laser-matter interaction studies. For many interaction experiments it is necessary to (1) achieve a nearly flat super-Gaussian irradiance distribution, (2) minimize scattering losses, and (3) ensure insensitivity to the laser wavefront nonuniformities. This article shows that these goals may be achieved using a distributed phase plate with a strictly continuous surface determined by a new phase-retrieval algorithm.

The first phase-plate designs intended for direct-drive spherical-implosion experiments were two-level plates consisting of an array of discrete rectangular or hexagonal subregions of either 0 or $\pi$ phase within the region.[1,2] In this case the far-field envelope is defined by the Fourier transform of the subregions and does not conform to a super-Gaussian shape. The lenslet array[3] provides an efficient method of obtaining a flatter irradiation profile; however, it is difficult to control the two-dimensional shape and power spectrum of this profile. Previously designed distributed phase plates (DPP's) with a strictly continuous phase[4] have achieved 96% on-target efficiency but have yielded only a Gaussian[5] or a low-order super-Gaussian far-field distribution. None of these methods provides the desired high-order super-Gaussian shape (see Fig. 63.29) often required for applications in laser-matter interactions.

Phase-retrieval algorithms, developed by Gerchberg and Saxton[6] and Feinup,[7] have been used to synthesize phase plates yielding a higher-order super-Gaussian profile in the far field.[8] We shall refer to this method as phase retrieval with random start (PRRS), as explained below. PRRS is quite general and may be applied to the synthesis of essentially any type of far-field distribution, but we will consider only super-Gaussian distributions in this study. PRRS has no phase discontinuities of magnitude $\pi$ but exhibits point singularities that cause scattering and line discontinuities of magnitude $2\pi$ that can cause scattering as a result of manufacturing errors.

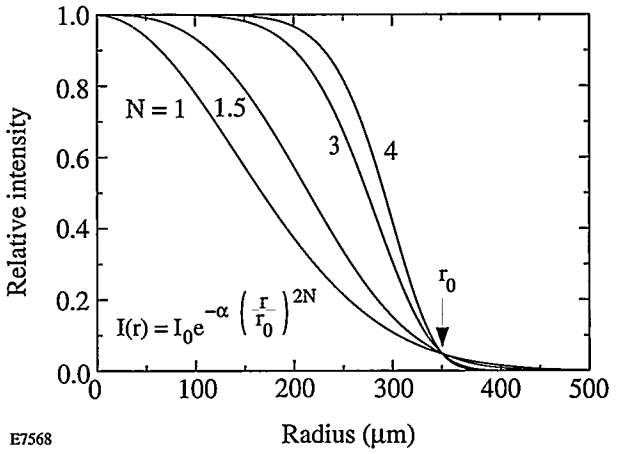


Fig. 63.29
Super-Gaussian irradiance profiles of the form $I(r) = I_0 \exp\left[-\alpha(r/r_0)^{2N}\right]$ for values of $N$ from 1 to 4, plotted with normalized peak irradiances and with $\alpha$ chosen so that all curves pass through 5% of the peak irradiance at the same radius $r_0$. Energy-normalized profiles would emphasize differences in peak irradiance or beam size. These curves illustrate the relative flatness associated with the higher-order super-Gaussian profiles.

To design a phase plate with the PRRS algorithm, one begins with a random noise distribution (no correlation between neighboring points) in the pupil and then performs four steps iteratively.[7] Figure 63.30 illustrates this process. First, each point in the near-field complex amplitude is normalized to achieve the desired near-field intensity profile, leaving the phase unchanged. Second, the complex amplitude is propagated to the far field. Third, each point in the far-field complex amplitude is normalized to achieve the desired intensity profile while preserving the phase. Fourth, the complex amplitude is propagated back to the near field. These four steps are repeated until the solution converges or the desired level of performance is achieved.

Once the phase-retrieval iteration process is finished, the phase of the complex amplitude distribution in the near field at step 4 determines the surface profile of the phase plate. Synthe-

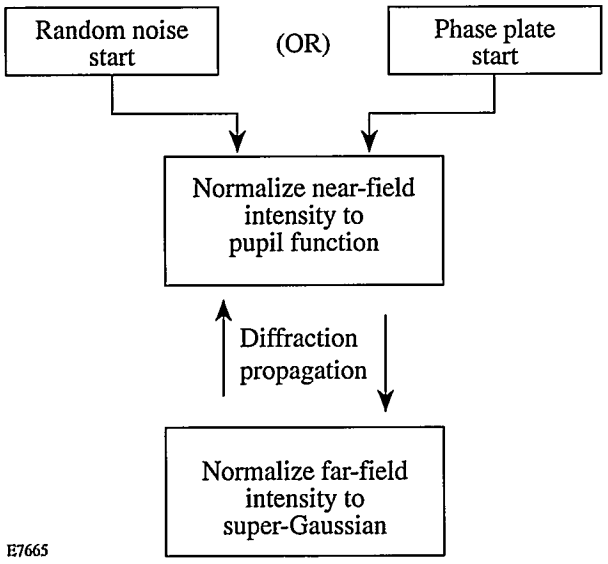


Fig. 63.30
Iterative procedure used to design phase plates according to the phase-retrieval method. Typically, random noise is used in the first pass through the process; however, other phase distributions can be used to reduce the total number of iterations required to achieve an accurate approximation to the desired far-field irradiance envelope.

sis of super-Gaussian far-field profiles by the phase-retrieval algorithm results in speckle-like phase patterns in both the near and far fields. Modulo $2\pi$ jumps arise if the range of the phase exceeds $2\pi$ because the arctangent function $\Psi = \tan^{-1}(\mathrm{Im}/\mathrm{Re})$ maps the phase into the range $-\pi \le \Psi \le \pi$. The loci of modulo $2\pi$ jumps form closed curves. In a kinoform the modulo $2\pi$ jumps are left in place; however, phase-unwrapping algorithms can be used to remove these jumps.[9]

Branch cuts are discontinuities of magnitude $2\pi$ terminated at each end by a pair of phase poles. Branch cuts, unlike modulo $2\pi$ jumps, cannot be phase unwrapped by the elementary unwrapping algorithms because they are line segments rather than closed curves.[9] Figure 63.31 illustrates a positive-negative pole pair with a branch cut between the poles. Phase poles are phase singularities that occur at the point where the loci of real zeros and imaginary zeros cross.[10] Near a phase pole the phase $\Psi$ is a helical function—one cycle of a screw—with a branch cut to constrain $-\pi \le \Psi \le \pi$. The approximate slope of the wavefront in the neighborhood of a circular pole is found by dividing the height of $\lambda$ by the circumference $2\pi r$, where $r$ is the distance from the pole, giving $\lambda/2\pi r$. This is the source of steep but smoothly varying wavefront slopes, which are a direct source of scattering. The association of wide-angle scattering with the location of poles has been numerically verified by blocking the on-target light in the far field, leaving only the wide-angle scattered light. The resulting distribution is backpropagated to the near field, in which high-intensity spots are found to be coincident with pole locations. Direct scattering occurs at the extreme slopes near poles and at non-$2\pi$ discontinuities. The $2\pi$ line discontinuities should, in theory, cause no scattering; however, they can act as indirect sources of scatter because of finite widths produced by limitations in the manufacturing process.

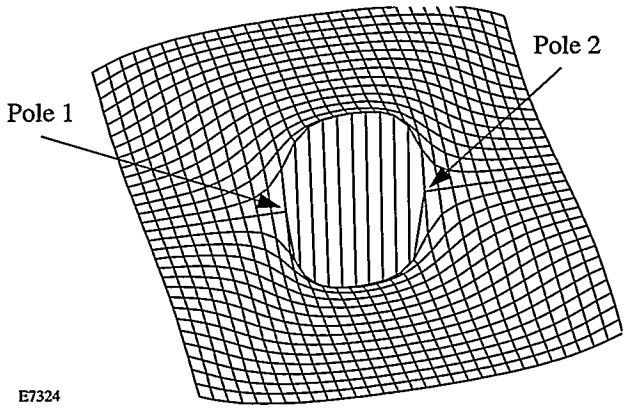


Fig. 63.31
Example of a horizontally oriented pair of positive (right) and negative (left) phase poles with a branch cut between the poles. The wavefront slope in the immediate region of each pole is approximately $\lambda/2\pi r$, where $r$ is the distance from the pole, causing wide-angle vortex scattering. Theoretically the branch cut is a perfectly sharp discontinuity of height $\lambda$; however, manufacturing limitations can result in a finite slope to the branch cut, causing scattering loss.

When performing the numerical diffraction calculations of the phase-retrieval algorithm, only the direct source of wide-angle scattering owing to the smooth-surface effects of the vortex phase near poles is observed. The indirect scattering effects of $2\pi$ discontinuities are not observed in numerical calculations and may be minimized in the design process either by a reduction of the net length of the discontinuities through phase unwrapping and a reduction in the number of poles or by manufacturing methods that reduce the discontinuity width. For a 0.351-$\mu$m wavelength, a 28-cm near-field pupil, a 180-cm focal length, and a 350-$\mu$m target radius, PRRS generates ~10,000 poles. Scattering from the vortex surfaces caused a direct scattering loss of ~5%. In this example, wide-angle scattering can be defined as the energy outside a radius of 500 $\mu$m. In addition to the 5% scattering loss due to vortex

surfaces, there are additional losses due to the $2\pi$ discontinuities: both modulo $2\pi$ jumps and branch cuts. If the number of poles can be reduced, then the direct scattering due to vortex surfaces and the indirect scattering due to branch cuts will be reduced.

A strictly continuous phase plate will have negligible scattering loss. Recently a continuous DPP has been developed, using a two-dimensional Fourier grating with random phase to produce a low-order super-Gaussian profile in the far field.[4] For the 60-beam OMEGA laser system, the smallest target radius is 350 $\mu$m and the $f$ number is ~6.4. A Fourier grating with a spatial period of 0.49 cm and an amplitude of 0.228 waves (at $\lambda = 351$ nm) was used to produce equal far-field modulation for the 0, +1, and −1 orders and generate approximately five major peaks in the far field to form a super-Gaussian envelope. A random phase with an rms value of 0.5 waves and autocorrelation diameter of 0.9 cm was added to the Fourier grating to fill in the gaps between the major peaks of the far field. Figure 63.32 illustrates the far-field patterns from (a) the Fourier grating and (b) a random phase distribution. The GLAD code[11] is used for the DPP design and analysis, in addition to various phase-retrieval algorithms.

The above hybrid DPP design, instead of random noise, was used as a starting point for the phase-retrieval algorithm for the design of the higher-order super-Gaussian DPP.[12] This algorithm is denoted as phase retrieval starting from the hybrid design (PRHD). As indicated in Table 63.I, only 1,400 poles were observed, compared with 10,000 poles for the PRRS. We used only two cycles of phase retrieval since more cycles did not improve the fit to the desired super-Gaussian and resulted in additional poles. Figure 63.33 compares the azimuthally averaged profiles of the desired fourth-order super-Gaussian profile with those produced by the starting hybrid DPP, PRRS, and PRHD, in which an ensemble average based on 100 different noise seeds was used for the random aspects of each design method. The azimuthal average provides strong noise smoothing for larger values of $r$ but no smoothing at $r = 0$. The ensemble average provides additional noise smoothing to display better the shape of the curves at small values of $r$.

PRHD provides the widest flat region in the center of the target area. As summarized in Table 63.I, the PRRS design has ~5% direct scattering outside the 500-$\mu$m radius, compared with 2% for the PRHD design. It is also expected that the indirect scattering that is due to $2\pi$ discontinuities will be much lower for the PRHD than the PRRS because there are only 1,400 poles, compared with 10,000 poles, giving a much lower net length of $2\pi$ discontinuities, which become important when manufacturing limitations are included.

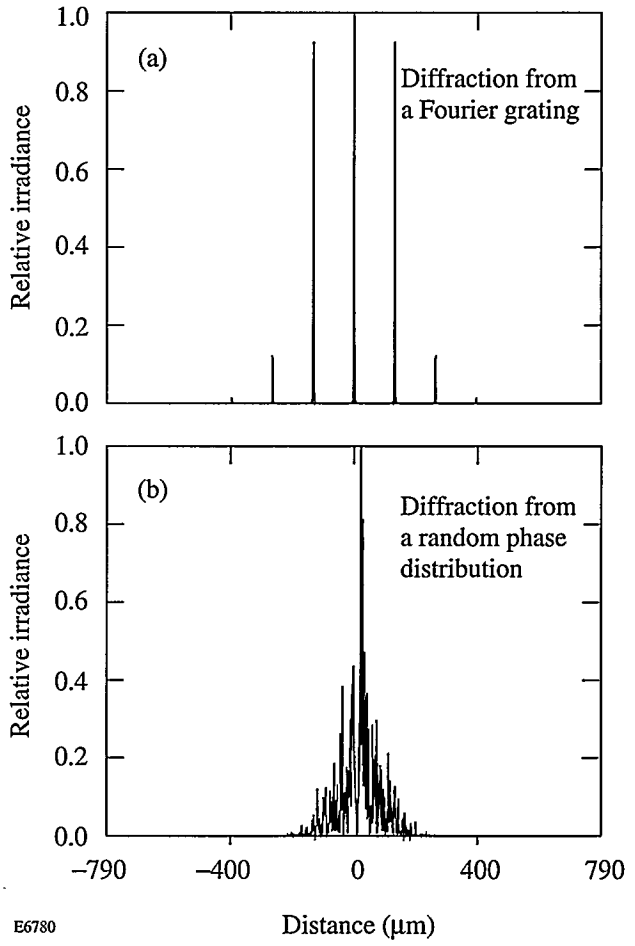


Fig. 63.32
Far-field patterns from (a) a Fourier grating and (b) a random phase distribution used as a starting point for the new phase-retrieval method of designing super-Gaussian DPP's. Since this hybrid DPP produces a far-field irradiance envelope closer to the desired envelope, fewer iterations are required for convergence to the desired super-Gaussian envelope.

Table 63.I: Pole counts and wide-angle scattering losses for the three design types.[(a)]

| Phase-plate type | Number of poles | Direct scattering outside 500-$\mu$m radius (%) | Approximate super-Gaussian order |
|---|---|---|---|
| PRRS | 10,000 | 5.0 | 4.0 |
| Hybrid DPP | 0 | 0.3 | 1.5 |
| PRHD | 1,400 | 2.0 | 4.0 |

[(a)] Only direct scattering due to vortices is included in the table.

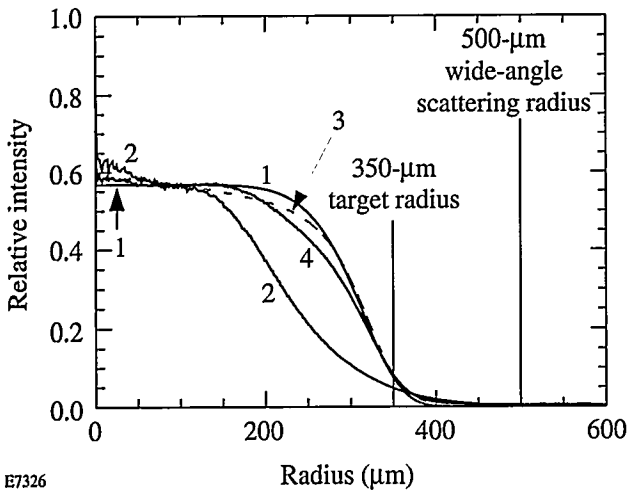


Fig. 63.33
Azimuthally averaged profiles of the fourth-order super-Gaussian function (curve 1), the hybrid DPP (curve 2), the PRRS (curve 3), and the PRHD (curve 4). The curves represent an ensemble average of 100 calculations done with different random seeds. Light that falls outside 500 μm is considered wide-angle scattering. The PRHD has a wider flat region in the center than does the PRRS.

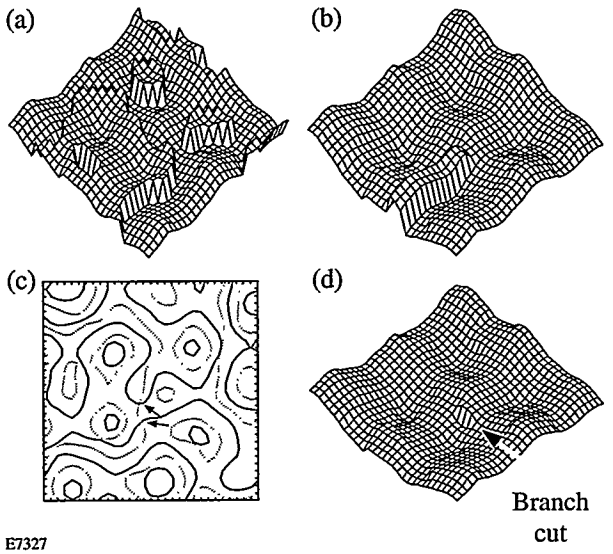


Fig. 63.34
(a) Phase plot of PRHD kinoform showing a 1.2-cm × 1.2-cm section of the 28-cm-diam beam. Islands and plateaus of height λ result in discontinuities of net length ~140 pixel lengths. (b) Conventional phase unwrapping, which ignores branch cuts, reduces the net length of the discontinuities. The phase-unwrapping algorithm fails at the branch cut between the vertically oriented pole pair near the center of the display, creating a spurious horizontal plateau of 28 pixel lengths. (c) Loci of real (solid lines) and imaginary (dotted lines) zeros. The two primary poles are marked. (d) Phase unwrapping with branch-cut recognition reduces the net discontinuity length to the length of the branch cut (approximately two pixel lengths).

Modulo $2\pi$ discontinuity scattering, unlike vortex surface scattering, may be reduced by phase unwrapping. Figure 63.34(a) shows a 1.2-cm × 1.2-cm section of the 28-cm-diam aperture with no phase unwrapping and represents the surface if the PRHD were to be implemented as a kinoform. The net discontinuity length for this small section is ~140 pixel lengths. Islands of $2\pi$ height are apparent. Figure 63.34(b) shows the result of a conventional phase-unwrapping algorithm that attempts to achieve continuity by first resolving the center column and then resolving the horizontal rows from the center to the left and from the center to the right.[9] The net scattering length is reduced to ~28 pixels. Figure 63.34(c) indicates the pole pair by the crossing of real and imaginary loci. The phase-unwrapping algorithm used in Fig. 63.34(b) did not recognize the branch cut and generated the 13-pixel-long plateau of high phase, seen in Fig. 63.34(c), as a spurious effect. Figure 63.34(d) shows the same small section after correction for the branch cut. The net discontinuity length has been reduced from approximately 140 to 2 pixel lengths.

## Summary

A new distributed phase plate that achieves a good approximation to a fourth-order super-Gaussian with very low scattering losses has been designed. Low scattering is achieved because the new design is nearly continuous, having fewer phase poles and a lower net length of $2\pi$ phase discontinuities. The net length of $2\pi$ discontinuity lines, which in practice are an additional source of scattering because of finite width when manufactured, may be reduced to a low level by a phase-unwrapping algorithm capable of treating branch cuts. Preliminary investigations suggest that even-higher-order super-Gaussian far-field profiles can be generated with this technique.

## ACKNOWLEDGMENT

Helpful discussions with Sham Dixit, David Freid, and James Feinup are acknowledged. This work was supported by the U.S. Department of Energy Office of Inertial Confinement Fusion under Cooperative Agreement No. DE-FC03-92SF19460, the University of Rochester, and the New York State Energy Research and Development Authority. The support of DOE does not constitute an endorsement by DOE of the views expressed in this article.

## REFERENCES

1. Y. Kato *et al.*, Phys. Rev. Lett. **53**, 1057 (1984).
2. Laboratory for Laser Energetics LLE Review **33**, NTIS document No. DOE/DP40200-65, 1987 (unpublished), p. 1.
3. X. Deng *et al.*, Appl. Opt. **25**, 377 (1986).

4. T. J. Kessler, Y. Lin, J. J. Armstrong, and B. Velazquez, Proc. Soc. Photo-Opt. Instrum. Eng. **1870**, 95 (1993).

5. J. W. Goodman, in *Laser Speckle and Related Phenomena*, Springer Series in Applied Physics, Vol. 9, edited by J. C. Dainty (Springer-Verlag, Berlin, 1984), Chap. 2, p. 9.

6. R. W. Gerchberg and W. O. Saxton, OPTIK **35**, 237 (1972).

7. J. R. Fienup, Appl. Opt. **21**, 2758 (1982).

8. S. N. Dixit *et al.*, Opt. Lett. **19**, 417 (1994).

9. J. M. Huntley, Appl. Opt. **28**, 3268 (1989).

10. B. Ya. Zel'dovich, N. F. Pilipetsky, and V. V. Shkunov, in *Principles of Phase Conjugation*, Springer Series in Optical Sciences, Vol. 42, edited by T. Tamir (Springer-Verlag, Berlin, 1985), p. 79.

11. GLAD is a general purpose laser system and physical-optics computer program. It is a proprietary product of Applied Optics Research, Tucson, AZ.

12. Y. Lin, T. J. Kessler, and G. N. Lawrence, Opt. Lett. **20**, 764 (1995).

# Electro-Optic Sampling of 1.5-ps Photoresponse Signals from $YBa_2Cu_3O_{7-\delta}$ Thin Films

Studies of the fast photoresponse of high-$T_c$ thin films may reveal important information on scattering mechanisms or nonequilibrium processes in high-$T_c$ materials. Optical pump-probe experiments on $YBa_2Cu_3O_{7-\delta}$ (YBCO) thin films have reported picosecond and subpicosecond time constants,[1,2] but the interpretation of the results is still controversial. Photoresponse experiments with current-biased samples may provide more direct information on nonequilibrium processes,[3–8] but the bandwidth of the oscilloscopes used in these experiments is usually the limiting factor in resolving fast voltage transients on the picosecond time scale. Photoresponse signals with widths ranging from 16 to 40 ps have been reported recently using fast oscilloscopes.[5,7,8] Electro-optic sampling,[9] on the other hand, offers improved time resolution in the subpicosecond regime and has been used to study superconducting electronics[10] and the propagation of picosecond pulses on superconducting coplanar transmission lines.[11] Electro-optic sampling has also been used recently to show that laser-induced switching of Pb transmission lines from the superconducting to the normal state occurs within 1 ps.[12]

This article describes experiments that, to the best of our knowledge, are the first to use electro-optic sampling to study the photoresponse of YBCO thin films. We have observed electrical transients as fast as 1.5-ps full-width at half-maximum (FWHM), which are the fastest photoresponse signals reported to date from a YBCO thin film. We have also found that picosecond transients can be seen in optically thick films (>100 nm), despite previous claims that fast transients can be seen only in ultrathin films with thicknesses of the order of 10 nm.

A schematic of the experimental setup is shown in Fig. 63.35. The *c*-axis YBCO films were grown epitaxially by laser ablation on 0.5-mm-thick $LaAlO_3$ substrates. Films with thicknesses of 100 and 200 nm were used. A coplanar transmission line structure[7] was patterned into the films using standard photolithographic techniques and a wet chemical etch. The center line of the coplanar waveguide (CPW) had a width of 130 $\mu$m, and the width of the gap to the ground lines was 336 $\mu$m. The length of the CPW was about 1.5 mm. A bias current could be applied to one end of the CPW, while the other end was terminated to the ground plane by a narrow bridge with a length of 100 $\mu$m. The bridge widths were 7 $\mu$m and 17 $\mu$m for the 100-nm film, and 10 $\mu$m for the 200-nm film.

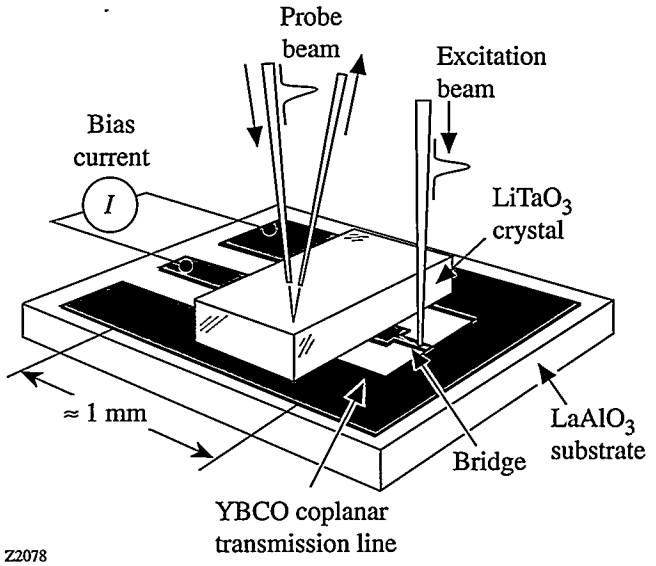


Fig. 63.35
Schematic of the experimental setup.

After processing, the 7-$\mu$m bridge of the 100-nm film had a zero-resistance critical temperature $T_{c0}$ of 90.5 K and a transition width of about 0.8 K. The resistivity $\rho$ at 100 K was 144 $\mu\Omega$ cm ($R$ = 205 $\Omega$), and the critical current $J_c$ at 77 K was about $2 \times 10^6$ A/cm$^2$ ($I_c$ = 12 mA) using a 10 $\mu$V/cm criterion for the onset of dissipation in the bridge. As described elsewhere,[7] the 10-$\mu$m bridge of the 200-nm film had $T_{c0}$ = 89 K, $\rho$(100 K) = 124 $\mu\Omega$ cm ($R$ = 62 $\Omega$), and $J_c = 1.5 \times 10^6$ A/cm$^2$ ($I_c$ = 29 mA).

A mode-locked Ti:sapphire laser operating at a repetition rate of 76 MHz was used to generate 150-fs pulses at a wavelength of 790 nm. To perform electro-optic sampling,[10] the pulses were split into two beams: an excitation beam for

inducing a photoreponse signal in the bridge, and a probe beam for monitoring the electric field from the resulting voltage transient in the $LiTaO_3$ crystal. Both beams were focused onto the sample by passing them through the same microscope objective, also used for viewing the illuminated region. The diameter of the spot size on the bridge was about 10 $\mu$m. The excitation beam was chopped by an acousto-optic modulator at a frequency of 1 MHz, and a translation stage provided the necessary time delay of the probe beam with respect to the excitation beam. The electric field in the electro-optic crystal was probed close to the edge of the center line of the CPW and about 400 to 500 $\mu$m from the position of the microbridge. A reflective dielectric coating on the bottom face of the 1-mm-thick $LiTaO_3$ crystal reflected the probe beam back out through the microscope objective to an analyzer that detected the change in polarization of the probe beam arising from the electric field of the photoresponse signal. Lock-in amplification techniques were then used to extract the electro-optic signal. After 30 averages for each waveform, a voltage resolution of about 0.5 mV for the photoresponse signals could be obtained. Due to large reflections from the end of the short transmission line, time delays beyond 40 to 50 ps could not be studied.

As described elsewhere,[7] the samples were mounted in vacuum on a cold finger cooled with liquid nitrogen. All the experiments discussed here were therefore carried out at a base temperature of 78.6 K, as measured by a temperature diode placed near the sample. It is important to note that increasing the average power $P_{av}$ of the excitation beam raised the average temperature of the film at the laser spot. It was estimated that the average temperature increase of the portion of the bridge illuminated by the beam was about 3 K/mW. Thus, for $P_{av} = 0.4$ mW incident on the bridge, the base temperature would increase to 79.8 K.

Figure 63.36 shows a 1.5-ps-wide voltage transient observed from the 7-$\mu$m bridge of the 100-nm film. The slow rise time and the faster fall time of the transient followed by oscillations suggest that the original photoresponse signal generated at the bridge has experienced some dispersion by the time it reaches the sampling point in the electro-optic crystal.[11] The inset of Fig. 63.36 shows a 1.8-ps-wide photoresponse signal from the 10-$\mu$m bridge of the 200-nm film. Figure 63.37 shows the dependence of the photoresponse signal on the bias current for the 7-$\mu$m bridge of the 100-nm film at a fixed fluence of 15 $\mu J/cm^2$. At high bias currents, as shown in Fig. 63.37(a), there is a fast transient less than 2 ps wide followed by a fast tail with a fall time of about 10 ps. At later

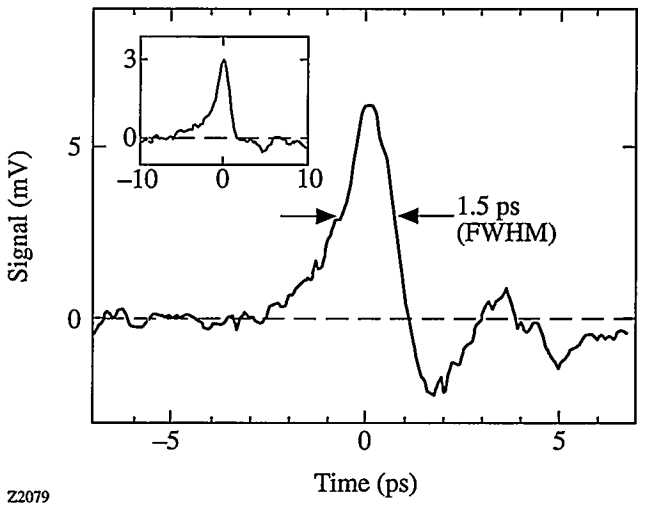


Fig. 63.36
Photoresponse signal from a 7-$\mu$m-wide bridge of a 100-nm-thick YBCO film at a bias current of 15 mA and a fluence of 15 $\mu J/cm^2$ ($P_{av} = 0.4$ mW). The full-width at half-maximum (FWHM) of the voltage transient is 1.5 ps. The inset shows a photoresponse signal from a 10-$\mu$m-wide bridge of a 200-nm-thick film at the same fluence but at a bias current of 60 mA. The width of the signal in the inset is about 1.8-ps FWHM.

times, a much slower component develops due to a resistive bolometric response of the film.[6,7] As the bias current is decreased, as in Fig. 63.37(b), the amplitude of the fast tail becomes much smaller with respect to that of the initial fast transient, and only a small amount of the resistive component remains. At lower bias currents, the fast tail and resistive component disappear completely, as shown in Fig. 63.37(c) and in the 15-mA case of Fig. 63.36, and only the picosecond transient remains, followed by a negative component in the signal with a decay time of about 15 ps.

We believe that the picosecond photoresponse transient (FWHM < 2 ps) is due to a kinetic inductive response given by $V = I\, dL/dt$, where $V$ is the voltage, $I$ is the bias current, and $L$ is the kinetic inductance of the bridge.[3,5–8] Figure 63.38 confirms the linear behavior of the amplitude of the picosecond photoresponse signal with the bias current, as predicted by a kinetic inductive response. The kinetic inductance of a superconducting bridge is inversely proportional to the superfluid density. In a purely kinetic inductive response, a positive voltage transient represents a net breaking of Cooper pairs, and a negative transient signifies a net recombination of excited quasiparticles back into Cooper pairs.[3] The negative response seen in Fig. 63.37(c) may be evidence for an effective nonequilibrium recombination time of about 15 ps in YBCO. Negative transients with durations of about 30 ps have been

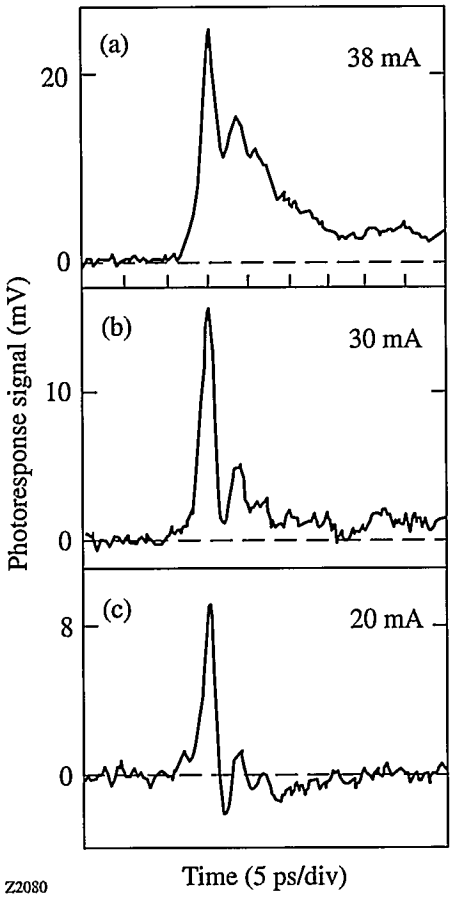


Fig. 63.37
Photoresponse signals from the 7-$\mu$m bridge of the 100-nm film for bias currents of (a) 38 mA, (b) 30 mA, and (c) 20 mA. The fluence was 15 $\mu$J/cm$^2$ ($P_{av}$ = 0.4 mW). Aside from the different bias currents, conditions were identical to those of the 15-mA case of Fig. 63.36. Notice the fast tail at high bias currents in (a) and (b), which then disappears at lower bias currents in (c). Also notice the negative component to the signal in (c).

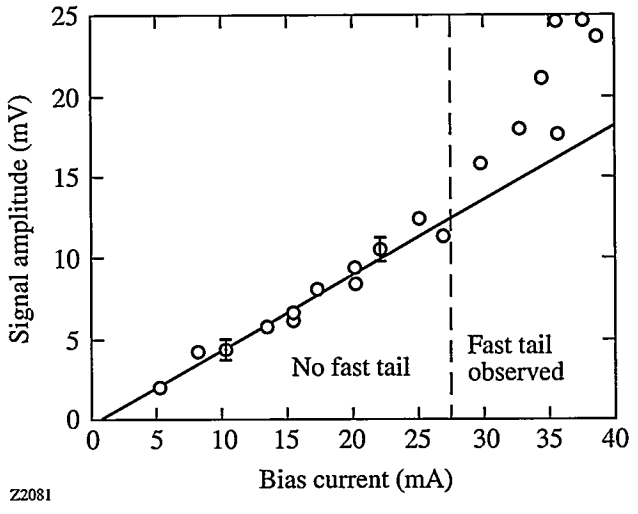


Fig. 63.38
Amplitude of the photoresponse signal (open circles) as a function of bias current for the 7-$\mu$m bridge of the 100-nm film at a fluence of 15 $\mu$J/cm$^2$ ($P_{av}$ = 0.4 mW). Above 28 mA, a fast tail is present, and the amplitude of the signal is not linear with the bias current. Below 28 mA, the fast tail disappears, and the response becomes linear with bias current. The solid line is a least-squares fit to the data below 28 mA. Error bars of ±0.5 mV are shown on two of the data points.

reported recently in photoresponse experiments on YBCO thin films using fast oscilloscopes.[7,8] The area under the negative part of the response in Fig. 63.37(c) is also approximately equal to the area under the faster positive component. This suggests that the positive transient arises mainly from a nonequilibrium (or nonbolometric) kinetic inductive mechanism,[3,5,8] as opposed to a change in the kinetic inductance arising from a purely thermal (or bolometric) response, which would not account for the observed negative transient.[6,7]

A kinetic inductive bolometric model,[6,7] however, predicts a voltage transient with an amplitude of about 30 mV and a width of 0.15-ps FWHM for the conditions given in Fig. 63.37(c). This would give a 3-mV signal after broadening to 1.5-ps FWHM, which is the same order of magnitude as the observed transient of about 9 mV. In a two-temperature nonequilibrium heating model with a ratio of phonon to electronic heat capacities of $C_{ph}/C_e = 40$ and an electron-phonon relaxation time of 1.5 ps,[13] the change in temperature $\Delta T_e$ of the electronic system is about 32 K. The electronic temperature would therefore exceed $T_c$, which might induce a transition in the bridge to the normal state. The resistance of the 7-$\mu$m × 100-$\mu$m × 100-nm bridge at 110 K is around 220 Ω, or about 22 Ω for a 10-$\mu$m section. At a bias current of 20 mA, this would give a voltage transient with an amplitude of 400 mV for a superconducting-to-normal-state transition, which is much larger than the observed signals.

The origin of the fast tail may be due to several mechanisms. At high bias currents (Fig. 63.37) or large fluences (not shown), where the fast tail is seen in the photoresponse signal, the time over which net pair breaking occurs may be extended, which would widen the positive response of the signal. The fast tail may also be due to fast vortex motion across the width of the bridge. Studies of flux-flow transistors have revealed vortex velocities as high as $6 \times 10^7$ cm/s.[14] The transit time across a 7-$\mu$m-wide bridge would therefore be about 12 ps, which is close to the observed fall time of about 10 ps for the fast tail. Recent studies on switching instabilities in current-biased YBCO thin films have reported lower vortex velocities

of the order of $2 \times 10^5$ cm/s,[15] which would not account for a 10-ps duration of the fast tail. Furthermore, the duration of the fast tail did not increase when a wider bridge with a width of 17 $\mu$m was used with a 10-$\mu$m laser focus. Experiments with larger beam focuses on wider bridges may be necessary to study this effect.

In conclusion, we have observed for the first time photoresponse signals less than 2 ps in duration from YBCO thin films using electro-optic sampling techniques. The picosecond transients were seen in optically thick films and at a repetition rate of 76 MHz. We believe that the fast picosecond response is due to a kinetic inductive mechanism, and that the fast tail may be due to ballistic vortex motion across the bridge. The fast response shown in this work makes YBCO films suitable for high-speed applications, e.g., as photodetectors operating above 100 GHz.

## ACKNOWLEDGMENT

This work was supported by the Ontario Centre for Materials Research and the Natural Sciences and Engineering Research Council of Canada and made use of the facilities of the Centre for Electrophotonic Materials and Devices. Research in Rochester was partially supported by the Army Research Office grant DAAH04-93-G-0211. Additional support was received from the Frank Horton Graduate Fellowship Program.

## REFERENCES

1. S. G. Han *et al.*, Phys. Rev. Lett. **65**, 2708 (1990); S. G. Han *et al.*, IEEE Trans. Magn. **27**, 1548 (1991).
2. T. Gong, L. X. Zheng, W. Xiong, W. Kula, Y. Kostoulas, R. Sobolewski, and P. M. Fauchet, Phys. Rev. B **47**, 14,495 (1993).
3. N. Bluzer, Phys. Rev. B **44**, 10,222 (1991); N. Bluzer, J. Appl. Phys. **71**, 1336 (1992); N. Bluzer, IEEE Trans. Appl. Supercond. **3**, 2869 (1993).
4. A. D. Semenov *et al.*, Appl. Phys. Lett. **63**, 681 (1993).
5. A. Ghis *et al.*, Appl. Phys. Lett. **63**, 551 (1993).
6. F. A. Hegmann and J. S. Preston, Phys. Rev. B **48**, 16,023 (1993).
7. F. A. Hegmann, R. A. Hughes, and J. S. Preston, Appl. Phys. Lett. **64**, 3172 (1994); F. A. Hegmann, R. A. Hughes, and J. S. Preston, in *High-Temperature Superconducting Detectors: Bolometric and Non-bolometric*, edited by M. Nahum and J.-C. Villegier (SPIE, Bellingham, WA, 1994), Vol. 2159, pp. 88–97.
8. M. A. Heusinger *et al.*, IEEE Trans. Appl. Supercond. **5**, 2595 (1995).
9. J. A. Valdmanis, G. Mourou, and C. W. Gabel, Appl. Phys. Lett. **41**, 211 (1982).
10. M. Currie, C.-C. Wang, D. Jacobs-Perkins, R. Sobolewski, and T. Y. Hsiang, IEEE Trans. Appl. Supercond. **5**, 2849 (1995).
11. D. R. Dykaar, R. Sobolewski, J. M. Chwalek, J. F. Whitaker, T. Y. Hsiang, G. A. Mourou, D. K. Lathrop, S. E. Russek, and R. A. Buhrman, Appl. Phys. Lett. **52**, 1444 (1988); M. C. Nuss *et al.*, Appl. Phys. Lett. **54**, 2265 (1989).
12. X.-H. Hu, T. Juhasz, and W. E. Bron, Appl. Phys. Lett. **59**, 3333 (1991).
13. G. N. Gol'tsman *et al.*, J. Supercond. **7**, 751 (1994); M. Lindgren *et al.*, Appl. Phys. Lett. **64**, 3036 (1994).
14. P. Bernstein *et al.*, J. Appl. Phys. **76**, 2929 (1994).
15. S. G. Doettinger *et al.*, Phys. Rev. Lett. **73**, 1691 (1994).

# Magnetorheological Finishing—A Deterministic Process for Optics Manufacturing

Finish polishing of optics with magnetic media has evolved extensively over the past decade. Of the approaches conceived during this time, the most recently developed process is called magnetorheological finishing (MRF). In MRF, a magnetic field stiffens a fluid suspension in contact with a workpiece. The workpiece is mounted on the rotating spindle of a computer-numerically-controlled (CNC) machine. Driven by an algorithm for machine control that contains information about the MRF process, the machine deterministically polishes out the workpiece by removing microns of subsurface damage, smoothing the surface to a microroughness of 10 Å rms, and correcting surface figure errors to less than 0.1 $\mu$m peak-to-valley (p-v). Spheres and aspheres can be processed with the same machine setup using the appropriate machine program. This article describes MRF and gives examples that illustrate the capabilities of a pre-prototype machine located at the Center for Optics Manufacturing (COM).

## Background

Finish polishing of optics is defined here to be the production of a surface to within 0.25 $\mu$m p-v of the specified figure, accompanied by sufficient material removal to eliminate subsurface damage and to achieve a microroughness of 10 Å rms. Classical finishing processes employ precisely shaped, viscoelastic pitch or polyurethane foam-faced laps to transfer pressure and velocity through an abrasive slurry to the workpiece. Material is removed by chemical and mechanical interactions among the abrasive (typically micron- to submicron-size cerium oxide or aluminum oxide), the carrier fluid (water), and the workpiece.

Strong technical and economic incentives exist for developing alternative finishing processes that use laps whose shapes are not permanently fixed, but can be controlled and changed with the application of an external field. The cost for design, manufacture, and storage of numerous fixed laps, each with a different surface curvature, would be eliminated. It would also be easy to create unique lap shapes for finishing aspheric and other nonstandard surfaces. Innovative work has been done by several research groups throughout the world to introduce magnetic media to the optics finishing process.

Magnetic media-assisted finishing has been studied in Japan for many years. In 1984, Y. Tani and K. Kawata[1] reported experiments with the geometry shown in Fig. 63.39. The principal of operation was the creation of magnetobuoyant forces that acted on nonmagnetic abrasives (silicon carbide, 4-$\mu$m diam, 40 vol.%) in a magnetic fluid (a ferrocolloid-magnetite, $Fe_3O_4$, 100- to 150-Å diam in eicosyl naphthalene), placed in a nonuniform magnetic field (1-kG approximate field strength). The magnetic field gradients created by a flat lap array of permanent magnets caused the abrasive grains to levitate upward into contact with the work. Motor-driven rotation of the main spindle caused the work (a set of three acrylic plates, 20 mm in diameter) to move over the abrasives that were localized in the regions of minimum magnetic field.

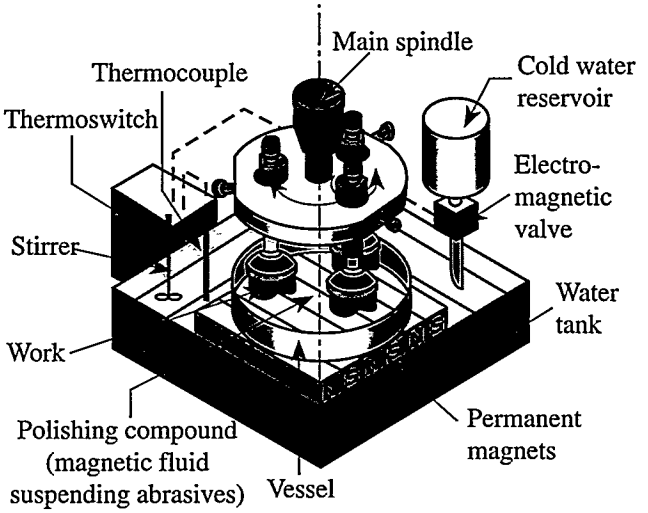


Fig. 63.39
Polishing of acrylic plates with SiC abrasives in a magnetic fluid composed of 150-Å-diam magnetite particles. The pole pieces serve as the reference lapping surface for the workpiece. (From Ref. 1.)

Material was removed at the rate of 2 μm/min across the entire part, and a 10× reduction in surface roughness to 400-Å Rmax was observed after 1 h. (Rmax denotes peak-to-valley roughness.) The authors noted significant thermal control problems in the slurry.

Related work was reported by Y. Saito *et al.* in 1987, again for acrylic plates in an aqueous-based ferrocolloid slurry.[2] Confinement of polishing abrasives to the work zone was a problem. The pressures generated by these two approaches were inadequate to polish glass, and there was no possibility for surface figure control.

Based upon work of Kurobe,[3] Suzuki *et al.*[4] made significant advances with the machine geometry shown in Fig. 63.40. By sealing the ferrocolloidal media in a brass trough with a flexible, polyurethane-rubber cover, they could direct considerably more pressure (10–25 kPa for 8–10 kG) to a colloidal silica slurry in contact with the work. It was possible to finish hard materials against a magnetically shaped polyurethane lap. Nonplanar surfaces could be polished by suitably contouring the magnet pole cap. In 1989, they reported smoothing a lithium niobate surface of 50-mm radius of curvature from 1500-Å to 100-Å Rmax (17 Å rms) in 30 min. The spherical surface figure error was reduced from 0.4 to 0.3 μm p-v.

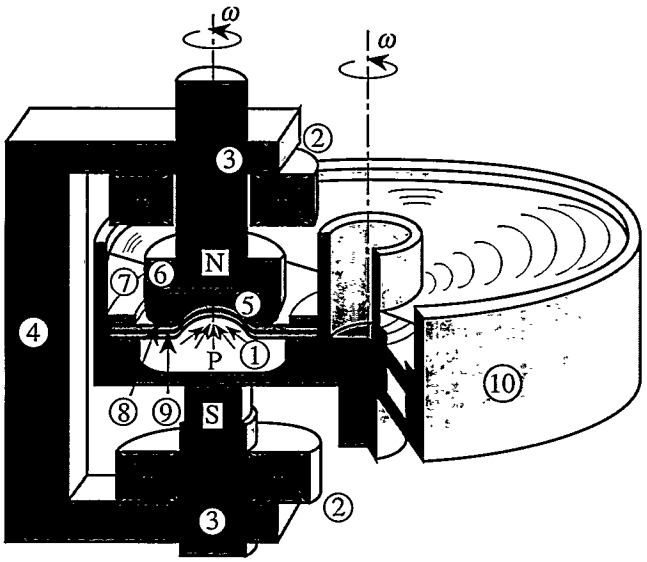


1. Magnetic fluid
2. Coil
3. Iron pole
4. Yoke
5. Workpiece
6. Jig or chuck
7. Polishing abrasive
8. Polyurethane pad
9. Rubber sheet
10. Brass vessel

G3838

Fig. 63.40
Apparatus for polishing with a pad whose shape is defined by a magnetic field acting on a confined magnetic fluid. (From Ref. 2.)

More recently, in 1993, these researchers demonstrated the ability to polish aspheric surfaces on 40-mm-diam Pyrex® glass parts with removal rates of 2 to 4 μm/h.[5] One drawback to this approach was a lack of edge control. Another serious impediment to commercialization was the need for an inventory of customized pole caps, uniquely shaped to each desired surface form.

**Introduction to Magnetorheological Finishing (MRF)**

The most recent approach to processing optics with magnetic fluids is magnetorheological finishing (MRF). This technology was initiated in Minsk, Belarus by Kordonski, Prokhorov, and coworkers,[6,7] as an outgrowth of work with intelligent fluids for clutches, shock absorbers, and vibration isolators. The concept of MRF is shown in Fig. 63.41. A suspension of noncolloidal magnetic particles and polishing abrasives is contained in a vessel, or trough. Rotation of the trough delivers the suspension to the surface of a spindle-mounted workpiece. With the application of a dc magnetic field in the vicinity of the workpiece, the suspension stiffens to form a small pressure spot that contacts and conforms to the workpiece. The magnetic-field-stiffened suspension constitutes a lap, and the constant flow of magnetic particles and

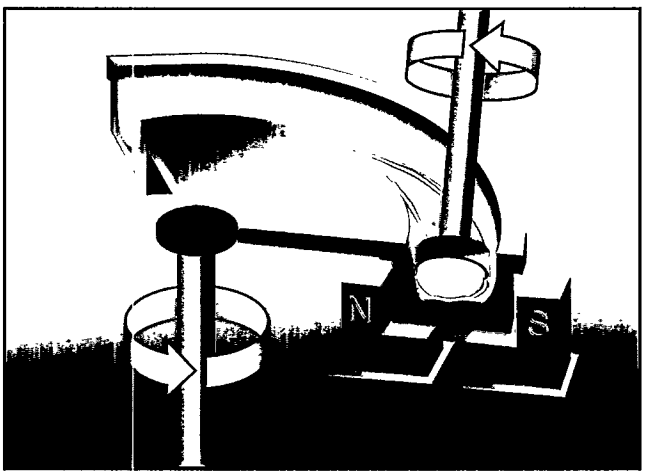


©Center for Optics Manufacturing, University of Rochester

G3839

Fig. 63.41
The MRF concept. A workpiece is immersed directly into the magnetorheological suspension for processing against a magnetic-field-stiffened, fluid lap.

polishing abrasives through the region of high pressure causes material removal at the workpiece surface. A key difference between the MRF process and that of Fig. 63.40 is that in MRF material removal takes place only in the vicinity of the small pressure spot rather than simultaneously over the whole surface of the workpiece. Other unique features of the MRF process are the controllable and conformal nature of the lap, the constant replenishment of the polishing zone with fresh suspension, and the continual removal of glass particles and heat generated in the polishing process.

A workpiece is polished by sweeping its surface through the zone of high pressure. Dwell time determines the amount of material that is removed. The illustration in Fig. 63.42 gives a cut-away view of the finishing process, where a spherical surface is shown in three orientations. The lens center is polished with the spindle normal to the bottom of the trough. Rotation of the spindle about the lens center of curvature causes annular regions of increasing diameter to come into the zone of high pressure for finishing. A key to the areal removal of subsurface damage, areal smoothing, and areal figure correction is the machine program that drives spindle motion at predetermined velocities through both positive and negative angles. Spherical or aspheric surfaces can be finished with the same machine setup, using customized machine programs.

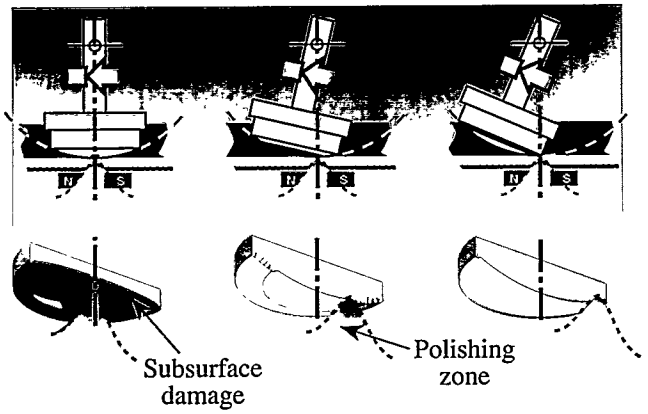


[©]Center for Optics Manufacturing, University of Rochester

G3840

Fig. 63.42
Polishing out a workpiece with the MRF process. Dwell time determines the ultimate surface shape and smoothness.

## Magnetic Suspension, Polishing "Spot," and Parameter Studies

The MR suspension consists of noncolloidal magnetic particles, ~4.5 $\mu$m in diameter, mixed in an aqueous slurry with nonmagnetic polishing abrasives (see Fig. 63.43). When circulating suspension passes into the high magnetic field (~4 kG) created by an electromagnet, the magnetic particles form chain-like structures. The result is an increase in the viscosity and yield (shear) stress of the suspension by two orders of magnitude. A localized pressure spot is formed against the surface of the workpiece, and material removal occurs as a result of chemomechanical interactions.

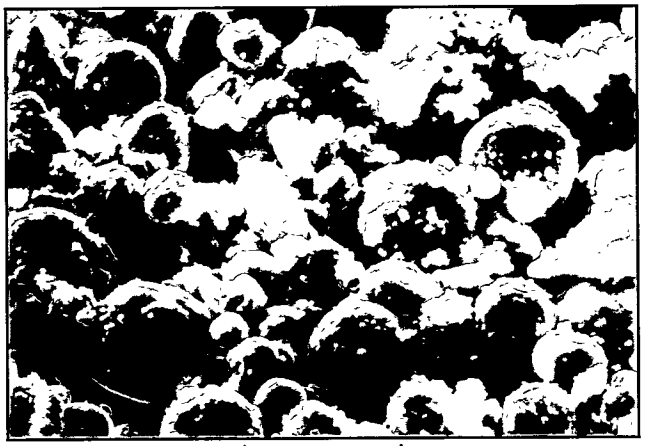


G3841

Fig. 63.43
Scanning electron micrograph of an MR suspension containing 4.5-$\mu$m (initial median size) spherical magnetic particles and 3.5-$\mu$m (initial median size) $CeO_2$ particles. The sample was analyzed after one week of use.

The MRF removal function in the zone of high pressure is specific to the machine platform, the magnetic field strength, the workpiece geometry, and the properties of the material being finished. All experimental results reported in this paper were obtained on a pre-prototype MRF machine whose configuration resembles that shown in Fig. 63.41. Figure 63.44 shows the fluid flow direction and removal "spot" for a 40-mm-diam BK7 glass lens with an 84-mm radius of curvature, immersed in the MR suspension for 5 s. The spindle arm was oriented at an angle of $\theta = 2°$ and was locked to prevent workpiece rotation. Interferometrically derived depth profiles show that the removal function has a backward "D" shape, with a region of peak removal at the point of deepest penetration of the lens surface into the suspension. The peak removal rate is 4.6 $\mu$m/min, and the volumetric removal rate is 0.48 $mm^3$/min.

Several parameter studies have been conducted to evaluate the sensitivity of the polishing spot to process parameters. There is a significant dependence upon material type. Fig-

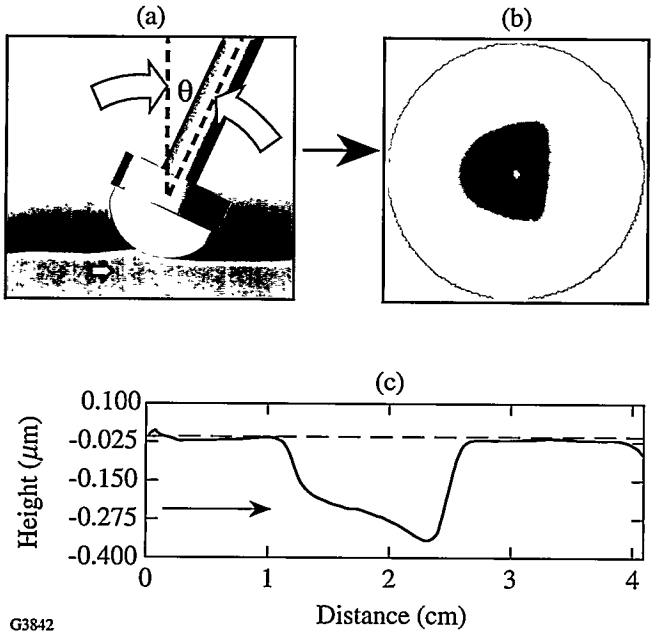


Fig. 63.44
MRF removal function on BK7 glass after 5 s. The "spot" areal size is approximately 2 × 2 cm for the conditions described in the text.

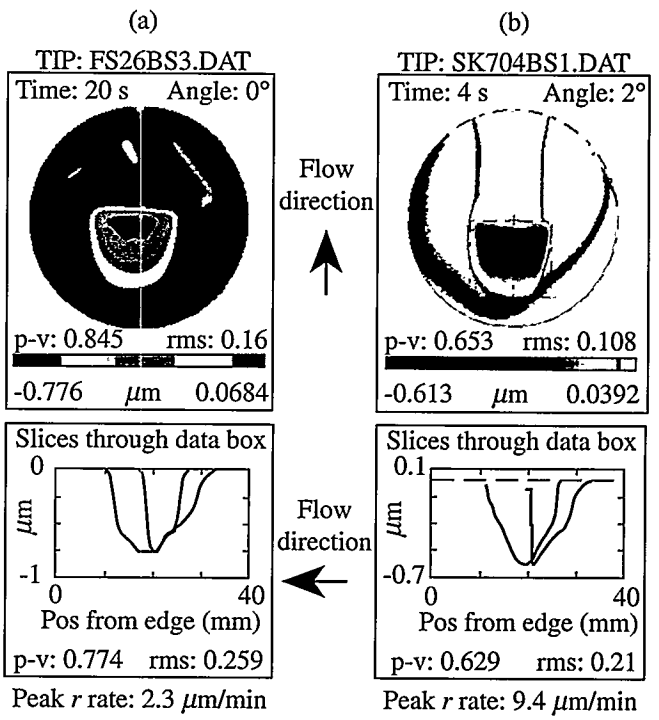


Fig. 63.45
Interferograms of removal "spots" for two different glass types under identical MR processing conditions. Depth-profile line scans shown below the spots are similar in shape.

ure 63.45 shows interferograms of spots taken on two different glass types. For the fused silica part, the spot is acquired by lowering the part into the suspension at normal incidence, turning the magnetic field on for 20 s, turning the field off, and raising the spindle-mounted part up and out of the suspension. Depth profile line scans, taken in orthogonal directions through the interferogram and displayed below the spot, give a peak removal rate of 2.3 μm/min for this glass. For the SK7 part, a spot is acquired by first turning on the magnetic field. The spindle-mounted part is then swept through an angle to the near-normal-incidence orientation in the suspension. It is kept there for a period of 4 s and then swept back out. Because of its composition and physical properties, SK7 polishes faster than fused silica. The measured peak removal rate is 9.4 μm/min. The spot shapes for these glasses are very similar. This is a characteristic of the MR process.

Figure 63.46 displays the peak and volumetric removal rates for a selection of seven optical glass types, measured under identical MR process conditions. There is a factor of nearly 4 increase in removal rate for F7 compared with fused silica (FS). The trend toward higher removal rates generally correlates with a decrease in silica content (change in chemistry of removal) and a drop in glass hardness (Knoop, Vickers, or lapping—change in mechanics of removal).

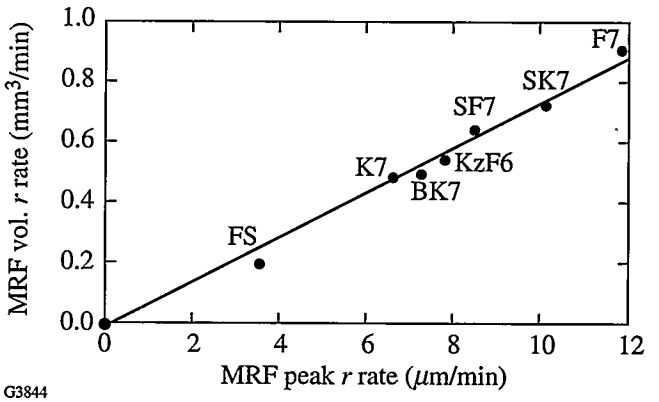


Fig. 63.46
Removal rates for several glass types under identical MR processing conditions. Softer glasses are generally seen to polish more rapidly.

Another parameter that has been studied is the sensitivity of final surface microroughness to glass type and to initial surface

microroughness. Areal polishing experiments, conducted on spherical parts generated with deterministic grinding processes[8] at COM, show that the smoothing process is more sensitive to the initial condition of the surface than to the glass type. Figure 63.47 gives the time evolution of surface microroughness for the same set of seven optical glasses (40-mm diam), measured with two different types of optical profilers. Both sets of data show that the final rms surface microroughness, independent of glass type, is ~10 Å. If the initial rms surface microroughness is less than a few hundred angstroms, smoothing occurs in 5 to 10 min. The rate of smoothing drops for rougher surface conditions.

### Deterministic MR Finishing of Convex Spherical and Aspheric Surfaces

Since 1993 a pre-prototype MRF machine has been used as a testbed for the development of software that enables technical personnel (not necessarily opticians) to deterministically finish optics.[9] The software is being developed for COM by Prof. Greg Forbes, Macquarie University, Sydney, Australia, and his graduate student, Mr. Paul Dumas of The Institute of Optics, University of Rochester. Most test parts for polishing experiments are prepared primarily on Opticam® CNC ring-tool generating machines at COM, although parts have also been provided by selected companies in the U.S. and elsewhere.

The Forbes/Dumas code requires three items as input: the shape and magnitude of the MRF removal function or "spot," the initial surface shape, and the processing objectives. The first item is obtained by generating a spot on a test piece of the same material type and shape to be finished. An interferogram of the removal spot, recorded by a Zygo Mark IV xp® interferometer, is acquired and loaded into the code. Alternatively, a previously recorded and stored spot profile may be called up from a database. The second input is the initial shape of the surface to be finished, which for a spherical surface is another interferogram showing initial deviation from a best-fit sphere. For an aspheric surface the input could be a surface profile obtained with a stylus instrument like the Rank Taylor Hobsen Form Talysurf®. The third input is the processing objective, which could be dc removal to eliminate subsurface damage, figure correction, or a combination of the two.

The Forbes/Dumas code runs on a PC. Using a series of complex algorithms, the code convolves the removal function with the initial surface shape to derive an operating program for the spindle-arm angular controller on the MRF machine. The code specifies angles and accelerations for the controller, the number of sweeps required between positive and negative angles, and the total estimated processing time. Finally, the code predicts the figure expected from the process cycle. The Forbes/Dumas code and the pre-prototype MRF machine controller are best understood with several examples.

1. Convex Spherical Parts from Fused Silica

One of several convex fused-silica parts (40-mm diam, 58-mm radius of curvature), generated on the Opticam® SX, was polished in three cycles to illustrate dc removal, figure correction, and surface smoothing. Results are given in Table 63.II. The first cycle lasted 32 min, removing 3 μm uniformly from the surface and reducing the areal surface roughness from 40 Å to 8 Å p-v (unfiltered, Zygo Maxim® 3D optical profiler). Symmetric surface wavefront error was held to an increase of 0.1 μm for 3 μm of material removed. (The configuration of MRF implemented in the pre-prototype machine does not permit efficient removal of any asymmetric features.) The second cycle (see below) brought figure error down from 0.42 μm to 0.14 μm. This was accomplished in 6 min with the (radially) selective removal of ~0.7 μm of material. A third cycle was implemented to remove an additional 3 μm of material while further reducing symmetric

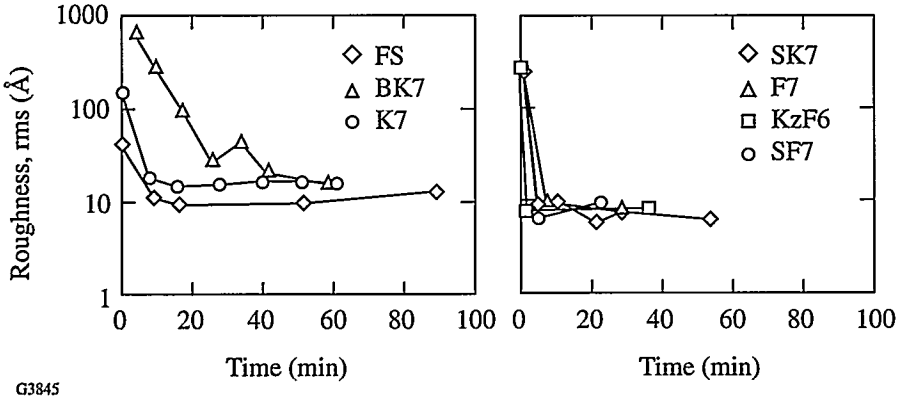


Fig. 63.47
Surface smoothing for a variety of 40-mm-diam glass parts with the same MRF process conditions. Final rms microroughness is ~10 Å. The smoothing time is 5–10 min for surfaces whose initial rms microroughness is under a few hundred angstroms.

are indicated on the left and relevant Form Talysurf® scans on the right. In the first MRF cycle, 12 μm of material were removed over a period of 100 min. The rms roughness was reduced from 9400 Å to 10 Å. All subsurface damage was eliminated. (HF acid etching on identical parts confirms that MRF does not introduce new subsurface damage.) The second figure correction run required 40 min of polishing time; 4 μm of material were removed. At the conclusion of this cycle the form error was reduced to 0.86 μm. These BK7 lenses were returned to TI and judged acceptable for inclusion in a breadboard of their deformable mirror device assembly, an integral part of TI's digital imaging technology.

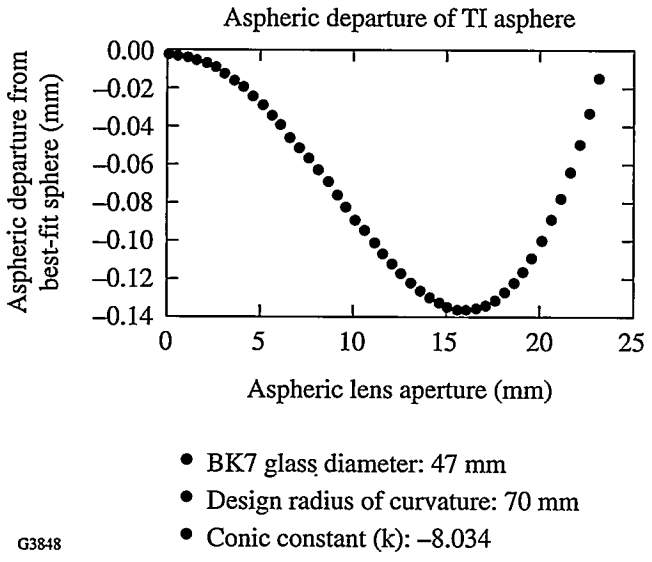


Fig. 63.50
Aspheric shape required for a collaborative deterministic manufacturing experiment with Texas Instruments.

## Summary

MRF is a promising new optics manufacturing technology. Fundamental to this technology is an environmentally safe, aqueous suspension of magnetic particles and polishing abrasives, whose viscosity is increased by orders of magnitude in a magnetic field. The stiffened suspension acts as a "spot" lap that conforms to and polishes out the surface of a workpiece immersed in it. In initial trials on a pre-prototype machine, MRF has shown an excellent capability for smoothing ground glass surfaces, correcting figure errors, and eliminating subsurface damage. Experiments have demonstrated that, with machine-control programs generated by a computer algorithm, both spheres and aspheres can be finished with the same machine setup, for a variety of optical glasses.

## ACKNOWLEDGMENTS

This work was carried out in collaboration with D. Golini and Y. Hsu of COM and with W. I. Kordonski, I. V. Prokhorov, E. Fess, D. Pietrowski, and V. W. Kordonski of Byelocorp Scientific, Inc. The authors acknowledge the expertise, dedication, and teamwork of Chris Dewever, Paul Dumas, Greg Forbes, Gennady Gorodkin, John Schaefer, Alan Tittle, and John Vakiner. Support for this effort was provided by Byelocorp Scientific, Inc. and the U.S. Army Materiel Command. Additional support was received from the Frank J. Horton Fellowship Program at the Laboratory for Laser Energetics. The pre-prototype MRF machine was manufactured for COM by CNC Systems, Inc., Ontario, NY.

| Cycle | Amount removed (μm) | Cycle time (min) | rms* roughness (Å) | p-v fig. (μm) |
|---|---|---|---|---|
| Initial | --- | --- | 9400 | 6.42 |
| #1: dc ssd removal/ smoothing | 12 | 100 | 10 | 4.40 |
| #2: figure correction | 4 | 40 | 10 | 0.86 |

*Zygo New View®, 20x Mirau

G3849

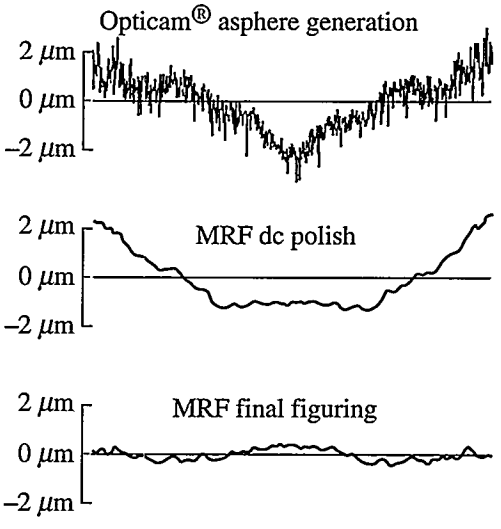


Fig. 63.51
Finishing of a 47-mm-diam asphere in two MR processing cycles. The entire polishing and figuring operation required 140 min of machine time.

## REFERENCES


1. Y. Tani and K. Kawata, CIRP Annals **33**, 217 (1984).
2. Y. Saito *et al.*, in the *Proceedings of the 6th International Conference on Production Engineering Osaka* (1987), pp. 335–340.
3. T. Kurobe, O. Imanaka, and S. Tachibana, Bull. Jpn. Soc. Precis. Eng. **17**, 49 (1983).
4. H. Suzuki *et al.*, Prec. Eng. **4**, 197 (1989).
5. H. Suzuki *et al.*, J. Jpn. Soc. Precis. Eng. **59**, 1883 (1993).
6. W. I. Kordonsky, in the *Third International Conference on Adaptive Structures,* edited by B. Wada, M. Natori, and E. Breitbach (Technomic, Lancaster, PA, 1993), pp. 13–27.
7. I. V. Prokhorov, W. I. Kordonsky, L. K. Gleb, G. R. Gorodkin, and M. L. Levin, in *OSA Optical Fabrication and Testing Workshop*, 1992 Technical Digest Series, Vol. 24 (Optical Society of America, Washington, DC, 1992), pp.134–136.
8. D. Golini and W. Czajkowski, *Laser Focus World*, July 1992, 146.
9. W. I. Kordonsky, I. V. Prokhorov, B. E. Kashevsky, S. D. Jacobs, B. E. Puchebner, Y. Hsu, D. Pietrowski, D. Strafford, and E. Fess, in *OSA Optical Fabrication and Testing Workshop*, 1994 Technical Digest Series, Vol. 13 (Optical Society of America, Washington, DC, 1994), pp.104–109.

# Initial Target Experiments on the Upgraded OMEGA Laser System

A major program to demonstrate the feasibility of direct-drive laser fusion is underway at LLE. The overall goal of this program is to develop an understanding of target physics at the 30-kJ level that will allow the performance of direct-drive capsules designed for use with the National Ignition Facility (NIF) at the 1- to 2-MJ level to be predicted with confidence. The majority of the experiments that will contribute to this goal will be performed with the 60 UV (351-nm) beams of the recently upgraded, 30-kJ OMEGA laser system. The key physics issues that will be examined, both experimentally and theoretically, include irradiation uniformity, laser energy coupling and transport, laser-plasma interaction physics, hydrodynamic stability, and hot-spot and main-fuel-layer physics.

In this article we summarize initial target experiments performed with the upgraded OMEGA laser system.[1] Targets consisted mainly of glass microballoons (GMB's) having high initial aspect ratios ($R/\Delta R$, where $R$ is the target radius and $\Delta R$ is the shell thickness) of ~150 to 300, filled with either pure deuterium or an equimolar mixture of deuterium and tritium at pressures ranging from 5 to 20 atm. These low-mass shells were accelerated to high implosion velocities. The compressed fuel was predicted to have a high electron temperature (up to 6 keV) and a density in the range of 0.2 to 2 g/cm$^3$. Diagnosis of target performance during the acceleration phase of the implosion was obtained from time- and space-resolved measurements of the x-ray emission from the laser-heated glass shells. Overall target performance was diagnosed by nuclear and particle instrumentation, from which estimates of the total thermonuclear yield and the fuel ion temperature were obtained. Neutron yields have been measured to be as high as $10^{14}$ (DT) and $1.1 \times 10^{12}$ (DD), and ion temperatures up to 13 keV have been inferred from a neutron time-of-flight detector. High fuel electron temperatures of 3 to 4 keV have been inferred from spectroscopic measurements.

The main objective of these initial experiments was the activation of several key diagnostic systems. An x-ray framing camera and a Kirkpatrick-Baez (KB) microscope were used to image the x-ray emission during the implosions. Copper and indium neutron activation counters were used to determine DT and DD neutron yields, and scintillator-photomultipliers were used to measure the neutron time-of-flight. Finally, a crystal spectrometer was fielded to measure the electron temperature from the continuum slope of the x-ray spectrum and from krypton K-shell spectroscopy.

### X-Ray Imaging

1. X-Ray Framing Camera

A series of experimental shots were devoted to the initial activation of one of the x-ray framing cameras. The camera is based on the high-speed gating of a 0.25-mm-thick microchannel plate with a channel-pore aspect ratio (length:diameter) of 40:1. The design and testing of the prototype for this camera are described in Ref. 2. The temporal resolution of the camera over a range of operating parameters was measured off-line using a short-pulse (300-fs) frequency-quintupled glass laser system. For the GMB's in this experimental series the camera was operated with an expected temporal resolution (gating time) of 35 to 40 ps.

Figure 64.1 shows a series of images recorded from shot 5067, sensitive to x rays in the spectral range above 3 keV. The target was a 20-atm DD-filled glass microballoon with an initial wall thickness of 2.3 $\mu$m and a diameter of 845 $\mu$m. The magnification was 6× and the calculated spatial resolution was ~10 $\mu$m in the target plane. The time delay between strips is 250 ps, and the delay between images on a given strip is 50 ps. The fogging around the images in the third and fourth strips is caused by high-energy x rays produced during the implosion and transmitted through the 50-$\mu$m Ta pinhole substrate. The vignetting seen in the four corner images is caused by a circular aperture in the pinhole mount. The x-ray emission comes primarily from overdense glass plasma with an electron temperature $\gtrsim$800 eV. During much of the implosion, before the glass has expanded significantly beyond its initial thickness, the location of the peak x-ray emission thus provides a good indication of the shell's location.

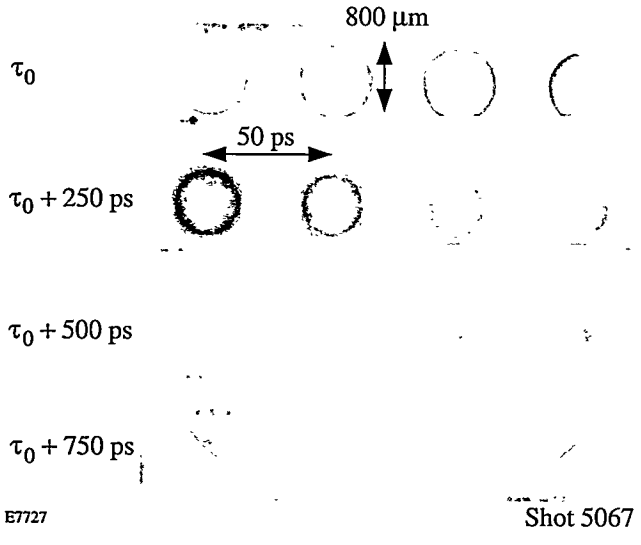


Figure 64.1
Framing-camera images of OMEGA shot 5067. The target was a glass microballoon with an initial wall thickness of 2.3 μm and a diameter of 845 μm. The time delay between strips is 250 ps, and the delay between images on a given strip is 50 ps, time increasing from left to right. The magnification is 6× and the calculated spatial resolution is ~10 μm.

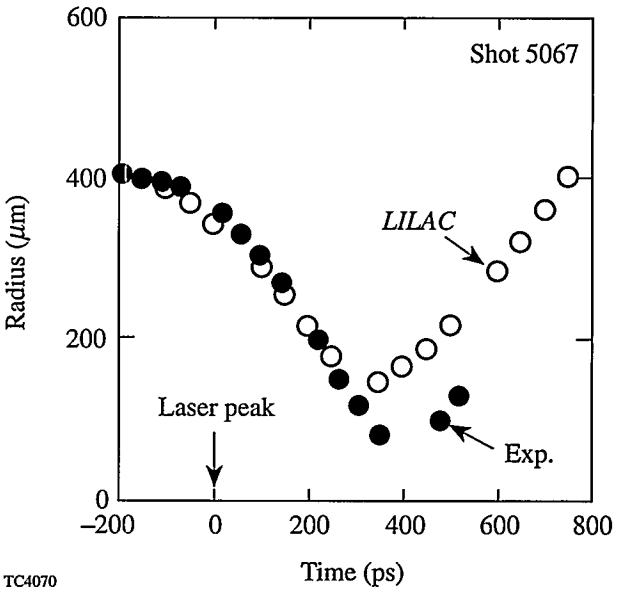


Figure 64.2
Radius of the peak x-ray emission contour for the target of Fig. 64.1 as a function of time. The solid circles are azimuthal averages obtained from the framing-camera images of Fig. 64.1, and the open circles are predictions of the one-dimensional code *LILAC*.

To obtain a more quantitative understanding of the framing-camera images, the azimuthally averaged radius of the peak emission contour for each frame of Fig. 64.1 has been plotted in Fig. 64.2 as a function of time. Predictions based on the one-dimensional code *LILAC* are also plotted. *LILAC* uses a straight-line radiation transport algorithm to replicate the images, with spatial smearing based on the resolution of the pinhole. The temporal response of the diagnostic is modeled as being Gaussian in shape, with a 40-ps FWHM. Since no absolute timing fiducial is currently available for the camera, the zero time reference between the two data sets was taken as being the one that gave the best fit between the two. The time $\tau_0$ of the first frame of Fig. 64.1 is then –200 ps, where $\tau = 0$ corresponds to the peak of the laser pulse. As can be seen, the predictions for the hydrodynamic motion of the shell are in good agreement with the experiment throughout the acceleration phase of the implosion ($\tau \lesssim 200$ ps). However, during the subsequent coast phase of the implosion and at the onset of stagnation, the experiment deviates from the *LILAC* prediction. Emission from the glass comes from smaller radii than predicted, with the radius of peak emission continuing to decrease linearly with time until its stagnation at ~350 ps. This departure from one-dimensional predictions may be due to the present level of laser-beam uniformity, in which case better results can be expected when beam smoothing is employed on the system. The successful deployment of this first x-ray framing camera and the data obtained from it will allow improvements in target drive to be assessed when beam-smoothing techniques are implemented.

2. Kirkpatrick-Baez Microscope

A Kirkpatrick-Baez (KB) microscope—one of a set of new microscopes that incorporate improvements over the design used previously at LLE[3]—has been used to obtain time-integrated x-ray images of the initial target implosions. The reflective optics are Ir coated, extending their useful band up to 8 keV, while the resolution at the center of the field of view is ~5 μm.[4] The KB microscopes thereby provide high-resolution, relatively hard x-ray images of target emission. They have been designed with precision pointing and focusing and are being fully calibrated in the x-ray laboratory at LLE. Eventually, the microscopes will be used for space-resolved continuum spectroscopy of implosions by incorporating a diffraction grating,[5] and for framed monochromatic imaging by attaching a crystal monochromator and a framing camera assembly.[4] The monochromator/framing camera attachment is being built by the laser fusion group at the Los Alamos National Laboratory.[6]

For the initial implosion experiments on OMEGA, a single KB microscope was deployed on the target chamber with a

simple arrangement of thin metallic filters. X-ray film (Kodak DEF) was used to record the images. Four images were obtained per shot through various filters. Since the targets used in these experiments were principally glass microballoons filled with either DD or DT, and since the glass contained a significant amount of a high-Z element (1%–2% $RbO_2$ molar), the shell emitted copious levels of relatively hard x rays (>4 keV). It was therefore necessary to filter the flux from the targets to limit the film exposure. Figure 64.3 shows the calculated response of the KB microscope versus energy for the Ir-coated mirrors and for a filtration of 203.2 μm of Be in combination with 101.6 μm of Al. The effective energy band is from 5 to 8 keV.

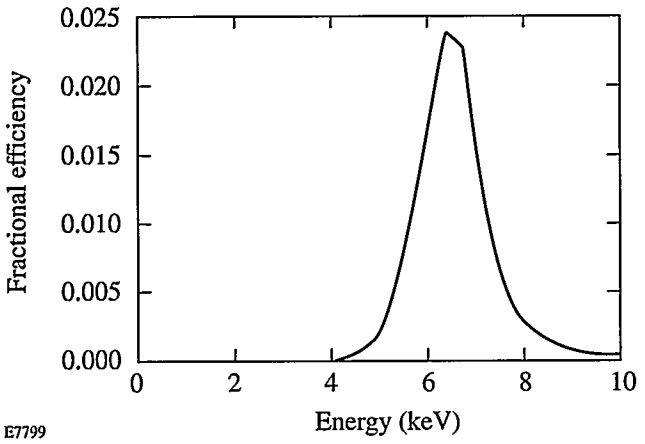


Figure 64.3
Calculated response of the KB microscope versus energy for 0.70° Ir-coated mirrors with a filtration of 203.2 μm of Be in combination with 101.6 μm of Al.

Figure 64.4 shows a comparison of pinhole camera and KB microscope images obtained on shot 5039. The target was a DT-filled glass microballoon overcoated with a 2-μm layer of CH. The increased resolution evident in the KB microscope image illustrates the benefit of the higher resolution and increased sensitivity of the KB microscope. The x-ray pinhole camera and the KB microscope were positioned within 10° of each other on the target chamber, minimizing differences due to view direction. They were similarly filtered so as to be sensitive to x rays of >5-keV energy. The pinhole size was 10 μm and the magnification was 4.0. The microscope was operated at a magnification of 12.9. Both images were recorded on Kodak DEF film. One benefit of the increased sensitivity of the microscope is the ability to operate at higher magnifications, thereby reducing film grain noise as a contribution to image blurring. Clearly the increased spatial resolution allows for the imaging of finer details in the stagnation core.

For purposes of comparison with the previously described framing-camera results, Fig. 64.5(a) shows an image from shot 5067. The stagnation core can again be seen in this image. In this shot, as with many others not shown here, the right-hand side of the shell is much brighter than the left-hand side. A significant part of this effect is due to a systematic focus offset of the beams illuminating the left side of the target, a problem that has since been corrected. Using an intensity-converted horizontal lineout through the image [shown in Fig. 64.5(b)], the diameter of the stagnated shell can be estimated to be 192 μm, based on the locations of peak emission on either side of the center. (The intensity conversions were accomplished using the semi-empirical formulas of Henke *et al.*[7] and assuming an energy of 6 keV for the optical densities measured

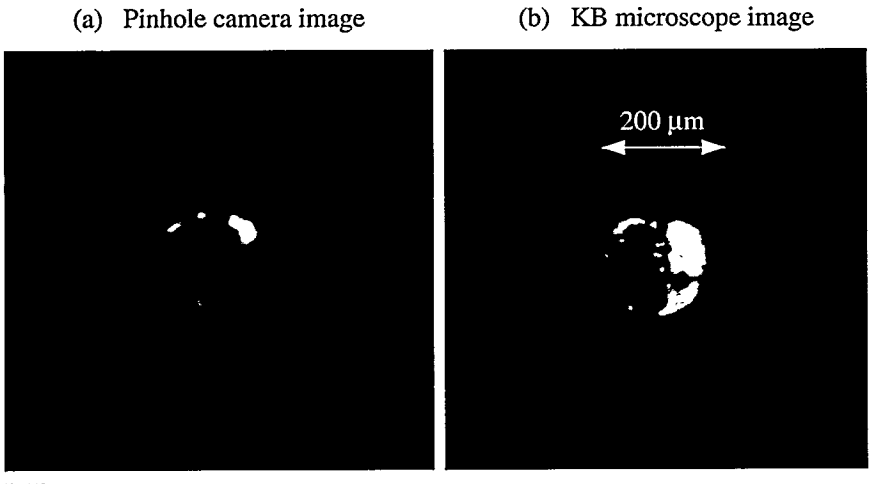


Figure 64.4
(a) Pinhole camera image and (b) KB microscope image of a 20-atm DT-filled glass microballoon of 840-μm diameter and 2-μm wall thickness, coated with 2 μm of CH (shot 5039). The two images have the same spatial scale and are viewed from within 10° of the same direction. The increased spatial resolution of the KB microscope is evident.

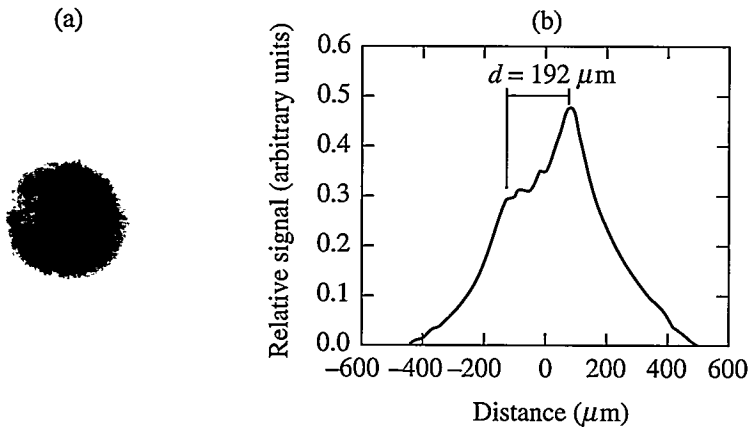


Figure 64.5
(a) KB microscope image of OMEGA shot 5067. The reflective optics are Ir coated, extending their useful band up to 8 keV, while the resolution at the center of the field of view is ~5 μm. (b) An intensity-converted horizontal lineout of the image in (a). The diameter of the stagnated shell is estimated to be ~192 μm.

in the DEF-recorded image.) *LILAC* predictions (Fig. 64.6) indicate a somewhat larger stagnated shell diameter of 275 μm. This disagreement is consistent with what was seen with the framing-camera data above.

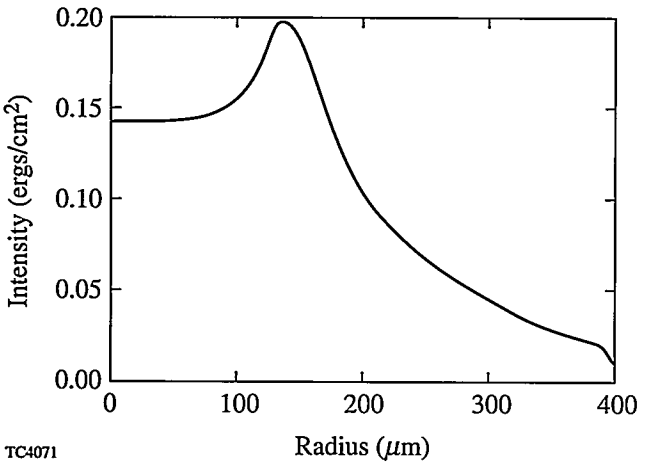


Figure 64.6
*LILAC* simulation of Fig. 64.5(b). The diameter of the stagnated shell, based on the location of peak emission, is predicted to be ~275 μm.

## Fusion Experiments

A set of diagnostics that provided measurements of the neutron yield and the fuel ion temperature was used for these initial experiments. The neutron yield was measured by activation methods and scintillator-photomultiplier systems. Ion temperatures were measured using current-mode, quenched-scintillator/fast-photomultiplier detectors, with signals recorded by wide-bandwidth transient digitizers. Several detectors for both yield and ion temperature were used for each experiment.

The activation systems include copper and sodium activation for the detection of 14.1-MeV neutrons produced by DT fuel mixtures, and indium activation for the measurement of 2.45-MeV neutrons produced by pure deuterium fuel. The activation systems have been calibrated by the associated particle technique in a collaborative effort with the State University of New York at Geneseo. Two of the activation samples are inserted near the target (copper sample at 40 cm, indium sample at 25 cm) by a pneumatically operated rapid extractor. This system automatically transports the sample to the counting area, allowing rapid measurement while reducing the radiation exposure of personnel. On high-yield DT fuel target shots, the copper activation sample is placed 6.6 m from the target chamber in a holder near the other diagnostics (see Fig. 64.7). The sodium activation system uses self-activation/self-detection of sodium in a sodium-iodide gamma-ray detector crystal, which is located 6.6 m from the target chamber.[8]

A scintillator-photomultiplier system is also used to measure yield. This instrument consists of several large scintillators mounted at 6.6 m from the target and used as neutron time-of-flight spectrometers. These "yield" scintillators have active volumes of 2,500 and 44,000 $cm^3$. The primary purpose of these devices is to allow the measurement of low primary and secondary yields. In the present high-yield experiments, the gain of the photomultipliers was reduced to prevent saturation. The data-acquisition subsystem consists of both transient recorders and, optionally, gated charge integrators. The charge integrators are gated to record individually the 2.45-MeV and the 14.1-MeV neutron signals for each detector. The scintillator yield measurements are calibrated *in situ* by comparison with the activation systems for both 2.45-MeV and 14.1-MeV neutrons.

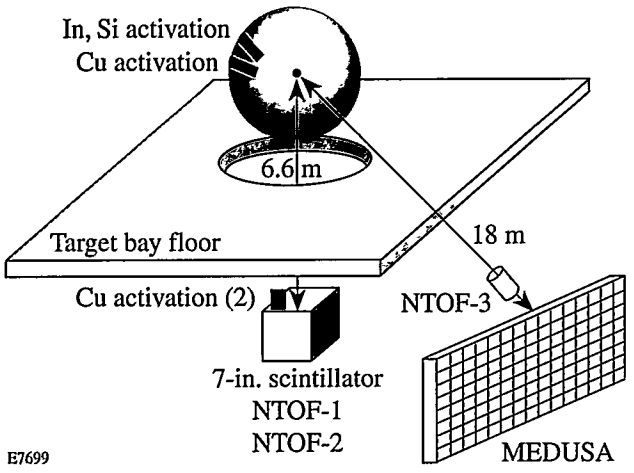


Figure 64.7
Schematic of the target chamber and the location of some of the neutron diagnostic systems.

Time-of-flight spectroscopy, using a GHz-bandwidth scintillator-photomultiplier-digitizer, currently provides ion-temperature measurements with low-temperature thresholds of 3.5 keV (for 14.1-MeV neutrons) and 0.2 keV (for 2.45-MeV neutrons). These detectors, along with the other scintillation detectors, are housed 6.6 m beneath the target chamber in a bunker with 20-cm-thick concrete walls and a 6-cm-thick lead faceplate to reduce the effects of prompt $n$-$\gamma$ radiation (see Fig. 64.7). An additional fast time-of-flight detector is being installed in the neutron diagnostic room at a distance of 18 m from the target chamber; this will provide the higher resolution required for low-temperature DT implosion experiments.

A series of experimental shots were designed to provide a wide range of DT and DD yields to aid in the calibration of the activation counters and scintillators. Table 64.I presents typical neutron data from five target shots. The system response (including the scintillator, photomultiplier, coaxial cable, and recording digitizer) for neutron time-of-flight measurements was determined by applying a short (100-ps) light pulse to the detector package. This system response was deconvolved from the raw experimental signal (an example of which is shown in Fig. 64.8) to obtain the neutron-averaged ion temperatures quoted in Table 64.I. The one-dimensional *LILAC* predictions for yield, neutron-averaged ion temperature, and convergence ratio are also included in Table 64.I. The five shots corresponded to a wide range of targets. Shot 5241, which gave the highest ion temperature, used a thin (2.7-$\mu$m) bare glass shell, while the other shots included plastic shells (shots 5212 and 5221) and plastic-coated glass shells (shots 5049 and 5276).

After the calibration series of shots, emphasis was placed on maximizing the yield in both DT and DD implosion experiments. The design of these experiments focused mainly on

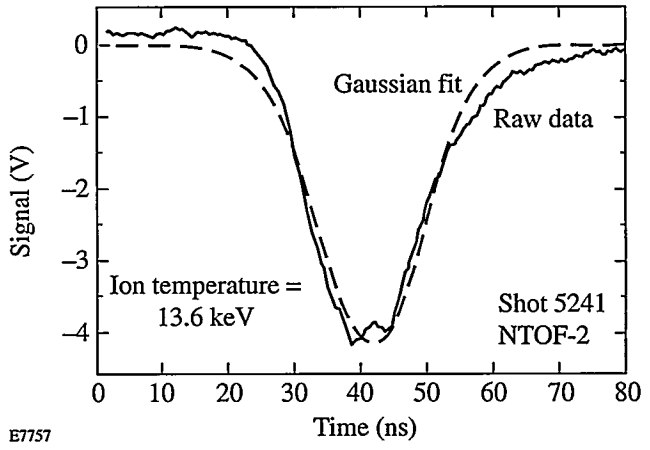


Figure 64.8
Signal obtained from a scintillator-photomultiplier neutron time-of-flight detector placed at 6.6 m from the target. The Gaussian fit to the raw data corresponds to an ion temperature of 13.6 keV.

Table 64.I: Summary of neutron yields and ion temperatures.

| | | Neutron Yield | | Ion Temperature (keV) | | Calculated |
|---|---|---|---|---|---|---|
| Shot Number | Fuel | Measured | Calculated | Measured | Calculated | Convergence Ratio |
| 5049 | DT | $1.0\times10^{14}$ | $2.0\times10^{14}$ | — | 15.0 | 4.4 |
| 5212 | DD | $5.9\times10^{10}$ | $1.7\times10^{11}$ | 4.7 | 2.3 | 19.3 |
| 5221 | DD | $4.8\times10^{10}$ | $1.6\times10^{11}$ | 6.1 | 2.4 | 19.0 |
| 5241 | DD | $5.7\times10^{11}$ | $9.3\times10^{11}$ | 13.6 | 17.0 | 5.2 |
| 5276 | DT | $4.9\times10^{13}$ | $1.7\times10^{14}$ | 7.8 | 9.3 | 8.6 |

reducing the calculated convergence ratio of the pellet during the implosion. The calculated convergence ratio is defined as the ratio of the initial fuel-pusher interface radius to the calculated radius of this same interface at stagnation. It is well established on the basis of stability considerations that one is able to obtain an increasing fraction of the one-dimensionally calculated neutron yield as the calculated convergence ratio is decreased.[9,10] With the limited set of targets available, several options were investigated to reduce the calculated convergence ratio of the implosions while maximizing the one-dimensional yield. A solution was found in overcoating the bare glass microballoons with several microns of parylene and then targeting OMEGA at tighter-than-normal focusing.

Results for the DT neutron yield as a function of UV energy on target are shown in Fig. 64.9. The maximum yield ($1.0 \times 10^{14}$) is the highest recorded to date from any laser system. It must again be noted that precision energy balance, power balance, and beam smoothing have not yet been implemented on OMEGA. Consistent with the discussion of the x-ray images above, the symmetry of the implosions may well have suffered from high initial levels of on-target irradiation nonuniformity. For the shot producing $10^{14}$ neutrons, the calculated convergence ratio was 4.4 and the yield was a fraction 0.52 of the one-dimensional yield. The fusion energy released from this shot was equal to 1% of the laser energy delivered to the target (1% of scientific breakeven).

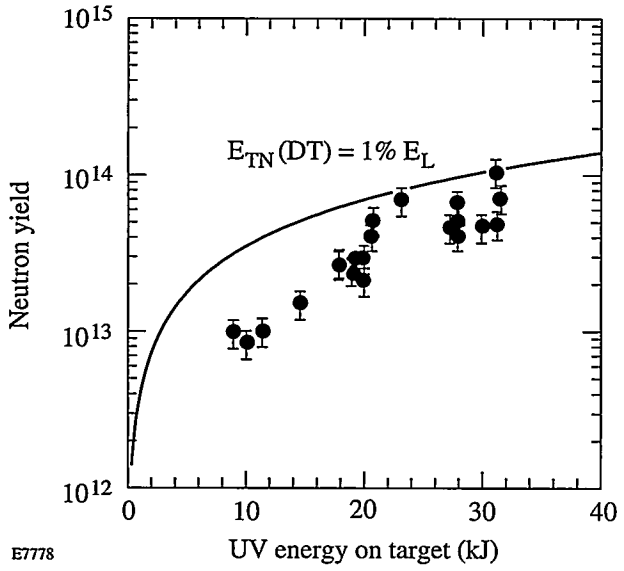


Figure 64.9
Performance summary of initial high-yield implosion experiments. The solid curve indicates the neutron yield corresponding to a fusion energy release equal to 1% of the UV energy on target (1% of scientific breakeven).

**X-Ray Spectroscopy**

It was predicted that high electron temperatures up to 5 keV could be achieved on OMEGA by using relatively thin shell targets. These temperatures would occur at modest compressed densities (~1 to 5 g/cm$^3$), and the ion temperatures would peak at above 10 keV at the center of the compressed core. New diagnostic techniques were thus developed for measuring these temperatures, using K-shell line and continuum spectroscopy of krypton-doped targets.[11,12] (See also the next article in this issue.) A series of krypton-doped, deuterium-filled targets were shot on OMEGA to test these predictions. A strong K-shell Kr spectrum was indeed observed, and high electron temperatures were determined, in close agreement with code predictions. These targets were similar to those of Table 64.I for which high ion temperatures were measured.

The krypton lines observed in these shots have the highest energies, 13 to 16 keV, that have been observed in laser-fusion experiments. Previously, only the $Kr^{+34}$ resonance line (at 13.1 keV) had been observed, using a Von-Hamos focusing spectrometer on the 24-beam OMEGA system operating in short-pulse mode (100 ps, 6 TW).[13]

Results from the present experiments are shown from two Kr-doped target shots for which the experimental parameters are listed in Table 64.II. In the first shot, a Si(111) diffracting crystal was used, tuned to detect the spectral range of 8 to 13 keV, while in the second shot a LiF(200) crystal was used, tuned to the range of 12 to 20 keV.

Figure 64.10 shows a comparison between the measured and simulated spectra from shot 4952. In Fig. 64.10(a), the raw experimental spectrum is shown in film density units. In Fig. 64.10(b), a time- and space-integrated *LILAC* simulation of the same spectrum is shown. This simulation was carried out using a non-LTE radiation transport postprocessor that includes a time-dependent multispecies ionization and level-population model based on a simple screened-hydrogenic description of the principal atomic states. Figure 64.11 shows a similar comparison between experiment and simulation for shot 5110. In both cases the simulated spectrum is plotted on a linear scale, in line with the fact that film density and exposure are approximately linear for the photon energy range detected (see below). The He-$\alpha$ line in Fig. 64.11 has a film density higher than 5 and saturates the film. Instrumental broadening of the lines has been included in the simulation. In comparing the measured and simulated spectra, it should be noted that *LILAC* does not calculate the satellite lines on the low-energy side of the He-$\alpha$ and He-$\beta$ lines, nor the lines above

Table 64.II: Experimental parameters of two CH target shots analyzed using krypton line and continuum spectroscopy.

| Shot No. | Target diameter ($\mu$m) | Target thickness ($\mu$m) | DD pressure (atm) | Krypton pressure (atm) | Laser energy (kJ) |
|---|---|---|---|---|---|
| 4952 | 870 | 10.0 | 10 | 0.03 | 23.6 |
| 5110 | 874 | 12.4 | 10 | 0.03 | 29.5 |

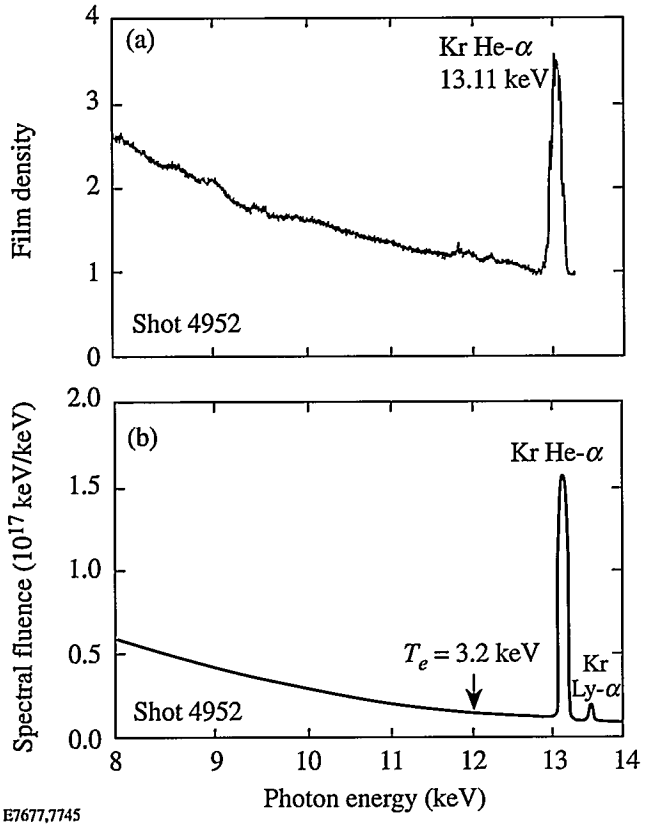


Figure 64.10
(a) Experimental spectrum from Kr-doped, DD-filled target shot 4952. (b) *LILAC* simulation of the same spectrum. The continuum slope around 12 keV in (b) implies $T_e = 3.2$ keV. Instrumental broadening of the calculated lines has been included. The simulation does not include the satellite lines on the low-energy side of the He-$\alpha$ line.

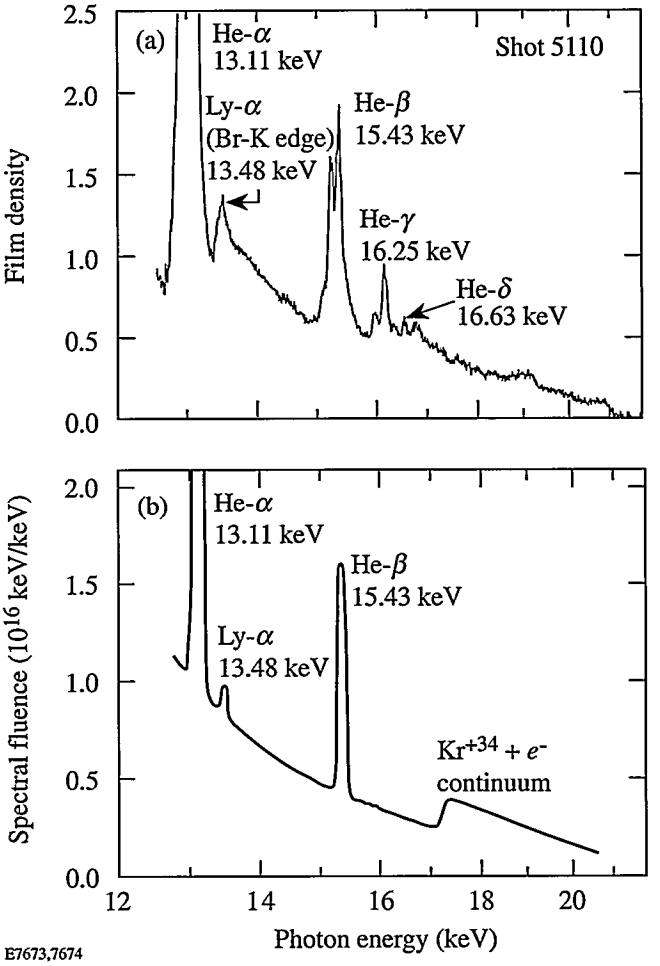


Figure 64.11
(a) Experimental spectrum from Kr-doped, DD-filled target shot 5110. The He-$\alpha$ line has a film density >5 and saturates the film. (b) *LILAC* simulation of the same spectrum. The simulation does not include the satellite lines on the low-energy side of the He-$\beta$ line or the lines above 16 keV. Instrumental broadening of the calculated lines has been included.

16 keV. Also, accounting for film and crystal calibration increases the experimental high-energy continuum and brings it into closer agreement with the simulated one.

To analyze the spectra quantitatively, the responses of the film (Kodak DEF) and the crystals (LiF and Si) have to be known. Henke[14] published a model for the response of DEF film and normalized it to experimental values below 10 keV. Using this model and updated x-ray absorption coefficients in the film constituents, we calculated the film response for photon energies below and above 10 keV. Figure 64.12 shows the results in the 1- to 30-keV range, for various film density values between $D = 0.5$ and $D = 3$ (in increments of 0.5), assuming that the film density was measured with a numerical

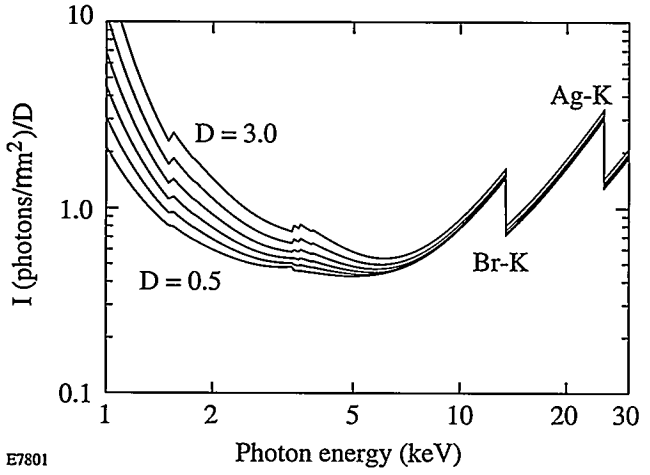


Figure 64.12
Calculated DEF film response for various film-density values between $D$ = 0.5 and $D$ = 3 (in increments of 0.5), assuming that the film density was measured with a numerical aperture of 0.25. Jumps in response due to the $K$ edges of Br and Ag are marked. Henke's model was used, with updated coefficients for x-ray absorption in the film constituents.

aperture of 0.25. Jumps in film response due to the $K$ edges of Br and Ag are marked. Figure 64.12 shows that for film densities below $D \sim 2$ and photon energies above ~6 keV, the film density is proportional to exposure. This is the reason for plotting the spectral fluence in Figs. 64.10 and 64.11 on a linear scale.

For the Si(111) crystal, published diffraction data[15] were used. For the LiF(200) crystal, published calibration data[16] were used as well, and they agree with previous data for LiF(200) crystals used at LLE.[17] It should be emphasized that for the purpose of temperature determination only the changes with photon energy of the film and crystal responses are required. Using the film exposure $I$(keV/cm$^2$) and the integrated crystal reflectivity $R$, the spectral fluence per unit solid angle of the target can be determined. For example, the resulting continuum fluence at a photon energy $E$(keV) is given by $S(\text{keV/keV}) = I(E)L^2 \tan\theta_B/(RE \cos\alpha)$, where $L$ is the target-film distance (along the ray), $\theta_B$ is the Bragg angle, and $\alpha$ is the angle of incidence on the film.

Using the film and crystal calibrations as described above, the spectral data were converted to spectral fluence in absolute units. The continuum slopes in the ranges 8 to 13 keV for Fig. 64.10 (shot 4952) and 16.5 to 20.5 keV for Fig. 64.11 (shot 5110) were used to estimate the electron temperature by fitting exponential curves. Figure 64.13 shows the result for shot 4952 where fitting to the high-energy part of the continuum yields a temperature of 3.1 keV. For shot 5110, the measured temperature was 4.0 keV. The simulated spectra show, in agreement with the experiment, that higher-energy portions of the continuum yield higher temperatures. This is because these portions are preferentially emitted at the higher-temperature regions (and times). The experimental result for shot 4952 agrees with the simulated temperature of 3.2 keV, obtained from the slope of the simulated spectrum in the same spectral range. The absolute magnitude of the continuum is lower than that of the simulated spectrum by only about a factor of 1.5; comparison of the absolute magnitude of spectral lines is complicated by such factors as detailed atomic physics modeling and the spatial distribution of the emitting source.

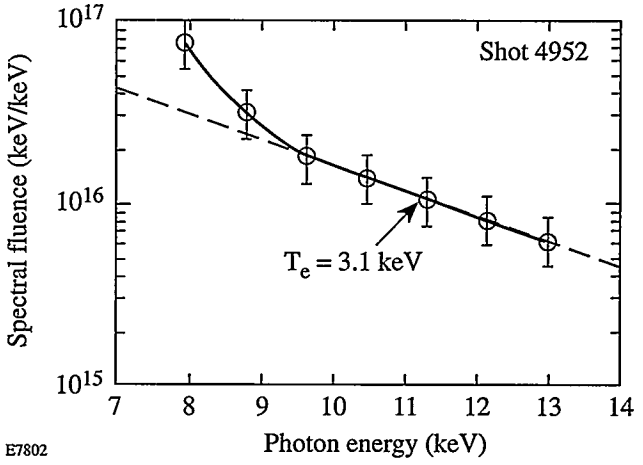


Figure 64.13
Experimental continuum spectrum of Fig. 64.10(a) after absolute calibration. The slope in the 10- to 13-keV range indicates an electron temperature of $T_e$ = 3.1 keV.

*LILAC* results show that the space-averaged temperatures around peak compression in these shots were 3 to 4 keV and the maximum temperatures were 5 to 6 keV. The ion temperatures in such thin-shell implosions are predicted to be significantly higher than the electron temperatures, consistent with the experimental results reported in Table 64.I.

An additional method for estimating the electron temperature involves the measured intensity ratio of the Lyman-$\alpha$ line of $Kr^{+35}$ to the helium-$\beta$ line of $Kr^{+34}$. As described in Ref. 11, this ratio is highly sensitive to the temperature below ~8 keV and changes very little with density. Also, the spectral lines chosen can have a relatively low opacity (unlike that of the He-$\alpha$ line); this is true for the krypton fill pressure and compression in these experiments. However, it was shown[18]

that a high opacity of the He-$\alpha$ line can indirectly increase the Lyman-$\alpha$ to helium-$\beta$ ratio for the same temperature; this is because the He-$\alpha$ opacity facilitates ionization of the helium-like state through $n=2$ excited $Kr^{+34}$ ions. Figure 64.14 shows curves of the calculated intensity ratio[12] of these two lines, with and without a correction for the opacity of the He-$\alpha$ line. The curve used here for the temperature determination corresponds to the opacity ($\tau = 15$) for shot 5110, estimated on the basis of *LILAC*-predicted profiles. A complication arises because the wavelength of the $K$ edge of Br (in the film grains) practically coincides with that of the Lyman-$\alpha$ line of $Kr^{+35}$, giving rise to a jump in the film response at that wavelength. The corresponding jump in the measured spectrum should be smaller than what is indicated in Fig. 64.12 because of the finite spectral resolution of the spectrometer (which blends the intensity around the jump). To account approximately for this effect, the continuum at energies above the $K$ edge was extrapolated toward lower energies and the resulting jump in the continuum was subtracted from the measured peak at 13.5 keV. The resulting estimated temperature (see Fig. 64.14) is 4.1 keV.

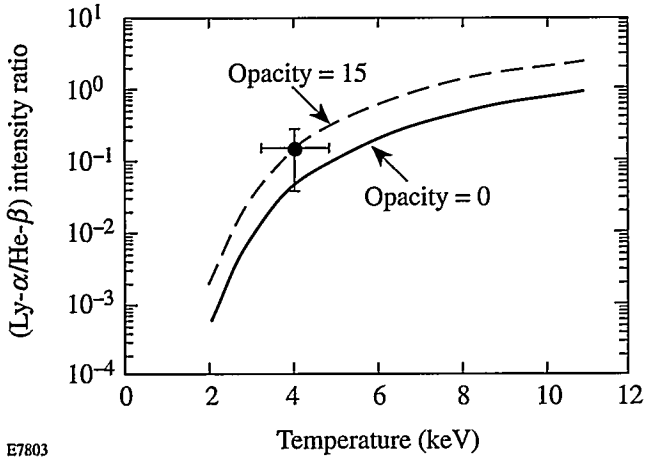


Figure 64.14
Electron-temperature determination by the measured intensity ratio of the Lyman-$\alpha$ to helium-$\beta$ lines. The curves of calculated intensity ratio are taken from Ref. 12. This ratio depends weakly on the density, but it does depend significantly on the opacity of the He-$\alpha$ line. The curve used here for the temperature determination corresponds to the estimated opacity ($\tau = 15$) for shot 5110.

In the future, the ion temperature in similar experiments will be measured through the Doppler broadening of Kr lines, using a recently completed focusing x-ray spectrograph of high spectral resolution. Finally, the measurements will be extended to include $L$-shell Kr lines. It is shown in the following article that the simultaneous measurement of $K$- and $L$-shell lines can be used to determine the fuel $\rho R$ and to study core-shell mixing.

## Summary

Initial target experiments have been performed with the upgraded OMEGA laser, using glass and CH microballoons filled with either pure deuterium or DT. During these experiments several key diagnostic systems have been activated including an x-ray framing camera, a Kirkpatrick-Baez (KB) microscope, copper and indium neutron activation counters, scintillator-photomultipliers, and a crystal spectrometer. The framing camera has been used to diagnose the target implosion dynamics, which agree well with predictions up to the stagnation phase. Deviations from predictions, also seen using the KB microscope, are consistent with the present lack of beam smoothing on the laser. Neutron yields up to $10^{14}$ (1% of scientific breakeven)—the highest recorded to date from any laser system—have been obtained from DT targets and fuel ion temperatures up to 13 keV have been measured. Spectroscopic diagnostics based on the continuum slope and krypton line ratios have demonstrated electron temperatures from 3 to 4.1 keV. Taken as a whole, these results demonstrate a successful integration of laser operations and target diagnostics into the OMEGA experimental system.

## ACKNOWLEDGMENT

This work was supported by the U.S. Department of Energy Office of Inertial Confinement Fusion under Cooperative Agreement No. DE-FC03-92SF19460, the University of Rochester, and the New York State Energy Research and Development Authority. The support of DOE does not constitute an endorsement by DOE of the views expressed in this article.

## REFERENCES

1. Laboratory for Laser Energetics LLE Review **63**, NTIS document No. DOE/SF/19460-91, 1995 (unpublished), p. 99.
2. D. K. Bradley, P. M. Bell, O. L. Landen, J. D. Kilkenny, and J. Oertel, Rev. Sci. Instrum. **66**, 716 (1995).
3. Laboratory for Laser Energetics LLE Review **46**, NTIS document No. DOE/DP/40200-156, 1991 (unpublished), p. 91.
4. F. J. Marshall and Q. Su, Rev. Sci. Instrum. **66**, 725 (1995).
5. F. J. Marshall, J. A. Delettrez, R. Epstein, and B. Yaakobi, Phys. Rev. E **49**, 4381 (1994).
6. J. A. Oertel, T. Archuleta, L. Clark, S. Evans, A. Hauer, F. J. Marshall, C. G. Peterson, T. Sedillo, C. Thorn, and R. G. Watt, in *Ultrahigh- and High-Speed Photography, Videography, and Photonics '95*, edited by D. R. Snyder and G. A. Kyrala (SPIE, Bellingham, WA, 1995), Vol. 2549, p. 82.

7. B. L. Henke, E. M. Gullikson, and J. C. Davis, At. Data Nucl. Data Tables **54**, 181 (1993).

8. R. A. Lerche, Lawrence Livermore National Laboratory Laser Program Annual Report 1978, UCRL-50021-78 (1979), p. 6-53.

9. Laboratory for Laser Energetics LLE Review **28**, NTIS document No. DOE/DP/40200-26, 1986 (unpublished), p. 159.

10. Laboratory for Laser Energetics LLE Review **40**, NTIS document No. DOE/DP/40200-102, 1989 (unpublished), p. 171.

11. Laboratory for Laser Energetics LLE Review **61**, NTIS document No. DOE/SF/19460-58, 1994 (unpublished), p. 1.

12. B. Yaakobi, R. Epstein, C. F. Hooper, D. A. Haynes, and Q. Su, submitted for publication to the Journal of X-Ray Science and Technology.

13. B. Yaakobi and A. J. Burek, IEEE J. Quantum Electron. **QE-19**, 1841 (1983).

14. B. L. Henke *et al.*, J. Opt. Soc. Am. B **3**, 1540 (1986).

15. G. Brogren and E. Lindén, Ark. Fys. **22**, 535 (1962).

16. D. B. Brown and M. Fatemi, J. Appl. Phys. **45**, 1544 (1974).

17. A. J. Burek and B. Yaakobi, Final Report to the National Bureau of Standards contract NB81NAHA2032 (1983), Appendix A.

18. C. J. Keane *et al.*, Phys. Fluids B **5**, 3328 (1993).

# Diagnosis of High-Temperature Implosions Using Low- and High-Opacity Krypton Lines

High-temperature laser target implosions can be achieved by using relatively thin-shell targets. Electron temperatures of up to 5 keV at modest compressed densities (~1 to 5 g/cm$^3$) are predicted for such experiments and have been diagnosed in an initial series of implosion experiments on the upgraded OMEGA laser (see the previous article). The corresponding ion temperatures are predicted to be higher, peaking above 10 keV at the target center. The possibility of using krypton doping for diagnosing the core temperature of imploding targets was discussed in an earlier issue of the LLE Review.[1] In that work, a simplified analysis for the case of optically thick lines was performed, using approximate Stark profiles. In the present work, the use of detailed Kr Stark profile calculations by C. F. Hooper *et al.* from the University of Florida improves and extends the earlier analysis. The use of krypton doping is a powerful technique for diagnosing target implosions, as the implosion dynamics are to lowest order independent of doping and different levels of doping can be used to permit the measurement of different quantities. For example, low doping levels allow low-opacity lines to be used to measure the ion temperature via Doppler broadening, while higher doping levels allow the density-radius product ($\rho R$) of the compressed fuel to be measured from high-opacity lines. In high-density implosions, low-opacity lines can be used to diagnose the density through Stark broadening, and higher-opacity lines can be used to estimate the extent of mixing.[1]

Calculations have been carried out using the *LILAC* code for a CH shell of 1-mm diameter and 10-$\mu$m thickness, filled with a 10-atm pressure of DT.[1] The laser energy was 30 kJ in a Gaussian pulse of 650-ps width. Results have shown that the core electron temperature and density are fairly uniform, at ~5 keV and ~4.5 g/cm$^3$, respectively. On the other hand, the ion temperature ranges from ~6 keV to ~12 keV and is centrally peaked. Code calculations have shown that the core temperatures are hardly changed by the addition of 0.01 atm of krypton. By adding 0.1 atm of krypton, the peak electron temperature drops a little to about 4 keV. The predicted spectra have been calculated by the *LILAC* code and a non-LTE post-processor, which includes transitions between actual atomic configurations, using Doppler and Stark profiles. The calculated line intensities even for the 0.01-atm case are very substantial (of the order of $10^{17}$ keV/keV), and the contrast of line to continuum is better than a factor of 4 for the He-$\beta$ line. Furthermore, the shape of the spectrum above ~10 keV at peak compression differs little from the time-integrated spectrum because most of the emission originates from peak compression. Thus, a time-integrated measurement in this spectral range yields the conditions at peak compression with reasonable reliability.[1]

### Diagnosis of Density Using Low-Opacity Lines

A recently developed multielectron line-profile formalism and code (MERL)[2,3] has been used to calculate Stark-broadened emission line profiles for the Kr K-shell lines. The analysis in this article relies in particular on the helium-$\beta$ transition ($3^1P$–$1^1S$), and the profiles shown here pertain to this line. Broadening due to perturbing ions is treated in the quasi-static ion approximation, and the dynamic effect of electrons is calculated using a second-order relaxation theory. Ion- and electron-radiator interactions are computed in the dipole approximation. Necessary atomic physics data (energy-level structure and reduced dipole matrix elements) were calculated using Cowan's[4] multiconfiguration atomic structure code, using the Hartree-Plus-Statistical-Exchange method for approximating the potential energy function due to the electrons, and including relativistic corrections.

Figure 64.15 shows examples of calculations carried out by the group at the University of Florida. The Stark profile of the helium-$\beta$ line of $Kr^{+34}$, of 0.8033-Å wavelength, is calculated for two densities: (a) $1 \times 10^{24}$ cm$^{-3}$ and (b) $5 \times 10^{24}$ cm$^{-3}$. It is assumed that the krypton constitutes a small fraction mixed into the fuel and that most of the perturbers are fuel ions. The effect of Doppler broadening is also calculated, at an assumed ion temperature of 10 keV. The shape of the Stark profile is significantly affected by relativistic effects in the atomic physics due to the relatively high nuclear charge $Z$ of krypton. There are two dipole-allowed transitions from the $1s3l$ upper-level manifold to the ground state. The unperturbed singlet-singlet

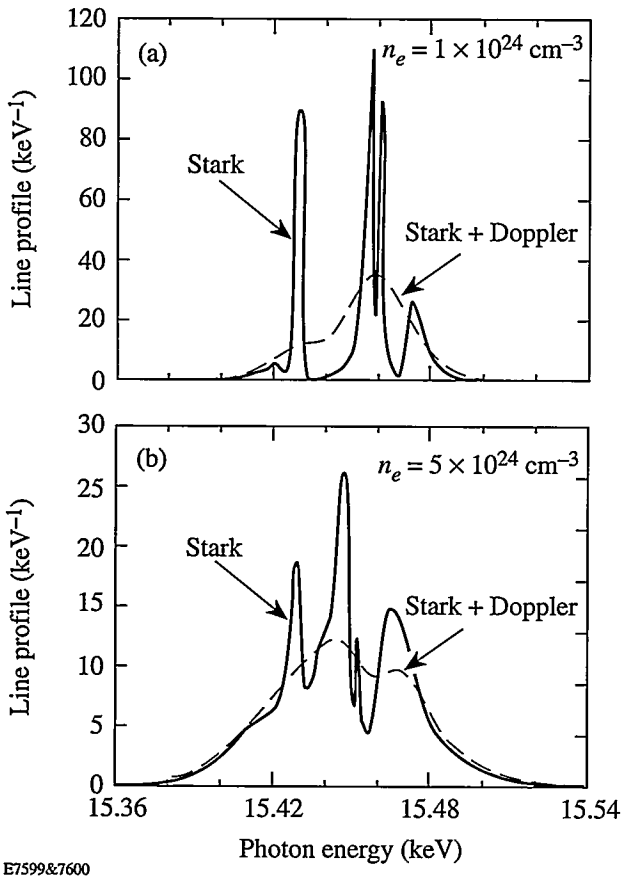


Figure 64.15
Calculated Stark profile of the He-$\beta$ line of $Kr^{+34}$ (solid line) and the combined Stark and Doppler profile corresponding to an ion temperature of 10 keV (dashed line). Electron densities $n_e$ of (a) $1 \times 10^{24}$ cm$^{-3}$ and (b) $5 \times 10^{24}$ cm$^{-3}$ were assumed.

transition is located at 15,451 eV, and the triplet-singlet transition is located at 15,426 eV. Additional peaks appear because of field mixing among the levels of the upper manifold.

Comparison of Figs. 64.15(a) and 64.15(b) clearly shows the effect of increasing density on the profile. The lower density, $1 \times 10^{24}$ cm$^{-3}$ (~4.5 g/cm$^3$), is at the upper end of the expected density range for the high-temperature target shots. The higher density, $5 \times 10^{24}$ cm$^{-3}$ (~22.5 g/cm$^3$), corresponds to future experiments where both high density and high temperature will be achieved. For the lower-density case the combined profile width is dominated by the Doppler broadening and can thus yield the ion temperature. To measure this width, a spectral resolution $\lambda/\Delta\lambda$ greater than ~1000 is required. This is not easily achievable with a flat crystal spectrometer, unless employed at a very large distance from the target; however, a Rowland-circle focusing spectrograph can readily achieve this.[5] In going from the lower density ($1 \times 10^{24}$ cm$^{-3}$) to the higher density ($5 \times 10^{24}$ cm$^{-3}$) the line width more than doubles, reflecting the increasing effect of the Stark broadening. It should be noted, however, that this broadening is mostly the result of the increase in intensity of forbidden components. Only at much higher densities will the total width of the manifold be determined by the Stark width rather than by the separation of the components. For the density range covered by Fig. 64.15, density signatures are provided by the width as well as the shape of the compound profile, which in turn is determined by the change in intensity and spectral position of the various components. In particular, in going from the lower to the higher density, the peak intensity of the compound profile shifts to lower energies by about 10 eV (due to the so-called "level repulsion" in second-order perturbation theory). To measure this shift, a spectral resolution $\lambda/\Delta\lambda$ greater than ~2000 is required.

### Diagnosis of $\rho R$ using High-Opacity Lines

Optically thick spectral lines can be used to deduce the $\rho R$ of the compressed core. The self-absorption of spectral lines (i.e., the absorption by the same transition as that of the emission line) affects both the emergent line intensity as well as its spectral shape. Self-absorption leads to broadening; for a spatially uniform temperature the spectral profile will tend to be flat-topped, whereas for a radially falling temperature the line profile may have a central minimum. In the past, the broadening due to self-absorption of the Lyman-$\alpha$ line of argon was employed to estimate the core $\rho R$.[6] As explained in Ref. 6, the density has to be known (by fitting Stark profiles to an optically thin line) to deduce the $\rho R$ from an optically thick line. Alternatively, the width of several optically thick lines in the same line series must be measured.[7] These methods can be employed here as well. However, we pursue an alternative method, based on the intensity of the optically thick line rather than its profile, which does not require a prior knowledge of the density or the use of additional lines.

The intensity of an optically thick line emerging from the plasma volume is related to the escape factor parameter, which has been the subject of numerous publications.[8–11] The escape factor $G$ is defined by

$$G(\tau_0) = \int_{-\infty}^{\infty} P(\delta E) \exp\left[-\tau_0 P(\delta E)/P(\delta E = 0)\right] d(\delta E), \quad (1)$$

where $\delta E$ is the energy separation from the unperturbed posi-

tion, $P(\delta E)$ is the line profile at $\delta E$ in inverse energy units, and $\tau_0 = \tau(0)$ is the optical depth at $\delta E = 0$. The line opacity $\tau(\delta E)$ can be expressed as [see Eq. (8-14) in Ref. 12]

$$\tau(\delta E) = \left(\pi e^2 h / Mmc\right) P(\delta E)\, f\, \rho R\, \varepsilon Q_n, \qquad (2)$$

where $M$ is the krypton ionic mass, $m$ is the electron mass, $e$ is the electron charge, $h$ is Planck's constant, $c$ is the speed of light, $f$ is the absorption oscillator strength of the line, $\rho R$ is the total areal density (mostly that of the fuel), $\varepsilon$ is the fraction of krypton in the fuel (by mass), and $Q_n$ is the fraction of krypton ions in the absorbing level (i.e., the lower level of the transition). The spectral position $\delta E = 0$, which is somewhat arbitrary, is taken to be 15,451 eV, the unperturbed position of the strongest line.

The escape factor $G(\tau_0)$ in spherical geometry, as given by Eq. (1), corresponds to a point source at the center of the sphere, with $\tau_0$ the opacity integrated over the radius. For a source uniformly distributed over the sphere, Mancini *et al.*[11] have shown that $G(\tau_0)$ for Holtsmarkian profiles and large opacities is about twice as large as for the point-source case. This indicates that knowing the temperature profile (or the spatial distribution of emitting and absorbing ions) is not critical when using the calculated escape factor for diagnostics. Thus, a two-temperature spatial profile (a hot spot surrounded by a cool absorbing layer) and a uniform temperature profile give an escape factor that differs by only a factor of 2 for any $\tau_0 >> 1$. To determine which geometry agrees better with the experiment we can examine two experimental signatures: (a) for a uniform source, the core image size at high photon energy will be about the same as that at low photon energy, whereas for a hot-spot source the former will be much smaller than the latter, and (b) for a uniform source the observed line profile will be flat-topped, whereas for a hot-spot source a self-reversal (or minimum) will be observed at the position of the profile peaks. Equation (1) applies to a two-temperature spatial profile but assumes that the line profile is the same in both the emission and absorption regions. This implies a uniform density since the density-dependent Stark broadening dominates the emergent profile for high opacities (see below). As an example, if the absorption line profile is half as wide as the emission profile (indicating a lower density by about a factor of 2.8), the escape factor can be shown to be larger by about 30%.

To obtain the escape factor $G(\tau_0)$ from Eq. (1) for our case, we use profiles such as those in Fig. 64.15. Figure 64.16 shows the escape factor as a function of the opacity at line center (15,451 eV), with and without the Doppler profile contribution. The curves are calculated for an ion temperature of 10 keV. The escape factor $G$ depends on the temperature only through the Doppler contribution. Figure 64.16 shows that we

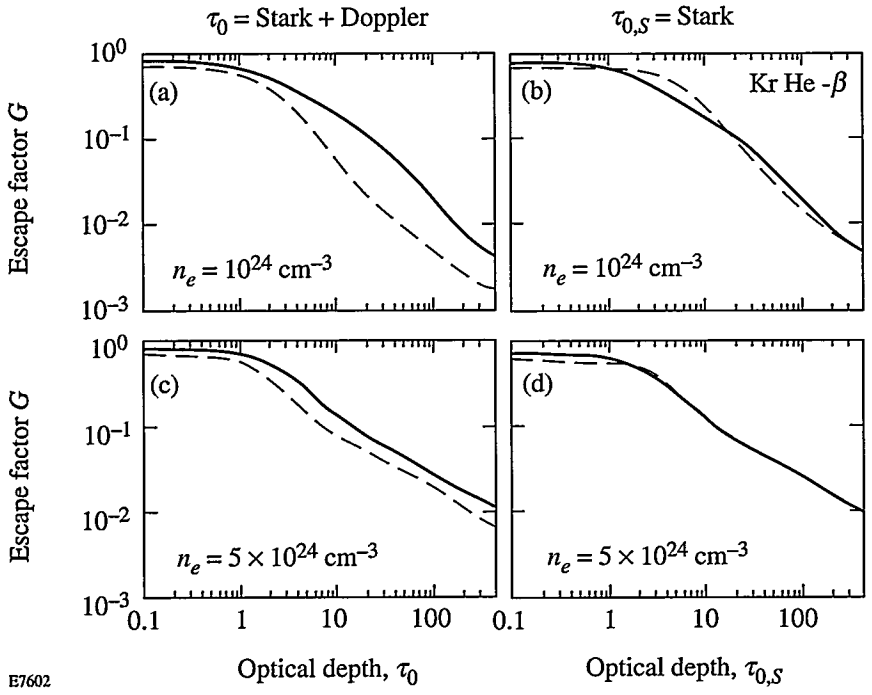


Figure 64.16
Calculated escape factor of the He-$\beta$ line of $Kr^{+34}$ for the two electron densities used in Fig. 64.15, as a function of the opacity at the line center (15,451 eV), without the Doppler contribution (solid curves) and with the Doppler contribution (dashed curves). In (a) and (c) the opacity $\tau_0$ at 15,451 eV relates to the total Stark + Doppler profile, while in (b) and (d) the opacity $\tau_{0,S}$ at 15,451 eV relates to the Stark profile only.

can almost eliminate this dependence by plotting $G$ as a function of $\tau_{0,S}$, the opacity at line center due to the Stark profile only. When changing from $\tau_0$ to $\tau_{0,S}$, the curves of total profile shift to opacity values that are larger (since $\tau_{0,S} > \tau_0$) by the ratio $\tau_{0,S}/\tau_0$. The two curves thus plotted are almost coincident. The reason for this is simple: The Doppler profile decays much faster, with increasing separation from line center, than the Stark profile. Thus, the far wings are relatively unaffected by Doppler broadening. However, the escape factor for high opacity values depends only on the far wings [see Eq. (1)]. Therefore, the escape factor for high opacities will be relatively independent of the temperature. Since the profile on the far wings is essentially identical to the Stark profile, the escape factor will depend only on the Stark opacity $\tau_{0,S}$ at line center.

A similar situation will arise if we include ion-dynamic effects in the calculation of the Stark profiles. Effects on the Stark profile of the motion of perturbing ions (which are otherwise assumed stationary) will depend also on the ion temperature and will affect mostly the line center rather than its wings. Thus, the opacity $\tau_{0,S}$ relates to the Stark profile without either the Doppler effect or the ion-dynamic effects.

Comparison of the profiles in Fig. 64.16 shows also the relative insensitivity of the escape factor to the density. As mentioned earlier, for a Holtsmarkian profile and high opacities $G(\tau_0)$ depends only on $\tau_0$ and not on the density (or the line width). For easier comparison, Fig. 64.17 shows the escape-factor curves from Figs. 64.16(b) and 64.16(d), calculated without the Doppler contribution, for the two densities $1 \times 10^{24}$ cm$^{-3}$ and $5 \times 10^{24}$ cm$^{-3}$. As seen, the two profiles overlap to within a factor of ~1.4. Similar agreement is obtained in comparing curves that do include the Doppler broadening. We can thus use Fig. 64.16 to find the quantity $\tau_{0,S}$ from a measured value of the escape factor, without a precise knowledge of the temperature or the density. The question before us now is what does the opacity $\tau_{0,S}$ depend on, i.e., what diagnostic information can be inferred from knowing $\tau_{0,S}$?

From Fig. 64.16, the escape factor for high opacity in the density range $(1–5) \times 10^{24}$ cm$^{-3}$ can be approximated by the relation

$$G(\tau_{0,S}) \sim 1.3/(\tau_{0,S})^{0.9} . \qquad (3)$$

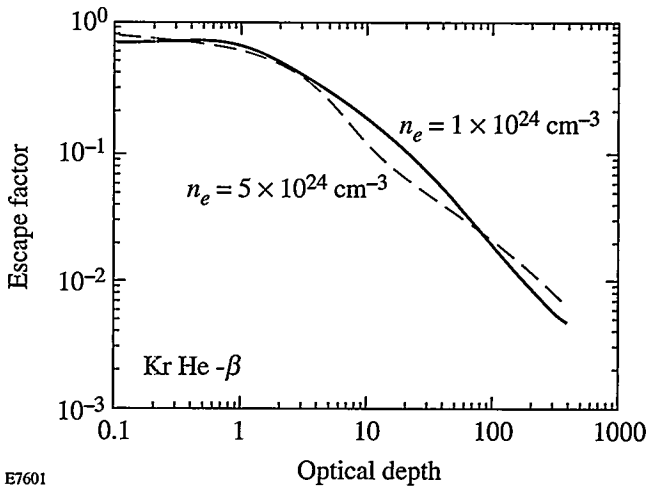


Figure 64.17
Calculated escape factor of the He-$\beta$ line of $Kr^{+34}$ for two electron densities, as a function of the opacity at line center (15,451 eV), without the Doppler contribution.

Only at much higher densities, where level mixing of the $n = 3$ manifold due to the plasma electric field becomes substantial, will this relation tend to that for the Holtsmarkian profile mentioned above. For that case it was shown earlier[1] that the density dependence of $\tau_{0,S}$ drops out but the determination of $\tau_{0,S}$ (through the measurement of the escape factor) can then yield information on possible mixing. For the density range discussed here, Eq. (3) does lead to a dependence of $\tau_{0,S}$ on the density (or on the $\rho R$), thus providing a diagnostic for $\rho R$. A method for measuring the escape factor was described in Ref. 1.

The diagnostic method for the fuel $\rho R$ consists of measuring the escape factor as outlined in Ref. 1, and then deducing $\tau_{0,S}$ from curves like those in Fig. 64.16. It follows from the definition of $\tau_0$ (Eq. 2) that if we substitute $\tau_{0,S}$ for $\tau_0$, the profile $P(\delta E = 0)$ appearing in Eq. (2) should refer to the pure Stark profile $P_S(\delta E = 0)$. This profile can be read off the calculated Stark profiles such as those in Fig. 64.15 and is obviously a function of the density. In the range $(1–5) \times 10^{24}$ cm$^{-3}$, $P_S(\delta E = 0)$ as a function of the density $\rho$ can be approximated as

$$P_S(\delta E = 0) \sim 0.4/\rho^{0.88} . \qquad (4)$$

In any practical case, the complete profile curves can be used rather than this approximate expression. Further, in an imploding spherical target the following relationship holds:

$$\rho R = \left(3M_F/4\pi\right)^{1/3} \rho^{2/3}, \tag{5}$$

in terms of the total fill mass $M_F$ (fuel and krypton). Combining Eqs. (2), (4), and (5) we can write

$$\rho R = 0.02 A^{3.125} \left(3M_F/4\pi\right)^{1.375} G^{3.437}, \tag{6}$$

where $A = \left(\pi e^2 h/Mmc\right) f \varepsilon Q_n$ [from Eq. (2)]. The quantity $Q_n$ has been shown[1] to be very close to unity over a wide temperature range. This relation is the basis for determining the fuel $\rho R$ from a measurement of the escape factor $G$. As mentioned above, actual calculated curves can be used rather than the approximations given in Eqs. (3) and (4).

Finally, we estimate the expected sensitivity of the method for measuring the fuel $\rho R$. To find $G$ from the intensity ratio of the helium-$\beta$ and Balmer-$\alpha$ lines,[1] with a precision of ±20%, the intensity of each of the lines (in relative units) has to be measured with a precision of ±10%. A method for the relative calibration of the two instruments measuring the two different wavelengths was described in Ref. 1. From Eq. (3), an error of ±20% in $G$ will result in an error of ±22% in $\tau_{0,S}$. Finally, from Eq. (6), the precision in determining the compressed fuel $\rho R$ will be better than a factor of 2.

## Summary

In summary, the use of krypton doping for diagnosing high-temperature, medium-density implosions has been discussed for two cases: low-opacity lines (achieved with low doping) and high-opacity lines. Using detailed Kr Stark profile calculations, it is found that the profiles of low-opacity lines in the expected density range are dominated by Doppler broadening; they can thus provide a measurement of the ion temperature if spectrometers of spectral resolution $\Delta\lambda/\lambda \geq 1000$ are used. For high-opacity lines, obtained with a higher krypton fill pressure, the measurement of the escape factor can yield the $\rho R$ of the compressed fuel. At higher densities, Stark broadening of low-opacity lines becomes important and can provide a measurement of the density, whereas lines of higher opacity can be used to estimate possible mixing.[1] These higher densities will arise in future experiments where high temperatures and high densities will be simultaneously achieved.

## ACKNOWLEDGMENT

This work was supported by the U.S. Department of Energy Office of Inertial Confinement Fusion under Cooperative Agreement No. DE-FC03-92SF19460, the University of Rochester, and the New York State Energy Research and Development Authority. The support of DOE does not constitute an endorsement by DOE of the views expressed in this article.

## REFERENCES

1. Laboratory for Laser Energetics LLE Review **61**, NTIS document No. DOE/SF/19460-58, 1994 (unpublished), p. 1.
2. L. A. Woltz and C. F. Hooper, Jr., Phys. Rev. A **38**, 4766 (1988).
3. R. C. Mancini *et al.*, Comput. Phys. Commun. **63**, 314 (1991).
4. R. D. Cowan, *The Theory of Atomic Structure and Spectra* (University of California Press, Berkeley, CA, 1981).
5. J. C. Kieffer *et al.*, Appl. Opt. **28**, 4333 (1989); B. Yaakobi, T. Boehly, and P. Audebert, Rev. Sci. Instrum. **61**, 1915 (1990).
6. B. Yaakobi, S. Skupsky, R. L. McCrory, C. F. Hooper, H. Deckman, P. Bourke, and J. M. Soures, Phys. Rev. Lett. **44**, 1072 (1980).
7. N. D. Delameter *et al.*, Phys. Rev. A **31**, 2460 (1985).
8. F. E. Irons, J. Quant. Spectrosc. Radiat. Transfer **22**, 1 (1979).
9. J. P. Apruzese, *ibid.* **34**, 447 (1985).
10. C. Chenais-Popovics *et al.*, *ibid.* **36**, 355 (1986).
11. R. C. Mancini, R. F. Joyce, and C. F. Hooper, Jr., J. Phys. B: At. Mol. Phys. **20**, 2975 (1987).
12. H. R. Griem, *Plasma Spectroscopy* (McGraw-Hill, New York, 1964).

# Simulations of Diagnostic Emission due to Fuel-Pusher Mixing in Laser-Driven Implosions

It is important to develop diagnostics of the Rayleigh-Taylor instability that occurs during the deceleration phase of inertial-confinement-fusion capsule implosions because this instability is a crucial factor limiting the capsule performance.[1] To simulate the effects of this instability and to assess possible diagnostic techniques, a mix model has been added to the one-dimensional (1-D) hydrocode *LILAC*.[2] This model includes the effects of turbulent mixing on the hydrodynamic motion as well as on the temperature and material-concentration profiles within the plasma. In the work described here, this model is used to simulate time-resolved images of implosions of a gas-filled capsule that is representative of the kind proposed for near-term experiments on the 30-kJ, 60-beam OMEGA laser. In particular, the use of emission from thin chlorine-doped layers in the pusher is considered as a means to track the growth of the mixed region near the fuel-pusher interface. It is shown how the onset of mix-induced emission varies over a series of polymer-shell targets that are identical, except that the additive layer is displaced by different amounts from the fuel-pusher interface in each target. It is also shown that the introduction of an additive layer sufficiently thick to produce adequate diagnostic emission has a minor effect on the implosion performance, compared with the effects of mix itself.

The Rayleigh-Taylor instability is the tendency of adjacent fluid layers to interpenetrate one another when the less dense of the two layers supports the denser layer under a gravitational or inertial force.[3] Under these circumstances, perturbations in their interface grow into buoyant bubbles of the lighter fluid that rise past sinking spikes of the heavier fluid.[4] As the depth of penetration becomes comparable to the lateral scale length of the bubble-spike structure, the interpenetration becomes more turbulent[4] and the state of the two fluids approaches that of a mixture.

This instability appears twice during a capsule implosion. The first occurrence, the acceleration-phase instability, starts at the very beginning of the implosion at the ablation front where the shell is being accelerated inward by the hot and relatively light plasma ablating from the capsule surface. This instability can be seeded by both initial surface imperfections in the shell and nonuniform laser irradiation. The second occurrence, the deceleration-phase instability, begins as the rising pressure in the fuel core decelerates the imploding shell. At this time, the inward radial acceleration reverses, and the instability moves to the inner side of the density peak in the pusher to the fuel-pusher interface, where the hot central fuel mass supports the cooler and denser pusher. Here, the unstable growth of the fuel-pusher interface is seeded by the accumulated distortion that feeds through from the ablation region. As pusher material mixes with the fuel, cooling by dilution causes the nuclear reaction rates to drop. In addition, the dispersal of the fuel into the pusher reduces the areal density of the fuel mass (the fuel-averaged density-radius product, $\rho R$), which is a key measure of how close to ignition the fuel has come. If the pusher contains a substance other than hydrogen, radiative losses will cool the fuel further. If this enhanced radiation loss can be observed either spectroscopically or with imaging, then it can be interpreted as evidence that mix has occurred.

Such a diagnostic represents a logical extension of the technique of using plastic-coated glass targets[5] and multilayer targets[6] in thermal transport experiments to measure the advance of the thermal front in the ablation region. Calculations of the growth of the mix region near the ablation front showed that mixing due to the acceleration-phase instability significantly augments thermal conduction in transporting the laser-driven heat front to the glass substrate layer, which accounted for emission from the glass appearing sooner than expected from simulations based on thermal transport alone.[6]

In adapting this technique to the deceleration-phase instability of the fuel-pusher interface, we consider a series of targets where a thin additive layer is placed at various distances $\Delta r$ from the inner surface of the pusher (see Fig. 64.18). The characteristic emission from the additive is delayed until the mixed region has grown through the underlying pure-CH polymer to include the additive layer. By measuring the delay

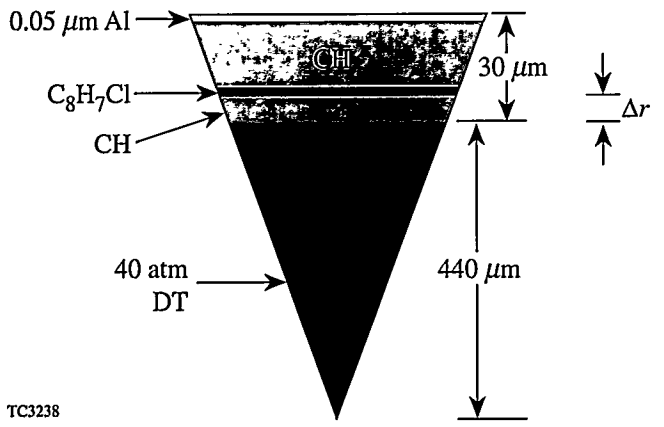


Figure 64.18
Section of the representative spherical capsule that will serve as the example in the calculations to follow. The $C_8H_7Cl$ additive layer is 2-μm thick. It is to be imploded with a square 13.5-TW pulse of 2.3-ns duration.

of the additive emission as a function of the initial position of the additive layer, the trajectory of the bubble surface, the outer boundary of the mixed region, can be inferred.

This technique is also a refinement of a method used in experiments on the Nova laser at the Lawrence Livermore National Laboratory where iodine was added to polymer shells to increase the emissivity of the pusher.[7] In other experiments,[8] chlorine was used as a pusher additive and argon as a fuel additive. The overall degree of mixing was inferred from the intensity of chlorine emission, relative to the intensity of the argon emission, and an average temperature of the mixed additive was obtained from the line ratios of the spectra of the additives. The use of thin additive layers and time-resolved measurements allows the growth of the mix region to be followed in time by associating the arrival of the outer mix-region boundary at the additive-layer radius with the onset of the characteristic additive emission. The idealizations of a distinct mix-region boundary at the bubble front and an abrupt onset of the diagnostic emission are only approximations, but they are useful for understanding the results of the simulations and for anticipating the results of actual experiments.

### Mix Modeling in One Dimension

In our spherically symmetric, purely 1-D simulation, the multidimensional bubble-spike structure and the subsequent turbulent structure are not described explicitly, leaving instead a fluid that is completely mixed at the atomic level. The mix model used within the 1-D hydrocode *LILAC* is formulated as a diffusive process that transports constituent concentrations and thermal energy within the boundaries of the mix region. These boundaries are the bubble and spike fronts obtained from perturbation mode amplitudes calculated from the 1-D hydrodynamics using a multimode Rayleigh-Taylor model similar to that of Haan.[9] The diffusion coefficient is the product of a velocity derived from the expansion of the mix region and a scale length $\lambda_{mix}$ characteristic of the mixing motion. At this point in the development of the 1-D mix model, this scale length is a free parameter, but work is now in progress to allow its value to be derived at each time from other physical parameters of the system being simulated. The inclusion of this 1-D mix model within *LILAC* allows for simulations that take into account the cooling effects of radiation and dilution and the associated reduction in the diagnostic emission and the neutron yield. These simulations also allow the hydrodynamics to respond to the moderated density and pressure profiles, as well as to the effects of the modified radiative properties of the mixed fluid.

An important consequence of this 1-D approximation is that the interpenetrating fluid elements share the same spherically averaged temperature profile. It is reasonable to expect that thermal conduction equilibrates temperatures rapidly over the short scale lengths of the interpenetrating fluid bubbles, spikes, fingers, and eddies, which will tend to evolve the temperature of the mixing region toward a spherically symmetric temperature profile common to all the constituents. To the extent that this is true, the temperature in the neighborhood of a particular ion of additive material will depend more on its radial coordinate than on information lost by disregarding the nonspherical fluid structure.

A difficulty with the 1-D mix model can occur when the mixed region is optically thick. In reality, or in a multidimensional description, this region could have optically thin spots that would allow radiation to escape that otherwise would not escape. Even a relatively subtle effect of this kind would limit the usefulness of a 1-D model for simulating quantitative line intensities, except when line-absorption effects are negligible or otherwise well understood. Also, emission that is particularly temperature sensitive could be misrepresented if spherical averaging were to smooth out some hot spots. However, the use of a local transport model in 1-D does preserve important elements of realism by evolving and distributing the constituent concentrations in a physically plausible way. This is an improvement over global approximations such as forcing flat concentration profiles throughout the mix region[8] or postulat-

ing analytical forms to interpolate the temperature, density, and concentration profiles between the boundaries of the mixed region. Modeling the mix of thermal energy along with the plasma constituents gives an effective enhancement of thermal transport consistent with the mix model. Also, by incorporating the mix model into the hydrodynamics, the mix-affected plasma profiles and pressure gradient remain consistent with the main hydrodynamic process that is the formation of the compressed core.

### Time-Dependent Pusher Emission

The capsule chosen to illustrate the model is shown schematically in Fig. 64.18. It is a 30-$\mu$m-thick CH polymer shell (the pusher), 940 $\mu$m in diameter, filled with 40 atm of DT. It is driven by a simple, flat-top, 13.5-TW pulse, 2.3 ns in duration. A 2-$\mu$m-thick layer of $C_8H_7Cl$ is added to this basic design at a distance $\Delta r$ from the initial pusher/fuel interface.

For illustrative purposes it is useful to talk of the onset of chlorine emission from this additive layer as a signal of the arrival of the bubble surface at the additive layer. This simplified interpretation is based on the assumption that the additive is heated to an emitting temperature immediately upon contact with the bubble front. However, the mix model used in the simulations makes no such assumption. It takes into account the delay required for the additive and the hot fuel to be transported into a common volume where a sufficient amount of additive can be brought to an emitting temperature so as to produce diagnosable radiation. Another simplification is to describe the mix region as having distinct boundaries. The mix model does employ such boundaries to delineate the mix region, but the actual modifications of the material content, temperature, and density profiles due to mix are obtained from a transport model.

Accepting for now this view that additive emission signals the arrival of the bubble front at the additive layer, Fig. 64.19 illustrates how the onset times of the additive emission can be used to track the trajectory of the bubble surface in a series of shots using capsules that are identical, except that the initial position $\Delta r$ of the additive layer is varied. This figure shows the trajectories of the DT/CH interface and Lagrangian markers at various $\Delta r$'s, together with the bounds of the predicted mixing region for two different surface finishes, for the illustrative capsule. The bounds of the mixing region correspond to the bubble and spike trajectories and are obtained as described above from the multimode Rayleigh-Taylor perturbation model adapted from the work of Haan.[9] Superimposed over the layer interface trajectories, they illustrate how the mixed region

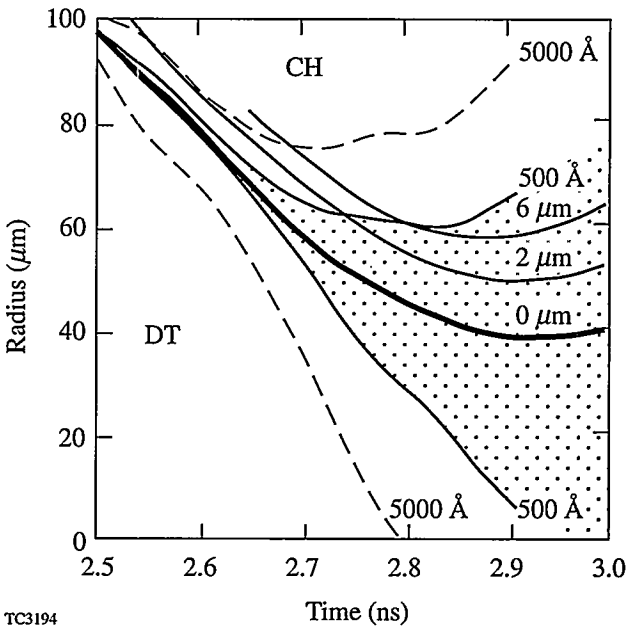


Figure 64.19
Calculated trajectories of the DT/CH interface (heavy line) and Lagrangian markers in the CH at initial distances $\Delta r$ of 2 $\mu$m and 6 $\mu$m from this interface. The curves labeled 500 Å and 5000 Å indicate the bounds of the predicted regions of DT-CH mixing for these initial rms surface finishes. The mix region includes both hot core material and relatively cool pusher material. Diagnostic emission from an additive layer in the pusher can occur when it is heated by contact with hot fuel in the mix region.

grows to include both hot core material and additive at times that depend on the initial perturbation and on the initial location of the additive layer. In the calculations for Fig. 64.19, the mix diffusion step has been omitted from the hydrodynamics. The feedback of mix on the hydrodynamics has potentially important effects on the amount of additive emission, but its effect on the trajectories shown here is small.

The heavy curve labeled 0 $\mu$m is the trajectory of the decelerating fuel-pusher interface. The zero of the time axis is the time of the start of the laser pulse. The curves labeled 2 $\mu$m and 6 $\mu$m are trajectories that would have been taken by additive layers if they had been displaced initially by these distances from the inner surface of the shell. The pair of curves labeled 500 Å are the mix-front trajectories calculated assuming an initial rms perturbation amplitude equal to this value whose modal decomposition is of the form $l^{-5/4}$, where $l$ is the spherical mode index. The dashed curve shows the much larger mixed region resulting from a 5000-Å surface perturbation. This rms perturbation amplitude should be comparable to an equivalent surface roughness, but a quantitative relationship

between surface roughness and the perturbation amplitude is not established at this time. Consequently, these results should be regarded as purely illustrative and not indicative of the performance of a capsule made to any given specification. Also, the relationship of this surface perturbation to an equivalent irradiation nonuniformity has not been determined.

The amplitudes of the fuel-pusher perturbation modes are set at the beginning of the shell deceleration to values obtained from the corresponding ablation-region mode amplitudes by applying the attenuation factor $\exp\left(-l\,\Delta r_s/r_a\right)$, mode by mode, where $r_a$ is the radius of the ablation surface and $\Delta r_s$ is the separation between the ablation surface and the fuel-pusher interface. This is the prescription suggested by Haan[9] for initializing mode amplitudes at a surface whose unstable perturbations are seeded by the instability that has grown at another surface. The form of this coupling factor corresponds to the decaying exponential dependence of the amplitude of a surface-wave eigenfunction on the distance from the perturbed surface. This correspondence is well motivated, but approximate, and requires further study.

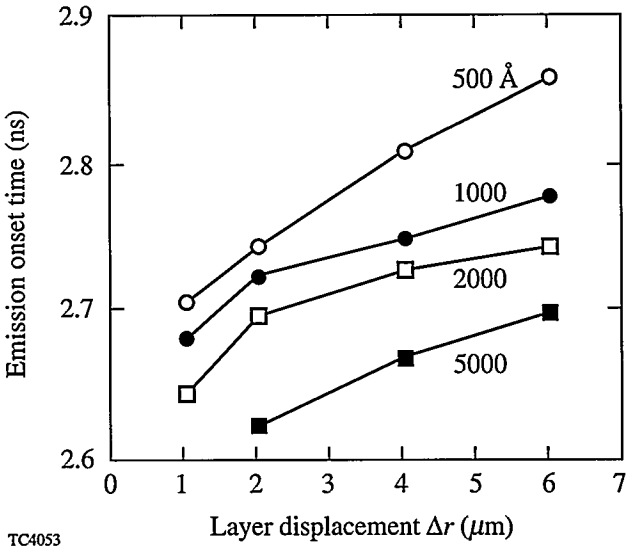


Figure 64.20
Time of onset of emission from the additive layer shown as a function of the initial additive layer displacement $\Delta r$ from the inside surface of the polymer shell, for various initial surface perturbations.

For the purposes of illustration, then, the crossing of the trajectory of the bubble front with the trajectory of the additive layer can be taken to give the time when the additive material enters the mixed region. Presumably, the amount of hot fuel in the mixed region at this time has raised the temperature to a level sufficient for the additive to emit. Figure 64.20, which gives the functional dependence of this estimated emission onset time on the additive layer displacement $\Delta r$ for a series of capsules with identical initial perturbations, shows that this onset time is delayed with more deeply inset additive layers and with smaller initial perturbations, as might be expected. Each curve was obtained from the bubble-front trajectory resulting from the corresponding initial surface perturbation. The points are the times at which this trajectory contacts an additive layer at the indicated initial displacement. Emission-onset timing data from an actual series of shots can be plotted in the same way. This data might not be so complete, however, because the onset time can be expected to become less distinct for additive layers inset by more than a few microns.

While Fig. 64.20 gives useful qualitative information, a mix transport model, such as the one described here, is required to provide more quantitative information. In particular, it can address the important questions of whether one obtains a coincidence of elevated temperature and additive concentration over a large enough volume to produce a signal that is distinct against the background of the polymer emission. This article concentrates on the detection of additive emission by imaging. It is found that distinct time-dependent additive emission is obtained in the cases simulated here, although not for as full a range of additive layer displacements as is shown in Figs. 64.19 and 64.20.

### Mix as a Diffusive Process

Once the growth and extent of the mix region have been obtained, a diffusive transport model is used to simulate the redistribution of the plasma constituents and thermal energy within this region. A natural way to regard mix in 1-D is that each zone in the numerical mesh exchanges a small amount of material with its closest neighbors at each time step. The finite-difference equation that describes this has the form of a diffusion equation. The diffusion coefficient is chosen to be the product of a mix velocity, taken from the velocities of the mix-region boundaries relative to the fluid velocities, and a mixing length. In all but one of the simulations described below, the mixing length is a free parameter. Results are obtained either for a fixed value chosen in advance or for a range of values to show how the outcome of the simulations can vary over the plausible limits of the model. "Flux limitation" is employed as well. The diffusive mass flux is forced to be less than a given multiple $F$ of the free-streaming mass flux given by the product of the mass density and the mix velocity. This feature prevents unphysically large mass fluxes in the presence of large density gradients. The flux-limit parameter $F$ is familiar from other

applications of diffusive transport[10] and is the second free parameter of this model. It is set equal to 2.0 in the calculations presented in this article. Once these two parameters are set, the concentration profiles of the mixed constituents and the mix-transported thermal energy density are then calculated in detail, according to local conditions, rather than from simpler unphysical and/or acausal assumptions such as instantaneous homogeneity within the mix region.

This model resembles the "$k$-$\varepsilon$" model in its use of diffusive transport to model turbulent transport,[11] but important differences exist. In the model used here, the momentum and kinetic energy of each fluid zone are conserved exactly, but there is no accounting for energy contained in the turbulent motion, in contrast to the $k$-$\varepsilon$ model. Another difference is that this model contains a multimode instability calculation done in parallel with the mix transport, while the $k$-$\varepsilon$ model includes no mode-spectral information. The mix-region model presented here offers the advantage of including the Haan multimode perturbation model with its phenomenology of the nonlinear growth of saturated modes. The spatial-spectral information kept by the multimode model is potentially important in the development of the mix-transport model beyond the version used to obtain the results shown below. For example, preliminary results have been obtained using a mixing scale length that is set equal to the rms perturbation wavelength averaged over the mode spectrum. This utilizes the spatial wavelength information in the perturbation mode spectrum, which is certainly a better strategy than using a fixed length chosen in advance. This derived scale length changes in time as the mode amplitudes themselves change and also as the transverse wavelengths of the individual modes decrease due to the mix region converging with the implosion.

An illustration of the direct effect of mix in 1-D simulations is provided by Fig. 64.21, which shows the spread of the concentration profile of the chlorine additive in the representative capsule shown in Fig. 64.18 for two values of $\Delta r$. In both cases the surface mass perturbation is set to 2000 Å with an $l^{-5/4}$ modal decomposition. Figure 64.21(a) shows the case where the initial additive layer is the innermost 2 $\mu$m of the pusher, and Fig. 64.21(b) shows the case where the additive layer is inset by 2 $\mu$m. The mixing length $\lambda_{mix}$ is chosen to be 100 $\mu$m. In each case the sequence of concentration profiles includes the deceleration phase up to just beyond peak compression. In both cases the additive layers remain substantially undisturbed until after 2.4 ns. The additive layer at the fuel-pusher interface shows a slight preliminary dispersal. The main difference between the two cases occurs just after 2.5 ns, where the additive layer at the fuel-pusher interface begins to disperse about 100 ps before the inset additive layer. By 2.8 ns, the additive profiles have become nearly identical. The difference between the profiles between 2.5 and 2.7 ns suggests that the displacement of the additive layer by 2 $\mu$m can result in an effect that can be seen with a temporal resolution around the 100-ps level.

### Effects of Mix on Capsule Performance

Simulating the emission from pusher additives requires mix modeling within hydrodynamic simulations to determine to what degree a given amount of additive perturbs the experiment, either by changing the hydrodynamic stability of the implosion or by quenching the diagnostic emission by dilution or by radiative cooling. The perturbative effect of a 2-$\mu$m additive layer at the inside surface of the shell can be evaluated from the results shown in Fig. 64.22 for implosions performed using a range of mixing scale lengths $\lambda_{mix}$. These simulations

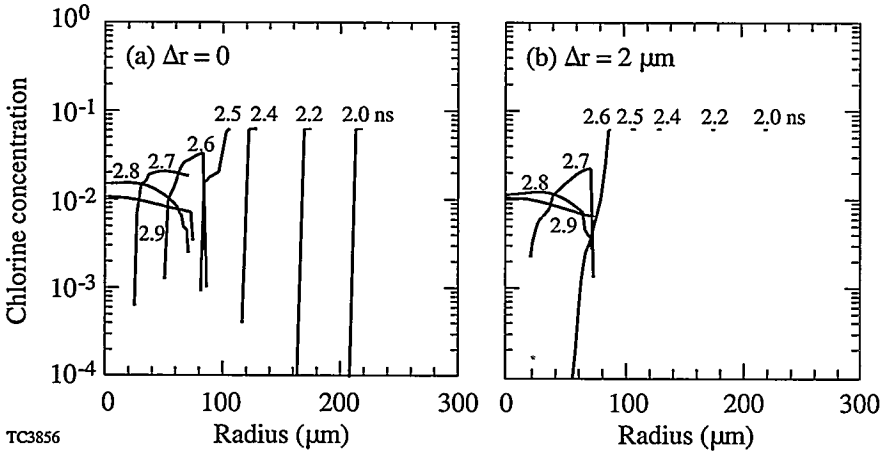


Figure 64.21
Sequences of chlorine concentration profiles for (a) $\Delta r = 0$ and (b) $\Delta r = 2$ $\mu$m. In each case the chlorine spreads as time increases, but the spreading is delayed, as expected, in the second case. These simulations were performed for an initial perturbation of 2000 Å and with $\lambda_{mix} = 100$ $\mu$m.

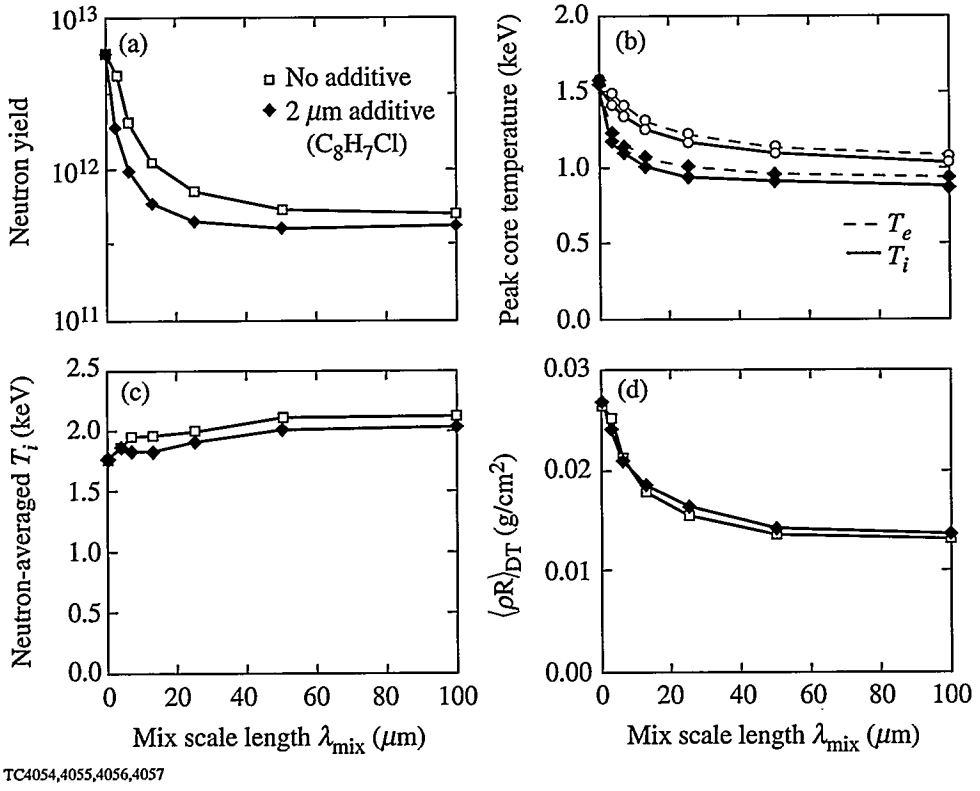


Figure 64.22
Effect of the diagnostic layer (2 μm of $C_8H_7Cl$) on (a) the neutron yield, (b) the peak electron and ion core temperatures, (c) the neutron-averaged ion temperature, and (d) the DT $\rho R$. Results are plotted as a function of the mix scale-length parameter $\lambda_{mix}$ for an initial surface perturbation of 2000 Å. The presence of the diagnostic layer is seen to have only a minor effect on the capsule behavior in comparison with the mix.

assume the same initial 2000-Å mass perturbation and $l^{-5/4}$ modal decomposition, which is severe enough to give a good indication of the worst-case effect of mix. The additive layer is placed at the fuel-pusher interface because this produces the maximum effect on the hydrodynamics. The mixing scale length is varied over the range from zero, which gives no mix at all, to 100 μm, where the net mixing rate is determined primarily by the flux limitation. In this case flux limitation restricts the speed of the mixing motion to no greater than 2.0 times the divergence speed of the bubble and spike surfaces, over and above the divergence of the 1-D fluid motion. Figure 64.22 shows that mix has a far greater impact on capsule performance than does the additive layer. Figure 64.22(a) shows that mix reduces the neutron yield substantially, corresponding to a small reduction in the ion temperature [which is shown in Fig. 64.22(b)]. The additional radiative cooling due to the additive is seen in Fig. 64.22(b) as a very slight additional reduction in temperature. Due to the strong dependence of the neutron-production rate on temperature, the effect of the additive on the total neutron yield is quantitatively significant, but it is clearly of secondary importance in comparison with the much greater effect of the much larger amount of pusher polymer that has been mixed in.

Figures 64.22(c) and 64.22(d) show the ion temperature and the peak value of $\langle \rho R \rangle_{DT}$, the radial integral of the DT mass density, both neutron averaged and thus relevant to nuclear diagnostics. The neutron-averaged ion temperature rises with mix due to the fact that quenching of neutron production within the mix region tends to shut off the yield from the cooler part of the core; this skews the neutron weighting of the temperature average toward the center of the capsule, which is hotter. The neutron-averaged ion temperature is not as sensitive to the presence of the additive as the neutron yield in Fig. 64.22(a). Note that $\langle \rho R \rangle_{DT}$ includes the DT mass only, wherever the mix might have taken it, and does not include the contribution of the pusher material. It is not the areal density of a distinct core. The neutron-averaged fuel areal density $\langle \rho R \rangle_{DT}$ de-

creases with increasing mix, but the additive has an almost negligible effect.

Figure 64.23 shows the neutron-production rates plotted as functions of time for a sequence of simulations with mixing lengths ranging from 0 to 100 $\mu$m. As above, this covers the range of mixing lengths from one that would give no mix at all to one that is large enough for the homogenizing effect of mix to be limited primarily by the flux limitation of the diffusion. A 2000-Å mass perturbation and $\Delta r = 0$ have been assumed in all cases. One striking aspect of the results shown in Fig. 64.23 is that the curves remain close to each other up to 2.6 ns where they abruptly diverge. Figure 64.21(a) shows that this is near the time when the entire inner 2 $\mu$m of pusher with the chlorine additive has just been drawn into the mix region, which is indicated by the tails on both ends of the concentration profile. By this time the mix region has expanded to include most of the fuel. This abrupt divergence of the neutron-production rates supports the interpretation that yield is effectively quenched by the arrival of pusher material, as was suggested above in explaining the results of Fig. 64.22.

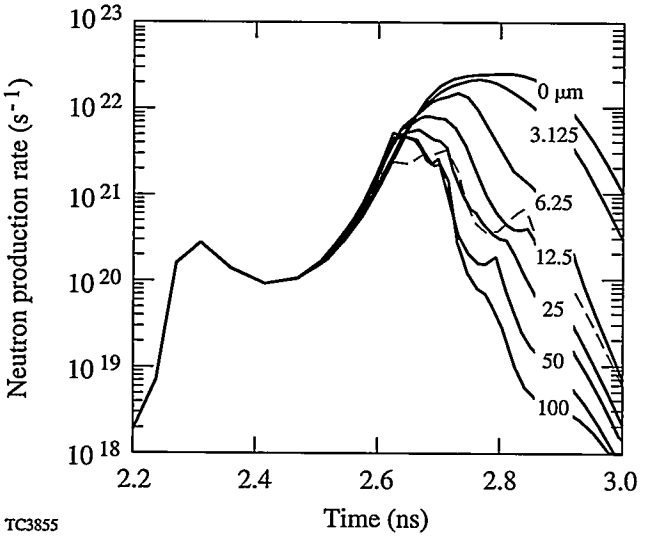


Figure 64.23
Neutron-production rate as a function of time for several values of the mix scale-length parameter $\lambda_{mix}$. The initial surface perturbation is 2000 Å. The dashed curve is obtained using a model where $\lambda_{mix}$ is chosen to be equal to the time-dependent rms spherical wavelength of the perturbation mode spectrum.

The dashed curve in Fig. 64.23 is obtained using a time-dependent mixing length chosen to be equal to the rms spherical wavelength of the perturbation mode spectrum. This represents an attempt to reduce the number of *ad hoc* parameters in the model. This choice of mixing length also results in an abrupt onset of quenching. The total yield obtained is very close to that obtained from the larger mixing lengths that give very rapid mixing, but later in the deceleration phase the neutron-production rate drops more slowly to values obtained at these later times with much shorter mixing lengths. This reflects the shortening of the average perturbation wavelength due to the spherical convergence of the mixing region, which in this case is a stronger effect than the tendency of the perturbation spectrum to evolve toward longer wavelengths as the shorter-wavelength perturbation modes saturate and fall behind the longer-wavelength modes.

### Effects of Mix on Images

Under conditions expected in the fuel-pusher mix, chlorine emission consists mostly of K-shell lines and bound-free continuum. Chlorine is distinctly more emissive than carbon under these conditions since carbon is then almost completely stripped and is seen mostly by its bound-free emission. Imaging implosions with emission in the 3- to 5-keV range isolates the chlorine continuum spectrally and enhances the contrast of emission from the hottest parts of the mixed region against the rest of the image. Chlorine is well suited as a pusher additive for the example described above because its K-shell lines occur just above the energies where the relatively cold pusher would attenuate emission from the center at times near peak compression. Avoidance of this attenuation is obviously important for observing mix with time-resolved spectroscopy.[12] The relative emission strength of chlorine over carbon allows small amounts of additive to be used. The detectability of the chlorine emission is limited by how well it competes with the continuum emission from the carbon, which is the main ingredient of the pusher and thus much more abundant. This is of particular concern when observing line emission from embedded additive layers since the additive lines must be observed against the background of continuum from all the carbon in the overlying layer of pure polymer.

Simulations of framing-camera images are obtained from integrating the equation of radiative transfer along straight-line photon paths through time-dependent emissivity and opacity profiles, taken from the 1-D hydrodynamic simulation, and into a model of a framing camera. The camera forms pinhole images on a photocathode. The images are transferred to a phosphor screen through a multichannel plate, which is triggered by a short electrical pulse propagating along a stripline over the plate. The model includes the camera geometry, the optics of finite pinholes, and a temporal response based on the calculated response of the multichannel plate to the electrical

pulse provided. The gating time is 45 ps, which represents a near-term development goal for this instrument. The intensity units in the plotted images are arbitrary since the camera model does not include information from an absolute calibration, but the relative intensities from frame to frame are consistent in these units. The spectral response of the camera includes that of the camera itself and foil filters of 25 $\mu$m of beryllium and 20 $\mu$m of titanium to center the net response within a window from about 3 to 5 keV.

Figure 64.24 shows a sequence of five framing-camera images, taken 50 ps apart, of the previously chosen polymer capsule with mix seeded by a 2000-Å exterior mass perturbation. The results from six simulations are superposed. Each curve represents the azimuthally averaged image intensity plotted as a function of radius. A mixing length of 100 $\mu$m is assumed. The value of the numeral labeling curves 0, 1, 2, and 4 is the initial displacement, in microns, of the additive layer outward from the inner surface of the pusher. The curve labeled

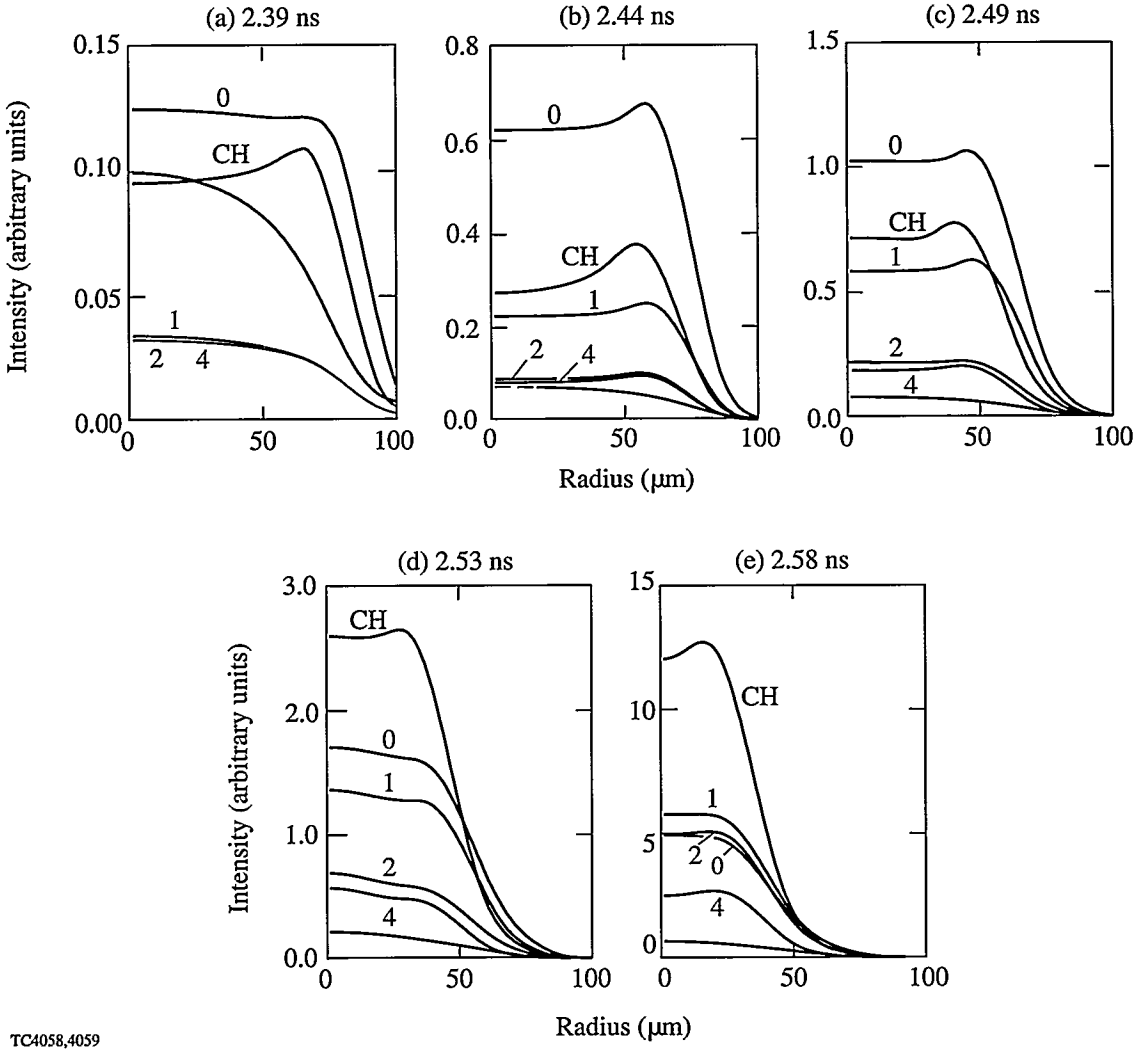


Figure 64.24
Simulated framing-camera images in the 3- to 5-keV range at times 45 ps apart ranging from (a) 2.39 ns to (e) 2.58 ns. The curves labeled 0 to 4 are for additive layer displacements of 0 to 4 $\mu$m, respectively; the curves labeled CH are for a pure CH pusher (no additive layer), and the dashed curves are for the case of no mix. Except for the dashed curves, the initial surface perturbation is 2000 Å and the mix scale-length parameter $\lambda_{mix}$ is 100 $\mu$m. Note the different intensity scales.

"CH" corresponds to a calculation with no additive layer, and the dashed curve is obtained from a simulation of the case "0," where the additive layer is at the fuel-pusher interface and where no mix takes place.

At the time of the first frame [Fig. 64.24(a)], mixing has already begun. The effect of this is seen in the brightness of image 0 relative to the dashed line, its unmixed counterpart. A comparison of image 0 with image CH, obtained with no additive, shows that the additive results in a brighter image, as is expected, but without limb brightening, in contrast to the distinct limb brightening of the image CH. The intrinsic emissivities of both capsules are, in fact, peaked at their fuel-pusher interfaces, but at this early time there remains enough cool additive surrounding the fuel-pusher mix region of the additive-layer capsule to form an attenuating layer that rounds off the image by a limb-absorption effect. This limb darkening is particularly strong for images 1, 2, and 4, where the entire additive layer is cold and absorbing. The conditions at the fuel-pusher interfaces of these three cases are essentially identical to those of the CH case where there is no additive, and the differences between their images and that of the CH case are almost entirely due to this absorption. The nearly complete indistinguishability of the 1, 2, and 4 curves is evidence that the additive layer has no other effect on the implosion.

At later times curves 1, 2, and 4 brighten, in the expected order, as fuel-pusher mixing overtakes the additive layers successively further from the fuel-pusher interface. For example, from frame (d) to frame (e), curve 2 brightens to become comparable in intensity to curves 0 and 1. This systematic effect of the additive-layer displacement on the time dependence of the additive emission would be worth looking for in an actual experiment. These images tend to become more limb brightened as the additive becomes more emissive than absorbing, but there is a competing effect favoring central emission as well, as is seen in frame (d).

The five frames show that the fuel cores contract by a factor of about 2 for each calculation over the 200 ps shown. Nevertheless, there are subtle differences in their dynamics that are caused by mix. These effects, in combination with rapidly increasing intensities, add a potentially significant bias to the comparison of the overall intensities of any two images at any given instant. Comparing image intensities at points of equal core compression, for example, could give different results. Thus some caution is required in comparing relative intensities in Fig. 64.24. The CH images of the pure polymer capsule in particular appear surprisingly bright, relative to the images of capsules with additive layers. The pure polymer capsule does, in fact, implode sooner than the additive-layer capsules and is found to reach peak compression about 30 ps earlier. Consequently, if the images were all compared at identical degrees of convergence, rather than at identical points in time, the intensity from the pure polymer capsule would be seen to be much more in line with those of the other images.

Relaxing the flux limitation by increasing the flux-limit parameter allows a greater concentration of chlorine to reach the spike front from the bubble front, and greater limb brightening is obtained. This is what would most likely result from a mix model that instantaneously homogenized all the material within the mix region, which is unphysical, at least from the point of view of the mix transport model used in this work.

Over the entire 200 ps spanned by these images, all the images brighten by nearly two orders of magnitude, except for the unmixed case, which lags far behind. This shows that mix can be expected to have a strong brightening effect on images of polymer-shell implosions, regardless of how they are modified by additive layers.

## Conclusions

In conclusion, experiments are proposed to diagnose pusher/fuel mixing in imploding gas-filled capsules using additive layers of chlorinated plastic at various distances from the initial pusher/fuel interface. A mix model has been developed to simulate these experiments. The model includes the self-consistent modifications to the capsule hydrodynamics that result from a time-dependent diffusive treatment of the mix region. These experiments appear promising, based on the present analysis. The proposed diagnostic technique is, of course, compatible with other diagnostics suggested elsewhere, such as detailed line-shape and line-ratio analysis, with or without a fuel additive.

## ACKNOWLEDGMENT

This work was supported by the U.S. Department of Energy Office of Inertial Confinement Fusion under Cooperative Agreement No. DE-FC03-92SF19460, the University of Rochester, and the New York State Energy Research and Development Authority. The support of DOE does not constitute an endorsement by DOE of the views expressed in this article.

## REFERENCES

1. J. Nuckolls, L. Wood, A. Thiessen, and G. Zimmerman, Nature **239**, 139 (1972).

2. Laboratory for Laser Energetics Report No. 16, 1973 (unpublished); Laboratory for Laser Energetics Report No. 36, 1976 (unpublished).

3. Lord Rayleigh, *Scientific Papers* (Cambridge University Press, Cambridge, England, 1900), Vol. II, pp. 200–207; G. I. Taylor, Proc. R. Soc. Lond. A **201**, 192 (1950).

4. F. H. Harlow and J. E. Welch, Phys. Fluids **9**, 842 (1966).

5. J. Delettrez, Can. J. Phys. **64**, 932 (1986) and references cited therein.

6. J. Delettrez, D. K. Bradley, and C. P. Verdon, Phys. Plasmas **1**, 2342 (1994).

7. B. A. Hammel *et al.*, ICF, LLNL Quarterly Report **1**, (1991), pp. 151–156.

8. T. R. Dittrich *et al.*, Phys. Rev. Lett. **73**, 2324 (1994).

9. S. W. Haan, Phys. Rev. A **39**, 5812 (1989).

10. R. C. Malone, R. L. McCrory, and R. L. Morse, Phys. Rev. Lett. **34**, 721 (1975).

11. S. Gauthier and M. Bonnet, Phys. Fluids A **2**, 1685 (1990).

12. R. Epstein, J. A. Delettrez, C. P. Verdon, D. Shvarts, and B. Yaakobi, Bull. Am. Phys. Soc. **39**, 1695 (1994).

# Distributed-Phase-Plate Design Using Simulated Annealing Algorithms

Methods of designing phase plates to achieve control of the far-field irradiance distribution for laser-induced plasma experiments have been under study for more than a decade. One important goal of phase-plate design is to generate the desired far-field spatial profile while minimizing wide-angle scattering outside this profile. This article reports a new algorithm that accomplishes this goal.

Many phase-plate designs reported in the literature have used the phase-retrieval algorithm. These designs achieve a good match to the high-order super-Gaussian distribution that is presumed to approximate the ideal far-field spatial profile. However, the resulting phase plates exhibit wide-angle scattering losses due to steep surface slopes near surface vortices and line discontinuities.[1,2] An article in a previous issue of the LLE Review[3] described an improved phase-retrieval procedure that reduces the number of pole discontinuities and thus the energy loss due to scatter. The present article reports a simulated-annealing algorithm that has resulted in a complete elimination of this source of loss.

Using the classical method of phase retrieval, it is not possible to specify arbitrary constraints or to custom design a cost function for a particular application. To achieve lower scatter by using a strictly continuous phase-plate surface, we have investigated simulated annealing because it allows us to invoke specific constraints, to design with arbitrary cost functions, and, potentially, to find the globally optimum solution for a given set of constraints.[4,5] Using simulated annealing we can specify separately the target far-field profile and the cost function. For example, we can design for specific speckle statistics given the constraint of a specified far-field profile. The cost function may be made sufficiently complex to combine with various weights a number of different factors of importance to a given application.

## Algorithm

Our implementation of simulated annealing consists of a number of steps. Starting from an initially aberration-free pupil distribution, a smoothed random wavefront of weak magnitude is constructed and added to the pupil. The far-field irradiance is then calculated by diffraction propagation using fast Fourier transform algorithms, and its azimuthal average $f(r)$ is compared with the desired far-field super-Gaussian irradiance envelope

$$I(r) = e^{-2(r/r_0)^M}, \tag{1}$$

where $M$ is the super-Gaussian order, $r$ is the transverse radius in the far field, and $r_0$ is the characteristic radius of the far-field distribution. A simple cost function $S$ is evaluated from $f(r)$ and $I(r)$ as

$$S = \int_0^\infty [f(r) - I(r)]^2 2\pi r dr. \tag{2}$$

Cost functions calculated in rectangular coordinates tend to over-constrain the design by reducing the speckle. Use of the azimuthal-average profile as in Eq. (2) provides noise averaging of the quasi-speckle pattern in the far field. Various perturbations of the phase plate are then tried, with the cost function reevaluated each time. If the cost function is lower, the perturbation is accepted and the modified phase plate becomes the basis of further trials. If the cost function is higher than that of the previous cycle, the trial perturbation will be accepted if a random number $X$, which is uniformly distributed between 0 and 1, is less than the simulated annealing probability $p$, defined as

$$p = e^{-\Delta S/T}, \tag{3}$$

where $\Delta S$ is the change in the cost function due to the perturbation and $T$ is a parameter known as the simulated annealing temperature, the analog of the temperature of an annealing oven. Since the initial, aberration-free pupil matches the target profile quite poorly, the initial cost function is high and $\Delta S$ is

quite high also; i.e., relatively small perturbations of the phase plate result in relatively large changes in $S$. The temperature $T$ is lowered over a number of iterations and serves to control the "cooling" rate of the process. A premise of the theory of simulated annealing is that if the process is cooled sufficiently slowly, local minima will be overcome, resulting in convergence to the global optimum.[4,5]

In our illustrative calculations, the diameter of the pupil was 14 cm, and the desired far-field distribution was a super-Gaussian of eighth order and 700-$\mu$m diameter. For a laser wavelength of 0.3511 $\mu$m there are about 150 speckles across this diameter. The far-field distribution was sampled using an array of 1024 × 1024 points. Although the beamlines of the OMEGA laser are 28 cm in diameter, the smaller 14-cm diameter was used to reduce computation time.

To find a continuous-surface phase plate that best achieves the desired far-field irradiance envelope, the trial perturbation to the phase plate consists of smoothed random surfaces guaranteeing that the sum of the accepted perturbations will also be strictly continuous. Each cycle of the simulated annealing process requires a unique surface perturbation. Smoothed random surface perturbations are constructed by taking a two-dimensional field of real random numbers and smoothing and scaling this distribution to obtain the desired variance and autocorrelation width. These surface perturbations are made unique by choosing a different random seed for each cycle. We have used an autocorrelation diameter of 0.8 cm, giving about 17.5 autocorrelation diameters over the 14-cm pupil width and a wavefront error of standard deviation 0.03 waves. Once the perturbation wavefront is formed, it is applied to the complex amplitude distribution in the pupil, the far-field distribution is calculated, and the change in cost function is computed.

Simulated annealing is well known to require extensive computational time. The difficulty of designing phase plates may be characterized by the size of a square computer array (represented as $N \times N$) needed to represent the phase plate. The number of distinct optical modes scales approximately as $N^2$, and the time per calculation step also scales as $N^2$. The largest array reported in the literature that has been used for phase-plate design was 128 × 128.[6] For the calculations described in this article, it was necessary to use arrays of 1024 × 1024, leading to an increase in calculation time of nearly four orders of magnitude when compared with studies with the array size 128 × 128.

The literature contains various prescriptions for cooling schedules to achieve optimum or near-optimum performance in a minimum time.[7–9] In most cases the cooling schedules are, at least in part, determined heuristically by numerical experiments for the particular type of problem of interest to the respective authors. To determine the feasibility of the simulated-annealing technique for our application, which includes a very large number of optical modes, we started with a purely cooling or quenching phase (distinct from simulated annealing) in which the temperature $T$ was set to zero; i.e., no reversal steps were allowed. Starting from an unaberrated pupil, we found the process converged in about 2,000 cycles. The minimized cost function resulting from this calculation ($S_1$) established a benchmark with which to compare the subsequent simulated annealing procedure. We then set the temperature $T$ so that the cost function rose to approximately four to five times $S_1$ and then cooled exponentially with a time constant of 1,500 cycles for the next 8,000 cycles. This second phase of the procedure is true simulated annealing since reversal steps are allowed, according to the temperature and current cost function. At the end of the simulated annealing phase, the cost function was reduced from its value $S_1$ at the end of the quenching phase by about a factor of 3. This calculation took about 120 h of CPU time on the Cray YMP-2 at LLE.

Figures 64.25 and 64.26, respectively, show the azimuthally averaged far-field profile for phase plates designed by phase retrieval and simulated annealing. Both designs were done for the same super-Gaussian profile with $M = 8$. Although the simulated annealing design was restricted to a continuous phase-plate surface, it achieved a much better fit to the desired super-Gaussian shape. The phase-retrieval design was well converged in about ten cycles, while the simulated-annealing design required 10,000 cycles. It is possible that other cooling schedules would give faster convergence and lower asymptotic cost functions.

The continuous-surface design has the advantage that it is free of steep surface slopes and discontinuities, resulting in low wide-angle scattering—an advantage not built into the cost function. The effect of wide-angle scattering is seen in Fig. 64.25 by the very slow decay at large radii, in contrast to Fig. 64.26, which shows rapid decay toward zero irradiance at large radii. In practice, the phase-retrieval design would produce more wide-angle scattering than shown in Fig. 64.25. This is because this design leads to steep surface slopes in the vicinity of surface vortices and $2\pi$ line discontinuities, which result in about 5%–10% wide-angle scattering. The effect of

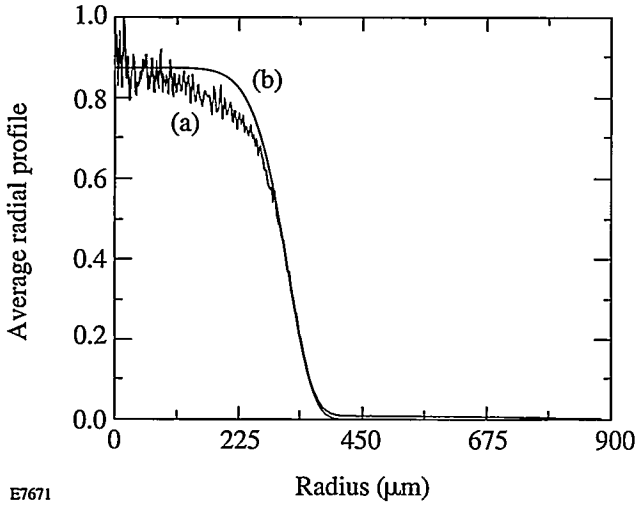


Figure 64.25
Azimuthal average of the far-field irradiance [curve (a)] due to a phase plate designed by the phase-retrieval algorithm, using the parameters defined in the text. The smooth line [curve (b)] is the ideal eighth-order super-Gaussian profile. The azimuthal average provides considerable smoothing of the data, particularly at the larger values of radius. The phase-retrieval solution shows shoulder droop and a rather slow decay to zero at large radius because of wide-angle scattering from steep surface slopes.

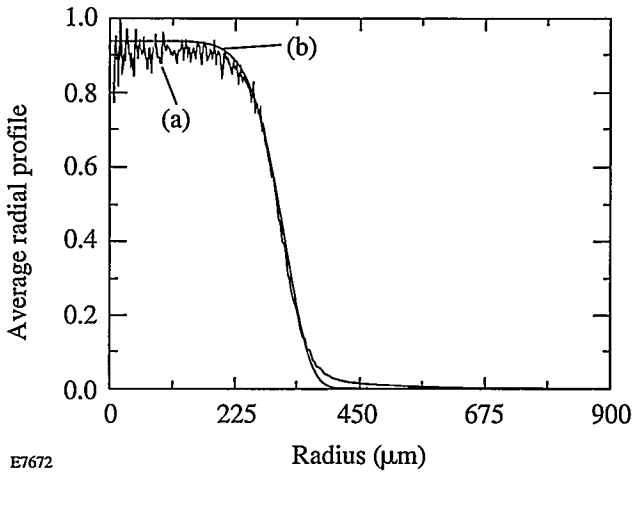


Figure 64.26
Azimuthal average of the far-field irradiance [curve (a)] due to a phase plate designed by the simulated-annealing algorithm. The conditions are the same as for Fig. 64.25, with curve (b) again the ideal profile. The shoulder of curve (a) is considerably more square than for phase retrieval, and the decay to zero is more rapid, indicating little wide-angle scattering because there are no steep surface slopes.

the line discontinuities does not appear in the calculation because the width of the discontinuities is effectively zero, but some finite width will inevitably be present in the manufactured phase plate.

Scans in two orthogonal directions of the target-plane irradiation profile from phase plates generated using the simulated-annealing algorithm are shown in Fig. 64.27. Unlike Figs. 64.25 and 64.26, no azimuthal averaging has taken place. The large (100% rms) modulations seen are characteristic of far-field phase-plate profiles. The small amount of energy loss outside a diameter of 800 μm is evident.

## Overlapping Laser Beams

Flat-foil Rayleigh-Taylor instability experiments require a large number of overlapping laser beams to supply the desired irradiance and uniformity. In particular, the lower-order modes of the irradiance pattern must be minimized to allow for uniform foil acceleration and a careful study of the instabilities associated with high-order modes. There are two primary approaches to obtaining a uniform focal plane envelope from a hexagonal set of six beams from the OMEGA system. The first approach involves using the current OMEGA phase plates, which produce weak super-Gaussian profiles, and offsetting the beams in the target plane by an amount chosen to optimize

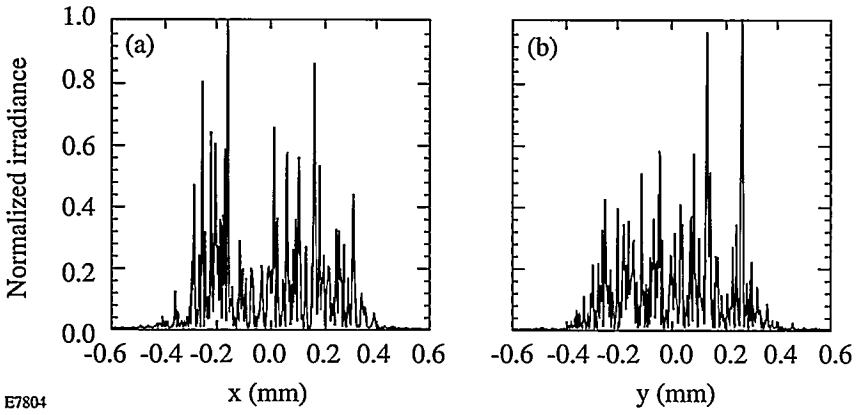


Figure 64.27
Target-plane irradiance profiles resulting from the simulated-annealing algorithm, (a) vertical and (b) horizontal, showing the high modulation speckle that is characteristic of phase converting a laser beam to over 100 times its intrinsic diffraction limit.

the flatness of the envelope. This method represents a compromise between unwanted modulation, energy loss, and envelope uniformity. The second method involves phase converting the laser beams to produce super-Gaussian beam profiles. This method is preferred because it leads to greater energy efficiency and a larger spatial region of uniform irradiation.

The two-dimensional irradiance pattern for six overlapping laser beams, each phase converted with a super-Gaussian phase plate designed by the simulated-annealing algorithm, is shown in Fig. 64.28. In this case the six beams have the same pointing, resulting in a smaller irradiated region than that produced by offsetting the beams radially from the center of the target. This plot shows the time-instantaneous speckle modulation, which is reduced from 100% to 40% due to the uncorrelated (intensity) addition of the six laser beams. The irradiated region is also seen to be circular, as desired. The encircled energy within an 800-$\mu$m spot is 97% for this design.

The azimuthally averaged profile of this irradiance distribution is shown as curve (a) in Fig. 64.29. Curve (b) is an eighth-order super-Gaussian profile, which is nearly the same as each individual beam envelope but a little wider because the beams irradiate the target at an angle of incidence of ~20°. Figure 64.30 shows vertical and horizontal cross sections of the six-beam irradiance on target, without azimuthal averaging. Comparing with Fig. 64.27, the modulation of the speckle is reduced from 100% to 40% due to the $\sqrt{6}$ statistical dependence. A certain amount of energy is lost in the wings of the irradiance distribution. Given that the most useful portion of the irradiance distribution is the flat portion in the center, there is a premium on producing the flattest individual profiles possible. These profiles should remain flat under many realizations of the laser-beam phase error. The needs of stability experiments thus provide an impetus for continued phase-plate design at LLE.

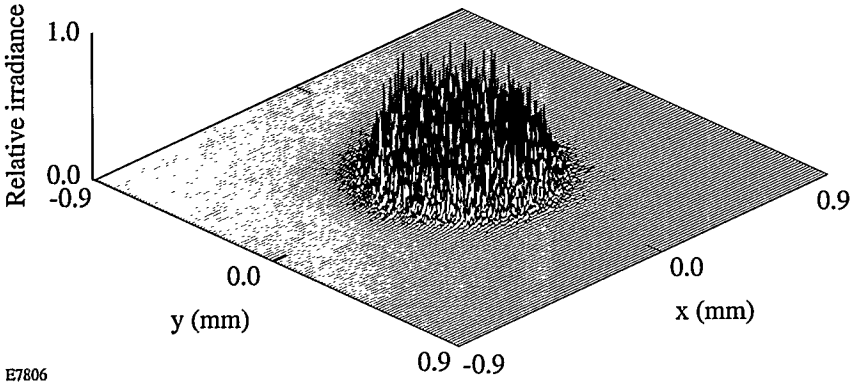


Figure 64.28
Target-plane irradiance pattern for six beams overlapped and focused onto a flat target, each beam phase converted with a super-Gaussian phase plate. The six beams form a hexagonal subset of the 60 OMEGA beams. For flat target irradiation, the speckle modulation is decreased by the square root of the number of overlapped laser beams.

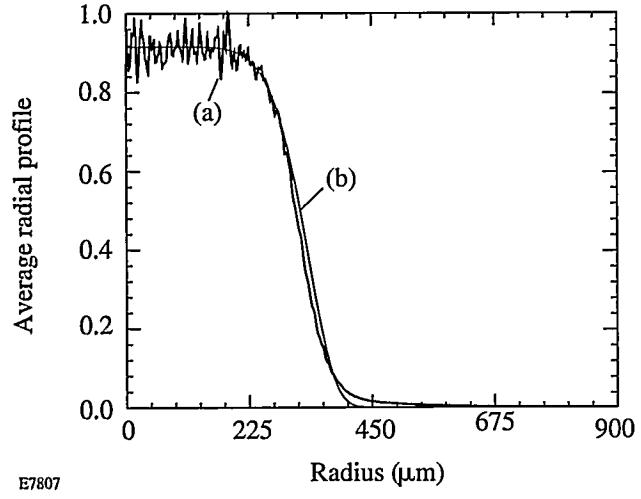


Figure 64.29
Azimuthally averaged profile of the two-dimensional irradiation pattern of Fig. 64.28. It is found that 97% of the energy is contained within an 800-$\mu$m-diameter circle. The 500-$\mu$m-diameter flat region can be extended by pointing the six beams away from the center of the target.

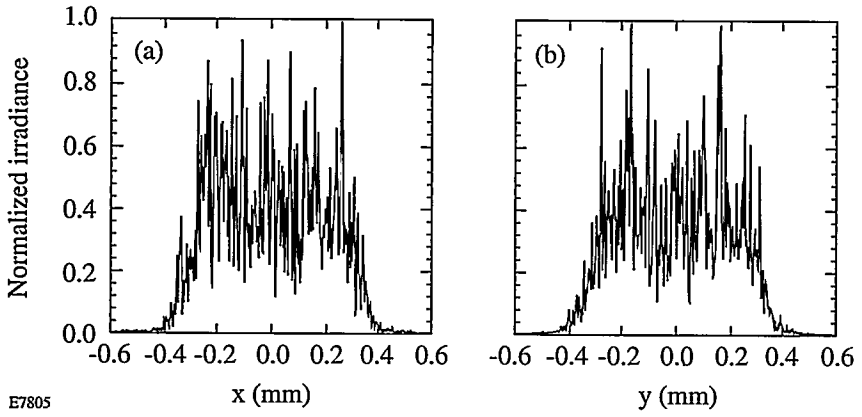


Figure 64.30
Target-plane irradiance profiles, (a) vertical and (b) horizontal, showing a reduction in speckle modulation compared with Fig. 64.27. This is characteristic of overlapping phase-converted laser beams. The contrast of the modulation is reduced from 100% to 40%, which is the expected $\sqrt{6}$ improvement in the time-instantaneous uniformity.

**Summary**

A simulated annealing algorithm has been developed to design distributed phase plates that produce super-Gaussian irradiance profiles. This approach uses a strictly continuous surface relief that minimizes wide-angle scattering. Phase plates produced using this algorithm perform better than those produced using the previous phase-retrieval algorithm, which suffer from steep surface slopes and line discontinuities. The new algorithm also allows great flexibility in defining the cost function and constraints to meet the requirements of the target experiments to be performed.

Super-Gaussian phase plates can be fabricated and used to conduct experiments involving multiple overlapping beams. This is important for studies of the Rayleigh-Taylor instability on flat targets. In addition to enhancing the energy efficiency, the simulated-annealing technique offers the capability of controlling the power spectrum of the individual beams used to irradiate targets.

Future work will involve reducing the computation time for the algorithm, decreasing the sensitivity of the phase-plate performance to the laser-beam phase errors, and gaining greater control of the power spectrum placed on target.

ACKNOWLEDGMENT

This work was supported by the U.S. Department of Energy Office of Inertial Confinement Fusion under Cooperative Agreement No. DE-FC03-92SF19460, the University of Rochester, and the New York State Energy Research and Development Authority. The support of DOE does not constitute an endorsement by DOE of the views expressed in this article.

REFERENCES

1. S. N. Dixit *et al.*, Opt. Lett. **19**, 417 (1994).
2. Y. Lin, T. J. Kessler, and G. N. Lawrence, Opt. Lett. **20**, 764 (1995).
3. Laboratory for Laser Energetics LLE Review **63**, NTIS document No. DOE/SF/19460-91, 1995 (unpublished), p. 126.
4. S. Kirkpatrick, C. D. Gelatt, Jr., and M. P. Vecchi, Science **220**, 671 (1983).
5. S. Kirkpatrick, J. Stat. Phys. **34**, 975 (1984).
6. S. Yin, M. Lu, C. Chen, F. T. S. Yu, T. D. Hudson, and D. K. McMillen, Opt. Lett. **20**, 1409 (1995).
7. H. Szu and R. Hartley, Phys. Lett. A **122**, 157 (1987).
8. N. Yoshikawa and T. Yatagai, Appl. Opt. **33**, 863 (1994).
9. K. Ergenzinger, K. H. Hoffman, and P. Salamon, J. Appl. Phys. **77**, 5501 (1995).

# Self-Interference Patterns and Their Application to Target Characterization

The uniformity requirements of direct-drive targets are stringent. The requirements on both sphericity and wall thickness uniformity are of the order of less than 1%. In the past, dual-beam interference microscopy has been used at LLE to characterize the wall thickness and uniformity of transparent targets.[1] With this technique, an interference pattern is formed between one beam that passes through the target and a second beam, split off from the first, that passes around the target. By comparison with computer-generated templates, these interference patterns can yield the wall thickness and its uniformity to a high degree of accuracy.[2]

This article describes an alternative interferometric technique that is simpler to use and that provides a rapid characterization of both the wall thickness and the uniformity of single-shell targets. These are typically polystyrene (CH) shells, which are selected prior to being coated with layers of various materials and/or filled with $D_2$, DT, or some other desired gas. These shells have the remarkable property that, when irradiated with a spatially incoherent, narrow-bandwidth light source and viewed using only a compound microscope, they display self-interference patterns (SIP's) such as the one shown in Fig. 64.31. These patterns are distinct concentric fringes when the target is uniform, but faint, distorted, or discontinuous fringes form when the target is nonuniform. Previously, SIP's have not been used because they are clearly observed only in targets of very high quality, with uniformity typically better than 1%.

This technique is currently being used for the preliminary selection of polystyrene shells typically of 800- to 1000-$\mu$m diameter and 5- to 12-$\mu$m wall thickness. The fringe locations have been modeled using ray tracing and agree well with actual measurements of well-characterized shells. Shells can be selected with the wall thickness known to $\pm 0.5$ $\mu$m and with uniformity better than 0.05 $\mu$m.

### Origin of the Self-Interference Pattern

SIP formation results from multiple reflections of rays within the shell walls. The three relevant beam paths are illustrated in Fig. 64.32. Beam 1 passes straight through the shell, beam 2 undergoes two reflections on the input side, and beam 3 undergoes two reflections on the output side. For a perfect shell, the emerging wavefronts of beams 2 and 3 are virtually identical, so they combine coherently and interfere with the wavefront of beam 1 to form the SIP. For an imperfect shell, in which the input and output thicknesses are different, a single SIP is not formed, but one observes a combination of two SIP's, one corresponding to the input side, (beams 1 and 2 interfering) and the other to the output side (beams 1 and 3).

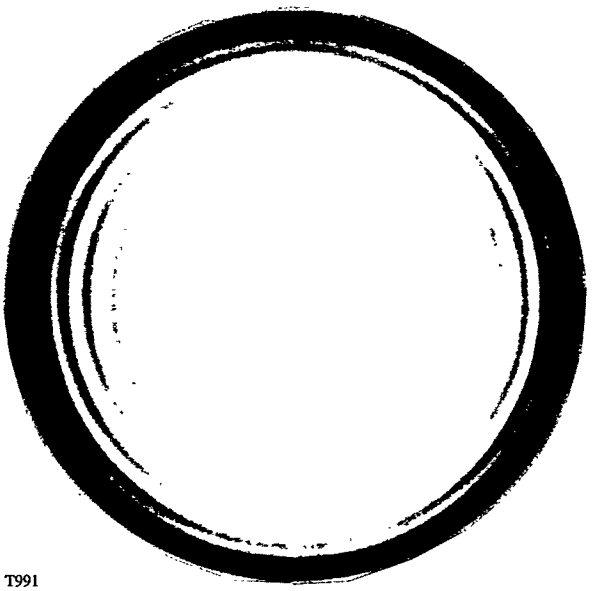
T991

Figure 64.31
A compound-microscope image of a self-interference pattern produced by a symmetric capsule when illuminated with narrow-bandwidth light. The polystyrene (CH) capsule has an 850-$\mu$m diameter and a 7-$\mu$m thickness.

In Fig. 64.32, all rays are shown backprojected (with dashed lines) to the point on the object plane ($z = 0$) from which they appear to come. Exact ray-tracing calculations show that a ray incident at a height $r_i$ appears to come from a height $r_a$ in the object plane where the difference between $r_i$ and $r_a$ is negligi-

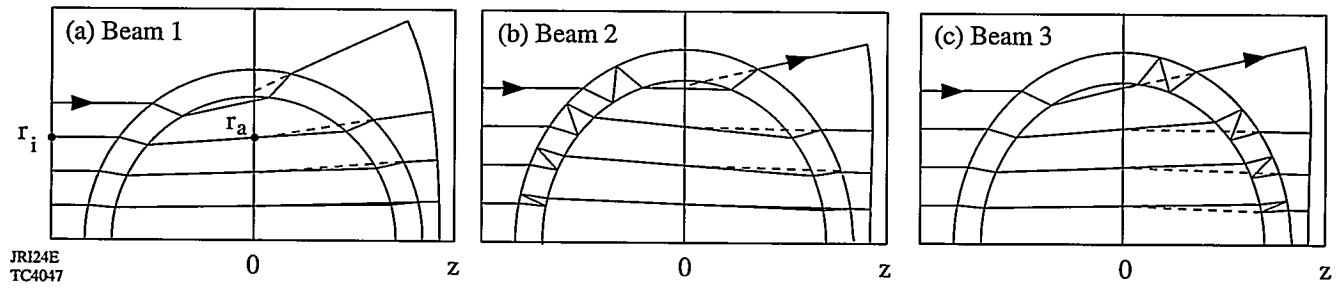


Figure 64.32
Ray paths through the target of (a) beam 1, (b) beam 2, and (c) beam 3. In each case the rays enter from the left, the emerging wavefront is drawn on the right, and the emerging rays are backprojected (dashed lines) to their apparent origin in the object plane ($z = 0$). For a perfect target, wavefronts 2 and 3 are virtually identical, add coherently, and form the self-interference pattern (SIP) through combination with wavefront 1.

bly small (typically less than 0.1 $\mu$m except very close to the edge of the target) for each of the three beam paths. This is true only for the object plane $z = 0$. Since the source is spatially incoherent, two rays can interfere only if they originate from the same incident ray. Thus, the only object plane that permits the SIP formation is the midplane $z = 0$. In this sense the fringes can be described as being localized in this plane. In contrast, if the illumination was spatially coherent as in the dual-beam interferometry technique described in Ref. 2, interference fringes could be obtained for any object plane.

For a spherically symmetric target, the locations of the interference fringes may be calculated by plotting the optical path difference $OPD_2$–$OPD_1$ between beams 2 and 1 as a function of apparent radius $r_a$ in the object plane (see Fig. 64.33). [$OPD_i$ is defined as the optical path difference (in centimeters) between a ray of beam $i$ ($i = 1$–3) and a reference ray passing through vacuum, but in Fig. 64.33 it is plotted in waves.] In this example, six bright fringes will be seen with optical path differences ranging from 29 to 24 waves, and the loci of greatest intensity in an interferogram can be simply constructed by drawing circles at the corresponding radii. For targets with nonuniformities in the $(x,y)$ plane, i.e., targets that are not rotationally symmetric about the $z$ axis, interferograms can be formed by tracing a grid of rays through the target and drawing a contour plot of the optical path difference with the contour levels chosen to be integer numbers of waves.[3]

In place of Fig. 64.33, the "universal curves" of Fig. 64.34 can be used to predict the behavior of all perfectly uniform targets of interest. In this figure, the optical path differences $OPD_1$ and $OPD_2$, and the difference $OPD_2$–$OPD_1$, are all

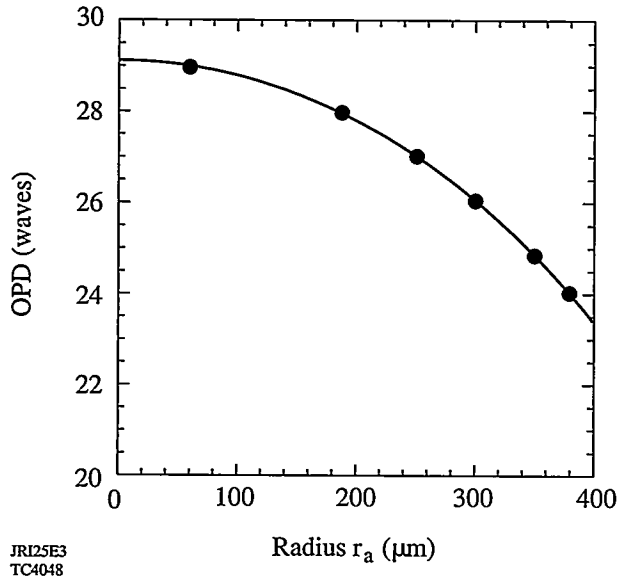


Figure 64.33
The optical path difference ($OPD_2$–$OPD_1$) between beam 2 and beam 1 for a representative CH target with an 850-$\mu$m outer diameter, a 5-$\mu$m thickness, and a refractive index at 546 nm of 1.59. The abscissa is the apparent radius $r_a$ in the object plane (see Fig. 64.32), which is almost identical to the incident radius $r_i$. The solid points correspond to integer values of optical path difference and thus give the radii of the centers of the bright fringes.

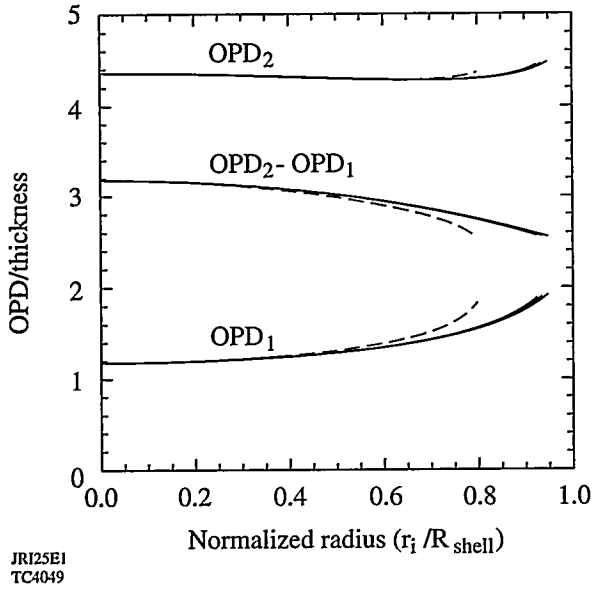


Figure 64.34
Universal curves governing the formation of the self-interference pattern. By plotting the OPD divided by the shell thickness $t$ on the vertical axis and the normalized radius ($r_i/R_{shell}$) on the horizontal axis, the three quantities $OPD_1/t$, $OPD_2/t$, and $OPD_2 - OPD_1/t$ are virtually independent of shell diameter and thickness. The curves shown here are for four shells with outer diameters ranging from 250 to 1500 $\mu$m and thicknesses ranging from 2 to 20 $\mu$m. The dashed curves correspond to a 250-$\mu$m diameter and a 20-$\mu$m thickness.

plotted against the normalized radius $r_i/R_{shell}$, where $R_{shell}$ is the average of the inner and outer shell radii. (Similar results are obtained by normalizing to either the inner or the outer radius.) Graphs are superposed for CH targets with outer diameter $d = 250$ to 1500 $\mu$m and thickness $t = 2$ to 20 $\mu$m; specifically, the four extreme combinations are included. All curves are virtually identical except for the low-aspect-ratio combination ($d = 250$ $\mu$m, $t = 20$ $\mu$m), which is not of current interest for experiments on OMEGA.

The values of OPD for rays passing through the center of a perfect target with respect to parallel rays passing external to the target are given by

$$OPD_1 = 2t(n-1), \tag{1}$$

$$OPD_2 = OPD_3 = 4tn - 2t, \tag{2}$$

$$OPD_2 - OPD_1 = 2tn. \tag{3}$$

For example, for $n = 1.59$ and a wavelength $\lambda = 546$ nm, as used throughout this article, the difference in $(OPD_2 - OPD_1)/t$ between the center and the edge is $\Delta(OPD_2 - OPD_1)/t = 0.62$. (The edge is understood to correspond to 95% of the inner-shell radius, i.e., approaching the last ray that will be transmitted through the target.) Thus, if $N$ bright fringes are counted, $\Delta(OPD_2 - OPD_1) \approx N\lambda$ and

$$t \approx N\lambda/0.62 = 0.88\ N\ \mu m. \tag{4}$$

The accuracy of Eq. (4) is limited by the accuracy with which $\Delta(OPD_2 - OPD_1)$ can be estimated by counting fringes. The method will work as long as the time difference between interfering rays $[(OPD_2 - OPD_1)/c$, where $c$ is the speed of light] is less than the coherence time of the source. For the low-pressure mercury vapor source[4] used in the work reported here, this criterion is satisfied for wall thicknesses $t \leq 15$ $\mu$m.

Ray trajectories have been calculated using both exact ray tracing and a paraxial approximation that includes third-order spherical aberration. The paraxial approximation does not accurately predict the wavefront near the edge of the target, where higher-order spherical aberration is present. However, the error incurred is approximately equal in each of wavefronts 1, 2, and 3. Thus, $\Delta(OPD_2 - OPD_1)$ and $\Delta(OPD_3 - OPD_1)$ are nearly identical for the paraxial and exact ray-tracing treatments, and results obtained by the two methods agree closely.

One notable property of the SIP is its sensitivity to $t$. For $n = 1.59$, the quantity detected is $OPD_2 - OPD_1 = 3.2t$ [from Eq. (3)] compared with $OPD_1 = 1.2t$ [from Eq. (1)] as would apply to conventional two-beam interferometry. This method is thus roughly three times more sensitive to changes in target thickness.

Another property of the SIP is that for very small differences between $t_L$ and $t_R$, the thicknesses on the left and right of the target in Fig. 64.32, respectively, a single interferogram is not formed. For a half-wave difference in the OPD along the

axis, enough to destroy the SIP, the necessary thickness difference is given by

$$2t_L n - 2t_R n = 0.5\ \lambda$$

or

$$t_L - t_R = 0.086\ \mu m, \qquad (5)$$

corresponding to a 1.2% peak-to-valley thickness variation for a typical 7-$\mu$m shell. Targets displaying a distinct SIP have a much better uniformity than this.

Some examples of calculated SIP's are given in Figs. 64.35–64.37. Figure 64.35 shows interferograms of three targets with various wall thicknesses, from which Eq. (4) can be verified. Figure 64.35(b) matches the experimental interferogram of Fig. 64.31 very well. Figure 64.36 shows interferograms of three targets with slightly different wall thicknesses $t$, to show the sensitivity of the SIP to $t$ as alluded to above. The OPD through the center changes by 0.29 waves for each 0.05-$\mu$m change in thickness. Each change is clearly distinguishable, especially if the location of the first or second clear fringe is measured. Finally, Fig. 64.37 shows a combination of two SIP's with a 1% nonuniformity. The nonuniformity is directed along the $z$ direction [Fig. 64.37(a)], at 45° to the $y$ and $z$ directions [Fig. 64.37(b)], and along the $y$ direction [Fig. 64.37(c)]. In each case the heavy and light lines indicate the two SIP's; in each of Fig. 64.37(a) and Fig. 64.37(b) a distinct SIP would not be seen in practice, so that the nonconcentricity would be easily detected. In Fig. 64.37(c), where the defect is aligned perpendicular to the viewing direction, an up-down shift can be observed in the calculated fringe pattern but would probably not be readily observed in practice. In Fig. 64.37(c) the two SIP's add coherently as the two thicknesses $t_L$ and $t_R$ are equal.

Actual target imperfections rarely match the simplified imperfections shown in Fig. 64.37. An example of an imperfect target is shown in Fig. 64.38. The fringes on the bottom are not too different from those of Fig. 64.31, but extra fringes are observed near the top where, clearly, the target contains a region of excessive thickness. There also appears to be some moiré beating in this area between the two SIP's, one of which is stronger because the microscope is focused closer to its plane of localization.

It does not require a large deviation from spherical symmetry for the two SIP's to not combine coherently. When the apparent positions $r_a$ in the object plane of the two rays associated with beam 2 and beam 3 (see Fig. 64.32) differ by the spatial coherence length of the light source imaged onto this plane, coherence is lost. An alternative and more general approach is to consider every incident ray, including rays other

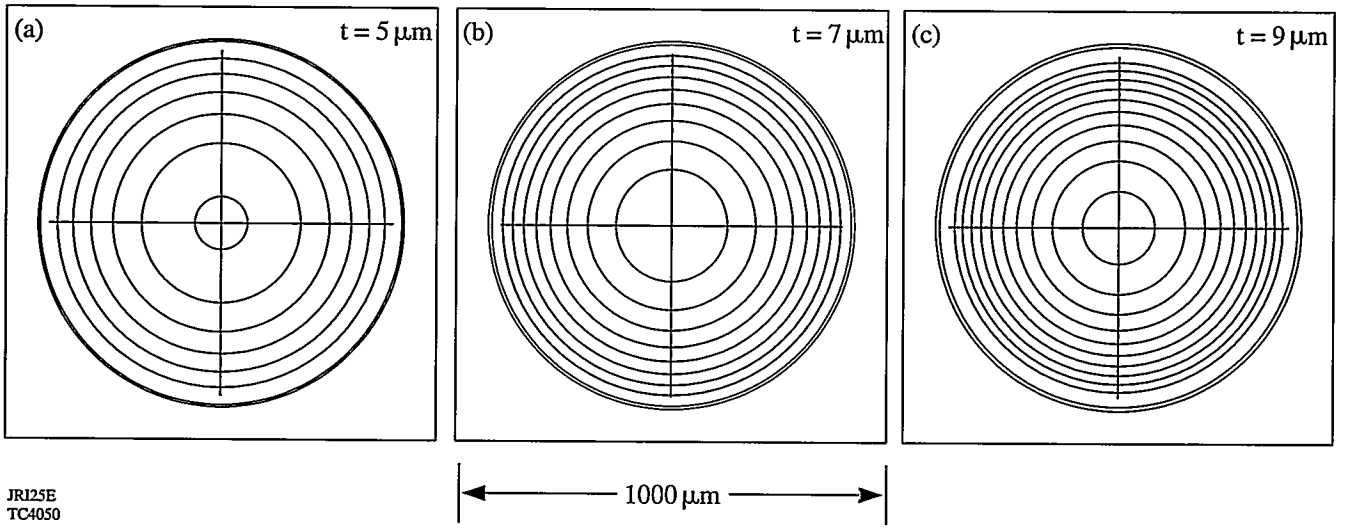


Figure 64.35
Calculated SIP's for three perfectly symmetric polystyrene targets, all with an outer diameter of 850 $\mu$m, but with thicknesses $t$ ranging from 5 to 9 $\mu$m. The outer circles indicate the edge of the target and the other circles are interference fringes. The SIP for $t = 5\ \mu$m corresponds to Fig. 64.33 and that for $t = 7\ \mu$m corresponds to Fig. 64.31. The target thickness in microns can be estimated by multiplying the number of bright fringes by 0.88.

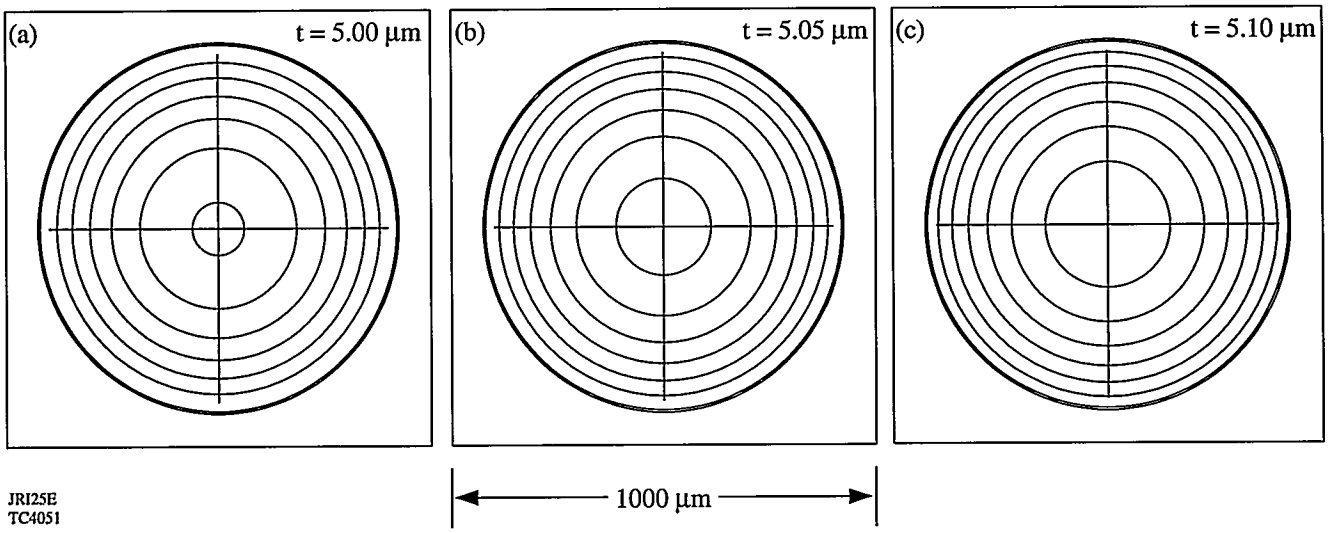


Figure 64.36
Calculated SIP's for three polystyrene targets with slightly different wall thicknesses. Thickness differences as small as 0.05 $\mu$m can be detected if attention is paid to the location of the inner fringes.

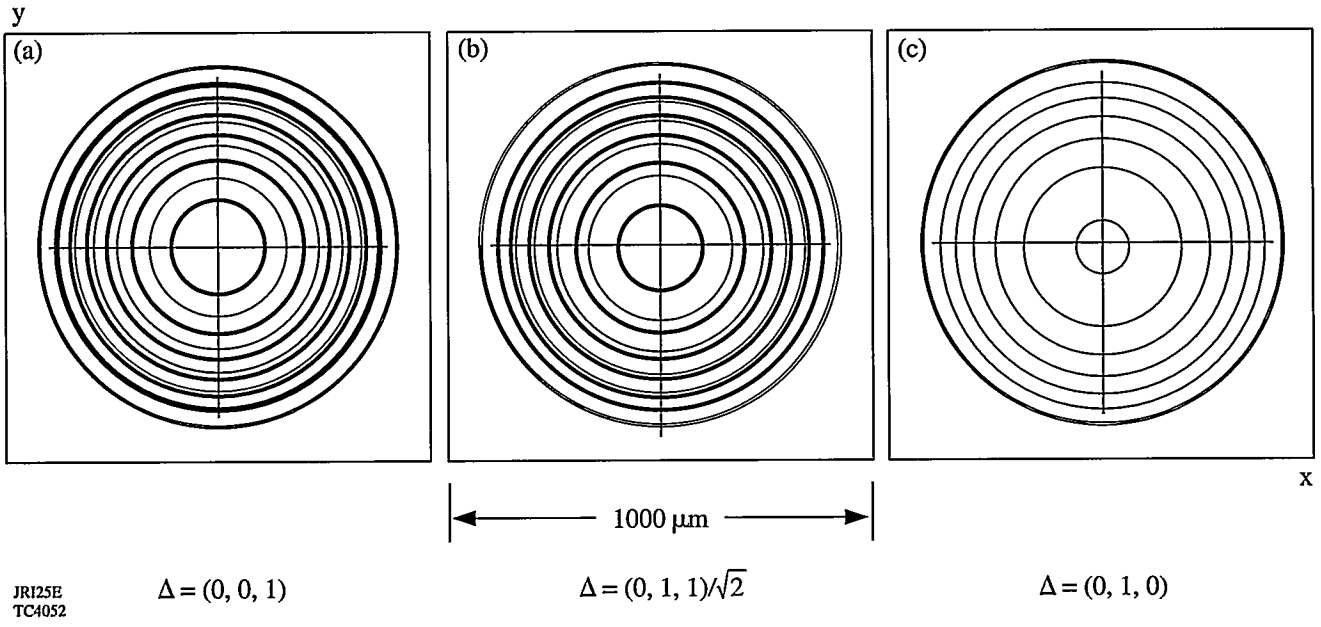


Figure 64.37
Calculated SIP's formed by interference between beams 1 and 2 (light lines) and between beams 1 and 3 (heavy lines) for a polystyrene target with a 1% thickness nonuniformity for three different orientations of the nonuniformity given by the unit vectors $\Delta$. (The inner surface is spherical but shifted 0.05 $\mu$m in the direction of $\Delta$.) In case (a) the two SIP's are out of phase by a half-wave in the center, so that no distinct interference pattern would be seen in practice. Thus, the existence of a distinct SIP indicates a target with better than 0.05-$\mu$m thickness uniformity.

than the parallel set shown in Fig. 64.32, as independent due to the spatially incoherent nature of the source. For each incident ray there are three emerging rays, corresponding to beam paths 1–3. Projecting their trajectories back, there will be a position where rays 1 and 2 cross for an ideal target, and a point of closest approach for a nonideal target. There will be a separate point of closest approach for rays 1 and 3. Constructive interference will occur if the backprojected rays pass sufficiently close to each other. For an ideal target, rays with different angles of incidence will cross in rotated midplanes but may still be close enough to each other in the object plane to interfere. Viewed alternatively, each angle of incidence will result in an interference pattern that appears to be formed within the target with a certain localization depth along the propagation direction; the patterns for different angles then add in intensity. This property of the system makes it unnecessary to illuminate the targets with collimated light and enhances the brightness of the images. It suffices to use a narrow-bandwidth extended source such as a low-pressure mercury-vapor lamp.

From Fig. 64.32, it is evident that the SIP is largely independent of the gas inside the target, whatever its pressure. This is because the interfering rays have a small angle and lateral displacement relative to each other; thus, they traverse almost the same optical path through the gas. This allows the target's wall thickness to be measured, after it is pressurized with fusion fuel, without accurate knowledge of the fill pressure. This is not possible with dual-beam interferometry since the optical path through the target is relative to an equivalent path in air. In this case, the difference between the refractive index of the fill gas and that of the surrounding air must be accounted for and subtracted from the total optical path length through the target to determine its wall thickness.

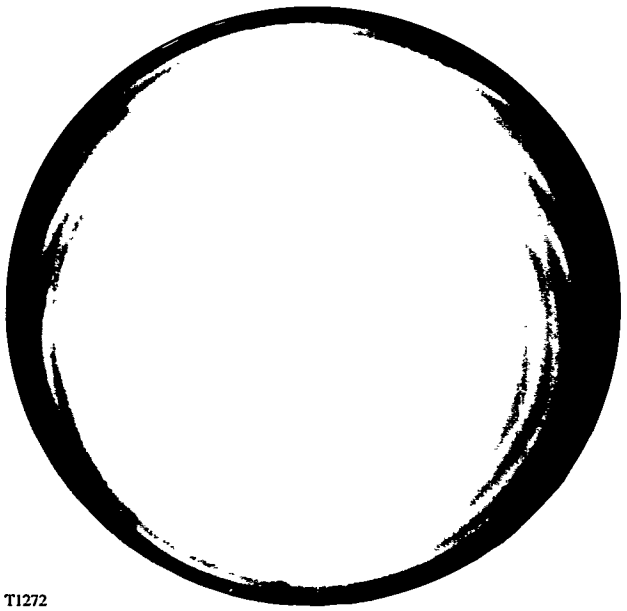

T1272

Figure 64.38
Example of an interference pattern formed from a poor-quality shell. Two SIP's are produced, as in Fig. 64.37, but they are not concentric.

**Fringe Visibility**

Uniform shells possess a relatively high fringe visibility with respect to nonuniform shells since the reflected wavefronts (beams 2 and 3) superpose both in space and phase, thereby interfering constructively to modify the amplitude of the transmitted wavefront (beam 1). Assume electric-field amplitude transmission coefficients $T_1$ and $T_2$ and a reflection coefficient $R$, respectively, at each interface. ($T_1$ and $T_2$ apply to rays passing from air to shell and from shell to air, respectively. Similar coefficients $R_1$ and $R_2$ could be defined, but they are equal in magnitude.) In practice, $T_1$, $T_2$, and $R$ will depend on the angle of incidence at each interface, but the assumption of single values for $T_1$, $T_2$, and $R$ will be good near the target center. For $n = 1.59$, $R=(n-1)/(n+1)=0.228$. Then the amplitudes of transmitted waves 1–3 are given respectively by

$$A_1 = A_0 T_1^2 T_2^2 ,$$

$$A_2 = A_0 T_1^2 T_2^2 R^2 , \tag{6}$$

$$A_3 = A_0 T_1^2 T_2^2 R^2 .$$

For a perfectly symmetric shell, waves 2 and 3 interfere constructively to produce a wave with amplitude

$$A_2 + A_3 = 2A_0 T_1^2 T_2^2 R^2 . \tag{7}$$

Interference between these two waves and the purely transmitted wave 1 gives amplitudes

$$A_1 \pm (A_2 + A_3) = A_0 T_1^2 T_2^2 \left(1 \pm 2R^2\right) \tag{8}$$

with ± indicating constructive (destructive) interference. The

fringe visibility is then

$$V \cong \frac{I_{max} - I_{min}}{I_{max} + I_{min}} = \frac{\left(1+2R^2\right)^2 - \left(1-2R^2\right)^2}{\left(1+2R^2\right)^2 + \left(1-2R^2\right)^2} \quad (9)$$

$$= \frac{4R^2}{1+4R^4}, \quad (10)$$

where $I_{max}$ and $I_{min}$ denote maximum and minimum intensities. Without waves 2 and 3 combining, Eq. (8) would be replaced by

$$A_1 \pm A_2 = A_0 T_1^2 T_2^2 \left(1 \pm R^2\right) \quad (11)$$

for interference between waves 1 and 2, with

$$V' = \frac{2R^2}{1+R^4}. \quad (12)$$

Thus, the visibility is greater by about a factor of 2 when waves 2 and 3 constructively interfere. For example, for $n = 1.59$, $R = (n-1)/(n+1) = 0.228$, $V = 0.206$, and $V' = 0.104$.

### Experimental Verification

The wall thicknesses of several glass shells were measured using dual-beam interferometry with an uncertainty of ±0.05 μm. Their outside diameters were also determined using a calibrated compound microscope to within ±3 μm. The refractive index of the glass shells was measured by fracturing shells from the same glass batch, immersing them in index-matching fluid, and varying the fluid temperature until the glass shards could not be differentiated from the fluid.[5] This method utilizes the temperature dependence of the refractive index of the index-matching fluid and results in a very sensitive refractive-index measurement with an uncertainty as low as ±0.0002. The shells were then imaged with the same compound microscope used to measure their outside diameter, but with a 10-nm-bandwidth interference filter centered on a 546-nm wavelength placed between its diffuser and condenser; this time the diameters of the SIP fringes were measured.

A comparison between the measured SIP fringe diameters and the calculated ones for a specific shell of thickness 2.89±0.05 μm is given in Table 64.III. Calculated fringe diameters are given for 2.89 μm and 2.93 μm. The latter thickness, well within the uncertainty of the thickness measurement, gives the better agreement between the measured and calculated SIP fringe diameters.

The SIP fringe diameters (when normalized to the shell diameter) are much less sensitive to small errors in the outside diameter than in the wall thickness because the universal curves of Fig. 64.34 depend primarily on the ratio $r_i/R_{shell}$. As noted above, the SIP is more sensitive to wall thickness variations than the dual-beam interferogram of the same target. In particular, the positions of the SIP innermost fringes provide information not so readily available from dual-beam interferometry because of the problem of establishing the piston, i.e., the absolute value of the optical path through the target center.

Table 64.III: A comparison between the calculated and measured SIP fringe diameters for a glass ($n$ = 1.4648±0.003) shell with a 255±3-μm outside diameter illuminated with 546-nm light with a 10-nm bandwidth. The measured wall thickness of 2.89±0.05 μm was obtained using a Mach-Zehnder interference microscope. The SIP fringe diameters were measured with a calibrated eyepiece reticule while viewing the shell through a compound microscope. A wall thickness of 2.93 μm gave the best agreement between the calculated and measured SIP fringe diameters and is within the uncertainty of the wall thickness measurement. (The outermost predicted fringe was not observed in the measured SIP.)

| Calculated fringe diameters (μm) | | Measured fringe diameters (μm) |
|---|---|---|
| $t$ = 2.89 μm | $t$ = 2.93 μm | |
| 94 | 110 | 112±5 |
| 160 | 168 | 167±3 |
| 202 | 210 | 206±3 |
| 238 | 242 | |

## Conclusions

The SIP fringe technique is now routinely used to preselect targets based on their wall thickness and nonconcentricity prior to high-precision interferometric characterization. This technique requires only a compound microscope with a narrow-bandwidth interference filter or a stereo microscope and a diffuse mercury-vapor illumination source. The wall thickness is determined to within ±0.5 $\mu$m by counting the number of fringes in the SIP, independent of the outside diameter, and the thickness uniformity is verified to an accuracy better than 0.05 $\mu$m. In addition, the wall thickness of gas-filled targets can be determined to the same accuracy without knowledge of the type of gas or its pressure.

## ACKNOWLEDGMENT

This work was supported by the U.S. Department of Energy Office of Inertial Confinement Fusion under Cooperative Agreement No. DE-FC03-92SF19460, the University of Rochester, and the New York State Energy Research and Development Authority. The support of DOE does not constitute an endorsement by DOE of the views expressed in this article.

## REFERENCES

1. G. M. Halpern *et al.*, J. Appl. Phys. 48, 1223 (1977).
2. R. Q. Gram, M. D. Wittman, C. Immesoete, H. Kim, R. S. Craxton, N. Sampat, S. Swales, G. Pien, J. M. Soures, and H. Kong, J. Vac. Sci. Technol. A 8, 3319 (1990).
3. M. K. Prasad, K. G. Estabrook, J. A. Harte, R. S. Craxton, R. A. Bosch, Gar. E. Busch, and J. S. Kollin, Phys. Fluids B 4, 1569 (1992).
4. Green Monochromatic Lamp, Edmund Scientific Co., 101 E. Gloucester Pike, Barrington, NJ 08007-1380.
5. R. P. Cargille Laboratories, Inc., Cargille Scientific, Inc., Cedar Grove, NJ 07009.

# Femtosecond Study of the Electronic Structure in Semiconducting Y-Ba-Cu-O

We have carried out femtosecond pump-probe studies of the electronic structure of semiconducting $YBa_2Cu_3O_x$ (YBCO). By separating photoinduced bleaching and free-carrier absorption, we have measured the charge-transfer gap. The recovery after the photoexcitation follows a stretched exponential law with a temperature-independent dispersion factor and a temperature-dependent decay time. At probe energies below 1.9 eV, a drastic decrease in bleaching is observed as a consequence of induced free-carrier absorption within the O-2*p* band, which leads us to the conclusion that the bandwidth of the O-2*p* band is approximately 1.9 eV.

Femtosecond spectroscopy has been a powerful tool in probing the properties of high-temperature superconductors (HTS), including the quasiparticle dynamics,[1-3] coherent phonons,[4,5] the electron-phonon coupling constant,[6–8] and the position of the Fermi level.[9–13] In the normal state of oxygen-rich YBCO with $x > 6.8$, the Fermi smearing model has been widely applied in describing the transient optical response, especially the sign change of the differential reflectivity when the probe is tuned across the Fermi level.[9–13] However, there is no general agreement over the dependence of the signal sign on doping, pump intensity, and temperature.

Recent femtosecond studies on insulating cuprates have observed both photobleaching and induced absorption.[14] The initial subpicosecond decay of the bleaching was assigned to two-magnon emission; however, the origin of the induced absorption below 1.6 eV was not fully understood. It is well accepted that semiconducting YBCO ($x < 6.3$) is a Mott-Hubbard insulator with a charge-transfer (CT) gap between the Cu-3*d* upper Hubbard band (UHB) and the O-2*p* band. Several corresponding band diagrams have been proposed based on Raman,[15] photoconductivity,[16] and photoluminescence[17] studies. Moreover, transient photoconductivity investigation has shown a long lifetime (>10 ns) for photoexcited carriers in insulating YBCO.[18]

In the present study, we explore the mechanisms of the nonequilibrium optical response in oxygen-poor semiconducting YBCO. We observe a stretched exponential recovery of the bleaching signals. We find that photoinduced, free-carrier absorption occurs at probe energies smaller than the bandwidth of the O-2*p* band. The interplay of free-carrier absorption and bleaching results in a significant enhancement of the recovery rate of the signal near the band edge. By investigating the relative contributions of the induced absorption and bleaching, we estimate that the bandwidth of the O-2*p* band is approximately 1.9 eV.

## Experiments

Our experiments were performed on 200-nm-thick epitaxial semiconducting YBCO films, which were deposited on MgO substrates using RF magnetron sputtering. Oxygen depletion was achieved by *in-situ* annealing of as-deposited films in 100 mTorr of Ar. Cryogenic testing of their electronic transport showed a behavior typical for a variable-length hopping.[19] The optical density was obtained using a Perkin-Elmer Lambda-9 spectrometer. The femtosecond response was investigated between room temperature and 12 K using a conventional pump-probe technique. Laser pulses of 120 fs in duration were generated by a colliding-pulse, mode-locked laser and further amplified by a copper vapor laser at an 8.5-kHz repetition rate. While the pump energy was fixed at 2 eV, variable probe energies were obtained from a white-light continuum. Pump and probe beams were cross polarized and focused on the 30-$\mu$m sample surface. With the pump energy of 10 nJ per pulse, the injected carrier density is estimated to be $\sim 10^{20}$ cm$^{-3}$. Lock-in and differential detection techniques were used to enhance the signal-to-noise ratio. Time-resolved transient changes in both reflection and transmission were measured simultaneously so that both the transient absorption ($\Delta\alpha$) and the unperturbed absorption coefficient ($\alpha_0$) could be obtained by a numerical fitting that included Fabry-Perot interferences.[20] The low-temperature measurements were

performed in a continuous-He-flow optical cryostat using 2-eV pump and probe pulses.

## Results and Discussion

Figure 64.39 shows the room-temperature linear absorption spectrum of an oxygen-depleted YBCO ($x \sim 6.0$) film. Two main absorption features near 1.78 and 2.8 eV are clearly resolved. These two peaks are related to the CT transition between the filled Cu-3*d* UHB and the empty O-2*p* band (in the hole picture).[15,16] In addition, a broad bandtail is observed below the fundamental absorption peak near 1.78 eV. Low-temperature photoconductivity studies have indicated that the lowest interband transition occurs at 1.5 eV.[17] Therefore, it can be concluded that all the probe energies (>1.65 eV) used in the present study are greater than the CT gap, and thus bleaching is expected as a result of band filling. Also shown in Fig. 64.39 are the values of $\alpha_0$ (solid dots) obtained from the numerical fitting of the pump-probe data. The good agreement between $\alpha_0$ from pump-probe experiments and the linear absorption curve demonstrates the effectiveness of the fitting program and gives additional confidence in our experimental results.

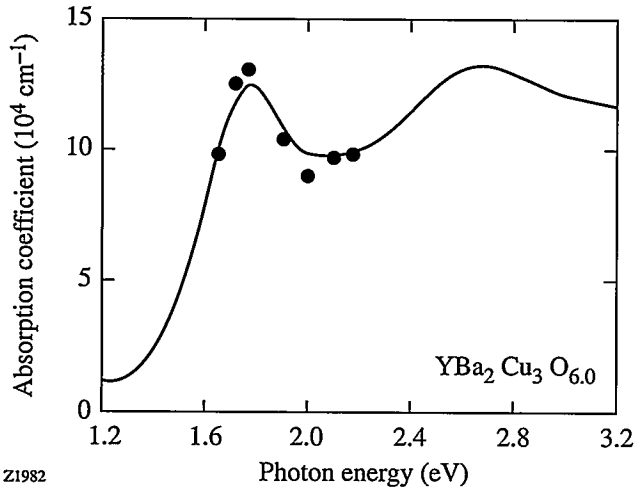


Figure 64.39
Absorption spectrum of semiconducting YBCO at room temperature. The solid dots are the values of linear absorption obtained from the pump-probe data.

Figure 64.40 displays the normalized transient absorption at probe energies from 1.65 eV (750 nm) to 2.1 eV (570 nm). As expected, bleaching ($\Delta\alpha < 0$) is observed at all wavelengths immediately after the excitation. The pulse-width-limited rise of the bleaching is due to the efficient redistribution of photoexcited carriers by carrier-carrier (CC) scattering. As in the case of conventional semiconductors, such as GaAs,[21] CC scattering occurs on a sub-100-fs time scale when the injected density is higher than $10^{19}$ cm$^{-3}$. The redistributed carriers occupy the previously empty states and, hence, block the possible transitions across the CT gap.

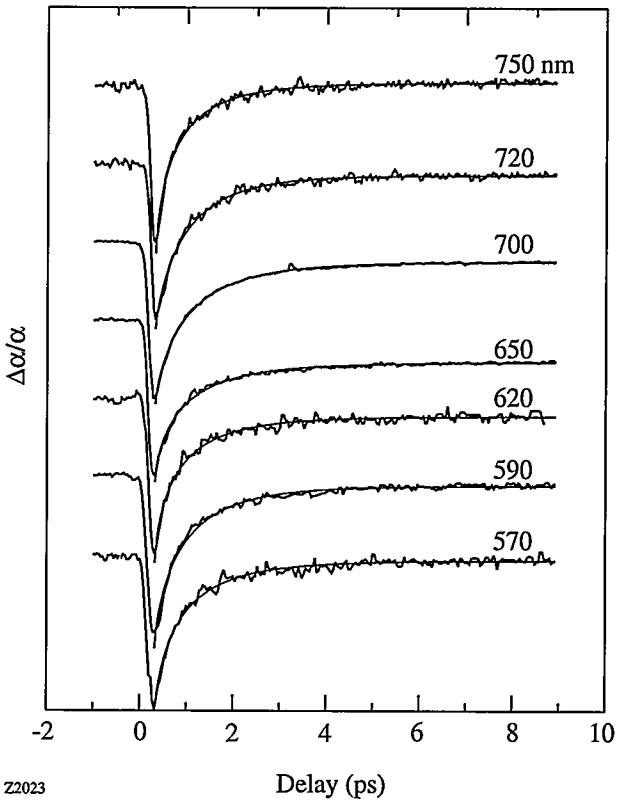


Figure 64.40
Time-resolved differential absorption $(\Delta\alpha/\alpha)$ of semiconducting YBCO at several probe wavelengths. The data are normalized and shifted vertically for clarity. The smooth lines are the fits using a stretched exponential.

The excess energy of the excited carriers is then transferred to the lattice. Since the carrier lifetime (~10 ns) is much longer than our 10-ps sampling window, one would expect carrier accumulation near the band edge prior to recombination. As a consequence, for photon energies near the band edge, the recovery of bleaching should become a slow process. In some cases, the bleaching could even increase with time as the carriers slowly cool down to near room temperature. We observe instead that the recovery is slowest around 1.9 eV (650 nm), rather than near the band edge (1.65 eV or 750 nm). Close to the band edge, the bleaching disappears in a few picoseconds, and the signal becomes positive after 5 ps

(Fig. 64.40), indicating induced absorption. The appearance of induced absorption at 1.65 eV suggests that the excited carriers can be further excited.

The relaxation measured by the recovery of the bleaching follows a stretched exponential and not a simple exponential. The smooth solid lines in Fig. 64.40 are fitted by a normalized stretched exponential plus a constant term, i.e., $-\Delta\alpha/\alpha = \exp\left[-(t/\tau)^{\beta}\right] + C_1$. While the first term models the relaxation of hot carriers, $C_1$ represents the excess heat that escapes by the much slower process of heat diffusion (bolometric process). The fitting provides constant values for $\tau \approx 0.6$ ps and $\beta \approx 0.7$ over the whole spectral range at room temperature. The stretched-exponential decay indicates the coexistence of multiple processes that cannot be represented by a unique time constant.[22,23]

In Fig. 64.41, the transient absorption spectra from Fig. 64.40 are plotted for different time delays. It takes 300 fs to reach the maximum bleaching, consistent with the pulse-width-limited rise time and fast CC scattering. Spectrally, the maximum bleaching is at 1.9 eV, an energy at which there is no peak in the linear absorption. There is also no observable spectral shift of the 1.9-eV peak with time over a 10-ps window. The decay in Fig. 64.41 shows that the slowest recovery occurs near 1.9 eV instead of at the band edge. In fact, at the band edge (1.65 eV) there is even a small increase in absorption after 5 ps, which indicates that, in this case, induced absorption overcomes bleaching. Therefore, the increase of the recovery rate below 1.9 eV results from induced absorption that cancels the bleaching. From the injected density of about $10^{20}$ cm$^{-3}$ and the magnitude of the induced absorption (about 300 cm$^{-1}$), we deduce a transition cross section of $\sim 3 \times 10^{-18}$ cm$^2$. Due to the partial cancellation of the induced absorption by the bleaching, the real transition cross section for free-carrier absorption could be larger than this. Nevertheless, the value of $\sim 3 \times 10^{-18}$ cm$^2$ is consistent with free-carrier absorption involving extended states and is much smaller than dipole-allowed absorption by carriers trapped in localized states. Therefore, the most likely bleaching cancellation process is free-carrier absorption inside the O-2*p* band.

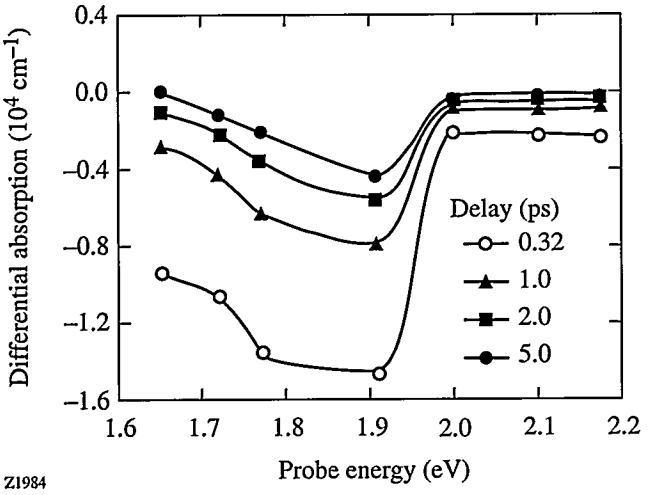


Figure 64.41
Differential absorption spectra at several delay times after the maximum bleaching.

Free-carrier absorption inside the O-2*p* band must depend strongly on the probe energy. At probe energies larger than the bandwidth of the O-2*p* band, no intraband transition is possible and only bleaching exists. Below that threshold energy, however, induced absorption and bleaching coexist and compensate each other. The net result is an increase in the recovery rate of bleaching and eventually induced absorption. Consequently, the fact that the fastest absorption recovery occurs near 1.9 eV corresponds to the threshold for free-carrier absorption and should be related to the bandwidth of the O-2*p* band. For smaller probe energies, the induced absorption becomes progressively stronger than bleaching because more occupied states are available for intraband transitions. As a result, the recovery rate of the differential signal increases drastically toward the lower energies (band edge) and starts to dominate at 1.65 eV (see Fig. 64.41).

Figure 64.42 shows the dependence of the time-resolved differential transmission $\Delta T/T$ on temperature. We note that the recovery of $\Delta T/T$ is faster at lower temperatures. As in Fig. 64.40, the relaxation process can be accurately fitted by a stretched exponential law (the smooth solid lines in Fig. 64.42). Figure 64.43 plots the time constant $\tau$ and the dispersion factor $\beta$ used for the stretched exponential fitting in Fig. 64.42. Unlike in the case of trapping where $\beta = T/T_0$,[22,23] our value of $\beta$ is independent of temperature. Simultaneously, $\tau$ shows a decrease with the temperature decrease, rather than an exponential increase. Therefore, our signals cannot be explained by a distribution of trapping states. The increased decay rate at low temperatures may be related to the emission of acoustic phonons.

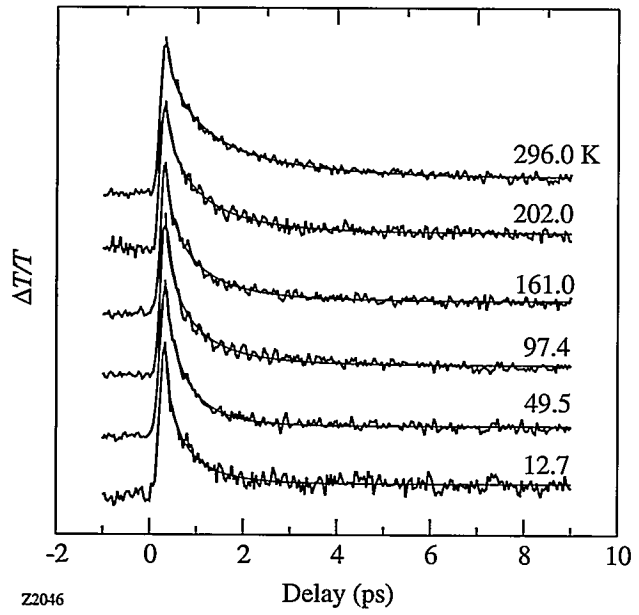


Figure 64.42
Time-resolved differential transmission $(\Delta T/T)$ of semiconducting YBCO at different temperatures. As in Fig. 64.40, the fitting by a stretched exponential is shown as smooth lines.

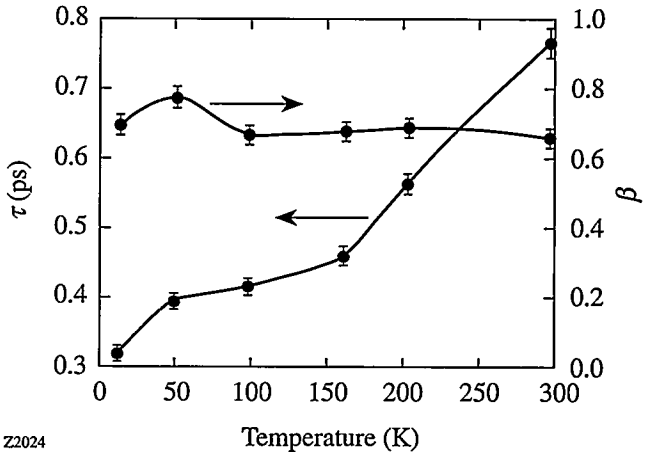


Figure 64.43
Stretched exponential parameters for transient transmission in Fig. 64.42 as a function of temperature. The solid lines are a guide to the eye.

## Conclusions

We have measured the transient optical response of semiconducting YBCO by femtosecond spectroscopy. Using probe pulses of different wavelengths, we have measured the free-carrier absorption within the O-2*p* band and bleaching across the CT gap. The hot carrier dynamics is described precisely by a stretched-exponential law. The temperature-independent dispersion factor ($\beta$) excludes transitions involving the trapping states within the CT gap. For probe energies above 1.9 eV, only bleaching contributes to the transient signals. Below 1.9 eV, photoinduced absorption due to free-carrier absorption inside the O-2*p* band coexists with the bleaching and results in a drastic decrease in the recovery time. Hence, the peak position of the bleaching at 1.9 eV is considered to be a measure of the bandwidth for the O-2*p* band.

## ACKNOWLEDGMENT

This research was supported by the Army Research Office Grant DAAH04-93-G-0211. Additional support was received from the Frank J. Horton Fellowship Program at the Laboratory for Laser Energetics.

## REFERENCES

1. S. G. Han *et al.*, Phys. Rev. Lett. **65**, 2708 (1990).
2. S. G. Han *et al.*, Phys. Rev. Lett. **67**, 1053 (1991).
3. G. L. Eesley *et al.*, Phys. Rev. Lett. **65**, 3445 (1990).
4. J. M. Chwalek *et al.*, Appl. Phys. Lett. **57**, 1696 (1990).
5. W. Albrecht, T. Kruse, and H. Kurz, Phys. Rev. Lett. **69**, 1451 (1992).
6. S. V. Chekalin *et al.*, Phys. Rev. Lett. **67**, 3860 (1991).
7. S. D. Brorson *et al.*, Phys. Rev. Lett. **64**, 2172 (1990).
8. A. L. Dobryakov *et al.*, Opt. Spectrosc. **76**, 871 (1994).
9. A. S. Kazeroonian *et al.*, Solid State Commun. **7**, 95 (1991).
10. D. H. Reitze *et al.*, Phys. Rev. B **46**, 14,309 (1992).
11. T. Gong, L. X. Zheng, W. Xiong, W. Kula, Y. Kostoulas, R. Sobolewski, and P. M. Fauchet, Phys. Rev. B **47**, 14,495 (1993).
12. W. Albrecht *et al.*, Appl. Phys. A, Solids Surf. **A56**, 463 (1993).
13. L. Shi, T. Gong, W. Xiong, X. Weng, Y. Kostoulas, R. Sobolewski, and P. M. Fauchet, Appl. Phys. Lett. **64**, 1150 (1994).

14. K. Matsuda *et al.*, Phys. Rev. B **50**, 4097 (1994).

15. E. T. Heyen, J. Kircher, and M. Cardona, Phys. Rev. B **45**, 3037 (1992).

16. G. Yu *et al.*, Phys. Rev. B **48**, 7545 (1993).

17. V. N. Denisov *et al.*, Phys. Rev. B **48**, 16,714 (1993).

18. G. Yu *et al.*, Solid State Commun. **72**, 345 (1989).

19. R. Sobolewski, W. Xiong, W. Kula, and J. R. Gavaler, Appl. Phys. Lett. **64**, 643 (1994).

20. M. Born and E. Wolf, ed. *Principles of Optics*, 6th ed. (Pergamon Press, Oxford, 1980), p. 630.

21. T. Gong, P. M. Fauchet, J. F. Young, and P. J. Kelly, Phys. Rev. B **44**, 6542 (1991).

22. H. Scher, M. F. Shlesinger, and J. T. Bendler, Phys. Today, 26 (1991).

23. R. A. Street, in *Hydrogenated Amorphous Silicon* (Cambridge University Press, Cambridge, 1991), p. 203.

# Laser Facility Report

This report summarizes activities on the OMEGA laser system from the commissioning shot series of the Key Decision 4 (KD4) campaign to the end of FY95. The KD4 series ended with the final system acceptance tests on 2 May 1995, which demonstrated that the system met and exceeded its performance goals. These results were reported in the previous issue of the LLE Review.[1] Following this campaign, the facility priorities during the third quarter of FY95 shifted to characterization and optimization of the laser and to diagnostic deployment on the target chamber, tasks that supported the experimental campaigns planned for the fourth quarter. Laser characterization included campaigns to collect detailed energy transport data in the OMEGA beamlines, while, in the target bay, many diagnostic systems were activated and the first 10-in.-manipulator (TIM) re-entrant diagnostic shuttle was installed. In addition, a facility improvement program was executed to address many issues that came up during the KD4 campaign.

The fourth quarter of FY95 was the first full quarter of operations on the upgraded OMEGA laser. The first implosion campaign (PP2) and flat-target campaign (S1) were successfully carried out. Results from the implosion campaign are reported in the first article of this issue. The laser system underwent significant improvements, with progress made in particular on the beam-timing, on-target pointing, and focusing systems. Beam-to-beam arrival time differences were measured with photodiodes and an oscilloscope, and all beams were adjusted to match a reference beam to <30 ps. The next-generation beam-timing instrument was tested and will be deployed during the next quarter to reduce beam-timing variations to less than 5 ps. Each target-shot day, pointing targets were shot with 60 beams to measure beam locations by comparing x-ray pinhole-camera images with calculated beam positions.[1] These shots were used to determine which beams needed to be realigned with the UV alignment system. A total of 35 of these pointing shots were taken. In addition, a number of pointing shots were taken for flat targets irradiated during the S1 campaign and also for spherical targets not located at the center of the chamber. Typical pointing results indicated that the rms deviation from the best calculated position was under 20 $\mu$m. Two focus scans were executed this quarter to characterize the UV focus performance. The final focus parameters for each beam were determined to an accuracy of $\pm 100$ $\mu$m, with the results of this study to be published next quarter.

Experimental campaigns this quarter resulted in a total of 150 target shots. This is consistent with plans to deliver 1000 target shots each year. In addition to the active shot campaigns, much work has been completed to prepare for the propagation of SSD laser pulses, separate backlighter sources, and timing-fiducial lasers. The SSD system and the backlighter source are scheduled for activation in the first quarter of FY96.

The shot summary for OMEGA this quarter is as follows:

| | |
|---|---|
| Driver | 187 |
| Beamline | 234 |
| Target | 150 |
| Total | 571 |

REFERENCES

1. Laboratory for Laser Energetics LLE Review 63, NTIS document No. DOE/SF/19460-91, 1995 (unpublished), p. 99.

# NLUF News

### Proposals for FY95

Eight proposals were submitted for consideration for FY95, as summarized in Table 64.IV. Two of them (186 and 188) are from principal investigators who submitted proposals for the first time. The proposals listed in Table 64.IV include three for x-ray spectroscopy measurements and one each for calibration of nuclear detectors, x-ray microscopy of ICF targets, high-resolution imaging, polymer shell characterization, and characterization of the critical surface.

These proposals were considered on 7 March 1995 by the voting members of the NLUF Steering Committee, listed in Table 64.V. The committee members include three from national laboratories, two from universities, and one from industry.

The approved FY95 proposals are listed in Table 64.VI, in order of technical merit as determined by the voting members of the Steering Committee. It is expected that the approved experiments will have OMEGA system time scheduled during calendar year 1996.

Table 64.IV: Proposals submitted for FY95.

| Proposal Number | Principal Investigator | Institution | Title |
|---|---|---|---|
| 186 | Stephen Padalino | State University of New York at Geneseo | Neutron Calibration Studies for MEDUSA |
| 187 | Hans R. Griem | University of Maryland | Spectroscopic Diagnostics on High-Density, Strongly Coupled ICF Plasmas |
| 188 | Qichang Su | Illinois State University | Krypton Spectroscopy Diagnostics of High-Temperature Implosions |
| 189 | Ping-chin Cheng | State University of New York at Buffalo | Development of High-Resolution X-Ray Microtomographic System for Characterizing ICF Targets for the OMEGA Upgrade Experiments |
| 190 | John F. Seely | Naval Research Laboratory | Monochromatic Two-Dimensional Imaging of Laser Targets |
| 191 | Arnold Honig | Syracuse University | New Techniques Applied to Cryogenic Polymer Shells: Emissivity and Accommodation Coefficients, Electron Spin Resonance for Temperature Determination and Levitation, and Nuclear Magnetic Resonance for Composition and Other Diagnostics of Deuterated Plasma Coatings |
| 192 | Katsuhiro Mizuno | University of California, Davis | The Ion Acoustic Decay Instability in the OMEGA Upgrade Laser Plasma—Applications to a Critical Surface Diagnostic, and Instability at Quarter Critical Density |
| 193 | Charles F. Hooper, Jr. | University of Florida | Time-Resolved Plasma Spectroscopy of Imploded Gas-Filled Microballoons: The Next Generation |

The first user experiment on the upgraded OMEGA laser system is the University of Maryland proposal (Number 187), which is expected to begin in January 1996. H. Griem and R. Elton from the University of Maryland have visited LLE to discuss this experiment. They will be mounting an XUV spectrometer on the OMEGA target chamber and are at present designing the mechanical mounts. LLE personnel are assisting them with preparations for this experiment.

**Proposals for FY96**

Nine proposals, summarized in Table 64.VII, have been submitted for consideration for FY96. The proposals include four for x-ray spectroscopy experiments and one each for cryogenic target characterization, nuclear calibration, hohlraum diagnostic development, high-resolution low-energy x-ray imaging of laser irradiation imprinting, and optical imaging of the critical surface. These proposals are presently being reviewed by the Steering Committee.

Table 64.V: Voting members of the NLUF Steering Committee.

| | |
|---|---|
| Dr. John Apruzese | Naval Research Laboratory |
| Dr. Michael J. Boyle | Bondtronix, Inc. |
| Prof. Chandrashekhar J. Joshi | University of California at Los Angeles |
| Dr. Joseph D. Kilkenny | Lawrence Livermore National Laboratory |
| Dr. Richard D. Petrasso | Massachusetts Institute of Technology |
| Dr. Jeffrey P. Quintenz | Sandia National Laboratory |

Table 64.VI: Approved FY95 NLUF proposals.

| Proposal Number | Principal Investigator | Institution |
|---|---|---|
| 192 | Katsuhiro Mizuno | University of California, Davis |
| 193 | Charles F. Hooper, Jr. | University of Florida |
| 188 | Qichang Su | Illinois State University |
| 191 | Arnold Honig | Syracuse University |
| 187 | Hans R. Griem | University of Maryland |

Table 64.VII: Proposals submitted for FY96.

| Proposal Number | Principal Investigator | Institution | Title |
|---|---|---|---|
| 194 | Hans R. Griem | University of Maryland | Electric Field Measurements from Satellites to Forbidden Line Ratios in an OMEGA Upgrade Laser-Produced Plasma |
| 195 | Arnold Honig | Syracuse University | Optical Imaging, Electron Spin Resonance, and Nuclear Magnetic Resonance Applied to Cryogenic Polymer ICF Targets for Low-Temperature Emissivity and Accommodation Coefficient, Levitation, and Quantitative Analysis of Fuel and Target Shell Material |
| 196 | Stephen Padalino | State University of New York at Geneseo | Calibration of Neutron Diagnostics for OMEGA |
| 197 | Joseph J. MacFarlane | University of Wisconsin, Madison | Development of Soft X-Ray Tracer Diagnostics for Hohlraum Experiments |
| 198 | Eugene Clothgiaux | Auburn University | Implementation of Novel X-Ray Polarization Diagnostics for OMEGA Upgrade at the National Laser Users Facility (NLUF) |
| 199 | John F. Seely | Naval Research Laboratory | High-Resolution Imaging of Early-Time Imprinting Using Normal-Incidence Multilayer Mirrors |
| 200 | Qichang Su | Illinois State University | Diagnosis of Core-Shell Mixing with Absorption and Emission Spectra of a Doped Layer |
| 201 | Katsuhiro Mizuno | University of California, Davis | The Ion Acoustic Decay Instability in the OMEGA Upgrade Laser Plasma—Applications to Optical Micrograph Image Diagnostic, and Instability at the Quarter Critical Density |
| 202 | Charles F. Hooper, Jr. | University of Florida | Time-Resolved Plasma Spectroscopy of Imploded Gas-Filled Microballoons: Continuum Lowering and Pusher Dynamics |

# Publications and Conference Presentations

## Publications


M. S. Adams, M. V. Fedorov, V. P. Krainov, and D. D. Meyerhofer, "Comparison of Quasiclassical and Exact Dipole Moments for Bound-Free Transitions in Hydrogen," Phys. Rev. A **52**, 125 (1995).

U. Alon, J. Hecht, D. Ofer, and D. Shvarts, "Power Laws and Similarity of Rayleigh-Taylor and Richtmyer-Meshkov Mixing Fronts at All Density Ratios," Phys. Rev. Lett. **74**, 534 (1995).

S. Augst and D. D. Meyerhofer, "Field Ionization of Noble Gas Atoms with a Keldysh Adiabaticity Parameter of One," Laser Phys. **4**, 1155 (1994).

R. Betti and J. P. Freidberg, "Stability Analysis of Resistive Wall Kink Modes in Rotating Plasmas," Phys. Rev. Lett. **74**, 2949 (1995).

R. Betti, V. Goncharov, R. L. McCrory, E. Turano, and C. P. Verdon, "Multiple Cutoff Wave Numbers of the Ablative Rayleigh-Taylor Instability," Phys. Rev. E. **50**, 3968 (1994).

T. R. Boehly, R. S. Craxton, T. H. Hinterman, P. A. Jaanimagi, J. H. Kelly, T. J. Kessler, R. L. Kremens, S. A. Kumpan, S. A. Letzring, R. L. McCrory, S. F. B. Morse, W. Seka, S. Skupsky, J. M. Soures, and C. P. Verdon, "The Upgrade to the OMEGA Laser System," Fusion Technol. **26**, 722 (1994); also in the *Proceedings of the IAEA Technical Committee Meeting on Drivers for Inertial Confinement Fusion*, Paris, France 14–18 November 1994, edited by J. Coutant (IAEA, 1995), pp. 79–86.

T. R. Boehly, R. S. Craxton, T. H. Hinterman, J. H. Kelly, T. J. Kessler, S. A. Kumpan, S. A. Letzring, R. L. McCrory, S. F. B. Morse, W. Seka, S. Skupsky, J. M. Soures, and C. P. Verdon, "The Upgrade to the OMEGA Laser System," Rev. Sci. Instrum. **66**, 508 (1995).

D. K. Bradley, P. M. Bell, O. L. Landen, J. D. Kilkenny, and J. Oertel, "Development and Characterization of a Pair of 30–40 ps X-Ray Framing Cameras," Rev. Sci. Instrum. **66**, 716 (1995).

X. D. Cao and D. D. Meyerhofer, "All-Optical Switching Via Collisions of Spatial Vector Solitons," Opt. Lett. **19**, 1711 (1994).

X. D. Cao and D. D. Meyerhofer, "Frequency-Domain Interferometer for Measurement of the Polarization Mode Dispersion in Single-Mode Optical Fibers," Opt. Lett. **19**, 1837 (1994).

X. D. Cao, D. D. Meyerhofer, and G. P. Agrawal, "Optimization of Optical Beam Steering in Nonlinear Kerr Media Via Spatial Phase Modulation," J. Opt. Soc. Am. B **11**, 2224 (1994).

X. D. Cao, L. Zheng, and D. D. Meyerhofer, "Measurement of Group-Velocity Walk-Off of Short Pulses in Nonlinear Crystals: A Novel Method," Opt. Lett. **20**, 392 (1995).

S.-H. Chen and S. Krishnamurthy, "Some Fundamental Issues Governing Thermotropic Chiral Nematic Copolymers," Polym. Preprints (Japan) **42**, 122 (1993).

S.-H. Chen, H. Shi, and J. Mastrangelo, "Novel Low Molar Mass Glass-Forming Liquid Crystals: Synthesis, Characterization and Morphological Stability," Polym. Preprints (Japan) **43**, 1674 (1994).

C. Y. Chien, G. Korn, J. S. Coe, J. Squier, G. Mourou, and R. S. Craxton, "Highly Efficient Second-Harmonic Generation of Ultra-Intense Nd:Glass Laser Pulses," Opt. Lett. **20**, 353 (1995).

M. J. Cumbo, D. Fairhurst, S. D. Jacobs, and B. E. Puchebner, "The Effect of Chemically Modulated Surface Charge in the Polishing of Optical Glass," in *Optical Fabrication and Testing Workshop*, Vol. 13, 1994 OSA Technical Digest Series (Optical Society of America, Washington, DC, 1994), pp. 134–137.

M. J. Cumbo, D. Fairhurst, S. D. Jacobs, and B. E. Puchebner, "Slurry Particle Size Evolution during the Polishing of Optical Glass," Appl. Opt. **34**, 3743 (1995).

M. Currie, C.-C. Wang, D. Jacobs-Perkins, R. Sobolewski, and T. Y. Hsiang, "An Optoelectronic Testing System of Rapid, Single-Flux Quantum Circuits," IEEE Trans. Appl. Supercond. **5**, 2849 (1995).

W. R. Donaldson and L. Mu, "Effect of Illumination Uniformity on GaAs Photoconductive Switches," IEEE J. Quantum Electron. **30**, 2866 (1994).

J. D. B. Featherstone, N. A. Barrett-Vespone, D. Fried, Z. Kantorowitz, J. Lofthouse, and W. Seka, "Rational Choice of Laser Conditions for Inhibition of Caries Progression," in *Lasers in Dentistry* (SPIE, Bellingham, WA, 1995), Vol. 2394, pp. 57–67.

D. Fried, R. E. Glena, J. D. B Featherstone, and W. Seka, "Multiple Pulse Irradiation of Dental Hard Tissues at $CO_2$ Laser Wavelengths," in *Lasers in Dentistry* (SPIE, Bellingham, WA, 1995), Vol. 2394, pp. 41–50.

D. Fried, R. E. Glena, J. D. B. Featherstone, and W. Seka, "Nature of Light Scattering in Dental Enamel and Dentin at Visible and Near Infrared Wavelengths," Appl. Opt. **34**, 1278 (1995).

P. D. Funkenbusch, Y. Y. Zhou, C. Lohnes, D. J. Quesnel, S. D. Jacobs, B. E. Puchebner, D. Golini, and A. Lindquist, "Deterministic Microgrinding of Glass with Polycrystalline Diamond Tools," in *Optical Fabrication and Testing Workshop*, Vol. 13, 1994 OSA Technical Digest Series (Optical Society of America, Washington, DC, 1994), pp. 36–39.

W. Gob, W. Lang, W. Kula, and R. Sobolewski, "Transport Properties and Superconducting Fluctuations in Oxygen Deficient Y-Ba-Cu-O Thin Films," Physica C **235–240**, 1535 (1994).

D. Gupta, W. R. Donaldson, and A. M. Kadin, "Energy Extraction from Superconducting Magnets Using Optically Activated YBa2$Cu_3O_{7-x}$ Switches," in *Optically Activated Switching IV*, edited by W. R. Donaldson (SPIE, Bellingham, WA, 1994), Vol. 2343, pp. 128–134.

D. Gupta, W. R. Donaldson, and A. M. Kadin, "Rapid Flux Motion and Critical State Dynamics in a Superconducting Disk," J. Appl. Phys. **78**, 372 (1995).

D. Gupta, W. R. Donaldson, and A. M. Kadin, "Transient Flux Dynamics in Optically Irradiated YBCO Thin-Film Switches," IEEE Trans. Appl. Supercond. **5**, 1371 (1995).

D. A. Haynes, Jr., C. F. Hooper, Jr., R. C. Mancini, D. K. Bradley, J. Delettrez, R. Epstein, and P. A. Jaanimagi, "Spectroscopic Analysis of Ar-Doped Laser-Driven Implosions," Rev. Sci. Instrum. **66**, 755 (1995).

F. A. Hegmann, D. Jacobs-Perkins, S. H. Moffat, C.-C. Wang, R. A. Hughes, M. Currie, P. M. Fauchet, T. Y. Hsiang, J. S. Preston, and R. Sobolewski, "Electro-Optic Sampling of 1.5-ps Photoresponse Signal from $YBa_2Cu_3O_{7-\delta}$ Thin Films," Appl. Phys. Lett. **67**, 285 (1995).

P. A. Jaanimagi, R. C. Elton, B. L. Welch, Y. Leng, and H. R. Griem, "Extending X-Ray Streak Camera Operation to Vacuum Ultraviolet Wavelengths," Rev. Sci. Instrum. **66**, 713 (1995).

S. D. Jacobs, "Finish Polishing of Optics with Magnetic Media," in *International Progress in Precision Engineering*, edited by M. Bonis *et al.* (Elsevier, 1995), pp. 357–360 (invited).

S. D. Jacobs, D. Golini, Y. Hsu, B. E. Puchebner, D. Strafford, W. I. Kordonsky, I. V. Prokhorov, E. Fess, D. Pietrowski, and V. W. Kordonsky, "Magnetorheological Finishing: A Deterministic Process for Optics Manufacturing," in the *International Conference on Optical Fabrication and Testing*, edited by Toshio Kasai (SPIE, Bellingham, WA, 1995), Vol. 2576, pp. 372–382 (invited).

S. D. Jacobs, D. Golini, Y. Hsu, B. E. Puchebner, D. Strafford, W. I. Kordonsky, I. V. Prokhorov, E. Fess, D. Pietrowski, and V. W. Kordonsky, "Magnetorheological Finishing: Toward Cylinders, Toroids, and Aspheric Optics," in *International Progress in Precision Engineering*, edited by M. Bonis *et al.* (Elsevier, 1995), pp. 371–374.

S. D. Jacobs, K. L. Marshall, and A. Schmid, "Liquid Crystals for Laser Applications," in CRC Handbook of Laser Science and Technology, Supplement 2: Optical Materials, edited by M. J. Weber (CRC Press, Boca Raton, FL, 1995), Sec. 14, pp. 509–577.

J. P. Knauer, R. L. Kremens, M. A. Russotto, and S. Tudman, "Using Cosmic Rays to Monitor Large Scintillator Arrays," Rev. Sci. Instrum. **66**, 926 (1995).

W. I. Kordonsky, I. V. Prokhorov, S. D. Jacobs, B. E. Puchebner, Y. Hsu, D. Pietrowski, and D. Stafford, "Glass Polishing Experiments Using Magnetorheological Fluids," in *Optical Fabrication and Testing Workshop,* Vol. 13, 1994 OSA Technical Digest Series (Optical Society of America, Washington, DC, 1994), pp. 107–109.

W. I. Kordonsky, I. V. Prokhorov, B. E Kashevsky, S. D. Jacobs, B. E. Puchebner, Y. Hsu, D. Pietrowski, and D. Stafford, "Basic Properties of Magnetorheological Fluids for Optical Finishing," in *Optical Fabrication and Testing Workshop*, Vol. 13, 1994 OSA Technical Digest Series (Optical Society of America, Washington, DC, 1994), pp. 104–106.

E. M. Korenic and K. L. Marshall, "Blending Polysiloxane 'Glass Resins' to Produce Optical Films with a Specific Refractive Index," Opt. Photonics News (Supplement) **6**(2) (1995).

W. Kula and R. Sobolewski, "Effect of Hydrogen Doping on Electrical Properties of Y-Ba-Cu-O Thin Films," Physica C **235–240**, 587 (1994).

W. Kula, W. Xiong, R. Sobolewski, and J. Talvacchio, "Laser Patterning of $YBa_2Cu_3O_x$ Thin Films Protected by *In-Situ* Grown $SrTiO_3$ Cap Layers," IEEE Trans. Appl. Supercond. **5**, 1177 (1995).

W. Lang, G. Heine, W. Kula, and R. Sobolewski, "Superconducting Fluctuations in $Bi_2Sr_2Ca_2Cu_3O_x$ Thin Films: Paraconductivity, Excess Hall Effect, and Magnetoconductivity," Phys. Rev. B **51,** 9180 (1995).

Y. Lin and T. J. Kessler, "Raman Scattering in Air: Four-Dimensional Analysis," Appl. Opt. **33**, 4781 (1994).

Y. Lin, T. J. Kessler, and G. Lawrence, "Distributed Phase Plates for Supergaussian Focal-Plane Irradiance Profiles," Opt. Lett. **20**, 764 (1995).

F. J. Marshall and Q. Su, "Quantitative Measurements with X-Ray Microscopes in Laser-Fusion Experiments," Rev. Sci. Instrum. **66**, 725 (1995).

J. C. Mastrangelo, T. N. Blanton, and S.-H. Chen, "Crystallization upon Thermal Annealing of a Glass-Forming Liquid Crystal in the Nematic Regime," Appl. Phys. Lett. **66**, 2212 (1995).

J. C. Mastrangelo, H. Shi, S.-H. Chen, and T. N. Blanton, "Design, Synthesis, and Stability of Organic Glasses for Advanced Optical Applications," in *Polymer Preprints* (American Chemical Society, August 1995), Vol. 36(2), pp. 43–44.

R. L. McCrory, "Progress Toward Ignition with Direct-Drive," in *Great Systems in Science and Technology,* edited by J. Horowitz and J. L. Lions (Mason Publishing, Paris, France, 1993), pp. 555–569.

C. J. McKinstrie, R. Betti, R. E. Giacone, T. Kolber, and E. J. Turano, "Two-Dimensional Stimulated Raman Scattering of Short Laser Pulses," Phys Rev. E **51**, 3752 (1995).

C. J. McKinstrie and E. A. Startsev, "Wave Propagation in a Drifting Plasma," Phys. Plasmas **5**, 3234 (1995).

K. Mizuno, R. Bahr, B. S. Bauer, R. S. Craxton, J. S. DeGroot, R. P. Drake, W. Seka, and B. Sleaford, "Direct Measurements of the Ion Acoustic Decay Instability in a Laser-Produced, Large-Scale, Hot Plasma," Phys. Rev. Lett. **73**, 2704 (1994).

C. I. Moore, J. P. Knauer, and D. D. Meyerhofer, "Observation of the Transition from Thomson to Compton Scattering in Multiphoton Interactions with Low-Energy Electrons," Phys. Rev. Lett. **74**, 2439 (1995).

L. Mu, W. R. Donaldson, J. C. Adams, and R. A. Falk, "Electromagnetic Wave Interaction with Laser-Induced Plasmas in GaAs," in *Optically Activated Switching IV*, edited by W. R. Donaldson (SPIE, Bellingham, WA, 1994), Vol. 2343, pp. 107–112.

W. Ng, B. E. Puchebner, and S. D. Jacobs, "Evaluation of Bound Abrasive Media for Fabrication of Ring Tool Polishers," in *Optical Fabrication and Testing Workshop,* Vol. 13, 1994 OSA Technical Digest Series (Optical Society of America, Washington, DC, 1994), pp. 114–116.

J. Peatross and D. D. Meyerhofer, "Angular Distribution of High-Order Harmonics Emitted from Rare Gases at Low Density," Phys. Rev. A **51**, R906 (1995).

B. E. Puchebner, A. Feltz, W. Ng, and S. D. Jacobs, "Coolant Performance in Bound Diamond Ring Tool Grinding of K7 Optical Glass," in *Optical Fabrication and Testing Workshop,* Vol. 13, 1994 OSA Technical Digest Series (Optical Society of America, Washington, DC, 1994), pp. 40–43.

B. E. Puchebner, A. Feltz, and S. Patterson, "The Effect of Additives in a Commercial Coolant on the Glass Grinding Process," in *Optical Fabrication and Testing Workshop,* Vol. 13, 1994 OSA Technical Digest Series (Optical Society of America, Washington, DC, 1994), p. 44.

D. Ress, L. B. DaSilva, R. A. London, J. E. Trebes, R. A. Lerche, and D. K. Bradley, "Novel X-Ray Imaging Methods at the Nova Laser Facility," Rev. Sci. Instrum. **66**, 579 (1995) (invited).

W. Seka, D. Fried, J. D. B. Featherstone, and S. F. Borzillary, "Light Deposition in Dental Hard Tissue and Simulated Thermal Response," J. Dent. Res. **74,** 1086 (1995).

W. Seka, D. Fried, J. D. B. Featherstone, and R. E. Glena, "Time-Dependent Reflection and Surface Temperatures during $CO_2$ Laser Irradiation of Dental Hard Tissues with 100-Microsecond Pulses," in *Proceedings of Lasers in Dentistry* (SPIE, Bellingham, WA, 1995), Vol. 2394, pp. 51–56.

H. Shi and S.-H. Chen, "Novel Glass-Forming Liquid Crystals. II. Systems Containing 1-phenyl-2-(6-cyanonaphth-2-yl) ethyne as a High Optical Birefringence Moiety," Liq. Cryst. **18**, 733 (1995).

H. Shi and S.-H. Chen, "Novel Glassy Nematic and Chiral Nematic Oligomers Derived from 1,3,5-Cyclohexanetricarboxylic and (1R,3S)-(+)-Camphoric Acids," Liq. Cryst. **17**, 413 (1994).

L. Shi, T. Gong, W. Xiong, X. Weng, R. Sobolewski, and P. M. Fauchet, "Femtosecond Optical Spectroscopy of Partially Deoxygenated Y-Ba-Cu-O Thin Films," in *Ultrafast Phenomena IX*, edited by P. F. Barbara, W. H. Knox, G. A. Mourou, and A. H. Zewail, Springer Series in Chemical Physics, Vol. 60 (Springer-Verlag, Berlin, 1994), pp. 327–328.

D. Shvarts, U. Alon, D. Ofer, R. L. McCrory, and C. P. Verdon, "Nonlinear Evolution of Multimode Rayleigh-Taylor Instability in Two and Three Dimensions," Phys. Plasmas **2,** 2465 (1995).

M. D. Skeldon, "Transverse Modulational Instabilities in the Presence of Stimulated Rotational Raman Scattering with a High-Energy Laser," Opt. Lett. **20**, 828 (1995).

M. D. Skeldon, A. Okishev, S. A. Letzring, W. R. Donaldson, K. Green, and W. Seka, "Optically Activated Switches for the Generation of Complex Electrical Waveforms with Multigigahertz Bandwidth," in *Optically Activated Switching IV*, edited by W. R. Donaldson (SPIE, Bellingham, WA, 1994), Vol. 2343, pp. 94–98.

R. Sobolewski and T. Y. Hsiang, "Progress in Ultrafast Superconducting Electronics," in *Superconductivity and Particle Detection*, edited by T. A. Girard, A. Morales, and G. Waysand (World Scientific, Singapore, 1995), pp. 279–289 (invited).

C.-C. Wang, M. Currie, and T. Y. Hsiang, "Ultrafast, Integrable, Optics-Based Interface between Superconducting and Room-Temperature Electronics," IEEE Trans. Appl. Supercond. **5**, 3156 (1995).

C.-C. Wang, M. Currie, D. Jacobs-Perkins, M. J. Feldman, R. Sobolewski, and T. Y. Hsiang, "Optoelectronic Generation and Detection of Single-Flux-Quantum Pulses," Appl. Phys. Lett. **66**, 3325 (1995).

C.-C. Wang, M. Currie, R. Sobolewski, and T. Y. Hsiang, "Subpicosecond Electrical Pulse Generation by Edge Illumination of Silicon and Indium Phosphide Photoconductive Switches," Appl. Phys. Lett. **67**, 79 (1995).

B. Yaakobi, R. Epstein, F. J. Marshall, D. K. Bradley, P. A. Jaanimagi, and Q. Su, "New Diagnostic Features in the Laser Implosion of Argon-Filled Targets," Opt. Commun. **111**, 556 (1994).

B. Yaakobi, R. Epstein, F. J. Marshall, D. K. Bradley, P. A. Jaanimagi, and Q. Su, "New Diagnostic Features in the Laser Implosion of Argon-Filled Targets," Rev. Sci. Instrum. **66**, 728 (1995).

B. Yaakobi, D. Shvarts, F. J. Marshall, R. Epstein, and Q. Su, "Target Imaging and Backlighting Diagnosis," Rev. Sci. Instrum. **66**, 731 (1995).

B. Yaakobi, Q. Su, F. J. Marshall, and R. Epstein, "Monochromatic Backlighting as a Laser-Fusion Diagnostic," J. X-Ray Sci. Technol. **5**, 73 (1995).

M. Yu, G. P. Agrawal, and C. J. McKinstrie, "Effect of Residual Dispersion in the Phase-Conjugation Fiber on Dispersion Compensation in Optical Communication Systems," IEEE Photonics Technol. Lett. **7**, 932 (1995).

M. Yu, G. P. Agrawal, and C. J. McKinstrie, "Pump-Wave Effects on the Propagation of Noisy Signals in Nonlinear Dispersive Media," J. Opt. Soc. Am. B **12**, 1126 (1995).

M. Yu, C. J. McKinstrie, and G. P. Agrawal, "Modulational Instabilities in Dispersion-Flattened Fibers," Phys. Rev. E **52**, 1072 (1995).

L. Zheng and D. D. Meyerhofer, "Cross-Correlation Technique for Single-Shot Measurements of Weak Light Pulses," Opt. Lett. **20**, 407 (1995).

## Conference Presentations

The following presentations were made at the OSA Annual Meeting/ILS-X '94, Dallas, TX, 2–7 October 1994:

W. I. Kordonsky and S. D. Jacobs, "Optical Finishing with Magnetorheological Fluids."

D. D. Meyerhofer, C. Bamber, T. Blalock, S. Boege, T. Kotseroglou, and A. C. Melissinos, "1-Hz, 1-ps, Terawatt, Chirped Pulse Amplification Laser System with a Nd:Glass Slab Amplifier."

C. I. Moore, J. P. Knauer, and D. D. Meyerhofer, "Relativistic Ponderomotive Acceleration of Electrons from a Laser Focus."

J. D. Zuegel and W. Seka, "Direct Measurements of Lower-Level Lifetime in Nd:YLF."

---

S. H. Chen, "Novel Low Molar Mass Glass-Forming Liquid Crystals: Synthesis, Characterization, and Morphological Stability," 43rd Symposium on Macromolecules, Fukuoka, Japan, 12 October 1994.

---

The following presentations were made at the 1994 Applied Superconductivity Conference, Boston, MA, 16–21 October 1994:

M. Currie, C.-C. Wang, D. Jacobs-Perkins, R. Sobolewski, and T. Y. Hsiang, "An Optoelectronic Testing System of Rapid, Single-Flux Quantum Circuits."

D. Gupta, W. R. Donaldson, and A. M. Kadin, "Transient Flux Dynamics in Optically Irradiated YBCO Thin Film Switches."

W. Kula, W. Xiong, R. Sobolewski, and J. Talvacchio, "Laser Patterning of $YBa_2Cu_3O_x$ Thin Films Protected by *in-situ* Grown $SrTiO_3$ Cap Layer."

C.-C. Wang, M. Currie, and T. Y. Hsiang, "Ultrafast, Integrable, Optics-Based Interface between Superconducting and Room-Temperature Electronics."

C.-C. Wang, M. Currie, D. Jacobs-Perkins, L. Shi, and T. Y. Hsiang, "Picosecond Cryogenic Nb/Si/Nb Metal-Semiconductor-Metal (MSM) Photodiode on Superconducting Microstrip Transmission Lines."

W. Xiong, M. Currie, W. Kula, and R. Sobolewski, "Thin-Film YBCO Photodetectors Based on Oxygen-Depleted Structures."

---

The following presentations were made at the XXVI Annual Symposium on Optical Materials for High Power Lasers, Boulder, CO, 24–26 October 1994:

S. S. Papernov and A. W. Schmid, "A Comparison of Laser-Induced Damage Micromorphology in Three Model Thin-Film Systems: $HfO_2$, $Y_2O_3$, and $Ta_2O_5$."

D. J. Smith, J. F. Anzellotti, A. W. Schmid, S. Papernov, Z. R. Chrzan, and S. J. Van Kerkhove, "Damage Fluence at 1054 nm and 351 nm of Coatings Made with Hafnium Oxide Evaporated from Metallic Hafnium."

---

M. D. Wittman, H. Kim, and A. S. Chow, "Determination of the Wall Thickness and Uniformity of Inertial-Fusion Capsules Using the Self-Interference Fringes Produced with Narrow-Bandwidth Illumination," 41st National Symposium of the American Vacuum Society, Denver, CO, 24–28 October 1994.

---

The following presentations were made at LEOS '94 7th Annual Meeting, Boston, MA, 31 October–3 November 1994:

W. R. Donaldson, L. Mu, D. Jacobs-Perkins, and T. Y. Hsiang, "Two-Dimensional Electro-Optic Sampling in GaAs Photoconductive Switches."

Y. Kostoulas, K. B. Ucer, L. Waxer, G. W. Wicks, I. A. Walmsley, and P. M. Fauchet, "Ultrafast Carrier Lifetime in Low-Temperature-Grown GaAs, InP, and InGaP."

---

The following presentations were made at SPIE's International Symposium on Photonic Sensors & Controls for Commercial Applications, Boston, MA, 31 October–4 November 1994:

D. Gupta, W. R. Donaldson, and A. M. Kadin, "Energy Extraction from Superconducting Magnets Using Optically Activated $YBa_2Cu_3O_{7-x}$ Switches."

L. Mu, W. R. Donaldson, J. C. Adams, and R. A. Falk, "Electromagnetic Wave Interaction with Laser-Induced Plasmas in GaAs."

M. D. Skeldon, A. Okishev, S. A. Letzring, W. R. Donaldson, K. Green, and W. Seka, "Optically Activated Switches for the Generation of Complex Electrical Waveforms with Multigigahertz Bandwidth."

---

The following presentations were made at the 36th Annual Meeting, APS Division of Plasma Physics, Minneapolis, MN, 7–11 November 1994:

R. Betti, H. L. Berk, and J. P. Freidberg, "Theory of the Beta-Induced Alfven Eigenmode."

R. Betti and J. P. Freidberg, "The Effect of Plasma Rotation on the Resistive Wall Mode."

T. R. Boehly, R. S. Craxton, P. A. Jaanimagi, J. H. Kelly, T. J. Kessler, R. L. Kremens, S. A. Kumpan, S. A. Letzring, R. L. McCrory, S. F. B. Morse, W. Seka, S. Skupsky, J. M. Soures, M. D. Tracy, and C. P. Verdon, "Initial Performance Results from the Upgraded OMEGA Laser."

A. V. Chirokikh, W. Seka, R. E. Bahr, R. S. Craxton, R. W. Short, A. Simon, and M. D. Skeldon, "Observations and Simulation of Stimulated Brillouin Scattering in Long-Scale-Length Laser Plasmas."

R. S. Craxton, M. Dunne, and O. Willi, "Competition between Target Self-Emission and Soft X-Ray Backlighting."

S. Cremer, J. P. Knauer, R. L. Kremens, M. A. Russotto, D. Shvarts, S. Skupsky, and C. P. Verdon, "Relation of Primary- to Secondary-Reaction Products to the Final Core Parameters of Pure Deuterium Targets in Laser Fusion Experiments."

J. A. Delettrez, D. K. Bradley, and C. P. Verdon, "A Mix Model in *LILAC* for the Linear and Weakly Nonlinear Regimes of the Rayleigh-Taylor Instability."

E. M. Epperlein and R. W. Short, "Nonlocal Electron Transport in the Presence of High-Intensity Laser Irradiation."

R. Epstein, J. A. Delettrez, C. P. Verdon, D. Shvarts, and B. Yaakobi, "Simulations of Spectral Signatures and Images of Core-Shell Mixing in Laser-Driven Implosions."

R. E. Giacone, C. J. McKinstrie, T. Kolber, and R. Betti, "Two-Dimensional Stimulated Brillouin Scattering."

V. Goncharov, R. Betti, R. L. McCrory, and C. P. Verdon, "The Effect of Thermal Conduction on the Ablative Rayleigh-Taylor Instability."

J. P. Knauer, P. W. McKenty, C. P. Verdon, S. G. Glendinning, S. V. Weber, D. M. Pennington, and R. J. Wallace, "Growth of Low-Amplitude Mass Perturbations due to the Rayleigh-Taylor Instability."

T. Kolber, C. J. McKinstrie, R. Betti, and R. E. Giacone, "The Effects of Realistic Geometry on Two-Dimensional Stimulated Brillouin Scattering."

R. L. Kremens, M. A. Russotto, and S. Tudman, "Simulation of 'Saturated' Operation of the MEDUSA Neutron Detector Array."

J. S. Li, C. J. McKinstrie, C. Joshi, and K. Marsh, "Thermal Filamentation of Counterpropagating Laser Beams."

F. J. Marshall, A. Hauer, J. Oertel, and R. Watt, "Monochromatic X-Ray Imaging of Laser-Fusion Targets."

C. J. McKinstrie, R. Betti, R. E. Giacone, and T. Kolber, "Stimulated Raman Scattering of Short Pulse Lasers."

W. Seka, A. V. Chirokikh, R. S. Craxton, R. E. Bahr, C. Labaune, H. A. Baldis, N. Renard, E. Schifano, A. Michard, S. Baton, B. Bauer, K. Baker, R. P. Drake, and K. Estabrook, "Stimulated Brillouin Scattering in Long-Scale-Length, Preformed Plasmas at 1 $\mu$m: Experiments and Simulations."

R. W. Short, "Smoothing of Speckle Irradiation Patterns by Temporal Evolution of the Target Corona."

D. Shvarts, U. Alon, D. Ofer, J. Hecht, R. L. McCrory, and C. P. Verdon, "Nonlinear Evolution of Multi-Mode Rayleigh-Taylor and Richtmyer-Meshkov Instabilities in Two and Three Dimensions."

A. Simon and R. W. Short, "Parametric Instability of Bernstein and Fluid Modes in Laser-Produced Plasma."

E. J. Turano, C. J. McKinstrie, and W. L. Kruer, "Relativistic Saturation of Forward Stimulated Raman Scattering."

---

T. R. Boehly, R. S. Craxton, T. H. Hinterman, P. A. Jaanimagi, R. L. Keck, J. H. Kelly, T. J. Kessler, R. L. Kremens, S. A. Kumpan, S. A. Letzring, R. L. McCrory, S. F. B. Morse, W. Seka, S. Skupsky, J. M. Soures, and C. P. Verdon, "The Upgrade to the OMEGA Laser System," IAEA, Paris, France, 14–18 November 1994.

---

A. Okishev, M. D. Skeldon, S. A. Letzring, W. Seka, and I. Will, "Nd:YLF Regenerative Amplifier for Pulse Shaping System of the 30-kJ (40-TW) UV OMEGA Laser System," OSA Topical Meeting: Advanced Solid-State Lasers, Memphis, TN, 30 January–2 February 1995.

---

The following presentations were made at the SPIE Conference–Biomedical Optics Conference '95, San Jose, CA, 5–10 February 1995:

J. D. B. Featherstone, N. A. Barrett-Vespone, D. Fried, Z. Kantorowitz, J. Lofthouse, and W. Seka, "Rational Choice of Laser Conditions for Inhibition of Caries Progression."

D. Fried, R. E. Glena, J. D. B Featherstone, and W. Seka, "Multiple Pulse Irradiation of Dental Hard Tissues at $CO_2$ Laser Wavelengths."

W. Seka, D. Fried, J. D. B. Featherstone, and R. E. Glena, "Time-Dependent Reflection and Surface Temperatures during $CO_2$ Laser Irradiation of Dental Hard Tissues with 50–500 $\mu$s Pulses."

---

The following presentations were made at the Tenth Target Fabrication Specialists' Meeting, Taos, NM, 6–10 February 1995:

C. M. Chen, H. Kim, M. Wittman, and S. Letzring, "Design of a Resonant Cavity for Plasma Heating Experiments."

H. Kim, E. L. Alfonso, and S.-H. Chen, "Fabrication of Plastic Shells by an Improved Microencapsulated Technique."

A. Simon, "Parametric Excitation of Electron Bernstein Waves in Laser-Produced Plasma."

E. J. Turano, C. J. McKinstrie, and R. E. Giacone, "Two-Dimensional Stimulated Raman Scattering of Short Laser Pulses."

---

The following presentations were made at the 1st Annual International Conference on Solid-State Lasers for Application to Inertial Confinement Fusion (ICF), Monterey, CA, 30 May–2 June 1995:

K. Green, W. R. Donaldson, R. Sobolewski, M. D. Skeldon, W. Seka, A. Okishev, and S. A. Letzring, "Transient Microwave Bandwidth Measurements of Illuminated Silicon Switches for Optical Pulse-Shape Control of Laser-Fusion Drivers."

J. H. Kelly, T. R. Boehly, J. M. Soures, D. L. Brown, R. Boni, R. S. Craxton, R. L. Keck, T. J. Kessler, R. L. Kremens, S. A. Kumpan, S. A. Letzring, S. J. Loucks, R. L. McCrory, S. F. B. Morse, W. Seka, S. Skupsky, and C. P. Verdon, "The Activation of the Upgraded OMEGA Laser at the University of Rochester."

R. L. McCrory, J. M. Soures, C. P. Verdon, A. Babushkin, T. R. Boehly, D. K. Bradley, R. S. Craxton, J. A. Delettrez, R. Epstein, P. A. Jaanimagi, S. D. Jacobs, R. L. Keck, J. H. Kelly, T. J. Kessler, H. Kim, J. P. Knauer, R. L. Kremens, S. A. Letzring, S. J. Loucks, F. J. Marshall, P. W. McKenty, S. F. B. Morse, A. Okishev, W. Seka, R. W. Short, M. D. Skeldon, S. Skupsky, and B. Yaakobi, "OMEGA Upgrade Laser System" (invited).

M. D. Skeldon, A. Okishev, A. Babushkin, and W. Seka, "Transient Stimulated Brillouin Scattering Pulse Compression for Photoconductive Switch Activation."

---

S. D. Jacobs, D. Golini, Y. Hsu, B. E. Puchebner, D. Strafford, W. I. Kordonsky, I. V. Prokhorov, E. Fess, D. Pietrowski, and V. W. Kordonsky, "Magnetorheological Finishing: A Deterministic Process for Optics Manufacturing," SPIE Japan Chapter International Joint Conference on Optical Fabrication and Testing and Applications of Optical Holography, Tokyo, Japan, 5-7 June 1995 (invited).

---

The following presentations were made at the Optical Interference Coatings Topical Meeting, Tucson, AZ, 5–9 June 1995:

J. F. Anzellotti, D. J. Smith, and Z. R. Chrzan, "The Improvement of Evaporated Dielectric Polarizer and Beam Splitter Coatings through the Use of Multiple Crystal Monitoring."

A. L. Rigatti, D. J. Smith, L. D. Lund, P. Glenn, and J. Glenn, "Characterization of Surface Particulate on Large Optics for Laser Fusion."

R. J. Sczupak and D. J. Smith, "A Single-Pass Laser Reflectometer: Conceptual Goals and Physical Results."

A. R. Staley and D. J. Smith, "Applications and Processes for High-Damage-Threshold Sol-Gel Coatings."

S. J. VanKerkhove and D. J. Smith, "Induced Stresses to Optical Substrates Due to High-Energy-Laser HR Thin Film Coatings."

---

The following presentations were made at The 1995 International Workshop on Superconductivity, Maui, HI, 18–21 June 1995:

R. Adam, W. Kula, R. Sobolewski, J. M. Murduck, and C. Patiette-Hall, "Photo-Induced Changes of the Transport Properties in Y-Ba-Cu-O Step-Edge Josephson Junctions."

W. Kula, R. Adam, and R. Sobolewski, "Y-Ba-Cu-O Thin Films with a Controlled, Oxygen In-Depth Profile for Hybrid Superconducting/Semiconducting Device Applications."

W. Kula, W. Xiong, B. McIntyre, R. Sobolewski, D. B. Dukes, and A. D. Caplin, "Characterization of Y-Ba-Cu-O Thin Films Containing Regions of Different Oxygen Content and Superconducting/Semiconducting Interfaces."

---

The following presentations were made at the Laser Optics '95 Conference, St. Petersburg, Russia, 27 June–1 July 1995:

J. H. Kelly, T. R. Boehly, J. M. Soures, D. L. Brown, R. Boni, R. S. Craxton, R. L. Keck, T. J. Kessler, R. Kremens, S. A. Kumpan, S. A. Letzring, S. J. Loucks, R. L. McCrory, S. F. B. Morse, W. Seka, S. Skupsky, and C. P. Verdon, "The Acti-

vation of the Upgraded OMEGA Laser at the University of Rochester."

A. Okishev, M. D. Skeldon, S. A. Letzring, W. R. Donaldson, A. Babushkin, and W. Seka, "Pulse-Shaping System for 60-Beam, 30-kJ (UV) OMEGA Laser."

---

The following presentations were made at the European Conference on Applied Superconductivity, Edinburgh, Scotland, 3–6 July 1995:

W. Kula, R. Adam, and R. Sobolewski, "Y-Ba-Cu-O Thin-Film Structures with a Nonuniform In-Depth Oxygen Concentration Profile."

C.-C. Wang, M. Currie, D. Jacobs-Perkins, R. Sobolewski, T. Y. Hsiang, and M. J Feldman, "Electro-Optic Measurements of Single-Flux Quantum Pulses."

---

The following presentations were made at SPIE's International Symposium on Optical Science, Engineering, and Instrumentation, San Diego, CA, 9–14 July 1995:

C. T. Cotton, "Design Considerations for the OMEGA Upgrade Final Focus Lens."

P. A. Jaanimagi and A. Mens, "Photoelectron Throughput in Streak Tubes."

B. E. Puchebner and S. D. Jacobs, "Development of New Bound Abrasive Polishers for Final Finishing of Optical Glasses."

---

T. Y. Hsiang, S. Alexandrou, R. Sobolewski, and C.-C. Wang, "Terahertz Dispersion of Coplanar Waveguides and Waveguide Bends," Progress in Electromagnetics Research Symposium, Seattle, WA, 24–28 July 1995 (invited).

---

J. C. Mastrangelo, H. Shi, S.-H. Chen, and T. N. Blanton, "Design, Synthesis, and Stability of Organic Glasses for Advanced Optical Applications," American Chemical Society National Meeting, Chicago, IL, 20–24 August 1995.

---

The following presentations were made at the OSA Annual Meeting, Portland, Oregon, 10–15 September 1995:

S. D. Jacobs, "Deterministic Magnetorheological Finishing of Spheres and Aspheres" (invited).

A. Schmid, T. Kessler, K. Marshall, and J. Armstrong, "Organic Thin Films on the 30-kJ OMEGA Glass Laser System Organic Thin Films."

D. J. Smith, "Optical Coating Technology for the Upgraded OMEGA Laser" (invited).

---

H. Kim, S. J. Pan, and P. C. Cheng, "X-Ray Microtomography for Characterizing Inertial Confinement Fusion Spherical Capsules," 13th International Vacuum Congress, 9th International Conference on Solid Surfaces, Yokohama, Japan, 25–29 September 1995.